c.1

LIBRARY
Michigan State
University

2520887

MICHIGAN STATE UNIVERSITY LIBRARIES
3 1293 00585 7200

This is to certify that the

dissertation entitled

Theoretical formulation and experimental investigation of a cylindrical cavity loaded with lossy dielectric materials

presented by

Haw-Hwa Lin

has been accepted towards fulfillment of the requirements for

Doctoral degree in Electrical Engineering

Major professor

Date 11/7/89

MSU is an Affirmative Action/Equal Opportunity Institution

O-12771

PLACE IN RETURN BOX to remove this checkout from your record.
TO AVOID FINES return on or before date due.

DATE DUE	DATE DUE	DATE DUE
MAR 2 6 2004		
JAN 0 5 2007		

MSU Is An Affirmative Action/Equal Opportunity Institution

Theoretical Formulation and Experimental Investigation of a Cylindrical Cavity Loaded with Lossy Dielectric Materials

by

Haw-Hwa Lin

A DISSERTATION

Submitted to
Michigan State University
in partial fulfillment of the requirements
for the degree of

DOCTOR OF PHILOSOPHY

Department of Electrical Engineering and System Science

1989

ABSTRACT

Theoretical Formulation and Experimental Investigation of a Cylindrical Cavity Loaded with Lossy Dielectric Materials

by

Haw-Hwa Lin

This dissertation presents a theoretical and experimental study of a cylindrical microwave cavity loaded with lossy dielectric materials. Theoretically the material-loaded cavity was formulated as a boundary value problem of a coaxially loaded waveguide connected to two homogeneous waveguides each with one end shorted. By means of mode-matching method, a set of homogeneous characteristic equations of the material-loaded cavity were derived. The resonant frequency (resonant length) associated with each cavity mode is then found as the zero of the set of the characteristic equations.

As an essential part of the cavity problem, the propagation characteristics and field patterns of waveguides coaxially loaded with lossy dielectric and isotropic plasma rods were studied numerically for various waveguide modes. These waveguide solutions were used to solve the lossy material rod loaded cavity problem. In particular the cavity-short type configuration was solved numerically yielding cavity resonant lengths, resonant frequencies and cavity Q vs the complex dielectric constant and size of the load for TM_{012}, TE_{011} and HE_{111} modes.

Two different experimental systems were employed in this research work. The first is a low power system, which was designed to characterize the empty and material loaded cavities. The second is a high power system, which was designed for efficient microwave heating of materials. The resonant frequencies, resonant lengths and quality factors measured with the low power system were used to verify theoretical results with materials of nylon and teflon rods, and a quartz tube containing ethylene glycol.

The influence of the graphite fiber orientation in composite epoxy slabs on the cavity electromagnetic field intensities and patterns was also studied with the low power system.

High power heating experiments were conducted to investigate the coupling of electromagnetic energy into lossy dielectric materials, including isotropic and anisotropic materials. Isotropic materials consisted of nylon and wet wood cylinders, and silicon wafers. Anisotropic material included graphite reinforced epoxy slabs. The heating experiments with nylon and wet wood cylinders demonstrated high coupling efficiency and the ability of on-line diagnosis of the complex dielectric constants of the load materials during heating using single-mode cylindrical cavity applicator. Heating uniformity and the factors that affect heating cycles were examined in these heating experiments using only a few watts of input power.

To my parents
Jyne-ming and Yu-ying Lin

and

My wife
Meijung

ACKNOWLEDGEMENTS

The author wishes to thank Dr. Jes Asmussen for his encouragement and guidance during the course of this investigation. Thanks are also extended to Ben Manring and Ron Fritz for their friendship and help with many of the experiments.

The author wishes to express his gratitude to his family for their emotional and financial support. Finally the author wishes to thank his wife, Meijung, for her understanding and encouragement throughout the duration of this work.

This research was supported in part by DARPA (U.S. Army Grant DAAG46-85-k-0006).

TABLE OF CONTENTS

LIST OF TABLES viii

LIST OF FIGURES ix

CHAPTER 1 INTRODUCTION 1

CHAPTER 2 LITERATURE REVIEW 6

2.1 Intorduction 6
2.2 Applications of microwave cavity applicator 7
2.2.1 Permittivity measurements 7
2.2.2 Microwave heating 22
2.2.3 Microwave plasma applications 25
2.3 Method of analyzing coaxially loaded cavity 27
2.3.1 Theoretical formulation 27
2.3.2 Mode designation 38

CHAPTER 3 THEORETICAL DEFINITION OF THE DIELECTRIC-LOADED CYLINDRICAL CAVITY 40

3.1 Introduction 40
3.2 Theoretical formulation of the dielectric-loaded cavity 40
3.3 Review of theoretical formulation of cylindrical waveguide 44
3.3.1 Cylindrical wave potential 44
3.3.2 The homogeneous cylindrical waveguide 48
3.3.3 The coaxially loaded cylindrical waveguide 54
3.4 Derivation of the cavity characteristic equation 70
3.4.1 Cavity-open type 70
3.4.2 Cavity-short type 76
3.4.3 Cavity-image type 79
3.5 Stored energy, absorbed power and quality factor for the dielectric-loaded cavity 82
3.5.1 Introduction 82
3.5.2 Stored energy 82
3.5.3 Absorbed power 87
3.5.4 Quality factor 90

CHAPTER 4 NUMERICAL SOLUTIONS AND TECHNIQUES 91

4.1 Introduction 91
4.2 Numerical technique 92

4.2.1 Muller's method 92
4.2.2 Root-searching algorithm 94
4.3 Numerical solutions 96
4.3.1 Introduction 96
4.3.2 Radial boundary value problem (dielectric-loaded waveguide problem) 96
4.3.3 Axial boundary value problem (dielectric-loaded cavity problem) 186

CHAPTER 5 EXPERIMENTAL SYSTEMS AND TECHNIQUES 235

5.1 Introduction 235
5.2 Experimental cavity design considerations and description 235
5.2.1 Experimental cavity design considerations 235
5.2.2 Experimental cavity description 243
5.3 Experimental systems and circuits 249
5.3.1 Experimental systems 249
5.3.2 Equivalent circuit of a material-loaded cavity applicator 256
5.4 Experimental procedures and techniques 261
5.4.1 Definitions 261
5.4.2 Low power swept-frequency measurements 263
5.4.3 High power single-frequency measurements 267

CHAPTER 6 EXPERIMENTAL RESULTS 272

6.1 Introduction 272
6.2 Low power measurements (verification of theory) 272
6.2.1 Introduction 273
6.2.2 TM_{012} mode 276
6.2.3 HE_{111} mode 278
6.2.4 Discussion 284
6.3 High power heating measurements 289
6.3.1 Heating of nylon 66 cylinders 289
6.3.2 Heating of wet wood cylinders 295
6.3.3 Heating of silicon wafer 299
6.3.4 Low power and high power heating of graphite reinforced epoxy slabs 301
6.3.5 Discussion 313

CHAPTER 7 SUMMARY AND RECOMMENDATIONS 314

7.1 Summary of results 314
7.1.1 Theoretical formulation and numerical analysis 314
7.1.2 Exprimental verificaition of theory and microwave heating of materials 315
7.2 Recommendations 318

7.2.1 Theory 318
7.2.2 Experiments 318

APPENDIX A FORMULAS FOR EVALUATING THE MATRIX ELEMENTS OF EQUATION 3.102 320

APPENDIX B IMPORTANT INTEGRALS USED IN THE ANALYTICAL FORMULATION OF A CYLINDRICAL CAVITY LOADED WITH LOSSY DIELECTRIC MATERIALS 324

REFERENCE 326

LIST OF TABLES

Table 6.1 Comparison between theoretical and experimental results for TM_{012} mode, (a) constant resonant length of 15.5 cm, (b) constant resonant frequency of 2.45 GHz 277

Table 6.2 Comparison between theoretical and experimental results for HE_{111} mode, (a) constant resonant length of 6.94 cm, (b) constant resonant frequency of 2.45 GHz 283

LIST OF FIGURES

Figure 1.1 Side-view of differnet cavity types, (a) cavity-open type, (b) cavity-short type and (c) cavity-image type 3

Figure 2.1 Cylindrical cavity loaded with dielectric rod 9

Figure 2.2 Cylindrical cavity loaded with dielectric disk 11

Figure 2.3 Block diagram of the active system 18

Figure 2.4 Cross-section of a waveguide applicator 24

Figure 2.5 Side-view of a multilayer dielectric resonator 32

Figure 2.6 Geometry of a dielectric resonator 36

Figure 3.1 Dielectric-loaded cavity dimensions 41

Figure 3.2 Coordinate system of the dielectric-loaded cavity 43

Figure 3.3 Cylindrical coordinates for the homogeneous waveguide 49

Figrue 3.4 Coordinate system for a coaxially loaded cylindrical waveguide 55

Figure 3.5 Coordinate system for the cavity-short type 77

Figure 3.6 Coordinate system for the cavity-image type 80

Figure 4.1a ω–β and ω–α diagram for TM_{01} mode, where a=1.27 cm, b=7/62 c, and ε=3.03-j0.39 102

Figure 4.1b ω–β and ω–α diagram for TE_{01} mode, where a=1.27 cm, b=7/62 c, and ε=3.03-j1.0 102

Figure 4.2a ω–β diagram for eight waveguide modes, where b/a=6 and ε=3.03-j0.039 104

Figure 4.2b ω–α diagram for eight waveguide modes, where b/a=6 and ε=3.03–j0.039 105

Figure 4.3a ω–β diagram for eight waveguide modes, where b/a=6 and ε=3.03-j0.39 107

, b/a=6 and $\kappa_0 a$=2.5 146

Figure 4.12f Electric field patterns for TE_{01} mode, where ε=3.03-j10.0
, b/a=6 and $\kappa_0 a$=2.5 147

Figure 4.13 Electric field patterns for TE_{01} mode for various κ0a,
where ε=3.03-j10.0 and b/a=6 149

Figure 4.14a Electric field patterns for TE_{01} mode, where ε=3.03-j0.039
, a=6.35 cm, b=7.62 cm and $\kappa_0 a$=3.26 150

Figure 4.14b Electric field patterns for TE_{01} mode, where ε=3.03-j0.039
, a=2.54 cm, b=7.62 cm and $\kappa_0 a$=3.26 151

Figure 4.14c Electric field patterns for TE_{01} mode, where ε=3.03-j0.039
, a=0.635 cm, b=7.62 cm and $\kappa_0 a$=3.26 152

Figure 4.15a ω–β diagram for HE_{111} mode for various ε", where b/a=6 and
ε'=3.03 154

Figure 4.15b Low frequency portion of the ω–β diagram for HE_{11} mode
shown in Figure 4.15a 155

Figure 4.15c ω–α diagram for HE_{11} mode for various ε", where b/a=6 and
ε'=3.03 156

Figure 4.16a ω–β diagram for HE_{11} mode for various a/b, where
ε=3.03-j0.039 158

Figure 4.16b ω–α diagram for HE_{11} mode for various a/b, where
ε=3.03-j0.039 159

Figure 4.17a Electric field patterns for HE_{11} mode, where ε=3.03-j0.039
, b/a=6 and $\kappa_0 a$=2.0 160

Figure 4.17b Electric field patterns for HE_{11} mode, where ε=3.03-j0.39
, b/a=6 and $\kappa_0 a$=2.0 161

Figure 4.17c Electric field patterns for HE_{11} mode, where ε=3.03-j1.0
, b/a=6 and $\kappa_0 a$=2.0 162

Figure 4.17d Electric field patterns for HE_{11} mode, where ε=3.03-j2.0
, b/a=6 and $\kappa_0 a$=2.0 163

Figure 4.17e Electric field patterns for HE_{11} mode, where ε=3.03-j2.5
, b/a=6 and $\kappa_0 a$=2.0 164

Figure 4.17f Electric field patterns for HE_{11} mode, where ε=3.03-j3.9 , b/a=6 and $\kappa_0 a$=2.0 165

Figure 4.17g Electric field patterns for HE_{11} mode. where ε=3.03-j5.0 , b/a=6 and $\kappa_0 a$=2.0 166

Figure 4.17h Electric field patterns for HE_{11} mode, where ε=3.03-j10.0 , b/a=6 and $\kappa_0 a$=2.0 167

Figure 4.18a Electric field patterns for HE_{11}mode, where ε=3.03-j0.039 , b/a=6 and $\kappa_0 a$=1.8 170

Figure 4.18b Electric field patterns for HE_{11} mode, where ε=3.03-j0.039 , b/a=6 and $\kappa_0 a$=0.65 171

Figure 4.18c Electric field patterns for HE_{11} mode, where ε=3.03-j0.039 , b/a=6 and $\kappa_0 a$=0.26 172

Figure 4.19a Electric field patterns for HE_{11}mode, where ε=3.03-j0.039 , a=6.35 cm, b=7.62 cm and $\kappa_0 a$=3.26 173

Figure 4.19b Electric field patterns for HE_{11}mode, where ε=3.03-j0.039 , a=2.54cm, b=7.62 cm and $\kappa_0 a$=1.3 174

Figure 4.19c Electric field patterns for HE_{11}mode, where ε=3.03-j0.039 , a=0.635 cm, b=7.62 cm and $\kappa_0 a$=0.326 175

Figure 4.20a ω–α and ω–β diagrams for TM_{01} mode waveguide loaded with isotropic plasma rod, where a=1.25 cm, b=4.75 cm, $N=10^{11}$ and ν/ω=0.1 178

Figure 4.20b ω–α and ω–β diagrams for TM_{01} mode waveguide loaded with isotropic plasma rod, where a=1.25 cm, b=4.75 cm, $N=10^{11}$ and ν/ω=1.0 179

Figure 4.20c ω–α and ω–β diagrams for TM_{01} mode waveguide loaded with isotropic plasma rod, where a=1.25 cm, b=4.75 cm, $N=10^{12}$ and ν/ω=0.1 180

Figure 4.20d ω–α and ω–β diagrams for TM_{01} mode waveguide loaded with isotropic plasma rod, where a=1.25 cm, b=4.75 cm, $N=10^{12}$ and ν/ω=1.0 1181

Figure 4.21a ω–α and ω–β diagrams for TM_{01} mode waveguide loaded with isotropic plasma rod, where a=1.25 cm, b=8.89 cm,

$N=10^{11}$ and $\nu/\omega=0.1$ 182

Figure 4.21b $\omega-\alpha$ and $\omega-\beta$ diagrams for TM_{01} mode waveguide loaded with isotropic plasma rod, where a=1.25 cm, b=8.89 cm, $N=10^{11}$ and $\nu/\omega=1.0$ 183

Figure 4.21c $\omega-\alpha$ and $\omega-\beta$ diagrams for TM_{01} mode waveguide loaded with isotropic plasma rod, where a=1.25 cm, b=8.89 cm, $N=10^{12}$ and $\nu/\omega=0.1$ 184

Figure 4.21d $\omega-\alpha$ and $\omega-\beta$ diagrams for TM_{01} mode waveguide loaded with isotropic plasma rod, where a=1.25 cm, b=8.89 cm, $N=10^{12}$ and $\nu/\omega=1.0$ 185

Figure 4.22a Resonant frequency vs. ε' for TM_{012} mode for various ε'', where a=0.635cm, b=7.62 cm and L_s=15.5 cm 187

Figure 4.22b Low dielectric constant portion of Figure 4.22a 188

Figure 4.22c Resonant frequency vs. ε' for TM_{012} mode for various ε'', where a=1.27 cm, b=7.62 cm and L_s=15.5 cm 190

Figure 4.23a Resonant frequency vs. ε' for HE_{111} mode for various ε'', where a=0.635 cm, b=7.62 cm and L_s=6.94 cm 191

Figure 4.23b Resonant frequency vs. ε' for HE_{111} mode for various ε'', where a=1.27 cm, b=7.62 cm and L_s=6.94 cm 192

Figure 4.24a Resonant frequency vs. ε' for TE_{011} mode for various ε'', where a=0.635 cm, b=7.62 cm and L_s=30.8 cm 193

Figure 4.24b Resonant frequency vs. ε' for TE_{011} mode for various ε'', where a=1.27 cm, b=7.62 cm and L_s=30.8 cm 195

Figure 4.25a Resonant frequency vs. ε' for TM_{012} mode for various ε'', where a=0.625 cm, b=8.89 cm and L_s=14.407 cm 196

Figure 4.25b Low dielectric constant portion of Figure 4.25a 197

Figure 4.26 Resonant frequency vs. ε' for HE_{111} mode for various ε'', where a=0.625 cm, b=8.89 cm and L_s=6.69 cm 198

Figure 4.27 Resonant frequency vs. ε' for TE_{011} mode for various ε'', where a=0.635 cm, b=8.89 cm and L_s=11.255 cm 199

Figure 4.28 Resonant frequency vs. a/b for various modes, where b=7.62 cm

and ε=3.03-j0.039 200

Figure 4.29 Resonant frequency vs. a/b for various modes, where b=8,89 cm and ε=3.03-j0.039 201

Figure 4.30a Resonant length vs. ε' for TM_{012} mode for various ε", where a=0.635 cm, b=8.89 cm and f_0=2.45 GHz 203

Figure 4.30b Enlargement of the low ε' portion of Figure 4.30a 204

Figure 4.31 Resonant length vs. a/b for various modes, where b=7.62 cm, ε=3.03-j0.039 and f_0=2.45 GHz 206

Figure 4.32a Q vs. ε' for TM_{012} mode for various ε", where a=0.635 cm, b=7.62 cm and f_0=2.45 GHz 208

Figure 4.32b Q_d vs. ε' for TM_{012} mode for various ε", where a=0.635 cm, b=7.62 cm and f_0=2.45 GHz 209

Figure 4.32c Q_{c1} vs. ε' for TM_{012} mode for various ε", where a=0.635 cm, b=7.62 cm and f_0=2.45 GHz 210

Figure 4.32d Q_{c2} vs. ε' for TM_{012} mode for various ε", where a=0.635 cm, b=7.62 cm and f_0=2.45 GHz 211

Figure 4.33a Q vs. ε' for HE_{111} mode for various ε", where a=0.635 cm, b=7.62 cm and f_0=2.45 GHz 213

Figure 4.33b Q_d vs. ε' for HE_{111} mode for various ε", where a=0.635 cm, b=7.62 cm and f_0=2.45 GHz 214

Figure 4.33c Q_{c1} vs. ε' for HE_{111} mode for various ε", where a=0.635 cm, b=7.62 cm and f_0=2.45 GHz 215

Figure 4.33d Q_{c2} vs. ε' for HE_{111} mode for various ε", where a=0.635 cm, b=7.62 cm and f_0=2.45 GHz 216

Figure 4.34a Q vs. ε' for TE_{011} mode for various ε", where a=0.635 cm, b=7.62 cm and f_0=2.45 GHz 217

Figure 4.34b Q_d vs. ε' for TE_{011} mode for various ε", where a=0.635 cm, b=7.62 cm and f_0=2.45 GHz 218

Figure 4.34c Q_{c1} vs. ε' for TE_{011} mode for various ε", where a=0.635 cm, b=7.62 cm and f_0=2.45 GHz 219

Figure 4.34d Q_{c2} vs. ε' for TE_{011} mode for various ε", where a=0.635 cm,

b=7.62 cm and f_0=2.45 GHz 220

Figure 4.35a Q vs. ε" for various modes, where ε'=3.03, a=0.635 cm, b=7.62 cm and f_0=2.45 GHz 222

Figure 4.35b Q_d vs. ε" for various modes, where ε'=3.03, a=0.635 cm, b=7.62 cm and f_0=2.45 GHz 223

Figure 4.35c Q_{c1} vs. ε" for various modes, where ε'=3.03, a=0.635 cm, b=7.62 cm and f_0=2.45 GHz 224

Figure 4.35d Q_{c2} vs. ε" for various modes, where ε'=3.03, a=0.635 cm, b=7.62 cm and f_0=2.45 GHz 225

Figure 4.36a Enlargement of the small ε" portion of Figure 4.35a 226

Figure 4.36b Enlargement of the small ε" portion of Figure 4.35b 227

Figure 4.36c Enlargement of the small ε" portion of Figure 4.35c 228

Figure 4.36d Enlargement of the small ε" portion of Figure 4.35d 229

Figure 4.37a Q vs. a/b for various modes, where ε=3.03-j0.039, b=7.62 cm and f_0=2.45 GHz 230

Figure 4.37b Q_d vs. a/b for various modes, where ε=3.03-j0.039, b=7.62 cm and f_0=2.45 GHz 231

Figure 4.37c Q_{c1} vs. a/b for various modes, where ε=3.03-j0.039, b=7.62 cm and f_0=2.45 GHz 232

Figure 4.37d Q_{c2} vs. a/b for various modes, where ε=3.03-j0.039, b=7.62 cm and f_0=2.45 GHz 233

Figure 5.1 Transverse electric and magnetic field patterns for various waveguide modes 238

Figure 5.2a Resonant frequncy vs. resonant length for a seven-inch cavity for various cavity modes 239

Figure 5.2b Resonant frequency vs. resonant length for a seven-inch cavity for various cavity modes in the frequency range of 1.6 to 3.2 GHz 240

Figure 5.3a Resonant frequency vs. resonant length for a six-inch cavity for various cavity modes 241

Figure 5.3b	Resonant frequency vs. resonant length for a six-inch cavity for various cavity modes in the frequency range of 1.6 to 3.2 GHz	242
Figure 5.4	Photograph of a seven-inch cavity	244
Figure 5.5	Side-view of a seven-inch cavity with fixed bottom plate	246
Figure 5.6	Side-view of a seven-inch cavity with removable bottom plate	247
Figure 5.7	Photograph of a six-inch cavity	250
Figure 5.8	Cut-away view of a precision six-inch cavity	251
Figure 5.9	Low power swept-frequency mode system diagram	252
Figure 5.10	High power single-frequency mode system diagram	253
Figure 5.11	Equivalent circuit of the material-loaded cavity	257
Figure 5.12	Q measurement using Q-curve	265
Figure 6.1	Configuration of the base plate	274
Figure 6.2	Microcoax probe and base plate dimensions	275
Figure 6.3	Field patterns for 0.635 cm teflon rod, TM_{012} mode, (a) actual magnitude and (b) comparison between theoretical and experimental results	279
Figure 6.4	Field patterns for 0.635 cm nylon rod, TM_{012} mode, (a) actual magnitude and (b) comparison between theoretical and experimental results	280
Figure 6.5	Field patterns for 1.27 cm nylon rod, TM_{012} mode, (a) actual magnitude and (b) comparison between theoretical and experimental results	281
Figure 6.6	Field patterns for 0.2 cm ethylene glycol, TM_{012} mode, (a) actual magnitude and (b) comparison between theoretical and experimental results	282
Figure 6.7	Field patterns for 0.635 cm teflon rod, HE_{111} mode, (a) actual magnitude and (b) comparison between theoretical and experimental results	285

Figure 6.8 Field patterns for 0.635 cm nylon rod, HE_{111} mode, (a) actual magnitude and (b) comparison between theoretical and experimental results 286

Figure 6.9 Field patterns for 1.27 cm nylon rod, HE_{111} mode, (a) actual magnitude and (b) comparison between theoretical and experimental results 287

Figure 6.10 Field patterns for 0.2 cm ethylene glycol, HE_{111} mode, (a) actual magnitude and (b) comparison between theoretical and experimental results 288

Figure 6.11a ε_r' of nylon 66 versus time 291

Figure 6.11b ε_r" of nylon 66 versus time 292

Figure 6.12a ε_r' of nylon 66 versus temperature 293

Figure 6.12b ε_r" of nylon 66 versus temperature 294

Figure 6.13a ε_r' of wet wood versus time 296

Figure 6.13b ε_r" of wet wood versus time 297

Figure 6.13c Coupling efficiency of wet wood heating versus time 298

Figure 6.14 Heating of 3-inch silicon wafer 300

Figure 6.15 Equilibrium temperature versus input power 302

Figure 6.16 Six inch cavity applicator loaded with graphite-epoxy slabe 304

Figure 6.17a Radial electric field versus ϕ at z=2.8 cm for TE^m_{112} mode, graphite-epoxy slab on bottom of cavity 305

Figure 6.17b Radial electric field vs. ϕ at z=4.65 cm for TE^m_{112} mode, graphite-epoxy slab on top of cavity 307

Figure 6.18a Equilibrium temperature vs. temperature probe position for TE^m_{112} mode, graphite-epoxy slab on bottom of cavity 308

Figure 6.18b Equilibrium temperature vs. temperature probe position for TE^m_{211} mode, graphite-epoxy slab on bottom of cavity 309

Figure 6.19a Temperature vs. time for the heating of graphite-epoxy slab

, input power=5W 311

Figure 6.19b Temperature vs. time for the heating of graphite-epoxy slab for power levels of 5 and 10 W, fiber orientation is perpendicular to the coupling prob 312

Chapter 1

INTRODUCTION

The microwave cavity applicator has many current and potential applications in industry and fundamental research, such as permittivity measurements, the heating and curing of epoxy and composite materials, the heating of food, semiconducting and biological materials as well as the use as microwave plasma and ion sources. Accordingly in recent years intense attention has been paid to the design and modeling of the microwave cavity applicator.

The design of a cavity applicator that is capable of coupling electromagnetic energy efficiently into the load is complex because energy transfer is a function of many variables that change as processing takes place. These variables include changes in dielectric properties, dimensions and temperature of the load material, the variations in the dimensions of the cavity applicator and the electromagnetic field patterns. For instance, as the material is heated during processing, the complex dielectric constant, temperature and the dimensions of the load change, which in turn alters the field patterns. Because of these changes, a mismatched, inefficient processing system often results. The energy transfer is also influenced by the operating frequency, the relative position of the load within the applicator and the shape of the load. For efficient energy transfer to load, the factors that influence the energy transfer need to be understood and taken into account in the design of the cavity applicator and some mechanism must be found to compensate for the varying material parameters to keep the material-loaded cavity matched during processing.

Hence it is useful to develop a theoretical model to study the energy transfer mechanism as a function of the parameters mentioned above. Based on the information attained from the model, it may then be possible to design an optimized cavity applicator and efficient and controllable microwave heating systems. The research

presented here is concerned with the development of efficient and controllable microwave applicators and associated heating systems. In particular it focuses on the theoretical modeling of idealized material loaded cylindrical cavities and the associated experimental verification with selected material loads.

This dissertation consists of theoretical and experimental parts. The objective of theoretical part is to develop a model of the cylindrical cavity loaded with lossy materials. From this model, the resonant frequency, resonant length, quality factor and the electromagnetic field patterns are investigated numerically as a function of the complex dielectric constant and size of the load material for a given mode. The objectives of the experimental part are to: (1) verify the theoretical model using selected load materials and resonant modes in the low power experiments, (2) design low power experiments to study the effect of anisotropic materials on the field patterns and (3) design high power heating experiments for efficient heating of rod and slab materials, including regular dielectric materials, semiconducting wafers and composite materials.

The overall layout of this dissertation is as follows. Chapter 2 presents a detailed literature review of the applications of the microwave cavity applicator as well as the methods that have been used to analyze dielectric-loaded cavity. The theoretical formulation of the cavity loaded with lossy dielectric materials is derived in Chapter 3. In general, the loaded cavity is treated as a boundary value problem of a coaxially loaded waveguide connected to two homogeneous waveguides each with one end shorted. The cavity walls are assumed to be perfectly conducting in this formulation. According to the cylindrical load material dimensions and positions in the cavity, three different material loaded cavity types, as shown in Figure 1.1, are classified: (1) cavity-open type, (2) cavity-short type, (3) cavity-image type. The classical EM analysis of the waveguide coaxially loaded with lossy dielectric rod was reviewed [87] and then a transcendental waveguide characteristic equation is derived. By means of

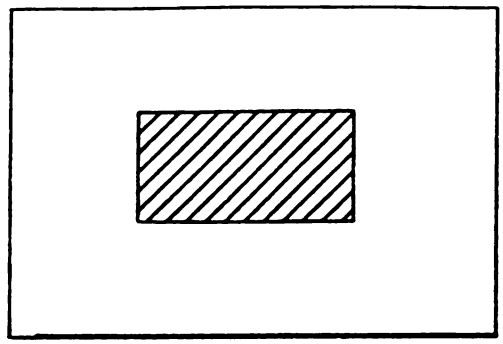

(a) cavity–open type

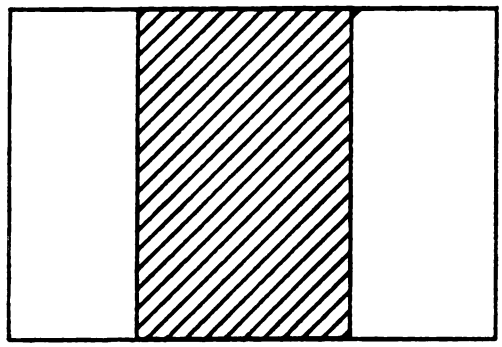

(b) cavity–short type

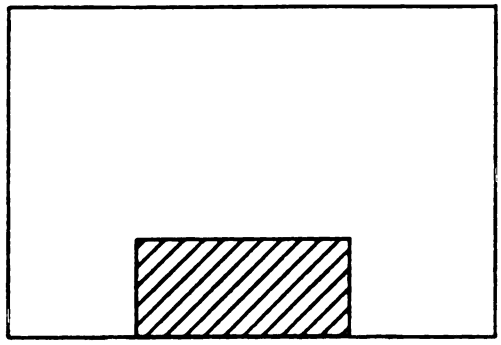

(c) cavity–image type

Figure 1.1 Side-view of different types of material-loaded cavity

mode-matching method, a set of the cavity characteristic equations is derived by enforcing axial boundary conditions of continuous tangential electric and magnetic fields over the waveguide-waveguide interfaces and vanishing tangential electric fields on the conducting walls. Also included in Chapter 3 is the derivation of the stored energy, absorbed power and quality factor of the material loaded cavity. The overall quality factor of the loaded cavity consists the quality factor due to the dielectric losses and the quality factor due to the conducting wall losses. Since in the theoretical model the cavity walls were assumed perfectly conducting, it is necessary to use perturbation method [87] for the calculation of the power absorbed by the conducting walls.

The description of the numerical algorithm and the numerical solutions of the characteristic equations derived in Chapter 3 are presented in Chapter 4. By solving the waveguide characteristic equations the $\omega - \beta$ and $\omega - \alpha$ diagrams are studied for eight waveguide modes, including TM_{0p}, TE_{0p} and hybrid modes. The $\omega - \beta$ and $\omega - \alpha$ characteristics and field patterns for TM_{01}, TE_{01} and HE_{11} modes are examined in detail as a function of the complex dielectric constant and radius of the dielectric material. In addition, a special case of the propagation characteristics of the waveguide loaded with isotropic cold plasma rod is investigated as a function of the electron density, normalized plasma collision frequency (relative to excitation frequency) and cavity radius for TM_{01} mode. Slow-wave and fast-wave regions are identified on the $\omega - \beta$ diagrams. The cavity characteristic equations of the cavity-short type are solved numerically for the resonant frequency and resonant length for TM_{012}, TE_{011} and HE_{111} mode, with the complex dielectric constant and rod radius as the running parameters. In addition, the overall quality factor, the quality factor due to the dielectric losses and the quality factor due to conducting wall losses are also investigated as a function of the complex dielectric constant and rod radius.

The description of experimental cavity applicators, experimental systems and techniques are introduced in Chapter 5. The design considerations of the cavity appli-

cator are discussed and the structures of the seven-inch and six- inch cavities are described briefly. Two experimental systems were employed for the experimental measurements. The first is a low power swept-frequency system used for the characterization of the empty and loaded cavity applicators. The second is the high power single-frequency systems for the microwave heating experiments. An equivalent circuit description of the material loaded cavity applicator is derived. Detailed descriptions of experimental procedures and techniques for the low power and high power experiments are also included.

Chapter 6 presents the results of the low power experiments designed to check the theoretical calculations and the results of the high power heating experiments designed to investigate the microwave heating of solid materials. In the low power verification experiments, load materials included teflon, nylon and ethylene glycol rods. In the high power heating experiments, load materials consisted of nylon and wet wood cylinders, silicon wafers and graphite reinforced epoxy slabs.

A summary of the work presented in the thesis is given in Chapter 7. Recommendations for future research are also included.

Chapter 2

LITERATURE REVIEW

2.1 Introduction

The utilization of microwave energy for the generation of heat was discovered accidently during testing of magnetrons at the Microwave and Power Tube Division of Raytheon in 1950. [1] Since then, microwave heating technology in industry has doubled every ten years. In the late 60's and early 70's microwave energy was used to dry potato chips and paper match books. In the 70's microwave heating were mainly for food processing, rubber processing and a few for the heating of solid materials [1], [2]. For the past ten years, microwave cavity applicator has been used widely for the heating of composite, semiconducting and biological materials, for sealing cartons and for the use as microwave plasma sources. Due to its growing applications in industry, extensive attention has been paid to the design and modeling of microwave cavity applicator.

It was not until 1951 that the first commercial available microwave oven was built as a floor model restaurant unit which led to the microwave home oven in 1960. All of the early industrial and domestic microwave ovens had a multimode resonant structure. The disadvantages of the multimode applicators are inefficiency, no on-line diagnosis and control of the heating processes. Although single mode cavity was utilized for measuring permittivity as early as 1960 [3], applications of single mode microwave applicators for rapid heating of nylon monofilament [2] and generation of plasma were reported in the 70's [4]. Since the advent of single mode applicator, the investigation of the coupling between electromagnetic and material and the development of on-line diagnosis during heating process have been made possible.

Theoretical modeling of material loaded microwave cavity is important for the understanding of electromagnetic/material interaction. Applying the theoretical model

to experiments, material properties during processing then may be diagnosed and precision control mechanism may be achieved. Many rigorous methods of analyzing dielectric loaded resonators have been developed during the last two decades [7], [8], [56] - [79]. Since most of the resonators have been used for such applications as temperature stable oscillators, low noise microwave synthesizers and bandpass filters, dielectrics considered in the modeling are generally low loss and high dielectric constant. In microwave heating, however, materials of various sizes, shapes and dielectric properties are encountered. Complex dielectric constant needs to be taken into account in the modeling. Although modeling approaches are similar, the numerical results of the lossy dielectric cases are quite different from those of the low loss (or lossless) dielectric cases.

In this chapter, applications of the single mode microwave cavity applicators during the past 25 years are reviewed and a literature survey of various methods of analyzing dielectric loaded cavities is presented.

2.2 Applications of microwave cavity applicator

2.2.1 Permittivity measurements

Interest in permittivity measurements at microwave frequencies has grown dramatically in the last few decades in order to characterize the properties of materials. For instance, in semiconductor industry, the permittivity of thin dielectric films has been received considerable attention due to its crucial role in the properties of semiconductor thin films and integrated circuits. The properties of thin biological films are important because their behavior at microwave frequencies is related to microwave biological hazards. Knowledge of the permittivity of industrial materials permits the optimization of the microwave heating process and real time control of the material properties to achieve desirable quality of the products.

Various methods for measuring the permittivity of dielectrics at microwave fre-

quencies have been seen in literature. These methods can be divided into two categories: (1) the transmission line methods and (2) the resonant cavity methods [84]. Since the permittivity measurement using microwave cavity applicator is of major concern in this dissertation, all the papers cited here make use of resonant cavity methods.

Careful study of the literature reveals that the complex dielectric constants of materials are determined either by exact formulation of the material loaded cavity or by cavity perturbation technique. Hence, the resonant cavity measurement techniques are further divided into exact formulation and perturbation technique two groups.

2.2.1.1 Exact formulation

The first tunable cylindrical cavity used for the measurements of the complex dielectric constant of a fairly low loss dielectric rod was demonstrated by J. K. Sinha and J. Brown in 1960 [3]. The cavity was excited at 9.375 GHz in TM_{01} or TE_{01} modes. As shown in Figure 2.1, a rod was placed into the cavity through a hole on the center of the bottom plate of the cavity but did not contact the top plate. The cavity resonant length L was plotted as a function of rod length l within the cavity. The propagation constant in the dielectric was obtained from the mean slope of above curve incorporated with the empty waveguide separation equation. Then, the relative dielectric constant was calculated by solving the characteristic and separation equations of the coaxially loaded waveguide. From the theoretical formulation of Q factor of the material loaded cavity and the Q measurements, the loss tangent was determined. The Q factor was measured by the insertion attenuation of the cavity at resonance. Measurements were made on polystyrene and titaniue dioxide but no comparison with published data was given.

Sinha and Brown failed to point out that one approximation was actually made when calculating the complex dielectric constants. That is, the real part of the dielectric constant was evaluated from the characteristic equation of coaxially loaded waveguide without including any losses.

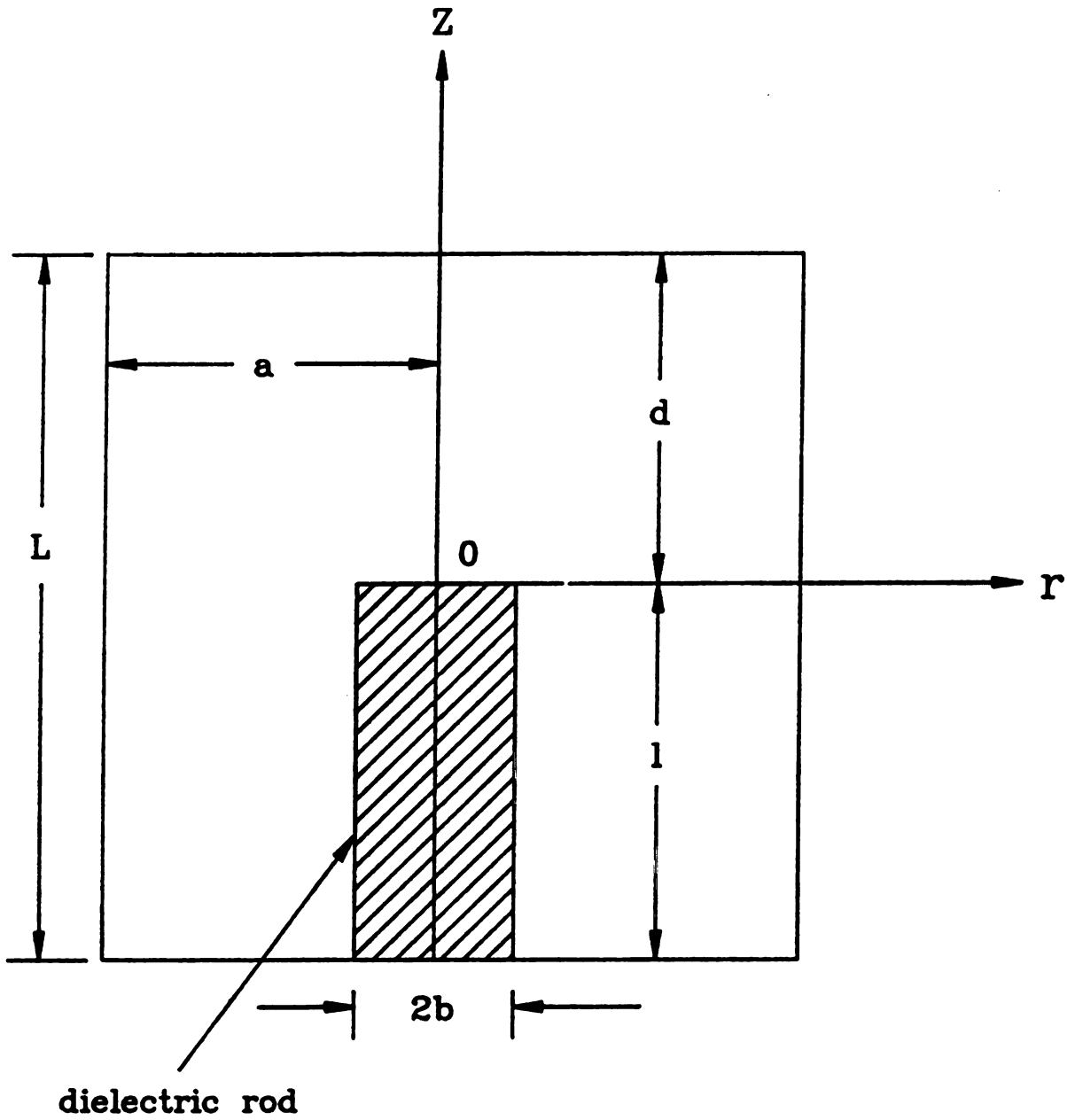

Figure 2.1 Cylindrical cavity loaded with dielectric rod

In 1964, D. T. Paris used a mode matching technique to formulate a slab-loaded TE_{01n} cylindrical cavity [5]. With this model, the complex permittivity of the sample materials was derived. Experiments were conducted using a right-circular cylindrical cavity in TE_{01n} mode. The configuration of the loaded cavity is depicted in Figure 2.2. A disc-shaped dielectric slab of thickness d completely filled the cross section of the cavity. The cavity was kept at resonance by adjusting the plunger position to the resonant length l. Two measurements, resonant frequencies and propagation constants were required to determine the complex dielectric constant. No experimental data was provided. Eight years later, J. Hanfling and L. Botte [6] also measured the dielectric constant of a disk in a cutoff circular waveguide cavity. But relation between the measured cavity resonant frequencies and the dielectric constant was established by means of the transverse-resonance procedure. The cavity was 0.9 inches in diameter and 1.895 inches long. Only real part of the dielectric constant of beryllia was measured and 0.1% accuracy was reported.

The dielectric properties of powder under controlled pressure were first measured by G. Roussy and M. Felden using a TE_{01n} mode cavity [7]. The material under test was contained in a tube of quartz, placed along the axis of the cavity. The lengths of the material and cavity were equal. They solved the loaded cavity problem as a section of a waveguide, loaded with multilayers of materials. Experiments were performed in two resonant modes, TE_{011} and TE_{012} modes, respectively. All the materials tested have dielectric constants less than 8-j0.01. Experimental results were within ±0.3% for the real part and within 0.5% for the imaginary one.

In a manner similar to Roussy and Felden, S. Li, et al. [8] also considered a lossy dielectric rod situated in the center of a cylindrical cavity, filling the whole length of the cavity. The cavity was operated in TM_{010} mode. A dispersion equation was derived by field matching technique, in which field components were expressed in series forms. For the first time in literature the perturbation introduced by the insertion

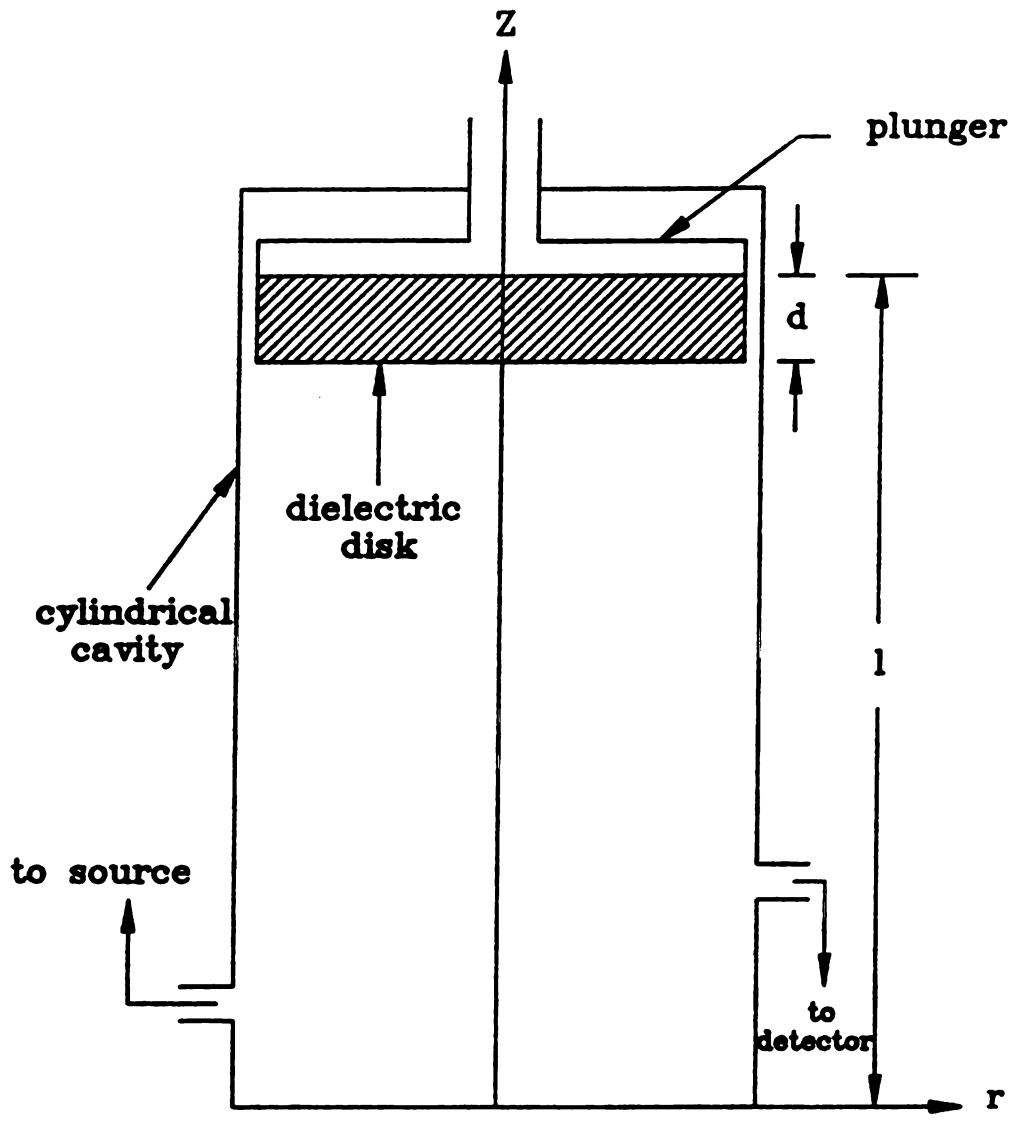

Figure 2.2 Cylindrical cavity loaded with dielectric disk

hole was taken into account in the formulation of the problem. Still, the cavity wall losses were calculated by means of cavity wall perturbation procedures. Measurements of resonant frequencies and cavity quality factors were taken for evaluating ε' and ε''. Reported experimental results show that the real and imaginary parts of the permittivities of various materials could be measured up to 77.4 and 13.1, respectively. The measurement errors arising from the theory and measurement system were less than 1 percent in ε' and 5 percent in ε''.

In 1982, C. B. Roseberg, N. A. Hermiz and R. J. Cook [9] demonstrated a reliable permittivity measurement technique on low-loss liquid. A single crystal quartz disc was fitted in an adjustable cylindrical TE_{01} cavity as a separator between the liquid and air filled regions. The disc was arranged to be half-guide wavelength thick and was positioned an integral number of half-guide wavelengths from the fixed end of the cavity. Resonance condition occurred by adjusting the movable top plated to an integral number of half-guide wavelengths above the separator, i.e., quartz disk. Mode matching technique was used to derived the relationship between the loaded quality factor and loss tangent. As are the cases in most papers, perturbation technique was involved in evaluating the cavity wall losses in order to reduce the complexity of calculation.

The real part of the complex permittivity was calculated from the usual guide wavelength formula with the measurements of the guide wavelength in the liquid filled region. Systematic errors arose from the uncertainties associated with the instruments used, from lack of uniformity of measured parameters over the system (e.g. temperature) and from practical departure from the theoretical model. It was shown that loss tangent could measured to an uncertainty of $\pm 3\times10^{-6}$ and relative permittivity to and uncertainty of ± 0.001. The largest ε' and loss tangent measured were 2.034 and 894×10^{-6}, respectively.

Unlike most experiments described in literature, Farooq [10] used a rectangular

cavity instead of cylindrical one. The dielectric test material was placed on the broad wall of the cavity and completely filled its cross section. Farooq demonstrated that this experiment had the advantage that the change in resonant parameters, i.e. resonant frequencies and cavity quality factors, were enlarged and the measurements of thin low loss material became easier. The derivation of the relationship between quality factor and loss tangent made use of mode matching technique. The range of application was considered best for values of loss factor from 10^{-4} to 10^{-2}. Materials under test were Polymethyl methacrylate and Polystyrene. Experimental results of the loss tangent were in good agreement with those of the published data for these materials.

As can be seen from the experiments described above, the shapes of the samples are either a long rod which is of the same length as that of the cavity, or a disk which completely fills the transverse cross section of the cavity. It is evident that one of the reasons why these sample shapes were chosen is to achieve mathematical simplicity. However, these configurations pose several serious problems. For disk-shaped sample, in many cases it is hard to get large enough samples to fill the cavity cross section, for example, in measurements on single crystals. Small air gaps exist between the sample and cavity walls, even with tight fitting. This gap effect was shown to give erroneous results when materials under test have large ε' and small ε'' [11]. For long rod sample, the sample was placed along the cavity axis parallel to the electric filed. As before, the fit of the sample is critical. For hard, brittle materials, attaining exact fit required is a problem because the ends of the sample rod tend to chip and crack [12]. For both configurations, the cavity must be disassembled for correct positioning of the sample. This leads to difficulties in reproducing the reference Q factor and the resonant frequency corresponding to the empty cavity.

2.2.1.2 Perturbation technique

Cavity perturbation techniques have been widely used to measure the complex dielectric constant ε of materials at microwave frequencies. These measurements are

performed by inserting a small, appropriately shaped sample into a resonant cavity and determining the properties of the sample from the resultant change in the resonant frequency and Q factor.

The basic assumption of the cavity perturbation is that the change in the overall geometrical configuration of the electromagnetic fields upon introduction of the sample must be small [13], [14]. In other words, the percentage change in the resonant frequency must be small. This assumption imposes limitations on the size and dielectric constant of the sample. For materials with large ε' (or large ε''), the size of the sample must be very small compared to that of the cavity in order to have minimal perturbation to the cavity resonance. On the other hand, if the complex dielectric constant of the material is small, the limitation on the ratio between the sizes of the sample to cavity may be relaxed.

According to the methods by which the frequencies of the microwave energy sources are controlled, two different experimental systems using perturbation techniques can be classified. A passive system is a system in which the frequency of the microwave source is constant in either CW or swept modes throughout experiments. The system is referred to as "passive" because the cavity applicator does not contribute to the generation of the microwave signals. An active system is a system in which the cavity resonance determines the frequencies of the microwave sources. Often, the active system is a close-loop circuit and the cavity resonance is tracked by phase-lock loop (PLL) technique. It has been shown that measurement automation can be easily accomplished in active frequency systems.

Passive systems

The earliest treatment of cavity perturbation using TM_{012} mode was conducted by E. F. Labuda and R. C. LeCraw [12]. A thin rod was placed in the center of a resonant cylindrical cavity. The length of the sample was of quarter-guide wavelength of the resonant cavity mode. Quasi-static approximations to the fields inside the

sample were made in the perturbation formula [15]. Reported data shows the accuracy of ε' to within 3% and ε'' to within 0.1%.

In 1971, W. Rueggeberg first showed the application of cavity perturbation to determine the complex dielectric constant of arbitrary dimensioned dielectric modules at microwave frequencies [16]. In his work, the sample under study need not meet the small volume requirement demanded by cavity perturbation. A mathematical relation that describes sample loss tangent was derived by the modification of the perturbation formula. In this modified formula, the derivative of the cavity resonant frequency with respect to dielectric constant of the material of a particular configuration under investigation, i.e. $\frac{df}{d\varepsilon}$, was included and no approximation to the field inside sample was made. Accordingly, there was no limitations on the volume and ε of the sample. A resonant frequency vs dielectric constant curve for a particular sample shape was established experimentally by measuring the resonant frequencies of a set modules with well known dielectric properties. The evaluation of an unknown sample requires the measurements of the resonant frequencies and the Q factors. The dielectric constant and derivative $\frac{df_1}{d\varepsilon}$, evaluated at f_1, are determined graphically. Then, using the modified perturbation formula, the loss tangent is readily determined.

Eldumiati and Haddad [11] showed that a reentrant cavity can be used to measure the conductivity and dielectric constant of a bulk semiconductor material by perturbation technique. In their experiments, a rectangular semiconductor sample was placed on the center of the bottom plate of the cavity, i.e., under the center post of the reentrant cavity. This sample arrangement has the following advantages: (1) the electric field is maximum in this region, which results in greater sample/electromagnetic interaction, and (2) the field is essentially uniform over the sample, provided the skin depth is larger than the sample dimension along the electric field. They demonstrated an revolutionary method that does not require Q factor measurements. The Q factors in

the perturbation formula for calculating ε'' and ε' were replaced by the change of the reflected power and the empty cavity coupling factor. Hence, a knowledge of the empty cavity coupling factor together with the measurements of the reflected power and resonant frequency are adequate for the determination of the complex dielectric constant $\hat{\varepsilon}$. As before, the field inside sample was approximated by quasi-static approximation. The empty cavity coupling factor, the change in reflected power and the resonant frequency shift were measured for the determination of the material complex permittivity.

Maria A. Rzepecka [17] presented a new method of using frequency counter for the determination of a cavity Q-factor instead of frequency markers techniques used by most investigators. She measured the dielectric constant $\hat{\varepsilon}$ of teflon, carbon tetrachloride, amyl alcohol, methyl alcohol, nitrobenzene and water by means of a rectangular cavity in TE_{013} and TE_{019} modes at 2.45 GHz. The Q-factor of the material loaded cavity in perturbation formula was expressed in terms of the empty cavity Q-factor, transmission coefficient for the empty cavity and transmission coefficient for the material loaded cavity. The uncertainties associated with the measured parameters and system instability in evaluating $\hat{\varepsilon}$ was examined in this paper.

A useful in depth literature review of cavity perturbation techniques and errors analysis were performed by Shuh-han Chao [14]. Chao employed the quasi-static approximation to formulate the total induced electric moments in the perturbation formula. He assumed that the electric field applied to the sample was uniform, provided a small sample was placed at the electric field maximum. In the error analysis, an analytical formula for calculating the errors caused by the measurement errors in the resonant frequency and the Q-factor were derived. The errors that have to do with the approximations made in the determination of the electric field inside the sample were not considered. He notes that, due to the conflicting requirements of small sample size for small perturbation error and large sample for small errors in the δf and δQ_0, an

optimum sample size for minimum errors can be found. Experiments were conducted by measuring the permittivity of small spheres in a iris-coupled TE_{103} rectangular cavity. The sample was held in a cylindrical styrofoam sample holder, which was placed at the geometrical center of the cavity. Measurements on the Q-factor and resonant frequency were made at 9.5928 GHz in swept frequency mode.

Active systems

An automatic digital method for measuring the dielectric constant of thin dielectric film using TE_{01n} cylindrical cavity at 9.3 GHz was reported by M. Rzepecka and M. Hamid [18] in 1972. The most significant improvement that they achieved over past investigators is the new Q factor measurement technique they proposed. The Q factor was determined by measuring the phase shift of the envelope of an amplitude modulated microwave signal when this signal was transmitted through a resonant cavity at resonance. The block diagram of the active system is shown in Figure 2.3. As is shown in this figure, the microwave signal was split into two parts. One part was amplitude modulated and passed through the test cavity, the other part went through a phase shifter and an attenuator. These two signals were mixed in the directional coupler and then fed into the detector. The output signal of the detector had a modulation component whose amplitude and phase depended on the difference between the microwave oscillator frequency and the cavity resonant frequency. This signal was compared with a reference signal from the modulation oscillator in a phase detector. The output dc signal from the phase detector, which was a function of the frequency difference mentioned above, was used to control the frequency of the microwave oscillator. This technique made the automation of the experimental system possible. However, the drawback of the phase measurement technique is that the circuitry is much more complex than that using resonant curve methods. The authors analyzed the errors present in the perturbation formula and in the measurements. The accuracy of evaluating ε' and ε'' relies on the accuracy of measuring the film thickness, cavity

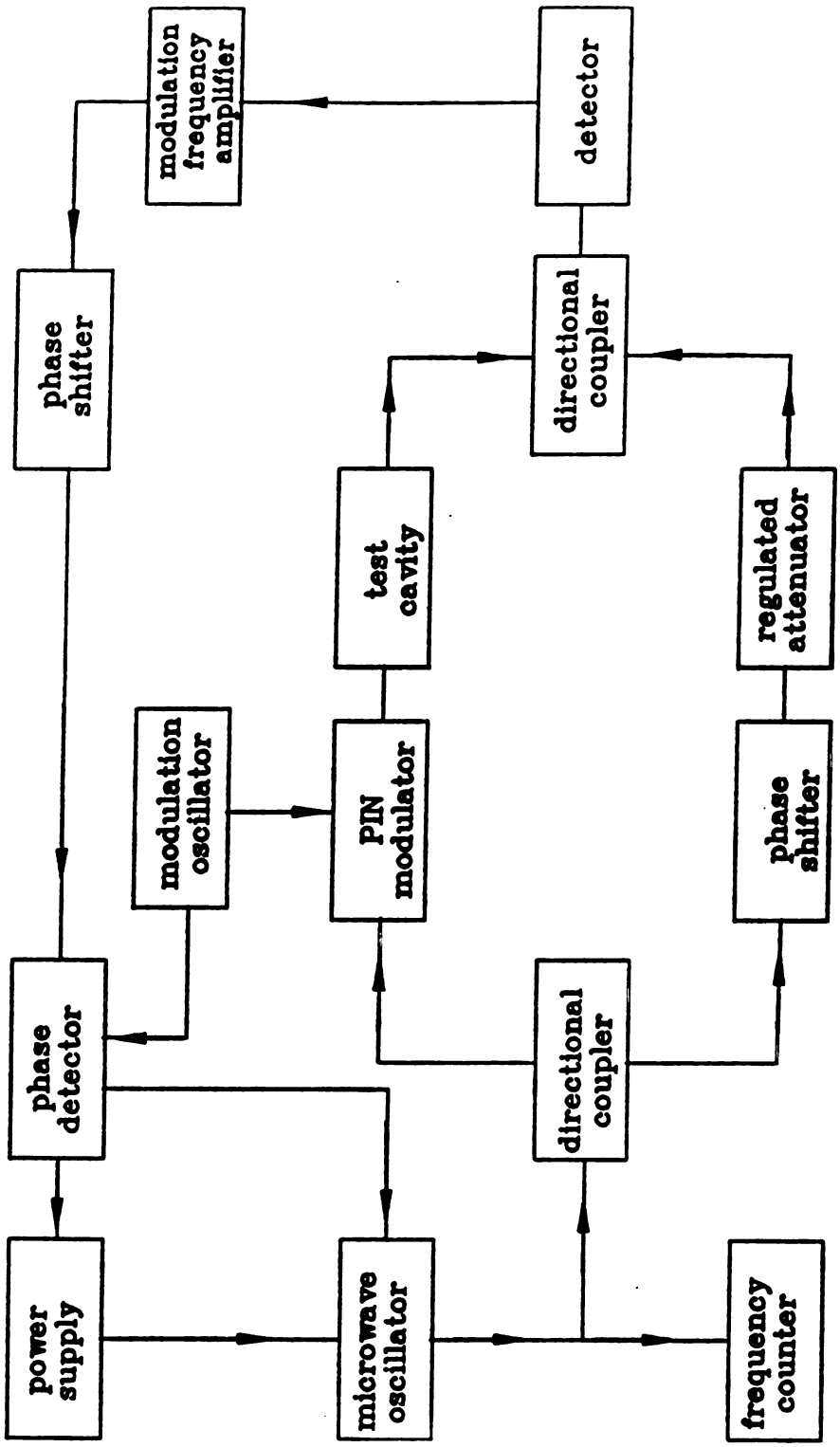

Figure 2.3 Block diagram of the active system

resonant frequency shift and Q factor. The main sources of measurement error are the errors related to frequency stabilizing circuit, variations of the cavity resonant during measurement, and the frequency counter. Cavity dimensions remained constant throughout experiments and cavity resonance was maintained by continuous adjustment of the frequency of the microwave oscillator via phase lock loop (PLL) circuit.

Based on this active frequency measurement scheme, C. Akyel, et al. developed microprocessor control techniques for dynamic measurements of complex dielectric constant using cavity perturbation [19]. In the experimental system, an electronic phase shifter introduces a periodic phase shift inside a closed loop circuit containing the cylindrical cavity applicator. An mechanical phase shifter adjusted by a microprocessor kept the cavity applicator at resonance. Both the resonant frequency shift and Q factor of the cavity were determined from the system oscillating frequencies, provided the phase shift caused by the resonant cavity was less than 15°. Limited by the small phase shift requirement, high accuracy can be achieved only if the frequency shift is smaller than 20 MHz and the loaded Q falls in the range from 500 to 6000.

One year later, C. Akyel and R. Bosisio [20] improved the above system by introducing Q-multiplier measurement mode. In this mode, the quality factor of the cavity applicator is increased whenever it is excessively decreased by sudden increases in the dielectric loss of the material load undergoing dynamic changes. The new system was able to measure the complex dielectric constant of sample material over a wider range of dielectric constants. No experimental results were reported in this paper.

Above work was again extended by Akyel, Labelle, Berteaud and Bosisio [21] to the computer aided permittivity measurements (CAPM) of moisten and Pyrolized materials. By means of this method, it is possible to directly relate the moisture content of sample materials exposed to strong electromagnetic fields to the dynamic changes observed in the complex dielectric constant at the test frequency. A rectangular TE_{103} mode cavity was excited at 2.45 GHz by two in-phase electric couplers to

prevent interference from higher order modes. The test sample material was a small piece of white bond paper which was first moistened and then rolled into a cylindrical form. The sample was held in the center of the cavity by a teflon sample holder. An AIM-65 microprocessor was able to calculate the percent moisture from the measured sample weights and the complex dielectric constants from the resonant frequencies and Q factors measurements by perturbation technique.

Experimental results show that both ε' and ε'' decrease essentially uniformly until the zero percent moisture level is reached. Beyond this level the ε'' increases rapidly while ε' remains nearly constant. It implies that the loss tangent $\tan\delta$ undergoes a radical change when the 0-percent moisture level is reached. This rapid change in the value of $\tan\delta$ offers a convenient means of detecting the 0-percent moisture level. The authors claim the precision of the moisture measurements is better than 0.1% and the precision of the dielectric measurements is better than 1% for ε' and better than 5% for ε''.

Using microwave cavity for the measurement of the complex dielectric constant of high loss liquids has been seen in several papers. In H.-J. Blume's report [22] a cylindrical cavity operated at 1.43 GHz in swept mode was used to measure the complex dielectric constant of polluted waters. Very small water sample in quartz tube of known volume was placed in the center of maximum electric field. Measurements on the input power, reflected power, coupling coefficient at resonance, frequency shift and resonant frequency are needed to calculated Q factor.

H. A. Buckmaster, et al. [23] used a variable length, nonresonant reflection cavity to measure ε of dilute aqueous KCI solutions. Comparison was made between the reflection and transmission type cavities. The complex permittivity was calculated from the attenuation per unit length and the phase shift per unit length. They demonstrated that high loss liquids could be determined more accurately using a variable-length transmission sample cell than using a variable length reflection sample cell.

Two different methods, single mode active cavity perturbation technique (SMAC) and time domain spectroscopy (TDS) were studied by C. Akyel et al. [24] to heat and measure, at the same time, the complex permittivity of various liquid dielectrics. The sample materials under test included ethanol, various solutions of methanol and decanol and mashed potatos. Comparison between these two methods was given. In SMAC methods, cavity was fixed in dimension [19]. Hence, some coupling variations were found during microwave heating cycles, which slightly affected the measurements. These changes were neglected in the calculation of the complex dielectric constants with perturbation formulas.

In TDS methods, a step voltage pulse produced by a fast-rising tunnel diode pulse generator was transmitted toward sample material. The voltage pulse propagated in the coaxial line until it reached the air-dielectric interface where a part of the pulse was reflected and the rest was transmitted into sample. The reflected signal was then detected by a wideband sampling oscilloscope. ε was determined by the scattering coefficient formula with the measured reflected voltage. In comparison with the experimental results obtained by SMAC, TDS may be more accurate. But the temperature permittivity hysteresis effect was observed from the SMAC results. It is not possible using TDS because of the nature of the pulse voltage heating.

In 1985, M. Martinelle, P. A. Rolla and E. Tombari [25] used a TE_{011} mode cylindrical cavity at 9.5 GHz for dynamic dielectric measurements during polymerization reaction. Possible volume or density changes of samples were taken into account in the perturbation formulas. Only ε' was measured in the experiments. Active frequency close-loop circuit was built to determine the frequency shift required in the formula for the evaluation of ε'. Later, in the same year, they proposed a method to determine the ε'' by power reflection coefficient measurements [26]. A first order perturbation formula was employed to calculate ε' and ε''. Measurements of the standing wave ratio (VSWR), empty cavity Q factor, empty cavity coupling coefficient and

filling factor were required for the calculation of ε''.

Experimental errors were analyzed for ε' and ε'', respectively. The error of ε' was mainly due to the Q factor changes which contributed more resonant frequency shift but was neglected in the first order approximation of the perturbation formula. The determination of ε'' by means of VSWR measurements was affected by a relative error, depending on the reflection coefficient value. The complex dielectric constant of chlorobenzene was measured and the error due to Q change was about 10^{-7}, due to reflection coefficient measurements was about 3×10^{-3}.

2.2.2 Microwave heating

In microwave heating, microwave energy is utilized to heat materials to achieve certain purpose. Wide variety of applications of this technology has been reported in the literature. Two categories can be classified among the most common applications: (1) dehydrating (water removal); and (2) enhance heating.

Dehydrating

Dehydrating of various materials is one the most traditional areas in which microwave heating has been applied. The forest industry has been using microwave to process large bundles of woods and plywood veneer, such as the redrying of veneer [27] and the drying of the glue between veneer sheets [28]. Since Sixties, microwave energy has been used to dry potato chips and paper match books [1]. More recently Thiebaut et al. [29] examined the dehydration of 13X zeolites using microwave energy in a TE_{011} cylindrical cavity. An evaluation of possible use of microwave and rf drying as a pretreatment step in the acid hydrolysis of corn stover was conducted by G. Lightsey's research group [30]. They conclude that microwave drying greatly reduces the process time compared to conventional drying.

The drying of plastic materials has drawn extensive attention. Since the tensile strength of specific plastics depends on the moisture content prior to extrusion,

moisture reduction is necessary. Lightsey [31] investigated the microwave drying of four common polymers. It is found that, compared to conventional drying techniques, reductions in drying time of 85 to 90 percent were achieved. In rubber processing and ceramic processing, using microwave energy for dehydration is becoming more and more attractive [1], [28].

Enhanced heating

Besides heating the water inside a material, microwaves have been used to heat the dielectric material in order to change the physical characteristics in known and controllable ways. This is the purpose of enhanced heating. Applications have been found in semiconductor processing, food processing and chemical processing.

A typical procedure in which semiconductor devices are fabricated from wafers entails heating the wafers during several process steps. In contemporary practice, wafers are routinely heated with resistance furnaces, infrared lamps, electron beams and lasers. Sirkis and Conrad [32], [33] used traveling waves to heat semiconductor ribbons and wafers directly without susceptor. Figure 2.4 displays the cross-section of a waveguide applicator. The semiconductor wafers were supported at each side by ceramic retainers. Experimental results show that 15 semiconductor ribbons or wafers could be heated uniformly at the same time.

In food processing, bacon cooking and meat tempering accounted for 79% of the installed microwave heating capacity as of 1984 [28]. Recently applications of microwave heating for stored-grain insect control and agriculture seed treatment have been reported [34]. An improvement of the nutritional quality of soybeans by continuous microwave heating was demonstrated by Vetsuypens and Loock [35].

In chemical processing, plastic processing, rubber processing and ceramic processing are the most promising areas of microwave heating applications. In addition to the drying of plastics mentioned previously, microwave energy has been proposed to enhance the polymerization process [25], [36]; to heat prior to extrusion; and to

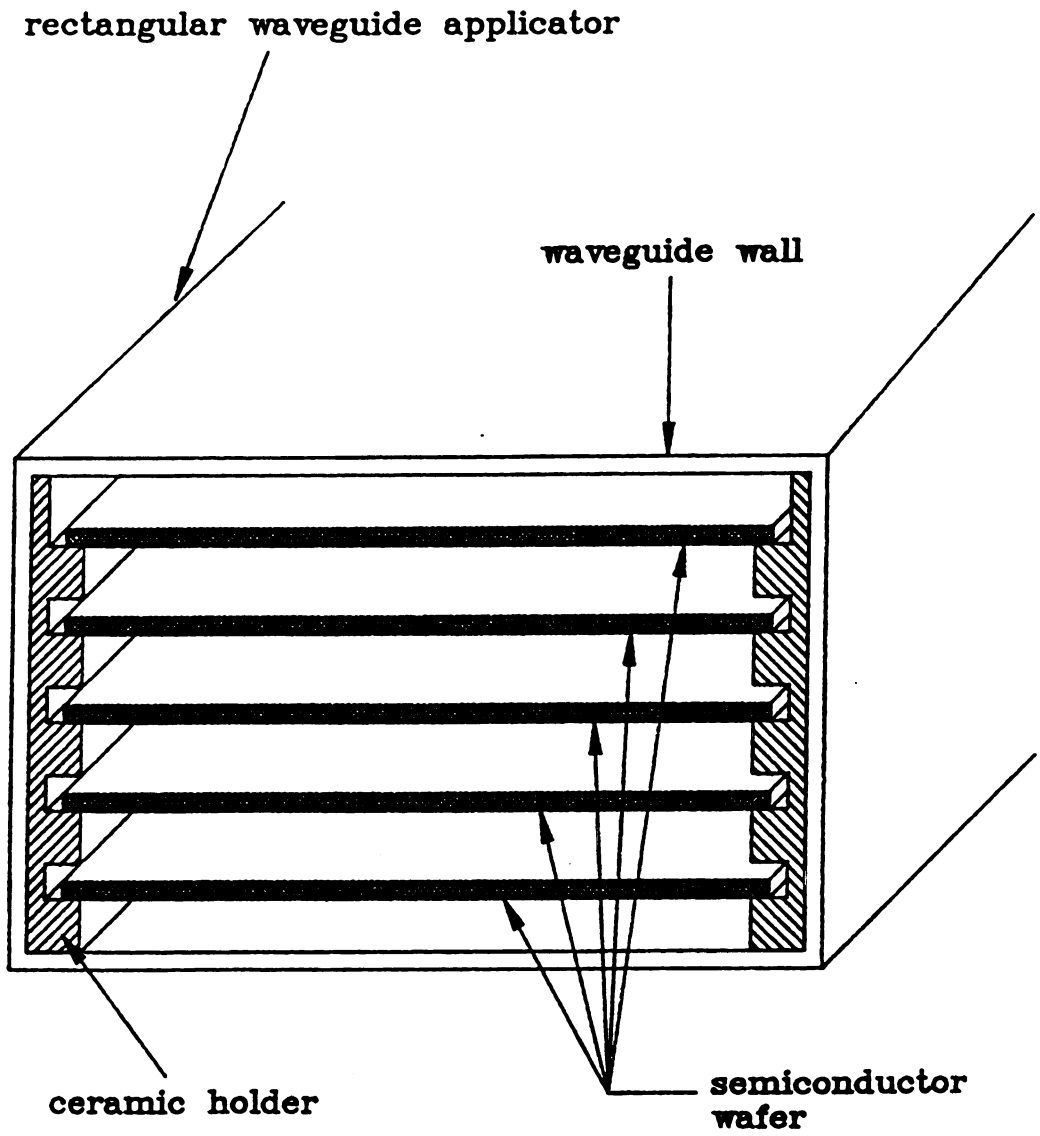

Figure 2.4 Cross-section of a waveguide applicator

stimulate specific chemical reactions [28]. Lightsey, George and Russel [31] proved that the use of microwave energy for curing plastics allows development of fast, more efficient and better controllable processing system than the processes that are commonly used at present. Strand [37] showed that the cure times of epoxy could be reduced 30-fold using microwave heating rather than conventional thermal heating. The utilization of microwave energy in rubber processing has been expanded from the initial application of extrusion curing to every facet of the rubber process. It includes tempering bales, devulcanizing, preheating prep and curing [1], [38]. Since microwave heating gives better heating control and efficiency and is not limited by thermal diffusion process, theoretically a material can be heated to any temperature wanted. This phenomena has been recently applied to the sintering and the joining of ceramics [39] - [42]. More recently researchers have paid attention to the application of microwave energy in composite materials. Park [43] investigated the sintering of zirconia- aluminia composites under 2.45 GHz microwave radiation. R.B. James [44] studied the microwave-induced surface melting of carbon composites and graphite by high power microwave pulses.

2.2.3 Microwave plasma applications

Using a microwave cavity applicator to generate microwave plasma has received much attention lately. The reason is that microwave plasma has been found many applications in industry and in fundamental researches. These applications include (1) microwave electrothermal and ion engines for spacecraft propulsion, (2) ion sources, (3) plasma etching and oxidation in semiconductor processing, (4) plasma induced chemical vapor deposition for growing diamond thin films.

Recent high pressure microwave discharge experiments [45] - [47] conducted at Michigan State University have demonstrated the potential application of microwave arcs as an electrothermal thruster concept. In these experiments, a high pressure

microwave discharge was established in a flowing gaseous propellant. The gas was heated to high temperatures and was passed through a nozzle, converting the gas thermal energy into thrust. Two different applicators have been used to sustain the discharges: a cylindrical cavity applicator and a compact coaxial applicator [46]. This electrodeless engine concept eliminates the electrode erosion and lifetime problems experienced in DC discharge. It is also expected to achieve much greater thruster level than can be obtained from electrostatic ion thruster.

Microwave plasma applicators [48] have demonstrated the ability of producing ion beams. A microwave cavity plasma disk ion source was shown to be able to operate over a large pressure, flow rate and absorbed power density ranges. The advantages of using microwave ion sources are no electrode problems such as discharge contamination with electrode materials, electrode lifetime constraints and the ion beam current density limits due to the presence of electrodes.

Polymer thin films are widely used in the semiconductor industry as insulators, planarizing layers and for patterning other materials. It has been shown that these polymers could be etched by using microwave plasmas. Hussla, et al. [49] used argon-ion plasma in their investigation of the silicon wafer temperature during the plasma etching process. Hopwood, et al. [50], [51] showed that a 2.45 MHz microwave plasma disk reactor (MPDR) could be used to generate plasmas for silicon etching. In their work, both CF_4/O_2 and SF_6/A_r plasmas were studied. It is found that by operating high-density plasmas at low pressures, ions were accelerated vertically to the wafer surface. Hence, considerable less undercutting was achieved than at high pressures. Microwave plasma oxidation for integrated circuit processing has also been demonstrated by using microwave plasma disk reactor [52], [53]. The oxidation rate was comparable to conventional thermal oxidations at 1000 C. However the temperature of the silicon wafer was less than 200 C. Low temperature is very important in VLSI processing since it reduces impurity motion, wafer warping and defect genera-

tion [52].

Recently considerable attention has been paid to the growth of diamond thin films. Because of all the useful properties diamond has, the potential applications of diamond thin film are numerous, such as high temperature and high power electronics and sensors, microwave and millimeter wave power device, printed circuit board, vacuum UV laser, cutting tools and tribological applications. The major difference between chemical vapor deposition (CVD) and plasma induced CVD is the energy source. The energy for the plasma CVD is supplied by plasma instead of heat in CVD. Basically, plasma CVD is performed by passing a mixture of hydrogen and methane into the deposition chamber and applying microwave power to induce glow discharge [54]. Microwave power breaks the methane into carbon and hydrogen. Atomic carbon deposits itself on the substrate in a configuration resembling the tetrahedral formation of diamond. Hydrogen atoms pick up dangling bonds on the surface from collapsing into a graphite form. In a pulsed microwave plasma CVD system, the introduction of hydrogen into deposition chamber is not necessary because the cooling process is rapid enough to prevent the transformation of metastable phases into graphite [55].

2.3 Methods of analyzing coaxially loaded cavity

2.3.1 Theoretical formulation

During the last two decades many rigorous methods have been developed to analyze dielectric resonators, such as the mode matching method, the finite element method, the Rayleigh-Rize method, moment method, and the transverse resonance method. Some of these methods are complicated and take up a great deal of computation time to achieve high accuracy. While some of them may be simplier and faster in computation but with less accuracy. There is no certain rule of choosing the methods. Nevertheless, depending on the resonator configuration, applications, dielectric

properties, and computation time and accuracy requeirments, one can select the most appropriate method for his application. The purpose of this section is to introduce those methods that are most frequently seen in literature. No attempt is made to compare them and to determine the most significant one.

Mode-matching method

Mode-matching method has been widely used for the analysis of open dielectric resonators and dielectric resonator with metallic boundaries. Basically, the structure of the resonator is divided into subregions. In each subregion the electromagnetic fileds are expressed as a linear combination of all possible eigenmodes with unknown coefficients. By enforcing the continuity conditions of the transverse electric and magnetic fields over the interfaces between subregions, a system composed of infinite number of homogeneous equations where each equation is described by infinite sum of terms is obtained. The vanishing determinant of the coefficient matrix of the system equations establishes the characteristic equation of the problem. Together with the separation equation associated with each subregion, the resonant frequency corresponding to various modes are solved numerically from the characteristic equation. For computation simplicity, a truncated system is usually considered. The size of the truncated determinant is determined by the convergence condition of the resonant frequency.

Using a mode-matching method to analyze microwave cavity loaded with a long dielectric rod has been reported by many researchers. A long dielectric rod is a rod which has the same length as that of the cavity. Axially independent modes were examined by Rossy and Felden [7], and by Shihe Li et al. [8]. Rossy and Felden studied the lossless case, while Li investigated a low loss dielectric rod with $\varepsilon'' = 0.04$. More complete analysis with the inclusion of hybrid modes was done by Kobayashi et al. [56], and by Zaki and Chen [57]. Only lossless dielectric materials were considered in both papers. In general, the loaded cavity was treated as a section of coaxi-

ally loaded waveguide, shorted at both ends. Kobayashi provided the design criteria for a dielectric resonator to accomplish possible highest quality factor for largest frequency separation between adjacent modes. In their analysis, the dielectric rod and the cavity walls were assumed lossless. Zaki and Chen not only calculated the resonant frequencies, Q-factors and mode charts, but also studied the effects of the relative dielectric sample dimensions on the Q-factor.

Sphicopoulos, Bernier and Gardiol [58] solved the problem of a cylindrical cavity loaded with many concentric dielectrics. The cavity was regarded as a waveguide loaded with multilayer dielectric tubes. Application of the boundary conditions on the conducting walls and continuity conditions between dielectric layers gave rise to a $N \times N$ homogeneous linear system equation. The resonant frequencies are the zeros of the determinant of the coefficient matrix. N is determined by the number of dielectric layers present in the cavity resonator. In this paper, losses in the dielectric and in the cavity walls were taken into account through the use of complex frequency and complex permittivity. The real part of each zero is the actual resonant frequency, while the imaginary part yields the unloaded Q-factor. In addition to the resonant frequency, mode conversions from homogeneous cavity to cavity loaded with two layers of dielectrics was examined and the field distributions for TE_{011} and HE_{111} modes were calculated. The lossy dielectric material considered has a complex dielectric constant of $\hat{\varepsilon} = 13.1 - j\,1.2\times10^{-2}$. Theoretical results were verified by experiments.

The earlies study of a microwave cavity centrally loaded with a finite dielectric cylinder using mode matching method was done by D. M. Bolle [59]. Bolle compared the results with those obtained from Slater's perturbation theory. No loss due to the dielectric material was considered. Later, Kobayashi, et al. [60], and Zaki and Chen [61], [62] investigated the same problem. They divided the resonator into two homogeneous waveguides and one dielectric-loaded waveguide three subregions. In other words, the resonator was treated as a three-layer problem. Boundary conditions and

continuity conditions were matched on the conducting walls and the interfaces between layers. Due to the structural symmetry, magnetic wall and electric wall boundary conditions were employed over the symmetry plane by some researchers [60], [61], [63]. It is worth noting that the resulting system equations is half of those without using the electric and magnetic walls boundary conditions.

Kobayashi also studied two extended cases:(1) long rod and (2) disk loaded cavities. Mode charts and resonant frequencies were calculated for various cavity modes. In zaki's paper [61], the transverse electric and magnetic field patterns at different axial positions for different modes were plotted.

A rectangular cavity loaded with low loss dielectric materials was analyzed by Leong, Kooi, and Yeo [64]. It is found that for low dielectric constant, ε'=2.58, three eigenmodes in each region was enough for good convergence, while for high dielectric constant ε'=95, convergence was achieved using six eigenmodes. The effect of dielectric loss on the resonant frequency and Q-factor was examined. Theoretical results show that the dielectric loss does not affect the resonant frequency for low loss dielectrics ($\tan\delta < 0.001$). Resonant frequency increases of less than 0.08 MHz was observed for a medium value of loss tangent of 0.03. The authors studied the temperature dependence of the resonant frequency and the output power variation of a cavity loaded with teflon over a temperature range from $23^{\circ}C$ to $72^{\circ}C$. Over this temperature range, the frequency decreased by 16 MHz.

Although the existence of complex modes [65], [66] in waveguide loaded with lossless dielectric material have been known since 60's, most researchers assume that all the modes in each of the subregions are either propagating or evanescent modes when mode matching method is applied. Not until 1988, Chen and Zaki [67] first included complex modes in the field expansions in the analysis of the lossless dielectric resonators using mode matching method. They successfully predicted all the resonant modes that were observed experimentally, which was impossible without

including the complex modes.

Studies of the multilayer dielectric resonator with metallic boundaries have been seen in literature [68] -[70]. As is shown in Figure 2.5, in the multilayer structure, a dielectric cylinder is placed in a metallic cylindrical cavity, which includes a dielectric support to hold the dielectric cylinder, one or two layers of dielectric substrates, and/or a dielectric post to tune out fabrication tolerance. Hence, the cavity is often divided into subregions of homogeneous waveguides and dielectric-loaded waveguides. Each layer corresponds to one of the waveguide subregions. Two basic assumptions were made as follows: (a) dielectric materials involved are isotropic and lossless, and (b) the metallic boundaries are perfectly conducting. As mentioned earlier, the electromagnetic fields in each subregion are expanded in terms of all possible eigenmodes existing in it. Boundary conditions are then made at the interface between dielectric layers (subregions).

Hong and Jansen [69] considered a 5-layer resonator structure. They found that 4 or 5 eigenmodes present in each layer were adequate for good convergence of resonant frequencies. Bonetti and Atia [68] investigates a 4-layer TE_{105} mode resonant cavity. Following the formulation of Zaki et al. [62], Vigneron and Guillon [70] studied a 3-layer asymmetric dielectric resonator. They solve for the resonant frequencies for both hybrid and axially symmetric modes. Generally, 6 expansion eigenmodes were required to achieve reasonable convergence.

Rayleigh-Ritz method

Recently Rayleigh-Ritz method [71] have been used to determine the resonant frequencies and Q-factor of dielectric-loaded microwave cavity with remarkable success. By using this method, the accuracy of solutions depend highly on the selection of basis functions. The basis functions are the solutions of Maxwell equations subject to appropriate boundary conditions, depending on what cavity structure is under study. Empty cavity solutions have been frequently employed as the basis [72] in the analysis

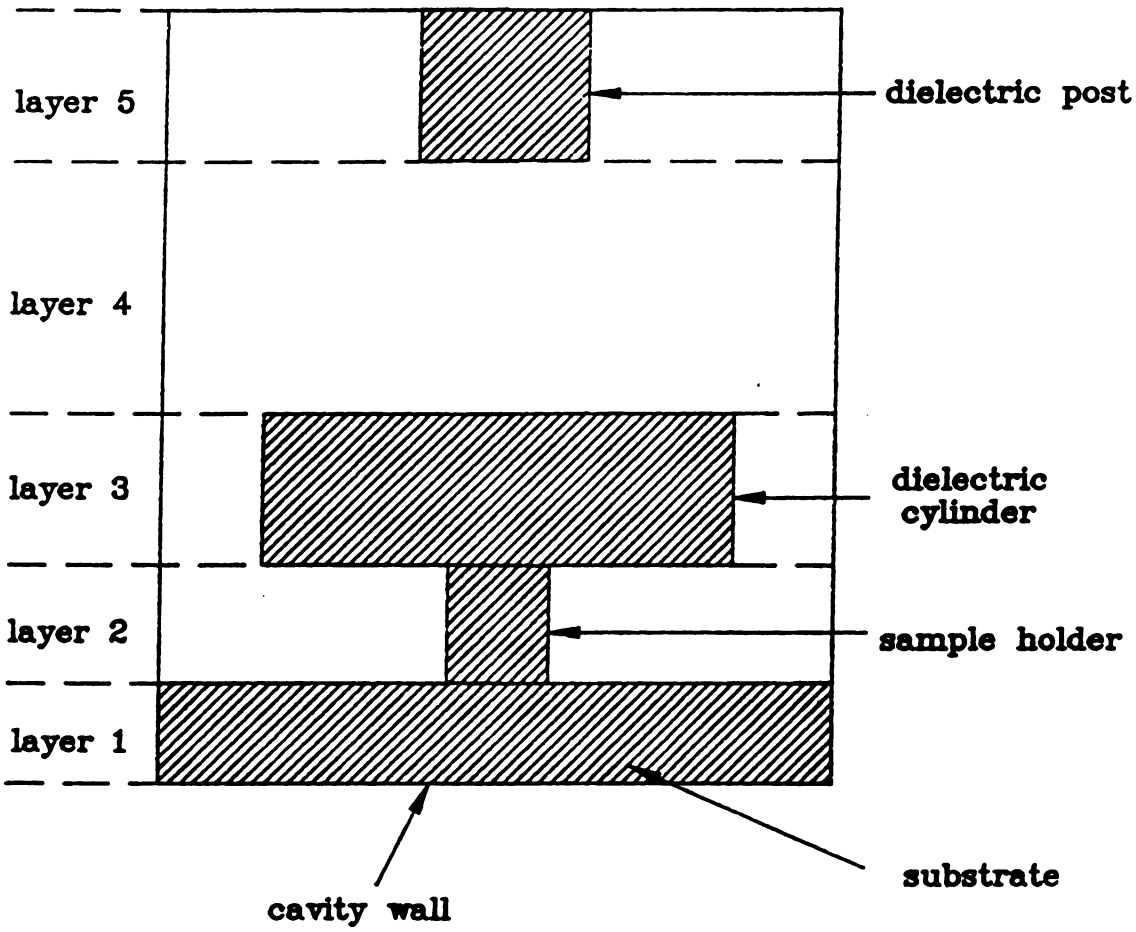

Figure 2.5 Side-view of a multilayer dielectric resonator

of lossless dielectric resonators. For the first time in 1983, the solutions of a partially filled cavity were used as the basis function by J. Krupka [73]. In this paper, Krupka demonstrated that the basis could be optimized through a proper choice of N basis functions from its infinite set to achieve the most accurate solutions. The optimization is easy because the resonant frequencies calculated by Rayleigh-Ritz method are lower bounded by the accurate solution [71]. According to this rule, N functions having the lowest frequency values among the infinite set are chosen to form the most significant basis. No loss was included in his analysis.

In addition to the choice of the basis, the dielectric constant of the basis cavity (partially filled cavity) also affects the convergence of the solutions. The optimal dielectric constant for certain cavity dimension is the one which has the lowest resonant frequency when only one basis, the predominant one, is used in the Rayleigh-Ritz method. The resonant frequency corresponding to this dielectric constant is taken as the starting point of the Rayleigh-Ritz method. With the optimized N basis functions and the optimaized dielectric constant of the basis cavity, the best convergence could be achieved by experimenting with N. Krupka calculated the resonant frequencies of a TE_{011} mode cavity as a function of N. It is found that for N > 10, significant convergence can be achieved.

By optimization of the basis, a high calculation accuracy of the resonant frequencies of the dielectric-loaded cavity is obtained. However, as the author noted, some difficulties arise because of the optimization. First, N transcendental equations need to be solved in order to determine the basis. Second, the new basis functions are more complicated than empty cavity basis functions. Therefore Krupka recommended that an optimized procedure be employed in the following cases: (1) when a very high accuracy of calculations is required, and (2) when the computation time must be short or/and the available computer memory is limited.

In the interest of calculating the resonant frequencies and Q-factor of MIC dielec-

tric resonators, Krupka took the electromagnetic fields of an auxiliary post dielectric resonator as the basis of Rayleigh-Ritz method [74]. The complex dielectric constants of the dielectric resonator and the substrate are $36.2 - j3.62\times10^{-3}$ and $3.03 - j1.65\times10^{-2}$, respectively. Because only nonradiating TE_{0nn} was looked for, the distance between conducting plates was smaller than half of the free space wavelength. Theoretical results were compared with the calculations obtained by mode-matching and Weinstein variational methods. It is intriguing to note that both mode-matching and Weinstein variational methods provides lower bounds for the accurate solutions, while Rayleigh-Ritz method provides upper bounds for them. The convergence of the Rayleigh-Ritz method is worse than mode-matching and Weinstein variational methods. However, on the other hand, Rayleigh-Ritz method leads to a simple eigenvalue problem which can be solved faster than the problem of searching the roots of the vanishing determinant which must be solved when those two methods are used.

A detailed comparison of the Rayleigh-Ritz method and the mode-matching method for computations of TE_{0nn}-mode resonant frequencies and Q-factors of dielectric-loaded microwave cavity was presented again by J. Krupka in 1988 [75]. In his analysis, all the dielectric materials were assume lossless. Computations were made for the dielectric resonator structure shown in Figure 2.6. Krupka demonstrated that, to achieve good convergence, 100 basis functions were required for Rayleigh-Rize method, while nine eigenmodes were used in the modal expansion in each subregion for mode-matching method. The computation time were approximately identical for both methods for various material/cavity dimensions and dielectric constants (10 seconds on a CDC 6600 computer per frequency value). It is seen that the discrepancy between resonant frequency values obtained by these two methods is not greater than 0.6 percent for the first six modes if the dielectric constant of the dielectric material is 10. However, the differences increase when the dielectric constant is 35 and the ratio of the length of the dielectric material to that of the cavity is less than

0.2, i.e., $p < 0.2$ as shown in Figure 2.6. This is due to the poor convergence of the Rayleigh-Rize method under these resonance conditions [73]. Krupka also examined the influences of the thickness of the substrate and the relative diameter (ratio of the diameters between dielectric material and cavity) on the resonant frequencies.

Moment method

Moment method has been used in the analysis of dielectric resonators in the last few years. In an attempt to find the TE_{i0k} mode resonant frequencies of a rectangular cavity containing a dielectric sample, Kedzior and Krupka made use of Galerkin method [72]. This is a well known moment method in which the set of testing functions is identical to the set of basis functions that expands the electric field (or magnetic field). Similar to mode-matching method a truncated system of linear equations was established in the formulation of the problem. The resonant frequencies were the zeros of the determinant of the coefficient matrix of the system equations.

Glisson and Kajfez [76] utilized moment method to formulate a microwave cavity loaded with lossless dielectric material with arbitrary cross section. Their approach was based on the solution of a surface integral. Numerical computations was made for a dielectric cylinder resonator without metallic boundaries. The values of the resonant frequencies and the values of the corresponding Q-factors were determined by the complex frequency technique [77]. The convergence condition of the solution was studied by increasing the number of points (N) on the generating arc. As was expected, the resonant frequencies and Q-factors showed good convergence as N is increased. Magnetic and electric surface currents, transverse electric and magnetic fields, and mode chart for various resonant modes were presented.

Finite element method

In order to investigate the cylindrical dielectric resonator in MIC applications, Kooi, Leong and Prakash [78] carried out the analysis using the finite element method. The resonator is a three layer problem, including dielectric post, substrate and empty

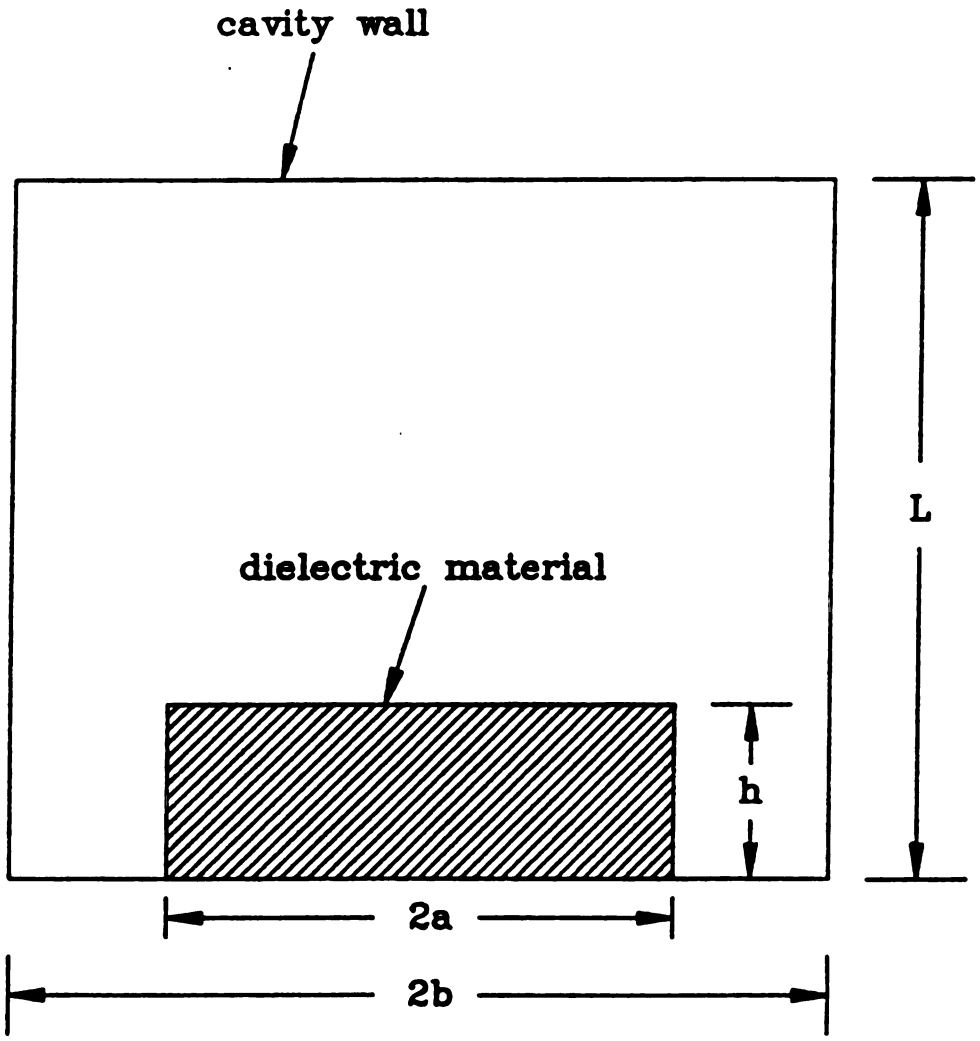

$p = h/L$

Figure 2.6 Geometry of a dielectric resonator

regions. The dielectric materials considered were lossless. Each region was divided into three-noded triangular elements. First-order polynomials were selected to approximate the variation of the electric field within each element. More elements were taken in the dielectric post region as most of the electromagnetic energy is confined in this region. Galerkin weighted residual approach was used to derive a system equations of each element. Putting together the system equations of each element yielded the overall system equations. The zeros of the determinant of the coefficient matrix are the resonant frequencies. The convergence condition was tested by increasing the number of elements. The authors suggested that higher accuracy in the computation of the resonant frequencies be achieved by using higher-order elements, instead of three-noded triangular elements. The resonant frequencies and Q-factors of TE_{018} mode were evaluated and compared to published data.

Transverse resonance method

The first report of using transverse resonance method to analyze a dielectric-loaded cylindrical cavity was done by Hanfling and Botte [6] in 1971. Recently, El-Sayed and Farghaly used this method to perform more detailed analysis of the influence of the load position on the resonant frequency of a dielectric-loaded rectangular cavity. [79] The cavity was loaded with a lossy dielectric slab, completely filling the cross section of the cavity. By means of the equivalent transmission line circuit of the loaded cavity, the characteristic equation was derived by matching the impedance in a properly selected reference plane. The resonant frequencies were computed for TE_{112}, TM_{112} and TM_{311} modes for various load locations within the cavity. They also examined the effects of the dielectric loss on the resonant frequencies. It is found that the resonant frequency vs dielectric constant curves exhibit oscillatory behavior. In general, the amplitude of oscillation is higher for a raised slab than when the slab is positioned at the bottom of the cavity. The dielectric loss factor has a rounding effect on the rapidly rising portions of resonant frequency vs dielectric con-

stant response.

2.3.2 Mode designation

Resonant modes of dielectric-loaded cavities are more complicated to designate than in homogeneous cavities. For axially symmetric modes, the classification of modes are simple. Since these modes are either pure TE or TM relative to cavity axis [80], they are denoted by TE_{0pq} or TM_{0pq} as in the case of homogeneous cavity, where p and q are integers. For nonaxially symmetric fields, the resonant modes are neither TE nor TM to any coordinate. These modes are termed hybrid modes. Several methods have been proposed for classifying hybrid modes, but no method has been universally accepted. Most schemes classify hybrid modes into one of two categories, HE_{npq} and EH_{npq}. However, the criterion used to determined whether a mode is HE or EH is still a subject of controversy.

One method is based on the relative contributions of E_z and H_z, i.e. the longitudinal field components, to the transverse field components at some reference point [60], [81]. If E_z is dominant over H_z, the mode is designated as EH_{npq}. If H_z is dominant over E_z, the mode is classified as HE_{npq}. Snitzer [82] proposed a method for designating hybrid modes by inspecting the ratio of the coefficients of E_z and H_z. If the sign of the ratio is the same as for the fundamental mode, which is conventionally referred to as HE_{111}, the hybrid modes are designated as HE_{npq}. On the other hand, if the sign of the ratio is opposite to that of HE_{111}, the modes are designated as EH_{npq}. Chou [83] and Sphicopoulos [58] classified the hybrid modes by examining the resonant modes in the limiting case of vanishing dielectric load. That is, the dielectric permittivity of the dielectric load is equal to that of the surrounding media or the volume of the dielectric load is forced to be zero. In this case, the dielectric-loaded cavity is in fact a homogeneous cavity. The hybrid modes are referred to as HE_{npq} if , in the limiting case, they are TE_{npq} mode. While EH_{npq} modes are those modes which convert to TM_{npq} modes in the limiting case. Zaki and Chen [61] introduced a totally different scheme

for mode designation. The resonant modes are classified as HEH_{nm}, HEE_{nm}, TEH_{0m}, TEE_{0m}, TMH_{0m} or TME_{0m}. This designation scheme is designed for structural symmetry resonators with electric wall and magnetic wall boundary conditions applied in the symmetry plane.

In this dissertation, the homogeneous cavity solutions are used as the initial approximations in the root searching algorithm. Each resonant mode of the dielectric-loaded cavity then corresponds to a mode in the homogeneous cavity. Accordingly, the mode designation scheme proposed by Chou and Sphicopoulos is employed here. In other words, hybrid modes are designated as HE_{npq} if they correspond to TE_{npq} in homogeneous cavity and as EH_{npq} if they correspond TM_{npq} homogeneous cavity modes. This method is simple and clear. It is simple in the sense that no calculation of the field components is required to distinguish the modes. It is clear because the dielectric- loaded cavity mode is related to the one in homogeneous cavity. As a result, the mode inversions can be investigated as the dielectric constant or the relative dimension of the dielectric load is changed.

Chapter 3

THEORETICAL DEFINITION OF THE LOSSY DIELECTRIC-LOADED CYLINDRICAL CAVITY

3.1 Introduction

This chapter presents the theoretical formulation of a cavity loaded with lossy dielectric materials. The material-loaded cavity is a a cylindrical cavity concentrically loaded with a cylindrical lossy material rod which partially fills the cavity. In the formulation, the material-loaded cavity is treated as a section of inhomogeneous cylindrical waveguide partially loaded with concentric cylindrical lossy dielectric rod, connected to two homogeneous cylindrical waveguides each with one end shorted. The mode matching method described in Chapter 2 is employed to derive the cavity characteristic equations. A review of the classical EM analysis of the homogeneous and coaxially loaded waveguides is presented in section 3.3. The cavity characteristic equations for three different cavity types, i.e., cavity-open, cavity-short and cavity-image types shown in Figure 1.1, are derived in section 3.4. The last section of this chapter is a detailed derivation of the stored energy, absorbed power and quality factor of the dielectric-loaded cavity.

3.2 Theoretical formulation of the dielectric loaded cavity

Figure 3.1 shows the geometry of the dielectric loaded cylindrical cavity. A dielectric cylinder of radius a and length l_2 is placed coaxially in a metallic cylindrical cavity of radius b and length L. A convenient way of analyzing the problem is to divide the structure of the loaded cavity shown in Figure 3.1 into four regions (I, II, III and IV). Regions III and IV represent a metallic homogeneous waveguide of radius b which is shorted at one end and is filled with dielectrics of permittivities $\hat{\varepsilon}_3$ and $\hat{\varepsilon}_4$, respectively. Regions I and II represent a section of a waveguide of radius b coaxially loaded with a concentric dielectric of radius a. Region I is the dielectric core of

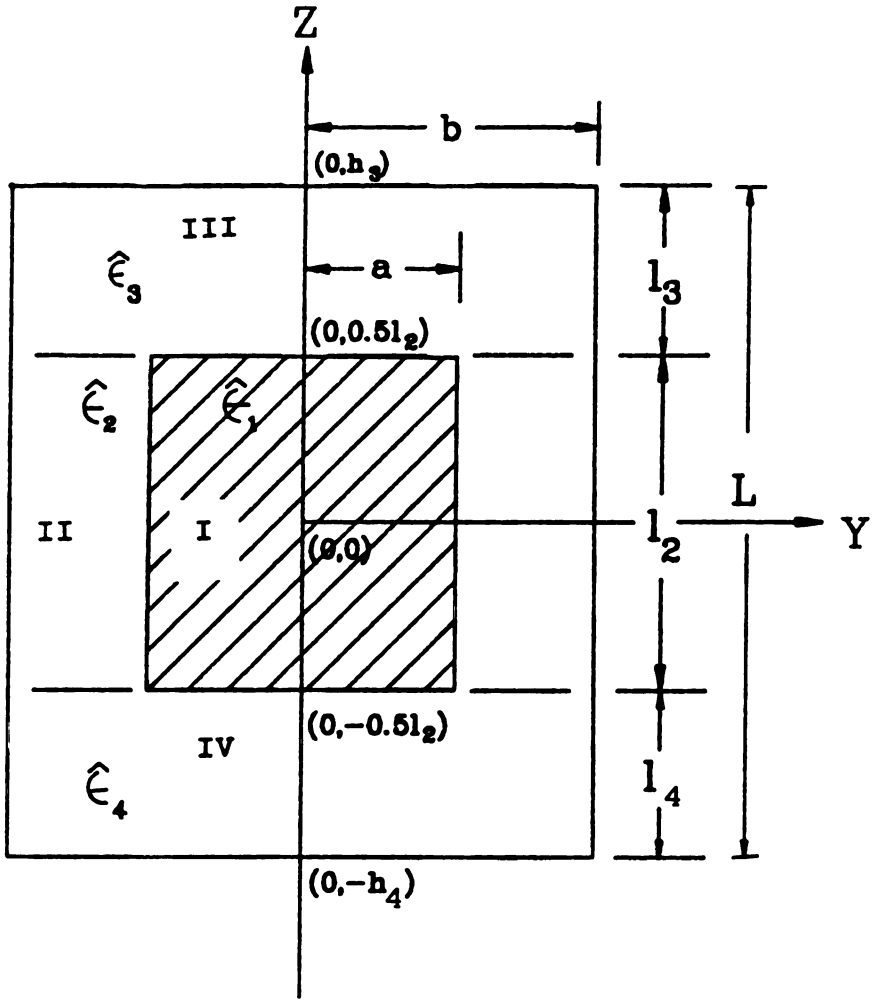

Figure 3.1 Dielectric–loaded cavity dimensions

permittivity $\hat{\varepsilon}_1$. Region II is the space between the metallic walls of the waveguide and the dielectric rod and filled with dielectric of permittivity $\hat{\varepsilon}_2$. As shown in Figure 3.1, l_3 and l_4 are the lengths of regions III and IV, respectively, and l_2 is the length of the coaxially loaded waveguide, i.e. regions I and II. The problem then reduces to a boundary value problem of a coaxially loaded waveguide connected to two homogeneous waveguides each with one end shorted.

The coordinate system to be used in the analysis of the dielectric loaded cavity problem is depicted in Figure 3.2. In this coordinate system the z-axis coincides with the axis of the loaded cylindrical cavity. The dielectric load is placed symmetrically about $\hat{z}$ in the cavity but not necessarily in the center of the cavity. It may be in any position on the cavity axis. Then, in general, the problem considered here has an asymmetrical structure and the mathematics is more complex if the origin is arranged in the center of the cavity. In order to have simplest mathematical expressions, the origin of the coordinate system is placed at the center of the dielectric load material.

The dielectric in each of the four regions is considered to be homogeneous, isotropic and lossy. The complex dielectric constant for each region is defined as

$$\hat{\varepsilon}_i = \varepsilon_i' - j\varepsilon_i'' - j(\frac{\sigma_i}{\omega}) = \varepsilon_0(\varepsilon_{r_i}' - j\varepsilon_{r_i}'') = \varepsilon_0 \hat{\varepsilon}_{r_i} \qquad i = 1, 2, 3, 4 \qquad (3.1)$$

where

$\hat{\varepsilon}_{r_i} = \varepsilon_{r_i}' - j\varepsilon_{r_i}''$

ε_i' = dielectric constant

ε_i'' = dielectric loss factor

ε_{r_i}' = relative dielectric constant

ε_{r_i}'' = effective relative dielectric loss factor

$\hat{\varepsilon}_{r_i}$ = relative complex dielectric constant

i = 1, 2, 3 and 4 are indices corresponding to regions I, II, III and IV, respectively.

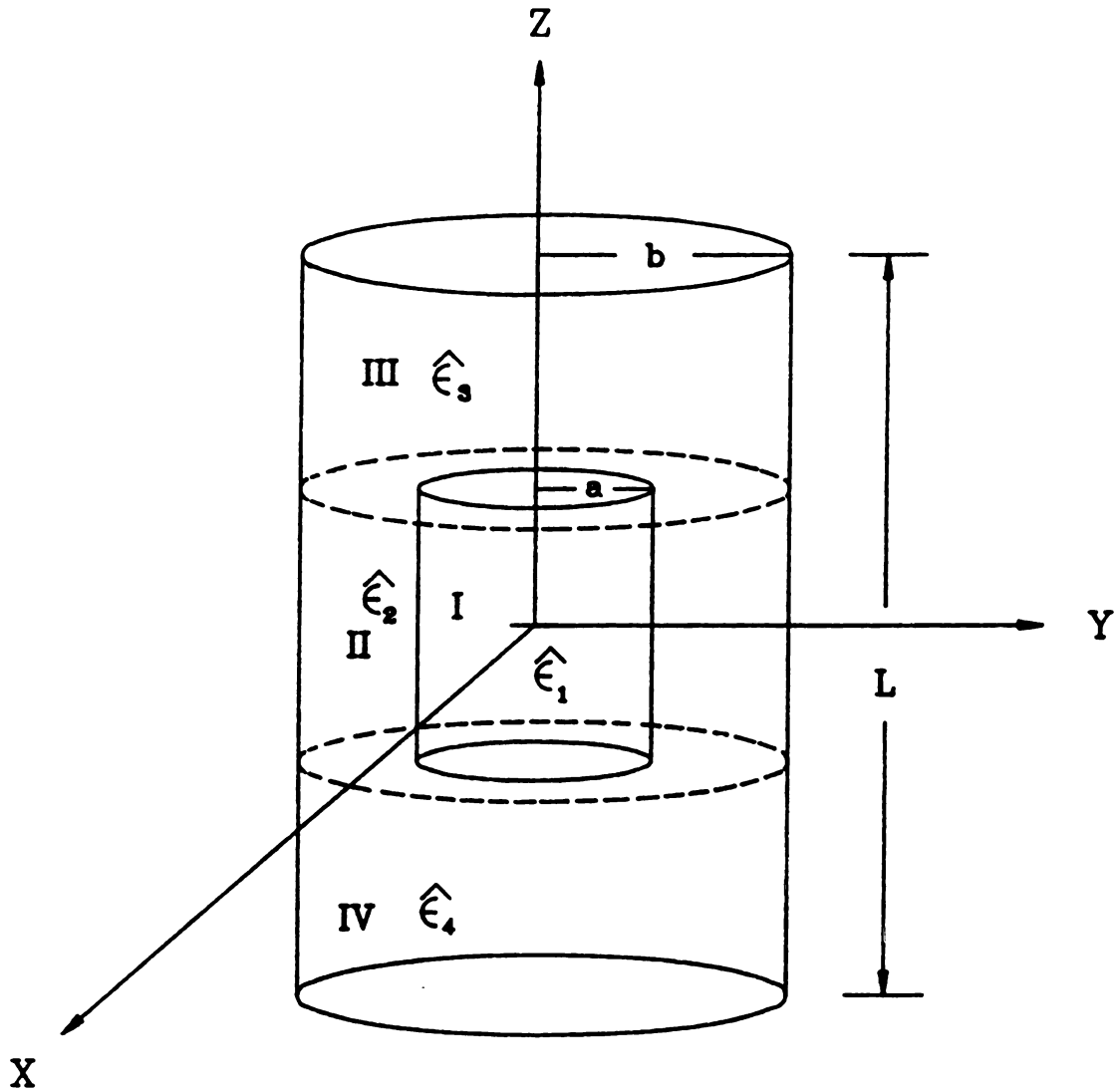

Figure 3.2 Coordinate system of the dielectric-loaded cavity

Both damping and conduction losses of the dielectrics are included in the effective relative loss factor, ε_{r_i}''. Often, the cavity is assumed to be filled with homogeneous dielectric, i.e., $\hat{\varepsilon}_2 = \hat{\varepsilon}_3 = \hat{\varepsilon}_4$. As mentioned earlier, the dielectric load material is of radius a, length l_2 and dielectric permittivity $\hat{\varepsilon}_1$. The radius of the dielectric load may be as large as that of the cavity, i.e., $0 < a \leq b$, and the length of the dielectric load may be as long as that of the cavity, $0 , l_2 \leq L$. When either $a = b$ and $l_2 = L$ or $\hat{\varepsilon}_1 = \hat{\varepsilon}_2 = \hat{\varepsilon}_3 = \hat{\varepsilon}_4$, the cavity is completely filled with the dielectric load material of complex dielectric constant $\hat{\varepsilon}_1$.

As can be seen from Figures 3.1 and 3.2, different load material dimensions and positions in the cavity result in a different boundary value problem. Variations of the problem can be identified by changing these parameters. In this dissertation, three different material loaded cavity types are classified according to the placement and size of the dielectric volume. In Figure 1.1a, the structure in which the dielectric cylinder load does not contact the conductor is call the cavity–open type. In Figure 1.1b, both ends of the long dielectric rod are in contact with the cavity conducting end plates. This structure is called cavity–short type. The structure shown in Figure 1.1c is called cavity–image type, in which one end of the dielectric disc contacts the cavity end plate. Each of the three different structures is subject to different axial boundary conditions. However, it is obvious that the cavity-short and the cavity-image types are two extended special cases of the cavity-open type. The solutions to the cavity-open type can be used to derive those to the other two structures. A detailed theoretical derivation of the characteristic equations for each of these structures is given in sections 3.3 and 3.4.

3.3 Review of theoretical formulation of cylindrical waveguide

3.3.1 Cylindrical wave potential

As mentioned in previous section, the dielectric loaded cylindrical cavity problem

shown in Figure 3.1 is viewed as a structure which consists of an open-ended waveguide and two homogeneous cylindrical waveguides shorted at one end. Hence, a knowledge of the solutions of the normal modes in these waveguides serves as the basis from which the cavity problem is formulated. In this section the cylindrical wave potentials for the dielectric loaded cylindrical waveguide are derived by solving for the solutions to the scalar Helmholtz equation in cylindrical coordinates. With the cylindrical wave potentials, normal modes in the coaxially loaded and homogeneous waveguides can be obtained by applying associated boundary conditions. Some of the basic and well known equations are given below.

The Maxwell's equations and associated constitutive relationships for a source free region are given by,

$$\nabla \times \vec{E} = -j\omega\vec{B} \tag{3.2a}$$

$$\nabla \cdot \vec{D} = 0 \tag{3.2b}$$

$$\nabla \times \vec{H} = j\omega\vec{D} \tag{3.2c}$$

$$\nabla \cdot \vec{B} = 0 \tag{3.2d}$$

$$\vec{D} = \hat{\epsilon}\vec{E} \tag{3.2e}$$

$$\vec{B} = \mu\vec{H} \tag{3.2f}$$

where $\hat{\epsilon}$ is the complex dielectric constant as defined in equation 3.1.

By introducing the magnetic vector potential $\vec{A}$ and electric vector potential $\vec{F}$, the field solutions result in

$$\vec{E} = -\nabla \times \vec{F} + \frac{1}{j\omega\hat{\epsilon}} \nabla \times \nabla \times \vec{A} \tag{3.3}$$

$$\vec{H} = \nabla \times \vec{A} + \frac{1}{j\omega\mu} \nabla \times \nabla \times \vec{F} \tag{3.4}$$

$\vec{A}$ and $\vec{F}$ are the solutions to the following wave equations and are called wave potentials.

$$\nabla^2 \vec{A} + \kappa^2 \vec{A} = 0 \tag{3.5a}$$

$$\nabla^2 \vec{F} + \kappa^2 \vec{F} = 0 \tag{3.5b}$$

where

$$\kappa = \omega\sqrt{\mu\hat{\epsilon}}$$

Note that in cylindrical coordinate system, $\hat{z}$ component of the wave potentials satisfies the scalar wave equation, or Helmholtz equation,

$$\nabla^2 \psi + \kappa^2 \psi = 0 \tag{3.6}$$

An arbitrary field in a homogeneous source free region can be expressed as the sum of a TM field and a TE field. A TM field is transverse magnetic to $\hat{z}$ with no H_z component and a TE field is transverse electric to $\hat{z}$ with on E_z component. A field TM to $\hat{z}$ can be obtained by setting $\vec{F} = 0$ and

$$\vec{A} = \hat{z}\psi \tag{3.7}$$

then

$$\vec{E} = -j\omega\mu\vec{A} + \frac{1}{j\omega\hat{\epsilon}} \nabla(\nabla\cdot\vec{A}) \qquad \vec{H} = \nabla \times \vec{A} \tag{3.8}$$

This can be expanded in cylindrical coordinates as,

$$\begin{aligned} E_\rho &= \frac{1}{j\omega\hat{\epsilon}} \frac{\partial^2\psi}{\partial\rho\,\partial z} & H_\rho &= \frac{1}{\rho} \frac{\partial\psi}{\partial\phi} \\ E_\phi &= \frac{1}{j\omega\hat{\epsilon}\rho} \frac{\partial^2\psi}{\partial\phi\,\partial z} & H_\phi &= -\frac{\partial\psi}{\partial\rho} \\ E_z &= \frac{1}{j\omega\hat{\epsilon}} \left(\frac{\partial^2}{\partial z^2} + \kappa^2\right)\psi & H_z &= 0 \end{aligned} \tag{3.9}$$

Similarly, a field TE to $\hat{z}$ can be obtained by setting $\vec{A} = 0$ and

$$\vec{F} = \hat{z}\,\psi \tag{3.10}$$

$$\text{then} \quad \vec{E} = -\nabla \times \vec{F} \qquad \vec{H} = -j\omega\hat{\epsilon}\vec{F} + \frac{1}{j\omega\mu} \nabla(\nabla\cdot\vec{F}) \tag{3.11}$$

Expanded in cylindrical coordinates, this is

$$\begin{aligned} E_\rho &= -\frac{1}{\rho}\frac{\partial\psi}{\partial\phi} & H_\rho &= \frac{1}{j\omega\mu} \frac{\partial^2\psi}{\partial\rho\,\partial z} \\ E_\phi &= \frac{\partial\psi}{\partial\rho} & H_\phi &= \frac{1}{j\omega\mu\rho} \frac{\partial^2\psi}{\partial\phi\,\partial z} \end{aligned} \tag{3.12}$$

$$E_z = 0 \qquad H_z = \frac{1}{j\omega\mu}\left(\frac{\partial^2}{\partial z^2} + \kappa^2\right)\psi$$

Once the scalar wave functions, ψ's, are solved from equation 3.6, the electric and magnetic fields can be derived according to equations 3.9 and 3.12. The scalar Helmholtz equation, equation 3.6, written in cylindrical coordinates is,

$$\frac{1}{\rho}\frac{\partial}{\partial\rho}\left(\rho\frac{\partial\psi}{\partial\rho}\right) + \frac{1}{\rho^2}\frac{\partial^2\psi}{\partial\phi^2} + \frac{\partial^2\psi}{\partial z^2} + \kappa^2\psi = 0 \tag{3.13}$$

Using the method of separation of variables, the solutions of ψ are expressed in the form

$$\psi = R(\rho)\,\Phi(\phi)\,Z(z) \tag{3.14}$$

Substitution of equation 3.14 into equation 3.13 and division by ψ yields

$$\frac{1}{\rho R}\frac{d}{d\rho}\left(\rho\frac{dR}{d\rho}\right) + \frac{1}{\rho^2\Phi}\frac{d^2\Phi}{d\phi^2} + \frac{1}{Z}\frac{d^2Z}{dz^2} + \kappa^2 = 0 \tag{3.15}$$

After some algebraic manipulations, the wave equation can be separated. Define κ_ρ as

$$\kappa_\rho^2 + \kappa_z^2 = \kappa^2 \tag{3.16}$$

and write the separated equations as

$$\begin{aligned}
&\rho\frac{d}{d\rho}\left(\rho\frac{dR}{d\rho}\right) + [(\kappa_\rho\rho)^2 - n^2]R = 0 \\
&\frac{d^2\Phi}{d\phi^2} + n^2\Phi = 0 \\
&\frac{d^2Z}{dz^2} + \kappa_z^2 Z = 0
\end{aligned} \tag{3.17}$$

The Φ and Z equations are harmonic equations, giving rise to harmonic functions, in general, denoted by $h(n\phi)$ and $h(\kappa_z z)$. The R equation is Bessel's equation of order n, solutions of which are denoted by $B_n(\kappa_\rho\rho)$. By choosing appropriate $h(n\phi)$, $h(\kappa_z z)$ and $B_n(\kappa_\rho\rho)$, the solutions to the Helmholtz equations are formed as

$$\psi = B_n(\kappa_\rho\rho)\,h(n\phi)\,h(\kappa_z z) \tag{3.18}$$

The choice of the Bessel functions is based on the behavior of the waves in the waveguide. Commonly used Bessel functions are $J_n(\kappa_\rho\rho)$, $N_n(\kappa_\rho\rho)$, $H_n^{(1)}(\kappa_\rho\rho)$ and

$H_n^{(2)}(\kappa_\rho\rho)$. These functions are linearly independent to one another. J_n and N_n are the Bessel functions of the first and second kinds, respectively. They exhibit oscillatory behavior for real κ_ρ and represent cylindrical standing waves. $H_n^{(1)}$ and $H_n^{(2)}$ are the Hankel functions of the first and second kinds, respectively. They represent cylindrical traveling waves, $H_n^{(1)}$ representing inward-traveling waves and $H_n^{(2)}$ representing outward-traveling waves. Note that only $J_n(\kappa_\rho\rho)$ functions are finite at $\rho = 0$, i.e., $J_n(0) \neq \infty$. Hence, if a field is to be finite at $\rho = 0$, $J_n(\kappa_\rho\rho)$ must be chosen for the Bessel function.

With properly selected harmonic functions and Bessel function, problems having cylindrical surface boundaries, such as the homogeneous and coaxially loaded cylindrical waveguides, can be solved by means of equations 3.9, 3.12 and 3.18.

3.3.2 The homogeneous cylindrical waveguide

As is shown in Figure 3.1, regions III and IV are two empty waveguides, shorted at one end, completely filled with homogeneous and isotropic dielectric. In this section, the modal fields in the homogeneous waveguide with one end shorted is derived.

Figure 3.3 depicts the cylindrical coordinate system for the analysis of the homogeneous waveguide, which models regions III and IV of Figure 3.2. Since fields are finite at $\rho = 0$ and travel along the $\hat{z}$ direction, the wave functions are of the form

$$\psi = \bar{a}\, J_n(\kappa_\rho\rho) \begin{Bmatrix} \sin n\phi \\ \cos n\phi \end{Bmatrix} e^{-\gamma z} \tag{3.19}$$

where $\bar{a}$ is an arbitrary constant. Either $\sin n\phi$ or $\cos n\phi$ may be chosen, except for the $n = 0$ case. Substituting equation 3.19 into equations 3.9 and 3.12 and applying the boundary conditions that $E_z = 0$ for *TM* modes and $E_\rho = 0$ for *TE* modes at the conducting walls $\rho = b$, the modal fields and eigenvalues for κ_ρ are determined

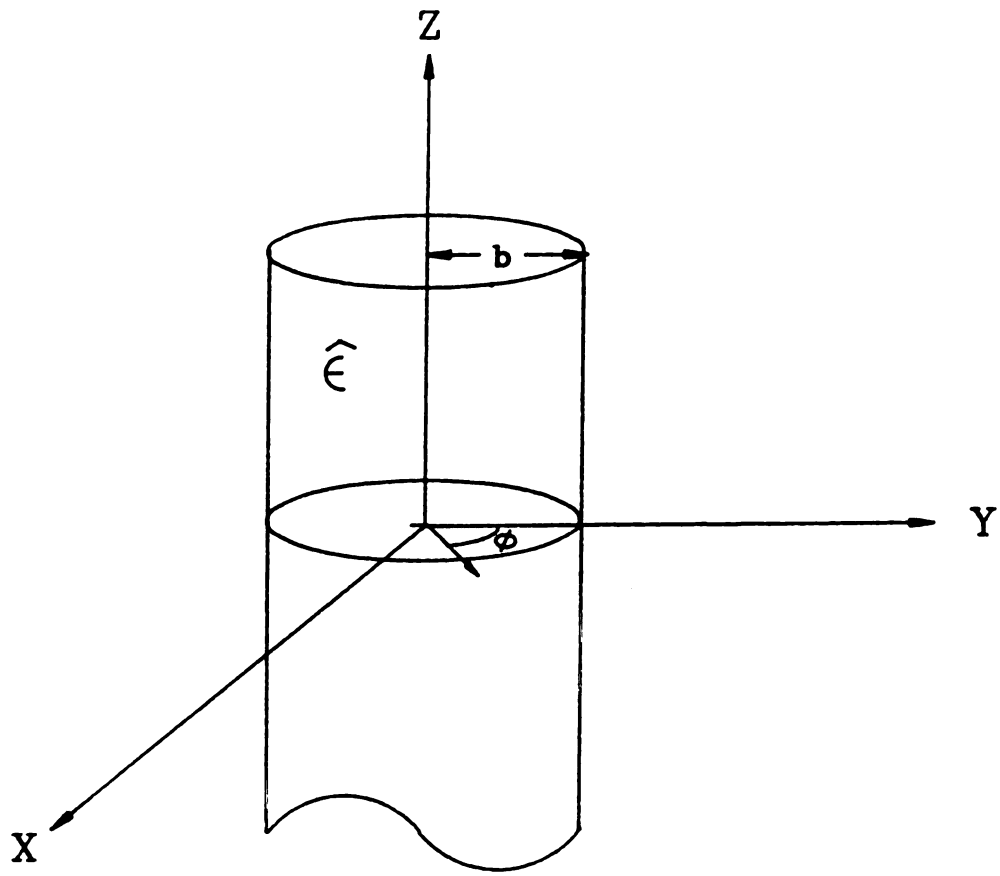

Figure 3.3 Cylindrical coordinates for the homogeneous waveguide

(1) TM_{np} modes

$$E_\rho^m = \bar{a}\ \left(\frac{j}{\omega\hat{\epsilon}}\right)\left(\nu\kappa_\rho\right) J_n'(\kappa_\rho\rho)\cos n\phi$$

$$E_\phi^m = \bar{a}\ \left(\frac{1}{j\omega\hat{\epsilon}}\right)\left(\frac{n\nu}{\rho}\right) J_n(\kappa_\rho\rho)\sin n\phi$$

$$E_z^m = \bar{a}\ \left(\frac{1}{j\omega\hat{\epsilon}}\right)\kappa_\rho^2 J_n(\kappa_\rho\rho)\cos n\phi \qquad (3.20a)$$

$$H_\rho^m = \bar{a}\ \left(-\frac{n}{\rho}\right) J_n(\kappa_\rho\rho)\sin n\phi$$

$$H_\phi^m = \bar{a}\ \left(-\kappa_\rho\right) J_n'(\kappa_\rho\rho)\cos n\phi$$

$$H_z^m = 0$$

where $\kappa_\rho = \frac{x_{np}}{b}$, x_{np} is the pth zero of J_n .

(2) TE_{np} modes

$$E_\rho^e = \bar{a}\ \left(-\frac{n}{\rho}\right) J_n(\kappa_\rho'\rho)\cos n\phi$$

$$E_\phi^e = \bar{a}\ \left(\kappa_\rho'\right) J_n'(\kappa_\rho'\rho)\sin n\phi$$

$$E_z^e = 0$$

$$H_\rho^e = \bar{a}\ \left(\frac{j}{\omega\mu}\right)\left(\nu\kappa_\rho'\right) J_n'(\kappa_\rho'\rho)\sin n\phi \qquad (3.20b)$$

$$H_\phi^e = \bar{a}\ \left(\frac{j}{\omega\mu}\right)\left(\frac{n\nu}{\rho}\right) J_n(\kappa_\rho'\rho)\cos n\phi$$

$$H_z^e = \bar{a}\ \left(\frac{1}{j\omega\mu}\right)\left(\kappa_\rho'^2\right) J_n(\kappa_\rho'\rho)\sin n\phi$$

where $\kappa_\rho' = \frac{x_{np}'}{b}$, x_{np}' is the pth zero of J_n' .

$$\nu^2 = -\kappa_z^2$$

The axial propagation factor $e^{-j\kappa_z z}$ and time variation factor $e^{j\omega t}$ are suppressed in equations 3.20a and 3.20b since they are common factors in all terms. Consequently, all the field expressions in the rest of this section imply the multiplication of the factors $e^{-j\kappa_z z}$ and $e^{j\omega t}$.

The transverse electric field of the normal modes without the arbitrary constant $\bar{a}$ can be expressed as

(1) TM_{np} modes

$$\begin{aligned}\hat{e}^{m}_{np} &= \hat{\rho}\, E^{m}_{\rho} + \hat{\phi}\, E^{m}_{\phi} \\ &= \left(\frac{j}{\omega\hat{\varepsilon}}\right)\left(\nu\kappa_{\rho}\right) J_{n}'(\kappa_{\rho}\rho)\, conn\phi\, \hat{\rho} \\ &\quad + \left(\frac{1}{j\omega\hat{\varepsilon}}\right)\left(\frac{n\nu}{\rho}\right) J_{n}(\kappa_{\rho}\rho)\, \sin n\phi\, \hat{\phi}\end{aligned} \tag{3.21}$$

(2) TE_{np} modes

$$\begin{aligned}\hat{e}^{e}_{np} &= \hat{\rho}\, E^{e}_{\rho} + \hat{\phi}\, E^{e}_{\phi} \\ &= \left(-\frac{n}{\rho}\right) J_{n}(\kappa_{\rho}'\rho)\, \cos n\phi\, \hat{\rho} \\ &\quad + \left(\kappa_{\rho}'\right) J_{n}'(\kappa_{\rho}'\rho)\, \sin n\phi\, \hat{\phi}\end{aligned} \tag{3.22}$$

The transverse magnetic fields of the normal modes without the arbitrary constant $\bar{a}$ are

(1) TM_{np} modes

$$\begin{aligned}\hat{h}^{m}_{np} &= \hat{\rho}\, H^{m}_{\rho} + \hat{\phi}\, H^{m}_{\phi} \\ &= \left(-\frac{n}{\rho}\right) J_{n}(\kappa_{\rho}\rho)\, \sin n\phi\, \hat{\rho} + \left(-\kappa_{\rho}\right) J_{n}'(\kappa_{\rho}\rho)\, \cos n\phi\, \hat{\phi}\end{aligned} \tag{3.23}$$

(2) TE_{np} modes

$$\begin{aligned}\hat{h}^{e}_{np} &= \hat{\rho}\, H^{e}_{\rho} + \hat{\phi}\, H^{e}_{\phi} \\ &= \left(\frac{j}{\omega\mu}\right)\left(\nu\kappa_{\rho}'\right) J_{n}'(\kappa_{\rho}'\rho)\, \sin n\phi\, \hat{\rho} \\ &\quad + \left(\frac{j}{\omega\mu}\right)\left(\frac{n\nu}{\rho}\right) J_{n}(\kappa_{\rho}'\rho)\, \cos n\phi\, \hat{\phi}\end{aligned} \tag{3.24}$$

In general, the transverse electric and magnetic normal modes are denoted as $\hat{e}_i$ and $\hat{h}_i$, respectively. They may be either TE or TM modes, where the subscript i represents one of the possible combinations of the mode designations, np.

To obtain the fields in regions III and IV, in which waves travel along both $+\hat{z}$ and $-\hat{z}$ directions, a homogeneous waveguide with one end shorted is considered. The transverse modal fields traveling in the $+\hat{z}$ direction are given by

$$\vec{E}_t^{+} = \bar{a}_i \, \hat{e}_i \, e^{-\gamma_i z} \tag{3.25a}$$

$$\vec{H}_t^{+} = \bar{a}_i \, \hat{h}_i \, e^{-\gamma_i z} \tag{3.25b}$$

The transverse modal fields traveling in $-\hat{z}$ direction are given by

$$\vec{E}_t^{-} = \bar{b}_i \, \hat{e}_i \, e^{\gamma_i z} \tag{3.26a}$$

$$\vec{H}_t^{-} = \bar{b}_i \, (-\hat{h}_i) \, e^{\gamma_i z} \tag{3.26b}$$

where $\bar{a}_i$ and $\bar{b}_i$ are arbitrary constants and subscript t represents the transverse field component. The transverse modal fields in the waveguide are the sum of the modal fields traveling in both directions. They are

$$\vec{E}_t = \vec{E}_t^{+} + \vec{E}_t^{-} = \hat{e}_i \, (\bar{a}_i e^{-\gamma_i z} + \bar{b}_i e^{\gamma_i z}) \tag{3.27a}$$

$$\vec{H}_t = \vec{H}_t^{+} + \vec{H}_t^{-} = \hat{h}_i \, (\bar{a}_i e^{-\gamma_i z} - \bar{b}_i e^{\gamma_i z}) \tag{3.27b}$$

As is shown in Figure 3.1, the boundary conditions in regions III and IV are that the transverse electric fields vanish on the end conducting walls. Since the approaches are similar, only region III is considered here. The transverse electric field is zero at the perfectly conducting $z = h_3$ plane, which forces equation 3.27a to be equal to zero for each mode, i.e.

$$\hat{e}_i \, (\bar{a}_i \, e^{-\gamma_i h_3} + \bar{b}_i e^{+\gamma_i h_3}) = 0 \qquad \text{for } \textit{all } \phi \text{ , and } 0 < \rho < b \tag{3.28}$$

An examination of equations 3.21 and 3.22 shows that $\hat{e}_i$ is not identically zero for all ϕ and $0 < \rho < b$. Thus, above equation is satisfied only if

$$\bar{a}_i \, e^{-\gamma_i h_3} + \bar{b}_i \, e^{+\gamma_i h_3} = 0 \tag{3.29}$$

Then $$\frac{\bar{a}_i}{\bar{b}_i} = - \frac{e^{\gamma_i h_3}}{e^{-\gamma_i h_3}} \tag{3.30}$$

Since both $\bar{a}_i$ and $\bar{b}_i$ are arbitrary constants, it makes no difference how they are chosen as long as they possess the relationship expressed in equation 3.30. One of the possible choice is

$$\bar{a}_i = c_i \, ^{\gamma_i h_3} \tag{3.31a}$$

$$\bar{b}_i = - c_i \, ^{-\gamma_i h_3} \tag{3.31b}$$

Substitution of $\bar{a}_i$ and $\bar{b}_i$ into equation 3.27a yields the transverse electric modal field

in region III.

$$\vec{E}_{t_i}^{III} = 2\, c_i\, \hat{e}_i\, \sinh\nu_i(h_3 - z)$$

Similarly, the transverse magnetic field in region III is obtained by substituting equation 3.31 into equation 3.27b. The resulting magnetic field is

$$\vec{H}_{t_i}^{III} = 2c_i\, \hat{h}_i\, \cosh\nu_i(h_3 - z)$$

where superscript III represents region III. Since $2c_i$ is an arbitrary constant corresponding to mode i, it can be replaced by some other arbitrary constant, say $\bar{a}_i$, without affecting the results. Rewriting the above equations below

$$\vec{E}_{t_i}^{III} = \bar{a}_i\, \hat{e}_i\, \sinh\nu_i(h_3 - z) \tag{3.32a}$$

$$\vec{H}_{t_i}^{III} = \bar{a}_i\, \hat{h}_i\, \cosh\nu_i(h_3 - z) \tag{3.32b}$$

Except subject to the boundary condition that the transverse electric field vanishes at $z = -h_4$, the derivation of the transverse modal fields in region IV is identical to that for region III. Substitutions of $-h_4$ for h_3 and $-\bar{b}_i$ for $\bar{a}_i$ in equation 3.32 result in the transverse electric and magnetic modal fields in region IV. These fields are

$$\vec{E}_{t_i}^{IV} = \bar{b}_i\, \hat{e}_i\, \sinh\nu_i(h_4 + z) \tag{3.33a}$$

$$\vec{H}_{t_i}^{IV} = -\bar{b}_i\, \hat{h}_i\, \cosh\nu_i(h_4 + z) \tag{3.33b}$$

The total transverse fields are the sum of all possible *TE* and *TM* modal fields. According to equations 3.32 and 3.33, the total transverse fields in regions III and IV are given in the following,

$$\vec{E}_t^{III} = \sum_i \bar{a}_i\, \hat{e}_i\, \sinh\nu_i(h_3 - z) \tag{3.34a}$$

$$\vec{H}_t^{III} = \sum_i \bar{a}_i\, \hat{e}_i\, \cosh\nu_i(h_3 - z) \tag{3.34b}$$

$$\vec{E}_t^{IV} = \sum_i \bar{b}_i\, \hat{e}_i\, \sinh\nu_i(h_4 + z) \tag{3.34c}$$

$$\vec{H}_t^{IV} = -\sum_i \bar{b}_i\, \hat{h}_i\, \cosh\nu_i(h_4 + z) \tag{3.34d}$$

3.3.3 The coaxially loaded cylindrical waveguide

The coordinate system and cross-section of a coaxially loaded cylindrical waveguide is shown in Figure 3.4. The metallic waveguide of radius b has perfectly conducting walls. Region I is a lossy dielectric rod of radius a. It has a complex relative dielectric constant $\hat{\varepsilon}_{r_1}$ and is placed symmetrically within the waveguide. Region II is the concentric area of complex relative dielectric constant $\hat{\varepsilon}_{r_2}$ between the dielectric rod and the conducting walls.

The electromagnetic fields in region I and II are the solutions to the source free Maxwell's equations subject to the boundary condition that the tangential electric and magnetic fields are continuous over the dielectric interface and the boundary condition that the tangential electric and magnetic fields are identically zero on the perfectly conducting surface at $r = b$. In section 3.3.1, the derivation of the general solutions of the source free Maxwell's equations was introduced. By choosing the appropriate forms of wave function ψ's, the EM fields in each region can be determined readily from equations 3.9 and 3.12 for TM and TE modes, respectively. According to equation 3.18, the wave functions in each of the two regions are given by

(I) Region I, $0 < \rho < a$

$$\psi^{m1} = A\, B_n^{m1}(\kappa_{\rho_1}\rho)\cos n\phi\, e^{-\gamma z}$$
$$\psi^{e1} = B\, B_n^{e1}(\kappa_{\rho_1}\rho)\sin n\phi\, e^{-\gamma z} \qquad n \neq 0 \qquad (3.35a)$$

$$\psi^{m1} = A\, B_0^{m1}(\kappa_{\rho_1}\rho)\, e^{-\gamma z}$$
$$\psi^{e1} = B\, B_0^{e1}(\kappa_{\rho_1}\rho)\, e^{-\gamma z} \qquad n = 0 \qquad (3.35b)$$

(II) Region II, $a < \rho < b$

$$\psi^{m2} = C\, B_n^{m2}(\kappa_{\rho_2}\rho)\cos n\phi\, e^{-\gamma z}$$
$$\psi^{e2} = D\, B_n^{e2}(\kappa_{\rho_2}\rho)\sin n\phi\, e^{-\gamma z} \qquad n \neq 0 \qquad (3.36a)$$

$$\psi^{m2} = C\, B_0^{m2}(\kappa_{\rho_2}\rho)\, e^{-\gamma z}$$
$$\psi^{e2} = D\, B_0^{e2}(\kappa_{\rho_2}\rho)\, e^{-\gamma z} \qquad n = 0 \qquad (3.36b)$$

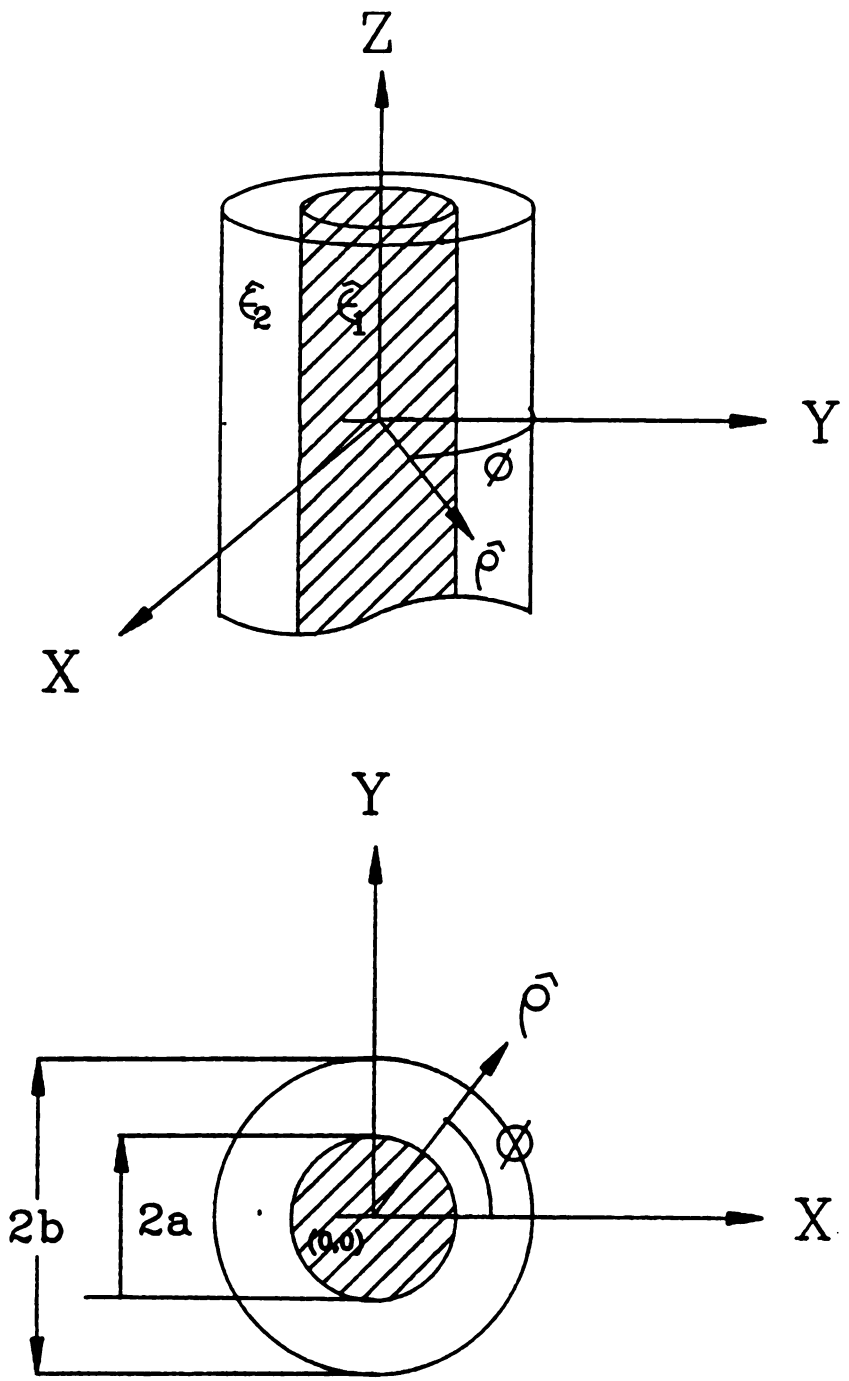

Figure 3.4 Coordinate system for a coaxially loaded cylindrical waveguide

where A, B, C, D = arbitrary constants

κ_{ρ_1}, κ_{ρ_2} = radial wavenumber in regions (I) and (II), respectively

γ = propagation constant

The superscripts m and e represent TM mode and TE mode and the superscripts 1 and 2 represent regions I and II. In each region, the γ's must satisfy the separation relationships

$$\kappa_{\rho_1}^2 = \kappa_1^2 + \gamma^2 \tag{3.37a}$$

$$\kappa_{\rho_2}^2 = \kappa_2^2 + \gamma^2 \tag{3.37b}$$

where $\kappa_1^2 = \omega^2\mu_1\varepsilon_1$, $\kappa_2^2 = \omega^2\mu_2\varepsilon_2$

$\gamma^2 = -\kappa_z^2$

In general, the electromagnetic fields which can exist within this waveguide structure are neither TE nor TM to any cylindrical coordinate except for rotationally symmetric fields, $n = 0$. These nonrotationally symmetric modes are hybrid modes, which have both axial electric and magnetic fields and angular variation of the fields ($n \neq 0$). In other words, TE and TM modes of the same angular variations couple into each other for $n \neq 0$ case, and the hybrid modes are the linear combination of these two modes. The coupling phenomenon will become clear when the boundary condition over the dielectric surface at $\rho = a$ is studied.

The factor $e^{-\gamma z}$ is suppressed from now on as this factor always occurs as a common factor in all terms. The TM mode electromagnetic fields in each of these two regions are determined by substituting the ψ^m's in equations 3.35 and 3.36 into equation 3.9. They are given by

Region (I)

(1) $n \neq 0$ (nonrotationally symmetric TM modes)

$$E_\rho^{m1} = A \left(\frac{j}{\omega\varepsilon_1}\right)\left(\kappa_{\rho_1}\gamma\right) B_n^{m1'}(\kappa_{\rho_1}\rho)\cos n\phi$$

$$E_\phi^{m1} = A \left(\frac{1}{j\omega\varepsilon_1}\right)\left(\frac{n\gamma}{\rho}\right) B_n^{m1}(\kappa_{\rho_1}\rho)\sin n\phi$$

$$E_z^{m1} = A \left(\frac{1}{j\omega\varepsilon_1} \right) \left(\kappa_{\rho_1}^2 \right) B_n^{m1}(\kappa_{\rho_1}\rho) \cos n\phi \tag{3.38}$$

$$H_\rho^{m1} = A \left(-\frac{n}{\rho} \right) B_n^{m1}(\kappa_{\rho_1}\rho) \sin n\phi$$

$$H_\phi^{m1} = A \left(-\kappa_{\rho_1} \right) B_n^{m1'}(\kappa_{\rho_1}\rho) \cos n\phi$$

$$H_z^{m1} = 0$$

(2) $n = 0$ (rotationally symmetric TM mode)

$$E_\rho^{m1} = A \left(\frac{1}{j\omega\varepsilon_1} \right) \left(\kappa_{\rho_1}\gamma \right) B_0^{m1'}(\kappa_{\rho_1}\rho)$$

$$E_\phi^{m1} = 0$$

$$E_z^{m1} = A \left(\frac{1}{j\omega\varepsilon_1} \right) \left(\kappa_{\rho_1}^2 \right) B_0^{m1}(\kappa_{\rho_1}\rho) \tag{3.39}$$

$$H_\rho^{m1} = 0$$

$$H_\phi^{m1} = A \left(-\kappa_{\rho_1} \right) B_0^{m1'}(\kappa_{\rho_1}\rho)$$

$$H_z^{m1} = 0$$

Region (II)

(1) $n \neq 0$ (nonrotationally symmetric TM modes)

$$E_\rho^{m2} = C \left(\frac{j}{\omega\varepsilon_2} \right) \left(\kappa_{\rho_2}\gamma \right) B_n^{m2'}(\kappa_{\rho_2}\rho) \cos n\phi$$

$$E_\phi^{m2} = C \left(\frac{1}{j\omega\varepsilon_2} \right) \left(\frac{n\gamma}{\rho} \right) B_n^{m2}(\kappa_{\rho_2}\rho) \sin n\phi$$

$$E_z^{m2} = C \left(\frac{1}{j\omega\varepsilon_2} \right) \left(\kappa_{\rho_2}^2 \right) B_n^{m2}(\kappa_{\rho_2}\rho) \cos n\phi \tag{3.40}$$

$$H_\rho^{m2} = C \left(-\frac{n}{\rho} \right) B_n^{m2}(\kappa_{\rho_2}\rho) \sin n\phi$$

$$H_\phi^{m2} = C \left(-\kappa_{\rho_2} \right) B_n^{m2'}(\kappa_{\rho_2}\rho) \cos n\phi$$

$$H_z^{m2} = 0$$

(2) $n = 0$ (rotationally symmetric TM modes)

$$E_\rho^{m2} = C \left(\frac{j}{\omega\varepsilon_2} \right) \left(\kappa_{\rho_2}\gamma \right) B_0^{m2'}(\kappa_{\rho_2}\rho)$$

$$E_\phi^{m2} = 0$$

$$E_z^{m2} = C \left(\frac{1}{j\omega\varepsilon_2} \right) \left(\kappa_{\rho_2}^2 \right) B_0^{m2}(\kappa_{\rho_2}\rho) \tag{3.41}$$

$$H_\rho^{m2} = 0$$

$$H_\phi^{m2} = C\ (-\kappa_{\rho_2})\ B_0^{m2'}(\kappa_{\rho_2}\rho)$$

$$H_z^{m2} = 0$$

In a similar fashion, the TE mode electromagnetic fields with unknown coefficients in each of the two regions are determined by substituting the ψ^e's in equations 3.35 and 3.36 into equation 3.12. They are

Region (I)

(1) $n \neq 0$ (nonrotationally symmetric TE modes)

$$E_\rho^{e1} = B\ \left(-\frac{n}{\rho}\right) B_n^{e1}(\kappa_{\rho_1}\rho)\cos n\phi$$

$$E_\phi^{e1} = B\ (\kappa_{\rho_1})\ B_n^{e1'}(\kappa_{\rho_1}\rho)\sin n\phi$$

$$E_z^{e1} = 0 \qquad (3.42)$$

$$H_\rho^{e1} = B\ \left(\frac{j}{\omega\mu_1}\right)(\kappa_{\rho_1}\gamma)\ B_n^{e1'}(\kappa_{\rho_1}\rho)\sin n\phi$$

$$H_\phi^{e1} = B\ \left(\frac{j}{\omega\mu_1}\right)\left(\frac{n\gamma}{\rho}\right) B_n^{e1}(\kappa_{\rho_1}\rho)\cos n\phi$$

$$H_z^{e1} = B\ \left(\frac{1}{j\omega\mu_1}\right)(\kappa_{\rho_1}^2)\ B_n^{e1}(\kappa_{\rho_1}\rho)\sin n\phi$$

(2) $n = 0$ (rotational symmetric TE modes)

$$E_\rho^{e1} = 0$$

$$E_\phi^{e1} = B\ (\kappa_{\rho_1})\ B_0^{e1'}(\kappa_{\rho_1}\rho)$$

$$E_z^{e1} = 0 \qquad (3.43)$$

$$H_\rho^{e1} = B\ \left(\frac{j}{\omega\mu_1}\right)(\kappa_{\rho_1}\gamma)\ B_0^{e1'}(\kappa_{\rho_1}\rho)$$

$$H_\phi^{e1} = 0$$

$$H_z^{e1} = B\ \left(\frac{1}{j\omega\mu_1}\right)(\kappa_{\rho_1}^2)\ B_0^{e1}(\kappa_{\rho_1}\rho)$$

Region (II)

(1) $n \neq 0$ (nonrotationally symmetric TE modes)

$$E_\rho^{e2} = D\ \left(-\frac{n}{\rho}\right) B_n^{e2}(\kappa_{\rho_2}\rho)\cos n\phi$$

$$E_\phi^{e2} = D\ (\kappa_{\rho_2})\, B_n^{e2'}(\kappa_{\rho_2}\rho)\sin n\phi$$

$$E_z^{e2} = 0 \tag{3.44}$$

$$H_\rho^{e2} = D\ \left(\frac{j}{\omega\mu_2}\right)(\kappa_{\rho_2}\gamma)\, B_n^{e2'}(\kappa_{\rho_2}\rho)\sin n\phi$$

$$H_\phi^{e2} = D\ \left(\frac{j}{\omega\mu_2}\right)\left(\frac{n\gamma}{\rho}\right) B_n^{e2}(\kappa_{\rho_2}\rho)\cos n\phi$$

$$H_z^{e2} = D\ \left(\frac{1}{j\omega\mu_2}\right)(\kappa_{\rho_2}^2)\, B_n^{e2}(\kappa_{\rho_2}\rho)\sin n\phi$$

(2) $n = 0$ (rotationally symmetric modes)

$$E_\rho^{e2} = 0$$

$$E_\phi^{e2} = D\ (\kappa_{\rho_2})\, B_0^{e2'}(\kappa_{\rho_2}\rho)$$

$$E_z^{e2} = 0 \tag{3.45}$$

$$H_\rho^{e2} = D\ \left(\frac{j}{\omega\mu_2}\right)(\kappa_{\rho_2}\gamma)\, B_0^{e2'}(\kappa_{\rho_2}\rho)$$

$$H_\phi^{e2} = 0$$

$$H_z^{e2} = D\ \left(\frac{1}{j\omega\mu_2}\right)(\kappa_{\rho_2}^2)\, B_0^{e2}(\kappa_{\rho_2}\rho)$$

The boundary conditions at the interface $\rho = a$ require that H_z, E_z, H_ϕ , and E_ϕ be continuous. The field components without superscripts represent the field components of hybrid mode, which is the sum of the TE and TM modes field components of the same angular variation. Matching the boundary conditions at $\rho = a$ leads to

(1) $E_{z_1} = E_{z_2}$

$$A\ \left(\frac{\kappa_{\rho_1}}{\kappa_{\rho_2}}\right)^2\left(\frac{\varepsilon_2}{\varepsilon_1}\right) B_n^{m1}(\kappa_{\rho_1}a) = C\ B_n^{m2}(\kappa_{\rho_2}a) \tag{3.46}$$

(2) $H_{z_1} = H_{z_2}$

$$B\ \left(\frac{\kappa_{\rho_1}}{\kappa_{\rho_2}}\right)^2 B_n^{e1}(\kappa_{\rho_1}a) = D\ \left(\frac{\mu_1}{\mu_2}\right) B_n^{e2}(\kappa_{\rho_2}a) \tag{3.47}$$

(3) $E_{\phi_1} = E_{\phi_2}$

$$A\ \left(\frac{n\gamma}{j\omega\varepsilon_1 a}\right) B_n^{m1}(\kappa_{\rho_1}a) + B\ \kappa_{\rho_1}\, B_n^{e1'}(\kappa_{\rho_1}a)$$

$$= C \left(\frac{n\gamma}{j\omega\varepsilon_2 a} \right) B_n^{m2}(\kappa_{\rho_2} a) + D \, \kappa_{\rho_2} B_n^{e2'}(\kappa_{\rho_2} a) \tag{3.48}$$

(4) $H_{\phi_1} = H_{\phi_2}$

$$A \left(-\kappa_{\rho_1} \right) B_n^{m1'}(\kappa_{\rho_1} a) + B \left(\frac{j}{\omega\mu_1} \right) \left(\frac{n\gamma}{a} \right) B_n^{e1}(\kappa_{\rho_1} a)$$

$$= C \left(-\kappa_{\rho_2} \right) B_n^{m2'}(\kappa_{\rho_2} a) + D \left(\frac{j}{\omega\mu_2} \right) \left(\frac{n\gamma}{a} \right) B_n^{e2}(\kappa_{\rho_2} a) \tag{3.49}$$

where $E_{z_1}, E_{\phi_1}, H_{z_1}, H_{\phi_1}$ = field components of hybrid modes in region I

$E_{z_2}, E_{\phi_2}, H_{z_2}, H_{\phi_2}$ = field components of hybrid modes in region II

Equations 3.46 through 3.49 are four linearly independent homogeneous equations with four unknown constants A, B, C, and D. A nontrivial solution exists only if the determinant of the coefficients of A, B, C, and D vanishes. For mathematical simplicity, define

$$F_1(\rho) = B_n^{m1}(\kappa_{\rho_1}\rho), \quad F_1 = F_1(a), \quad F_1' = F_1'(a) = \kappa_{\rho_1} B_n^{m1'}(\kappa_{\rho_1} a)$$

$$F_2(\rho) = B_n^{e1}(\kappa_{\rho_1}\rho), \quad F_2 = F_2(a), \quad F_2' = F_2'(a) = \kappa_{\rho_1} B_n^{e1'}(\kappa_{\rho_1} a)$$

$$F_3(\rho) = B_n^{m2}(\kappa_{\rho_2}\rho), \quad F_3 = F_3(a), \quad F_3' = F_3'(a) = \kappa_{\rho_2} B_n^{m2'}(\kappa_{\rho_2} a)$$

$$F_4(\rho) = B_n^{e2}(\kappa_{\rho_2}\rho), \quad F_4 = F_4(a), \quad F_4' = F_4'(a) = \kappa_{\rho_2} B_n^{e2'}(\kappa_{\rho_2} a)$$

Substitution of these expressions into equations 3.46 through 3.49 gives

$$\begin{aligned}
&A \left(\varepsilon_2 \kappa_{\rho_1}^2 \right) F_1 - C \left(\varepsilon_1 \kappa_{\rho_2}^2 \right) F_3 = 0 \\
&B \left(\mu_1 \kappa_{\rho_1}^2 \right) F_2 - D \left(\mu_1 \kappa_{\rho_2}^2 \right) F_4 = 0 \\
&A \left(\frac{n\gamma}{j\omega\varepsilon_1 a} \right) F_1 + B \, F_2' - C \left(\frac{n\gamma}{j\omega\varepsilon_2 a} \right) F_3 - D \, F_4' = 0 \\
&A \left(-F_1' \right) + B \left(\frac{j}{\omega\mu_1} \right) \left(\frac{n\gamma}{a} \right) F_2 + C \, F_3 - D \left(\frac{j}{\omega\mu_2} \right) \left(\frac{n\gamma}{a} \right) F_4 = 0
\end{aligned} \tag{3.50}$$

Hence, the characteristic equation for the dielectric loaded cylindrical waveguide in determinant form is

$$\begin{vmatrix} (\varepsilon_2\kappa_{\rho_1}^2)F_1 & 0 & -(\varepsilon_1\kappa_{\rho_2}^2)F_3 & 0 \\ 0 & (\mu_2\kappa_{\rho_1}^2)F_2 & 0 & -(\mu_1\kappa_{\rho_2}^2)F_4 \\ (\frac{n\gamma}{j\omega\varepsilon_1 a})F_1 & F_2' & -(\frac{n\gamma}{j\omega\varepsilon_2 a})F_3 & -F_4' \\ -F_1' & (\frac{j}{\omega\mu_1})(\frac{n\gamma}{a})F_2 & F_3' & -(\frac{j}{\omega\mu_2})(\frac{n\gamma}{a})F_4 \end{vmatrix} = 0 \qquad (3.51)$$

After some basic matrix operations, above expression becomes

$$\begin{vmatrix} (\varepsilon_2\kappa_{\rho_1}^2)F_1 & (\varepsilon_1\kappa_{\rho_2}^2)F_3 & 0 & 0 \\ -F_1' & -F_3' & (\frac{j}{\omega\mu_1})(\frac{n\gamma}{a})F_2 & (\frac{j}{\omega\mu_2})(\frac{n\gamma}{a})F_4 \\ (\frac{n\gamma}{j\omega\varepsilon_1 a})F_1 & (\frac{n\gamma}{j\omega\varepsilon_2 a})F_3 & F_2' & F_4' \\ 0 & 0 & (\mu_2\kappa_{\rho_1}^2)F_2 & (\mu_1\kappa_{\rho_2}^2)F_4 \end{vmatrix} = 0 \qquad (3.52)$$

The determinant is arranged in such a way that columns one through four are the coefficient column vectors of the unknown constants A, C, B, and D, respectively. Since A and C are the unknown coefficients of TM modes and B and D are the unknown coefficients of TE modes, the first and second coefficient column vectors of the determinant are corresponding to TM modes and the third and fourth coefficient column vectors of the determinant are corresponding to TE modes. With this determinant arrangement, equation 3.52 gives physical insight into the dielectric-loaded waveguide problem. It becomes manifest when $n = 0$ case is studied. Careful examination of equation 3.52 shows that for rotational symmetric modes, $n = 0$, TE and TM modes are decoupled. For $n = 0$, equation 3.52 is given by

$$\begin{vmatrix} (\varepsilon_2\kappa_{\rho_1}^2)F_1 & (\varepsilon_1\kappa_{\rho_2}^2)F_3 & 0 & 0 \\ -F_1' & -F_3' & 0 & 0 \\ 0 & 0 & F_2' & F_4' \\ 0 & 0 & (\mu_2\kappa_{\rho_1}^2)F_2 & (\mu_1\kappa_{\rho_2}^2)F_4 \end{vmatrix} = 0 \qquad (3.53)$$

which reduces to

$$\begin{vmatrix} (\varepsilon_2 \kappa_{\rho_1}^2) F_1 & (\varepsilon_1 \kappa_{\rho_2}^2) F_3 \\ -F_1' & -F_3' \end{vmatrix} \begin{vmatrix} F_2' & F_4' \\ (\mu_2 \kappa_{\rho_1}^2) F_2 & (\mu_1 \kappa_{\rho_2}^2) F_4 \end{vmatrix} = 0 \tag{3.54}$$

Note that the first determinant is the determinant of the coefficients of A and C, which are corresponding to TM modes, and the second determinant is the determinant of the coefficients of B and D, which are corresponding to TE modes. Hence the solutions of equation 3.53 separate into the solutions of the characteristic equation

$$\begin{vmatrix} (\varepsilon_2 \kappa_{\rho_1}^2) F_1 & (\varepsilon_1 \kappa_{\rho_2}^2) F_3 \\ -F_1' & -F_3' \end{vmatrix} = 0 \tag{3.55}$$

for TM modes ($n = 0$), and the solutions of the characteristic equation

$$\begin{vmatrix} F_2' & F_4' \\ (\mu_2 \kappa_{\rho_1}^2) F_2 & (\mu_1 \kappa_{\rho_2}^2) F_4 \end{vmatrix} = 0 \tag{3.56}$$

for TE modes ($n = 0$). As an observation from equations 3.48 and 3.49, it is evident that the coupling between nonrotationally symmetric ($n \neq 0$) TE and TM modes is due to the coupling across the $r = a$ boundary of the E_ϕ field components and H_ϕ field components. For rotationally symmetric modes ($n = 0$), E_ϕ components of TM modes and H_ϕ components of TE modes both are identically zero, which result in the decoupling between TE and TM modes.

Once the proper wave functions in each region are picked, the complete dielectric-loaded waveguide problem is described by the characteristic equations, equations 3.52, 3.55 and 3.56, along with the separation equations, equations 3.37a and 3.37b. In region I, the field must be finite at $\rho = 0$; hence

$$F_1(\rho) = F_2(\rho) = J_n(\kappa_{\rho_1} \rho) \tag{3.57}$$

In region (II), due to the conducting walls at $\rho = b$, the Bessel functions are in oscillatory forms. So, $F_3(\rho)$ and $F_4(\rho)$ are chosen as

$$F_3(\rho) = A_1 J_n(\kappa_{\rho_2}\rho) + A_2 N_n(\kappa_{\rho_2}\rho) \tag{3.58}$$

$$F_4(\rho) = A_3 J_n(\kappa_{\rho_2}\rho) + A_4 N_n(\kappa_{\rho_2}\rho) \tag{3.59}$$

The $N_n(\kappa_{\rho_2}\rho)$, which is the Bessel function of the second kind, is included because of no singularity point in region (II). To satisfy $E_z = 0$ at $\rho = b$, $F_3(b)$ is zero according to equation 3.40; hence

$$\frac{A_1}{A_2} = -\frac{N_n(\kappa_{\rho_2}b)}{J_n(\kappa_{\rho_2}b)} \tag{3.60}$$

Since A_1 and A_2 are arbitrary constants, it doesn't matter how they are chosen as long as equation 3.60 is satisfied. Define

$$A_1 = N_n(\kappa_{\rho_2}b)\,, \qquad A_2 = -J_n(\kappa_{\rho_2}b)$$

Substituting into equation 3.58, $F_3(\rho)$ becomes

$$F_3(\rho) = N_n(\kappa_{\rho_2}b)\,J_n(\kappa_{\rho_2}\rho) - J_n(\kappa_{\rho_2}b)\,N_n(\kappa_{\rho_2}\rho) \tag{3.61}$$

To satisfy $E_\phi = 0$ at $\rho = b$, $E_\phi^{m2} + E_\phi^{e2}$, the ϕ component of the hybrid mode electric field in region II is identically zero on the conducting walls. From equations 3.44 and 3.40 with $F_3(b) = 0$, one can conclude that $F_4'(b) = 0$. Accordingly, the relationship between A_3 and A_4 is given by

$$\frac{A_3}{A_4} = -\frac{N_n'(\kappa_{\rho_2}b)}{J_n'(\kappa_{\rho_2}b)} \tag{3.62}$$

Again, A_3 and A_4 are arbitrary constants, they can be chosen as

$$A_3 = N_n'(\kappa_{\rho_2}b)\,, \qquad A_4 = -J_n'(\kappa_{\rho_2}b)$$

Substituting into equation 3.59, $F_4(\rho)$ is expressed as,

$$F_4(\rho) = N_n'(\kappa_{\rho_2}b)\,J_n(\kappa_{\rho_2}\rho) - J_n'(\kappa_{\rho_2}b)\,N_n(\kappa_{\rho_2}\rho) \tag{3.63}$$

Instead of in the determinantal forms, the characteristic equations shall be expressed in the forms which are suitable for computer programming. After some algebraics, the determinant of equation 3.52 is carried out. It is

$$\left(\mu_1 \kappa_{\rho_2}^2 F_2' - \mu_2 \kappa_{\rho_1}^2 \frac{F_2 F_4'}{F_4}\right)\left(\varepsilon_1 \kappa_{\rho_2}^2\right) F_1' - \varepsilon_2 \kappa_{\rho_1}^2 \frac{F_1 F_3'}{F_3}\Big) + \left(\frac{n\gamma}{\omega a}\right)^2 \left(\kappa_{\rho_2}^2 - \kappa_{\rho_1}^2\right) F_1 F_2 = 0 \tag{3.64}$$

Using equations 3.57, 3.61, and 3.62, the following relations are obtained,

$$F_1' = F_2' = \kappa_{\rho_1} J_n'(\kappa_{\rho_1} a) \tag{3.65a}$$

$$\frac{F_2 F_4'}{F_4} = J_n(\kappa_{\rho_1} a)\kappa_{\rho_2} \frac{N_n'(\kappa_{\rho_2} b) J_n'(\kappa_{\rho_2} a) - J_n'(\kappa_{\rho_2} b) N_n'(\kappa_{\rho_2} a)}{N_n'(\kappa_{\rho_2} b) J_n(\kappa_{\rho_2} a) - J_n'(\kappa_{\rho_2} b) N_n(\kappa_{\rho_2} a)} \tag{3.65b}$$

$$\frac{F_1 F_3'}{F_3} = J_n(\kappa_{\rho_1} a)\kappa_{\rho_2} \frac{N_n(\kappa_{\rho_2} b) J_n'(\kappa_{\rho_2} a) - J_n(\kappa_{\rho_2} b) N_n'(\kappa_{\rho_2} a)}{N_n(\kappa_{\rho_2} b) N_n(\kappa_{\rho_2} a) - J_n(\kappa_{\rho_2} b) N_n(\kappa_{\rho_2} a)} \tag{3.65c}$$

Above expressions can be further simplified by defining

$$R_n(\kappa_{\rho_2}\rho) = J_n(\kappa_{\rho_1} a) \frac{N_n(\kappa_{\rho_2} b) J_n(\kappa_{\rho_2}\rho) - J_n(\kappa_{\rho_2} b) N_n(\kappa_{\rho_2}\rho)}{N_n(\kappa_{\rho_2} b) J_n(\kappa_{\rho_2} a) - J_n(\kappa_{\rho_2} b) N_n(\kappa_{\rho_2} a)} \tag{3.66}$$

$$P_n(\kappa_{\rho_2}\rho) = J_n(\kappa_{\rho_1} a) \frac{N_n'(\kappa_{\rho_2} b) J_n(\kappa_{\rho_2}\rho) - J_n'(\kappa_{\rho_2} b) N_n(\kappa_{\rho_2}\rho)}{N_n'(\kappa_{\rho_2} b) J_n(\kappa_{\rho_2} a) - J_n'(\kappa_{\rho_2} b) N_n(\kappa_{\rho_2} a)} \tag{3.67}$$

Substitution of these expressions into equations 3.65b and 3.65c yields

$$\frac{F_2 F_4'}{F_4} = \kappa_{\rho_2} P_n'(\kappa_{\rho_2} a) \tag{3.68}$$

$$\frac{F_1 F_3'}{F_3} = \kappa_{\rho_2} R_n'(\kappa_{\rho_2} a) \tag{3.69}$$

By means of equations 3.65a, 3.68 and 3.69, equation 3.64 is given by

$$\left(\mu_1 \frac{J_n'(\kappa_{\rho_1} a)}{\kappa_{\rho_1}} - \mu_2 \frac{Pn'(\kappa_{\rho_2} a)}{\kappa_{\rho_2}}\right)\left(\varepsilon_1 \frac{J_n'(\kappa_{\rho_1} a)}{\kappa_{\rho_1}} - \varepsilon_2 \frac{R_n'(\kappa_{\rho_2} a)}{\kappa_{\rho_2}}\right)$$

$$+ \left(\frac{n\gamma}{\omega a} \right)^2 \left(\frac{1}{\kappa_{\rho_1}^2} - \frac{1}{\kappa_{\rho_2}^2} \right)^2 J_n^2(\kappa_{\rho_1} a) = 0 \tag{3.70}$$

where $\mu_1 = \mu_0 \mu_{r1}$, $\mu_2 = \mu_0 \mu_{r2}$

$\varepsilon_1 = \varepsilon_0 \varepsilon_{r1}$, $\varepsilon_2 = \varepsilon_0 \varepsilon_{r2}$

For the purpose of numerical programming, it is convenient to express equation 3.70 in the following form,

$$\kappa_0^2 a^2 V_n W_n + U_n^2 = 0 \tag{3.71}$$

where

$$V_n = \left[\mu_{r_1} \frac{J_n'(\kappa_{\rho_1} a)}{\kappa_{\rho_1} a} - \mu_{r_2} \frac{P_n'(\kappa_{\rho_2} a)}{\kappa_{\rho_2} a} \right] \tag{3.72}$$

$$W_n = \left[\varepsilon_{r_1} \frac{J_n'(\kappa_{\rho_1} a)}{\kappa_{\rho_1} a} - \varepsilon_{r_2} \frac{R_n'(\kappa_{\rho_2} a)}{\kappa_{\rho_2} a} \right] \tag{3.73}$$

$$U_n = n\gamma a \, J_n(\kappa_{\rho_1} a) \left(\frac{1}{(\kappa_{\rho_1} a)^2} - \frac{1}{(\kappa_{\rho_2} a)^2} \right) \tag{3.74}$$

Equation 3.71 is the coaxially loaded waveguide characteristic equation for any waveguide modes. If $n = 0$, U_0 vanishes and equation 3.71 reduces to

$$V_0 W_0 = 0 \tag{3.75}$$

Similar to the previous analysis, the characteristic equations for rotationally symmetric TE and TM modes can be separated from above equation and are given, respectively, by

$$W_0 = 0 \quad \text{(TM modes for } n = 0 \text{)} \tag{3.76a}$$

$$V_0 = 0 \quad \text{(TE modes for } n = 0 \text{)} \tag{3.76b}$$

By solving the characteristic equation 3.71 and the separation equation 3.37, the complete dispersive characteristics of the dielectric-loaded waveguide can be obtained. Then, by use of these solutions, the field components in each of the two regions are determined for various modes. All the unknown coefficients A, B, C, and D for TE and TM modes shall be expressed in terms of one unknown coefficient A by solving the system equations 3.46 through 3.49. Substitution of appropriate Bessel functions for B_n's in these equations leads to

$$B = \left(\frac{\mu_1}{j\omega\varepsilon_1\mu_0} \right) \alpha A \tag{3.77}$$

$$C = \left(\frac{\varepsilon_2}{\varepsilon_1}\right) \left(\frac{\kappa_{\rho_1}}{\kappa_{\rho_2}}\right)^2 \left(\frac{J_n(\kappa_{\rho_1}a)}{N_n(\kappa_{\rho_2}b)J_n(\kappa_{\rho_2}a) - J_n(\kappa_{\rho_2}b)N_n(\kappa_{\rho_2}a)}\right) A \tag{3.78}$$

$$D = \left(\frac{\mu_2}{\mu_1} \right) \left(\frac{\kappa_{\rho_1}}{\kappa_{\rho_2}} \right)^2 \left(\frac{\mu_1}{j\omega\varepsilon_1\mu_0} \right) \alpha \cdot \left(\frac{J_n(\kappa_{\rho_1}a)}{N_n'(\kappa_{\rho_2}b)J_n(\kappa_{\rho_2}a) - J_n'(\kappa_{\rho_2}b)N_n(\kappa_{\rho_2}a)} \right) A \tag{3.79}$$

where $$\alpha = \frac{U_n}{a\, V_n} \tag{3.80}$$

The electromagnetic field components of the hybrid ($n \neq 0$), TE ($n = 0$), and TM ($n = 0$) modes can now be rewritten with one unknown coefficient A for each region in the following. Each of these field components are summarized in the equations below for regions I and II.

Region (I) ($0 < \rho < a$)

(1) Hybrid modes ($n \neq 0$)

$$E_{\rho_1} = A \left\{ \left(\frac{j}{\omega\varepsilon_1} \right) \left(\kappa_{\rho_1}\gamma \right) J_n'(\kappa_{\rho_1}\rho) + \alpha \left(-\frac{n}{\rho} \right) \left(\frac{\mu_1}{j\omega\varepsilon_1\mu_0} \right) J_n(\kappa_{\rho_1}\rho) \right\} \cos n\phi \tag{3.81a}$$

$$E_{\phi_1} = A \left\{ \left(\frac{1}{j\omega\varepsilon_1} \right) \left(\frac{n\gamma}{\rho} \right) J_n(\kappa_{\rho_1}\rho) + \left(\alpha\kappa_{\rho_1} \right) \left(\frac{\mu_1}{j\omega\varepsilon_1\mu_0} \right) J_n'(\kappa_{\rho_1}\rho) \right\} \sin n\phi \tag{3.81b}$$

$$E_{z_1} = A \left(\frac{1}{j\omega\varepsilon_1} \right) \left(\kappa_{\rho_1}^2 \right) J_n(\kappa_{\rho_1}\rho) \cos n\phi \tag{3.81c}$$

$$H_{\rho_1} = A \left\{ \left(-\frac{n}{\rho} \right) J_n(\kappa_{\rho_1}\rho) + \left(\alpha\kappa_{\rho_1}\gamma \right) \left(\frac{1}{\omega^2\mu_0\varepsilon_1} \right) J_n'(\kappa_{\rho_1}\rho) \right\} \sin n\phi \tag{3.81d}$$

$$H_{\phi_1} = A \left\{ (- \kappa_{\rho_1}) J_n'(\kappa_{\rho_1}\rho) + \alpha \left(\frac{n\gamma}{\rho} \right) \left(\frac{1}{\omega^2\mu_0\hat{\varepsilon}_1} \right) J_n(\kappa_{\rho_1}\rho) \right\} \cos n\phi \qquad (3.81e)$$

$$H_{z_1} = A \ \alpha (\kappa_{\rho_1}^2) \left(- \frac{1}{\omega^2\mu_0\hat{\varepsilon}_1} \right) J_n(\kappa_{\rho_1}\rho) \sin n\phi \qquad (3.81f)$$

(2) TM modes ($n = 0$)

$$E_{\rho_1}^{m} = A \ (\kappa_{\rho_1}\gamma) J_0'(\kappa_{\rho_1}\rho)$$

$$E_{\phi_1}^{m} = 0$$

$$E_{z_1}^{m} = A \left(\frac{1}{j\omega\hat{\varepsilon}_1} \right) (\kappa_{\rho_1}\gamma) J_0(\kappa_{\rho_1}\rho) \qquad (3.82)$$

$$H_{\rho_1}^{m} = 0$$

$$H_{\phi_1}^{m} = A \ (- \kappa_{\rho_1}) J_0'(\kappa_{\rho_1}\rho)$$

$$H_{z_1}^{m} = 0$$

(3) TE modes ($n = 0$)

$$E_{\rho_1}^{e} = 0$$

$$E_{\phi_1}^{e} = A \ (\kappa_{\rho_1}) \left(\frac{\mu_1}{j\omega\hat{\varepsilon}_1\mu_0} \right) J_0'(\kappa_{\rho_1}\rho)$$

$$E_{z_1}^{e} = 0 \qquad (3.83)$$

$$H_{\rho_1}^{e} = A \ (\kappa_{\rho_1}\gamma) \left(\frac{1}{\omega^2\mu_0\hat{\varepsilon}_1} \right) J_0'(\kappa_{\rho_1}\rho)$$

$$H_{\phi_1}^{e} = 0$$

$$H_{z_1}^{e} = A \ (\kappa_{\rho_1}^2) \left(- \frac{1}{\omega^2\mu_0\hat{\varepsilon}_1} \right) J_0(\kappa_{\rho_1}\rho)$$

Region (II) ($a < \rho < b$)

(1) Hybrid modes ($n \neq 0$)

$$E_{\rho_2} = A \left\{ \gamma \left(\frac{j}{\omega\hat{\varepsilon}_1} \right) \left(\frac{\kappa_{\rho_1}^2}{\kappa_{\rho_2}} \right) R_n'(\kappa_{\rho_2}\rho) \right.$$

$$+\alpha\left(-\frac{n}{\rho}\right)\left(\frac{\mu_2}{j\omega\hat{\varepsilon}_1\mu_0}\right)\left(\frac{\kappa_{\rho_1}}{\kappa_{\rho_2}}\right)^2 P_n(\kappa_{\rho_2}\rho)\Bigg\}\cos n\phi \tag{3.84a}$$

$$E_{\phi_2} = A\left\{\left(\frac{1}{j\omega\hat{\varepsilon}_1}\right)\left(\frac{n\gamma}{\rho}\right)\left(\frac{\kappa_{\rho_1}}{\kappa_{\rho_2}}\right)^2 R_n(\kappa_{\rho_2}\rho)\right.$$

$$\left.+\alpha\left(\frac{\mu_2}{j\omega\hat{\varepsilon}_1\mu_0}\right)\left(\frac{\kappa_{\rho_1}^{\,2}}{\kappa_{\rho_2}}\right)P_n'(\kappa_{\rho_2}\rho)\right\}\sin n\phi \tag{3.84b}$$

$$E_{z_2} = A\left(\frac{1}{j\omega\hat{\varepsilon}_1}\right)\left(\kappa_{\rho_1}^{\,2}\right)R_n(\kappa_{\rho_2}\rho)\cos n\phi \tag{3.84c}$$

$$H_{\rho_2} = A\left\{\left(-\frac{n}{\rho}\right)\left(\frac{\hat{\varepsilon}_2}{\hat{\varepsilon}_1}\right)\left(\frac{\kappa_{\rho_1}}{\kappa_{\rho_2}}\right)^2 R_n(\kappa_{\rho_2}\rho)\right.$$

$$\left.+(\alpha\gamma)\left(\frac{1}{\omega^2\mu_0\hat{\varepsilon}_1}\right)\left(\frac{\kappa_{\rho_1}^{\,2}}{\kappa_{\rho_2}}\right)P_n'(\kappa_{\rho_2}\rho)\right\}\sin n\phi \tag{3.84d}$$

$$H_{\phi_2} = A\left\{\left(-\frac{\hat{\varepsilon}_2}{\hat{\varepsilon}_1}\right)\left(\frac{\kappa_{\rho_1}^{\,2}}{\kappa_{\rho_2}}\right)R_n'(\kappa_{\rho_2}\rho)\right.$$

$$\left.+\alpha\left(\frac{n\gamma}{\rho}\right)\left(\frac{1}{\omega^2\mu_0\hat{\varepsilon}_1}\right)\left(\frac{\kappa_{\rho_1}}{\kappa_{\rho_2}}\right)^2 P_n(\kappa_{\rho_2}\rho)\right\}\cos n\phi \tag{3.84e}$$

$$H_{z_2} = A\ \alpha\left(-\frac{1}{\omega^2\mu_0\hat{\varepsilon}_1}\right)\left(\kappa_{\rho_1}^{\,2}\right)P_n(\kappa_{\rho_2}\rho)\sin n\phi \tag{3.84f}$$

(2) TM modes ($n = 0$)

$$E_{\rho_2}^{\,m} = A\ (\alpha)\left(\frac{j}{\omega\hat{\varepsilon}_1}\right)\left(\frac{\kappa_{\rho_1}^{\,2}}{\kappa_{\rho_2}}\right)R_0'(\kappa_{\rho_2}\rho)$$

$$E_{\phi_2}^{\,m} = 0$$

$$E_{z_2}^{m} = A \left(\frac{1}{j\omega\hat{\varepsilon}_1} \right) \left(\kappa_{\rho_1}^{2} \right) R_0(\kappa_{\rho_2}\rho) \tag{3.85}$$

$$H_{\rho_2}^{m} = 0$$

$$H_{\phi_2}^{m} = A \left(-\frac{\hat{\varepsilon}_2}{\hat{\varepsilon}_1} \right) \left(\frac{\kappa_{\rho_1}^{2}}{\kappa_{\rho_2}} \right) R_0'(\kappa_{\rho_2}\rho)$$

$$H_{z_2}^{m} = 0$$

(3) TE modes ($n = 0$)

$$E_{\rho_2}^{e} = 0$$

$$E_{\phi_2}^{e} = A \left(\frac{\mu_2}{j\omega\hat{\varepsilon}_1\mu_0} \right) \left(\frac{\kappa_{\rho_1}^{2}}{\kappa_{\rho_2}} \right) P_0'(\kappa_{\rho_2}\rho)$$

$$E_{z_2}^{e} = 0 \tag{3.86}$$

$$H_{\rho_2}^{e} = A \left(\gamma \right) \left(\frac{1}{\omega^2\mu_0\hat{\varepsilon}_1} \right) \left(\frac{\kappa_{\rho_1}^{2}}{\kappa_{\rho_2}} \right) P_0'(\kappa_{\rho_2}\rho)$$

$$H_{\phi_2}^{e} = 0$$

$$H_{z_2}^{e} = A \left(-\frac{1}{\omega^2\mu_0\hat{\varepsilon}_1} \right) \left(\kappa_{\rho_1}^{2} \right) P_0(\kappa_{\rho_2}\rho)$$

These expressions are the modal fields of dielectric-loaded waveguide. The total field exists in the waveguide is a linear combination of these modal fields multiplied by the propagating factor $e^{-\gamma}$. For lossless dielectric material, $\hat{\varepsilon}_r$ reduces to a real number that results in either purely real or purely imaginary γ. The modal field with real γ represents evanescent modes, which is decaying along $\pm \hat{z}$ direction, while the one with imaginary γ represents propagating mode, which propagates along $\pm \hat{z}$ direction. For lossy dielectric material, the complex valued dielectric constant $\hat{\varepsilon}_r$ gives rise to complex propagation constant γ. The modal fileds having complex γ are no longer purely propagating or evanescent mode, they are complex modes, which propagate and decay at the same time along $\pm \hat{z}$ direction. In a similar manner, the radial wavenumbers, κ_{ρ_1} and κ_{ρ_2}, may also be complex numbers when a lossy dielectric is present. Instead of pure standing wave patterns, the complex wavenumbers mean rather complicated field

distributions in the radial direction. The numerical investigations of the electromagnetic field distribution in the dielectric-loaded waveguides will be present in chapter 4.

3.4 Derivation of the cavity characteristic equation

3.4.1 Cavity-open type

In this section the cavity characteristic equation for the cavity-open type is derived by enforcing the boundary conditions in the axial direction, i.e., $\hat{z}$ direction. As is shown in Figure 3.1, the cavity consists of four regions. In each of these regions, the total fields are expressed as a linear combination of appropriate waveguide modes. The transverse electric and magnetic fields are then matched over the interfaces, i.e. $z = \pm\frac{l_2}{2}$, between the homogeneous waveguides and the coaxially loaded waveguide. This gives rise to a system composed of an infinite number of equations where each of the equations is described by an infinite sum of terms.

The total transverse electric and magnetic fields in regions III and IV are given in equations 3.34a through 3.34d. In the coaxially loaded waveguide region ($-\frac{l_2}{2} < z < \frac{l_2}{2}$), the total transverse fields are the linear combination of the transverse components of the hybrid, TE or TM modes derived in section 3.3.3. They are

$$\vec{E}_t^{\,c} = \sum_i \hat{E}_i \left(A_i\, e^{-\gamma_i z} + B_i\, e^{\gamma_i z} \right) \tag{3.87a}$$

$$\vec{H}_t^{\,c} = \sum_i \hat{H}_i \left(A_i\, e^{-\gamma_i z} - B_i\, e^{\gamma_i z} \right) \tag{3.87b}$$

where

$\gamma_i^2 = \kappa_{\rho_{1_i}}^2 - \kappa_1^2 \qquad \kappa_1^2 = \omega^2\mu_1\hat{\varepsilon}_1$ in region I

$\gamma_i^2 = \kappa_{\rho_{2_i}}^2 - \kappa_2^2 \qquad \kappa_2^2 = \omega^2\mu_2\hat{\varepsilon}_2$ in region II

A_i , B_i = arbitrary constants

$\hat{H}_i$, $\hat{E}_i$ = transverse modal fields in coaxially loaded waveguide, regions I and II

The superscript c represents coaxially loaded waveguide and the subscript i represents the possible existing mode. $\hat{H}_i$ and $\hat{E}_i$ are expressed in equations 3.81 through 3.86. In order to satisfy the continuity conditions of the transverse electric and magnetic fields over the interfaces $z = \pm \frac{l_2}{2}$, it is important that the angular variation of the fields be the same in each of the four regions shown in Figure 3.1. Also note that the fields in the cavity belong to either one of the following three categories: (1) TE modes in each of the regions I, II, III and IV; (2) TM modes in each of the regions I, II, III and IV; (3) combination of TE and TM modes in regions III and IV, and hybrid modes in regions I and II. From now on it is assumed that regions II, III and IV are filled with identical dielectrics, i.e., $\varepsilon_2 = \varepsilon_3 = \varepsilon_4$.

The boundary conditions at $z = \pm \frac{l_2}{2}$ require that the transverse electric and magnetic fields be continuous over the interfaces, i.e., at $z = + \frac{l_2}{2}$,

$$\vec{E}_t^{\,III} = \vec{E}_t^{\,c} \qquad \vec{H}_t^{\,III} = \vec{H}_t^{\,c} \tag{3.88a}$$

and at $z = - \frac{l_2}{2}$,

$$\vec{E}_t^{\,IV} = \vec{E}_t^{\,c} \qquad \vec{H}_t^{\,IV} = \vec{H}_t^{\,c} \tag{3.88b}$$

From equations 3.34 and 3.87, it is found that

$$\sum_j \tilde{a}_j \, \hat{e}_{3_j} \sinh\nu_{3_j}(h_3 - \frac{l_2}{2}) = \sum_i \hat{E}_i \, (A_i \, e^{-\gamma_i \frac{l_2}{2}} + B_i \, e^{\gamma_i \frac{l_2}{2}}) \tag{3.89a}$$

$$\sum_j \tilde{a}_j \, \hat{h}_{3_j} \cosh\nu_{3_j}(h_3 - \frac{l_2}{2}) = \sum_i \hat{H}_i \, (A_i \, e^{-\gamma_i \frac{l_2}{2}} - B_i \, e^{\gamma_i \frac{l_2}{2}}) \tag{3.89b}$$

$$\sum_j \tilde{b}_j \, \hat{e}_{4_j} \sinh\nu_{4_j}(h_4 - \frac{l_2}{2}) = \sum_i \hat{E}_i \, (A_i \, e^{\gamma_i \frac{l_2}{2}} + B_i \, e^{-\gamma_i \frac{l_2}{2}}) \tag{3.89c}$$

$$- \sum_j \tilde{b}_j \, \hat{h}_{4_j} \cosh\nu_{4_j}(h_4 - \frac{l_2}{2}) = \sum_i \hat{H}_i \, (A_i \, e^{\gamma_i \frac{l_2}{2}} - B_i \, e^{-\gamma_i \frac{l_2}{2}}) \tag{3.89d}$$

The arbitrary constants $\tilde{a}_j$, $\tilde{b}_j$ can be extracted from above expressions by means of the

orthogonality relationships of the modal fields of the homogeneous waveguide [85]. Define the inner product

$$< \hat{u}_i \ , \hat{v}_j > = \int_s \hat{u}_i \cdot \hat{v}_j^* \ ds \tag{3.90}$$

where s represents the guide cross section, $\hat{v}_j^*$ is the complex conjugate of $\hat{v}_j$. Then, the orthogonality properties of the normal waveguide mode can be made as follows,

$$< \hat{e}_j \ , \hat{e}_i > = \begin{cases} 0 & i \neq j \\ c_j & i = j \end{cases} \tag{3.91a}$$

$$< \hat{h}_j \ , \hat{h}_i > = \begin{cases} 0 & i \neq j \\ s_j & i = j \end{cases} \tag{3.91b}$$

where $\hat{e}_j \ , \hat{e}_i =$ transverse electric modal fields of TE (TM) mode

$\hat{h}_j \ , \hat{h}_i =$ transverse magnetic modal fields of TE (TM) mode

$c_j \ , s_j =$ normalization factors

It is worth noting that if $\hat{e}_j$ and $\hat{h}_j$ represent the transverse modal fields of a TE mode while $\hat{e}_i$ and $\hat{h}_i$ representing the transverse modal fields of a TM mode, then

$$< \hat{e}_j \ , \hat{e}_i > = 0 \qquad \text{for } \textit{all } i \text{ and } j \tag{3.92a}$$

$$< \hat{h}_j \ , \hat{h}_i > = 0 \qquad \text{for } \textit{all } i \text{ and } j \tag{3.92b}$$

Taking the dot product of the electric field equation 3.89a with $\hat{e}_{3_i}^*$, and the magnetic field equation 3.89b with $\hat{h}_{3_i}^*$ and integrating over the waveguide cross section, using the orthogonality relationships of the normal modes, two homogeneous linear equations with unknown constants $\tilde{a}_j$, A_i's and B_i's are obtained.

$$\tilde{a}_j \ c_{3_j} \ \sinh\nu_{3_j}(h_3 - \frac{l_2}{2}) = \sum_i (A_i \ e^{-\gamma_i \frac{l_2}{2}} + B_i \ e^{\gamma_i \frac{l_2}{2}}) < \hat{E}_i \ , \hat{e}_{3_j} > \tag{3.93a}$$

$$\tilde{a}_j \ s_{3_j} \ \cosh\nu_{3_j}(h_3 - \frac{l_2}{2}) = \sum_i (A_i \ e^{-\gamma_i \frac{l_2}{2}} - B_i \ e^{\gamma_i \frac{l_2}{2}}) < \hat{H}_i \ , \hat{h}_{3_j} > \tag{3.93b}$$

In a similar manner, equations 3.89c and 3.89d reduce to two homogeneous linear equations with unknown constants $\tilde{b}_j$, A_i's and B_i's.

$$\tilde{b}_j \, c_{4_j} \, \text{sinhv}_{4_j}(h_4 - \frac{l_2}{2}) = \sum_i (A_i \, e^{\gamma_i \frac{l_2}{2}} + B_i \, e^{-\gamma_i \frac{l_2}{2}}) < \hat{E}_i \, , \hat{e}_{4_j} > \tag{3.94a}$$

$$- \tilde{b}_j \, s_{4_j} \, \text{coshv}_{4_j}(h_4 - \frac{l_2}{2}) = \sum_i (A_i \, e^{\gamma_i \frac{l_2}{2}} - B_i \, e^{-\gamma_i \frac{l_2}{2}}) < \hat{H}_i \, , \hat{h}_{4_j} > \tag{3.94b}$$

where

$$c_{3_j} = < \hat{e}_{3_j} \, , \hat{e}_{3_j} > , \qquad s_{3_j} = < \hat{h}_{3_j} \, , \hat{h}_{3_j} > \tag{3.95a}$$

$$c_{4_j} = < \hat{e}_{4_j} \, , \hat{e}_{4_j} > , \qquad s_{4_j} = < \hat{h}_{4_j} \, , \hat{h}_{4_j} > \tag{3.95b}$$

Equations 3.93a through 3.94b can be simplified by defining

$$\bar{c}_j = c_{3_j} \, \text{sinhv}_{3_j}(h_3 - \frac{l_2}{2}) \tag{3.96a}$$

$$\bar{s}_j = s_{3_j} \, \text{coshv}_{3_j}(h_3 - \frac{l_2}{2}) \tag{3.96b}$$

$$\tilde{c}_j = c_{4_j} \, \text{sinhv}_{4_j}(h_4 - \frac{l_2}{2}) \tag{3.96c}$$

$$\tilde{s}_j = s_{4_j} \, \text{cosv}_{4_j}(h_4 - \frac{l_2}{2}) \tag{3.96d}$$

Substituting into equation 3.93a through 3.94b yields

$$\tilde{a}_j \, \bar{c}_j = \sum_i (A_i \, e^{-\gamma_i \frac{l_2}{2}} + B_i \, e^{\gamma_i \frac{l_2}{2}}) < \hat{E}_i \, , \hat{e}_{3_j} > \tag{3.97a}$$

$$\tilde{a}_j \, \bar{s}_j = \sum_i (A_i \, e^{-\gamma_i \frac{l_2}{2}} - B_i \, e^{\gamma_j \frac{l_2}{2}}) < \hat{H}_i \, , \hat{h}_{3_j} > \tag{3.97b}$$

$$\tilde{b}_j \, \tilde{c}_j = \sum_i (A_i \, e^{\gamma_i \frac{l_2}{2}} + B_i \, e^{-\gamma_i \frac{l_2}{2}}) < \hat{E}_i \, , \hat{e}_{4_j} > \tag{3.97c}$$

$$- \tilde{b}_j \, \tilde{s}_j = \sum_i (A_i \, e^{\gamma_i \frac{l_2}{2}} - B_i \, e^{-\gamma_i \frac{l_2}{2}}) < \hat{H}_i \, , \hat{h}_{4_j} > \tag{3.97d}$$

The $\tilde{a}_j$'s and $\tilde{b}_j$'s can be easily eliminated from above equations by dividing equations

3.97a and 3.97c with equations 3.97b and 3.97d, respectively.

$$\frac{\bar{c}_j}{\bar{s}_j} = \frac{\sum_i \left(A_i \, e^{-\gamma_i \frac{l_2}{2}} + B_i \, e^{\gamma_i \frac{l_2}{2}} \right)}{\sum_i \left(A_i \, e^{-\gamma_i \frac{l_2}{2}} - B_i \, e^{\gamma_i \frac{l_2}{2}} \right)} \cdot \frac{\bar{x}_{ji}}{\bar{y}_{ji}} \tag{3.98a}$$

$$-\frac{\tilde{c}_j}{\tilde{s}_j} = \frac{\sum_i \left(A_i \, e^{\gamma_i \frac{l_2}{2}} + B_i \, e^{-\gamma_i \frac{l_2}{2}} \right)}{\sum_i \left(A_i \, e^{\gamma_i \frac{l_2}{2}} - B_i \, e^{-\gamma_i \frac{l_2}{2}} \right)} \cdot \frac{\tilde{x}_{ji}}{\tilde{y}_{ji}} \tag{3.98b}$$

where

$$\bar{x}_{ji} = < \hat{E}_i \, , \hat{e}_{3_j} > , \qquad \bar{y}_{ji} = < \hat{H}_i \, , \hat{h}_{3_j} > \tag{3.98c}$$

$$\tilde{x}_{ji} = < \hat{E}_i \, , \hat{e}_{4_j} > , \qquad \tilde{y}_{ji} = < \hat{H}_i \, , \hat{h}_{4_j} > \tag{3.98d}$$

Multiplying out equations 3.98a and 3.98b gives a system of equations in A_i's and B_i's.

$$\sum_i A_i \, \bar{Y}_{ji} + B_i \, \bar{X}_{ji} = 0 \tag{3.99a}$$

$$\sum_i A_i \, \tilde{X}_{ji} + B_i \, \tilde{Y}_{ji} = 0 \tag{3.99b}$$

where

$$\bar{X}_{ji} = e^{\gamma_i \frac{l_2}{2}} \left(\bar{s}_j \, \bar{x}_{ji} + \bar{c}_j \, \bar{y}_{ji} \right) \tag{3.100a}$$

$$\bar{Y}_{ji} = e^{-\gamma_i \frac{l_2}{2}} \left(\bar{s}_j \, \bar{x}_{ji} - \bar{c}_j \, \bar{y}_{ji} \right) \tag{3.100b}$$

$$\tilde{X}_{ji} = e^{\gamma_i \frac{l_2}{2}} \left(\tilde{s}_j \, \tilde{x}_{ji} + \tilde{c}_j \, \tilde{y}_{ji} \right) \tag{3.100c}$$

$$\tilde{Y}_{ji} = e^{-\gamma_i \frac{l_2}{2}} \left(\tilde{s}_j \, \tilde{x}_{ji} - \tilde{c}_j \, \tilde{y}_{ji} \right) \tag{3.100d}$$

The matrix form of the system of infinite equations in equation 3.99 is expressed as

$$\begin{bmatrix} \tilde{X} & \tilde{Y} \\ \bar{Y} & \bar{X} \end{bmatrix} \begin{bmatrix} A \\ B \end{bmatrix} = 0 \tag{3.101}$$

where the element values of the submatrices $\bar{X}$, $\bar{Y}$, $\tilde{X}$ and $\tilde{Y}$ (i.e., $\bar{X}_{ji}$, $\bar{Y}_{ji}$, $\tilde{X}_{ji}$ and $\tilde{Y}_{ji}$) are determined with the aide of equations 3.100a through 3.100d. The subscript i represents the mode number of the dielectric-loaded waveguide modes and the subscript j represents the mode number of the homogeneous waveguide modes.

A nontrivial solution exists only if the determinant of the coefficient matrix is zero, that is

$$\det \begin{bmatrix} \bar{X} & \tilde{Y} \\ \bar{Y} & \tilde{X} \end{bmatrix} = 0 \tag{3.102}$$

The resonant frequencies of the dielectric-loaded cavity of the cavity-open type are the roots of equation 3.102. In theory, the sizes of the submatrices $\bar{X}$, $\bar{Y}$, $\tilde{X}$ and $\tilde{Y}$ are infinite because there are infinite numbers of modes existing in both the homogeneous and the dielectric-loaded waveguides, respectively. But in practice, for numerical computation, the infinite matrices $\bar{X}$, $\bar{Y}$, $\tilde{X}$ and $\tilde{Y}$ are truncated at a certain number N of the homogeneous waveguide and the dielectric-loaded waveguide modes. Then, the frequency is varied and the determinant in equation 3.102 is computed for each frequency. The frequencies giving zero value of the determinant are approximations to the resonant frequencies.

The size of the determinant N is determined by the convergence condition of the roots of the determinant, and the convergence toward the resonant frequency is achieved when the size N is increased. The size of the system is increased by taking more and more modes in the dielectric-loaded cavity. The modes in each of the three subregions are chosen as follows : for nonaxially symmetric modes ($n \neq 0$), 2N hybrid modes are taken in regions I and II, the coaxially loaded waveguide region, and N-TE modes and N-TM modes in regions III and IV; for axially symmetric modes ($n = 0$), N-TE (N-TM) modes are taken in regions I and II, and N-TE (N-TM) modes in regions III and IV.

Analytic expressions for the inner product terms of equations 3.95a, 3.95b, 3.98c and 3.98d, and the element values of the submatrices $\bar{X}$, $\bar{Y}$, $\tilde{X}$ and $\tilde{Y}$ of equations 3.100a through 3.100d are given in Appendix A.

3.4.2 Cavity-short type

The cavity-shorted type can be treated as a special case of the cavity-open type by forcing the lengths of the two homogeneous waveguides to be zero. As a result, all the analysis in previous section applies here except that l_3 and l_1 are taken to be zero while doing the numerical computation. Even though the homogeneous waveguides do not exist in the cavity-short type, the normal modes of the homogeneous waveguide are still included in the computations. The involvement of the modal fields of the homogeneous waveguides results in more numerical computation time due to the large size of system equations.

The analysis of the cavity-short type can be made more straightforward and much simpler if the homogeneous waveguide regions are excluded. As shown in Figure 1.1b, the cavity configuration of this problem can be viewed as a dielectric-loaded waveguide shorted at both ends. The axial boundary conditions require that the transverse electric and magnetic fields vanish on the conducting end plates. The coordinate system is defined in Figure 3.5. The transverse electric and magnetic fields of the dielectric-loaded waveguide are given by equations 3.87a and 3.87b. The boundary conditions of zero transverse electric field on the end conducting walls lead to

$$\sum_i \hat{E}_i \, (A_i + B_i) = 0 \qquad \text{for } \textit{all } \phi \text{ and } \rho \tag{3.103a}$$

$$\sum_i \hat{E}_i \, (A_i \, e^{-\gamma_i L} + B_i \, e^{\gamma_i L}) = 0 \qquad \text{for } \textit{all } \phi \text{ and } \rho \tag{3.103b}$$

According to equations 3.81 through 3.86, it is found that $\hat{E}_i$'s are not functions of z and do not identically equal zero over $z = L$ plane. Examination of equations 3.103a and 3.103b reveals that they are identically zero if only if

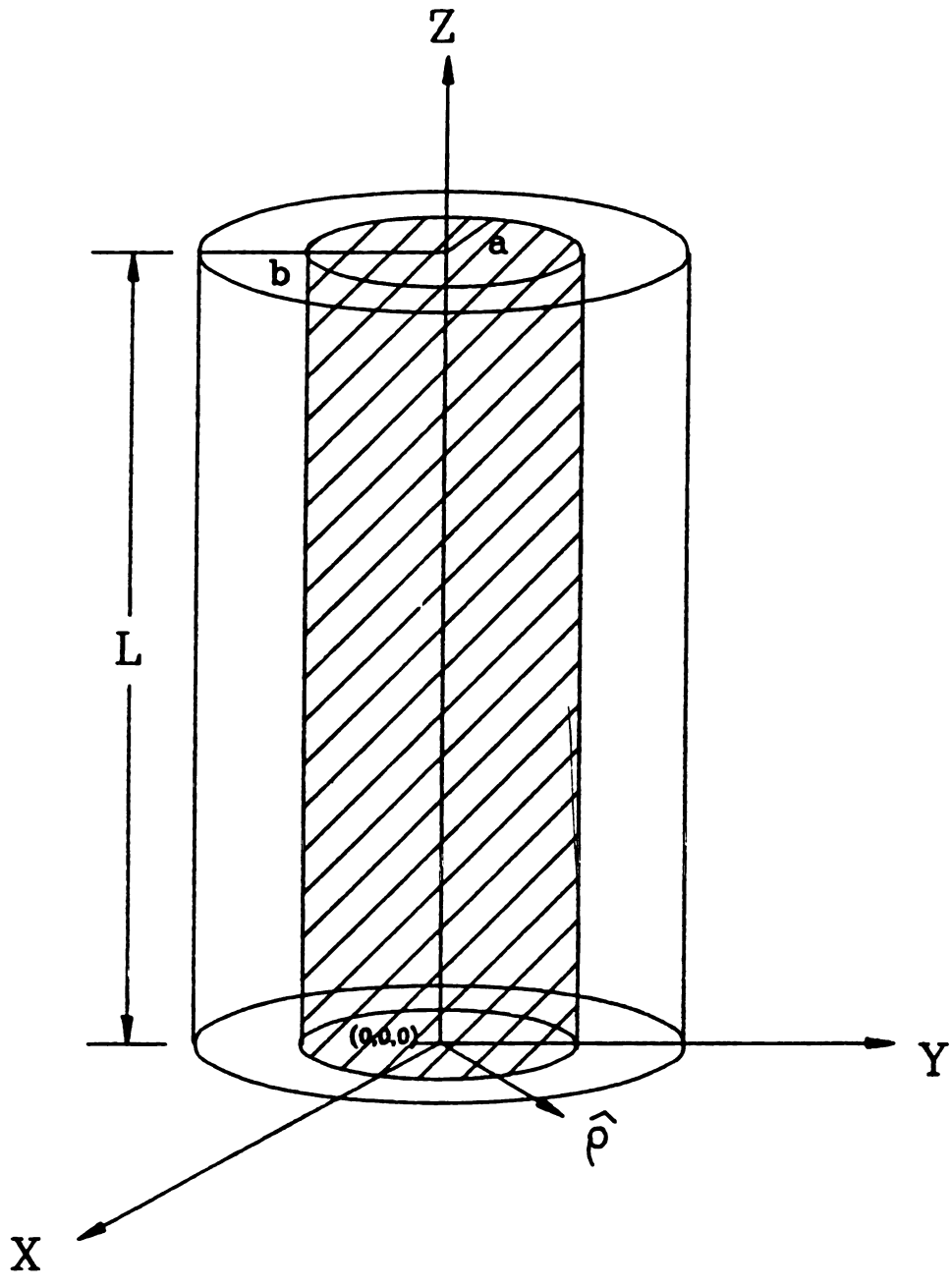

Figure 3.5 cavity–short type

$$A_i + B_i = 0 \tag{3.104a}$$

and

$$A_i\, e^{-\gamma_i L} + B_i\, e^{\gamma_i L} = 0 \tag{3.104b}$$

From above expressions and knowing that A_i and B_i are not zero for all i, the following condition is reached, that is

$$\sinh\gamma_i L = 0 \tag{3.105}$$

The subscript i is dropped from now on because above relation holds for any modes. Since $\gamma^2 = -\kappa_z^2$, equation 3.105 can be rewritten as

$$\sin\kappa_z L = 0 \tag{3.106a}$$

so $$\kappa_z = \frac{q\,\pi}{L} \qquad q = 0, 1, 2, \ldots . \tag{3.106b}$$

Substituting $-\kappa_z^2$ for γ^2 in equations 3.37a and 3.37b, the separation equations become

$$\kappa_{\rho_1}{}^2 + \kappa_z^2 = \kappa_1{}^2 \tag{3.107a}$$

$$\kappa_{\rho_2}{}^2 + \kappa_z^2 = \kappa_2{}^2 \tag{3.107b}$$

where

$$\kappa_1{}^2 = \omega^2\mu_1\varepsilon_1\,, \qquad \kappa_2{}^2 = \omega^2\mu_2\varepsilon_2 \tag{3.107c}$$

From the characteristic equation in 3.71 and the separation equations in 3.107, along with the propagation constant κ_z defined in 3.106, the resonant frequencies of the cavity-short type are readily determined. The present approach without including the two homogeneous waveguide regions avoids the computation of an infinite system equations. Apparently, the numerical computation procedures are simpler and the computation time is less.

The solutions of the cavity-short type problem are very useful for the understanding of the more general case, the cavity-open type problem. They are utilized to verify

the solutions of a special case of the cavity-open type in which the lengths of the homogeneous waveguides are zero.

3.4.3 Cavity-image type

The cavity-image type problem can be solved in many ways. It can be treated as a special case of cavity-open type problem by forcing the length of one of the homogeneous waveguide regions to be zero, say, $l_2 = 0$. Electric wall modal analysis also can be used to analyze this problem [60]. As is shown in Figure 3.6a, the transverse electric fields are zero on the conduction wall in the $z = 0$ plane, this problem becomes a cavity-open type problem with cavity length of $2L$ and s symmetric with respect to z-plane. In this section, the cavity-image type problem is considered as a coaxially loaded waveguide connected to a homogeneous waveguide, both waveguides are shorted at one end.

Following the cavity-short type analysis in previous section, the coordinate system of the cavity-image type is shown in Figure 3.6b. One of the homogeneous waveguide regions, region IV shown in Figure 3.1, is excluded form the cavity-open type problem. This problem now is subject to the boundary conditions that the transverse electric and magnetic fields are continuous over $z = \frac{l_2}{2}$ plane and the transverse electric filed is zero on the conduction end plates in $z = 0$ plane.

The transverse field components in region III are expressed in equations 3.34a and 3.34b. The transverse field components in regions I and II are expressed in equations 3.87a and 3.87b. To satisfy the boundary conditions, three homogeneous linear equations result :

$$\sum_i \hat{E}_i \left(A_i \, e^{-\gamma_i \frac{l_2}{2}} + B_i \, e^{\gamma_i \frac{l_2}{2}} \right) = \sum_j \tilde{a}_j \, \hat{e}_{3_j} \, \sinh\nu_{3_j}(h_3 - \frac{l_2}{2}) \tag{3.108a}$$

$$\sum_i \hat{H}_i \left(A_i \, e^{-\gamma_i \frac{l_2}{2}} - B_i \, e^{\gamma_i \frac{l_2}{2}} \right) = \sum_j \tilde{a}_j \, \hat{h}_{3_j} \, \cosh\nu_{3_j}(h_3 - \frac{l_2}{2}) \tag{3.108b}$$

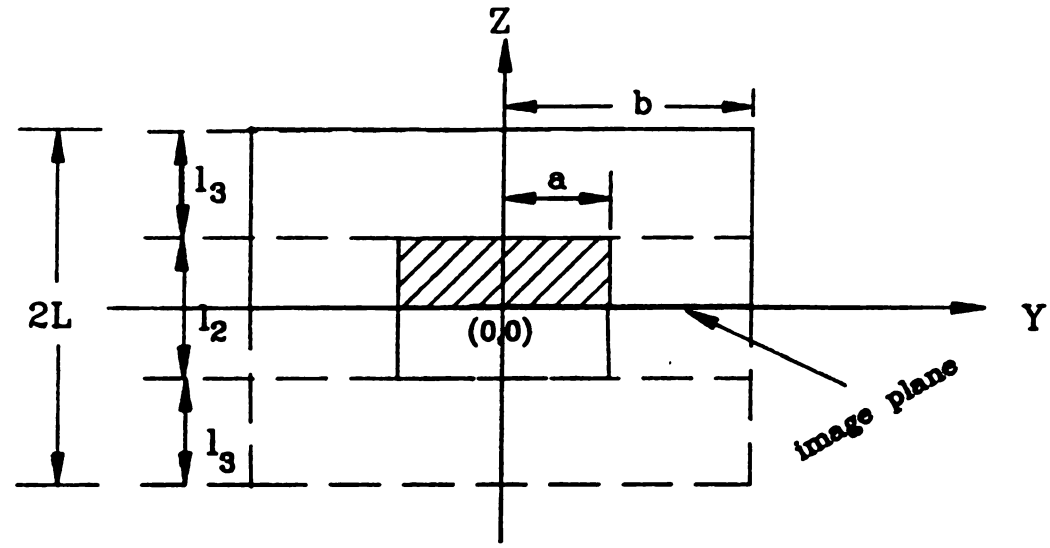

(a)

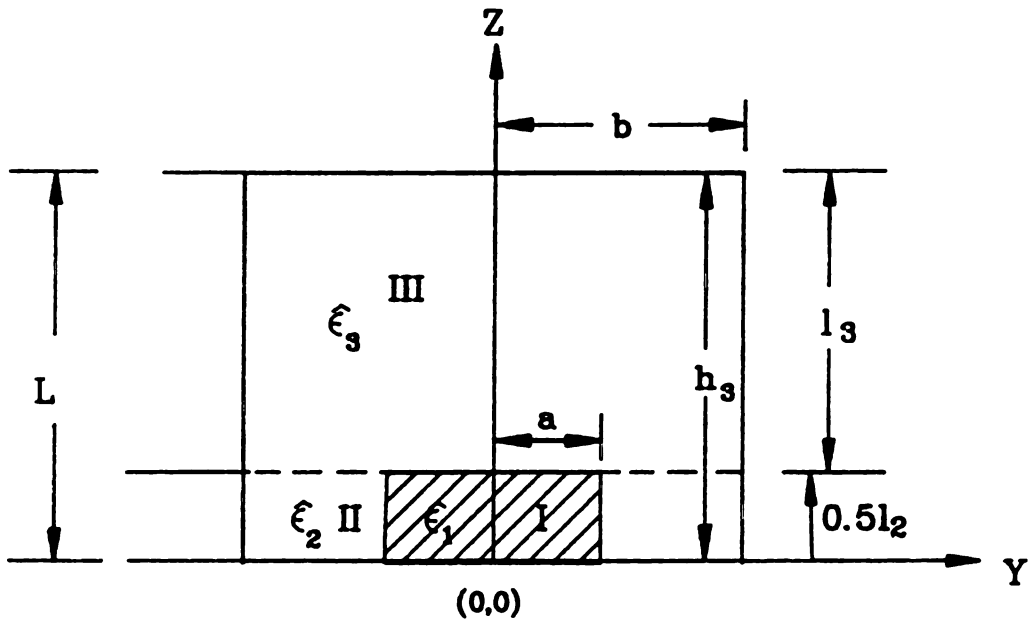

(b)

Figure 3.6 coordinate system for the cavity–image type

$$\sum_i \hat{E}_i \, (A_i + B_i) = 0 \tag{3.108c}$$

From equation 3.108c, it is obvious that

$$A_i = - B_i \qquad \text{for all i} \tag{3.109}$$

Using the orthogonality properties of the modal fields of the homogeneous waveguide and equation 3.109, two linearly independent homogeneous equation are obtained. They are

$$\bar{a}_j \, \bar{c}_j = \sum_i A_i \, (e^{-\gamma_i \frac{l_2}{2}} - e^{\gamma_i \frac{l_2}{2}}) < \hat{E}_i \, , \hat{e}_{3_j} > \tag{3.110a}$$

$$\bar{a}_j \, \bar{s}_j = \sum_i A_i \, (e^{-\gamma_i \frac{l_2}{2}} + e^{\gamma_i \frac{l_2}{2}}) < \hat{H}_i \, , \hat{h}_{3_j} > \tag{3.110b}$$

Dividing 3.110a by 3.110b yields

$$\frac{\bar{c}_j}{\bar{s}_j} = \frac{- \sum_i A_i \sinh(\gamma_i \frac{l_2}{2}) \, \bar{x}_{ji}}{\sum_i A_i \cosh(\gamma_i \frac{l_2}{2}) \, \bar{y}_{ji}} \tag{3.111}$$

where $\bar{c}_j$, $\bar{s}_j$, $\bar{x}_{ji}$ and $\bar{y}_{ji}$ are defined in equations 3.96a, 3.96b and 3.99c. After some algebraics, equation 3.111 becomes

$$\sum_i A_i \, \bar{X}_{ji} = 0 \tag{3.112a}$$

where

$$\bar{X}_{ji} = \sinh(\gamma_i \frac{l_2}{2}) \, \bar{x}_{ji} \, \bar{s}_j + \cosh(\gamma_i \frac{l_2}{2}) \, \bar{y}_{ji} \, \bar{c}_j \tag{3.112b}$$

Equation 3.112a has a nontrivial solution only if the determinant of the coefficient matrix is zero, i.e.,

$$\det \left[\bar{X}_{ji} \right] = 0 \tag{3.113}$$

where the element values $\bar{X}_{ji}$ are computed according to equation 3.112b. The

resonant frequencies of the cavity-image type problem are the roots of equation 3.113. As was discussed in section 3.4.1, for the purpose of numerical computation, a truncated system is considered in equation 3.113. The size of the matrix is determined by the convergence conditions of the resonant frequencies. More cavity modes taken into account will result in larger matrix size but better convergence.

Although solving the roots of the determinant of a truncated matrix to obtain the resonant frequencies is needed as is the case for the cavity-open type, there is a major advantage over the analysis described in section 3.4.1. Comparison of equation 3.102 and 3.113 reveals that the matrix size in the present analysis in which only one homogeneous waveguide region is considered has reduced to one half of that presented in section 3.4.1. As far as the computation time is concerned, smaller determinant size means faster numerical computation.

3.5 Stored energy, absorbed power and quality factor

3.5.1 Introduction

The energy stored in the cavity and The power losses due to the conducting walls and the dielectric losses are investigated in the following two sections. These results will be used to calculate the quality factor Q of the dielectric-loaded cavity. The power loss due to the coupling structure is neglected to avoid the complexity of input probe analysis. The cavity structure shown in Figure 3.1 will be considered throughout this section.

3.5.2 Stored energy

The energy stored U in the cavity is composed of the energies stored in the two homogeneous waveguide regions, inside the lossy dielectric cylinder, and in the region between the lossy dielectric cylinder and the conducting waveguide walls, i.e., region (II-2). Thus

$$U = U_1 + U_2 + U_3 + U_4 \tag{3.114}$$

where

U_1 = energy stored inside the lossy dielectric material, i.e., region I

U_2 = energy stored in region II

U_3 = energy stored in region III

U_4 = energy stored in region IV

The dielectric materials filling regions II, III and IV are assumed lossless. In other words, $\hat{\varepsilon}_2$, $\hat{\varepsilon}_3$ and $\hat{\varepsilon}_4$ are actually real-valued numbers. The time average electric and magnetic energies are given by,

$$U_e = \frac{1}{2\omega} \text{Im} \left(\iiint j\omega\hat{\varepsilon} \, |\vec{E}|^2 \, dv \right) \tag{3.115a}$$

$$U_m = \frac{1}{2\omega} \text{Im} \left(\iiint j\omega\mu_0 \, |\vec{H}|^2 \, dv \right) \tag{3.115b}$$

where

$$\hat{\varepsilon} = \varepsilon' - j\varepsilon''$$

Since the total energy stored in the cavity passes between electric and magnetic fields, it may be calculated by finding the energy storage in electric fields at the instant when these are a maximum. Thus the total energy is

$$U = 2U_e = \frac{1}{\omega} \text{Im} \iiint j\omega\hat{\varepsilon} \, |\vec{E}|^2 \, dv = \varepsilon' \iiint |\vec{E}|^2 \, dv \tag{3.115c}$$

The modal fields in each region were derived in sections 3.3.2 and 3.3.3, and are rewritten as:

Regions I and II : $-\frac{l_2}{2} < z < \frac{l_2}{2}$

$$\vec{E}^c = \hat{E} \left(A \, e^{-\gamma z} + B \, e^{\gamma z} \right) + \hat{z} \, E_z \left(A \, e^{-\gamma z} - B \, e^{\gamma z} \right) \tag{3.116a}$$

$$\vec{H}^c = \hat{H} \left(A \, e^{-\gamma z} - B \, e^{\gamma z} \right) + \hat{z} \, H_z \left(A \, e^{-\gamma z} + B \, e^{\gamma z} \right)$$

Region III : $\frac{l_2}{2} < z < h_3$

$$\vec{E}^{III} = \bar{a} \, \hat{e}_3 \sinh\nu_3(h_3 - z) + \hat{z} \, \bar{a} \, e_{3z} \cosh\nu_3(h_3 - z) \tag{3.116b}$$

$$\vec{H}^{III} = \tilde{a}\ \hat{h}_3 \cosh\nu_3(h_3 - z) + \hat{z}\ \tilde{a}\ h_{3z} \sinh\nu_3(h_3 - z)$$

Region IV : $-h_1 < z < -\frac{l_2}{2}$

$$\vec{E}^{IV} = \tilde{b}\ \hat{e}_4 \sinh\nu_4(h_1 + z) - \hat{z}\ \tilde{b}\ e_{4z} \cosh\nu_4(h_1 + z) \qquad (3.116c)$$

$$\vec{H}^{IV} = -\tilde{b}\ \hat{h}_4 \cosh\nu_4(h_1 + z) + \hat{z}\ \tilde{b}\ h_{4z} \sinh\nu_4(h_1 + z)$$

where e_{3z}, e_{4z}, h_{3z} and h_{4z} z-component modal fields of the homogeneous waveguides, are given in equations 3.20a and 3.20b, $\hat{e}_3$, $\hat{e}_4$, $\hat{h}_3$ and $\hat{h}_4$, transverse modal fields of the homogeneous waveguide, are given in equations 3.21 through 3.23, and E_z and H_z, z-component model fields of the dielectric-loaded waveguide, $\vec{E}$ and $\vec{H}$, transverse modal fields of the dielectric-loaded waveguide, are expressed in equations 3.81 through 3.86. A, B, $\tilde{a}$ and $\tilde{b}$ are the associated amplitudes in these subregions. Since the eigenmodes are linearly independent, the energy stored are actually the sum of the stored energies of all possible modes excited in the dielectric-loaded cavity. The subscript i is eliminated because it is understood that only one mode is considered at this time, and the result is valid for all modes.

The energy stored in each of the subregions are readily obtained from equations 3.115c through 3.116c.

$$U_1 = \varepsilon_1' \int_0^{2\pi}\int_0^{a}\int_{-\frac{l_2}{2}}^{\frac{l_2}{2}} \left\{ |\vec{E}\,(Ae^{-\gamma z} + Be^{\gamma z})|^2 + |E_z\,(Ae^{-\gamma z} - Be^{\gamma z})|^2 \right\} \rho\, d\phi\, d\rho\, dz$$

$$U_2 = \varepsilon_2' \int_0^{2\pi}\int_a^{b}\int_{-\frac{l_2}{2}}^{\frac{l_2}{2}} \left\{ |\vec{E}\,(Ae^{-\gamma z} + Be^{\gamma z})|^2 + |E_z\,(Ae^{-\gamma z} - Be^{\gamma z})|^2 \right\} \rho\, d\phi\, d\rho\, dz$$

$$U_3 = \varepsilon_3' \int_0^{2\pi}\int_0^{b}\int_{\frac{l_2}{2}}^{h_3} |\tilde{a}|^2 \left\{ |\hat{e}_3 \sinh\nu_3(h_3 - z)|^2 + |e_{3z} \cosh\nu_3(h_3 - z)|^2 \right\} \rho\, d\phi\, d\rho\, dz$$

$$U_4 = \varepsilon_4' \int_0^{2\pi}\int_0^{b}\int_{-h_1}^{-\frac{l_2}{2}} |\tilde{b}|^2 \left\{ |\hat{e}_4 \sinh\nu_4(h_1 - z)|^2 + |e_{4z} \cosh\nu_4(h_1 + z)|^2 \right\} \rho\, d\phi\, d\rho\, dz$$

The integrals can be calculated in a closed form, and the detailed derivations are given in Appendix (B). The results of the integrals are listed below,

$$U_1 = (\varepsilon_1'\pi|\kappa_{\rho_1}|^2)\left\{\left[(|c_1|^2+|c_2|^2)\cdot(\bar{t}_{n-1}+\bar{t}_{n+1})+(c_1c^*{}_2+c^*{}_1c_2)\cdot(\bar{t}_{n-1}-\bar{t}_{n+1})\right]\right.$$
$$\times\left[(|A|^2+|B|^2)S_2^+ + (AB^*+A^*B)S_2^-\right] + \left(\frac{2}{\omega^2}\frac{|\kappa_{\rho_1}|^2}{|\varepsilon_1|^2}\bar{t}_n\right)$$
$$\left.\times\left[(|A|^2+|B|^2)S_2^+ - (AB^*+A^*B)S_2^-\right]\right\} \qquad (3.117a)$$

$$U_2 = (\varepsilon_2'\pi)\frac{|\kappa_{\rho_1}|^4}{|\kappa_{\rho_2}|^2}\left\{\left[(|A|^2+|B|^2)S_2^+ + (AB^*+A^*B)S_2^-\right]\times\right.$$
$$\left[(\bar{t}_{n+1}+\bar{t}_{n-1})(|c_1|^2|A_n|^2+|c_3|^2|C_n|^2)\right.$$
$$+(g_{n-1}+g_{n+1})(|c_1|^2|B_n|^2+|c_3|^2|D_n|^2)$$
$$-(q_{n-1}+q_{n+1})(|c_1|^2A_nB_n^*+|c_3|^2C_nD_n^*)$$
$$-(q_{n-1}^*+q_{n+1}^*)(|c_1|^2A_n^*B_n+|c_3|^2C_n^*D_n)$$
$$+(\bar{t}_{n-1}-\bar{t}_{n+1})(c_1c_3^*A_nC_n^*+c_1^*c_3A_n^*C_n)$$
$$+(g_{n-1}-g_{n+1})(c_1c_3^*B_nD_n^*+c_1^*c_3B_n^*D_n)$$
$$-(q_{n-1}-q_{n+1})(c_1c_3^*A_nD_n^*+c_1^*c_3A_n^*D_n)$$
$$\left.-(q_{n-1}^*-q_{n+1}^*)(c_1c_3^*B_nC_n^*+c_1^*c_3B_n^*C_n)\right]+$$
$$\left[(|A|^2+|B|^2)S_2^+-(AB^*+A^*B)S_2^-\right]\times\left[\left(\frac{2}{\omega^2}\frac{|\kappa_{\rho_2}|^2}{|\varepsilon_1|^2}\right)\right.$$
$$\left.\left.\times(|A_n|^2\bar{t}_n+|B_n|^2g_n-A_nB_n^*q_n-A_n^*B_nq^*{}_n)\right]\right\} \qquad (3.117b)$$

$$U_3 = \left(\frac{\varepsilon_3'\pi}{2\omega^2}\right)\left(\frac{\kappa_\rho^2}{|\varepsilon_3'|^2}\right)\left\{\left[\frac{|v_3|^2}{2}(p^m{}_{n+1}+p^m{}_{n-1})(S_3^+-S_3^-)\right]+\right.$$
$$\left.\left[(\kappa_\rho^2p^m{}_n)(S_3^++S_3^-)\right]\right\} \qquad \text{——— } TM \qquad (3.117c)$$

$$= \frac{\pi \varepsilon_3'}{4} (\kappa_\rho')^2 (S_3^+ - S_3^-) (p^e_{n+1} + p^e_{n-1}) \qquad \text{——— } TE$$

$$U_4 = (\frac{\varepsilon_4' \pi}{2\omega^2}) (\frac{\kappa_\rho^2}{|\varepsilon_4'|^2}) \left\{ \left[\frac{|v_4|^2}{2} (p^m_{n+1} + p^m_{n-1}) (S_4^+ - S_4^-) \right] + \left[(\kappa_\rho^2 p^m_n) (S_4^+ + S_4^-) \right] \right\} \qquad \text{——— } TM \qquad (3.117d)$$

$$= \frac{\pi \varepsilon_4'}{4} \kappa_\rho'^2 (S_4^+ - S_4^-) \cdot (p^e_{n+1} - p^e_{n-1}) \qquad \text{——— } TE$$

where

$$p^m_n = \int_0^b \rho \, J_n^2(\kappa_\rho \rho) \, d\rho \ , \quad \kappa_\rho = \frac{x_{np}}{b}$$

$$p^e_n = \int_0^b \rho \, J_n^2(\kappa_\rho' \rho) \, \rho \ , \quad \kappa_\rho' = \frac{x_{np}'}{b}$$

$$\tilde{t}_n = \int_0^a |J_n(\kappa_{\rho_1}\rho)|^2 \, \rho \, d\rho \qquad \bar{t}_n = \int_a^b |J_n(\kappa_{\rho_2}\rho)|^2 \, \rho \, d\rho$$

$$g_n = \int_a^b |N_n(\kappa_{\rho_2}\rho)|^2 \, \rho \, d\rho$$

$$q_n = \int_a^b J_n(\kappa_{\rho_2}\rho) \, N_n^*(\kappa_{\rho_2}\rho) \, \rho \, d\rho \qquad q_n^* = \int_a^b J_n^*(\kappa_{\rho_2}\rho) \, N_n(\kappa_{\rho_2}\rho) \, \rho \, d\rho$$

$$S_2^+ = \frac{\sinh(\gamma + \gamma^*) \frac{l_2}{2}}{\gamma + \gamma^*} \qquad S_2^- = \frac{\sinh(\gamma - \gamma^*) \frac{l_2}{2}}{\gamma - \gamma^*}$$

$$S_3^+ = \frac{\sinh(v_3 + v_3^*) l_3}{v_3 + v_3^*} \qquad S_3^- = \frac{\sinh (v_3 - v_3^*) l_3}{v_3 - v_3^*}$$

$$S_4^+ = \frac{\sinh(v_4 + v_4^*) l_1}{v_4 + v_4^*} \qquad S_4^- = \frac{\sinh(v_4 - v_4^*) l_1}{v_4 - v_4^*}$$

$$A_n = \frac{J_n(\kappa_{\rho_1} a) \, N_n(\kappa_{\rho_2} b)}{N_n(\kappa_{\rho_2} b) \, J_n(\kappa_{\rho_2} a) - J_n(\kappa_{\rho_2} b) \, N_n(\kappa_{\rho_2} a)}$$

$$B_n = \frac{J_n(\kappa_{\rho_1} a) \, J_n(\kappa_{\rho_2} b)}{N_n(\kappa_{\rho_2} b) \, J_n(\kappa_{\rho_2} a) - J_n(\kappa_{\rho_2} b) \, N_n(\kappa_{\rho_2} a)}$$

$$C_n = \frac{J_n(\kappa_{\rho_1} a) \, N_n'(\kappa_{\rho_2} b)}{N_n'(\kappa_{\rho_2} b) \, J_n(\kappa_{\rho_2} a) - J_n'(\kappa_{\rho_2} b) \, N_n(\kappa_{\rho_2} a)}$$

$$D_n = \frac{J_n(\kappa_{\rho_1} a)\, J_n'(\kappa_{\rho_2} b)}{N_n'(\kappa_{\rho_2} b)\, J_n(\kappa_{\rho_2} a) - J_n'(\kappa_{\rho_2} b)\, N_n(\kappa_{\rho_2} a)}$$

The energies stored in subregions III and IV are classified according to TM and TE modes due to the fact that these modes are linearly independent in homogeneous waveguides, as a result, the stored energies corresponding to each mode can be computed separately. In the dielectric-loaded waveguide the modes are generally neither TE nor TM to any cylindrical coordinate, they are hybrid modes except for rotationally symmetric fields. Consequently, the stored energy in subregions I and II, U_1 and U_2, are computed for hybrid one. The analytic expressions for above parameters are also given in Appendix (B).

3.5.3 Absorbed power

The total power couples into the cavity in steady state includes the power dissipated on the metal walls as well as the power delivered to the lossy dielectric material. If the dielectric is of low loss material, most of the input power is dissipated in the conducting walls, as a result, the metal wall losses become dominant. On the other hand, if the cavity is loaded with high loss material, the power absorbed by the cavity is mainly the power absorbed by the dielectric material. The average density of power dissipated in the dielectric is expressed as

$$\begin{aligned} p_d &= \omega\, \varepsilon_1'' \, |\vec{E}|^2 \\ &= \omega \varepsilon_1'' \left[|\hat{E}\, (A\, e^{-\gamma z} + B\, e^{\gamma z})|^2 + |E_z\, (A\, e^{-\gamma z} - B\, e^{\gamma z})|^2 \right] \end{aligned} \tag{3.118a}$$

ant the total power absorption in the dielectric, dielectric loss, is simply a volume integral of p_d of the entire dielectric material.

$$P_d = \int_v p_d \, dv = \int_0^{2\pi} \int_0^{a} \int_{-\frac{l_2}{2}}^{\frac{l_2}{2}} \omega \varepsilon_1'' \, |\vec{E}|^2 \, \rho \, d\phi \, d\rho \, dz \tag{3.118b}$$

By close examination of the energy stored in the dielectric material U_1, it is found that the dielectric loss is the product of the stored energy in the dielectric and the loss tangent. Accordingly, the dielectric loss P_d is merely proportional to U_2 given in equation 3.116b, and that is

$$P_d = (\omega \frac{\varepsilon_1''}{\varepsilon_1'}) U_2 \tag{3.119}$$

The power lost in the metal walls is given by

$$P_c = \mathrm{Re} \int\int_s (\vec{E} \times \vec{H}^*) \cdot d\vec{s} \tag{3.120}$$

where s denotes surface of the conducting walls. Since $\vec{E}$ and $\vec{H}$ were obtained under the assumption of perfect conducting cavity walls, P_c is not exact in the sense that the boundary condition on the cavity walls are no longer true. Though the tangential component of $\vec{E}$ is not quite zero at the conductor, however, for good conductors, it is very small, the fields are only slightly perturbed from the perfect conducting wall solutions. Based on the perturbational method, the perfect conducting wall solution is used to approximate $\vec{H}$ at the conductor, and equation 3.120 is used to approximate the power dissipated in the metal walls. Thus,

$$P_c = R_s \int\int_s |H_{tan}|^2 \, ds$$

$$= P_{c2} + P_{c3} + P_{c4}$$

where

R_s = intrinsic resistance of the metal

H_{tan} = tangential component magnetic field on metal surface

P_{c2} = power dissipated in the metal walls in region II

P_{c3} = power dissipated in the metal walls in region III

P_{c4} = power dissipated in the metal walls in region IV

P_{c2}, P_{c3} and P_{c4} are given below,

$$P_{c2} = (2 \pi R_s b) \left\{ (\bar{P}_{c2} + \bar{\bar{P}}_{c2}) (|A|^2 + |B|^2) S_2^+ + (\bar{P}_{c2} - \bar{\bar{P}}_{c2}) (AB^* + A^*B) S_2^- \right\}$$

$$P_{c3} = (\frac{R_s \pi \kappa_p^2}{2}) \left\{ (b J_n'^2(\kappa_p b)) (S_3^+ + S_3^-) + (p^m{}_{n+1} + p^m{}_{n-1}) \right\} \quad \text{—— } TM$$

$$= (\frac{R_s \pi}{2 \omega^2 \mu^2}) \left\{ (b J_n^2(\kappa_p' b)) \left[(\frac{n^2 |v_3|^2}{b^2}) (S_3^+ + S_3^-) + \kappa_p'^4 (S_3^+ - S_3^-) \right] + (|v_3|^2 \kappa_p'^2) (p^e{}_{n+1} + p^e{}_{n-1}) \right\} \quad \text{—— } TE$$

$$P_{c4} = (\frac{R_s \pi \kappa_p^2}{2}) \left\{ (b J_n'^2(\kappa_p b)) (S_4^+ + S_4^-) + (p^m{}_{n+1} + p^n{}_{n-1}) \right\} \quad \text{—— } TM$$

$$= (\frac{R_s \pi}{2 \omega^2 \mu^2}) \left\{ (b J_n^2(\kappa_p' b)) \left[\frac{n^2 |v_4|^2}{b^2} (S_4^+ + S_4^-) + \kappa_p'^4 (S_4^+ - S_4^-) \right] + (|v_4|^2 \kappa_p'^2) (p^e{}_{n+1} + p^e{}_{n-1}) \right\} \quad \text{—— } TE$$

where

$$\bar{P}_{c2} = \left\{ \frac{|\varepsilon_2|^2}{|\varepsilon_1|^2} \frac{|\kappa_{\rho_1}|^4}{|\kappa_{\rho_2}|^2} |R_n'(\kappa_{\rho_2} b)|^2 + (\frac{n}{b})^2 (\frac{|\alpha \gamma|^2}{|\varepsilon_1|^2}) (\frac{1}{\omega^4 \mu_0{}^2}) \times \frac{|\kappa_{\rho_1}|^4}{|\kappa_{\rho_2}|^4} |P_n(\kappa_{\rho_2} b)|^2 - 2 \mathrm{Re} \left\{ (\frac{\varepsilon_2}{\omega^2 \mu_0 |\varepsilon_1|^2}) (\alpha \gamma)^* \times (\frac{n}{b}) (\frac{|\kappa_{\rho_1}|^4}{|\kappa_{\rho_2}|^2 \kappa_{\rho_2}{}^*}) R_n'(\kappa_{\rho_2} b) P_n^*(\kappa_{\rho_2} b) \right\} \right\}$$

$$\bar{\bar{P}}_{c2} = (\frac{1}{\omega^4 \mu_0{}^2}) \frac{|\alpha \kappa_{\rho_1}{}^2|^2}{|\varepsilon_1|^2} |P_n(\kappa_{\rho_2} b)|^2$$

3.5.4 Quality factor Q for dielectric loaded cavity

A quality factor Q for the dielectric-loaded cavity may be defined as

$$Q = \omega_0 \frac{U}{P}$$

where ω_0 is the resonant angular frequency, U is the total time-average energy stored, and P is the average power loss. As was mentioned in previous section, the time-average power dissipation consists of two parts, the power loss due to the dielectric material and that due to the metal walls, namely,

$$P = P_c + P_d$$

Consequently, it is convenient to express the Q in terms Q_c and Q_d corresponding to the losses P_c and P_d to have a better understanding of the effects of the losses in the various parts of the loaded cavity.

$$\frac{1}{Q} = \frac{1}{Q_d} + \frac{1}{Q_c}$$

where

$$Q_d = \omega_0 \frac{U}{P_d}$$

$$Q_c = \omega_0 \frac{U}{P_c}$$

ω_0 = resonant angular frequency

It is of great interest to understand how the loss of the dielectric affects the Q. Since the resonant frequency and Q are the two measurable experimental data, knowing the effects of the dielectric constants on them in theory will help interpret experimental results and improve on-line diagnosis microwave material processing techniques. From the measured Q's and resonant frequencies, the dielectric properties of the material may be predicted and the beginning and termination of the material heating cycles may be determined.

Chapter 4

NUMERICAL SOLUTIONS AND TECHNIQUES

4.1 Introduction

The characteristic equations for the dielectric-loaded waveguide and the dielectric-loaded cavity were derived in chapter 3. In this chapter these transcendental equations are solved numerically using Muller's method [71, 86]. Muller's method has been used on computers to find any prescribed number of zeros, real or complex, of an arbitrary function with remarkable success. In section 4.2.1 a brief description of Muller's method is given. In addition, the root-searching algorithm and the determination of the initial approximation is described in section 4.2.2.

The dielectric-loaded waveguide is known as a radial boundary value problem because the material discontinuities occur at the dielectric-dielectric interface in the radial direction. In section 4.3, the changes in the propagation characteristics as a function of ε_r', ε_r'' and rod radius are investigated. The ω–κ diagrams for eight waveguide modes, i.e. TM_{01}, TM_{02}, TE_{01}, TE_{02}, HE_{11}, HE_{21}, EH_{11} and EH_{12} are presented. In order to have a better understanding of the changes of the propagation characteristics as one of the waveguide parameters (ε_r', ε_r'', and rod radius) varies, the $\omega - \kappa_z$ diagrams and electromagnetic field patterns for TM_{01}, TE_{01} and HE_{11} modes are studied in more detail. The dielectric rod under study includes lossy dielectric materials and isotropic lossy cold plasma.

The dielectric-loaded cavity is referred to as axial boundary value problem due to the fact that the electromagnetic field continuity conditions are enforced over the material discontinuities in the axial direction. In section 4.4, the resonant frequency, resonant length and quality factor of the dielectric-loaded cavity for TM_{012}, TE_{012} and HE_{111} modes are determined as a function of ε_r', ε_r'' and rod radius. In addition, a comparison between the exact formulation and the perturbation technique for TM_{012} mode is

presented.

4.2 Numerical technique

4.2.1 Muller's method

Most numerical methods for searching roots of an arbitrary function can only find an isolated zero of the function once an approximation to that zero is known. These methods are not very satisfactory when all the roots are required or when good initial approximations are not available. Some methods may need the evaluation of the derivative of the function, which may turn out to be very difficult because of the complexity of the function itself.

A method, developed by Muller and hence called Muller's method, can numerically find the complex roots of an arbitrary function on computers. This method is iterative, converges almost quadratically in the vicinity of a root and does not require the computation of the derivative of the function. Both complex and real roots can be obtained even when these roots are not simple. Moreover, the method is global in the sense that an initial approximation needs not to be supplied. In addition, if an approximation to the zeros is provided, less computation time is required using Muller's method.

Muller's method is an extension of the secant method. In the secant method, a second order polynominal $P(x)$ is established by passing through $\{x_i\ , f(x_i)\}$ and $\{x_{i-1}\ , f(x_{i+1})\}$, where x_i and x_{i-1} are the approximations to a root of $f(x) = 0$. The next approximation x_{i+1} is then determined as the zero of $P(x)$. In Muller's method, the next approximation x_{i+1} is found as the zero of the parabola which goes through the three points $\{x_i\ , f(x_i)\}$, $\{x_{i-1}\ , f(x_{i-1})\}$, and $\{x_{i-2}\ , f(x_{i-2})\}$. The following parabola

$$P(x) = f(x_i) + (x - x_i)c_i + f[x_i\ , x_{i-1}\ , x_{i-2}](x - x_i)^2 \tag{4.1}$$

is an unique parabola which agrees with the function $f(x)$ at the three points x_i, x_{i-1}, x_{i-2}, with

$$c_j = f[x_i, x_{i-1}] + f[x_i, x_{i-1}, x_{i-2}](x_i - x_{i-1}) \tag{4.2}$$

$$f[x_i, x_{i-1}] = \frac{f(x_i) - f(x_{i-1})}{x_i - x_{i-1}} \tag{4.3}$$

$$f[x_i, x_{i-1}, x_{i-2}] = \frac{f[x_i, x_{i-1}] - f[x_{i-1}, x_{i-2}]}{x_i - x_{i-2}} \tag{4.4}$$

Thus any zero λ of the parabola $P(x)$ satisfies

$$\lambda - x_i = \frac{-2f(x_i)}{c_i \pm \{c_i^2 - 4f(x_i) f[x_i, x_{i-1}, x_{i-2}]\}^{1/2}} \tag{4.5}$$

The sign before the radical is selected so that the denominator is the largest in magnitude. If the right-hand side of equation (4.5) is labeled as h_{i+1}, then the next approximation to a zero of $f(x)$ is taken to be

$$x_{i+1} = x_i + h_{i+1} \tag{4.6}$$

The process is then repeated using x_{i-1}, x_i, x_{i+1} as the three basic approximations. The iteration process is stopped until either of the following criteria is satisfied for prescribed ε_1, ε_2:

$$\text{(a)} \quad \frac{|x_i - x_{i-1}|}{|x_i|} < \varepsilon_1 \tag{4.7}$$

$$\text{(b)} \quad |f(x_i)| < \varepsilon_2 \tag{4.8}$$

or until the prescribed number of iterations is exceeded.

To find more than one zero, Muller's method employs a procedure known as deflation. For instance, if one zero ξ_1 has already been found, the next zero will be calculated by working with the new function

$$f_1(x) = \frac{f(x)}{x - \xi_i} \tag{4.9}$$

If r zeros ξ_1, ..., ξ_r have already been found, the next root is obtained by working with the deflated function

$$f_r(x) = \frac{f(x)}{(x-\xi_1)(x-\xi_2)\cdots(x-\xi_r)} \tag{4.10}$$

4.2.2 Root-searching algorithm

The complex characteristic equations in equations 3.71 and 3.102 for the dielectric-loaded waveguide are solved numerically using Muller's method. There are very many roots inherent in these complex transcendental equations and each of the roots corresponds to a unique waveguide mode. As a result, how to locate the correct root for a particular mode is nontrivial. An iterative root-searching algorithm, which uses the homogeneous waveguide as the initial approximations in Muller's method, is developed here. This algorithm not only identifies each of the infinite modal solutions but also gives clear insight into how the mode changes as ε_r' and ε_r'' are varied from 1 and 0, respectively. A detailed description of the algorithm is presented in the following.

The waveguide configuration is shown in Figure 3.5. By letting the dielectric constant of the dielectric rod equal to that of the surrounding media, i.e., $\hat{\varepsilon}_1 = \hat{\varepsilon}_2$, the dielectric-loaded waveguide becomes a homogeneous waveguide. Then, using the well known homogeneous waveguide solutions as the initial approximation in the Muller's method and incrementing $\hat{\varepsilon}_1$ slightly, the solution corresponding to the new inhomogeneous waveguide is obtained. Replacing the initial approximation by the solutions just attained and incrementing $\hat{\varepsilon}_1$ again, the solution associated with the new dielectric constant of the dielectric rod is evaluated. Solutions obtained at each iteration are utilized as the approximations for the next iteration. The iterative process continues until the preset dielectric constant of the dielectric rod is reached.

Throughout this chapter, region II is assumed to be filled with air, i.e., $\hat{\varepsilon}_2 = \varepsilon_0$.

The dielectric permittivity of the dielectric rod is complex. In other words, the dielectric material in region II can be either lossless or lossy. For lossless dielectric rod, only the real part of the dielectric constant is incremented in the computation process while the imaginary part is set to be zero. For lossy dielectric material, both the imaginary and real parts of the relative dielectric constant are incremented from free space permittivity toward the preset value. However, they do not change simultaneously. The computation process is a two-step process. First, the real part of the dielectric constant is increased to a preset value, with the imaginary part equal to zero. Then, the dielectric loss is incremented and the real part remains unchanged for the rest of the computation. There is no special order to which part of the dielectric constant is incremented first. The numerical results are not affected if the imaginary part of the dielectric constant is incremented ahead of the real part and vice versa.

Note that only one part of the dielectric constant is changed and only one root is searched for at each iteration in the Muller's method. This is because there are many roots corresponding to various modes embedded in the transcendental equations. Some of the roots may exist in a very tight neighborhood. A large disturbance in the variable parameters, such as the complex dielectric constant, may result in solution corresponding to undesired mode. This is known as modal jump in this dissertation. In addition, if more than one root is desired at one time, it becomes extremely difficult to identify the modes of the solutions. Consequently, in order to avoid modal jump during computation and to be able to identify the root, only one zero at a is investigated. In order to remain on this zero a very small step size is added to the variable parameter during each iteration process. Adequate step size of the variable parameter is determined by trial and error.

The numerical technique for solving the cavity problem is identical to what just described above except that the homogeneous cavity solutions are used as the initial approximations. A three-layer dielectric- loaded cavity, as shown in Figure 3.1, is

considered here. For simplicity, it is assumed the dielectric materials in regions II, III and IV are the same and equal to air, i.e. $\hat{\varepsilon}_2 = \hat{\varepsilon}_3 = \hat{\varepsilon}_4 = \varepsilon_0$. Then the resonant frequency, resonant length and quality factor vs. ε_{r_1}', ε_{r_1}'' and dielectric load radius are obtained by following the empty cavity solutions. Note that for simplicity, in the following sections $\hat{\varepsilon}_r$ represents the complex dielectric constant in region I.

4.3 Numerical solutions

4.3.1 Introduction

The numerical solutions given in this section are divided into two categories: (1) radial boundary value problem solutions and (2) axial boundary value problem solutions. As mentioned in section 4.1, the radial boundary value problem corresponds to the coaxially loaded waveguide, and the axial boundary value problem corresponds to the dielectric-loaded cavity.

In section 4.3.2 the $\omega - \kappa_z$ solutions of various waveguide modes of the coaxially loaded waveguide are evaluated. These solutions are computed for different running parameters such as the dielectric permittivity and dielectric material radius. These dielectric-loaded waveguide solutions are essential for studying the dielectric-loaded cavity problem.

In section 4.3.3, the resonant frequency and the resonant length of the dielectric-loaded cavity are calculated as a function of ε_r', ε_r'' and load radius for various cavity modes. In addition, the influence of the complex dielectric constant and dielectric sample volume on the quality factor is also examined.

4.3.2 Radial boundary value problem (dielectric loaded waveguide problem)

In this section, the $\omega - \kappa_z$ solutions for the coaxially loaded waveguide are evaluated for eight waveguide modes, which include TM_{0p}, TE_{0p} and hybrid modes. The influence of the perfectly conducting walls on the propagation characteristics and

electromagnetic field patterns are examined by varying b/a ratio, where b is the radius of the waveguide and a is the radius of the dielectric material. In addition, the changes in the propagation characteristics and EM field patterns as a function of ε_r' and ε_r'' are studied.

The separation and characteristic equations for the coaxially loaded waveguide are given in equations 3.37 and 3.71, respectively. The subscript 1 and 2 represents the regions I and II shown in Figure 3.4. Here, nonmagnetic materials are considered, i.e., $\mu_{r_1} = \mu_{r_2} = 1$. Region II is assumed to be filled with air, i.e., $\varepsilon_{r_2} = 1$. Equations 3.37 and 3.71 are rewritten as

$$X^2 = W^2 \varepsilon_{r_1} + Z^2 \tag{4.11a}$$

$$Y^2 = W^2 + Z^2 \tag{4.11b}$$

$$W^2 V_n W_n + U_n^2 = 0 \tag{4.11c}$$

where

$$V_n = \frac{J_n'(X)}{X} - \frac{P_n'(Y)}{Y} \tag{4.12a}$$

$$W_n = \varepsilon_{r_1} \frac{J_n'(X)}{X} - \frac{R_n'(Y)}{Y} \tag{4.12b}$$

$$U_n = n\ Z\ J_n(X) \left(\frac{1}{X^2} - \frac{1}{Y_2} \right) \tag{4.12c}$$

$$X = \kappa_{\rho_1} a$$

$$Y = \kappa_{\rho_2} a$$

$$Z = \gamma a$$

$$W = \kappa_0 a$$

where P_n and R_n are expressed in equations 3.66 and 3.67, respectively. Substituting

equations 4.12a through 4.12c into equation 4.11c gives the following transcendental equation.

$$W^2 \left(\frac{J_n'(X)}{X} - \frac{P_n'(Y)}{Y} \right) \left(\varepsilon_{r_1} \frac{J_n'(X)}{X} - \frac{R_n'(Y)}{Y} \right)$$

$$+ n^2 Z^2 J_n^2(X) \left(\frac{Y^2 - X^2}{X^2 Y^2} \right)^2 = 0 \qquad (4.13a)$$

Since Y and Z can be expressed in terms of X by means of equations 4.11a and 4.11b, equation 4.13 is in fact a transcendental equation with one unknown X. X is the root to be determined. For axially symmetric modes, n=0, TE and TM modes decouple, as already been demonstrated in chapter 3. These modes of the dielectric loaded waveguide are still denoted by TM_{0p} or TE_{0p} modes, in accordance with their physical nature. The characteristic equations for these modes are given as

$$\varepsilon_{r_1} J_0'(X)\, Y - R_0'(Y)\, X = 0 \qquad \text{for } TM_{0p} \text{ modes} \qquad (4.13b)$$

$$J_0'(X)\, Y - P_0'(Y)\, X = 0 \qquad \text{for } TE_{0p} \text{ modes} \qquad (4.13c)$$

For nonaxially symmetric modes, i.e. $n \neq 0$, due to the existence of both axial electric and magnetic field components, the waveguide modes are no longer TE or TM with respect to any coordinates. These modes are called hybrid modes. They are denoted by HE_{np} or EH_{np} depending on their nature in the limiting case when the relative dielectric constant of the dielectric material is one. HE_{np} modes corresponds to TE_{np} homogeneous waveguide modes, while EH_{np} modes corresponds to TM_{np} homogeneous waveguide.

As mentioned in section 4.2.2, equation 4.13 has many roots and each root is associated with one waveguide mode. These roots are searched iteratively starting from empty waveguide solutions . The separation equations for empty cylindrical waveguide are given below.

$$(\frac{x_{np}a}{b})^2 = \kappa_0^2 a^2 + \gamma^2 a^2 \qquad \text{for } TM_{np} \text{ modes} \tag{4.14a}$$

$$(\frac{x_{np}'a}{b})^2 = \kappa_0^2 a^2 + \gamma^2 a^2 \qquad \text{for } TE_{np} \text{ modes} \tag{4.14b}$$

It is obvious that the initial approximation to X, the normalized radial wavenumber, should be

$$X_0 = \begin{cases} \frac{x_{np}}{b}a & \text{for } TM_{np} \text{ modes} \\ \frac{x_{np}'}{b}a & \text{for } TE_{np} \text{ modes} \end{cases}$$

where

a = radius of dielectric material

b = radius of circular waveguide

The subscript 0 denotes the initial approximation with the relative permittivity being one, i.e., $\varepsilon_{r_1} = 1$. X_0 is in fact the cutoff wave number of the empty cylindrical waveguide [87], normalized by the rod radius.

Complete $\omega - \kappa_z$ solutions are obtained in two steps. First, the computer program searches for roots iteratively at a fixed frequency, starting from X_0 by incrementing dielectric constant until the desired value is reached. Then, the complete $\omega - \kappa_z$ solutions are evaluated iteratively by varying incrementally the operating frequency, while the dielectric permittivity is kept constant during the computation process.

4.3.2.1 $\omega - \kappa$ diagrams and electric field patterns

4.3.2.1.1 Introduction

A waveguide loaded with lossy dielectric material has different propagation characteristics and field patterns from those of a homogeneous waveguide. It is of

interest to study the changes in the dielectric loaded waveguide modes as a function of the size and permittivity of the dielectric load, as well as the operating frequency. The waveguide under investigation in this section is a cylindrical waveguide of radius b, loaded with a lossy dielectric rod of radius a and dielectric constant $\hat{\varepsilon}_r = \varepsilon_r' - j\varepsilon_r''$, as is shown in Figure 3.4. The region between dielectric rod and waveguide walls is assumed to be an air-filled region, i.e. $\hat{\varepsilon}_2 = \varepsilon_0$. Nylon is chosen as an example dielectric material in this section. Since nylon is a low loss dielectric material with $\hat{\varepsilon}_r$ = 3.03-j0.039 and commonly used in the laboratory, the characteristics and EM field patterns of a nylon rod loaded waveguide can easily be verified by experiments. All the dielectric-loaded waveguide examples demonstrated in the following sections use either nylon rod or variations of nylon which have ε_r' or ε_r'' equal to that or nylon.

In order to show the general trend of the changes in the propagation characteristics as ε_r'' is varied, the $\omega - \kappa_z$ diagrams of eight waveguide modes are examined. These eight modes cover both axial symmetric and asymmetric modes, including two TM, two TE and four hybrid modes. Following these examples is a detailed study of the propagation characteristics and field patterns of TM_{01}, TE_{01} and HE_{11} modes as one of the waveguide parameters, such as a/b, ε_{r_1}' and ε_{r_1}'', is changed. These three modes are the frequently used waveguide modes for microwave material processing and for generating microwave plasma in the laboratory. In addition, a waveguide loaded with isotropic cold plasma rod is also examined under a variety of experimental conditions that are of interest to electric propulsion discharges and diamond thin film deposition discharges.

Since the dielectric rod is lossy, κ_z is complex, i.e. $\kappa_z = \beta - j\alpha$, where β is the propagation constant ($\beta = 2\pi / \lambda_g$) and α is the attenuation constant in the $\hat{z}$ direction. By solving equation 4.13 for $\kappa_0 a$ vs. $\kappa_z a$ with $\hat{\varepsilon}_{r_1}$, $\hat{\varepsilon}_{r_2}$ and b/a specified, $\kappa_0 a$ vs. βa and $\kappa_0 a$ vs. αa diagrams can be generated for each waveguide mode. Interesting electromagnetic properties can be obtained from such diagrams. Because of the lossy guiding

structure, the waveguide modes are either propagating modes but subject to attenuation in $\hat{z}$-direction, or nonpropagating modes, which decay exponentially in $\hat{z}$ - direction with no wave propagation. As will be seen in the following examples, α and β do not vanish simultaneously, that is, κ_z never goes to zero at any frequency. Therefore, there is no longer a well-defined cutoff frequency. In order to identify the propagating, highly damped propagating and nonpropagating modes, in this dissertation a new cutoff frequency is defined. Cutoff is defined as the frequency at which $\alpha\lambda_0=1$, where λ_0 is the free space wavelength. According to this definition, a cutoff line, on which $\alpha\lambda_0=1$, can be drawn on the $\omega - \alpha$ diagram. A cutoff point is found as the intersection of the cutoff line and $\omega - \alpha$ curve.

To demonstrate the concept of the new cutoff frequency and cutoff line, the $\omega - \kappa_z$ diagrams for a waveguide coaxially loaded with lossy dielectric rod are shown in Figures 4.1a and 4.1b for TM_{01} and TE_{01} modes, respectively, where a=1.27 cm and b=7.62 cm. As shown in Figure 4.1a, the normalized cutoff wavenumber $\kappa_c a$ is 0.36. Since β is always larger than zero, only propagating and highly damped propagating regions are identified. In the propagating region, i.e. $\kappa_0 a > 0.36$ in this case, $\beta > 0$ and $\alpha\lambda_0 < 1$. While in the highly damped propagating region, i.e. $\kappa_0 a < 0.36$, $\beta > 0$ and $\alpha\lambda_0 > 1$. In other words, in the highly damped propagating region a wave will suffer an attenuation $\geq$ 1/e after traveling one free space wavelength. Figure 4.1b depicts a case where propagating, highly damped propagating and nonpropagating modes exist. As shown, $\beta=0$ for $\kappa_0 a < 0.35$ and the cutoff line intersects $\omega - \alpha$ curve at $\kappa_0 a=0.625$, i.e. $\kappa_c a=0.625$. Hence, propagating region is in the frequency region of $\kappa_0 a > 0.625$. Highly damped propagating region is in the frequency region of $0.625 > \kappa_0 a > 0.35$. As $\kappa_0 a < 0.35$, the TE_{01} mode is in the nonpropagating region. Note that, as demonstrated in this example, a mode below cutoff could be either highly damped propagating mode or nonpropagating mode, depending on if β is zero.

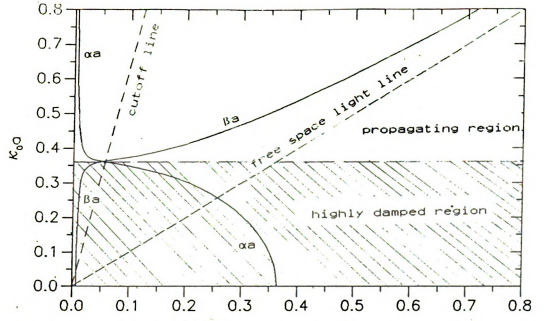

Figure 4.1a w-β and w-α diagram for TM_{01} mode, where a=1.27 cm, b=7.62 cm and ε=3.0-j0.39

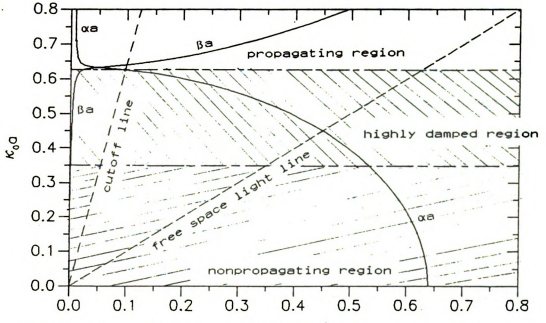

Figure 4.1b w-β and w-α diagram for TE_{01} mode, where a=1.27 cm, b=7.62 cm and ε=3.0-j1.0

4.3.2.1.2 $\omega - \kappa_z$ diagrams for eight waveguide modes

Figure 4.2a shows the $\kappa_0 a - \beta a$ diagram for a waveguide centrally loaded with a nylon rod with, $\hat{\varepsilon}_r$ = 3.03 - j0.039 and b/a = 6. Eight loaded waveguide modes, i.e. TM_{01}, TM_{02}, TE_{01}, TE_{02}, HE_{11}, HE_{21}, EH_{11} and EH_{21}, are presented in this figure. The $\omega - \beta$ diagram is separated into three regions by the free space light line and the light line in dielectric material, in this case nylon. Region 1 is the fast wave portion of the curves, in which the phase velocity v_ϕ of electromagnetic modes is faster than the speed of light in free space. Region 2 is the slow wave region where v_ϕ is smaller than the speed of light in free space.

The electromagnetic modes illustrated in Figure 4.2a exhibit both slow wave and fast wave characteristics. HE_{11}, TM_{01}, TE_{01} and HE_{21} cross the free space light line and become slow waves before $\kappa_0 a$ = 2.1. While TM_{02}, TE_{02}, EH_{21}, and EH_{11} remain in fast wave region for $\kappa_0 a$ < 3.6. Not until $\kappa_0 a$ reaches 4.9, do all these four modes cross into the slow wave region. Above $\kappa_0 a$ = 4.9, all the slow wave modes shown in Figure 4.2a approach the nylon light line asymptotically as frequency is increased. It is important to note that even though TE_{01} and EH_{11} are degenerate modes in homogeneous waveguide, they possess different dispersion characteristics and different cutoff frequency as will be seen later in Figure 4.2b in the dielectric loaded waveguide. As shown, TE_{01} mode becomes a slow wave at $\kappa_0 a$ = 1.6, while EH_{11} does not cross the free space light line until $\kappa_0 a$ = 4.9.

Figure 4.2b depicts the $\omega - \alpha$ diagram for the case of Figure 4.2a. It is seen that the relative order of the cutoff frequencies among these eight modes are essentially the same as in the limiting case when these modes are empty waveguide modes, i.e. when $\hat{\varepsilon}_{r_1} = \hat{\varepsilon}_{r_2}$ = 1.0. However, the cutoff frequencies are shifted down from the empty waveguide mode. For instance, the normalized cutoff wavenumber $\kappa_c a$ is 0.4 for empty waveguide TM_{01} mode but is 0.368 for loaded waveguide TM_{01} mode. When compared with Figure 4.2a, it is found that for propagating modes, slow waves are

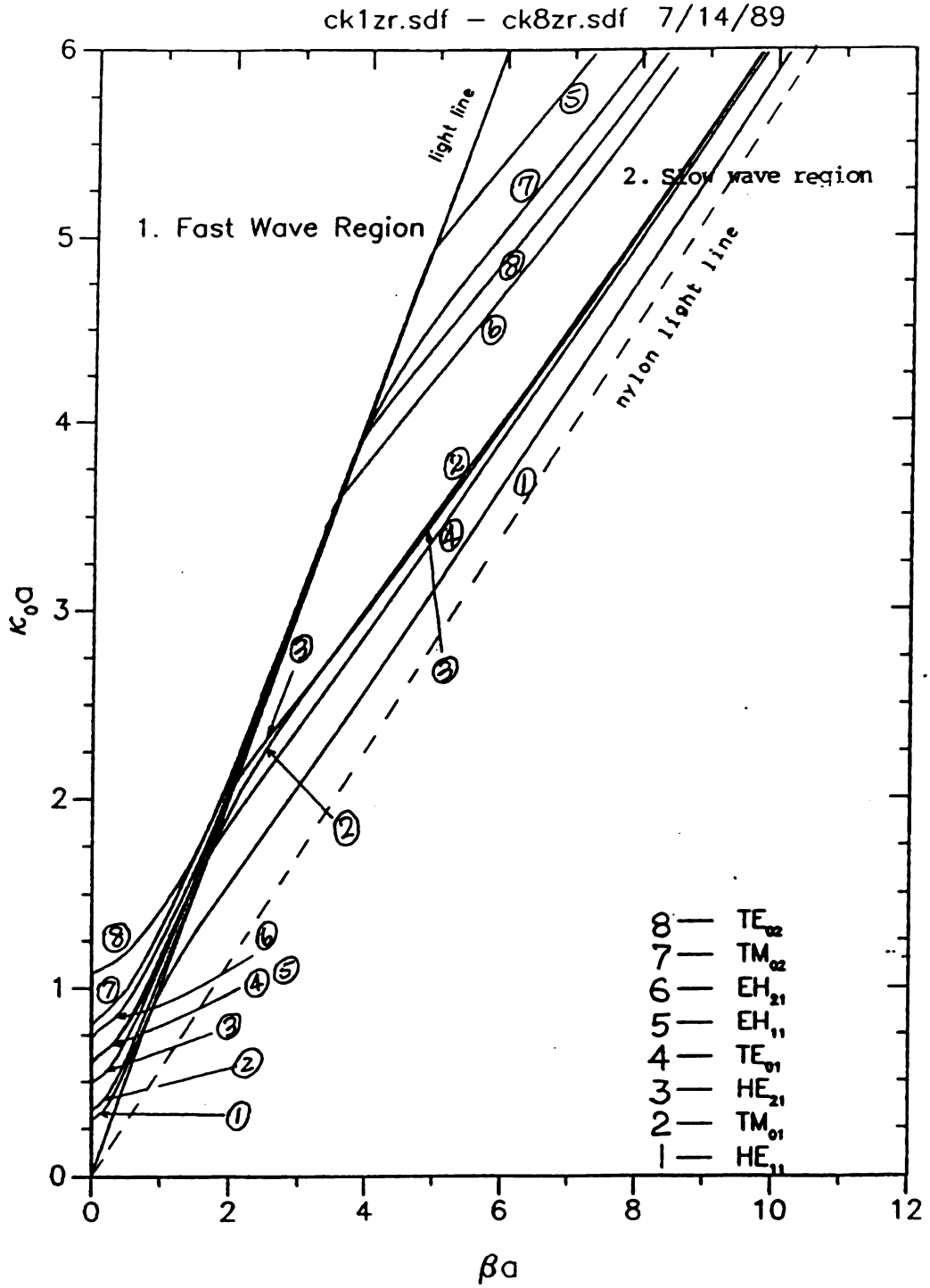

Figure 4.2a w-β diagram for eight waveguide modes, b/a=6, ε=3.03-j0.039.

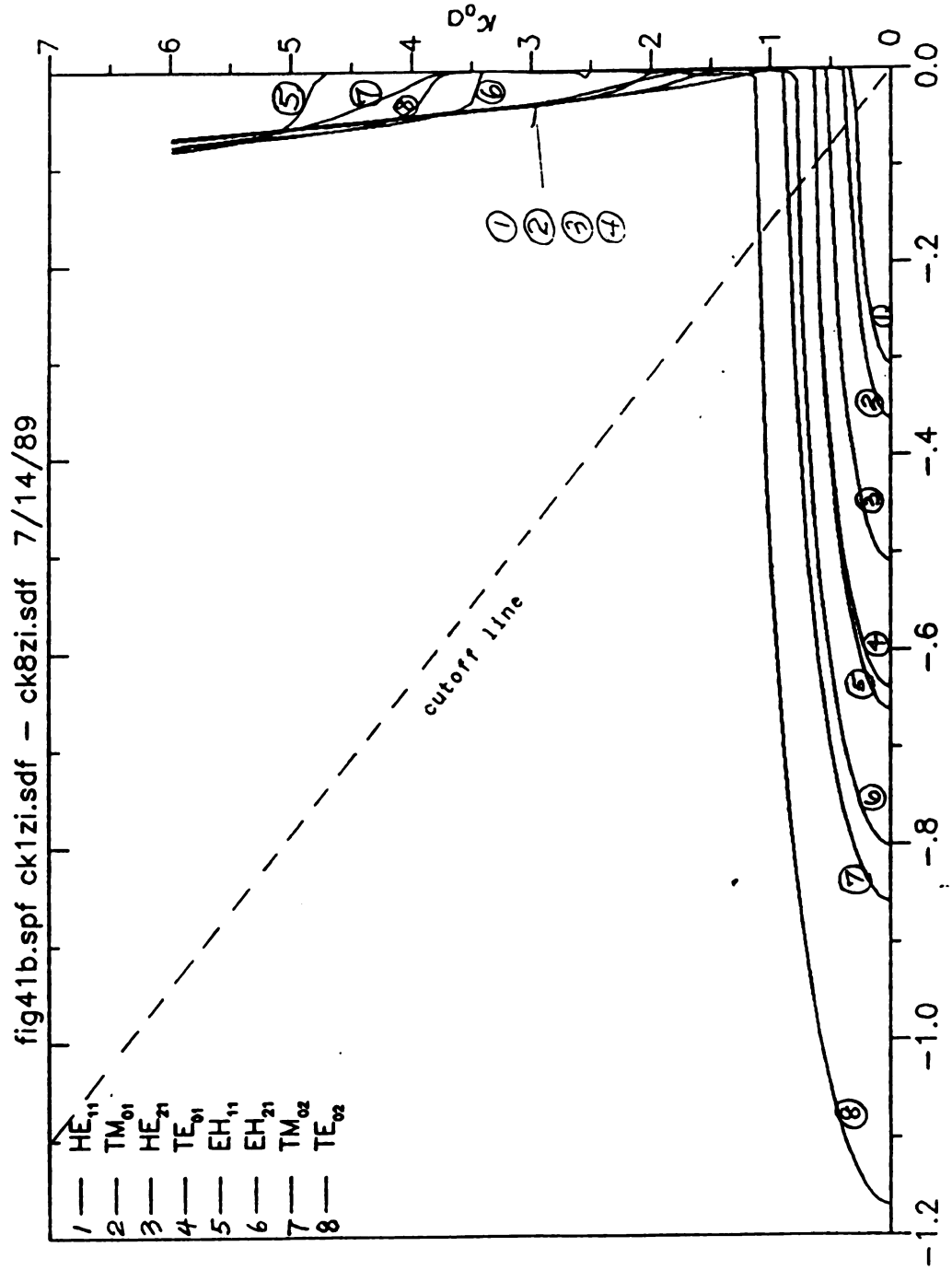

Figure 4.2b w-α diagram for eight waveguide modes, b/a=6, ε=3.03-j0.039.

subject to larger attenuation than fast waves at a fixed $\kappa_0 a$, while each mode is highly damped below cutoff due to $\alpha\lambda_0 > 1.0$. Also seen is that above cutoff α increases when the mode crosses over into the slow wave region.

Because the operating frequency considered in this dissertation is primarily at 2.45 GHz and the largest radius of the dielectric materials is less than 5 cm, $\kappa_0 a$ for all cases is well below 3.0. As a result, all the $\omega - \kappa_z$ diagrams under investigation later are limited to $\kappa_0 a$ less than 3.0.

The dispersion characteristics of a waveguide loaded with lossy dielectric rod varies as the dielectric loss of the dielectric rod changes. Figure 4.3a displays the $\omega - \beta$ diagrams for a rod having $\hat{\varepsilon}_r$ = 3.30 -j0.39 with b/a = 6. The dielectric loss is ten times larger than the case of Figure 4.2. It is observed that HE_{11}, TM_{01}, TE_{01}, and EH_{21} still become slow waves as frequency increases. In comparison with Figure 4.2a, the crossings where these modes enter slow wave region change little for HE_{11}, TM_{01} and TE_{01} modes but become lowered for EH_{21}. How the crossings are influenced by the change in ε_r'' will be more clear later in this section when the propagation characteristics of TM_{01}, TE_{01} and HE_{11} are examined for a wider range of ε_r''. TM_{02}, TE_{02}, HE_{21} and EH_{11} stay in fast wave region for $\kappa_0 a < 3.0$. A close look at the low frequency portion, as shown in Figure 4.3b, discloses that the propagation constants for TM_{01}, TM_{02} and EH_{11} modes do not vanish for any frequency. This type of phenomenon has been previously found in plasma loaded cylindrical waveguide [88].

In comparison with Figure 4.2b, the $\omega - \alpha$ curves displayed in Figure 4.3c show that the cutoff frequencies for all modes are shifted up slightly as ε_r'' is increased. Except for HE_{21} mode, the attenuation constants above cutoff for each mode is increased. At high frequency, i.e. $\kappa_0 a > 2.0$, the increases in α for HE_{11}, TM_{01}, TE_{01} and EH_{21} are much larger than those for EH_{11}, TM_{02} and TE_{02}. For example, at $\kappa_0 a$ = 2.5, the attenuation αa for TM_{01} grows from 0.025 to 0.22, while the αa for TM_{02} increases from almost zero to approximate 0.006 as ε_r'' is changed from 0.039 to 0.39. By

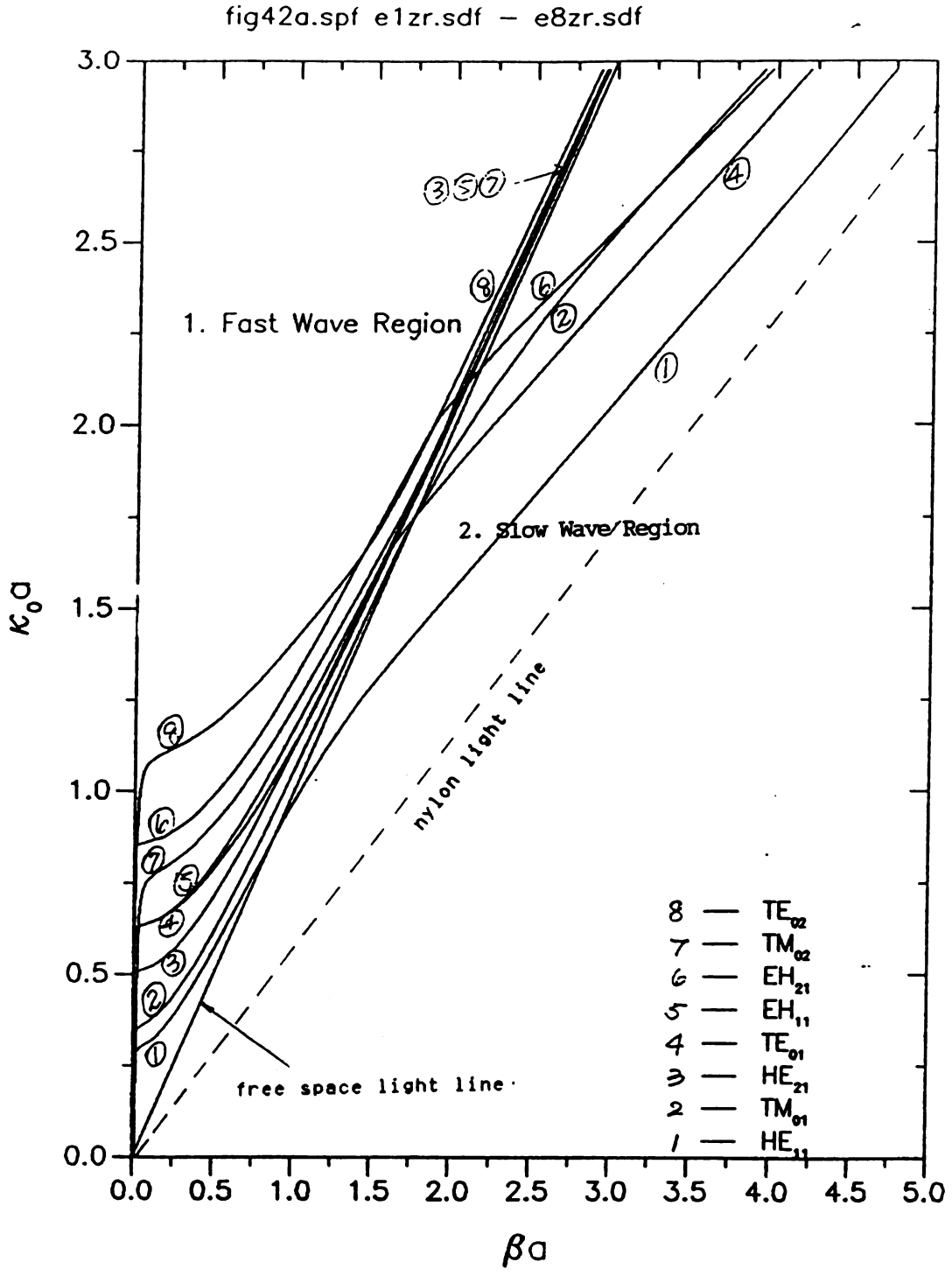

Figure 4.3a w-β diagram for eight waveguide modes, b/a=6, ε=3.03-j0.39.

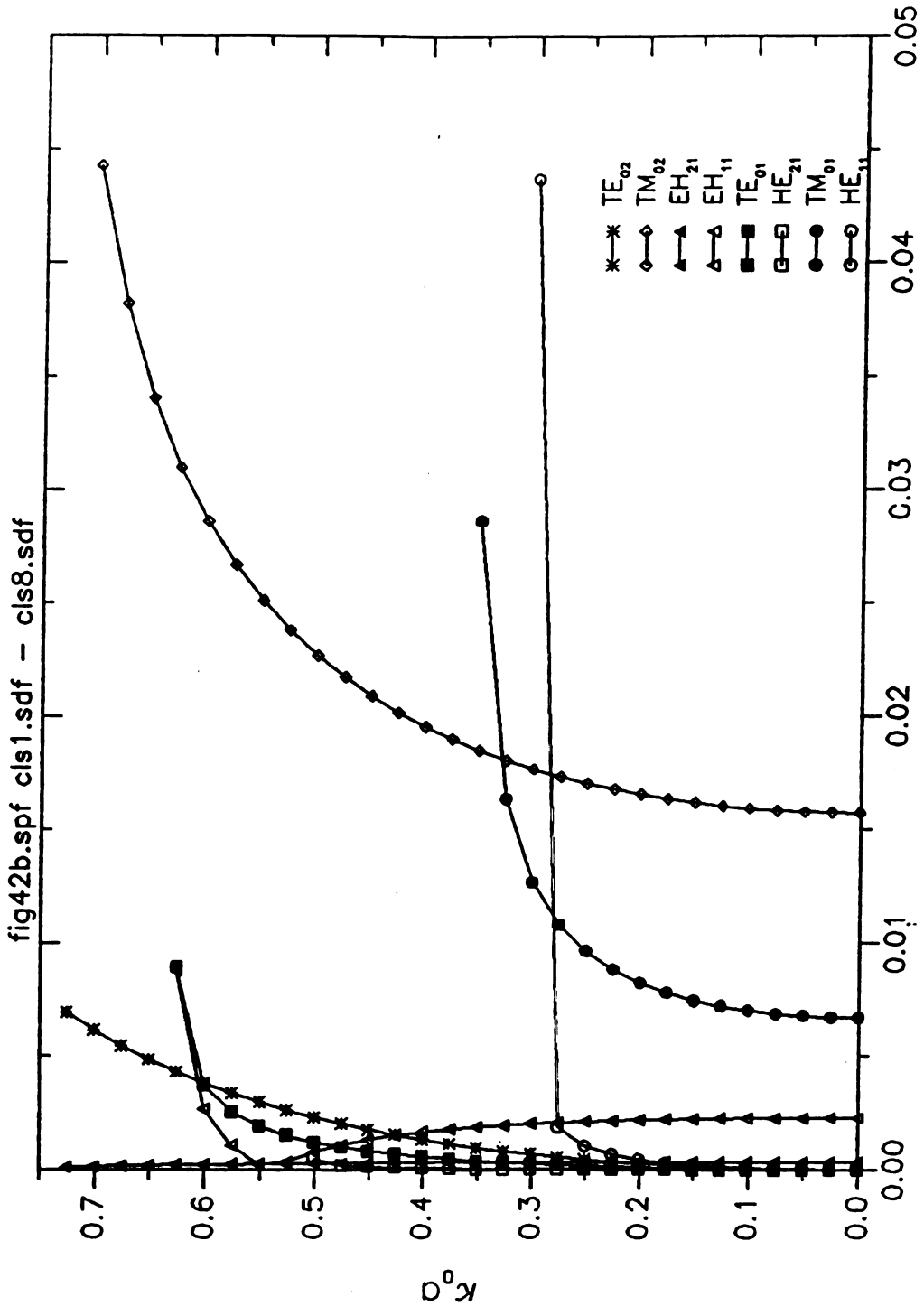

Figure 4.3b Low frequency portions of the w-β diagram for eight waveguide modes, b/a=6, ε=3.03-j0.39.

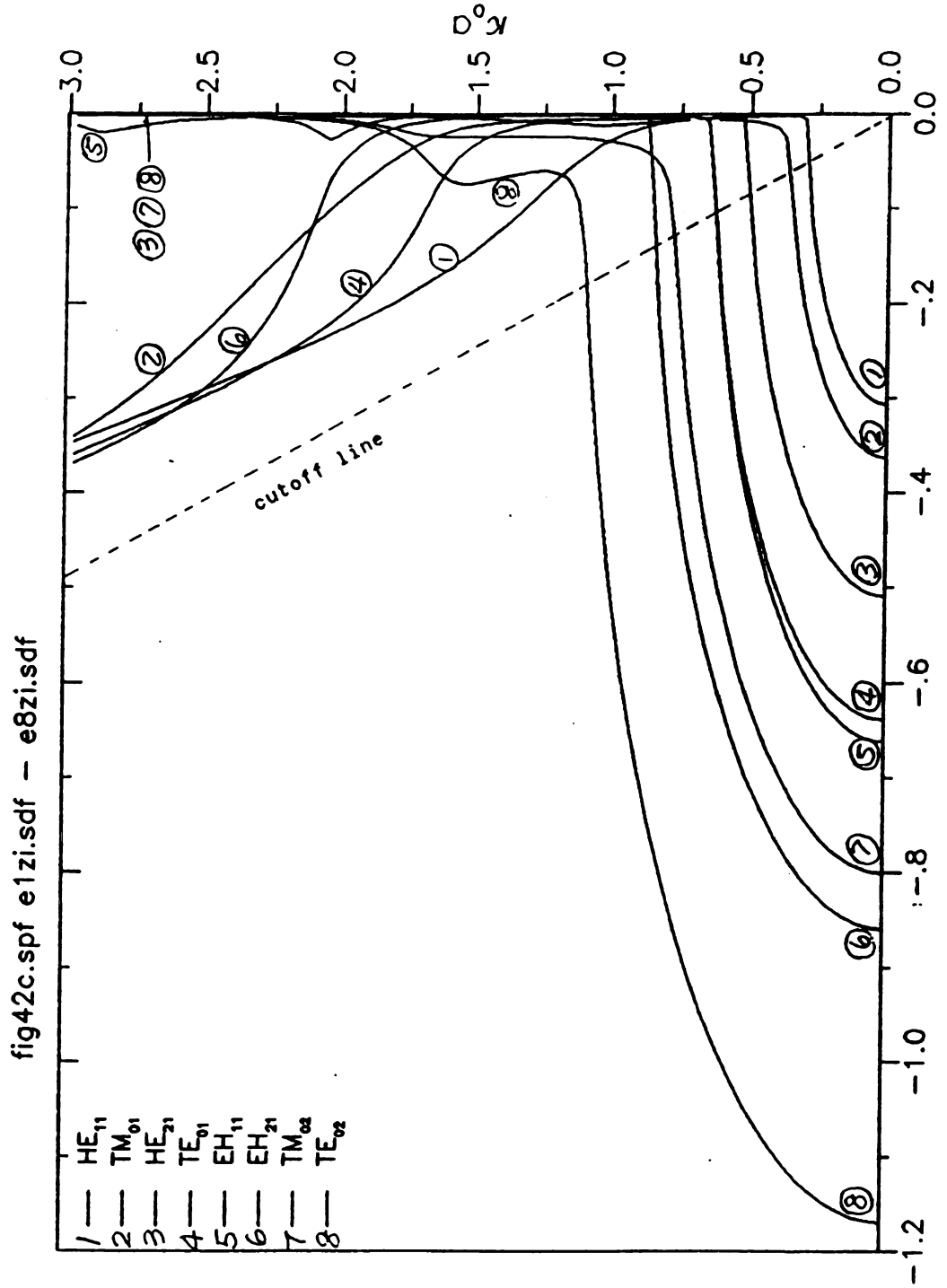

Figure 4.3c w-α diagram for eight waveguide modes, b/a=6, ε=3.03-j0.39.

comparing Figures 4.2a and 4.3a, it is found that in both cases, in the frequency range of $\kappa_0 a > 2.0$, HE_{11}, TM_{01}, TE_{01} are slow waves, and EH_{11}, TM_{02} and TE_{02} are fast waves. Above $\kappa_0 a = 2.125$, an increase in ε_r'' gives rise to the transformations of EH_{21} fast wave into EH_{21} slow wave and HE_{21} slow wave into HE_{21} fast wave. According to the above observations, above cutoff the attenuation will decrease when the mode is transformed into a fast wave mode from a slow wave mode as ε_r'' is increased. On the other hand, the attenuation increases if a fast wave mode becomes a slow wave as a result of an increase in ε_r''. Because the propagation constants for TM_{01}, TM_{02} and EH_{11} are always greater than zero, the three modes are highly damped propagating modes below the cutoff frequency.

Figure 4.4a through Figure 4.4c display the $\omega - \beta$ and $\omega - \alpha$ diagrams of a waveguide loaded with a rod where b/a = 6 and which has losses of $\varepsilon_r'' = 10$. As can be seen in Figure 4.4a, in the high frequency range, where $\kappa_0 a > 2.0$, all dispersion curves are asymptotic to the free space light line. Accordingly, no slow wave exists at higher frequencies. However, as depicted in Figure 4.4b, which is the enlargement of the low frequency range of Figure 4.4a, the $\omega - \beta$ curves for TM_{01}, TM_{02} and EH_{11} modes are in the slow wave region at very low frequencies and do not go to zero. Figure 4.4c, which is the $\omega - \alpha$ diagram, shows that, at high frequencies the attenuations for most modes are reduced when compared with the case of Figure 4.3c. However, the attenuation for TM_{01} mode in the frequency range between cutoff and $\kappa_0 a = 2.5$ is increased. More significant increase in α is seen for EH_{11} mode when ε_r'' is increased from 0.39 to 10. In comparison with Figure 4.3c, the cutoff frequency for HE_{11} is lowered, while for other modes the cutoff frequencies are shifted up. As will be demonstrated later, the changes in the attenuation for each mode is dependent on the changes in the EM field distribution within the waveguide as one of the waveguide parameters is varied. In the following examples, it will be seen that the variations in the field patterns resulted from an increase in ε_r'' are different among TM_{01}, TE_{01}

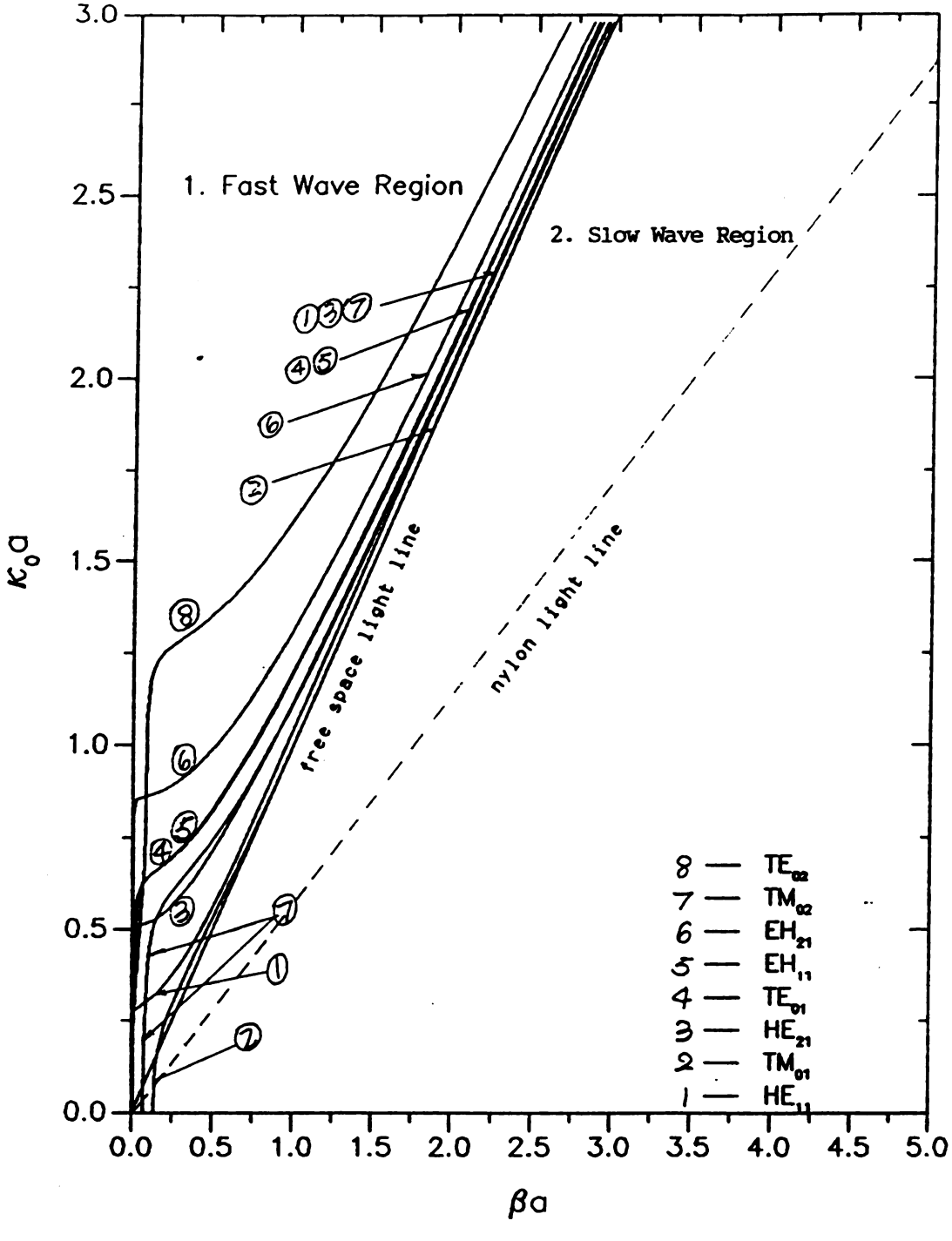

Figure 4.4a w-β diagram for eight waveguide modes, b/a=6, ε=3.03-j10.0.

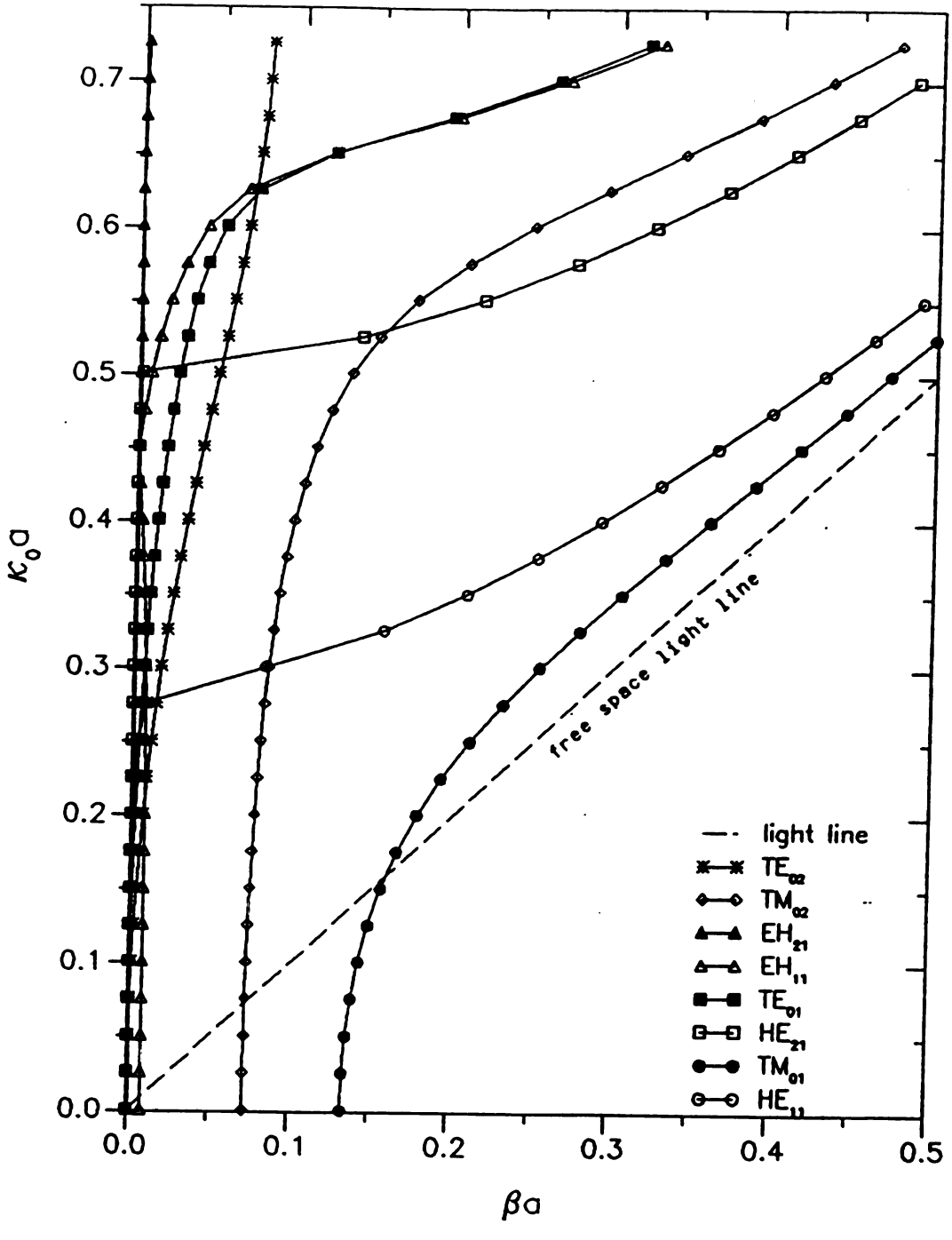

Figure 4.4b Low frequency portions of the w-β diagram for eight waveguide modes, b/a=6, ε=3.03-j10.0.

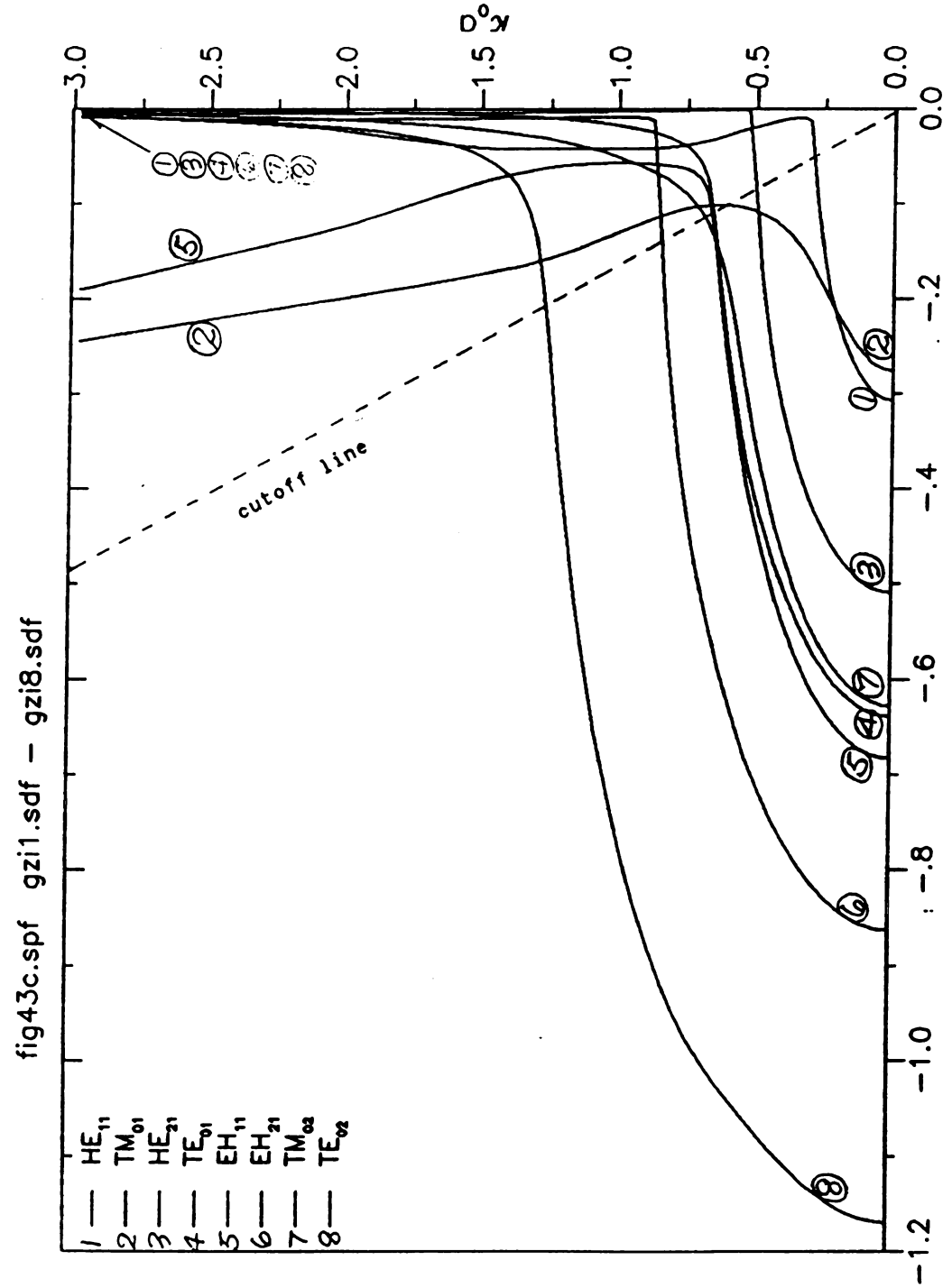

Figure 4.4c w-α diagram for eight waveguide modes, b/a=6, ε=3.03-j10.0.

and HE_{11} modes.

From Figure 4.2 through Figure 4.4, the dispersion characteristics for various modes have been demonstrated from low loss to high loss cases. It has been shown that different modes undergo different changes in the $\omega - \kappa_z$ characteristics as the dielectric loss of the dielectric material changes. It is interesting to find if there are certain ways of predicting the trend of these changes for each mode. To do so, the $\omega - \kappa$ diagrams and electromagnetic field distributions within the waveguide for TM_{01}, TE_{01}, and HE_{11} modes are examined in detail below.

4.3.2.1.3 $\omega - \kappa_z$ diagrams and field EM field patterns for TM_{01} mode

(A) $\omega - \kappa_z$ diagrams

Figures 4.5a, 4.5b and 4.5c are the $\omega - \beta$ and $\omega - \alpha$ diagrams for TM_{01} mode with a = 1.27 cm, b = 7.62 cm and $\varepsilon_r' = 3.03$. In each diagram, there are a family of curves where each curve corresponds to a specific dielectric loss ε_r''. A wide range of dielectric losses, from $\varepsilon_r'' = 0.039$ to 10.0, is investigated. As shown in Figure 4.5a, the $\omega - \beta$ curves can be divided into two groups: (1) $\varepsilon'' \leq 1.5$, and (2) $\varepsilon_r'' \geq 3.9$. For the group where $\varepsilon_r'' \leq 1.5$, the dispersion curves will cross free space light line and approach the nylon light line asymptotically at high frequencies. Crossings occur at about $\kappa_0 a \approx 2.0$. For those curves that cross free space light line, the crossing $\kappa_0 a$ is higher for larger ε_r''. If $\varepsilon_r'' \leq 1.5$, TM_{01} mode may be either slow wave or fast wave, depending on the operating frequency. Below $\kappa_0 a = 2.0$, the $\omega - \beta$ curves lie in the fast wave region, while when $\kappa_0 a$ is larger than 2.5, the $\omega - \beta$ curves lie in the slow wave region. As shown, the dispersion curves for group (2), where $\varepsilon_r'' \geq 3.9$, are in the fast wave region and become asymptotic to the free space light line in the high frequency range. In Figure 4.5b, which is the enlargement of the low frequency portion of Figure 4.5a, it is found that as $\varepsilon_r'' > 0.039$, β is always larger than zero. In the next example, it is seen that although $\beta > 0$ in the low frequency range, these modes are highly attenuated modes

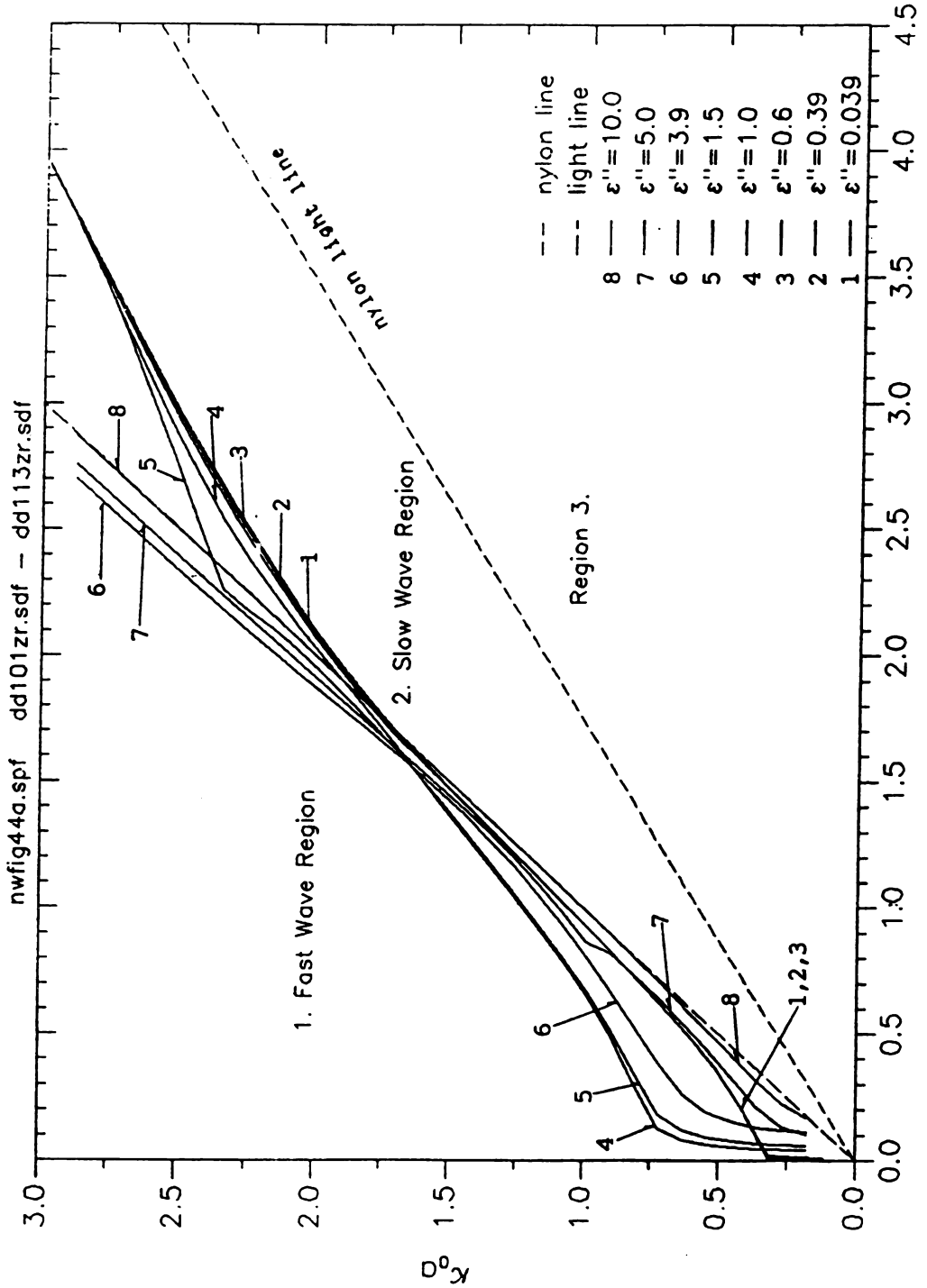

Figrue 4.5a w-β diagram for TM₀₁ mode for various ε'', b/a=6, ε'=3.03.

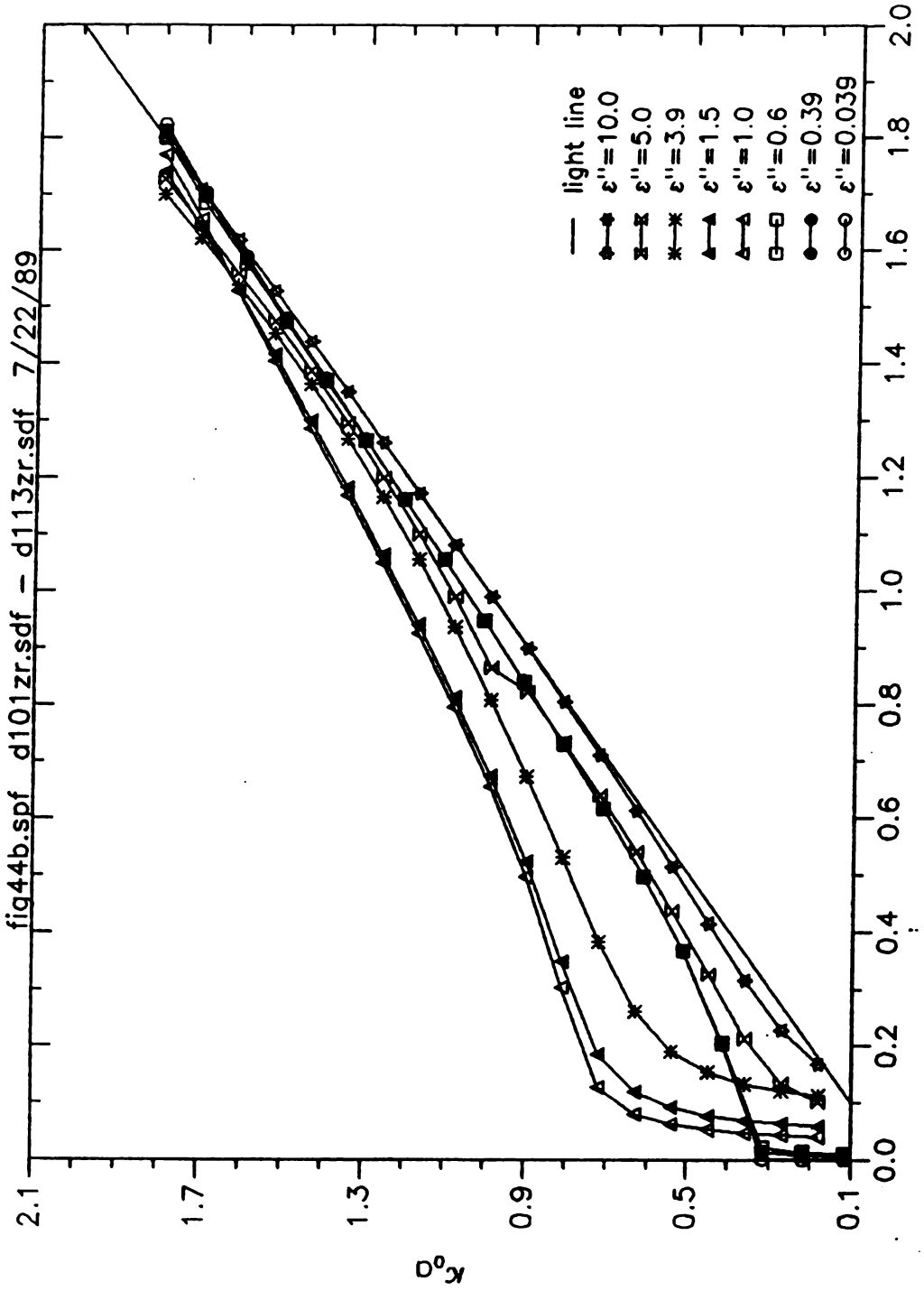

Figure 4.5b Low frequency portion of the w-β diagram for TM$_{01}$ mode for various ε'', b/a=6, ε=3.03

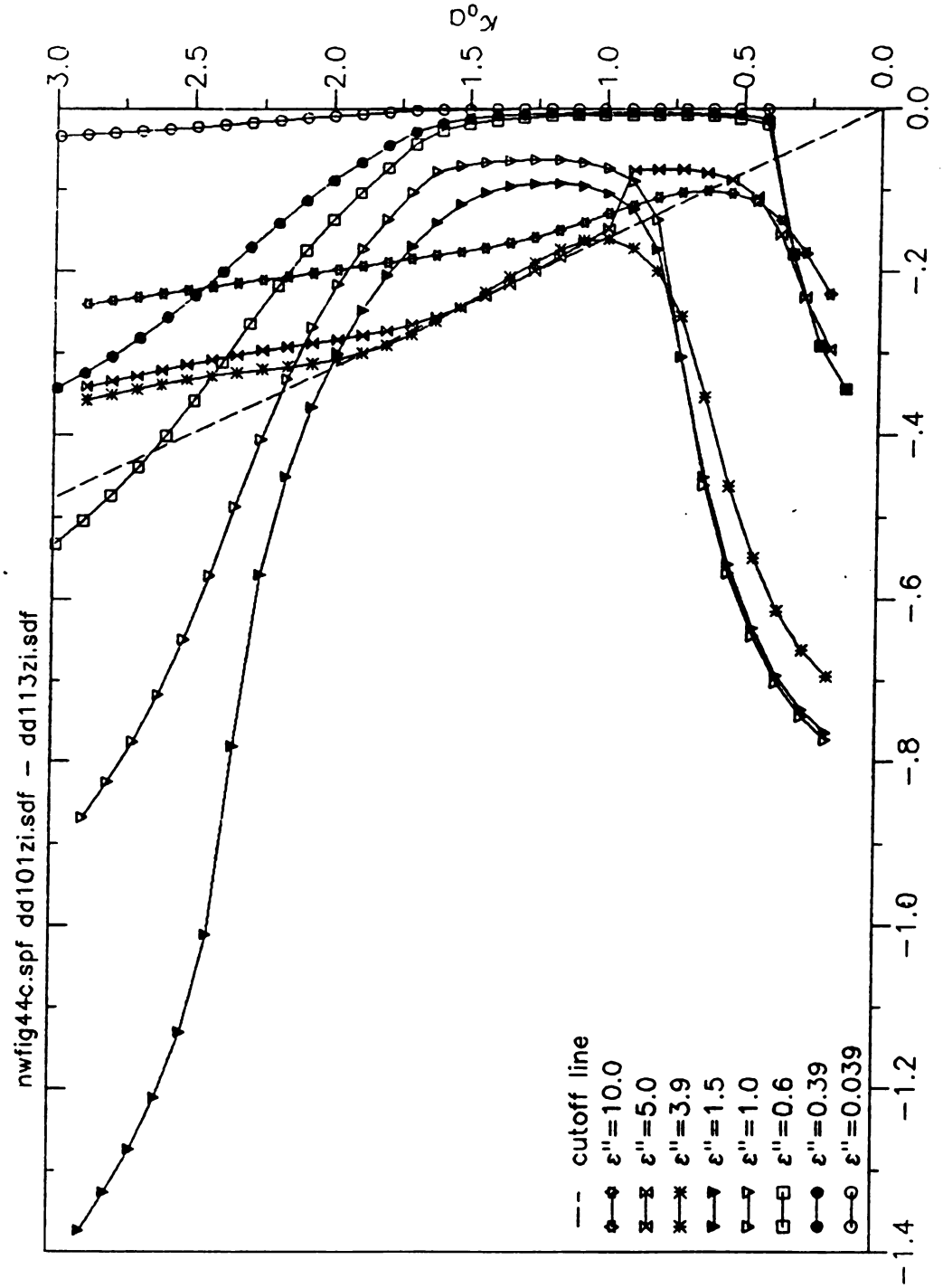

Figure 4.5c w-α diagram for TM_{01} mode for various ε'', b/a=6, ε'=3.03.

due to large attenuation constant.

From the $\omega - \alpha$ diagram shown in Figure 4.5c, some interesting phenomena associated with increasing ε_r'' are observed. In the range of $\kappa_0 a > 2.0$, the attenuation constant increases with increasing ε_r''. The largest attenuation occurs at $\varepsilon_r'' = 1.5$. Further increase in ε_r'' results in decreasing attenuation, such as the cases for ε_r'' equal to 3.9, 5.0, and 10.0. Comparing Figures 4.5a and 4.5c reveals that group (1) is in slow wave region, and group (2) is in fast wave region, provided $\kappa_0 a > 2.0$. It indicates that attenuation for slow waves increase with increasing ε_r'', but for fast waves attenuation reduces with increasing ε_r''. Interestingly, it is found a mode may have more than one cutoff frequency as is shown in Figure 4.5c. For example, as $\varepsilon_r'' = 1.5$, the $\omega - \alpha$ curve intersects with the cutoff line at two points, i.e. $\kappa_0 a = 0.875$ and 1.875. For $\kappa_0 a >$ 1.875 or < 0.875, the TM_{01} mode is highly damped propagating mode since $\alpha\lambda_0 > 1$. Although in the frequency range of $1.875 > \kappa_0 a > 0.875$ $\alpha\lambda_0$ is less than one, the attenuation is still large.

Figures 4.6a and 4.6b show the $\omega - \beta$ and $\omega - \alpha$ diagrams, respectively, for various a/b, with $\hat{\varepsilon}_r$ = 3,03 -j 0.039. As is indicated in Figure 4.6a, no matter what the ratio of a/b is, TM_{01} mode enters slow wave region at $\kappa_{0a} = 1.7$. In other words, the crossing is identical for all a/b ratios. As shown in Figure 4.6b, when $\kappa_0 a < 1.25$, TM_{01} are subject to larger attenuation for larger rod radius at a fixed $\kappa_0 a$. The cutoff wavenumbers are shifted up with increasing rod radius. However, as compared with the empty cavity cutoff wavenumber, all the cutoff wavenumbers are lowered. Note that, by comparing Figure 4.6a and 4.6b, the transition from below cutoff to above cutoff is seen to become more gradual as rod radius increases.

(B) EM Field patterns

Two steps are involved in the computation of the field patterns. The first step is to evaluate the propagation constant γ for given frequency ω and complex dielectric constant $\hat{\varepsilon}_r$ using the computer program developed for the computation of the ω–κ_z

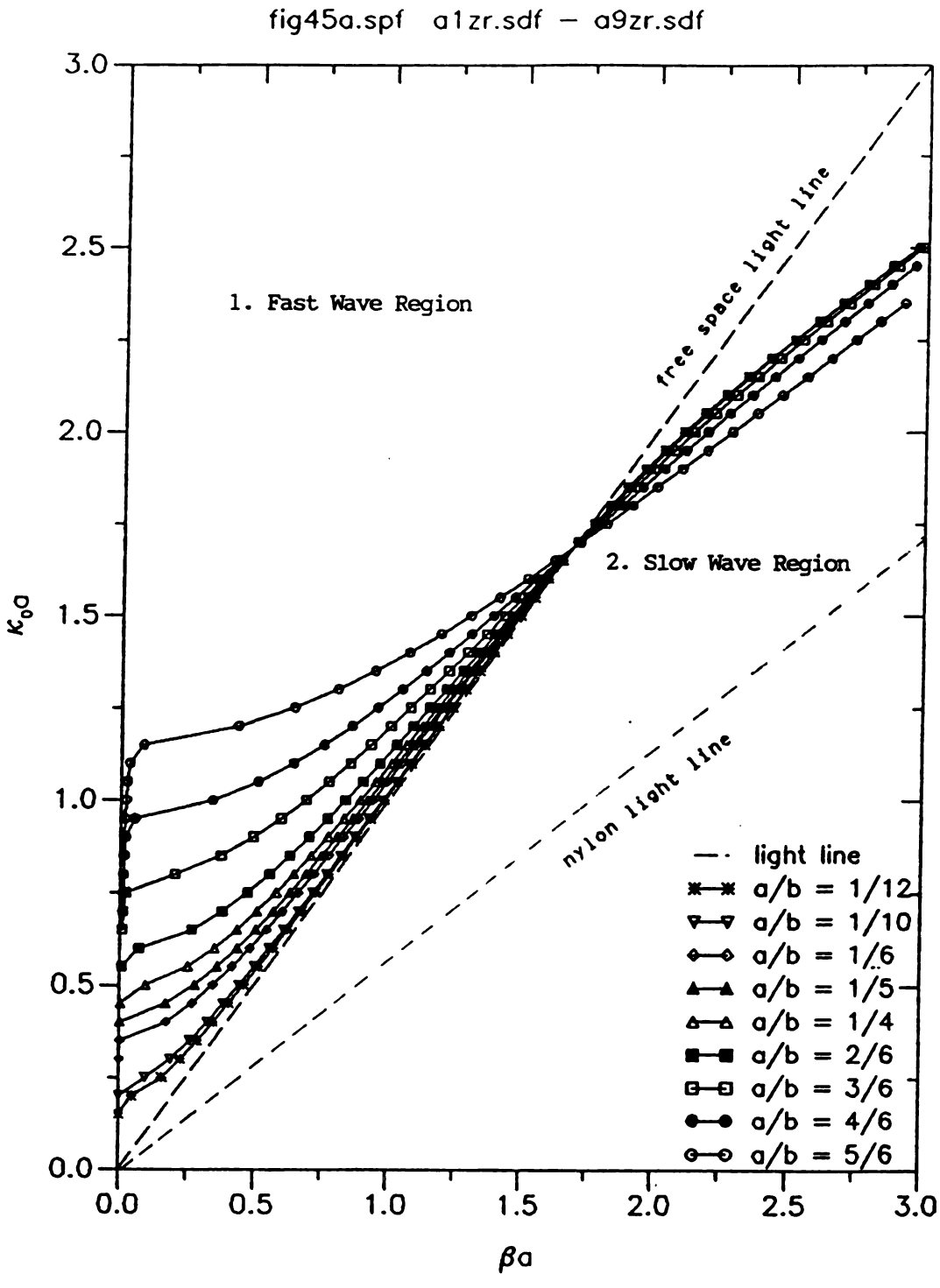

Figure 4.6a w-β diagram for TM_{01} mode for various a/b, ε=3.03-j0.039.

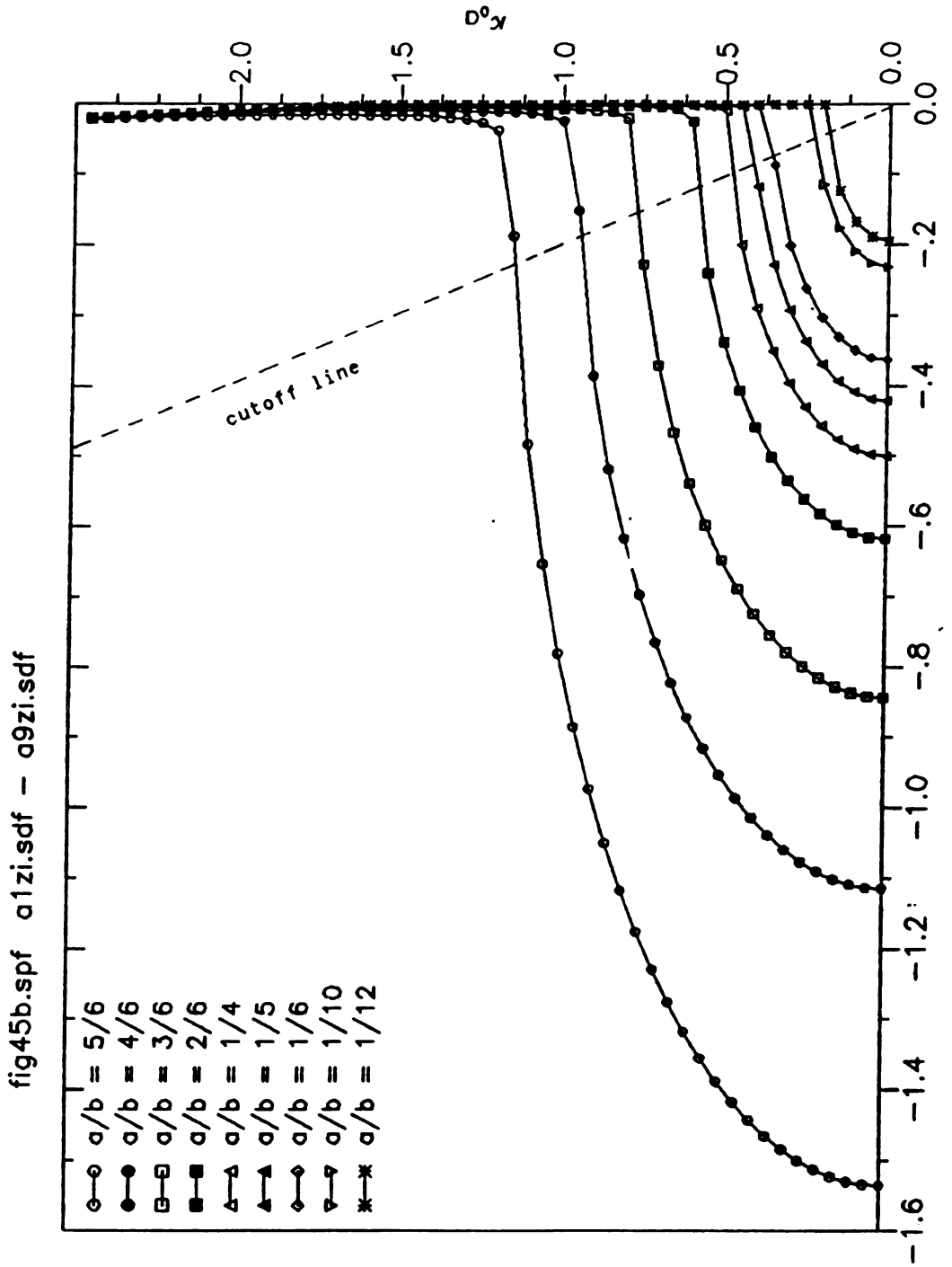

Figure 4.6b w-α diagram for TM_{01} mode for various a/b, ε=3.03-j0.039.

diagram. The field patterns of the coaxially loaded waveguide are then obtained by substituting γ into equations 3.81 through 3.86. The field patterns of E_z, E_ρ, and E_ϕ presented below are the radial variations of the square of the magnitude of each components at a certain waveguide cross section. Field patterns are normalized with respect to the largest value among the three components. For instance, electric fields are normalized by the maximum of $|E_\rho|^2_{max}$, $|E_z|^2_{max}$, and $|E_\phi|^2_{max}$. TM_{01} mode has only two electric field components, i.e. E_z and E_ρ. Since E_z is the dominant component, $|E_z|^2$ and $|E_\rho|^2$ are normalized with respect to $|E_z|^2_{max}$. The dashed line shown in the following figures represents the dielectric rod surface.

Figures 4.7a through 4.7g display the electric fields with $\kappa_0 a$ = 2.7, b/a = 6, and ε_r' = 3.03, for various ε''. Two different y-axis scales are shown in these figures, the one on the right hand side is for the ρ component and the left hand side is for the z component. The main reason why $\kappa_0 a$ = 2.7 was chosen is to illustrate the transition between TM_{01} slow wave and fast wave as ε_r'' changes. The operating frequency is 8.9 GHz for waveguide dimensions of a = 1.27 cm and b = 7.62 cm. Figure 4.7a is the field patterns of a waveguide centrally loaded with a nylon rod where ε_r = 3.03 - j0.039. It is seen that a large portion of the electric energy is confined in the dielectric rod. Both $|E_z|^2$ and $|E_\rho|^2$ vanish on the conducting walls. Also found is the large difference between the magnitude of E_ρ and E_z. As shown, the relative $|E_z|_{max}$=1 and the relative $|E_\rho|_{max} \approx 6.5\times10^{-5}$. As the dielectric loss ε_r'' is gradually increased up to 1.5, the relative field patterns, shown in Figures 4.7b through 4.7d, undergo hardly any changes. In other words, for $\varepsilon_r'' \leq 1.5$ most of the EM energy is distributed in the dielectric rod region. As demonstrated in Figure 4.7e, when ε_r'' = 3.9, the relative field patterns are altered and most of the EM energy is now distributed in the air-filled region. Note that the field in the rod is no longer a standing wave pattern but decays from the boundary. Further increasing the dielectric loss, as is shown in Figures 4.7f and 4.7g, two major changes in the field patterns are observed: (1) rapid decay of

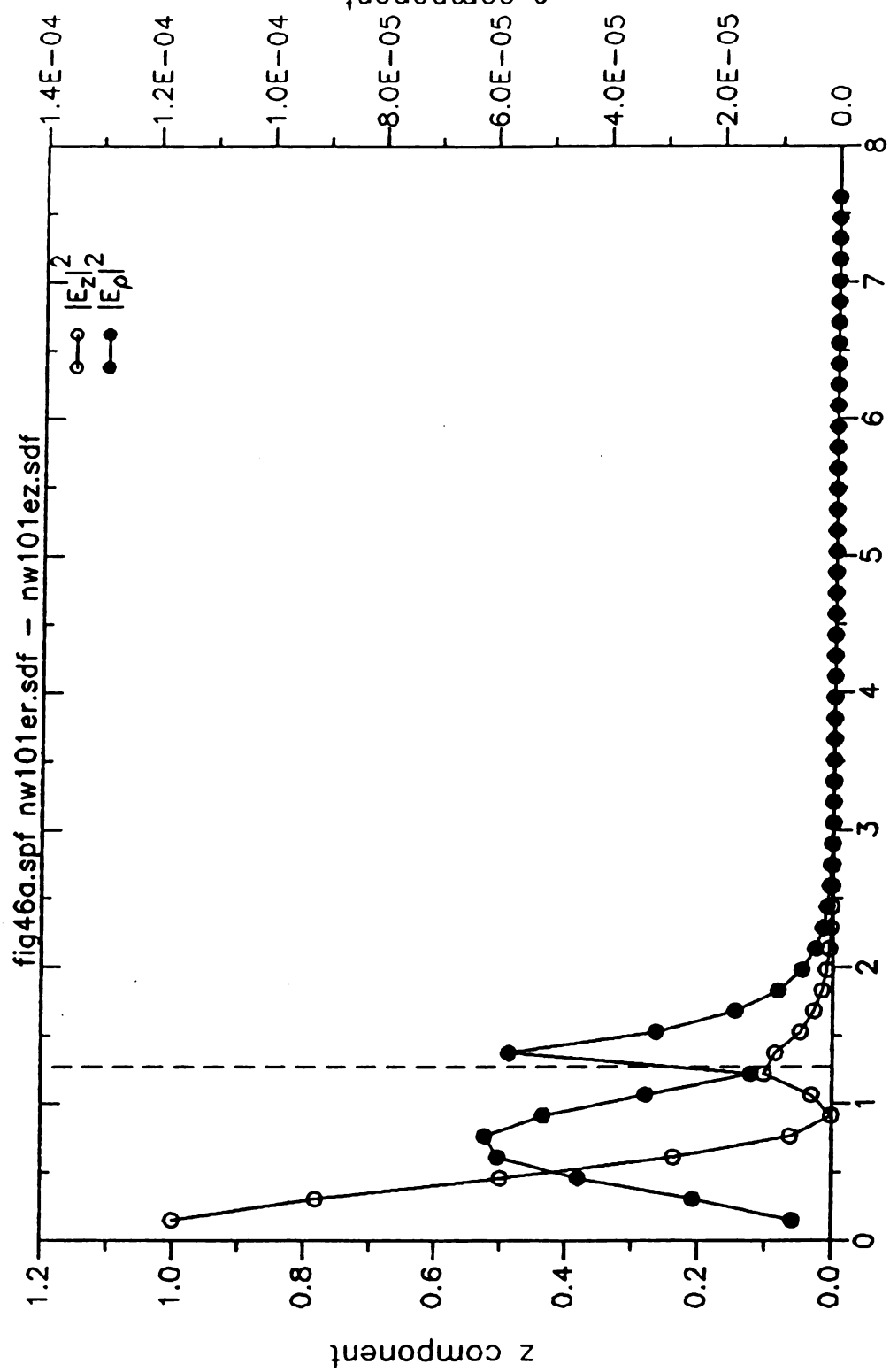

Figure 4.7a Electric field patterns for TM_{01} mode, ε=3.03-j0.039, b/a=6, $k_0 a$=2.7.

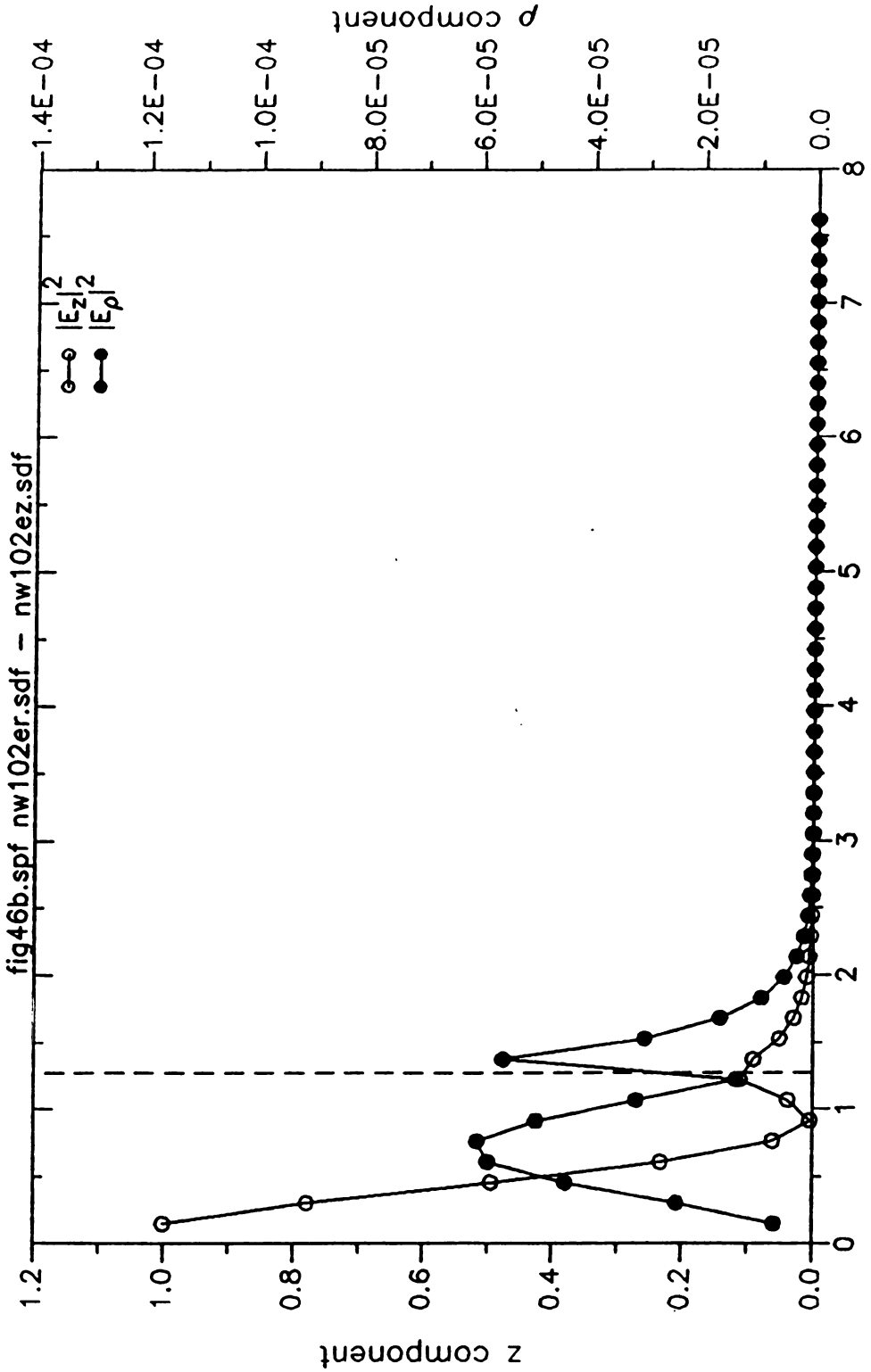

Figure 4.7b Electric field patterns for TM_{01} mode, ε=3.03-j0.39, b/a=6, k_0a=2.7.

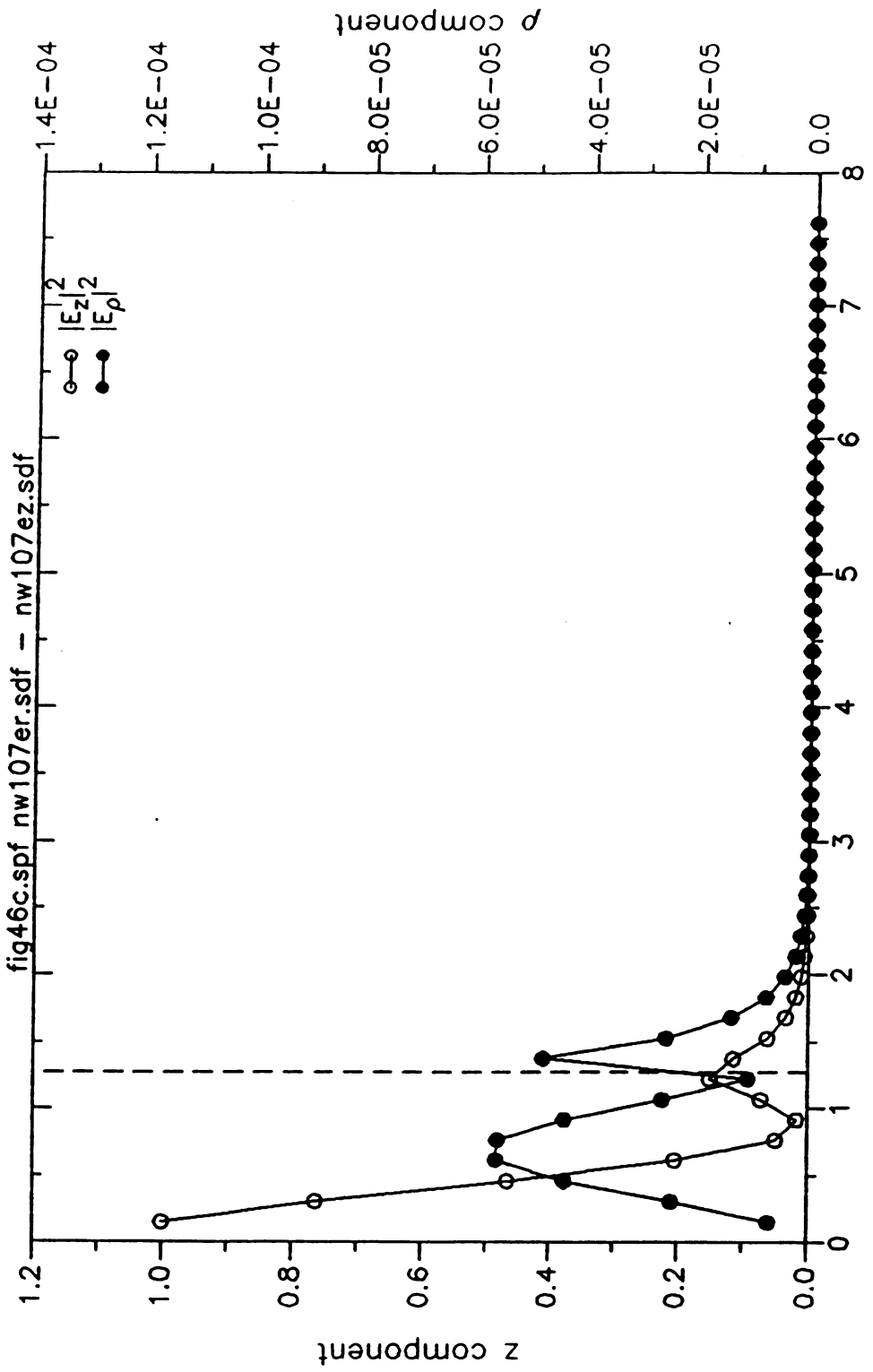

Figure 4.7c Electric field patterns for TM_{01} mode, ε=3.03-j1.0, b/a=6, $k_0 a$=2.7.

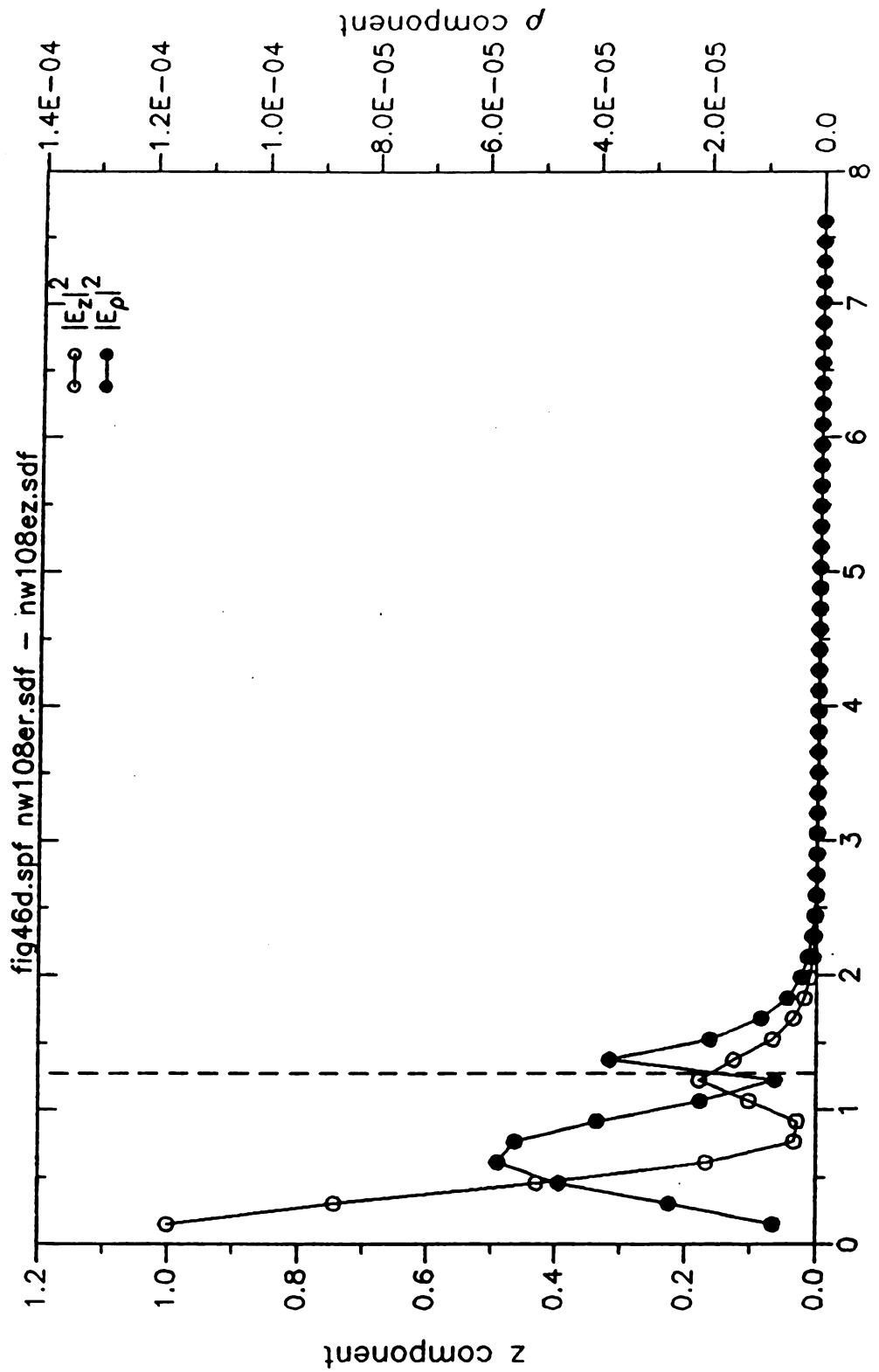

Figure 4.7d Electric field patterns for TM_{01} mode, ε=3.03-j1.5, b/a=6, k_0a=2.7.

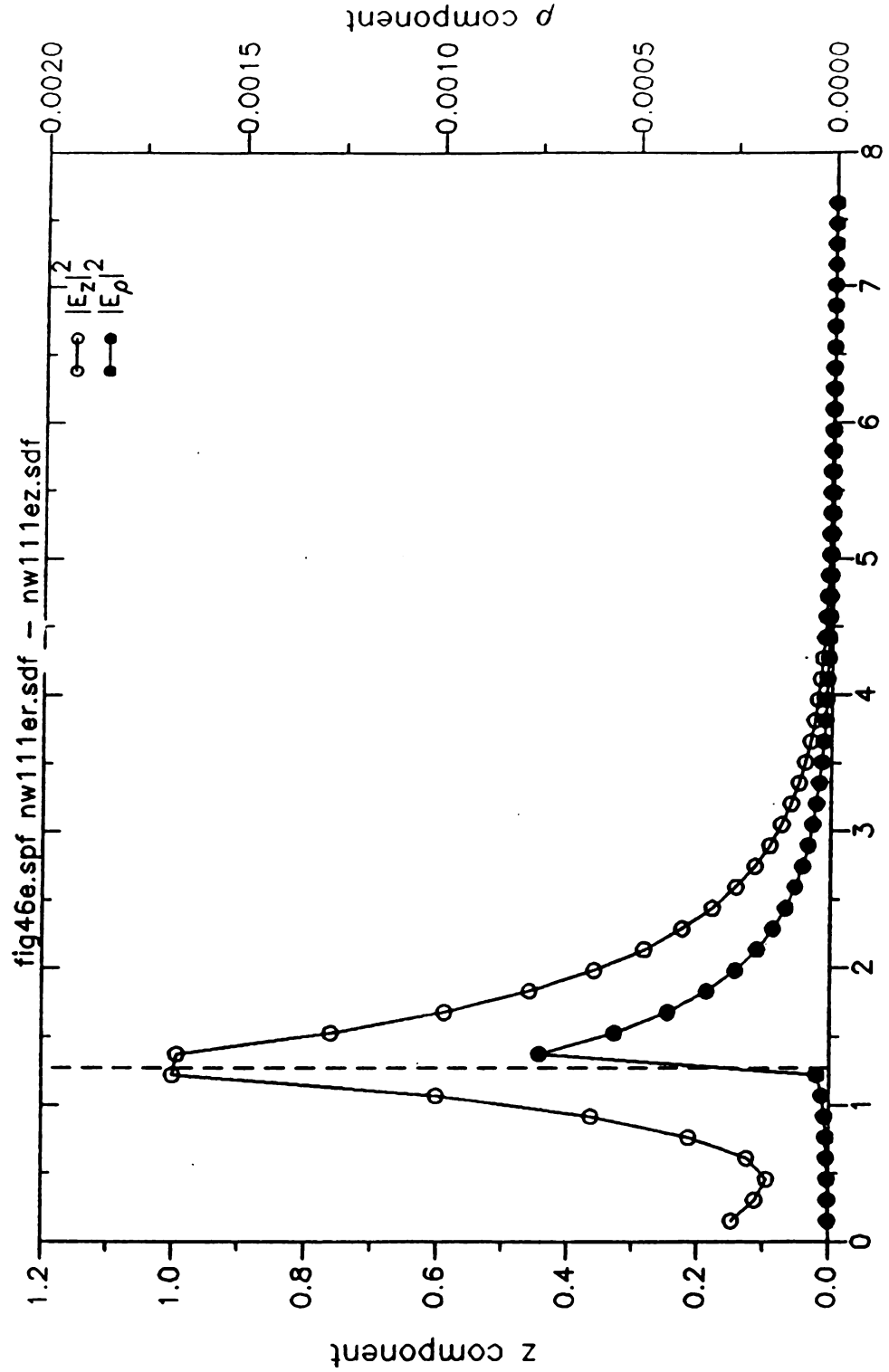

Figure 4.7e Electric field patterns for TM_{01} mode, ε=3.03-j3.9, b/a=6, k_0a=2.7.

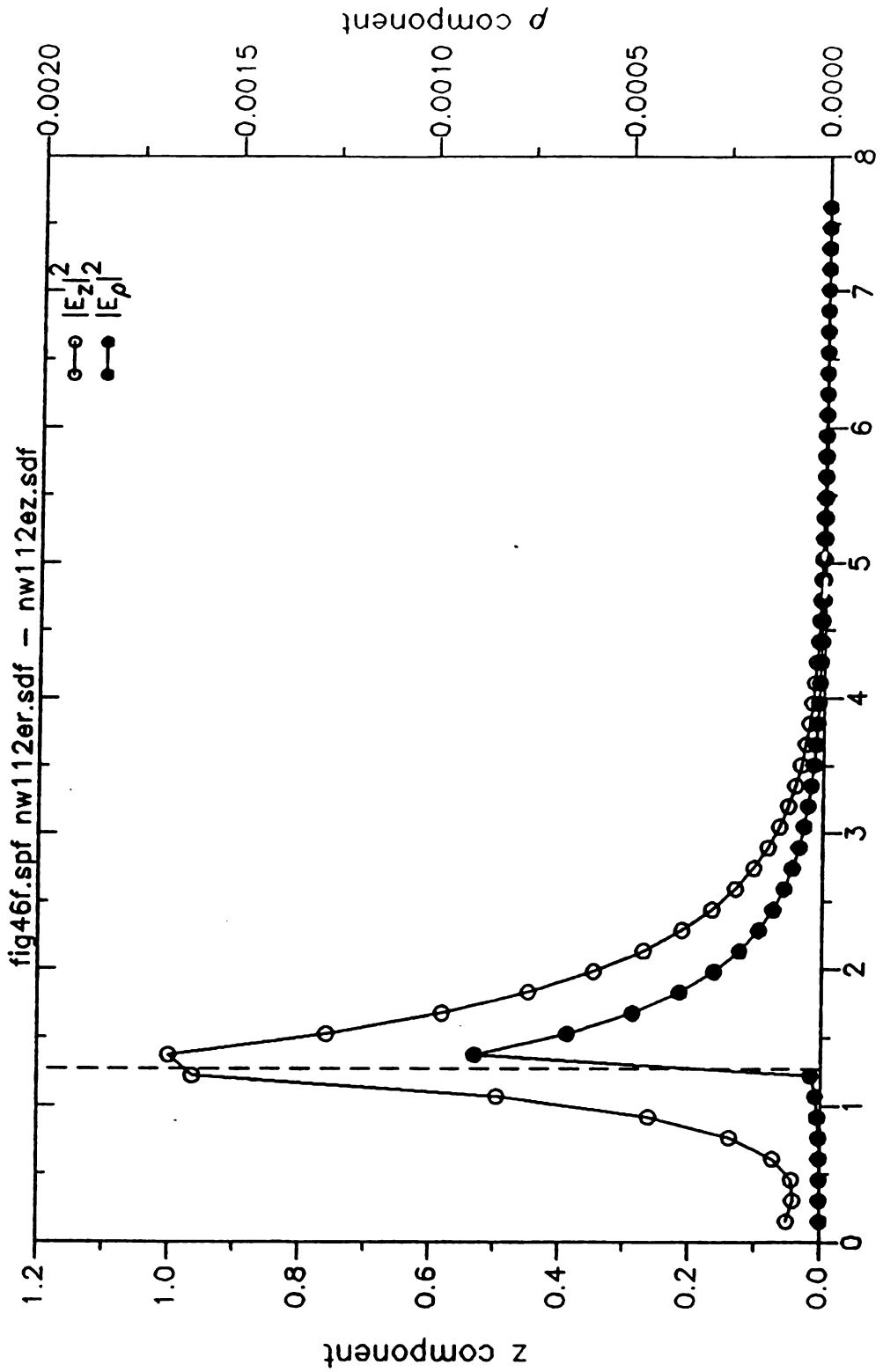

Figure 4.7f Electric field patterns for TM_{01} mode, ε=3.03-j5.0, b/a=6, $k_0 a$=2.7.

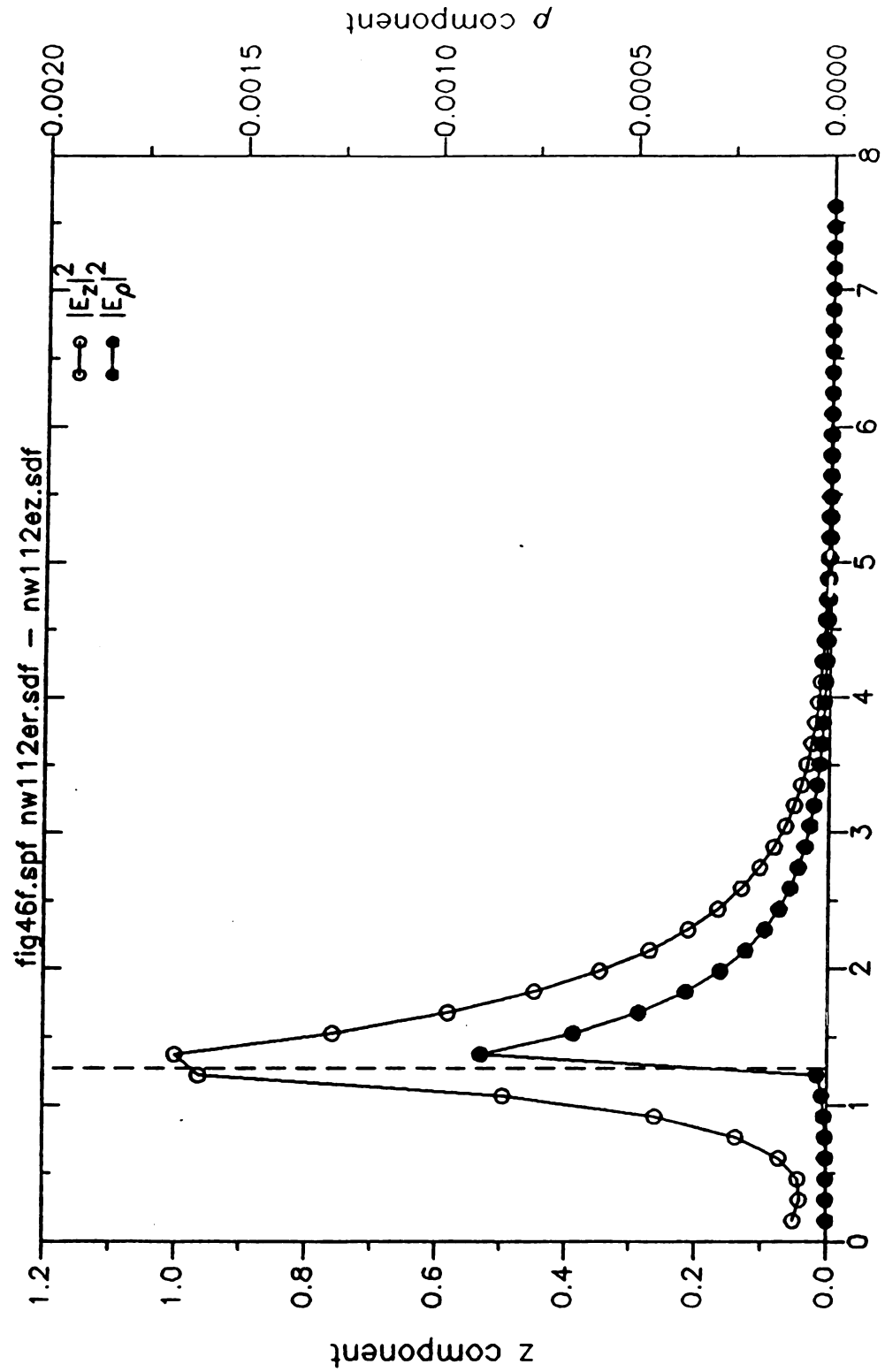

Figure 4.7f Electric field patterns for TM_{01} mode, ε=3.03-j5.0, b/a=6, $k_0 a$=2.7.

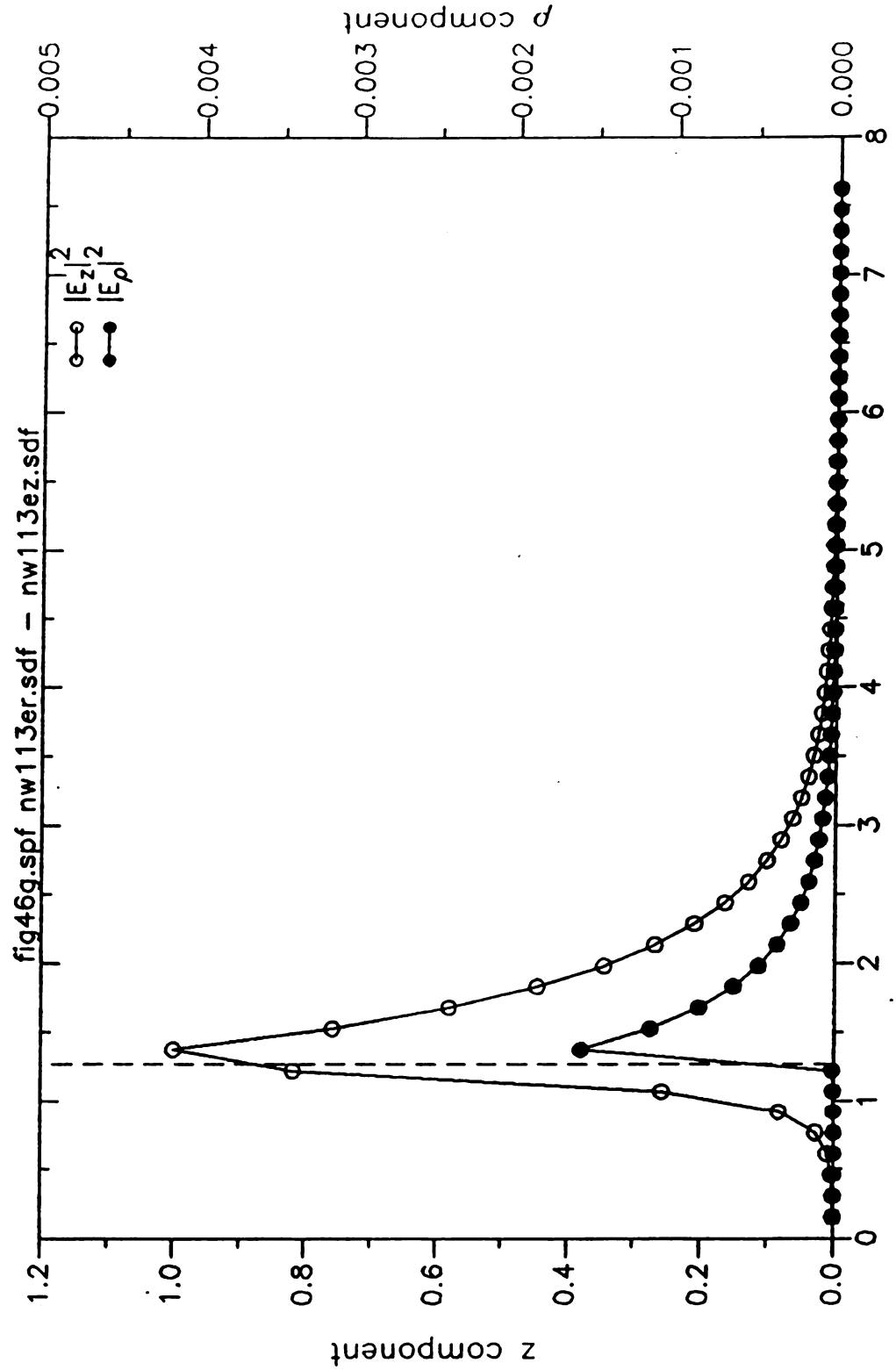

Figure 4.7g Electric field patterns for TM_{01} mode, ε=3.03-j10.0, b/a=6, k_0a=2.7.

$|E_z|$ in the rod from the boundary, e.g., more and more $|E_z|^2$ is "expelled" from the dielectric rod and (2) $|E_\rho|^2_{max}$ has grown dramatically. According to Figures 4.7e through 4.7g, most of the EM energy is distributed in the air-filled region as $\varepsilon_r'' \geq 3.9$. However most of the energy remains around the rod and E_z and E_ρ are still tightly bound to the region around the rod. The explanation for the rapid decay of $|E_z|$ in the rod as ε_r'' is increased is the skin effect. As ε_r'' gets larger, the dielectric rod becomes more like a conductor. As a result, the field in the rod is quickly damped and confined to a region closed to the boundary. Skin depth is the distance where the field in the rod is attenuated to 1/e of its magnitude on the dielectric boundary. The skin depth is determined by the equivalent conductivity, i.e. $\sigma=\omega\varepsilon''$.

By knowing that at $\kappa_0 a = 2.7$, TM_{01} is a slow wave if $\varepsilon_r'' \leq 1.5$, a fast wave if $\varepsilon_r'' \geq 3.9$, two observations are obtained from Figures 4.7a through 4.7g. First of all, for slow waves, most of the EM energy is confined in the dielectric rod and for fast waves most of the EM energy is distributed in the air-filled region. Secondly, a change in ε_r'' will result in a redistribution of the EM field patterns within the waveguide. The EM energy distributed in rod may increase or decrease with increasing ε_r''. Based on the observations, the changes in α as ε_r'' is increased at high frequency, as is shown in Figures 4.2b, 4.3c, 4.4c and 4.5c, can be explained from the view point of electromagnetic energy redistribution within the waveguide. For a slow wave, if an increase in ε_r'' still results in a slow wave and the EM field distributions do not undergo much alteration, and attenuation is increased since most of the EM energy is confined in rod. If an increase in ε_r'' transforms a slow wave into a fast wave, attenuation is reduced because of the removal of EM energy from rod into air-filled region. On the other hand, attenuation becomes larger if an increase in ε_r'' yields a transition from fast wave into slow wave. For fast waves, increasing ε_r'' leads to a decrease in attenuation because part of the EM energy is shielded from the rod as a result of an increase in ε_r''. In short, attenuation is decreased if an reduction of EM energy in rod occurs as ε_r'' is

changed. Attenuation is increased if a change in ε_r'' focuses more EM energy into rod.

Previous examples have showed that changing dielectric loss could move propagating TM_{01} mode from slow waves to fast wave because of the redistribution of electromagnetic energy within the dielectric loaded waveguide. The next two examples, shown in Figure 4.8a and 4.8b, demonstrate the influence of the operating frequency on the field patterns. The waveguide and dielectric rod dimensions are identical to the cases given in Figure 4.7, i.e. a = 1.27 cm and b = 7.62 cm. Nylon rod was selected as the low loss dielectric material. In Figure 4.8a, $\kappa_0 a$ = 0.65, which is resulted from 2.45 GHz operating frequency. It is shown that almost all of E_ρ is distributed in the air-filled region. Although $|E_z|_{max}$ occurs in the dielectric rod, the majority of the energy of E_z is confined in the air-filled region. This TM_{01} mode is a fast wave. By examining Figure 4.5a, the $\omega - \beta$ diagram for TM_{01} mode with b/a = 6, it is indeed a fast wave at $\kappa_0 a$ = 0.65 if $\hat{\varepsilon}_r$ = 3.03 - j0.039. Figure 4.8b depicts the electric field patterns of TM_{01} mode at $\kappa_0 a$ = 0.3, which corresponds to 1.22 GHz operating frequency. Obviously, the energy distributed in the dielectric rod is much less than that in air-filled region. According to Figure 4.5a, this is a nonpropagating mode. The high frequency example of $\kappa_0 a$ = 2.7 has already been given in Figure 4.7a. From these examples, it is found that changing operating frequency not only changes the field patterns but also alters the operating points on the $\omega - \kappa_z$ curves, which determines the electromagnetic wave to be a fast wave, a slow wave or even a nonpropagating mode.

According to waveguide perturbation theory [89], electromagnetic fields of the loaded waveguide will change as the rod radius is increased. It is of interest to investigate if there is any way of predicting the changes of the field patterns as b/a varies. To do so, the fields of a waveguide loaded with nylon rod are shown in Figures 4.9a through 4.9c for various rod radii. Note that even though the operating frequency is identical at 2.45 GHz in these examples, $\kappa_0 a$ is different corresponding to different rod radius. For small rod radius, TM_{01} mode is most likely in the fast wave region.

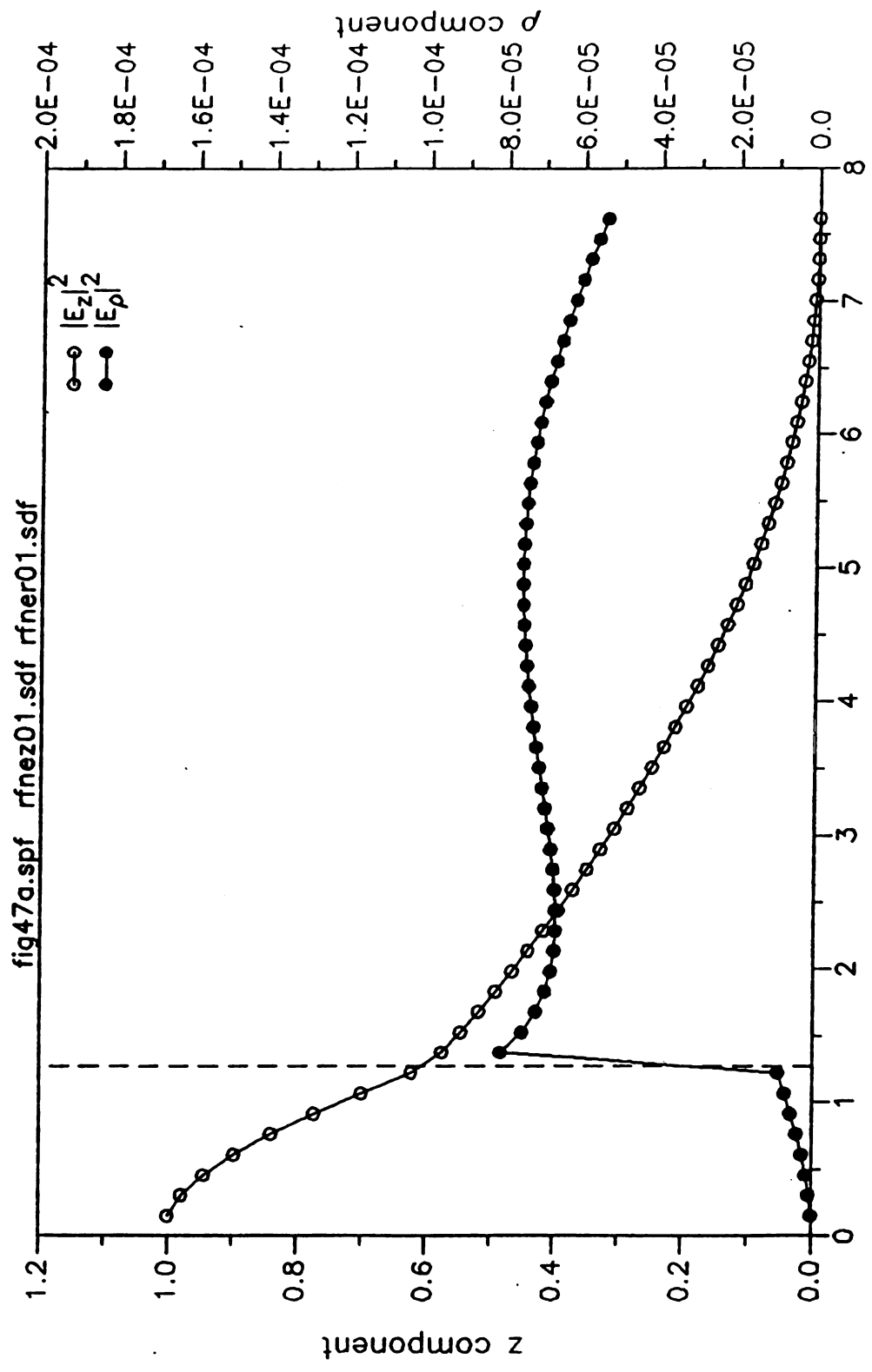

Figure 4.8a Electric field patterns for TM_{01} mode, ε=3.03-j0.039, b/a=6, $k_0 a$=0.65.

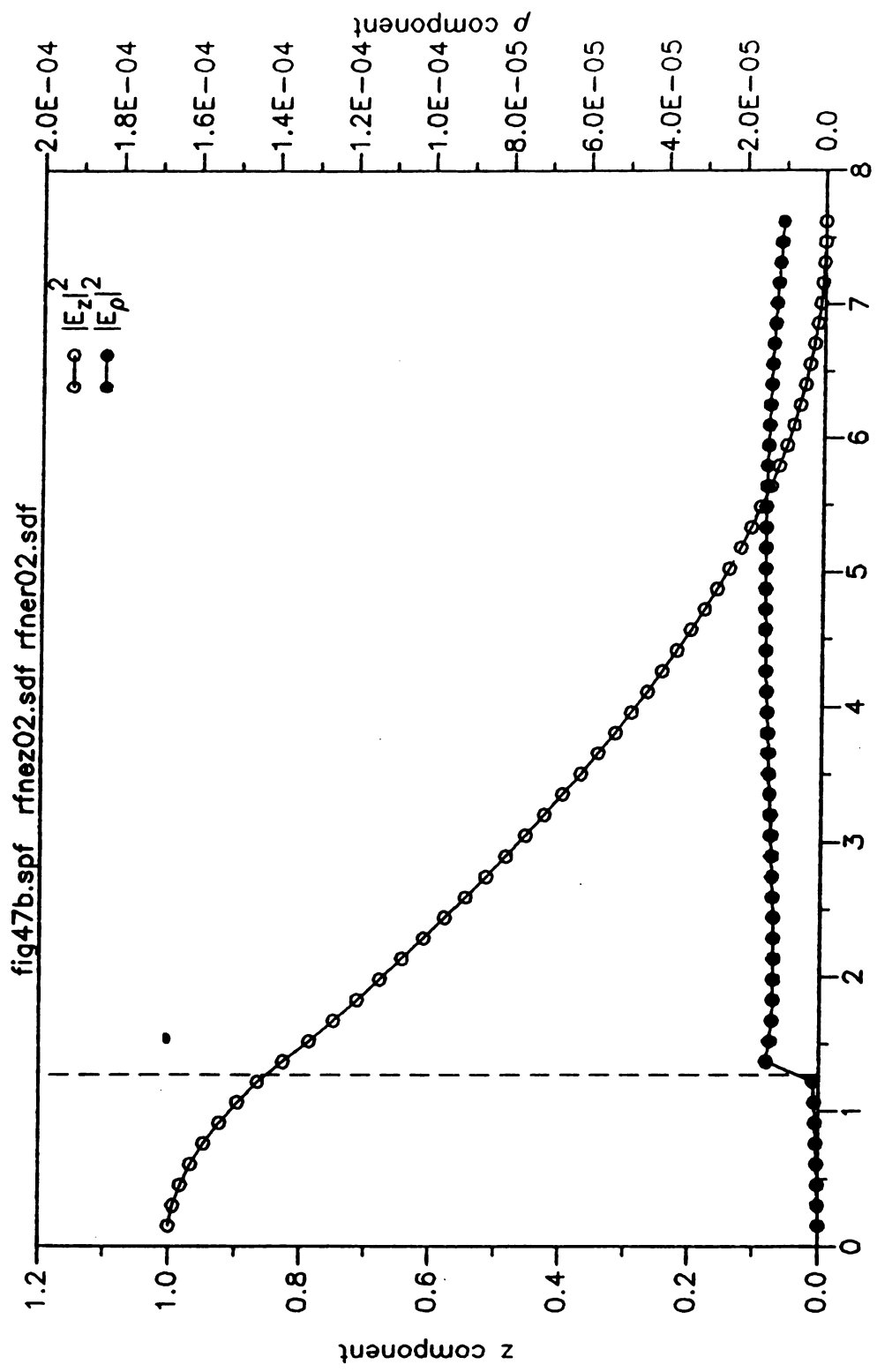

Figure 4.8b Electric field patterns for TM_{01} mode, ε=3.03-j0.039, b/a=6, k_0a=0.3.

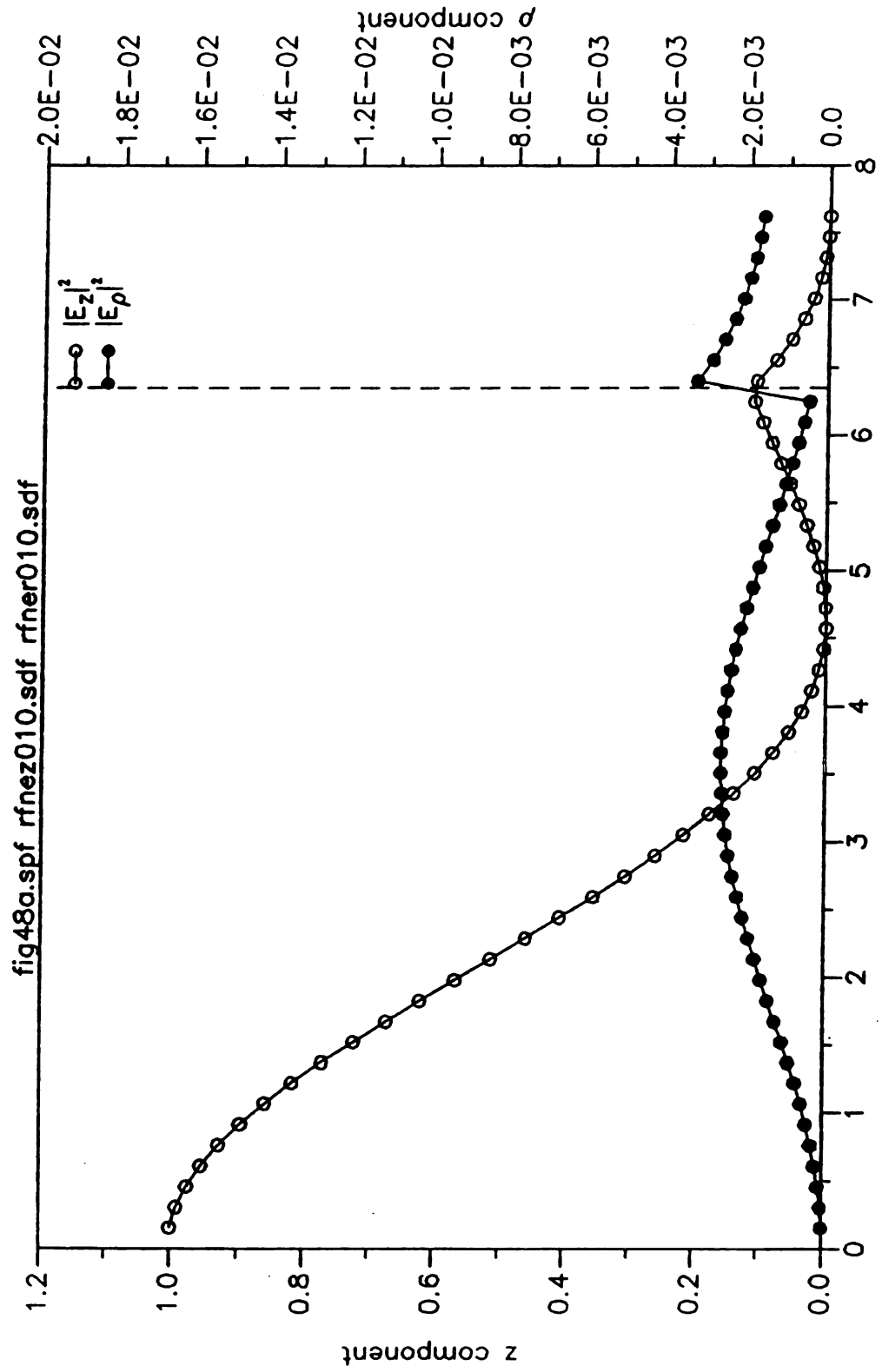

Figure 4.9a Electric field patterns for TM_{01} mode, ε=3.03-j0.039, a=6.35 cm, b=7.62 cm, k_0a=3.258.

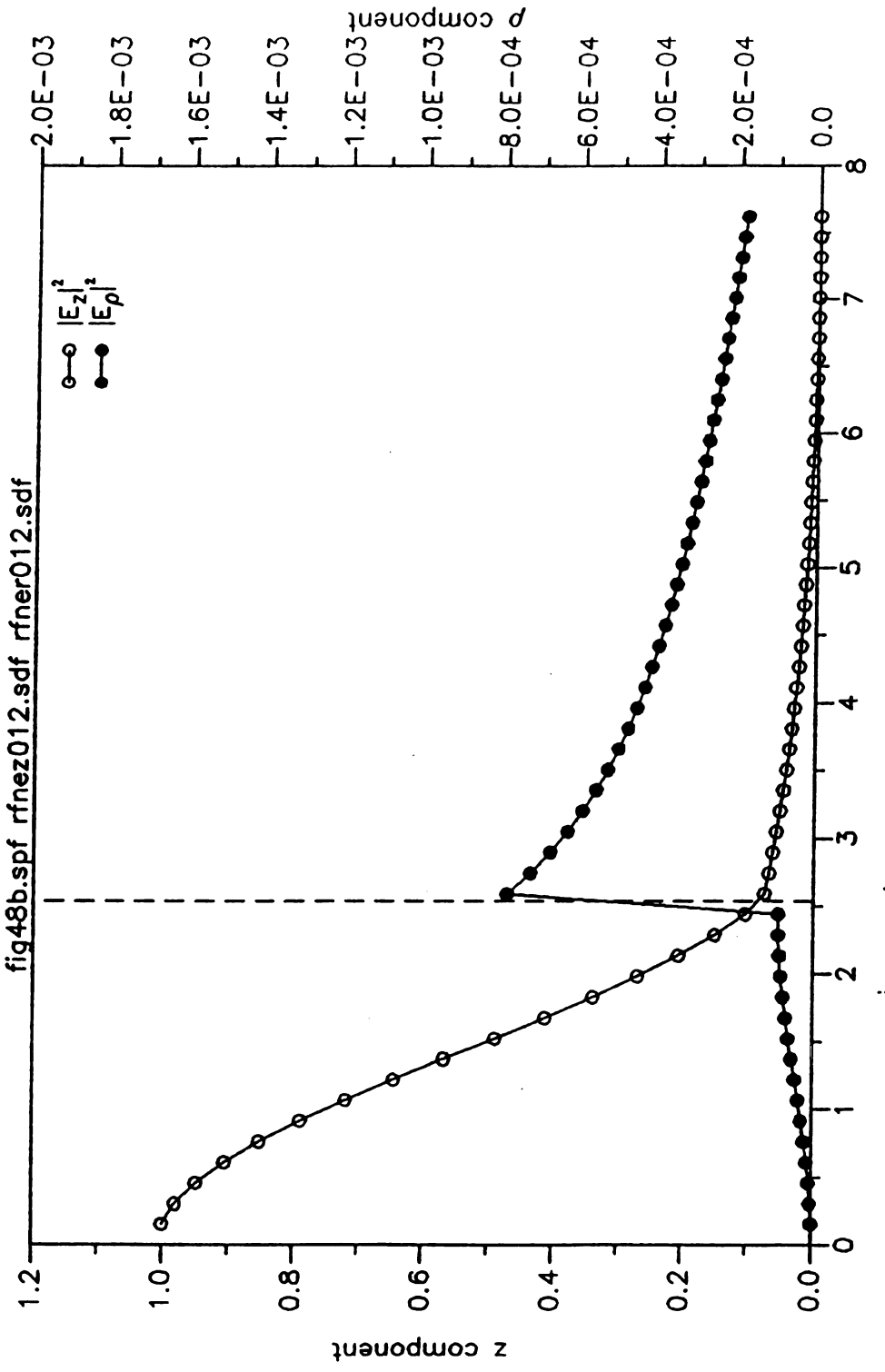

Figure 4.9b Electric field patterns for TM_{01} mode, ε=3.03-j0.039, a=2.54 cm, b=7.62 cm, k_0a=1.303.

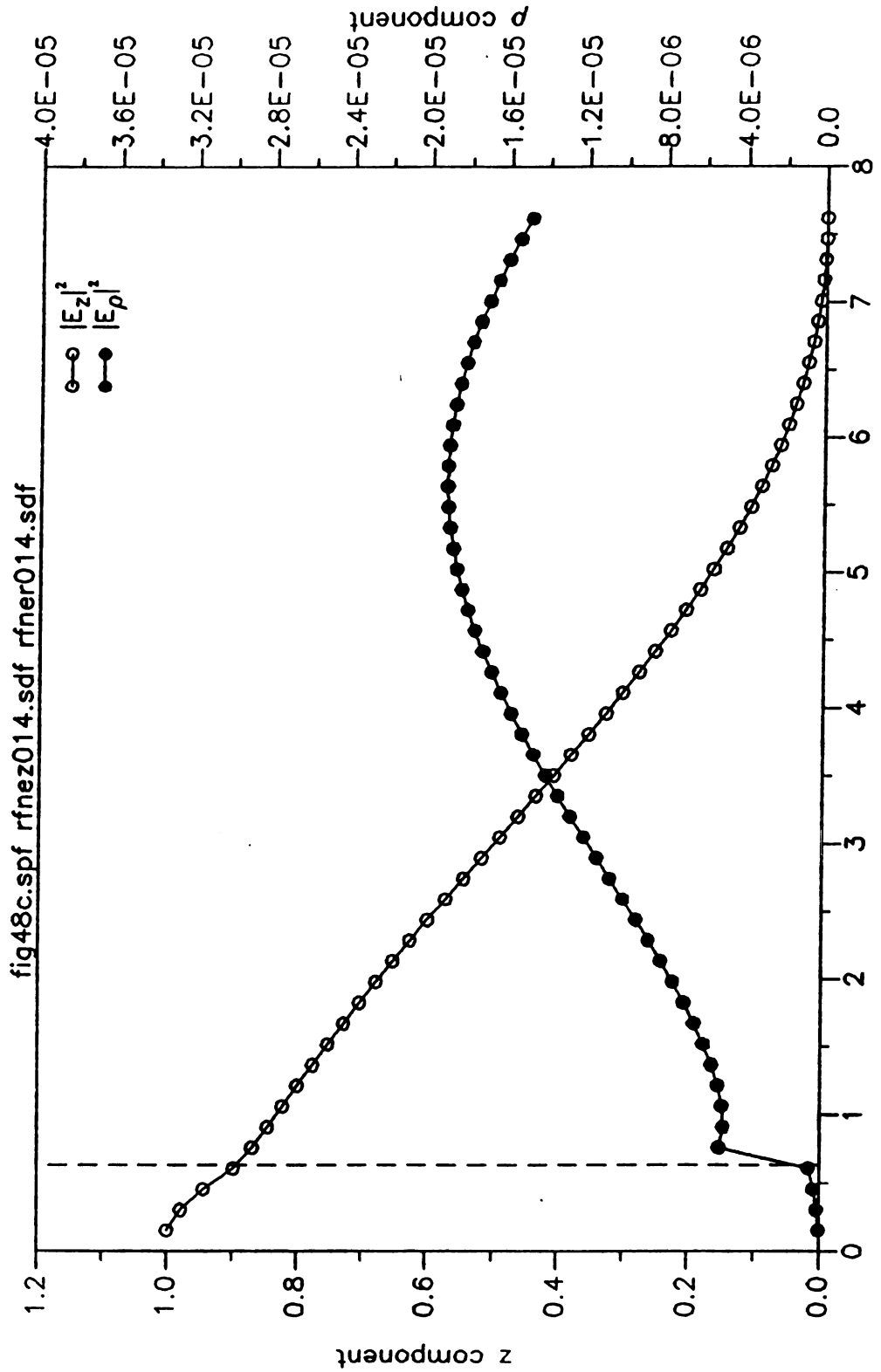

Figure 4.9c Electric field patterns for TM_{01} mode, ε=3.03-j0.039, a=0.635 cm, b=7.62 cm, k_0a=0.325.

As rod radius is increased, EM wave may become a slow wave due to the increase in $\kappa_0 a$. The waveguide radius considered in Figures 4.9a, 4.9b and 4.9c is 7.62 cm.

In Figure 4.9a, the rod radius is 6.35 cm which yields $\kappa_0 a$ = 3.26. As can be determined from Figure 4.6a, such a propagating TM_{01} mode is a slow wave. It is consistent with the field patterns shown in Figure 4.9a that most of the electric energy exists in the dielectric rod. In this example, $\frac{|E_z|^2_{max}}{|E_\rho|^2_{max}}$ is approximately 300. As the rod radius is reduced to 2.54 cm, which is the case depicted in Figure 4.9b, $\kappa_0 a$ is equal to 1.303. According to Figure 4.6a, the EM wave is still in slow wave region but about to transform to a fast wave. By comparing Figure 4.9b with Figure 4.9a, it is obvious that less electromagnetic energy is confined in the dielectric rod region. Neverthless, the electric energy distributed in the dielectric rod still dominates. Hence, it is still a slow wave. Interestingly, $\frac{|E_z|^2_{max}}{|E_\rho|^2_{max}}$ is increased to 1250. In Figure 4.9c, the rod radius is decreased to 0.635 cm and the corresponding $\kappa_0 a$ is 0.325. It is seen that the electromagnetic energy in the air-filled region is well beyond that in the dielectric rod region. Obviously, this is a fast wave, which agrees with the conclusion that could be drawn from Figure 4.6a. $\frac{|E_z|^2_{max}}{|E_\rho|^2_{max}}$ is risen up to 5×10^4 in this example.

4.3.2.1.4 $\omega - \kappa_z$ diagrams and field patterns for TE_{01} mode

(A) $\omega - \kappa_z$ diagrams

Figure 4.10a and 4.10b show the $\omega - \alpha$ and $\omega - \beta$ diagrams for TE_{01} mode as a function of ε_r'' with ε_r' = 3.03 and b/a =6. As is shown in Figure 4.10a, the dispersion curves can be divided into two groups:(1) $\varepsilon_r'' \le 0.5$ and (2) $\varepsilon_r'' \ge 1.0$. For group (1) the dispersion curves cross the free space light line and enter the slow wave region at $\kappa_0 a$ = 1.6. Eventually these curves become asymptotic to the nylon light line in high frequency range. It is found the intersections $\kappa_0 a$, at which fast waves cross over the free

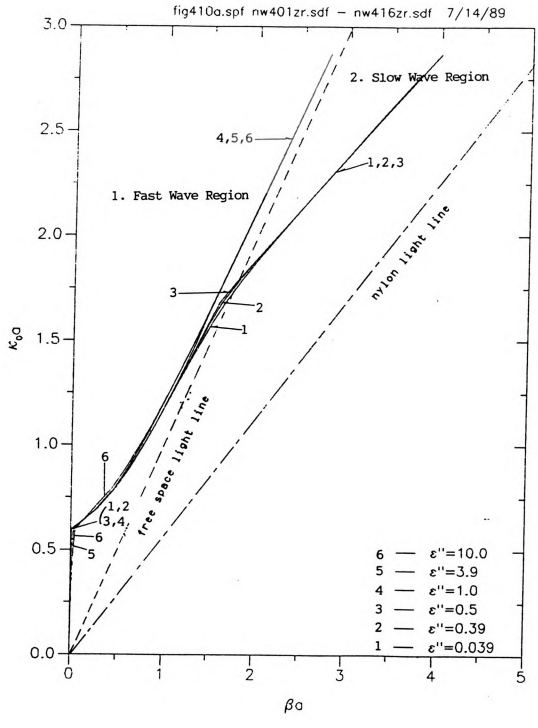

Figrue 4.10a w-β diagram for TE_{01} mode for various ε'', b/a=6, ε'=3.03.

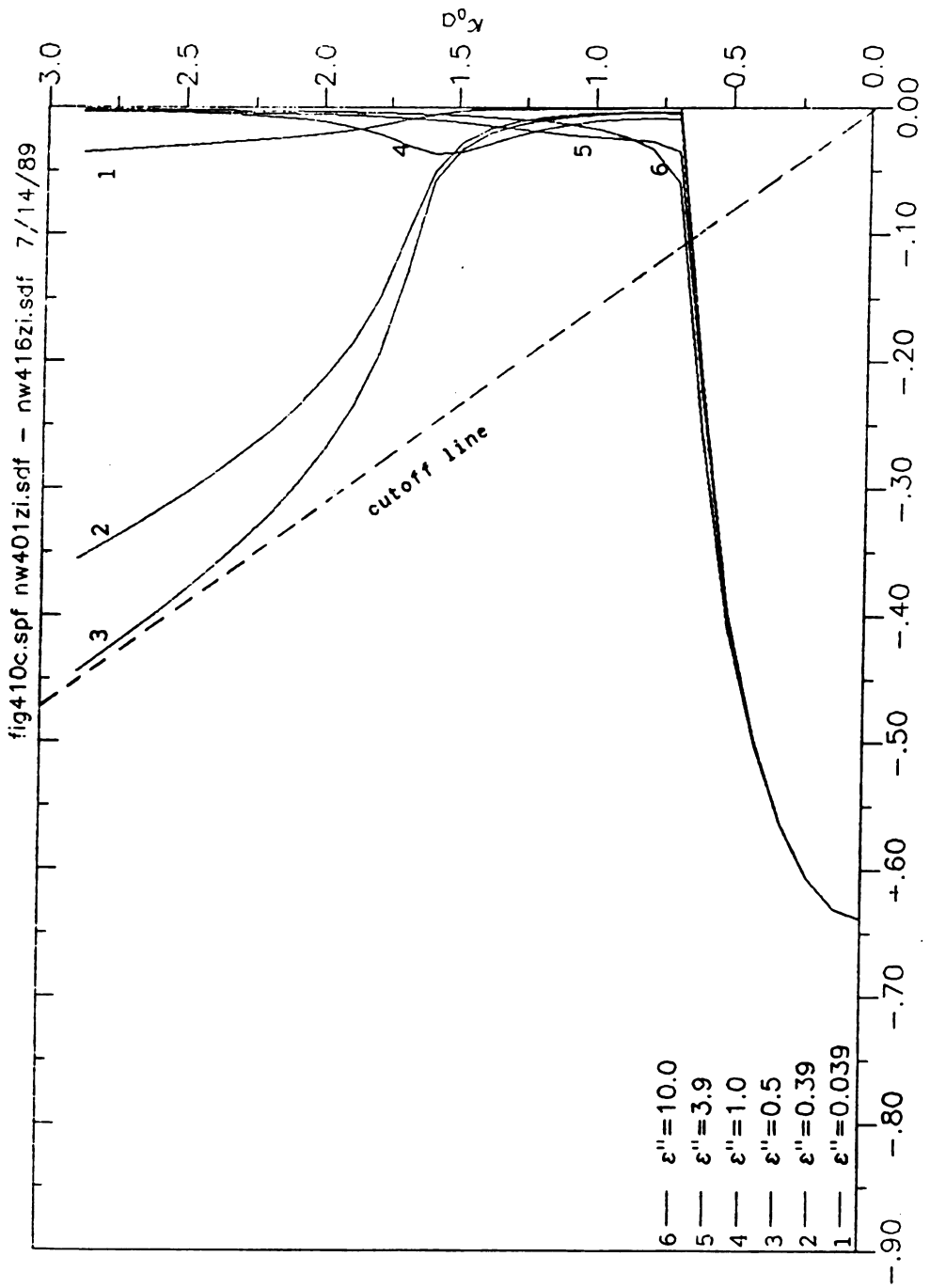

Figure 4.10b ω-α diagram for TE_{01} mode for various ε'', b/a=6, ε'=3.03.

space light line, is higher for larger ε_r''. The dispersion curves of group (2) stay in fast wave region and approaches the free space light line asymptotically at high frequency.

The $\omega - \alpha$ diagram displayed in Figure 4.10b shows that for group (1), increasing ε_r'' yields an increase in attenuation, provided $\kappa_0 a$ is larger than 0.5. On the other hand, the attenuation constants for group (2) are very small in the high frequency region. As shown in Figure 4.10a, at $\kappa_0 a > 1.6$, group (1) is in slow wave region, while group (2) is in fast wave region. Again, the cutoff frequency is increased with increasing ε_r''.

Figure 4.11a and 4.11b display the $\omega - \beta$ and $\omega - \alpha$ diagrams for a waveguide loaded with a nylon rod for various rod radii. The dispersion curves shown in Figure 4.11a point out that the intersections with the free space light line increase as a result of an increase in rod radius. All the $\omega - \beta$ curves cross the free space light line before $\kappa_0 a = 2.3$ and become asymptotic to the nylon light line at high frequency. As depicted in Figure 4.11b, in the frequency range of $\kappa_0 a < 2.0$, attenuation increases as a result of an increase in rod radius. Note that when $\kappa_0 a > 2.0$, $\kappa_0 a - \alpha a$ curves converges. It implies that at high frequency the attenuation constant α corresponding to larger rod radius is smaller. Also seen is that the larger the rod radius, the higher the normalized cutoff wavenumber. All the normalized cutoff wavenumbers are shifted down from the empty TE_{01} normalized wavenumber.

(B) Field patterns

The changes of the electric field of TE_{01} mode as a function of ε_r'' are displayed in Figures 4.12a through 4.12f when $\kappa_0 a$=2.5. If the rod radius is 1.25 cm and the waveguide radius is 7.62 cm, the corresponding operating frequency is 9.4 GHz. TE_{01} has only one electric field component E_ϕ. Thus only $|E_\phi|^2$ is shown in the following examples and its magnitude is normalized with respect to $|E_\phi|^2_{max}$. As is depicted in Figures 4.12a, 4.12b, and 4.12c, $|E_\phi|^2$ is confined in the rod and changes only slightly as ε_r'' is increased from 0.039 to 0.5. Figure 4.12d displays the distribution of $|E_\phi|^2$ for $\varepsilon_r'' = 1.0$. In comparison with Figure 4.12c, it is found that $|E_\phi|^2_{max}$ and most of the

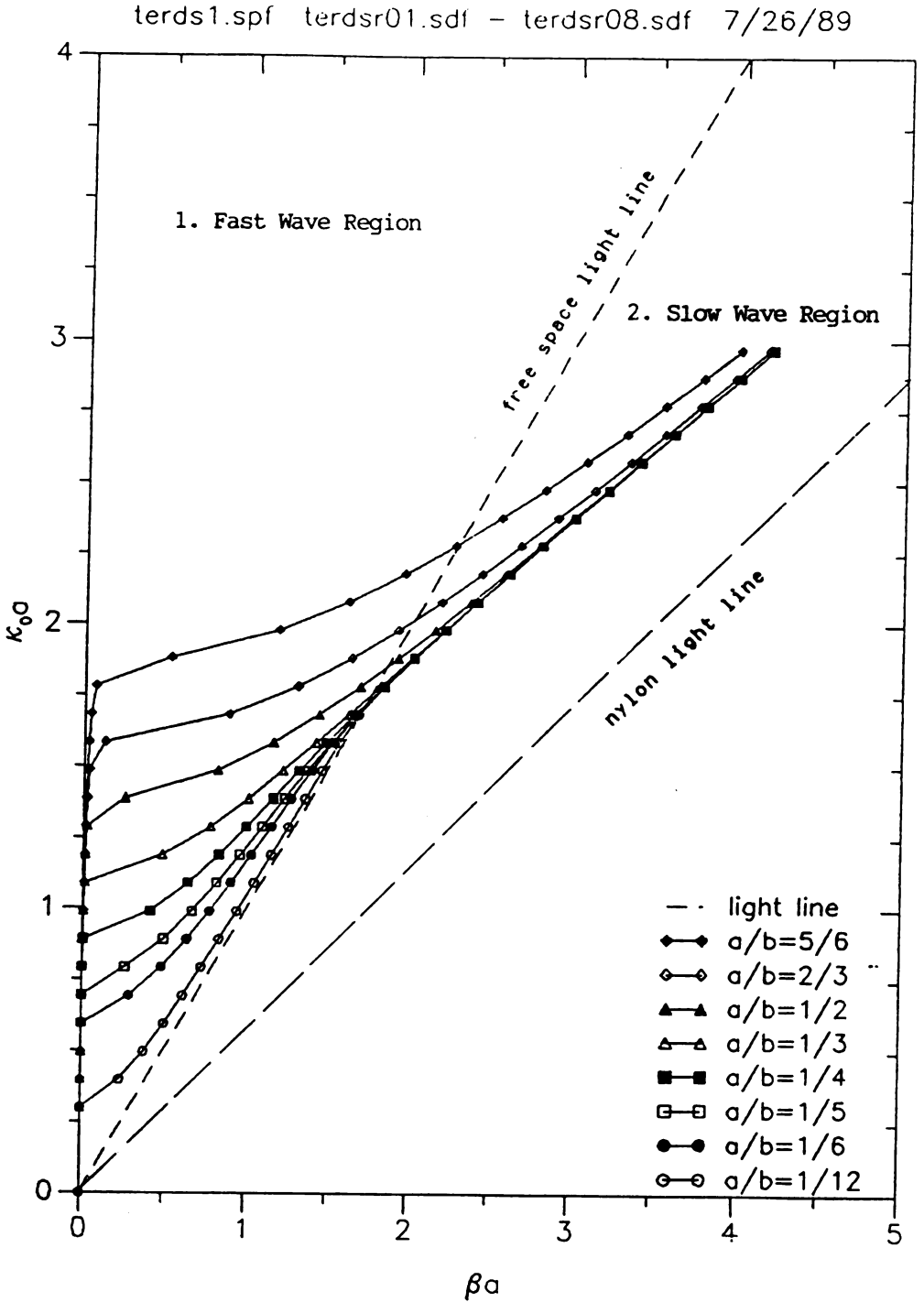

Figure 4.11a ω-β diagram for TE_{01} mode for various a/b, ε=3.03-j0.039.

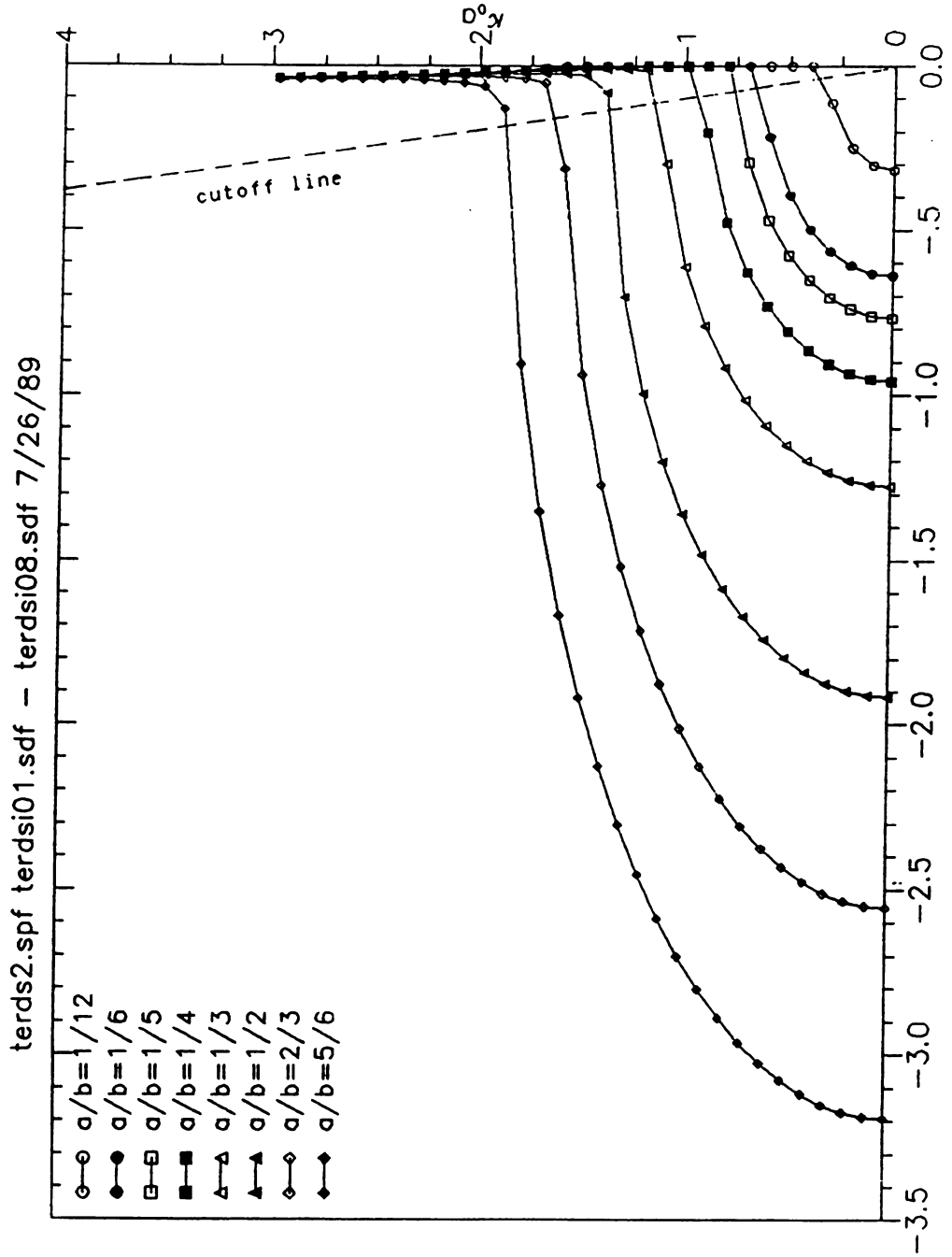

Figure 4.11b w-α diagram for TE_{01} mode for various a/b, ε=3.03-j0.039.

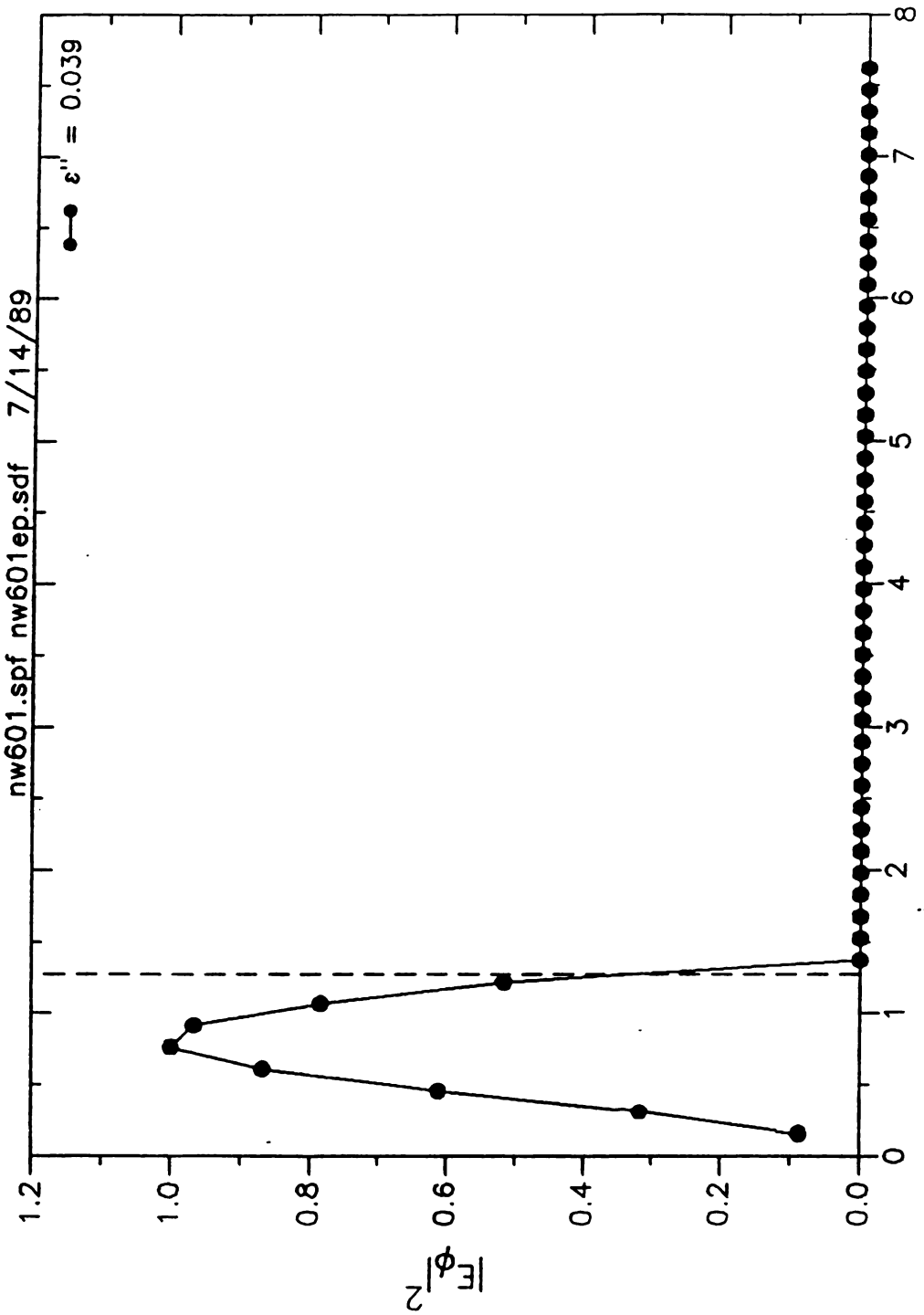

Figure 4.12a Electric field patterns for TE_{01} mode, ε=3.03-j0.039, b/a=6, k$_0$a=2.5.

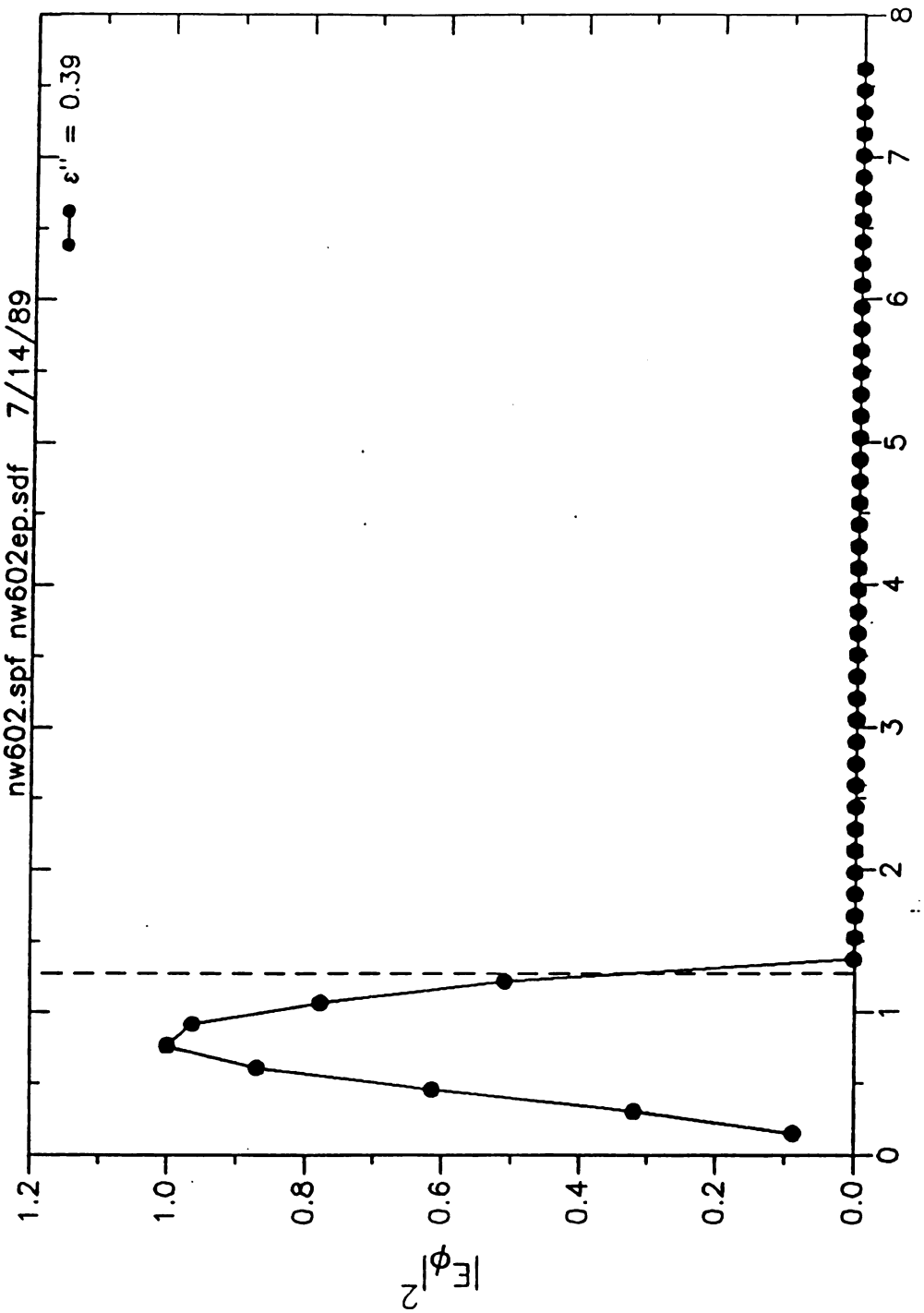

Figure 4.12b Electric field patterns for TE_{01} mode, ε=3.03-j0.39, b/a=6, k0a=2.5.

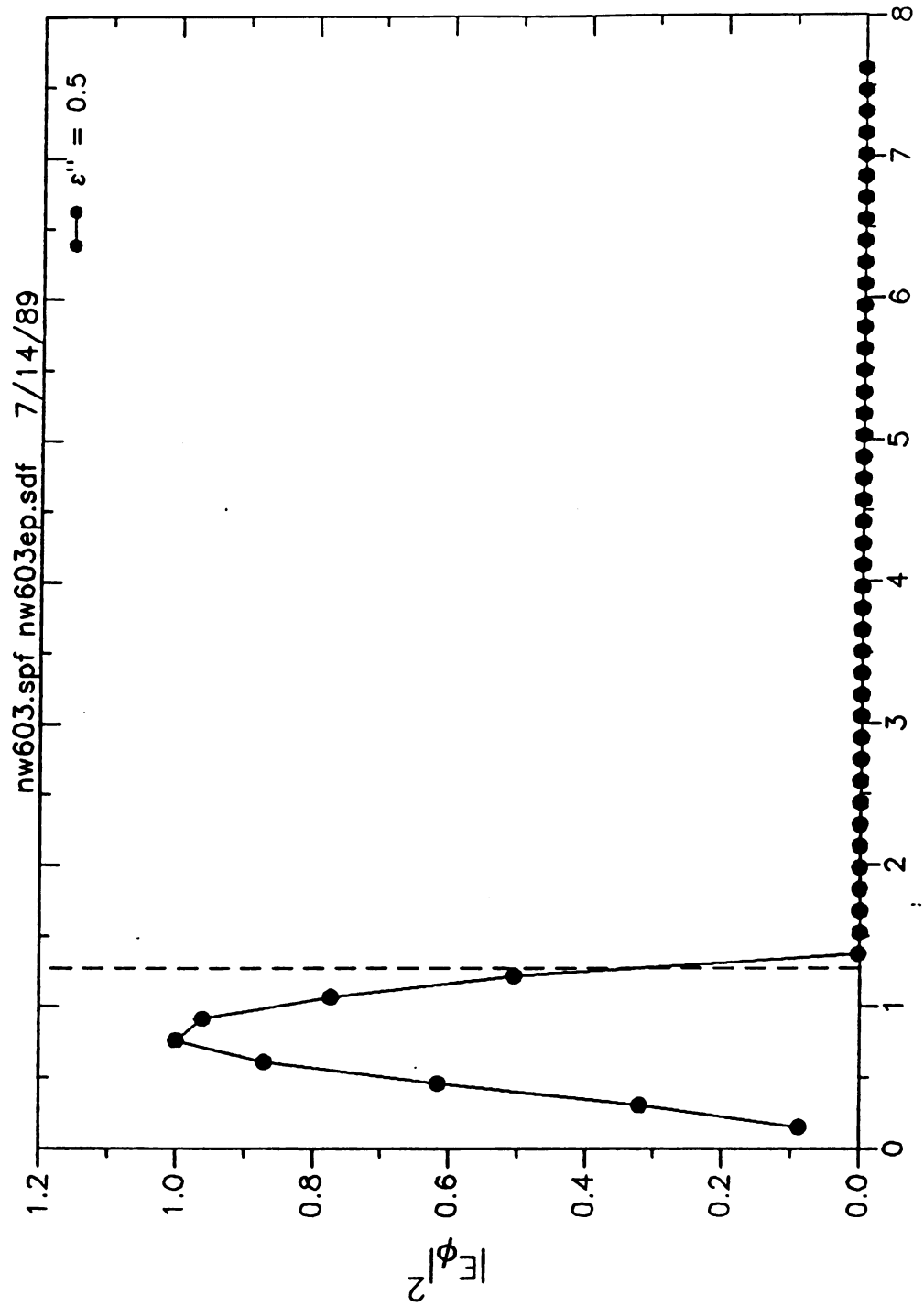

Figure 4.12c Electric field patterns for TE_{01} mode, ε=3.03-j0.5, b/a=6, k_0a=2.5.

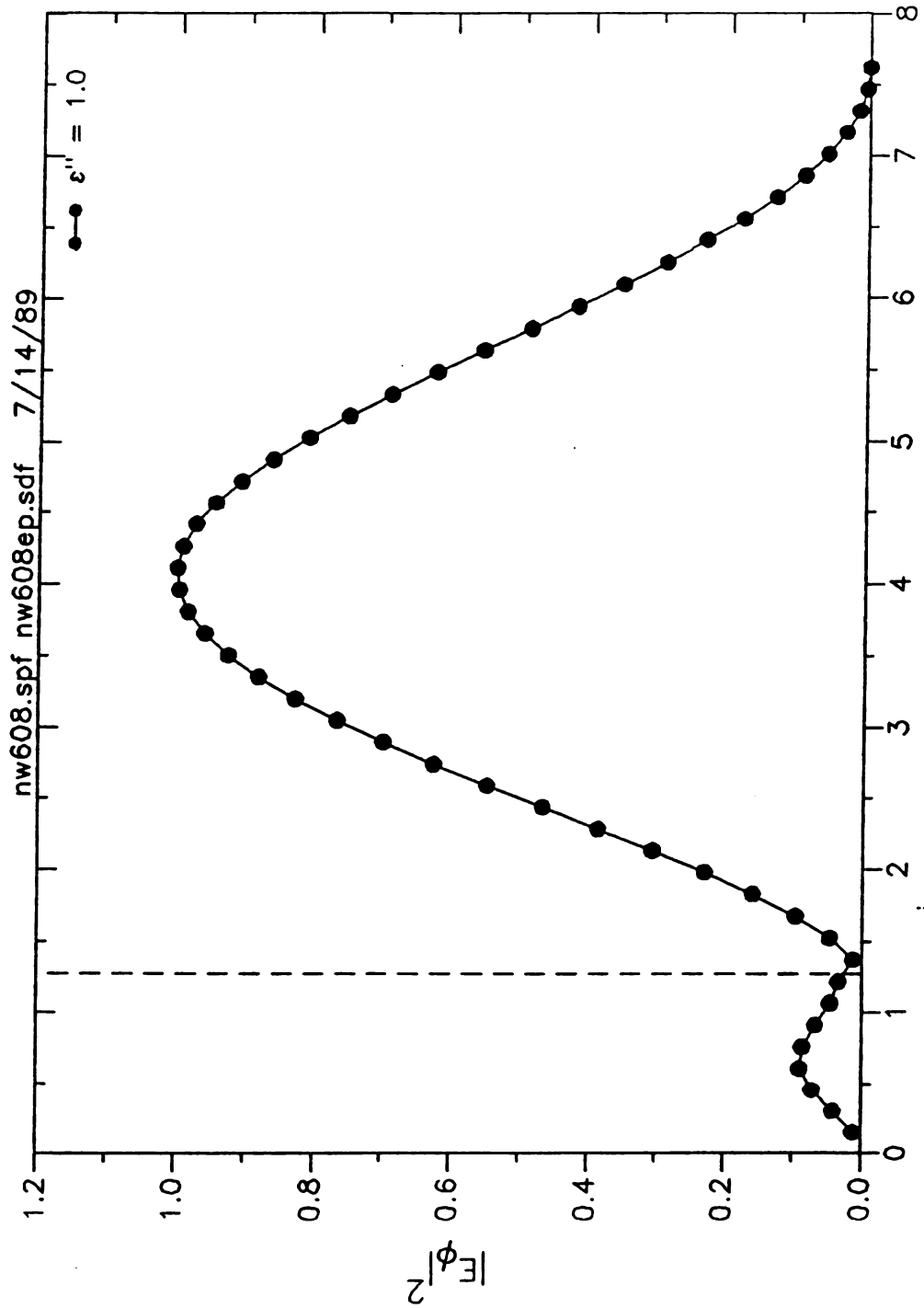

Figure 4.12d Electric field patterns for TE_{01} mode, ε=3.03-j1.0, b/a=6, k_0a=2.5.

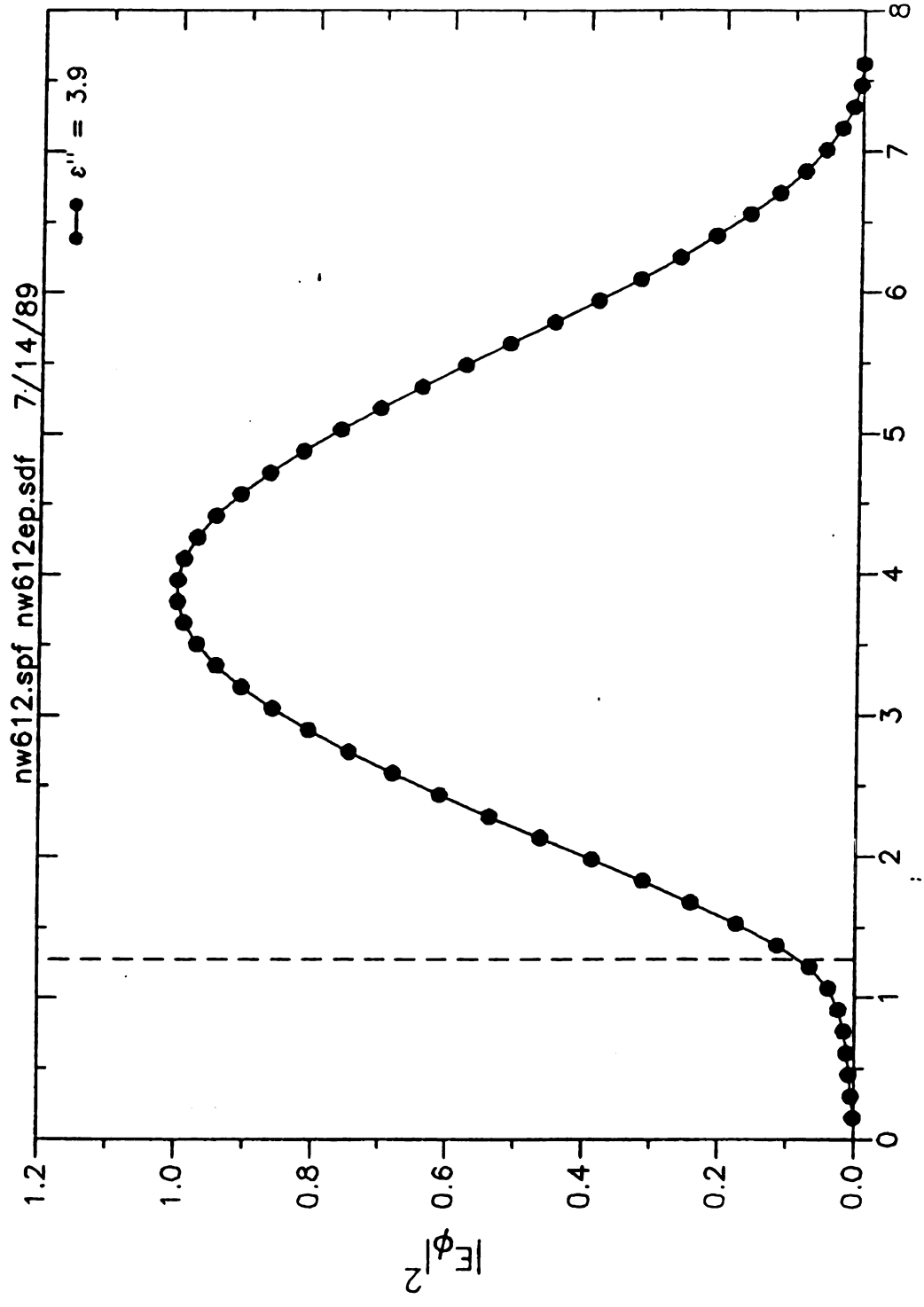

Figure 4.12e Electric field patterns for TE_{01} mode, ε=3.03-j3.9, b/a=6, k_0a=2.5.

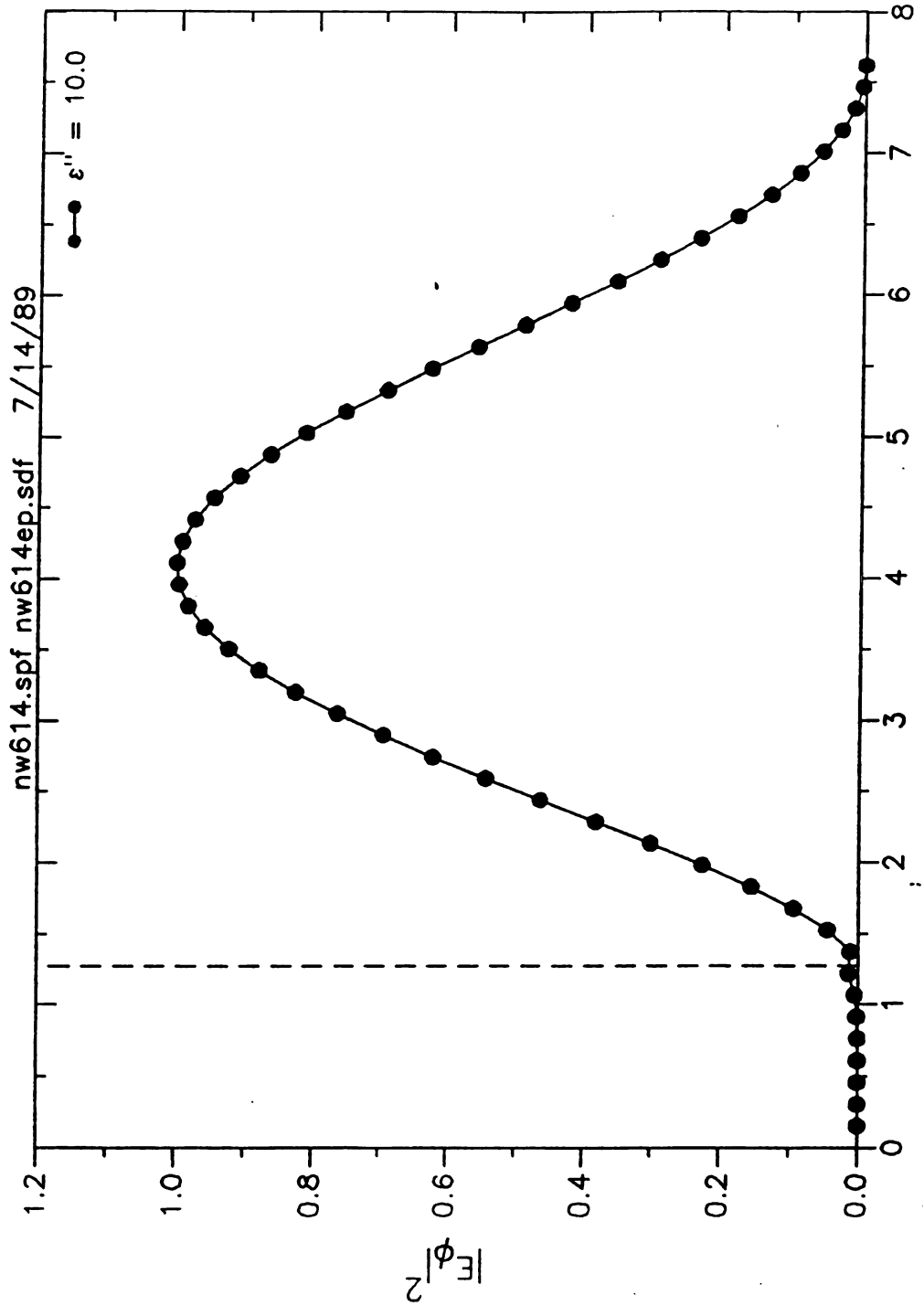

Figure 4.12f Electric field patterns for TE_{01} mode, $\varepsilon=3.03-j10.0$, $b/a=6$, $k_0a=2.5$.

electric energy have been shifted into the air-filled region due to an increase in ε_r'' from 0.5 to 1.0. The redistribution of $|E_\phi|$ results in not only a fast wave TE_{01} mode, as shown in Figure 4.10a, but also a large reduction in attenuation, as depicted in 4.10b. Further increases in ε_r'', as shown in Figures 4.12e and 4.12f, will reduce the amount of $|E_\phi|^2$ confined in rod and almost all of $|E_\phi|$ is sinusoidally distributed in the air-filled region. Note that this behavior is similar to that discovered for the TM_{01} mode, i.e. as ε_r'' increases the electromagnetic field is shielded from the material rod.

Figure 4.13 displays the distributions of $|E_\phi|^2$ of a waveguide loaded with a nylon rod for $\kappa_0 a$ = 0.65, 1.2, and 2.5. For waveguide dimensions of a = 1.27 cm and b = 7.62 cm, $\kappa_0 a$ = 0.65, 1.2 and 2.5 correspond to operating frequencies of 2.45 GHz, 4.523 GHz and 9.423 GHz, respectively. At $\kappa_0 a$ = 0.65, most of $|E_\phi|^2$ is distributed in the air-filled region and $|E_\phi|^2_{max}$ is also located in this region. As $\kappa_0 a$ is increased to 1.2, $|E_\phi|^2_{max}$ moves towards rod surface but is still positioned in the air-filled region. It is of interest to see that although most of the electric energy is still confined in the air-filled region, $|E_\phi|^2$ in rod has grown as much as 2.2 times larger as compared with $\kappa_0 a$ = 0.65. When $\kappa_0 a$ is 2.5, almost all of the electric energy is restained in the rod. Note that for the case of ε_r''=0.039, Figure 4.10a indicates that the TE_{01} mode is near cutoff at $\kappa_0 a$=0.65, a fast wave at $\kappa_0 a$=1.2 and a slow wave at $\kappa_0 a$=2.5.

The influence of rod radius on the electric field distribution is demonstrated in Figures 4.14a through 4.14c for an excitation of 2.45 GHz in a waveguide of 7.62 cm radius which is loaded with a nylon rod with radii of a = 6.35 cm, 2.54 cm and 0.635 cm, respectively. Figure 4.14a shows the field pattern for a = 6.35 cm. Most of the electric energy is distributed in the rod. As the rod radius is reduced to 2.54 cm, the field distributions shown in Figure 4.14b indicates that the energy distributed in rod is about the same as that in the air-filled region, but $|E_\phi|^2_{max}$ is still located in the rod. For a = 0.635 cm, as can seen in Figure 4.14c, the energy stained in the air-filled region is dominant over that in the rod.

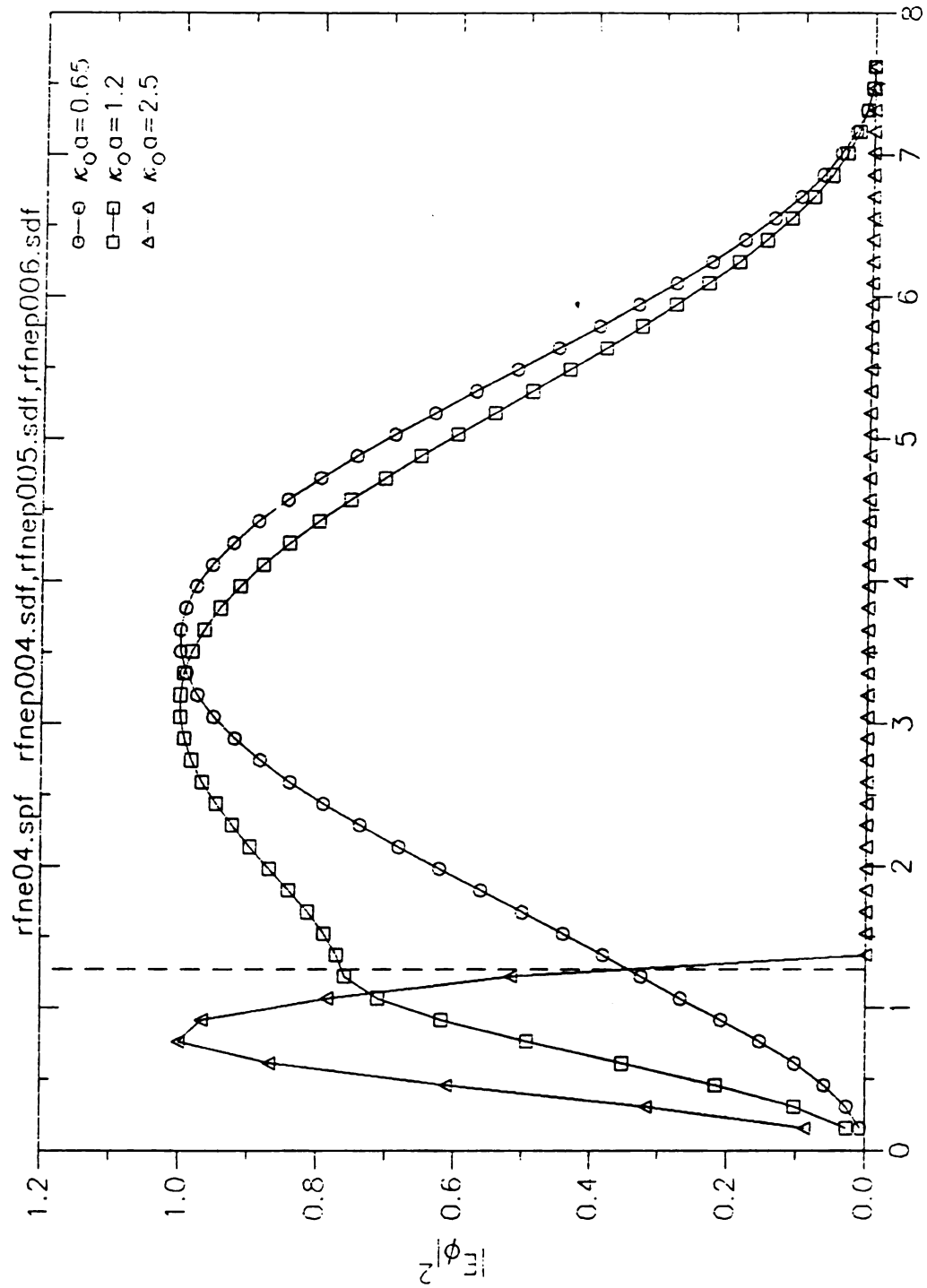

Figure 4.13 Electric field patterns for TE_{01} mode for various $k_0 a$, c=3.03-j0.039, b/a=6.

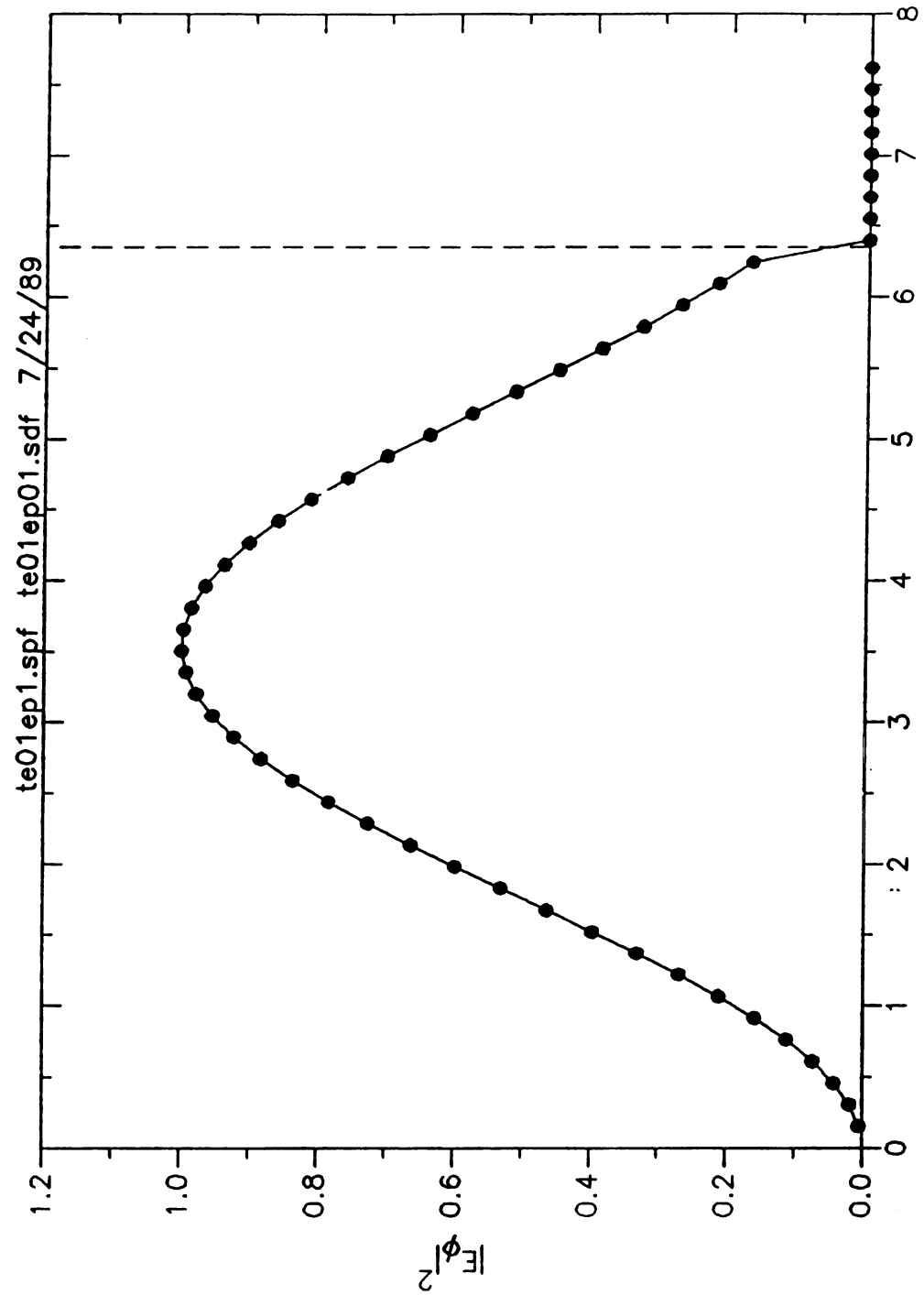

Figure 4.14a Electric field patterns for TE_{01} mode, c=3.03-j0.039, a=6.35 cm, b=7.62 cm, k_0a=3.26.

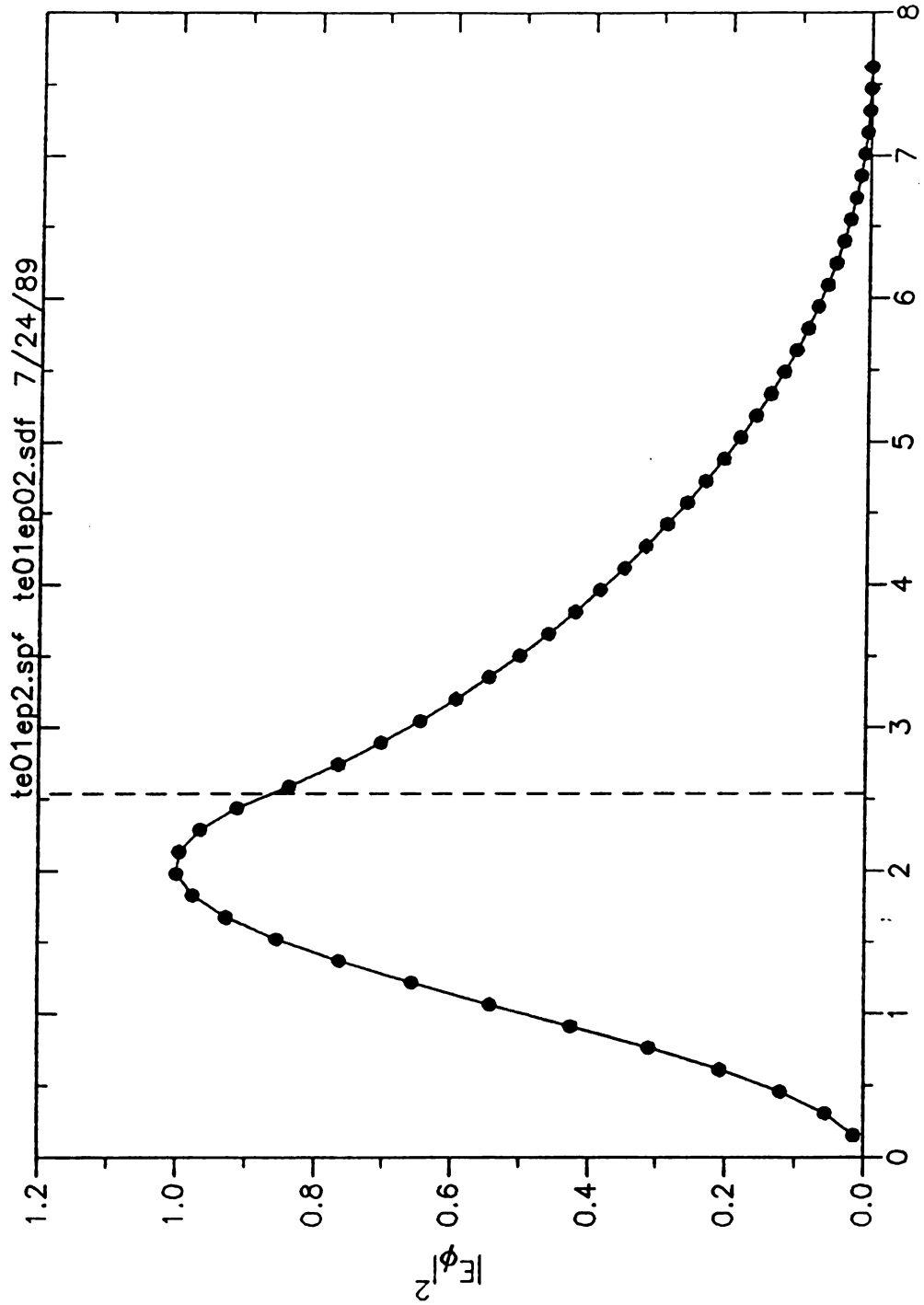

Figure 4.14b Electric field patterns for TE_{01} mode, ε=3.03-j0.039, a=2.54 cm, b=7.62 cm, k_0a=1.3.

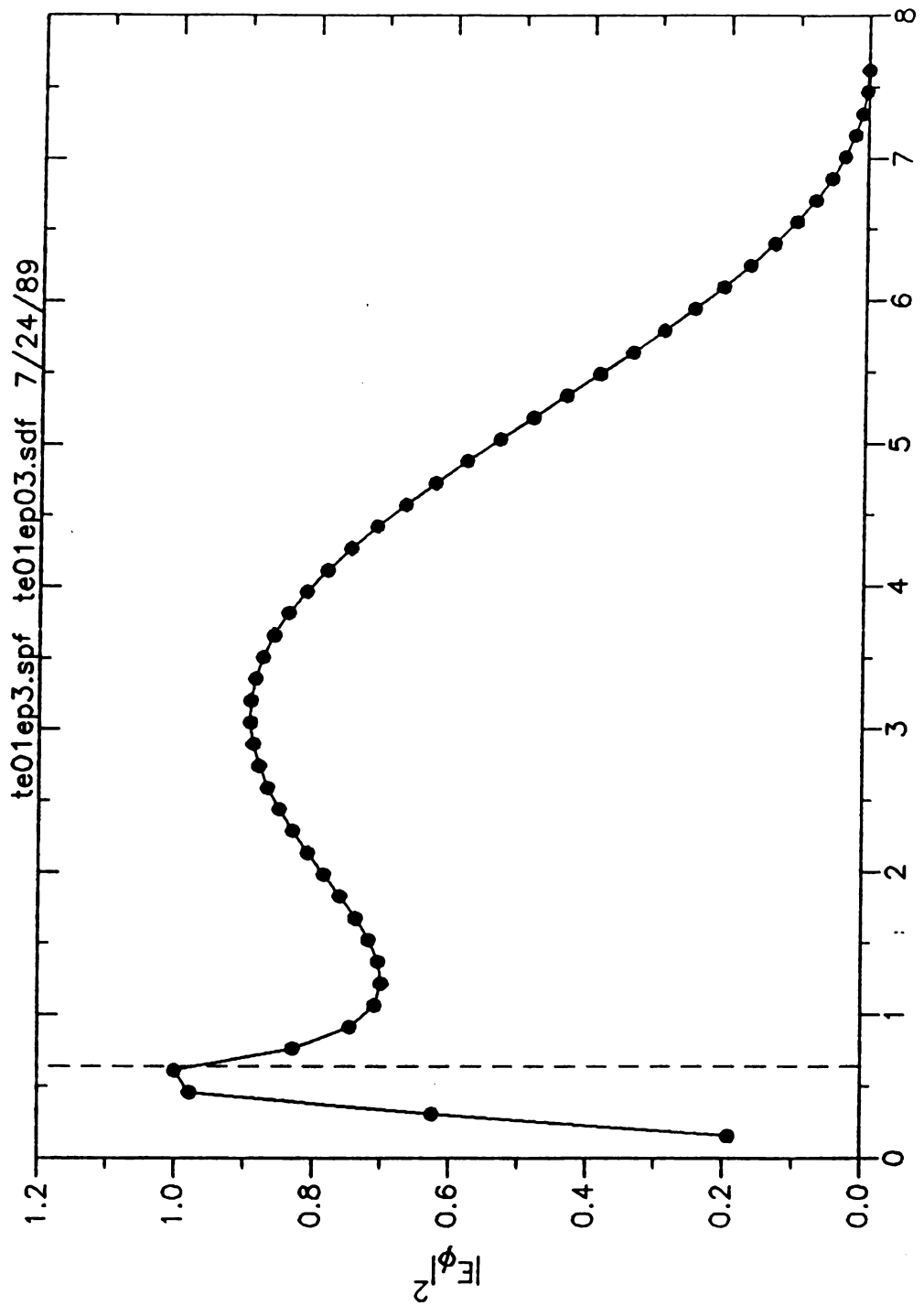

Figure 4.14c Electric field patterns for TE_{01} mode, c=3.03-j0.039, a=0.635 cm, b=7.62 cm, k₀a=0.326.

According to the dispersion characteristics and field patterns for TM_{01} and TE_{01} modes illustrated above, it is found that TM_{01} mode is a better mode for microwave heating than TE_{01} mode. First of all, TM_{01} mode stays in the slow wave region for a larger range of ε_r'' than TE_{01} mode. As noted earlier, most of the electromagnetic energy of the slow wave is confined in the dielectric material. In other words, TM_{01} mode can be used for microwave heating of materials for a wider range of the dielectric losses. Secondly, the large difference between the relative magnitude of the E_z and E_ρ for TM_{01} mode provides an easy way of coupling electromagnetic energy into the dielectric rod. That is, for TM_{01} mode, only very small E_ρ been excited will give rise to relative large E_z in the dielectric rod.

4.3.2.1.5 $\omega - \kappa_z$ diagrams and field patterns for HE_{11} mode

(A) $\omega - \kappa_z$ diagrams

Figures 4.15a through 4.15c depict the $\omega - \beta$ and $\omega - \alpha$ diagrams for HE_{11} mode for various ε_r''. The waveguide has a radius of 7.62 cm radius and is loaded with a dielectric rod of 1.27 cm radius and dielectric constant of $\varepsilon_r' = 3.03$. As the cases for TM_{01} and TE_{01} shown in Figure 4.6a and 4.10a, two groups of dispersion curves can be identified in Figure 4.15a. Group (1) is the family of curves which has $\varepsilon_r'' \leq 2.0$. The $\omega - \beta$ curves for this group cross the free space light line before $\kappa_0 a < 1.4$. Group (2) is the family of curves which has $\varepsilon_r'' \geq 2.5$ and stays in the fast wave region for $\kappa_0 a < 3.0$. At high frequency, the dispersion curves of group (1) approach the nylon light line asymptotically, while the dispersion curves of group (2) converge to the free space light line. As can be seen in Figure 4.15b, the $\kappa_0 a$ crossings for group (1) increase with increasing ε_r''.

The $\omega - \alpha$ diagram displayed in Figure 4.15c shows that above $\kappa_0 a = 1.0$ the attenuation for group (1) increases as ε_r'' is increased decrease in α is observed when ε_r'' is increased from 2.0 to 2.5. For group (2), at high frequency an increase in ε_r'' may

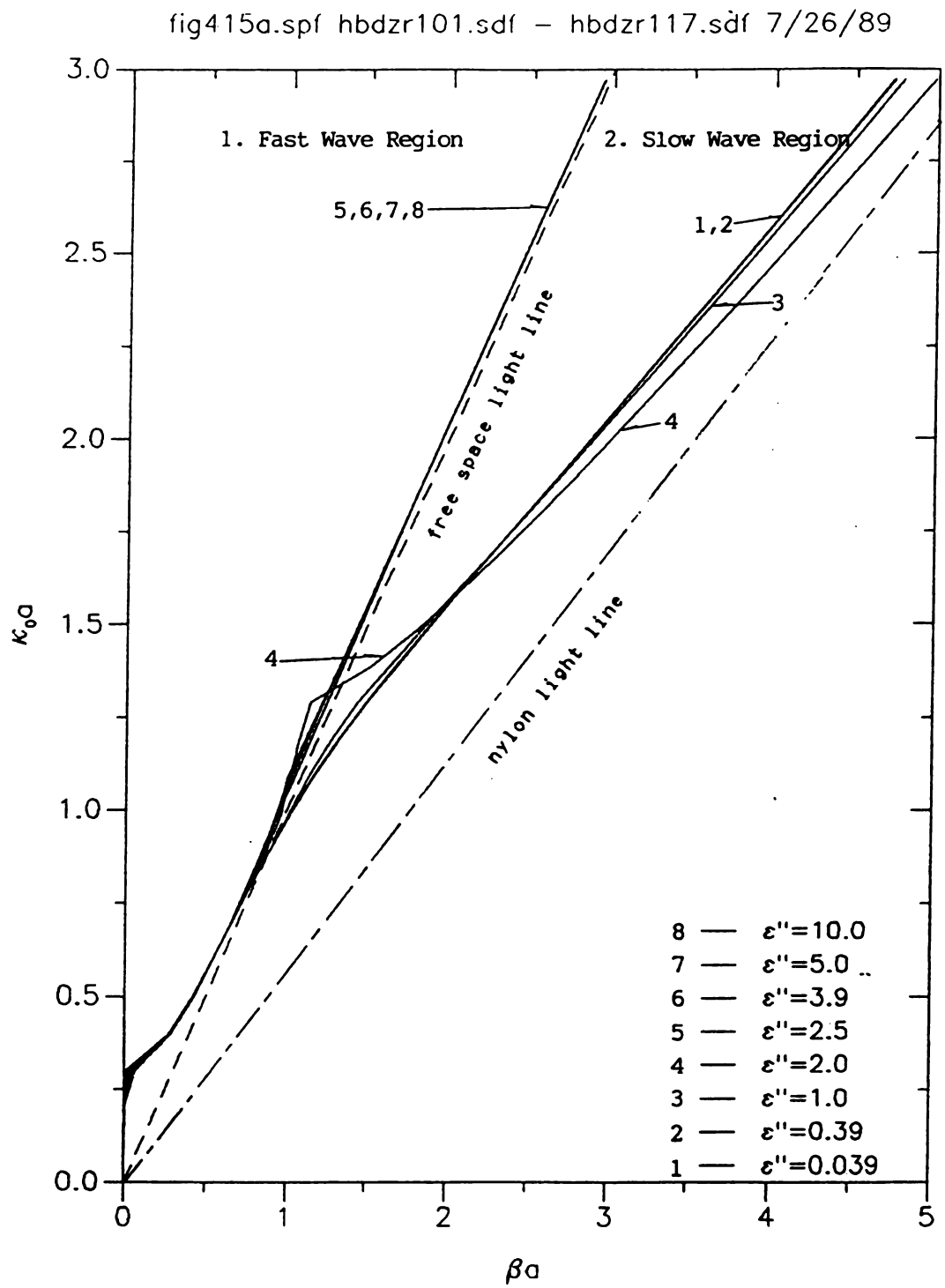

Figrue 4.15a ω-β diagram for HE_{11} mode for various ε", b/a=6, ε'=3.03.

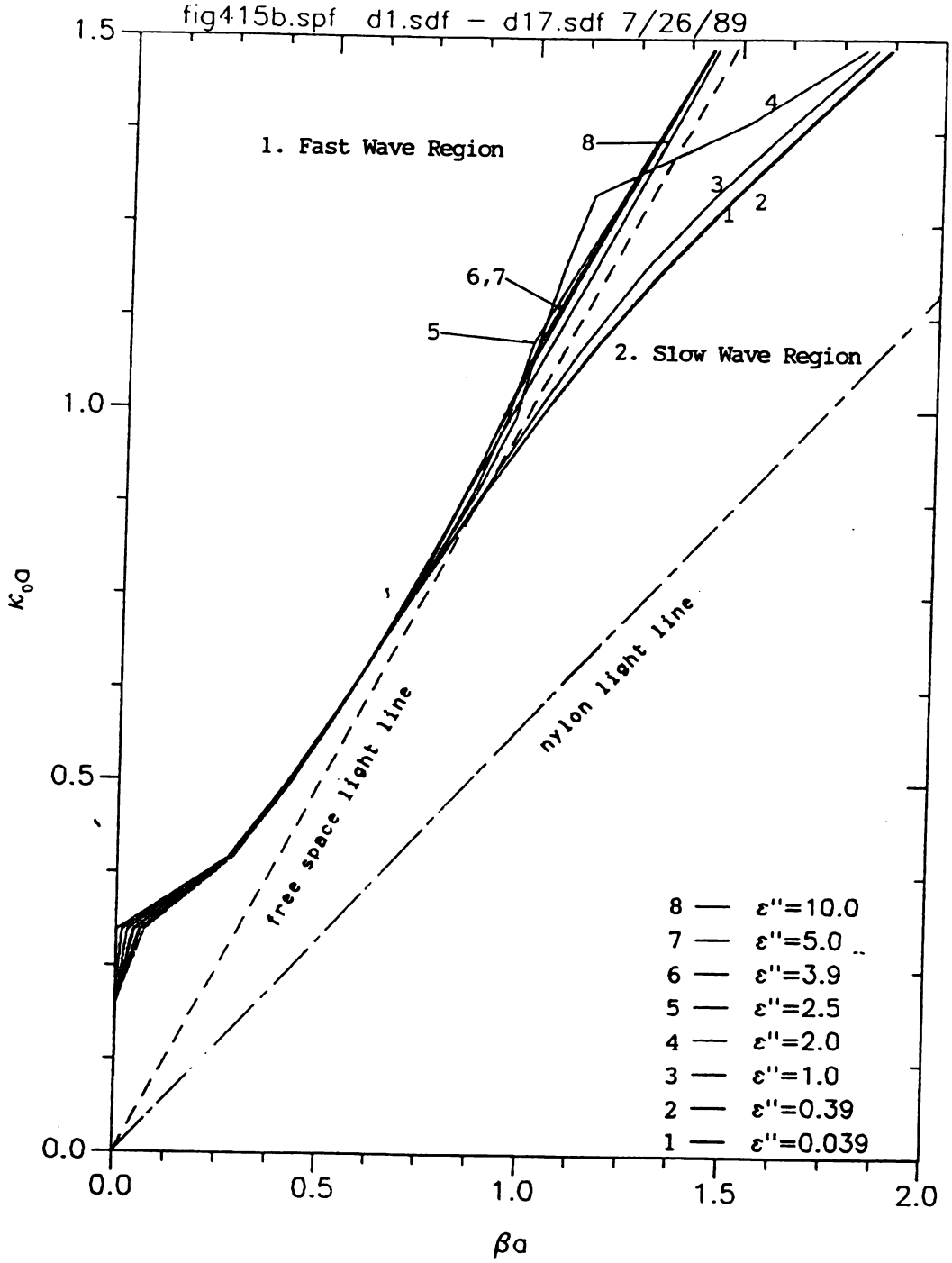

Figure 4.15b Low frequency portion of the w-ß diagrm for HE_{11} mode for various ε", b/a=6, ε=3.03

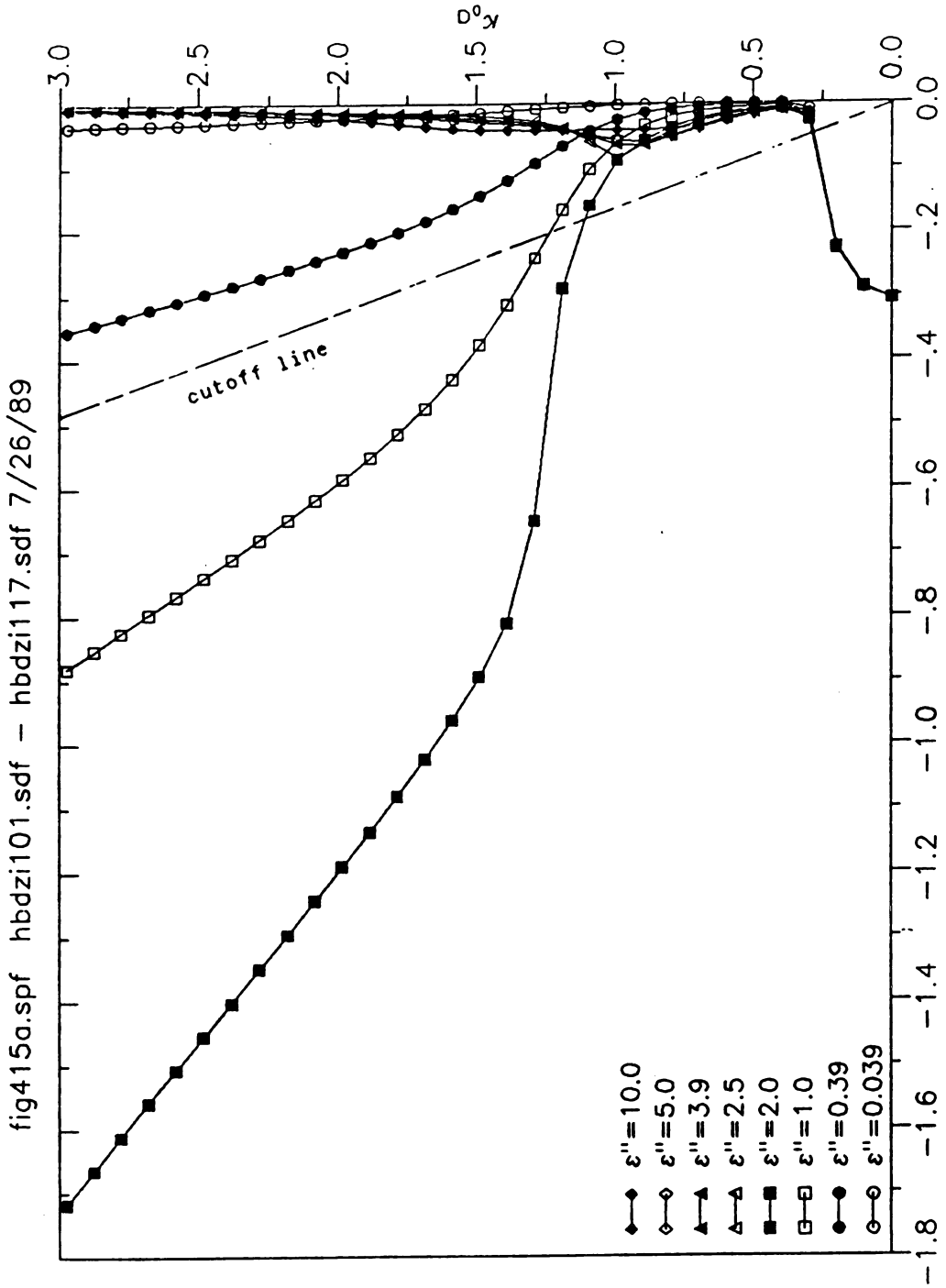

Figure 4.15c w-α diagram for HE11 mode for various ε'', b/a=6, ε'=3.03.

result in a reduction or an increase in α, depending on the frequency. The field patterns given in section (B) will shed light on the changes of α due to the changes in EM field distributions resulting from an increase in ε_r'' at high frequency. By comparing Figures 4.15a and Figure 4.15c, it is seen that group (1) is in slow wave region and group (2) is in fast wave region, provided $\kappa_0 a > 1.4$. The $\omega - \alpha$ curves at low frequency, i.e. $\kappa_0 a < 0.35$, are barely altered as ε_r'' is changed. There are two cutoff frequencies for each of $\varepsilon_r'' = 0.39$, 1.0 and 2.0 curves. Only one cutoff frequency exists for $\varepsilon_r'' = 0.039$, 2.5, 3.9, 5.0 and 10.0. The cutoff frequency in the low frequency range, i.e. $\kappa_0 a < 0.5$, is slightly increased as ε_r'' is increased.

The $\omega - \beta$ and $\omega - \alpha$ curves as a function of rod radius are shown in Figures 4.16a and 4.16b. It is of interest to see that the intersections of the $\omega - \beta$ curves with the free space light line, as shown in Figure 4.16a, increase with increasing rod radius. All $\omega - \beta$ curves cross the free space light line before $\kappa_0 a = 1.25$ and become asymptotic to the nylon light line at high frequency. As depicted in Figure 4.16b, the normalized cutoff wave number for each $\omega - \alpha$ curve is increased as rod radius is increased and is smaller than the empty TE_{11} cutoff wave number. Above cutoff, i.e. at $\kappa_0 a > 1.5$, αa converges for all a/b ratios. Below cutoff, increasing ε_r'' yields an increase in αa at a fixed $\kappa_0 a$.

(B) Field patterns

Figures 4.17a through 4.17h show the electric field patterns of HE_{11} mode for a variety of ε_r'' at $\kappa_0 a = 2.0$. In these examples, the radii of rod and the waveguide are 1.27 cm and 7.62 cm, respectively. Accordingly, the operating frequency corresponding to $\kappa_0 a = 2.0$ is 7.52 GHz. The ε_r' of dielectric rod is 3.03. HE_{11} has three electric field components, E_z, E_ρ and E_ϕ.

The field patterns shown in Figures 4.17a through 4.17d are the field patterns for group (1), i.e. $\varepsilon_r'' \leq 2.0$, depicted in Figure 4.17a. A close examination of the field distributions discloses that most of the electric energy is distributed within the dielectric

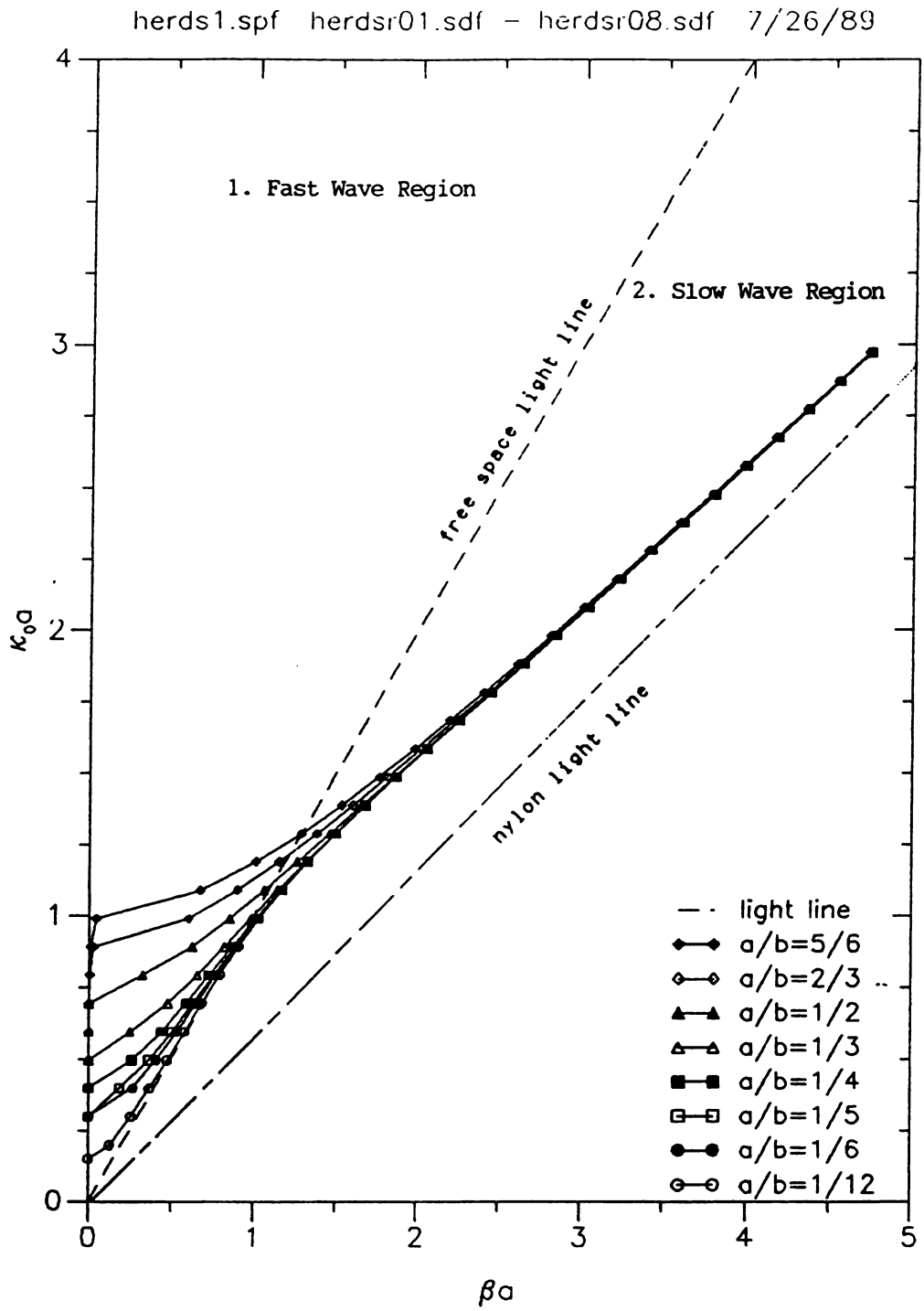

Figure 4.16a w-β diagram for HE_{11} mode for various a/b, ε=3.03-j0.039.

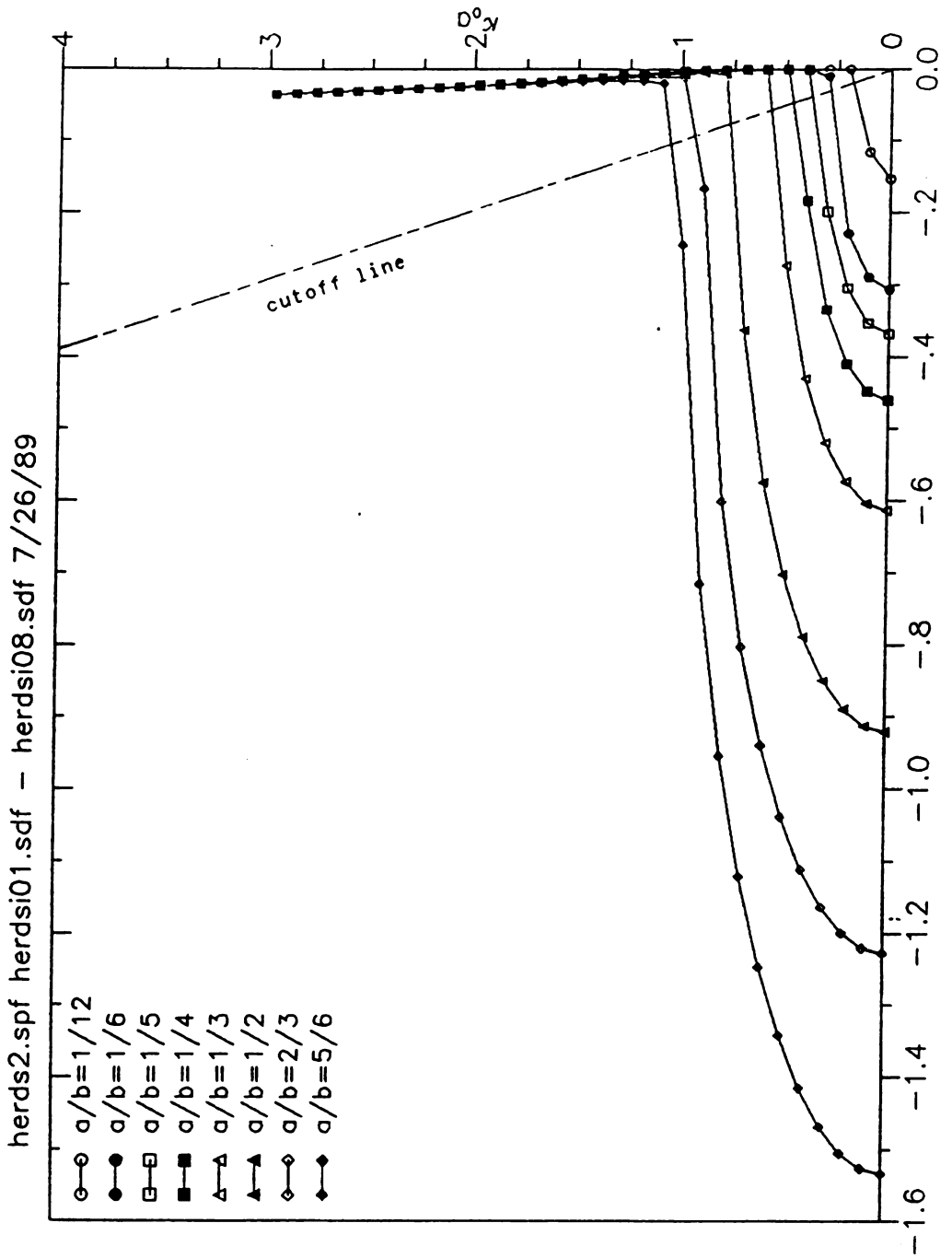

Figure 4.16b w-α diagram for HE11 mode for various a/b, ε=3.03-j0.039.

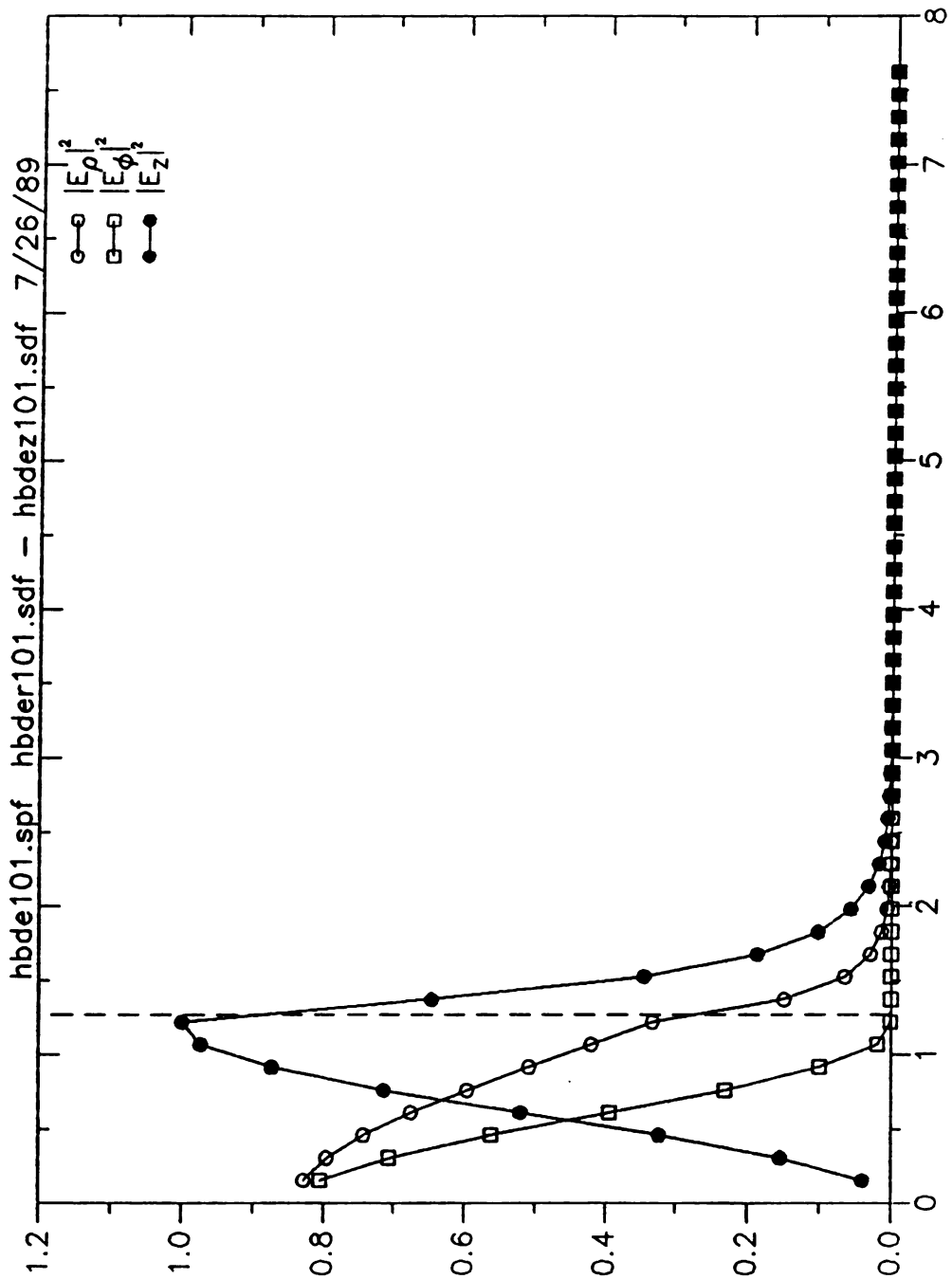

Figure 4.17a Electric field patterns for HE_{11} mode, ε=3.03-j0.039, b/a=6, k_0a=2.0.

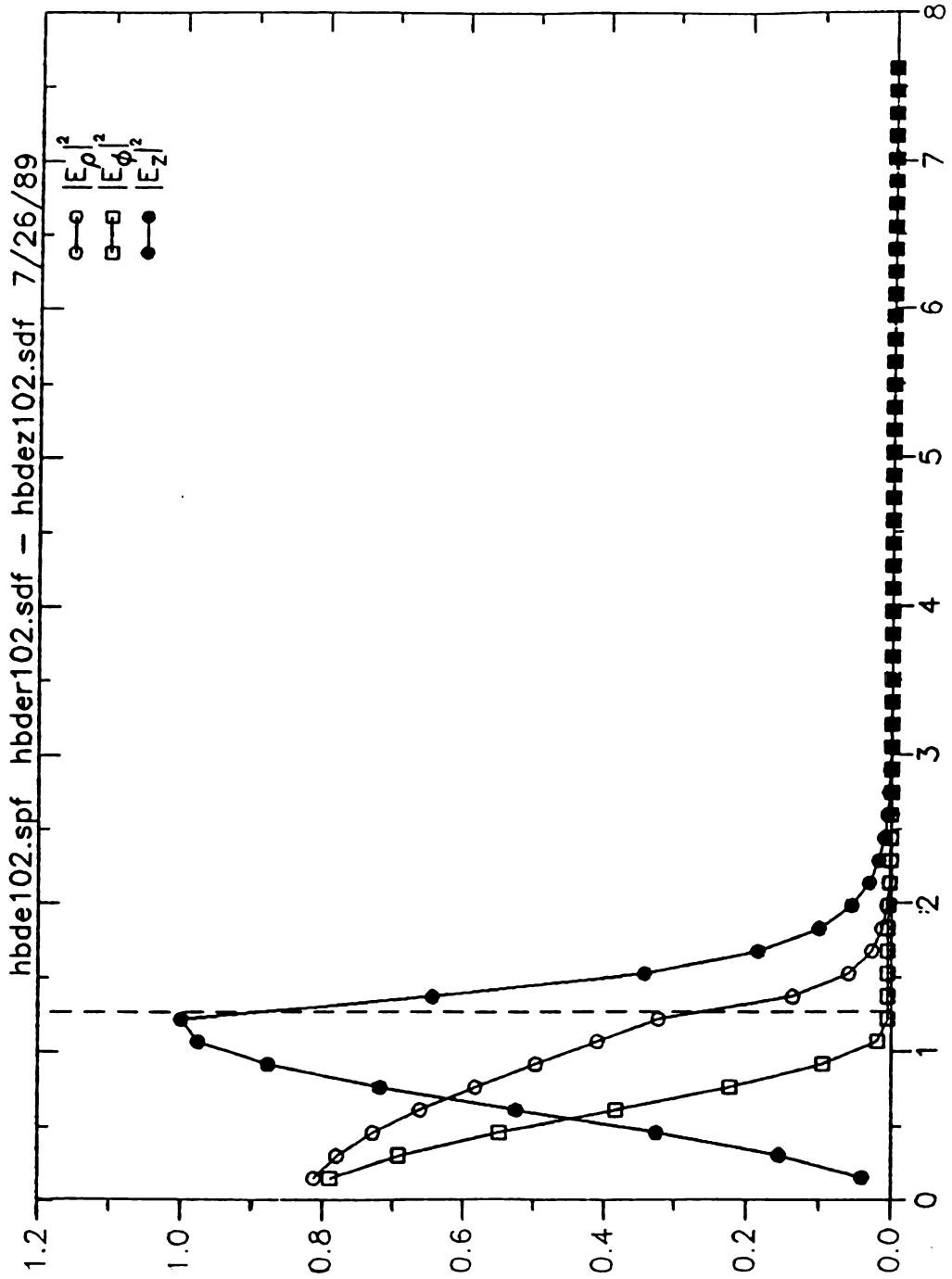

Figure 4.17b Electric field patterns for HE11 mode, ε=3.03-j0.39, b/a=6, koa=2.0.

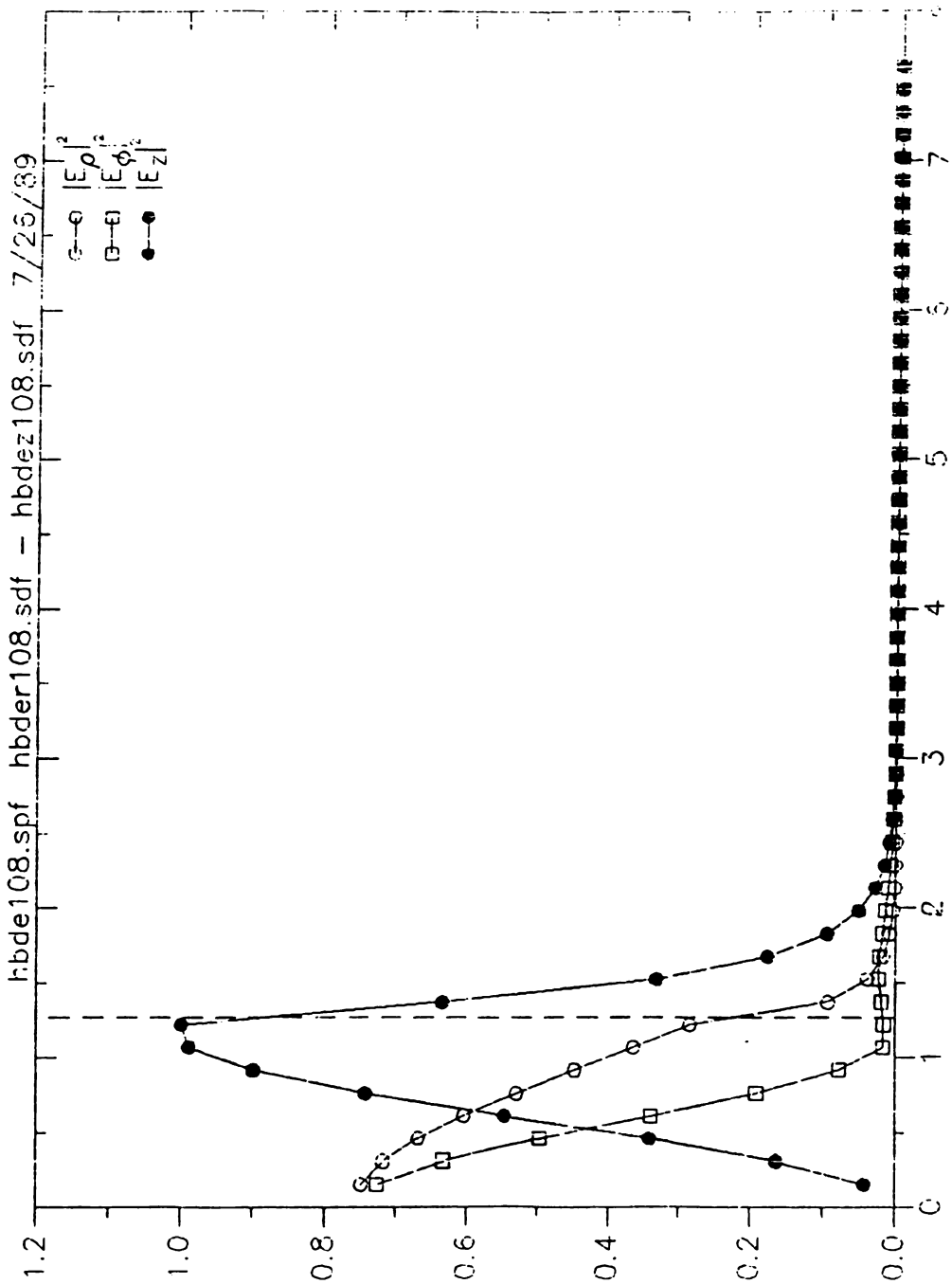

Figure 4.17c Electric field patterns for HE_{11} mode, ε=3.03-J1.0, b/a=6, k0a=2.0.

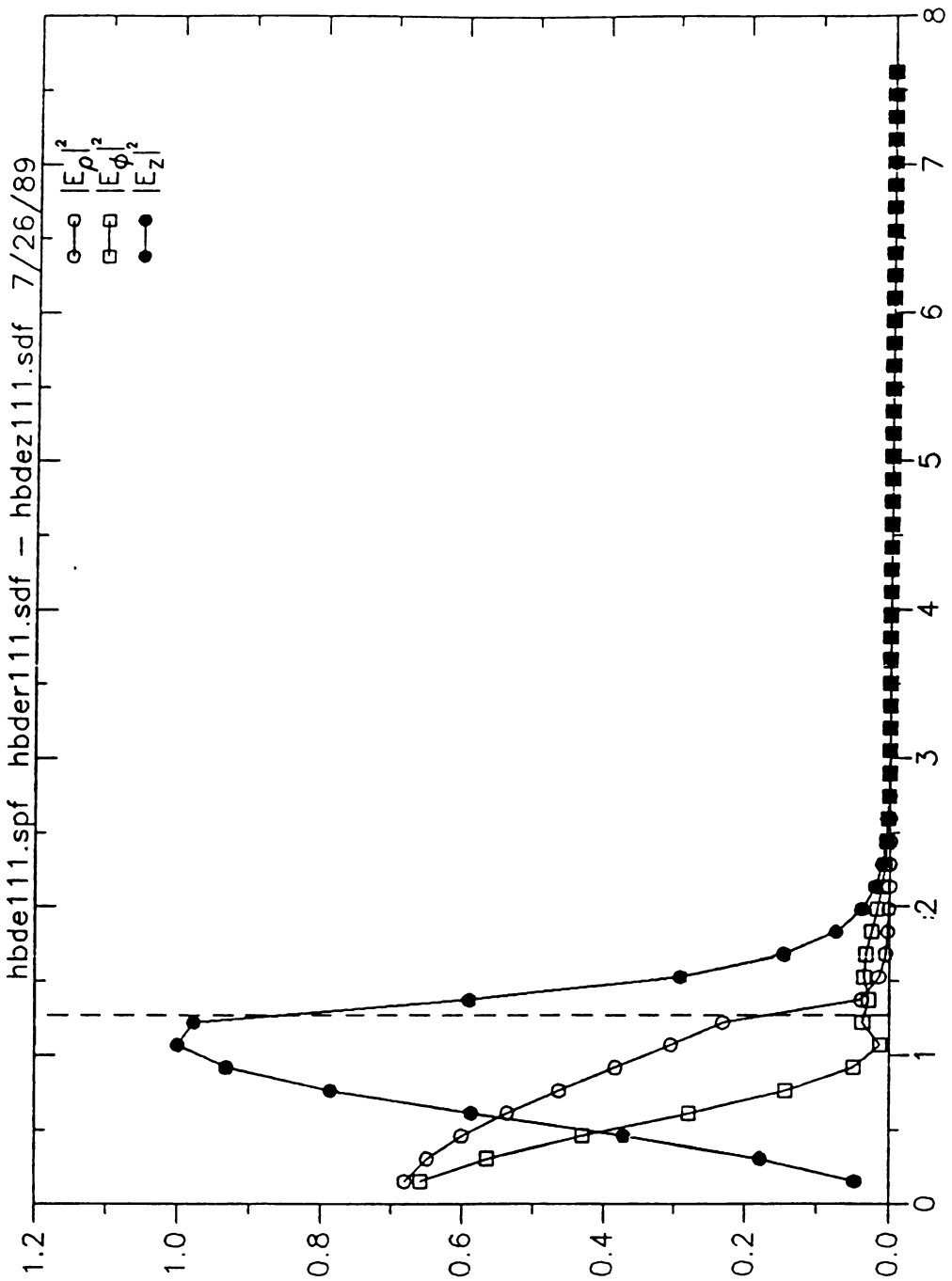

Figure 4.17d Electric field patterns for HE_{11} mode; c=3.03-12.0, b/a=6, k_0a=2.0.

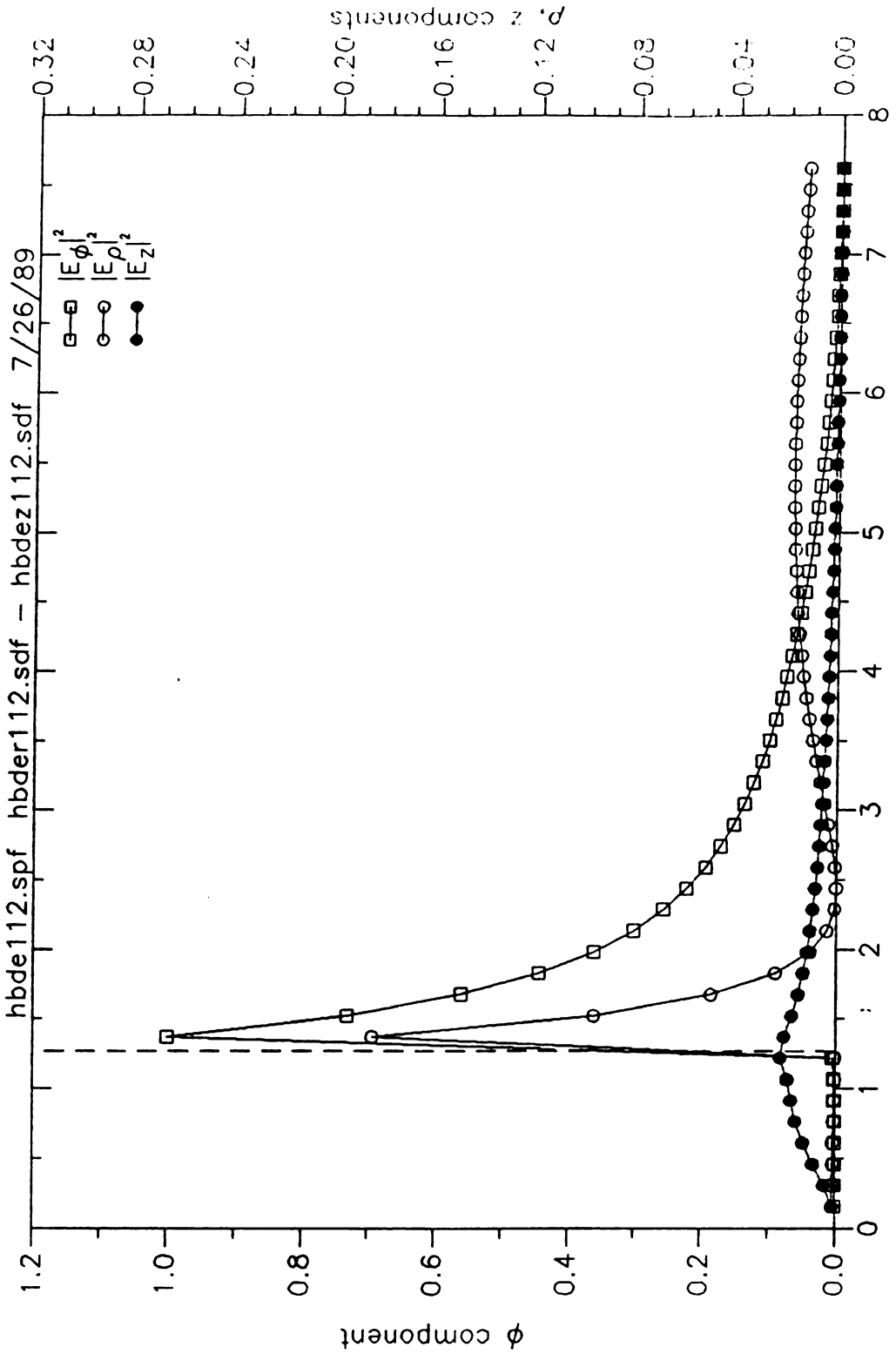

Figure 4.17e Electric field patterns for HE_{11} mode, ϵ=3.03-j2.5, b/a=6, k_0a=2.0.

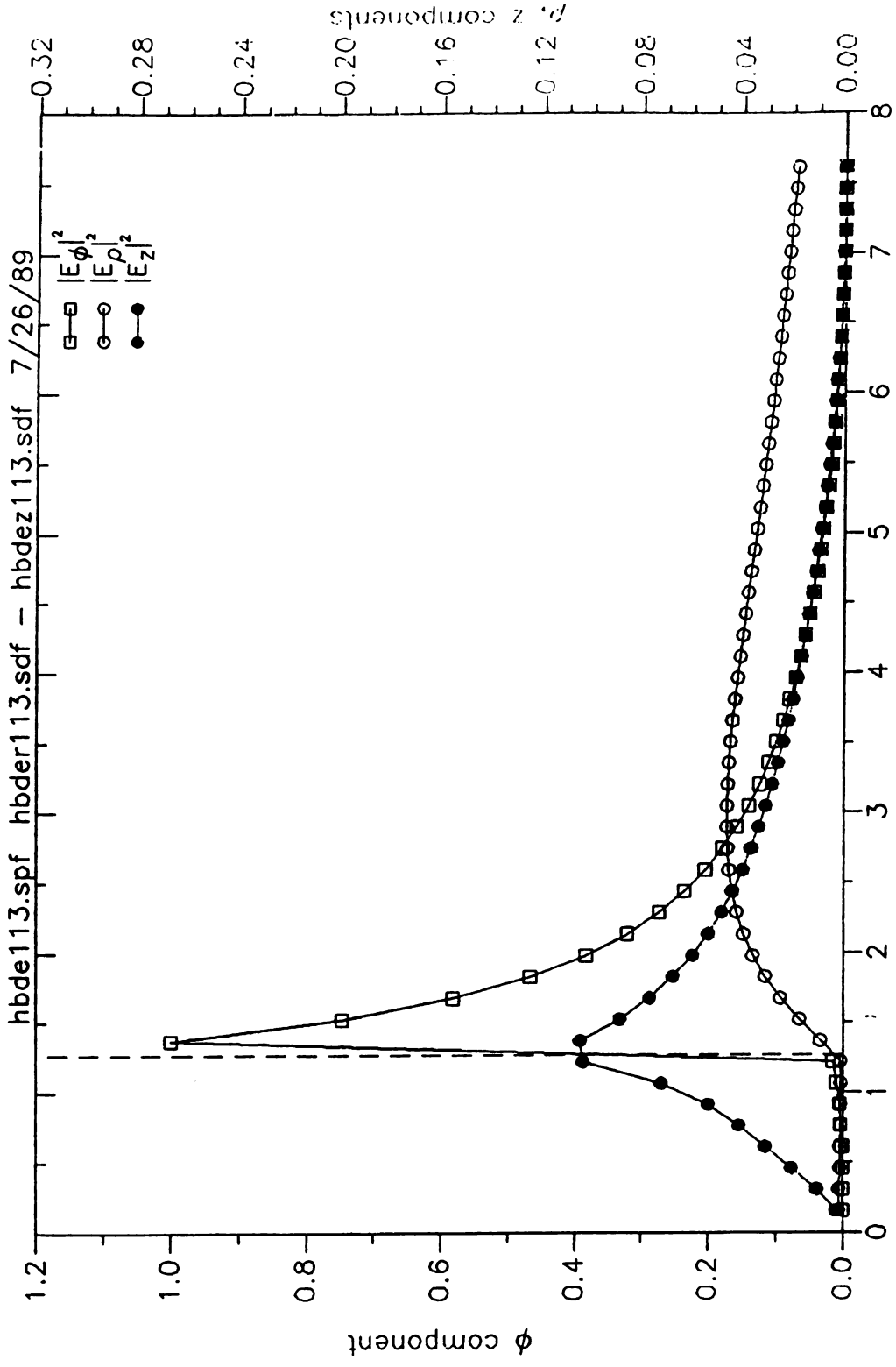

Figure 4.17f Electric field patterns for HE_{11} mode, ε=3.03-j3.9, b/a=6, k_0a=2.0.

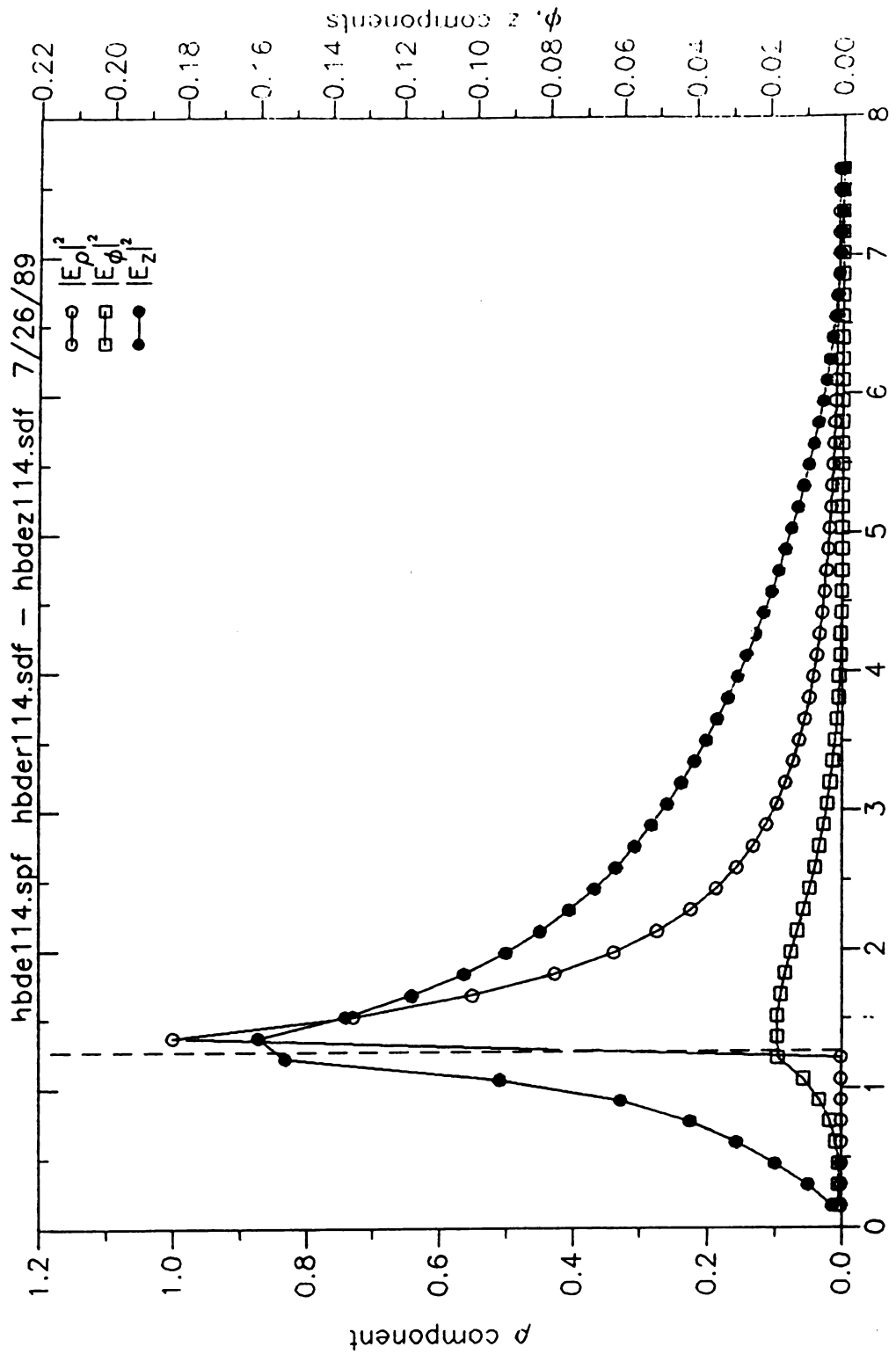

Figure 4.17g Electric field patterns for HE_{11} mode, ε=3.03-j5.0, b/a=6, k_0a=2.0.

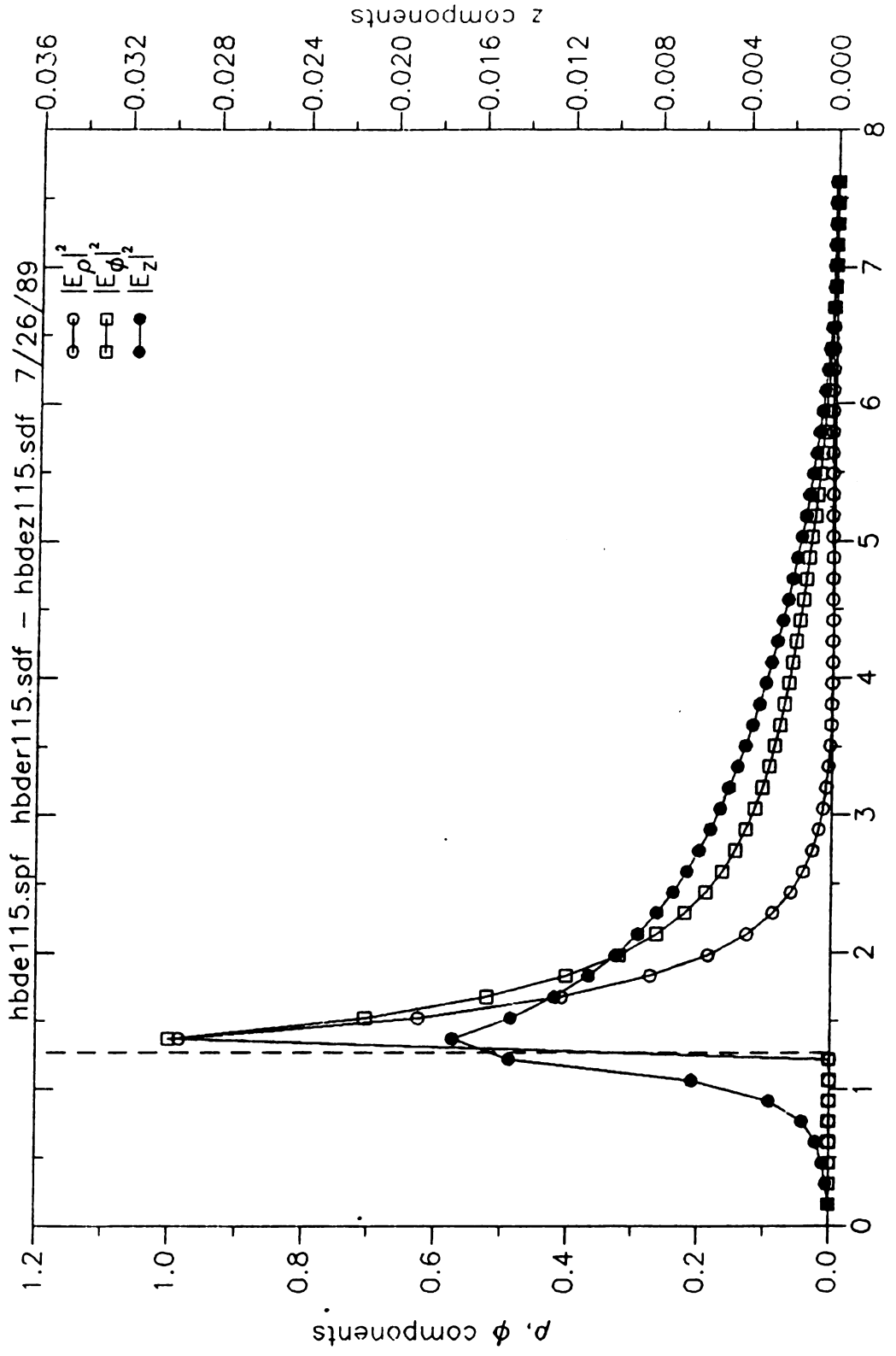

Figure 4.17h Electric field patterns for HE_{11} mode, ε=3.03-j10.0, b/a=6, k_0a=2.0

rod. Only minor changes in the fields are observed as ε_r'' varies. By comparing Figure 4.17a and 4.17d, it is seen that $|E_\rho|^2$ and $|E_\phi|^2$ in rod has dropped as much as 0.85 times due to an increase in ε_r'' from 0.039 to 2.0. In Figure 4.17d, $|E_z|^2$ is still the dominant field component, but $|E_z|^2_{max}$ has slightly moved from the dielectric surface toward the center of dielectric rod. Note that $|E_\rho|^2_{max}$ in air-filled region grows to 0.04 from zero, $|E_\phi|^2_{max}$ drops from 0.25 to 0.2 and $|E_\phi|^2$ in the air-filled region becomes more tightly bounded to the rod surface as a result of the increase in ε_r''. Apparently, the energy stored in the dielectric rod does not undergo much change as ε_r'' varies from 0.039 to 2.0. Again, the field patterns show why the attenuation for group (1) shown in Figure 4.15c increases as ε_r'' is increased at high frequency.

The field patterns for group (2) are presented in Figures 4.17e through 4.17h. Figure 4.17e depicts the electric fields corresponding to $\varepsilon_r'' = 2.5$. In comparison with Figure 4.17d, it is found not only almost of the EM energy is now confined in the air-filled region, but the dominant field component is $|E_\phi|$ instead of $|E_z|$. Obviously, the cause of the enormous reduction in α displayed in Figure 4.15c as ε_r'' is changed from 2.0 to 2.5 is due to the EM energy redistribution within the waveguide as ε_r'' varies. Also, the transition of most of the EM energy from rod into air-filled region moves the HE_{11} slow wave into fast wave region, as can be seen in Figure 4.15a. When ε_r'' is increased to 3.9, the field patterns shown in Figure 4.17f indicates that the distributions of $|E_\phi|$ and $|E_z|$ have changed and the energy of E_z restrained in rod has also increased. However, most of the EM energy is still confined in the air-filled region. Figure 4.17g shows the field patterns of the case where $\varepsilon_r'' = 5.0$. When compared with Figure 4.17f, it is found that E_ρ is the dominant component and $|E_\phi|^2_{max}$ is almost ten times smaller as a result of the increase in ε_r''. Although the distributions of $|E_z|$ are not altered much but $|E_z|^2_{max}$ is increased from 0.1 in Figure 4.17e to 0.15. It is interesting to see that when $\varepsilon_r'' = 10.0$, which is shown in Figure 4.17h, $|E_\phi|$ becomes the dominant field and gains as much as 67 times due to the increase in ε_r'' from 5.0 to

10.0. In the mean time, $|E_z|^2_{max}$ reduces from 0.155to 0.0165. The field distributions displayed in Figures 4.17e through 4.17h do not indicate a general pattern of the change of the EM fields as ε_r'' is increased, as was seen for TM_{01} and TE_{01}. It may be because of the existence of all the six field components, any change in ε_r'' gives rise to much more complicated perturbation to HE_{11} mode than to TE_{01} and TM_{01} modes.

The next three Figures, Figure 4.18a, 4.18b and 4.18c, depict the field patterns of a waveguide loaded with a nylon rod for different $\kappa_0 a$. The waveguide dimensions are identical to the examples given in Figure 4.17. As shown in Figure 4.18a, where $\kappa_0 a$ = 1.8, $|E_z|$ is the largest field component and most of the EM energy is distributed in the nylon rod. Apparently, this is a slow wave. In Figure 4.18b, the field patterns correspond to $\kappa_0 a$ = 0.65. It is seen that $|E_\rho|$ is the dominant field and the EM energy distributed in the air-filled region is much larger than that in the nylon rod. Obviously, a slow wave has been transformed into a fast wave due to the reduction of the operating frequency from $\kappa_0 a$ = 1.8 to $\kappa_0 a$ = 0.65. When $\kappa_0 a$ = 0.26, the field patterns given in Figure 4.18c show that the EM energy confined in nylon rod is increased, however, the majority of the EM energy is still distributed in the air-filled region.

The changes of the field distributions as a function of rod radius are investigated in Figures 4.19a, 4.19b and 4.19c. In these examples, a cavity of 7.62 cm radius is loaded with a nylon rod and excited at 2.45 GHz. In Figure 4.19a, the rod radius is 6.35 cm, which results in $\kappa_0 a$ = 3.25. It is found that $|E_\rho|^2_{max}$ and $|E_\phi|^2_{max}$ are equal and are located in the center of nylon rod. Also seen in Figure 4.19a is that most of the EM energy is confined in rod. As the rod radius is decreased to 2.54 cm, the filed patterns depicted in Figure 4.19b show that the EM energy distributed in air-filled region is well beyond that in the nylon rod. A significant reduction in $|E_\phi|^2$ is observed due to an decrease in rod radius. Figure 4.19c presents the field patterns of a rod of 0.635 cm radius.

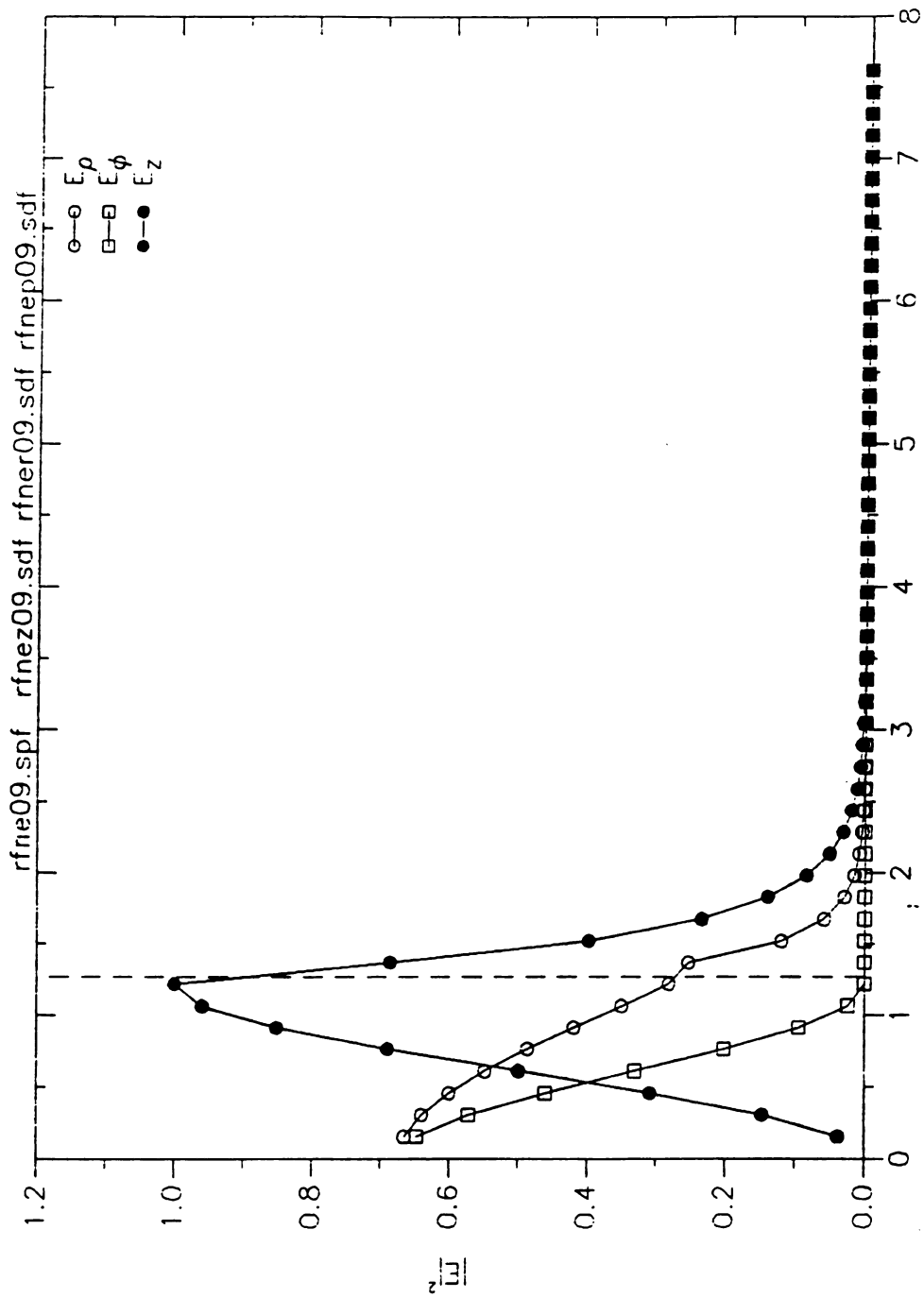

Figure 4.18a Electric field patterns for HE_{11} mode, ε=3.03-j0.039, b/a=6, k_0a=1.8.

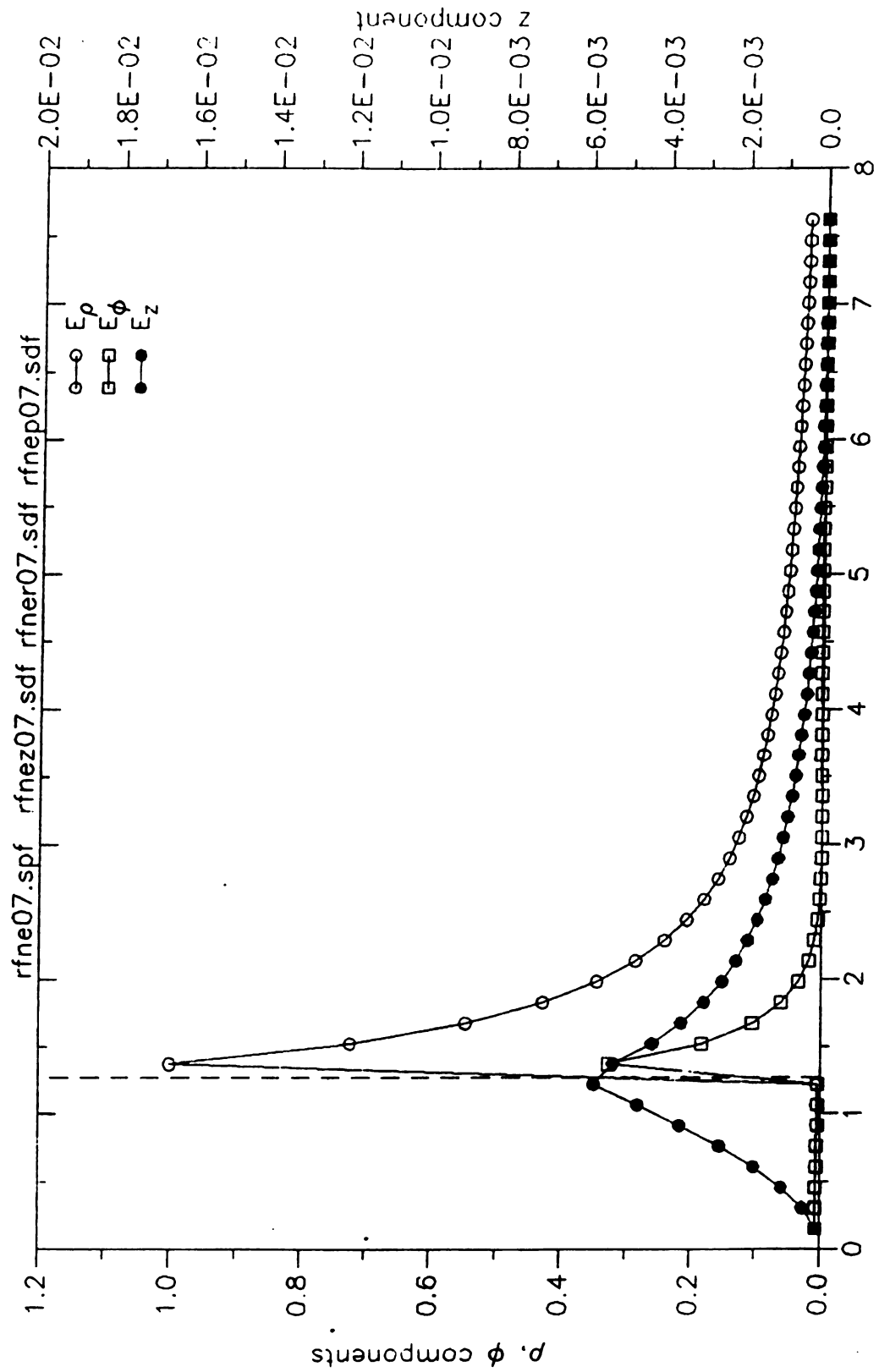

Figure 4.18b Electric field patterns for HE_{11} mode, ε=3.03-j0.039, b/a=6, k_0a=0.65

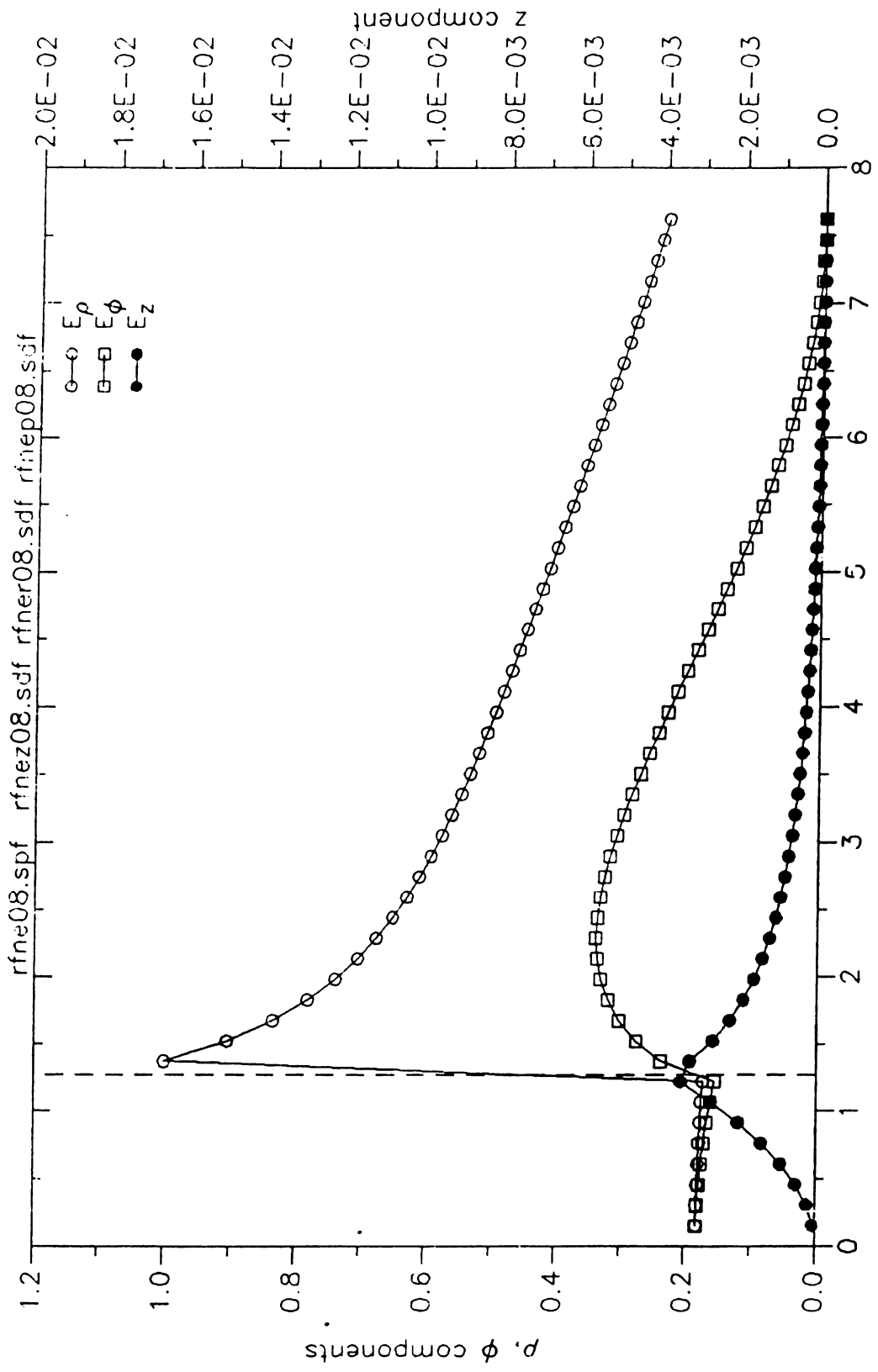

Figure 4.18c Electric field patterns for HE_{11} mode, $\varepsilon = 3.03 - j0.039$, b/a=6, $k_0 a = 0.26$

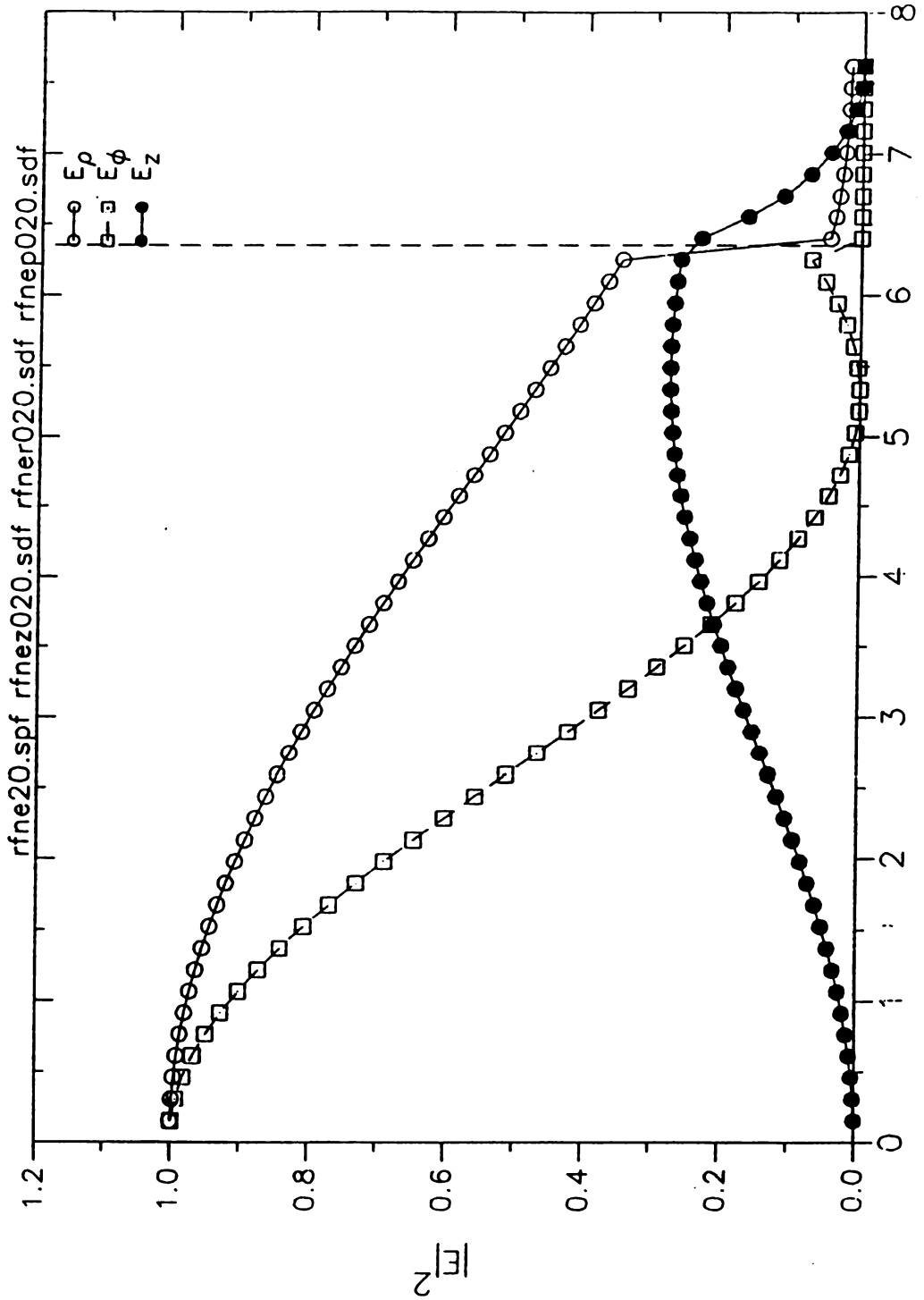

Figure 4.19a Electric field patterns for HE_{11} mode, ϵ=3.03-j0.039, a=6.35 cm, b=7.62 cm, k_0a=3.26.

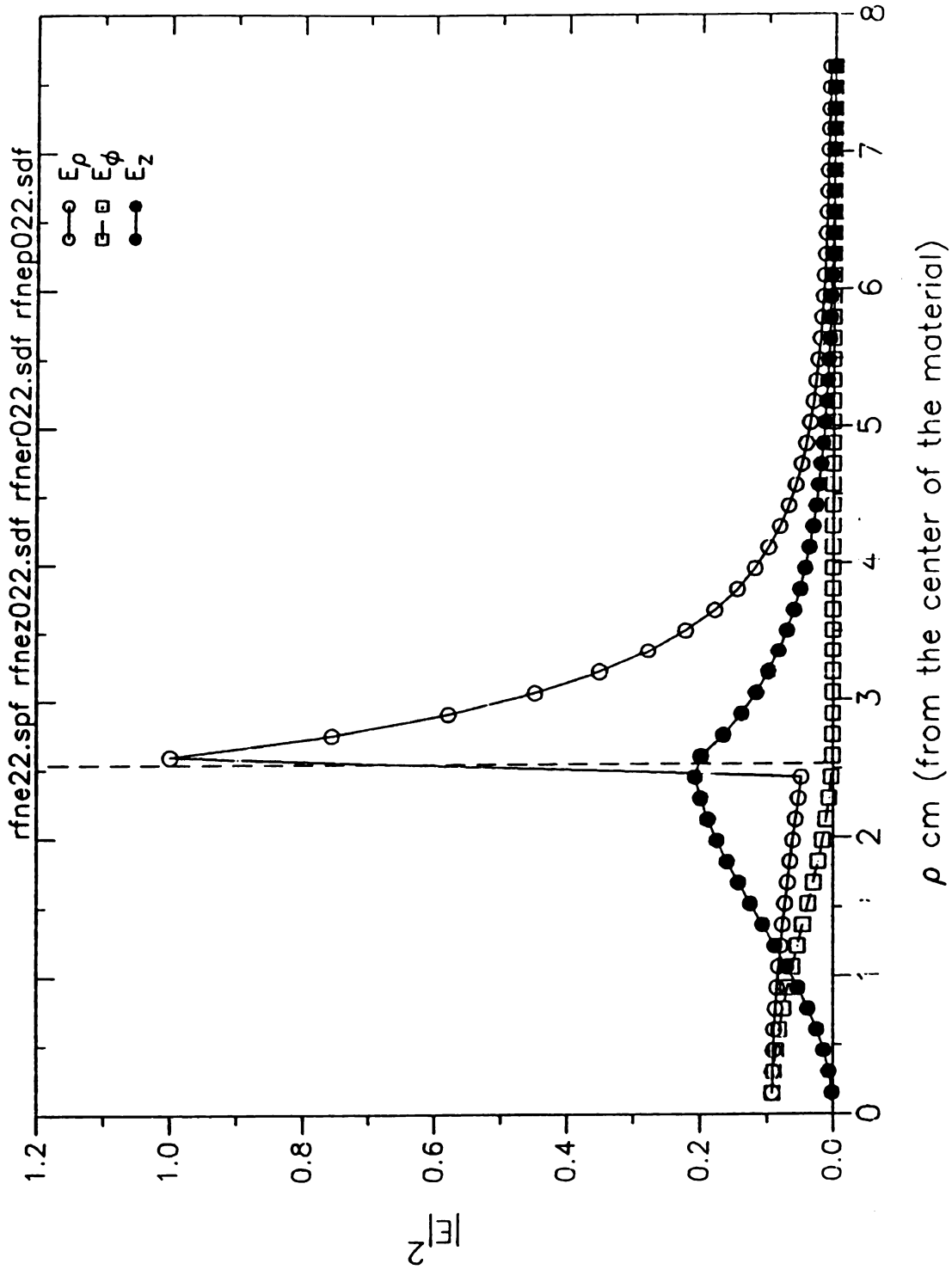

Figure 4.19b Electric field patterns for HE_{11} mode, c=3.03-j0.039, a=2.54 cm, b=7.62 cm, k_{0a}=1.3.

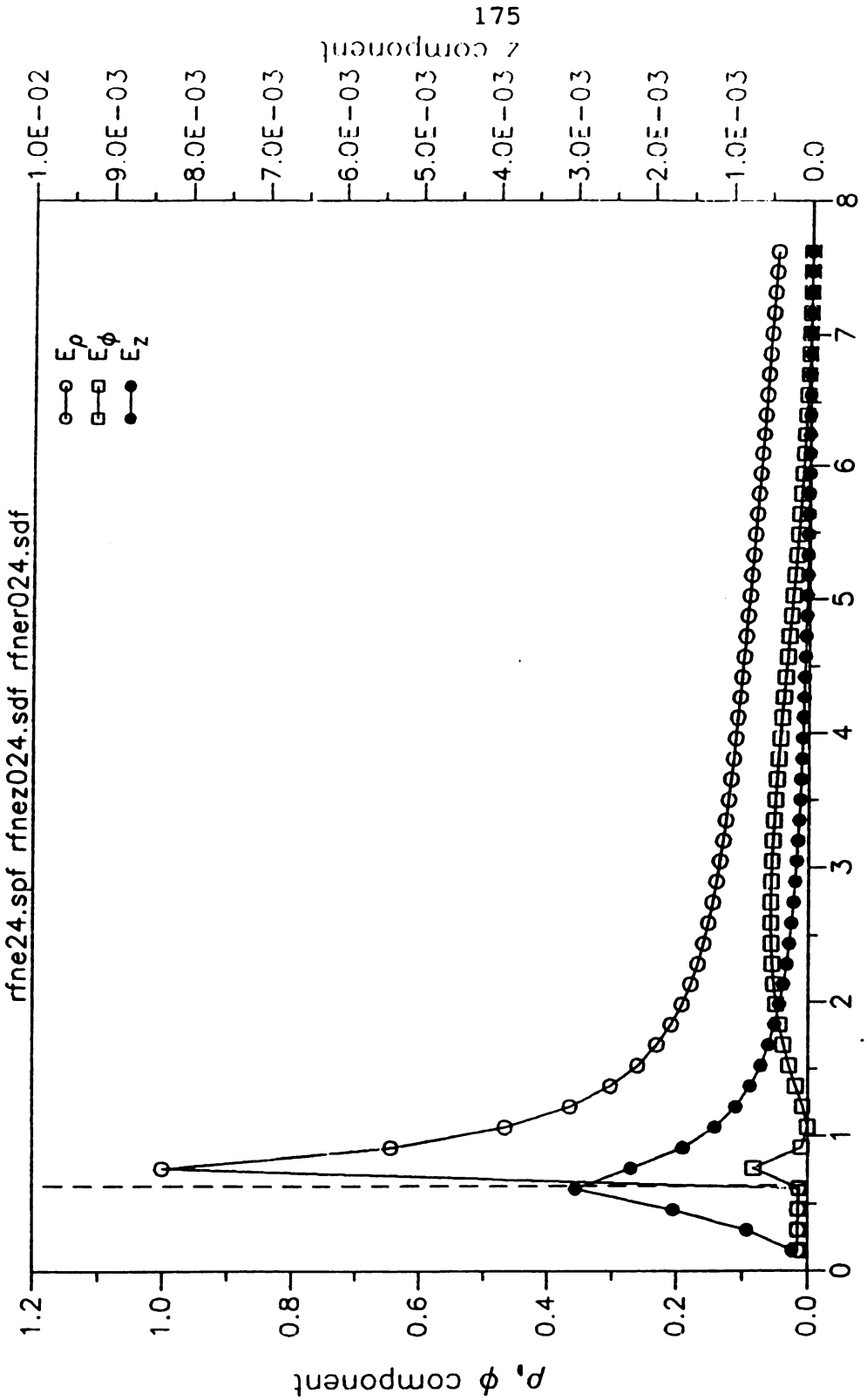

Figure 4.19c Electric field patterns for HE_{11} mode, c=3.03-j0.039, a=0.635 cm, b=7.62 cm, k_0a=0.326.

Although the field distributions are altered from those shown in Figure 4.19b as rod radius is decreased, most of the EM energy is still restrained in the air-filled region.

4.3.2.1.6 Propagation characteristics of a waveguide loaded with plasma rod

This section presents the $\omega - \beta$ and $\omega - \alpha$ diagrams of a waveguide loaded with isotropic, cold plasma rod for a variety of experimental conditions that are of interest to electric propulsion discharges and diamond thin film discharges. An equivalent dielectric constant can be defined for the isotropic plasma rod [88] as

$$\hat{\varepsilon} = \varepsilon_0 \left[1 - \frac{\omega_{p_e}^2}{\nu_e^2 + \omega^2} - j \frac{\nu_e}{\omega} \frac{\omega_{p_e}^2}{\nu_e^2 + \omega^2} \right] \tag{4.16}$$

$$= \varepsilon_0 (\varepsilon_r' - j \varepsilon_r'')$$

where

$$\varepsilon_r' = 1 - \frac{\omega_{p_e}^2}{\nu_e^2 + \omega^2} \tag{4.17}$$

$$\varepsilon_r'' = \frac{\nu_e}{\omega} \frac{\omega_{p_e}^2}{\nu_e^2 + \omega^2} \tag{4.18}$$

$$\omega_{p_e} = \sqrt{\frac{N_0 e^2}{m_e \varepsilon_0}} \tag{4.18}$$

ω_{p_e} = plasma electron frequency,

ν_e = effective electron-neutral particle collision frequency,

m_e = electron mass,

N_0 = electron number density,

e = electronic charge.

To facilitate the numerical computations, equations 4.17 and 4.18 are expressed in terms of $\frac{\omega_{p_e}}{\omega}$ and $\frac{\nu_e}{\omega}$ as the following equations,

$$\varepsilon_r' = 1 - \frac{\omega_{p_e}^2}{\omega^2} \frac{1}{1 + (\frac{\nu_e}{\omega})^2} \tag{4.19a}$$

$$\varepsilon_r'' = \frac{\omega_{p_e}^2}{\omega^2} \frac{\frac{\nu_e}{\omega}}{1 + (\frac{\nu_e}{\omega})^2} \tag{4.19b}$$

As can be seen in equation 4.19a, ε_r' is negative if $1 + \frac{\nu_e^2}{\omega^2} < \frac{\omega_{p_e}^2}{\omega^2}$. The negative dielectric constant property of isotropic cold plasma makes it distinct from the ordinary dielectric materials. In addition, according to equations 4.19a and 4.19b, ε_r' and ε_r'' are a function of angular frequency for specified $\frac{\nu_e}{\omega}$ and N_0, which in turn specifies ω_{p_e}. Hence, different points on the $\omega - \kappa_z$ curves for a waveguide loaded with isotropic cold plasma rod correspond to different plasma equivalent permittivities. Note also that for fixed N_0 and $\frac{\nu_e}{\omega}$, as ω approaches 0, ε_r' and ε_r'' approach $-\infty$ and $+\infty$, respectively. In this limit, $\frac{\nu_e}{\omega}$ is constant, i.e. $\nu_e \to 0$ as $\omega \to 0$ so that $\frac{\nu_e}{\omega}$ is constant.

Solving for $\kappa_0 a$ vs βa and $\kappa_0 a$ vs αa, the following conditions were investigated numerically. Two plasma waveguide geometries for the TM_{01} mode were considered. The circular waveguide radii are 4.75 cm and 8.89 cm, respectively, and the radius of the uniform, cold, lossy plasma rod is 1.25 cm. The electron density and plasma collision frequency that are examined for each waveguide geometry are listed below.

(1) $N_0 = 10^{11}/cm^2$ and $10^{12}/cm^2$

(2) $\frac{\nu_e}{\omega} = 1.0$ and 0.1

The results are displayed in Figures 4.20 through 4.21. This problem has been solved before [88] but is plotted differently here. On the dispersion diagrams, 2.45 GHz ($\kappa_0 a$=0.641) is shown as a horizontal line. The points where this line intersects the $\kappa_0 a$-βa and $\kappa_0 a$-αa curves are the operating points at 2.45 GHz.[1] Note the presence of the backward and slow waves, as reported earlier [88, 90], in these diagrams.

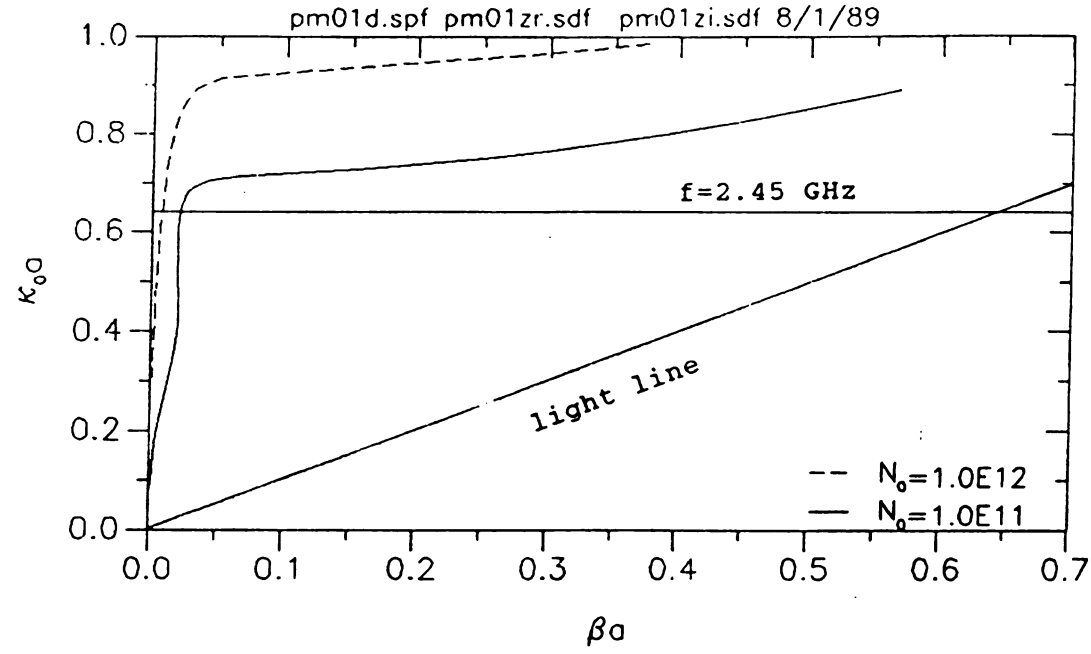

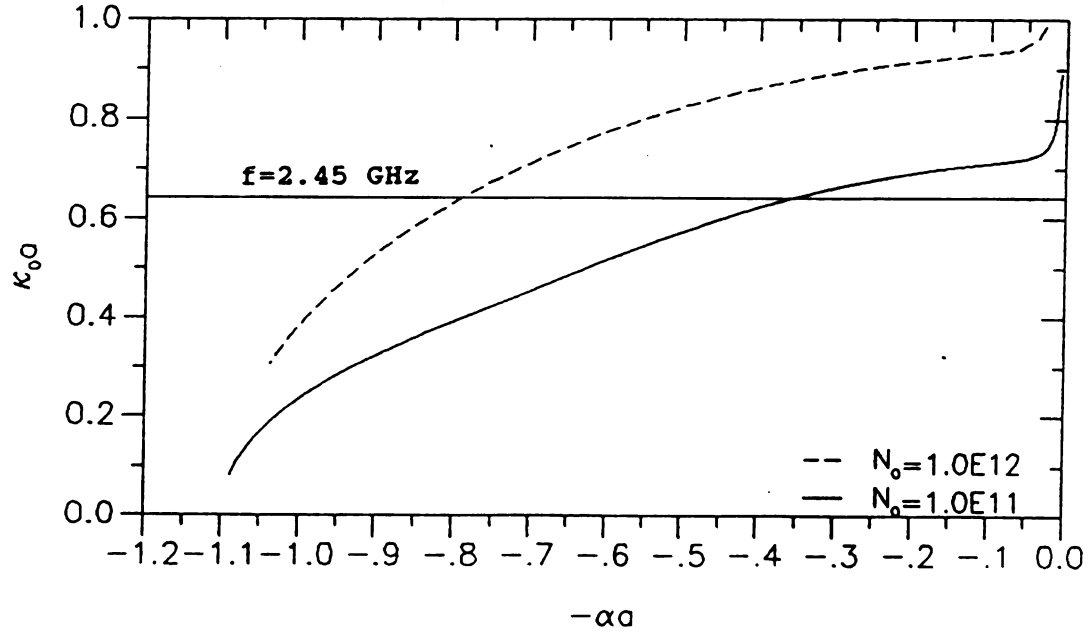

Figure 4.20a **w-β and w-α diagrams for TM_{01} mode for a waveguide loaded with plasma rod, where a=1.25 cm, b=4.75 cm and ν/ω=0.1**

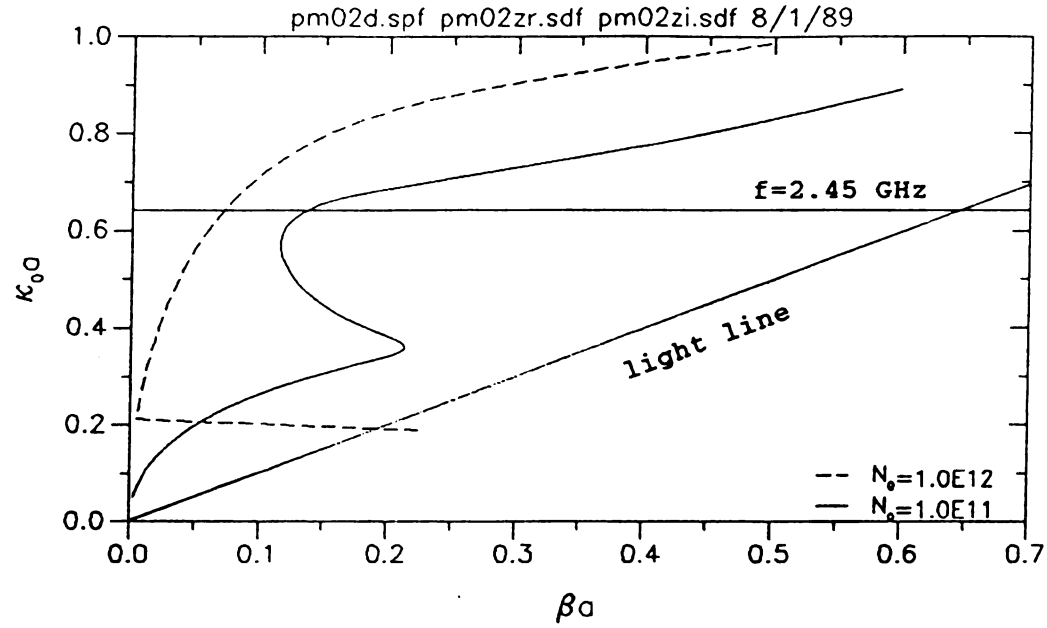

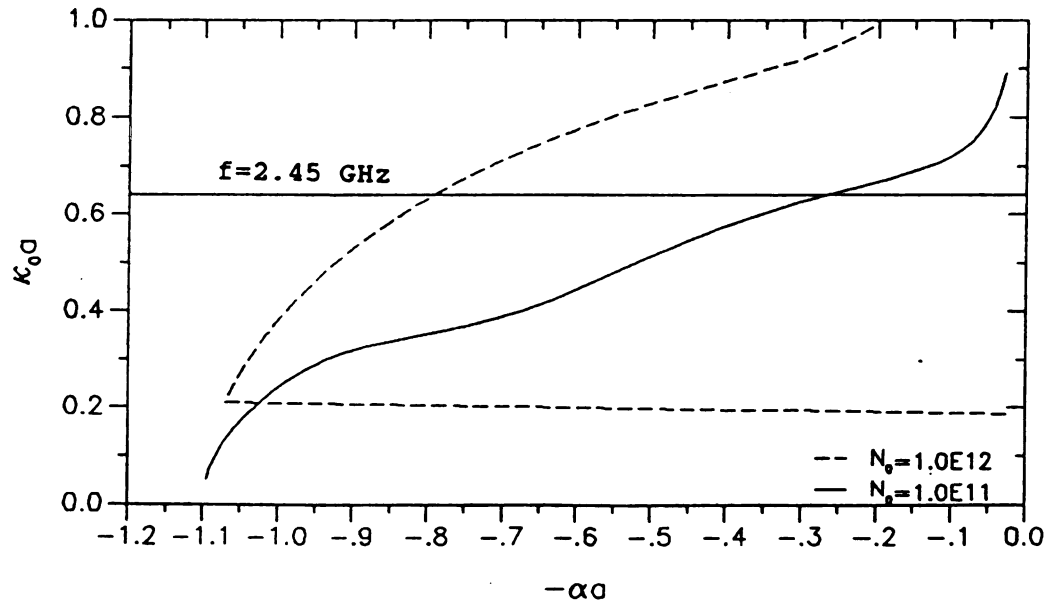

Figure 4.20b w-β and w-α diagrams for TM_{01} mode for a waveguide loaded with plasma rod, where a=1.25 cm, b=4.75 cm and ν/ω=1.0

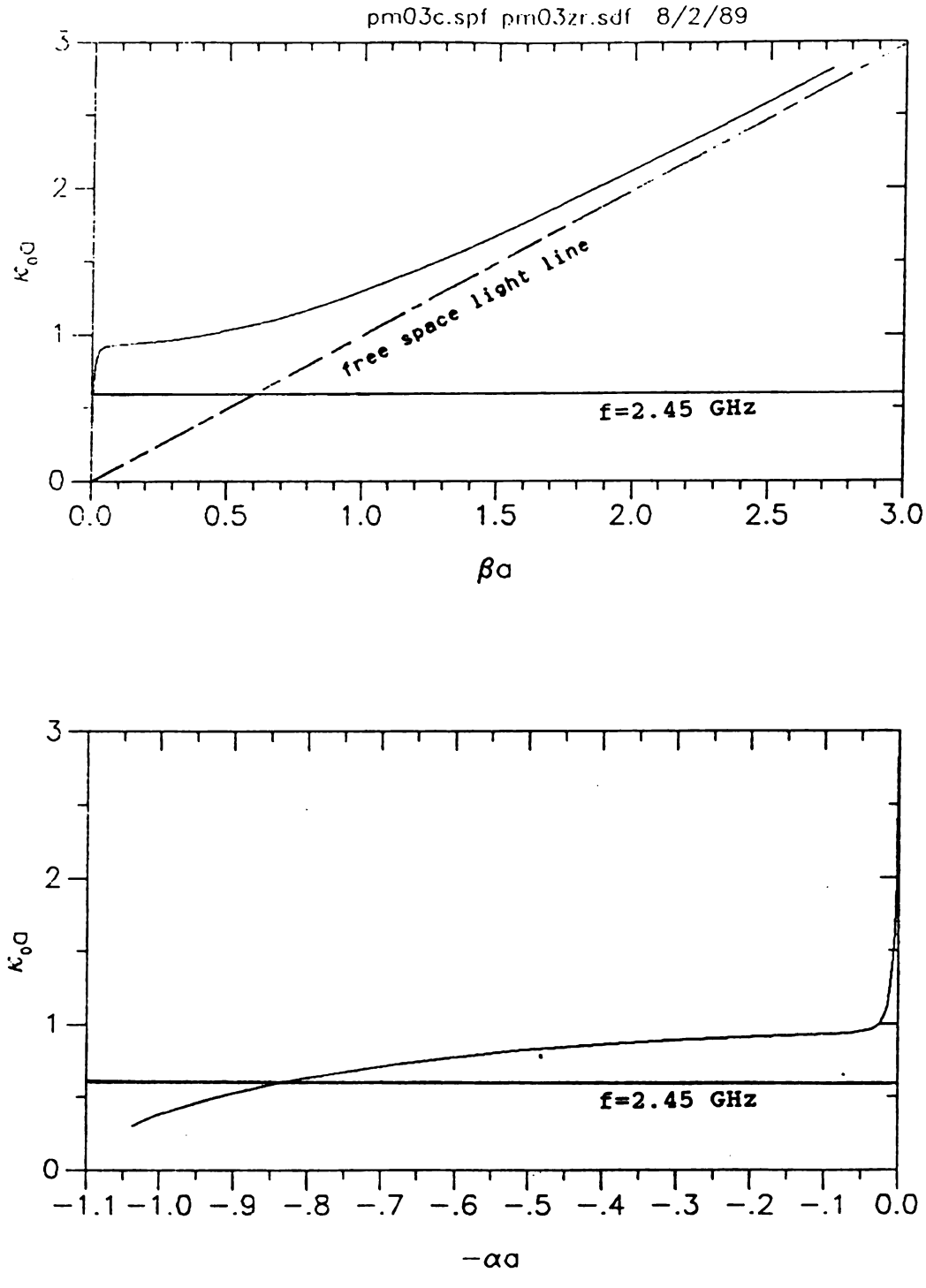

Figure 4.20c ω–β and ω–α diagrams for TM_{01} mode waveguide loaded with isotropic plasma rod, a=1.25 cm, b=4.75 cm, $N=10^{12}$, $\frac{\nu}{\omega}=0.1$.

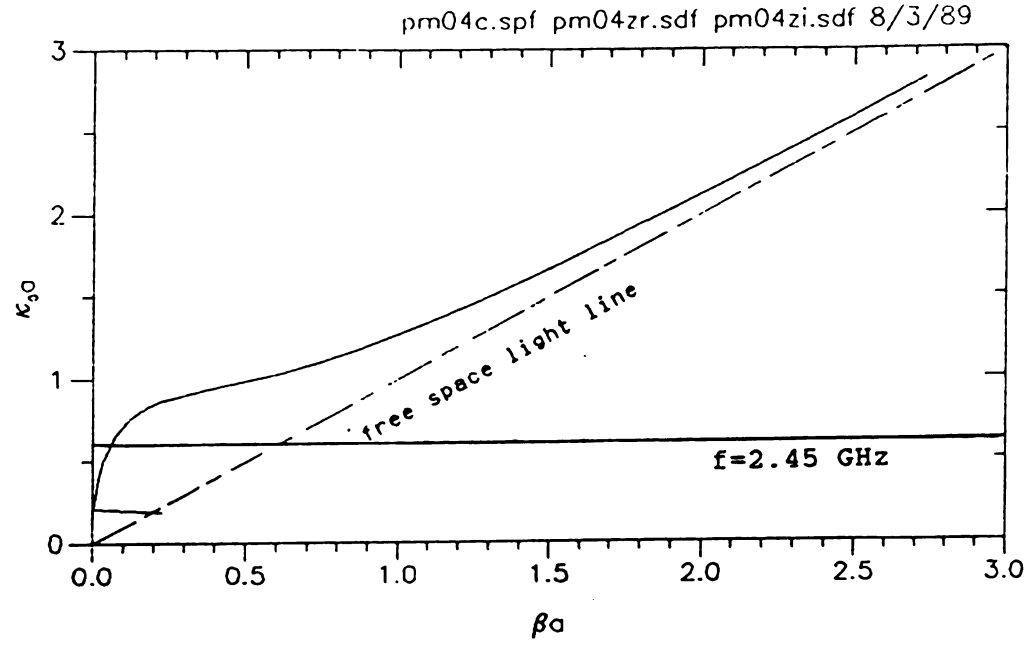

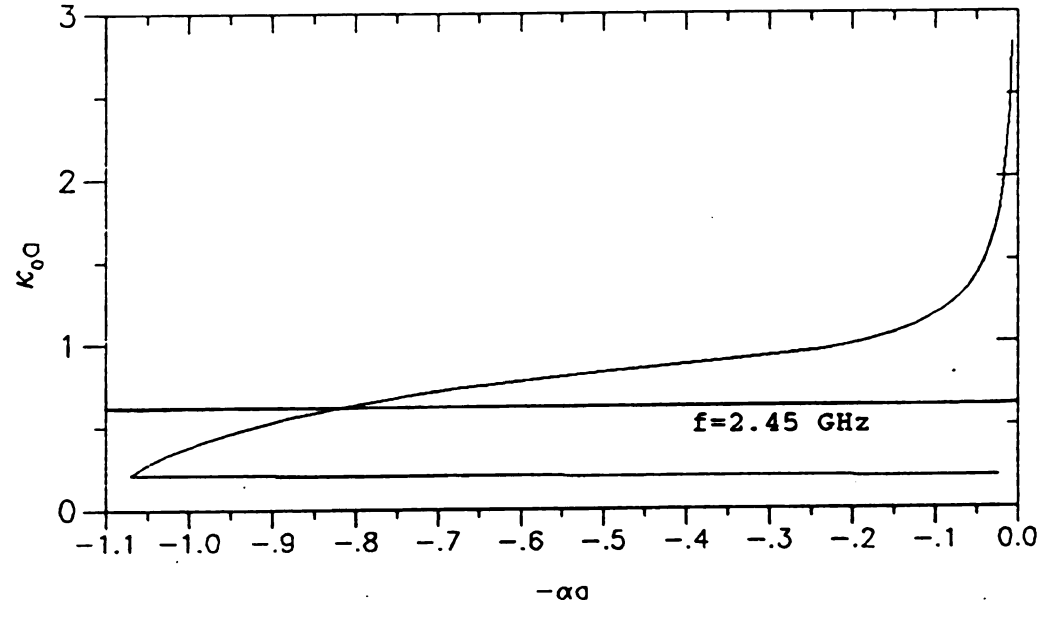

Figure 4.20d ω–β and ω–α diagrams for TM_{01} mode waveguide loaded with isotropic plasma rod, a=1.25 cm, b=4.75 cm, N=10^{12}, $\frac{\nu}{\omega}$=1.0.

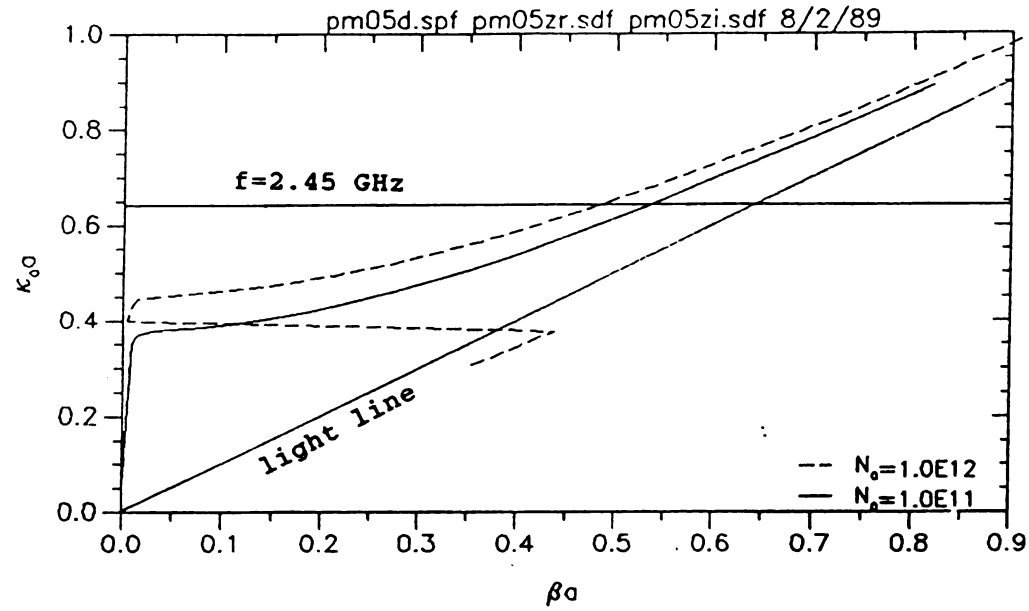

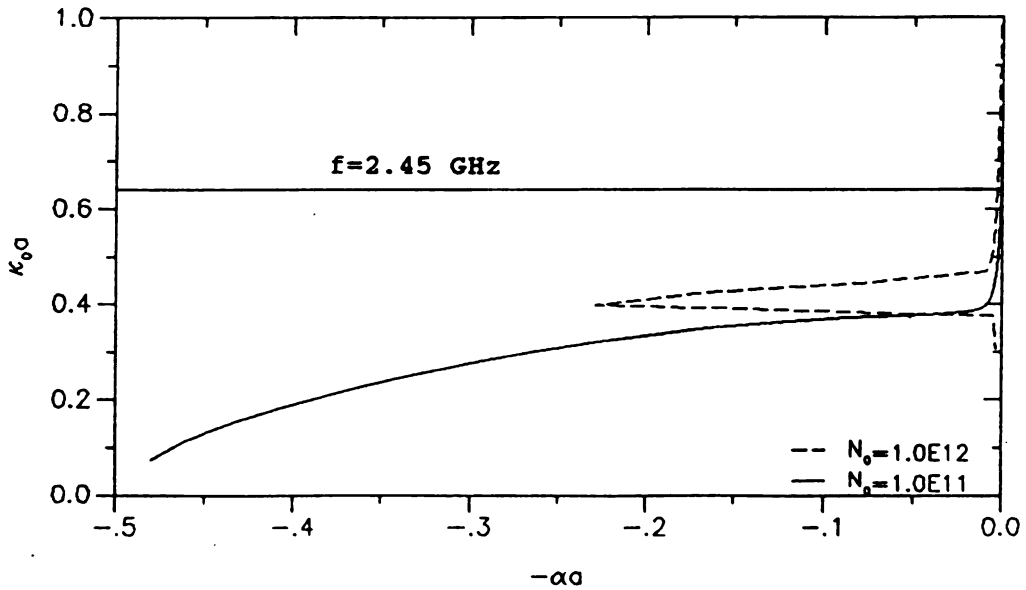

Figure 4.21a w-β and w-α diagrams for TM_{01} mode for a waveguide loaded with plasma rod, where a=1.25 cm, b=8.89 cm and ν/ω=0.1

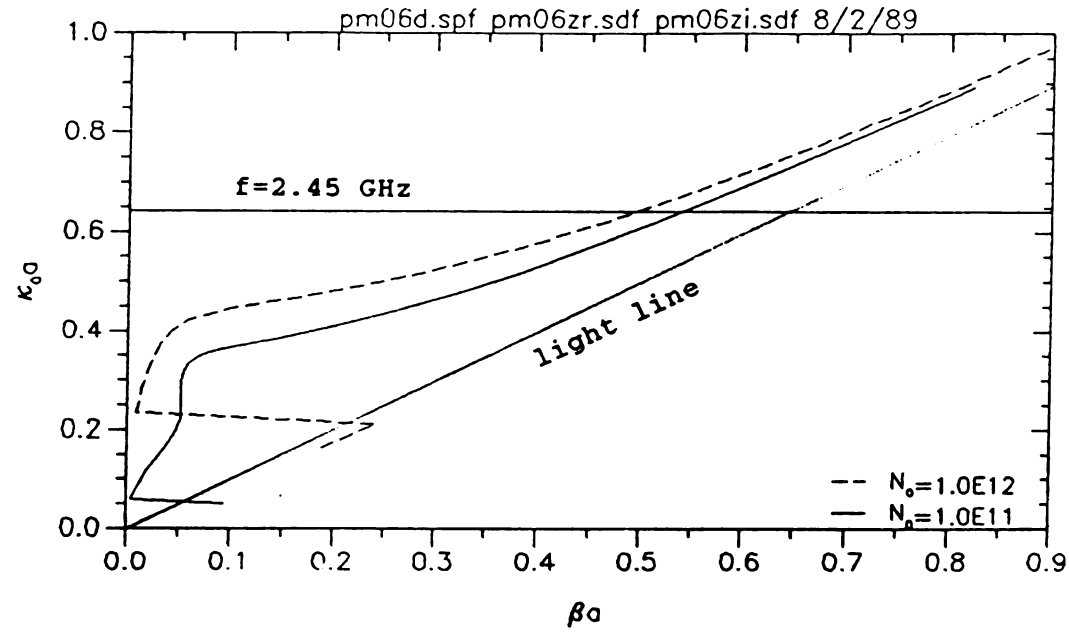

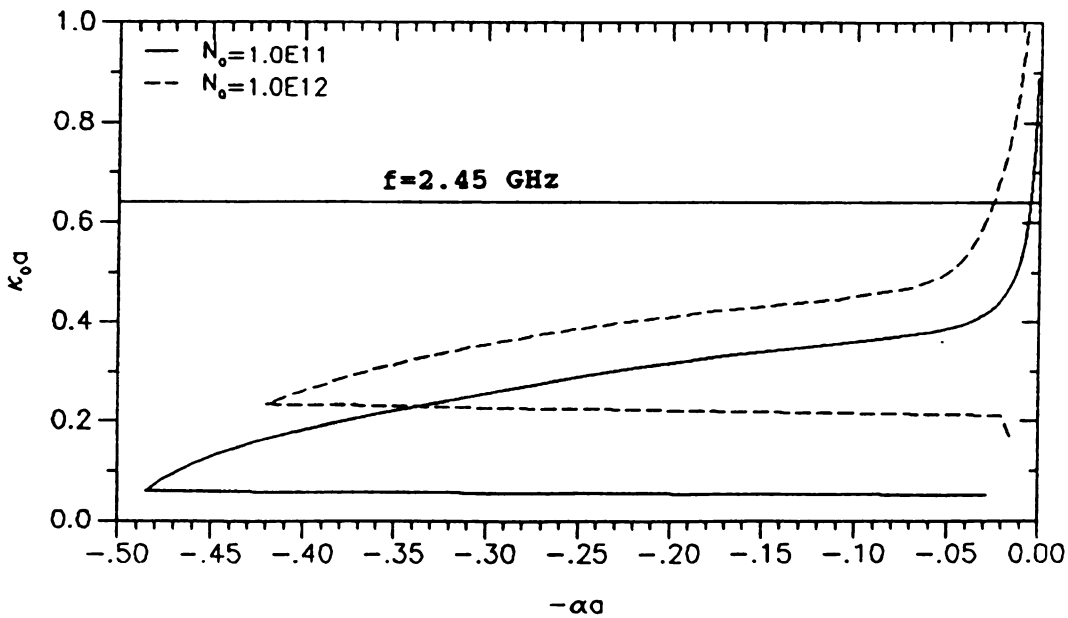

Figure 4.21b w-β and w-α diagrams for TM_{01} mode for a waveguide loaded with plasma rod, where a=1.25 cm, b=8.89 cm and ν/ω=1.0

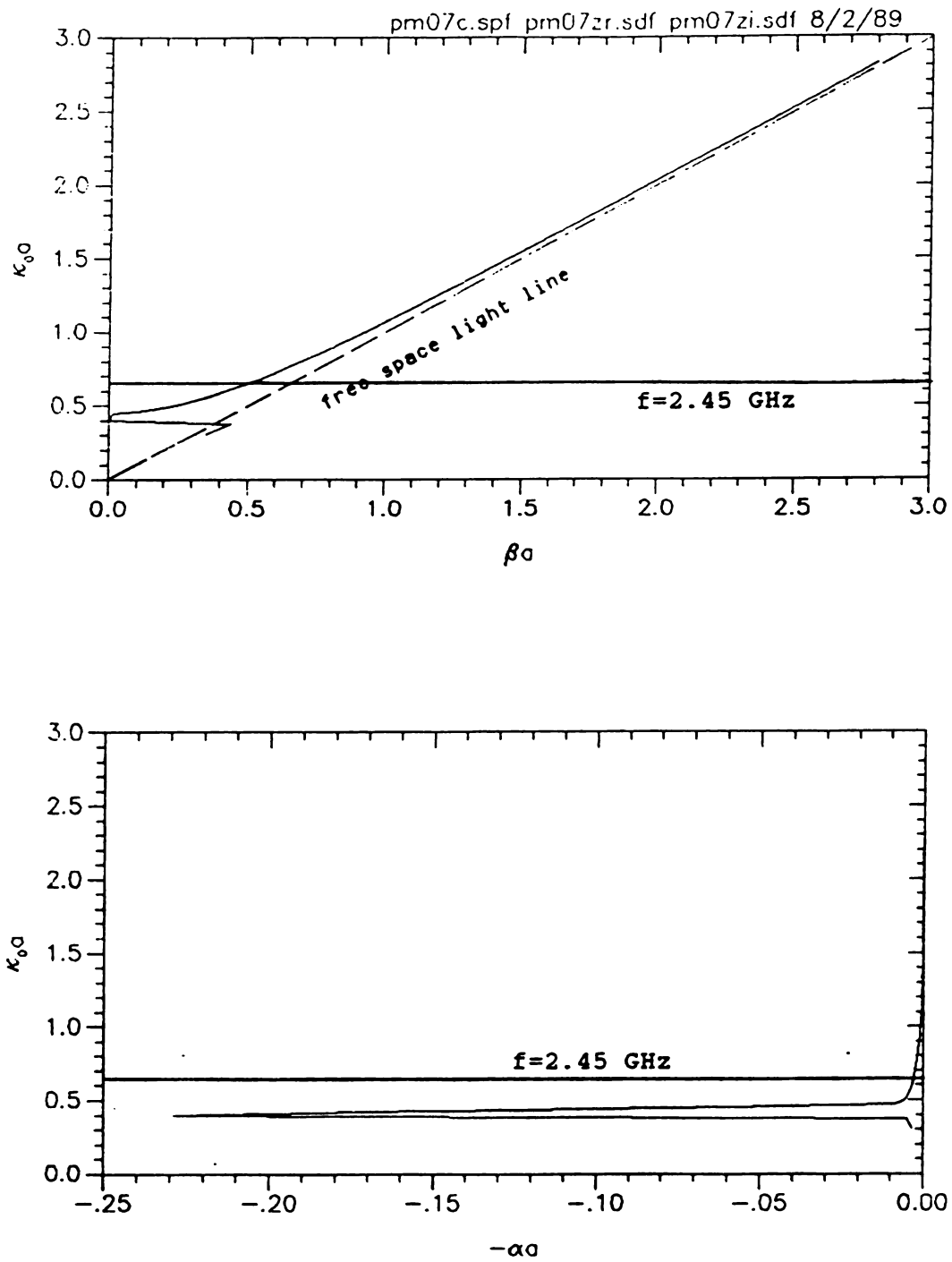

Figure 4.21c ω–β and ω–α diagrams for TM_{01} mode waveguide loaded with isotropic plasma rod, a=1.25 cm, b=8.89 cm, N=10^{12}, $\frac{\nu}{\omega}$=0.1.

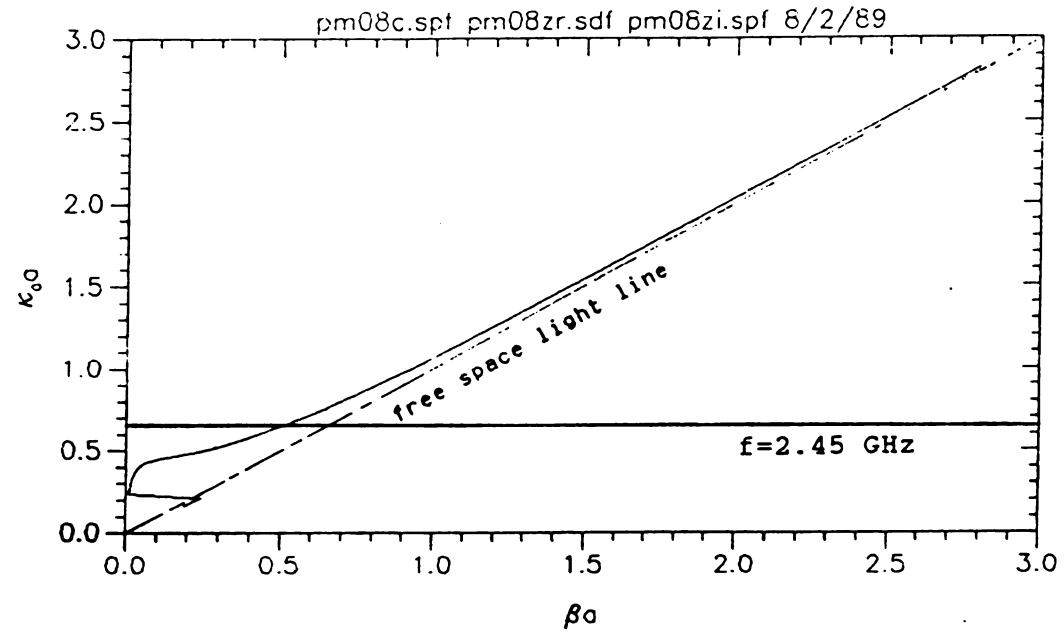

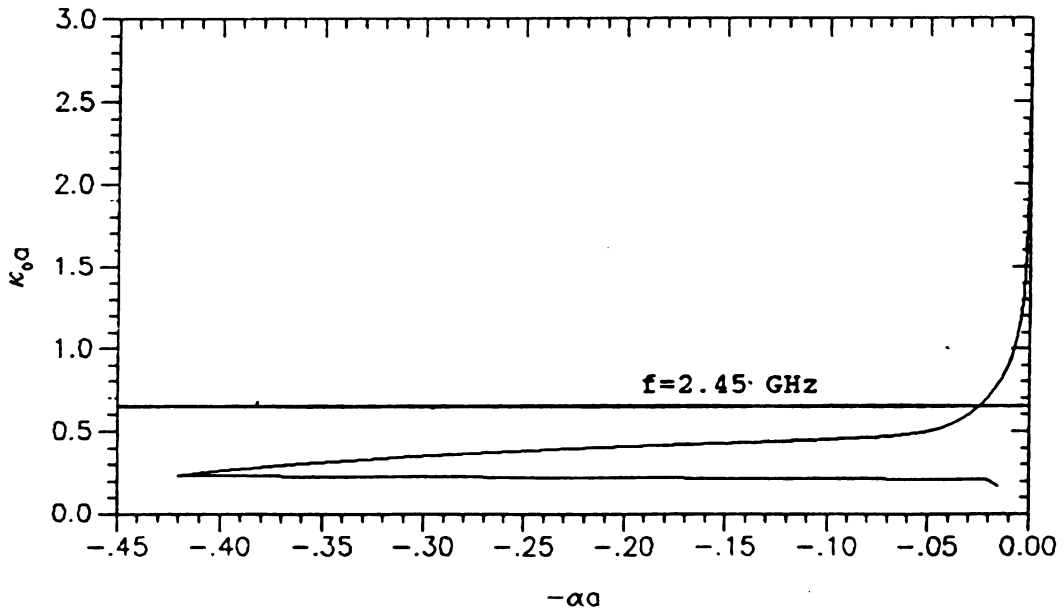

Figure 4.21d ω–β and ω–α diagrams for TM_{01} mode waveguide loaded with isotropic plasma rod, a=1.25 cm, b=8.89 cm, N=10^{12}, $\frac{v}{\omega}$=1.0.

These curves demonstrate that the numerical technique can be applied to uniform, cold, lossy plasma rod loaded circular waveguide. The numerical routine is available for diamond thin film and microwave electrothermal thruster experimentalists to apply to their particular discharge applications.

4.3.3 Axial boundary value problem (dielectric-loaded cavity problem)

4.3.3.1 Introduction

Numerical results of the cavity-short type material load which is described in section 3.42 are presented. Equations 3.71, 3.106b, 3.107a and 3.107b are solved for the resonant frequency and resonant length for TM_{012}, HE_{111} and TE_{011} modes under different material loading conditions. The changes of the resonant frequency (or resonant length) as a function of ε_r', ε_r'' and rod radius are investigated in section 4.3.3.2 below. In addition, the quality factors of the material loaded cavity are calculated for various ε_r', ε_r'' and rod radii.

4.3.3.2 Resonant frequency and resonant length for TM_{012}, HE_{111} and TE_{011} modes

Figures 4.22 through 4.27 show the change of the resonant frequency (f_r) as a function of ε_r' for a variety of ε_r'', where the cavity radius is 7.62 cm. Figures 4.22a and 4.22b depict the f_r vs. ε_r' diagrams for TM_{012} mode at a fixed cavity length L_s = 15.5 cm where the rod radii are 0.635 cm and 1.27 cm, respectively. The 15.5 cm cavity length corresponds to a 2.45296 GHz TM_{012} empty cavity resonance. As is shown in Figure 4.22a, the resonant frequency decreases with increasing ε_r'. It is of interest to see that for $\varepsilon_r' < 7.0$, larger ε_r'' results in higher resonant frequency at a fixed ε_r'. When ε_r' is constant but > 7.0, the resonant frequency decreases as ε_r'' increases. All the resonant frequency curves intersect at $\varepsilon_r' = 7.0$. Hence, for the cavity radius and rod radius given in Figure 4.22a, the dielectric-loaded TM_{012} cavity is resonant at 2.375 GHz at ε_r'=7.0 for any ε_r''. The low dielectric constant portion ($\varepsilon_r' < 10$) in

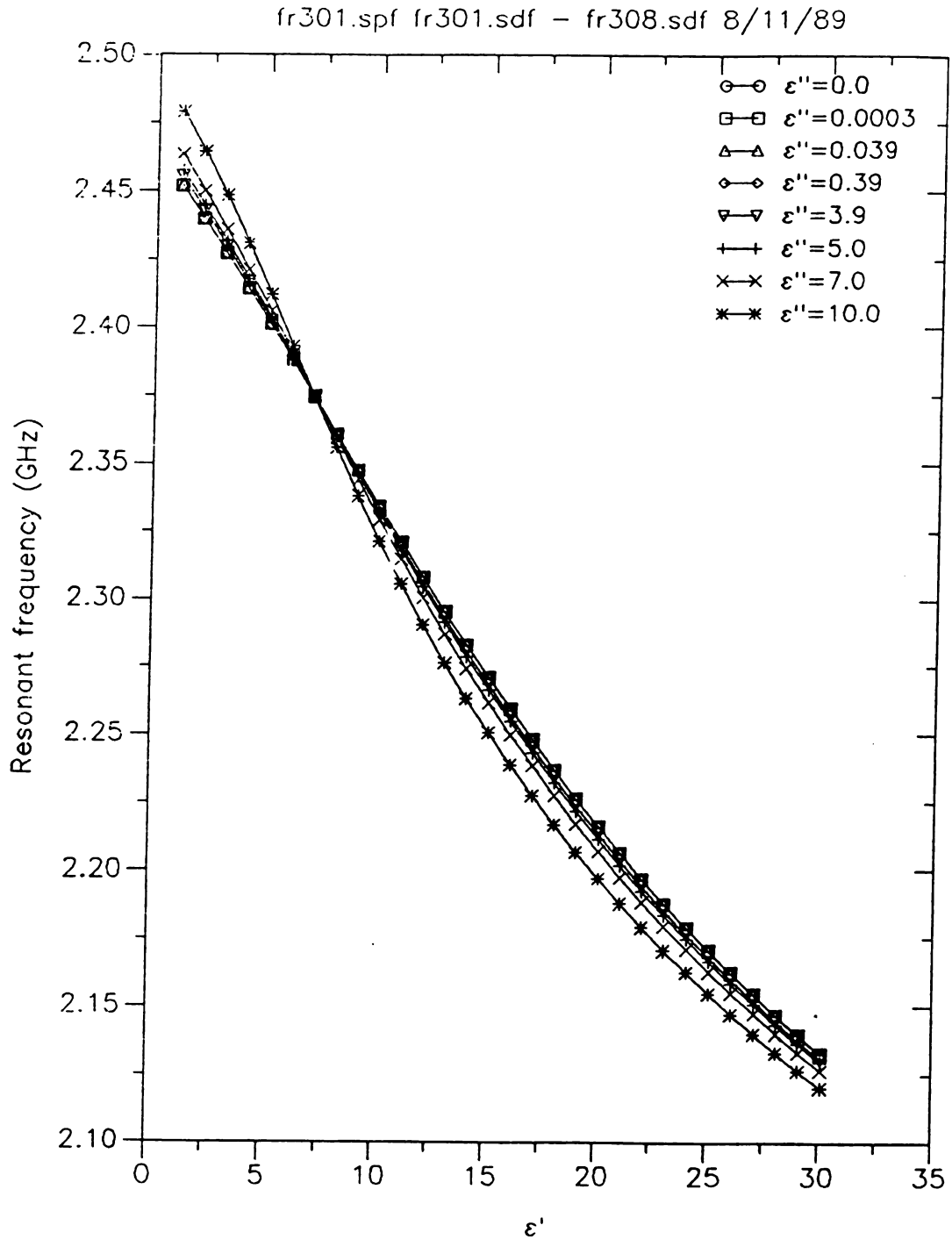

Figrue 4.22a Resonant frequency vs. ε' for TM_{012} mode for various ε", a=0.635 cm, b=7.62 cm and L_s=15.5 cm.

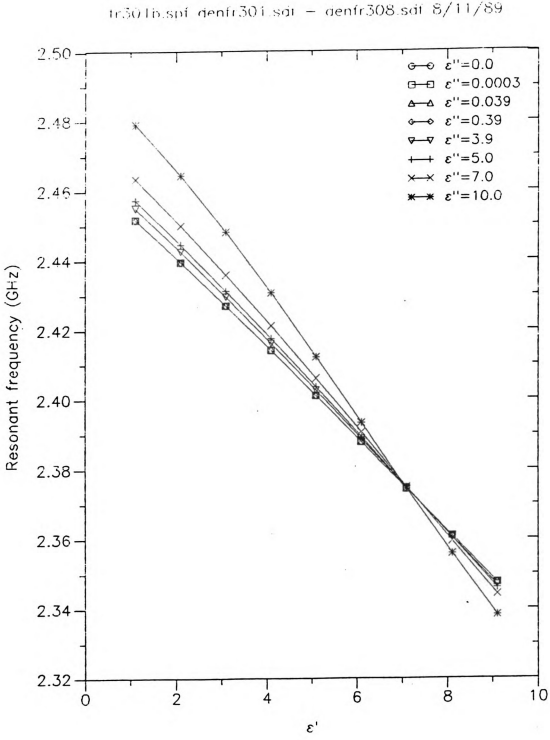

Figure 4.22b Low dielectric constant portion of Figure 4.22a

Figure 4.22a is displayed in Figure 4.22b. Figure 4.22c displays the case of a=1.27 cm. For $\varepsilon_r'' < 7.0$, the resonant frequency is reduced as ε_r' is increased. When $\varepsilon_r'' = 10$, the resonant frequency increases with increasing ε_r' until $\varepsilon_r' = 4.1$, after the point, an increase in ε_r' yields a decrease in the resonant frequency. Except for $\varepsilon_r'' = 3.9$ and 5.0, all the resonant frequency are shifted down from the empty cavity resonant frequency, 2.45296 GHz. The resonant frequency for $\varepsilon_r'' = 3.9$ and 5.0 are higher than 2.45296 GHz if $\varepsilon_r' < 1.25$. When $\varepsilon_r' > 1.25$, higher ε_r'' give rise to a lower resonant frequency at a given ε_r' for all the curves shown.

Figure 4.23a shows the case of a=0.634 cm and $L_r = 6.94$ cm for a 2.44994 GHz HE_{111} mode. The resonant frequency vs. ε_r' are almost identical when $\varepsilon_r'' < 3.9$. It is found that for $\varepsilon_r' < 13.5$, increasing ε_r'' will decrease f_r, and the opposite is true for $\varepsilon_r' > 13.5$. At $\varepsilon_r' = 13.5$, the resonant frequency is about 2.4088 GHz for all ε_r'' given in this example. The resonant frequency for $\varepsilon_r'' < 3.9$ are decreased with increasing ε_r'. When $\varepsilon_r'' \geq 3.9$, there is a ε_r' region where the resonant frequency is increased with increasing ε_r'. Outside this region, an increase in ε_r' will reduce the resonant frequency. All the resonant frequency are shifted down from the HE_{111} empty cavity resonant frequency. The example shown in Figure 4.23b is the same as Figure 4.23a except that the rod radius is twice as large. Again, the f_r vs. ε_r' curves are almost identical and are a decreasing function of ε_r' if $\varepsilon_r'' < 3.9$. For $\varepsilon_r'' = 3.9$, 5.0 and 7.0, increasing ε_r' will decrease the resonant frequency. It is interesting to see that when $\varepsilon_r'' = 10.0$, an increase in ε_r' result in an increase in f_r. For a given ε_r', increasing dielectric loss may give rise to either an increase or a decrease in the resonant frequency, depending the value of ε_r'. Except for the case of $\varepsilon_r'' = 10$, the resonant frequencies shown in Figure 4.23b are lower than the empty cavity resonance.

Figure 4.24a plots the f_r vs. ε_r' diagram for TE_{011} with a = 0.635. As shown, all the resonant frequencies are decreased with increasing ε_r'. The f_r vs. ε_r' curves do not vary much for $\varepsilon_r'' < 3.9$. At a given ε_r', increasing ε_r'' will increase the resonant

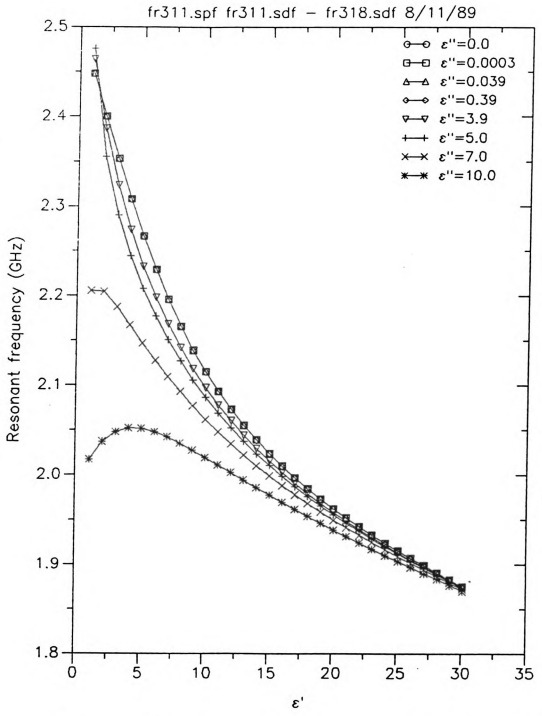

Figure 4.22c Resonant frequency vs. ε' for TM_{012} mode for various ε'', a=1.27 cm, b=7.62 cm, L_d=15.5 cm.

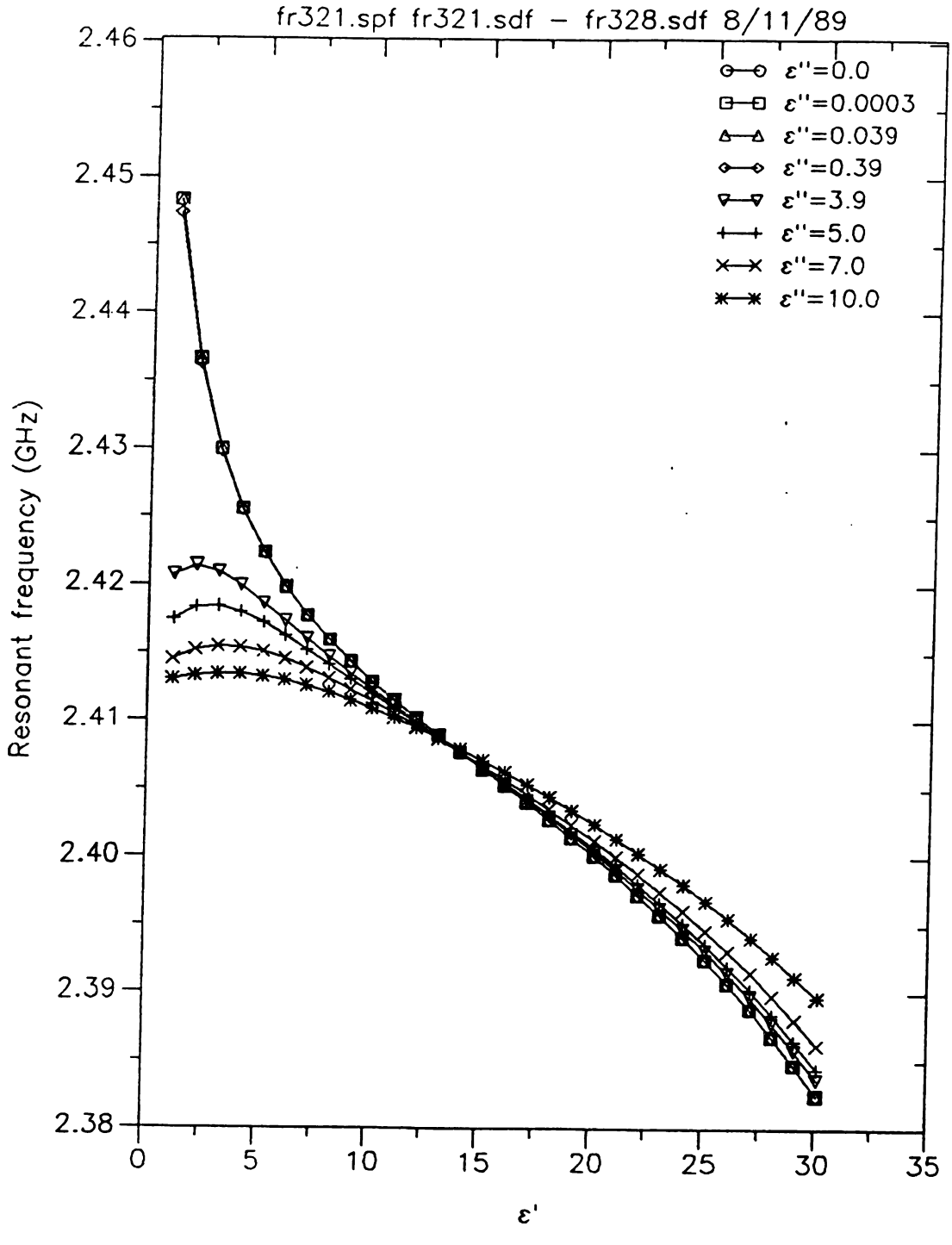

Figure 4.23a Resonant frequency vs. ε' for HE_{111} mode for various ε", a=0.635 cm, b=7.62 cm, L_m=6.94 cm.

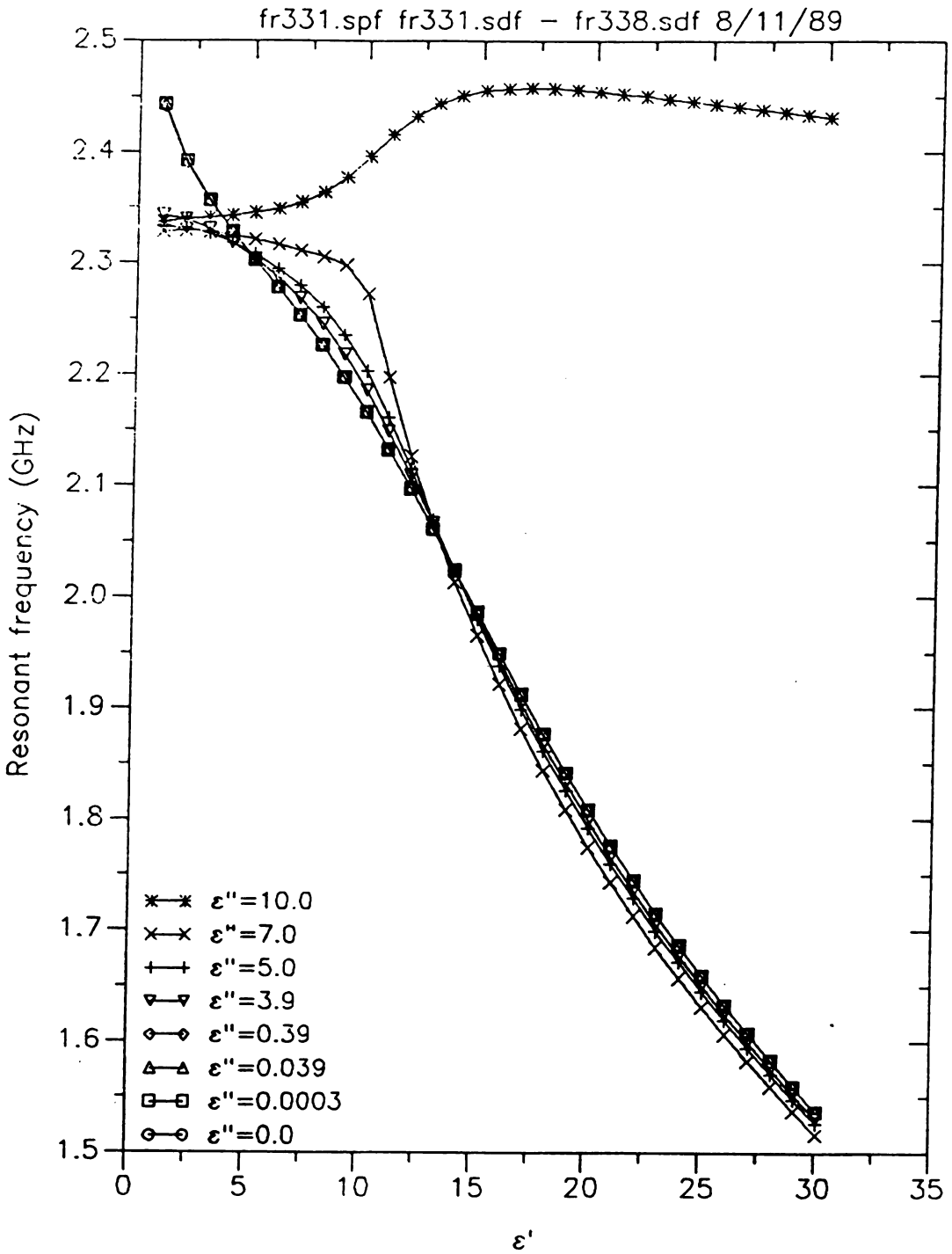

Figure 4.23b Resonant frequency vs. ε' for HE_{111} mode for various ε", a=1.27 cm, b=7.62 cm, L_s=6.94 cm.

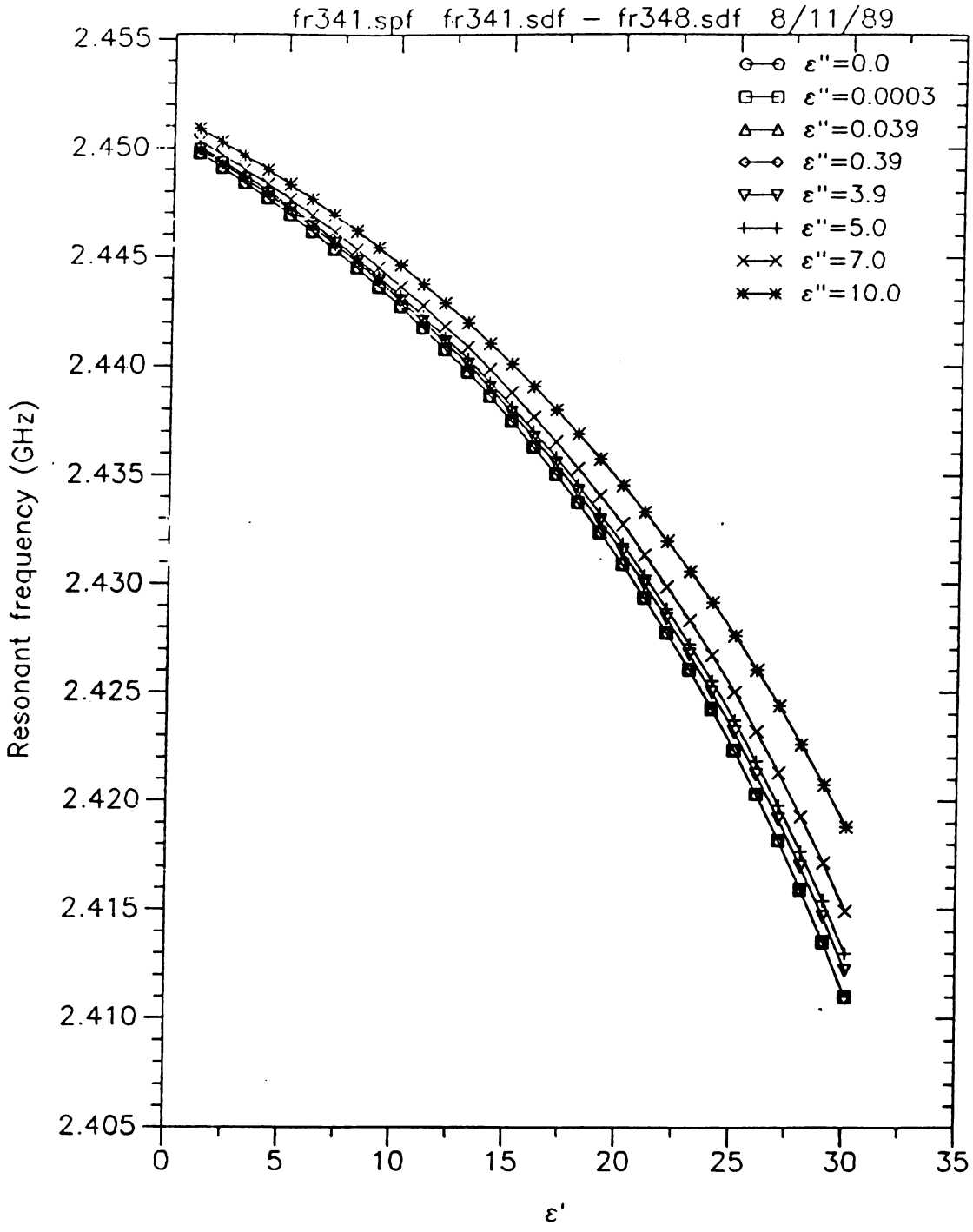

Figure 4.24a Resonant frequency vs. ε' for TE_{011} mode for various ε", a=0.635 cm, b=7.62 cm and L_s=30.8 cm.

frequency. It is seen for very low ε_r', the resonant frequency may be higher than the empty cavity resonance due to the increase in ε_r''. Figure 4.24b depicts a TE_{011} cavity loaded with a rod of 1.27 cm radius. The variations of the resonant frequency vs. ε_r' are quite different from those seen in Figure 4.24a. For $\varepsilon_r'' < 10.0$, the resonant frequency is decreased when ε_r' increases. When $\varepsilon_r'' = 10.0$, the resonant frequency increases as ε_r' increases and is always larger than the TE_{011} empty cavity resonance.

The next three figures, Figures 4.25, 4.26, and 4.27, are the f_r vs. ε_r' diagrams for a seven-inch cavity, where a = 0.625 cm and b = 8.9 cm. Each diagram has a family of curves and each curve corresponds to a specific dielectric loss. Figure 4.25 shows TM_{012} mode, where the cavity length is 14.407 cm. HE_{111} and TE_{011} modes are shown in Figure 4.26 and 4.27, respectively , and the corresponding cavity lengths are 6.69 cm and 11.255 cm. Note that the a/b ratio associated with the seven-inch cavity is smaller than that shown in Figures 4.22a, 4.23a, and 4.24a.

The variations of f_r as a function of a/b ratio are examined in Figure 4.28 for TM_{012}, HE_{111} and TE_{011} modes. In this example, the radius of the cavity is 7.62 cm and the load material is nylon, i.e. $\hat{\varepsilon}_r$=3.03-j0.039. The cavity lengths associated with TM_{012}, HE_{111} and TE_{011} modes are 15.5, 6.94 and 30.8 cm, respectively. Note that the empty cavity resonant frequency corresponding to the cavity length stated above is 2.45296 GHz for TM_{012} and 2.45 GHz for TE_{111} and TE_{011} modes. The resonant frequency of the cavity completely filled with materials with $\hat{\varepsilon}_r$=3.03-j0 is 1.409 GHz for TM_{012} and 1.4075 GHz for TE_{111} and TE_{011} modes. As shown, the resonant frequency decreases with increasing rod radius for each mode illustrated. Also note that when $a/b \rightarrow 0$, the resonant frequency approaches the empty cavity resonance and when $a/b \rightarrow 1$, the resonant frequency approaches the corresponding resonant frequency of the homogeneous cavity that is filled with dielectric material where $\hat{\varepsilon}_r$=3.03-j0. Figure 4.29 shows the resonant frequency vs. a/b diagram for a seven inch cavity, i.e. b=8.9 cm, loaded with nylon rod. The cavity lengths for TM_{012}, HE_{111} and TE_{011} modes are

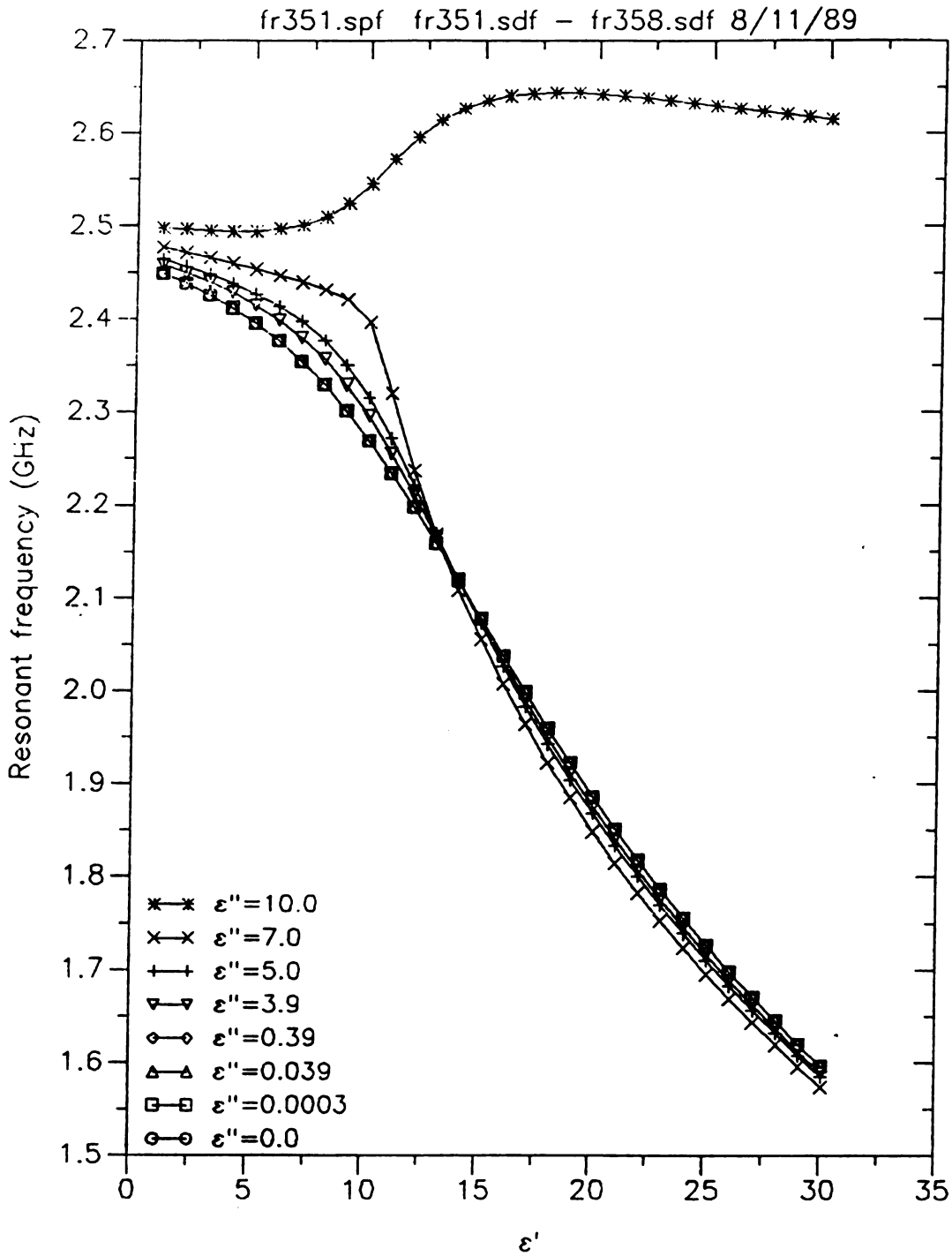

Figure 4.24b Resonant frequency vs. ε' for TE_{011} mode for various ε", a=1.27 cm, b=7.62 cm and L_s=30.8 cm.

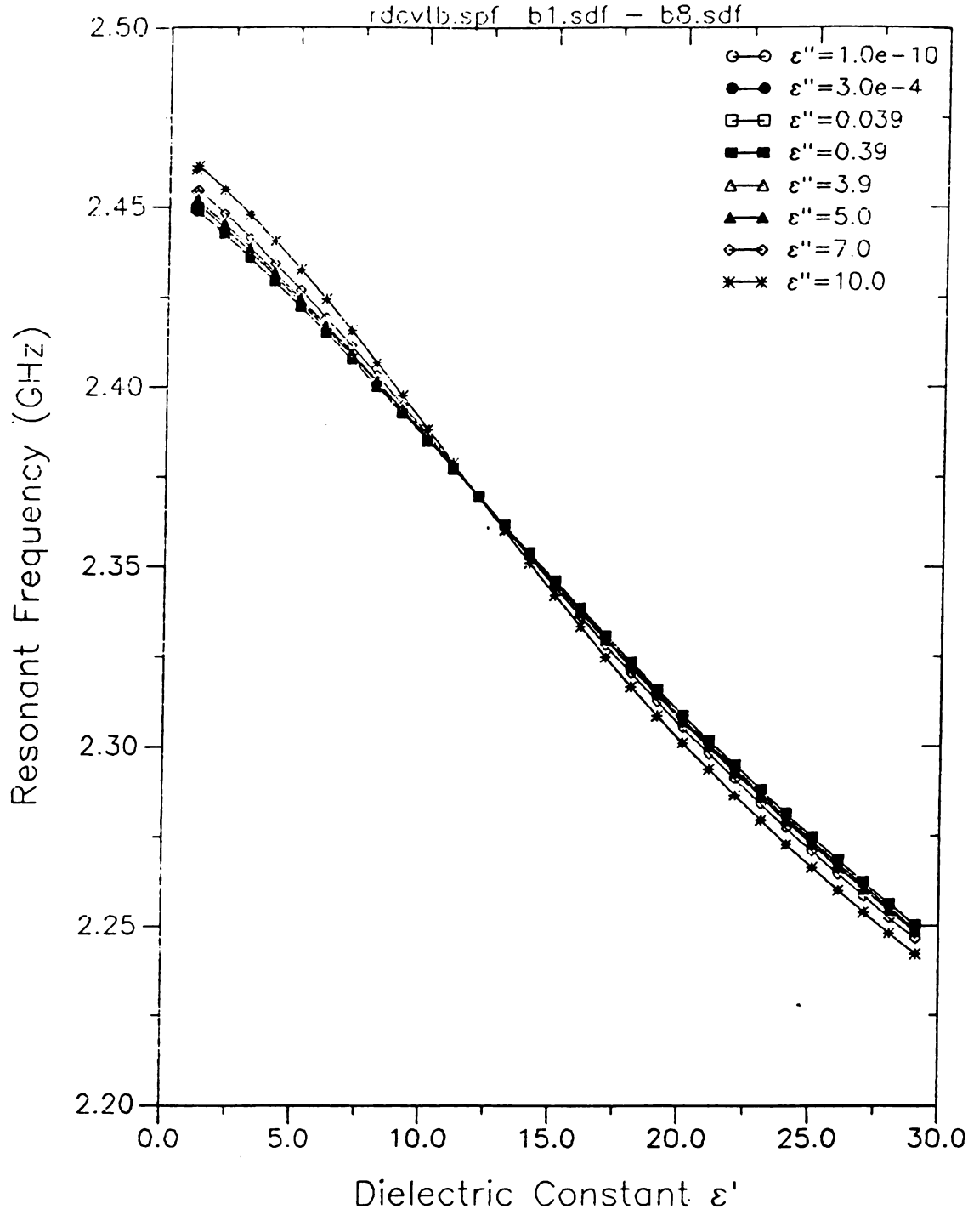

Figure 4.25a Resonant frequency vs ε' for TM_{012} mode for various ε", where a=0.635 cm, b=8.89 cm and L_s=14.407 cm

rdcvtbb.spf denb1.sdf denb8.sdf

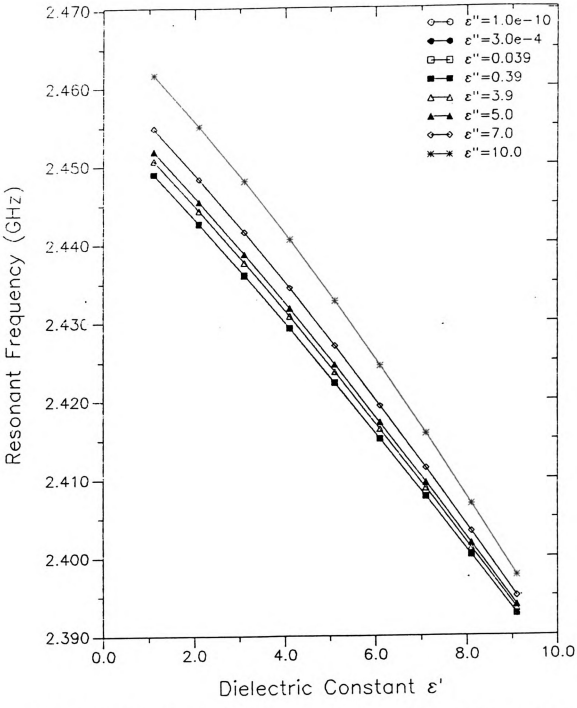

Figure 4.25b Low dielectric constant portion of Figure 4.25a

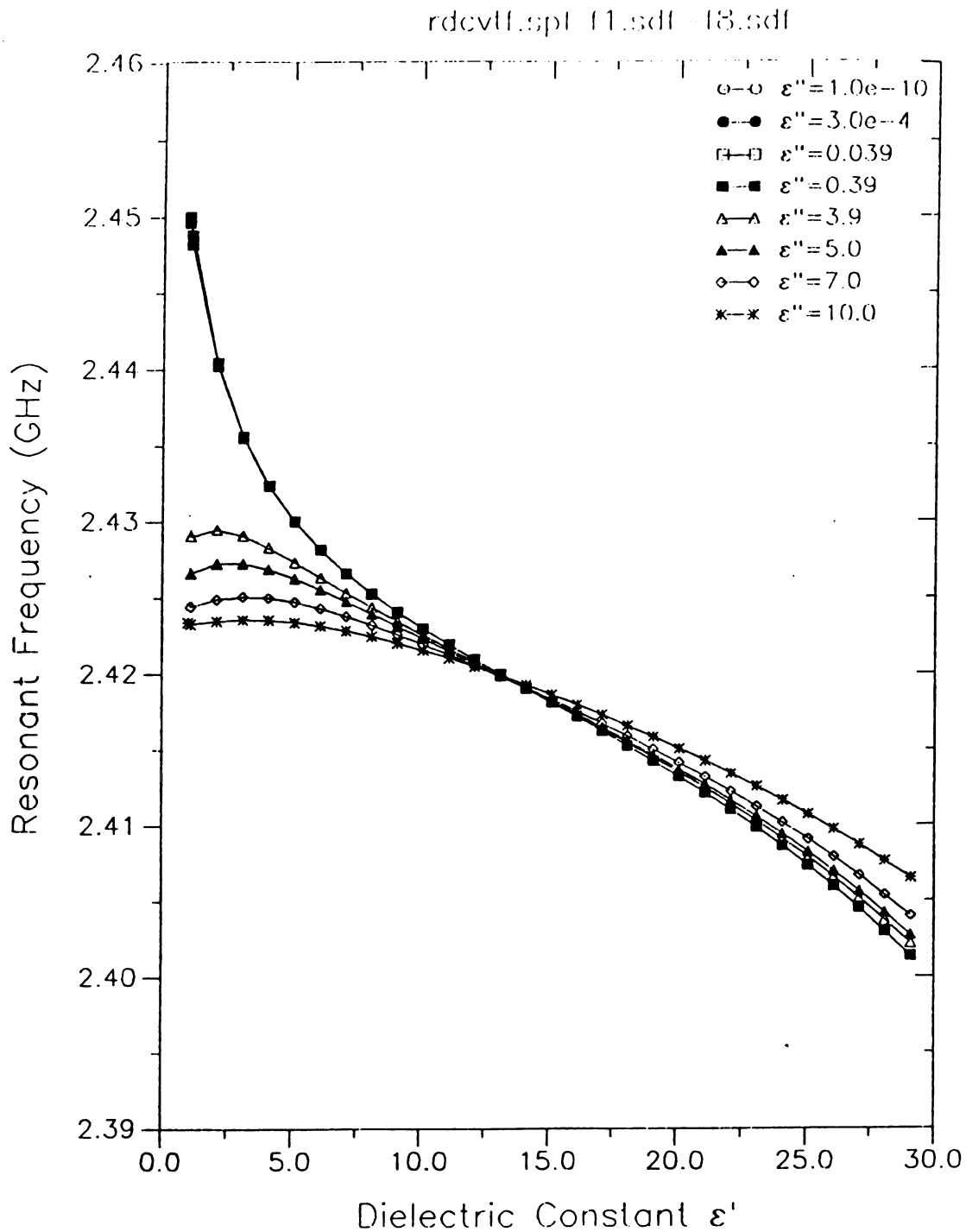

Figure 4.26 Resonant frequency vs. ε' for HE_{111} mode for various ε". a=0.625 cm, b=8.89 cm and L_m=6.69 cm.

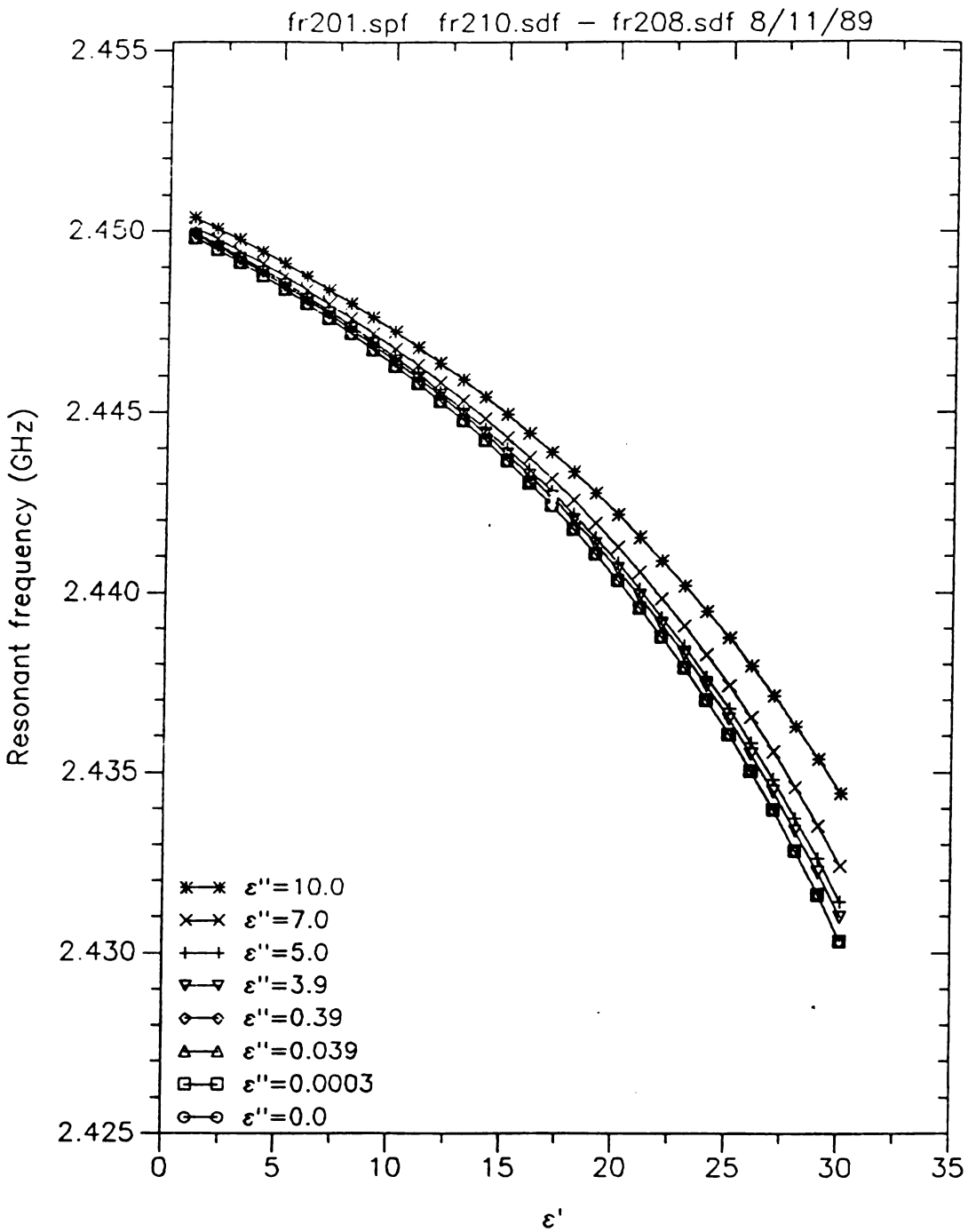

Figure 4.27 Resonant frequency vs. ε' for TE_{011} mode for various ε", a=0.635 cm, b=8.89 cm and L_s=11.255 cm.

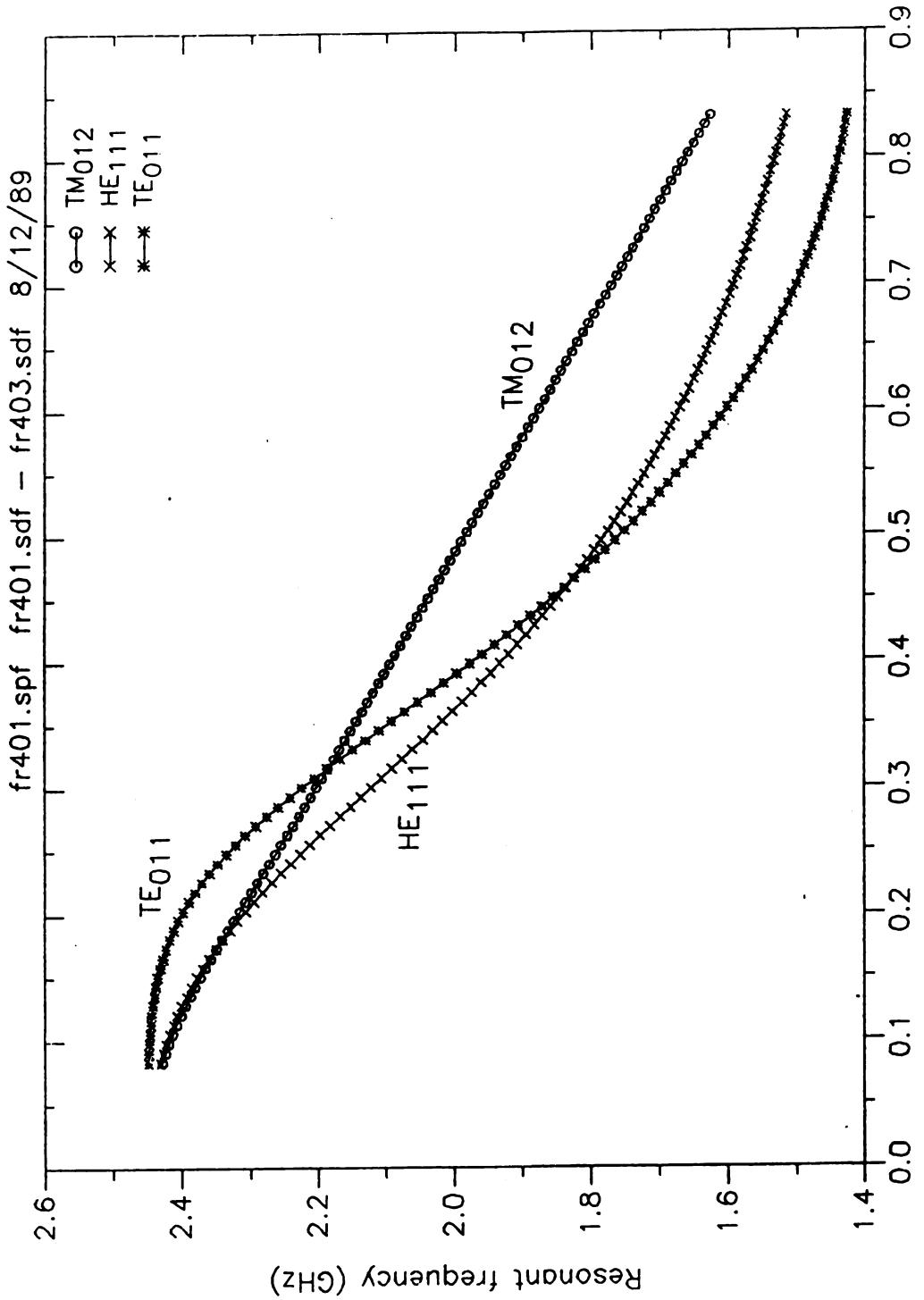

Figure 4.28 Resonant frequency vs. a/b for various modes, where b=7.62 cm, ε=3.03-j0.039.

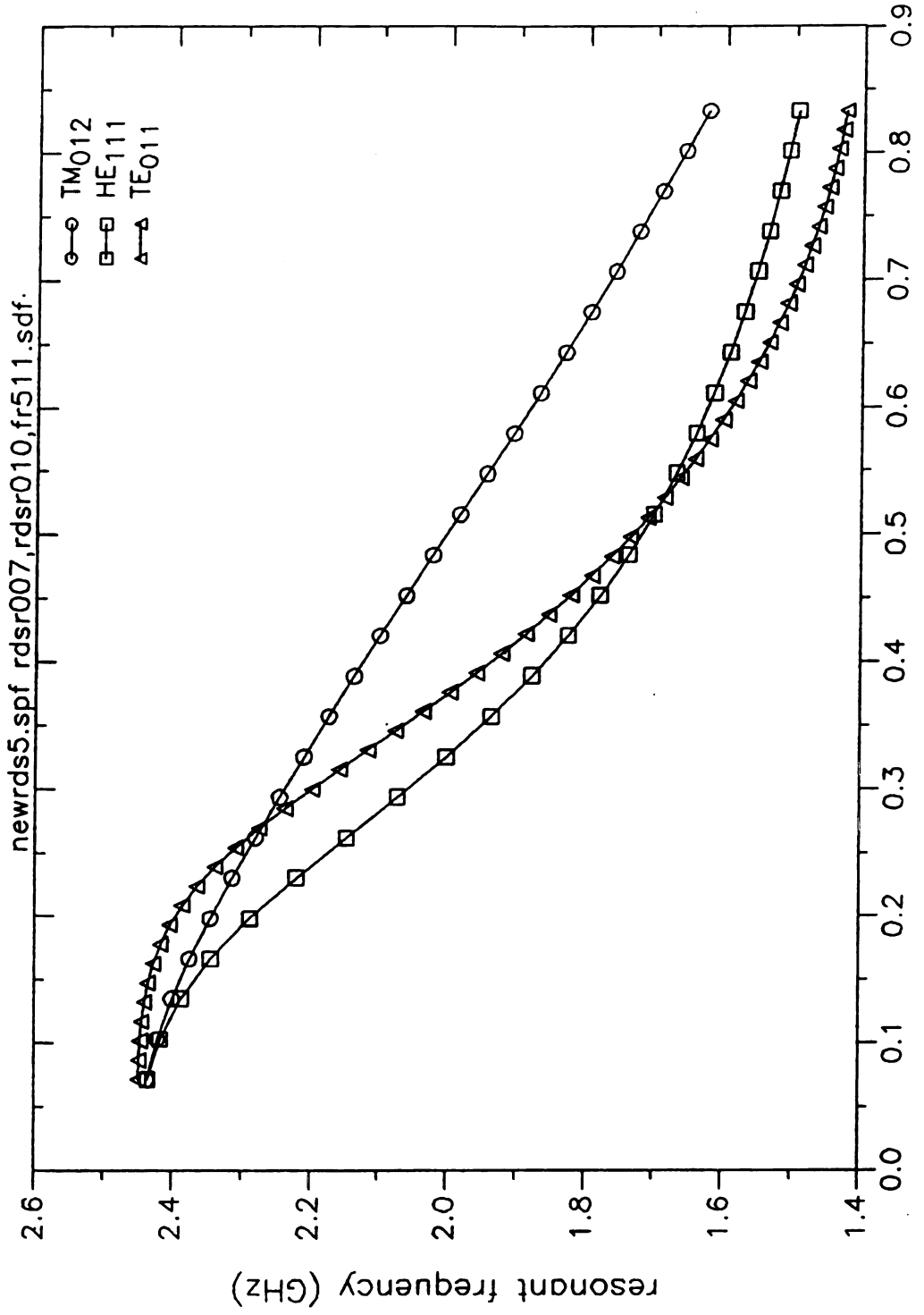

Figure 4.29 Resonant frequency vs. a/b for various modes, where b=8.89 cm, ε=3.03-j0.039.

14.407, 6.69 and 11.255 cm, respectively.

Perturbation technique has been widely used to determine the change in the eigenlength (or eigenfrequency) of a material loaded cavity, due to a change in the dielectric property of the material load. Based on the eigenlength shifts (or eigenfrequency shifts), the dielectric property of the load can be predicted. Often the fields within the loaded cavity are approximated by the empty cavity fields in the perturbation formula. If the field patterns within the loaded cavity are not altered much from those of the empty cavity, the approximations can give reasonably accurate results. On the other hand, if the the material load causes great changes of the empty cavity field patterns, perturbation technique may yield incorrect results. Comparisons of the exact solution and perturbation formula are given in Figures 4.30a and 4.30b.

The resonant length perturbation formula is similar to the resonant frequency perturbation formula given in equation 5.15a. The only differences are for the resonant length perturbation formula f_r is the constant operating frequency and f_{r0} is replaced by

$$f_{r0} = \frac{3\times10^8}{b}\sqrt{x_{np}^2+(\frac{q\pi b}{L_s})^2}$$

where L_s is the resonant length, b is the cavity radius and npq is the mode index. In this example, TM_{012} is excited at 2.45 GHz in a seven inch cavity and the rod radius is 0.635 cm, i.e. x_{01}=2.405, f_r=2.45 GHz, b=8.9 cm and a=0.635 cm.

As displayed in Figure 4.30a, the straight line represents perturbation solutions. The other curves are calculated by the exact formulation. It is interesting to see that for ε_r' larger than 38, the perturbation formula deviates away from the exact solutions. In between ε_r' = 10.0 and 38, larger ε_r'' gives rise to greater difference between the perturbation and exact solutions at a given ε_r'. Figure 4.30b shows the low dielectric constant portion of Figure 4.30a. In this particular example, it is found that perturbation formula only works for very small ranges of ε_r' and ε_r''. Note that the rod radius is very

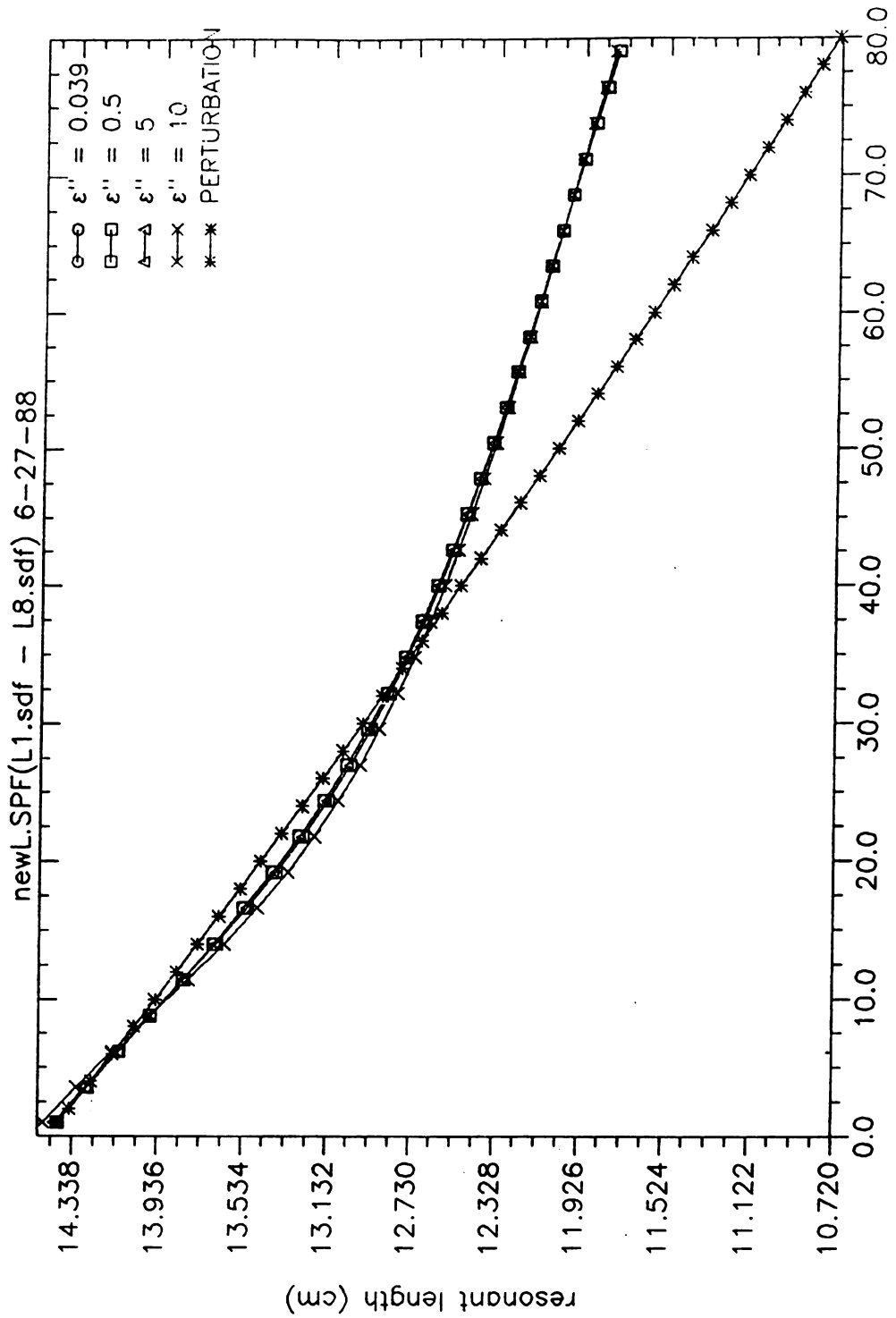

Figure 4.30a Resonant length vs. ε' for TM_{011} mode for various ε", a=0.635 cm, b=8.89 cm and f_0=2.45 GHz.

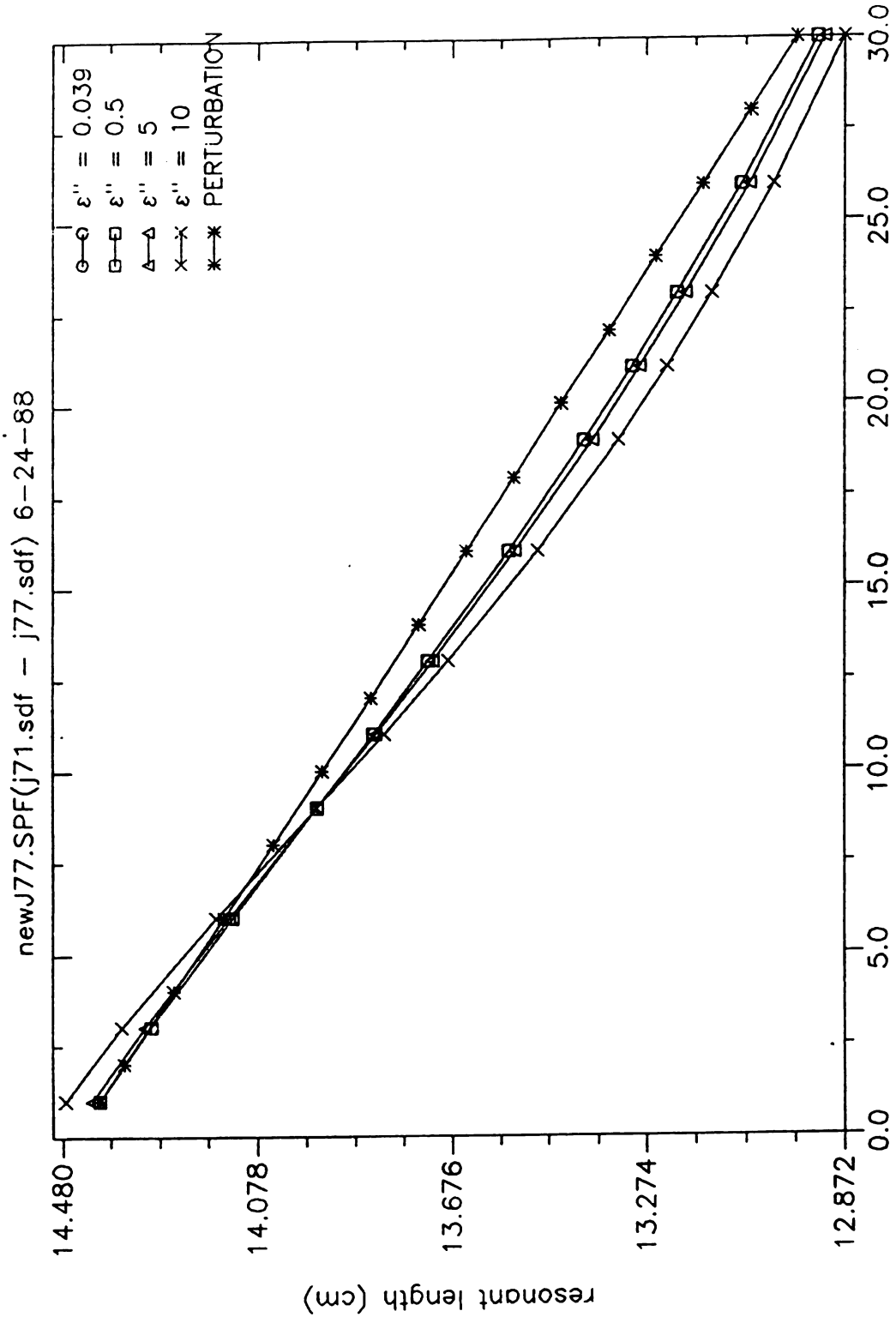

Figure 4.30b Enlargement of the low ε' portion of Figure 4.30a.

small compared to the cavity radius. If the rod radius increases and hence larger perturbation is caused to the empty cavity resonance, the perturbation formula may yield erroneous results even for very small ε_r' and ε_r''.

By comparing the f_r vs. ε_r' curves among the exact solutions shown in Figure 4.30a, it is observed that the resonant length decreases as ε_r' increases. In the range of $\varepsilon_r' < 7.0$, at a given ε_r', an increase in ε_r'' gives rise to an increase in the resonant length. For $60 > \varepsilon_r' > 7.0$, the resonant length is reduced with increasing ε_r'' at a specified ε_r'. As $\varepsilon_r' > 60$, all the resonant length vs. ε_r' curves converge. Figure 4.30b presents a close look at the low dielectric constant range.

Figure 4.31 depicts the resonant length vs. a/b for TM_{012}, HE_{111} and TE_{011} modes. The radius of the cavity is 7.62 cm and the dielectric material is nylon. The cavity is excited at 2.45 GHz. At the 2.45 GHz resonant frequency, the resonant length of the empty cavity is 15.530 cm for TM_{012}, 6.94 cm for TE_{111} and 30.8 cm for TE_{011}, and the resonant length of the homogeneous cavity that is filled with material of $\hat{\varepsilon}_r=3.03-j0$ is 7.52 cm for TM_{012}, 3.653 cm for TE_{111} and 4.255 cm for TE_{011}. As shown, the resonant length decreases with increasing rod radius. It is of interest to see that at $a/b=0.25$, TM_{012} and TE_{011} degenerate. Also seen is that as $a/b \rightarrow 0$, the resonant length approaches the empty cavity resonant length and when $a/b \rightarrow 1$, the resonant length approaches the resonant length of the homogeneous cavity filled with material with $\hat{\varepsilon}_r=3.03-j0$.

4.3.3.3 Quality factor

In this section, the quality factors of TM_{012}, HE_{111} and TE_{011} modes are studied as a function of ε_r', ε_r'' and rod radius. As mentioned in chapter 3, the quality factor Q can be expressed in terms of the quality factor due to the conducting wall losses and the quality factor due to the dielectric losses. Hence, the quality factor is written as

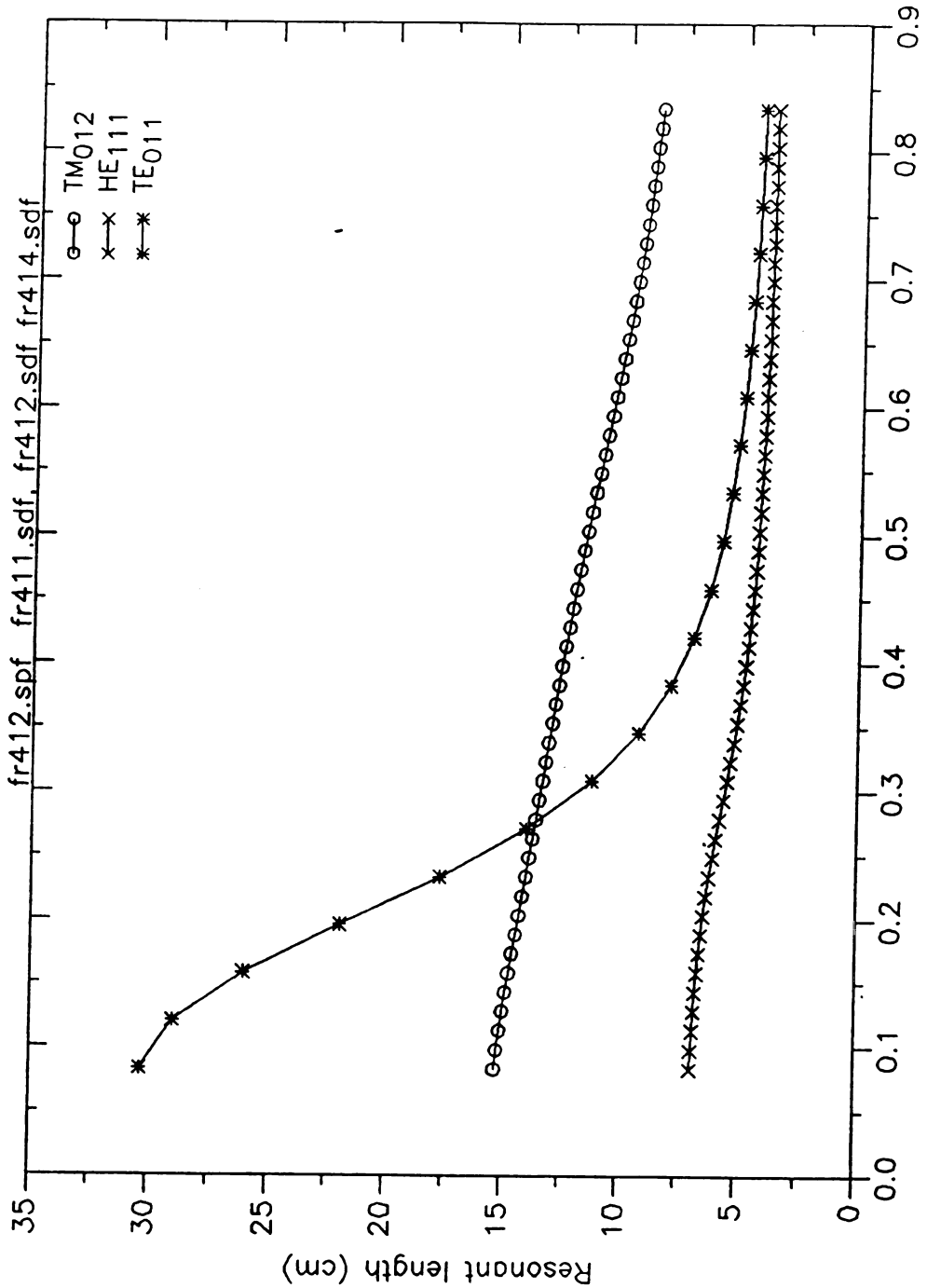

Figure 4.31 Resonant length vs. a/b for various modes, b=7.62 cm, ε=3.03-j0.039 and f_o=2.45 GHz.

$$\frac{1}{Q} = \frac{1}{Q_d} + \frac{1}{Q_{c1}} + \frac{1}{Q_{c2}} \tag{4.15}$$

where

Q_d : the quality factor due to dielectric losses,

Q_{c1} : the quality factor due to the lateral conducting walls,

Q_{c2} : the quality factor due to the end conducting walls.

The quality factors due to the conducting wall losses are obtained by perturbation theory [13]. In the following examples, Q, Q_d, Q_{c1} and Q_{c2} are examined to see the influence of the dielectric losses and conducting wall losses on the overall quality factor.

Figures 4.32a through 4.32d show Q, Q_d, Q_{c1} and Q_{c2} for TM_{012} mode, respectively, as a function of ε_r' for some selected ε_r''. The excitation frequency is 2.45 GHz in this example and in the later cases. The radii of the cavity and dielectric rod are 7.62 and 0.635 cm, respectively. Note that in order to keep the cavity at resonance at 2.45 GHz for various loading, the resonant length must vary for different loading conditions, i.e. for different ε_r'. As shown in Figure 4.32a, the overall quality factor Q increases gradually as ε_r' increases. For a given ε_r', increasing ε_r'' yields a decrease in Q. In comparison with Figure 4.32b, Q_d is approximately the same as Q. As depicted in Figures 4.32c and 4.32d, Q_{c1} and Q_{c2} do not change much for all the losses illustrated. Q_{c1} increases with increasing ε_r', while Q_{c2} is constant for all ε_r'.

Obviously, in this example Q_d is the dominant quality factor that determines the Q. Q decreases with increasing ε_r'' is because of the increase of power dissipation in the dielectric rod as a result of an increase in ε_r'', provided the shielding effect, as noted earlier in section 4.3.3.2, does not occur as ε_r'' increases. The increase of Q as ε_r' increases is most likely due to the redistribution of the field patterns, which gives rise to more stored energy as ε_r' increases. As mentioned earlier, the cavity length must vary as ε_r' changes to maintain the cavity at resonance. Since the cavity length

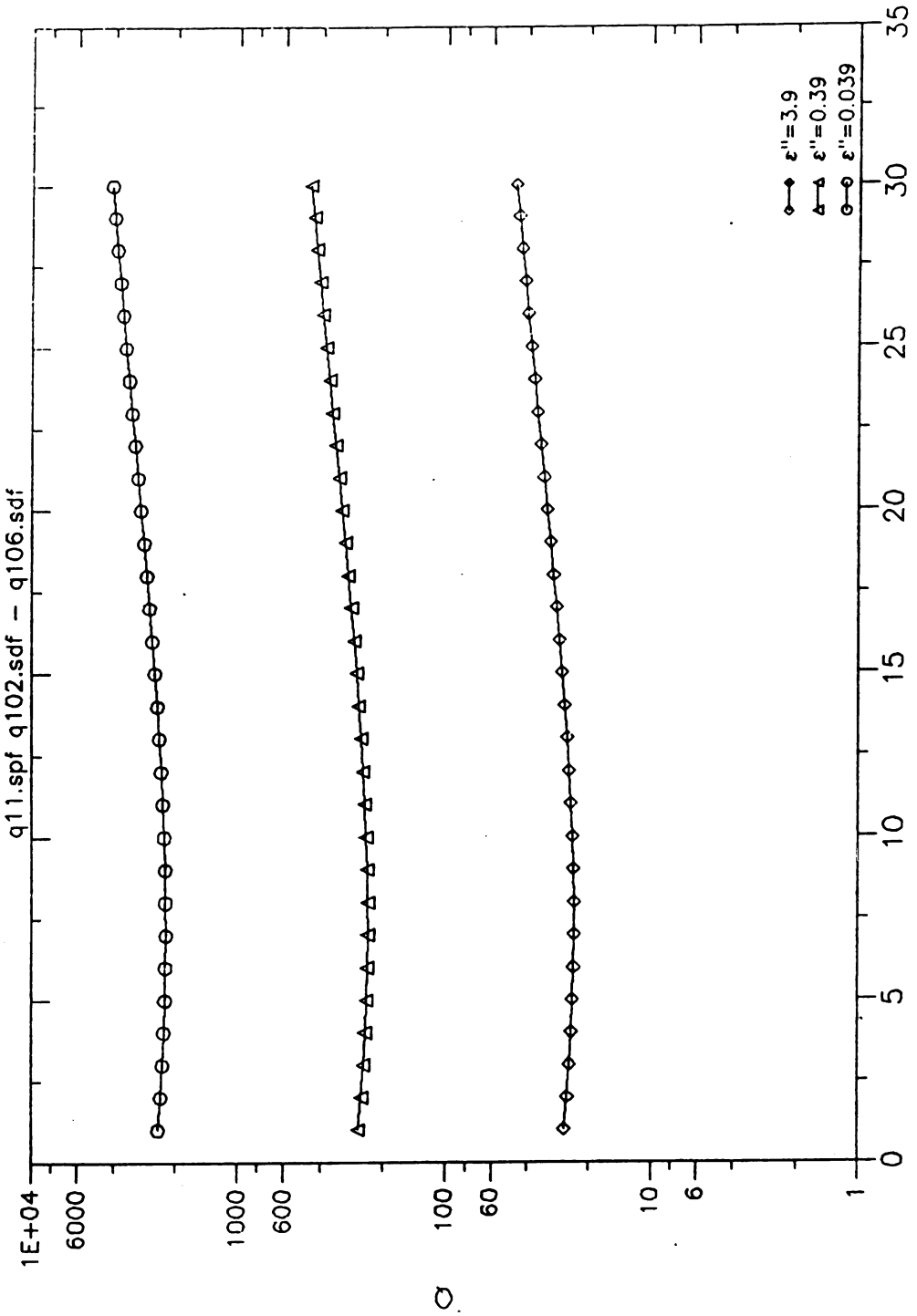

Figure 4.32a Q vs. ε' for TM_{011} mode for various ε'', where a=0.635 cm, b=7.62 cm and f_0=2.45 GHz.

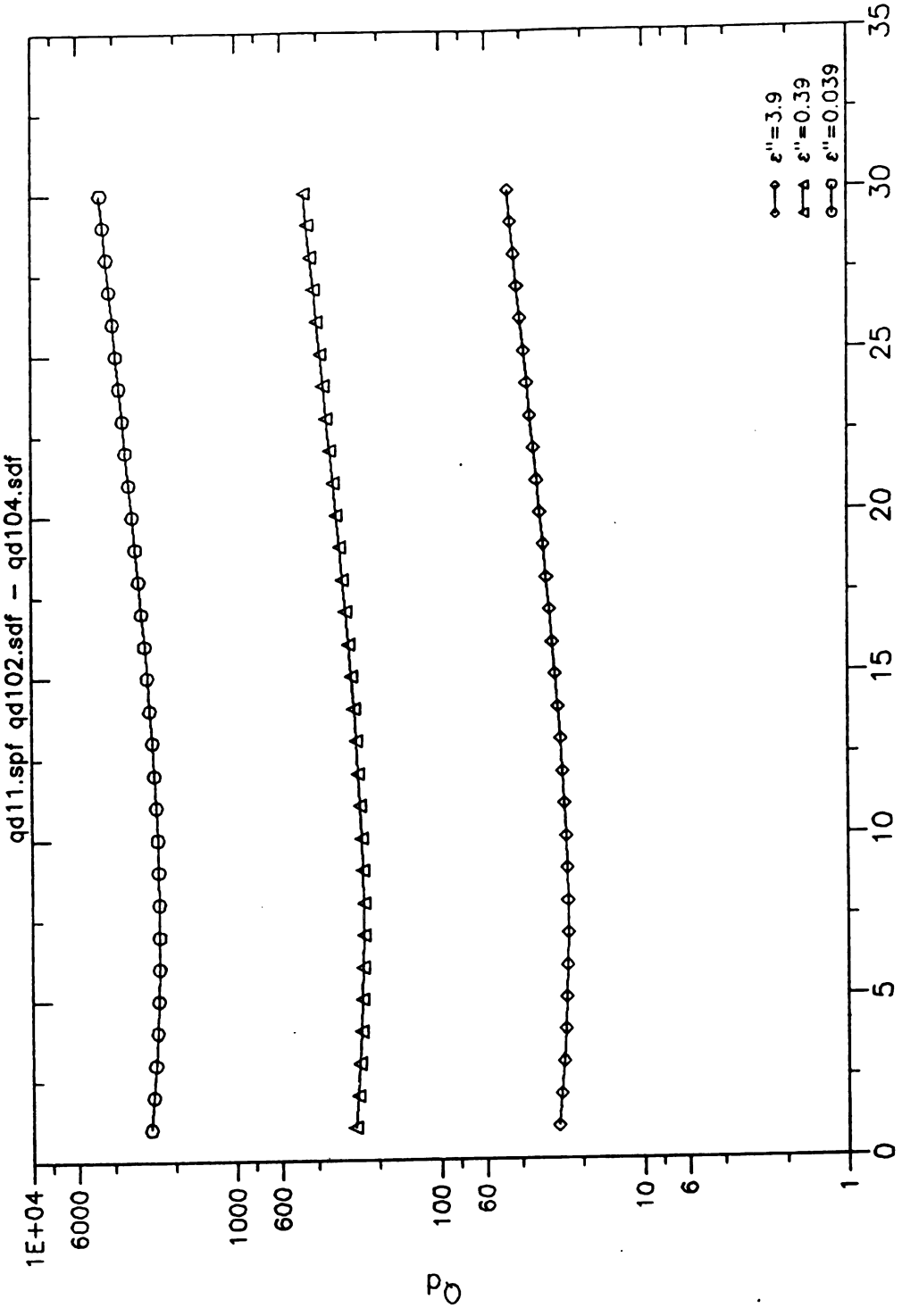

Figure 4.32b Q_d vs. ε' for TM_{011} mode for various ε'', where a=0.635 cm, b=7.62 cm and f_o=2.45 GHz.

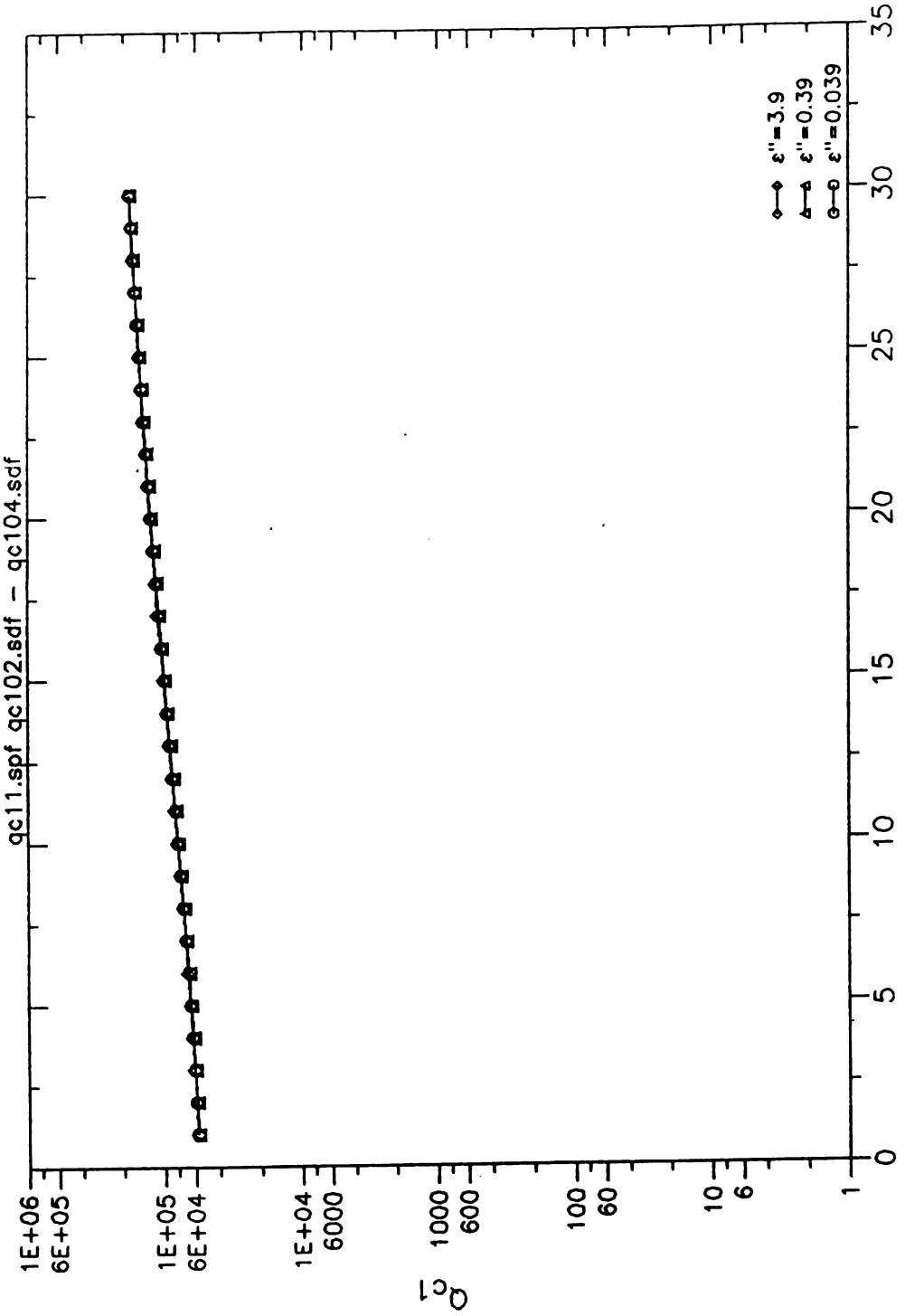

Figure 4.32c Q_{c1} vs. ε' for TM_{012} mode for various ε'', where a=0.635 cm, b=7.62 cm and f_0=2.45 GHz.

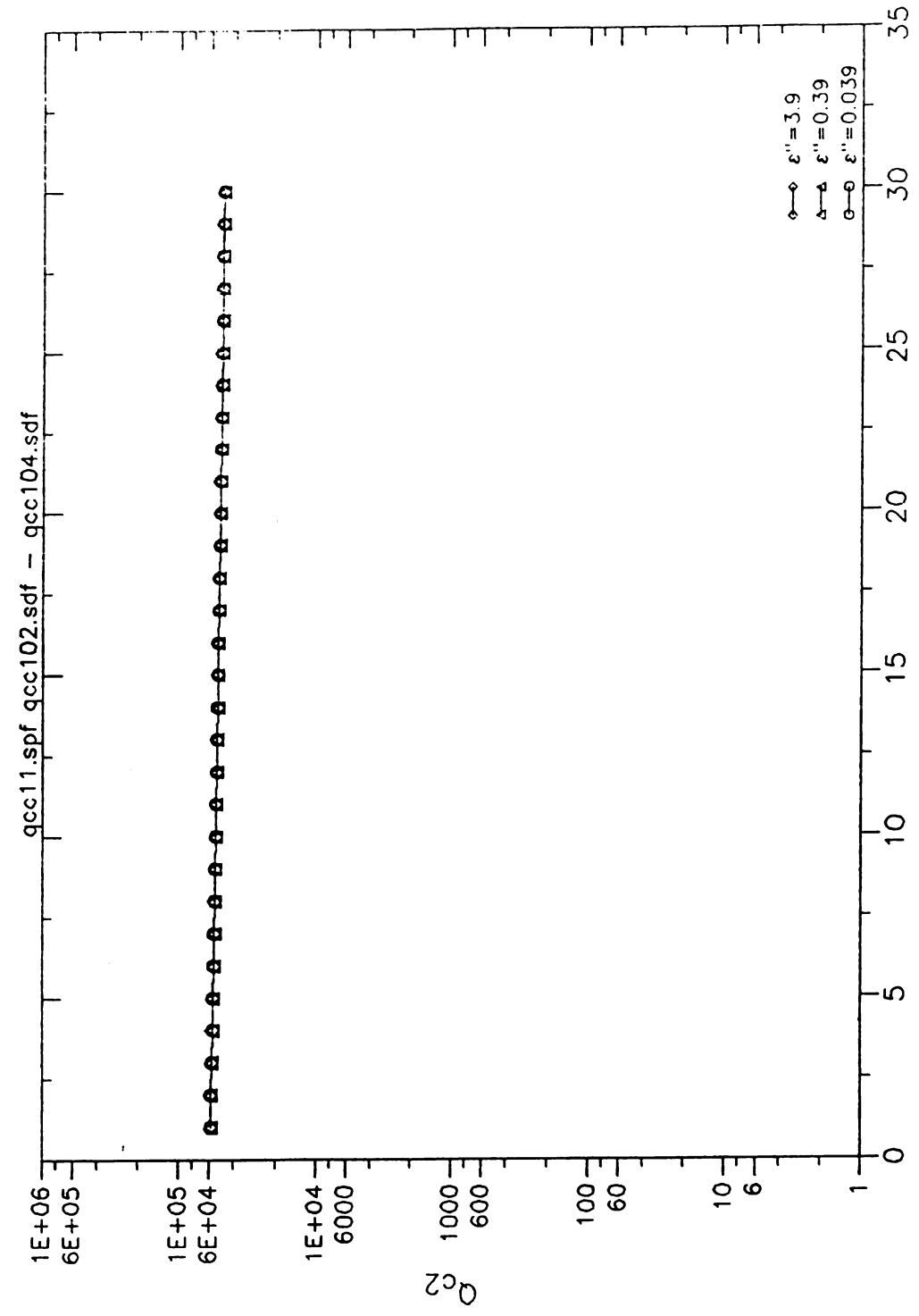

Figure 4.32d Q_{c2} vs ε' for TM_{012} mode for various ε'', where a=0.635 cm, b=7.62 cm and f_0=2.45 GHz

decreases with increasing ε_r', the lateral conducting wall losses reduces as ε_r' increases. This explans why Q_{c1} increases with increasing ε_r', as shown in Figure 4.32c.

Figures 4.33a through 4.33d display the Q, Q_d, Q_{c1} and Q_{c2} of HE_{111} mode, respectively. The cavity geometry is the same as the case of Figure 4.32. Similar to the case of TM_{012} mode, the Q shown in Figure 4.33a increases with increasing ε_r'. For $\varepsilon_r' > 2.5$, an increase in ε_r'' yields a decrease in Q. When $\varepsilon_r' < 2.5$, the Q corresponding to ε_r''=3.9 is less than the Q corresponding to ε_r''=0.039 but larger than that corresponding to ε_r''=0.39. Explanation for this phenomenon is that as ε_r'' is increased from 0.39 to 3.9, EM fields are shielded from the dielectric rod, as shown in Figures 4.17a through 4.17h, which causes the decrease of the power dissipated in the dielectric rod and hence the increase of Q. Again, the Q_{c1} and Q_{c2} shown in Figures 4.33c and 4.33d are almost constant for all the ε_r' and ε_r'' illustrated. Note that Q_{c1} is much larger than Q_{c2}. This indicates that the losses due to the end plates are much larger than those due to the lateral conducting walls.

The quality factors of TE_{011} are shown in Figures 4.34a through 4.34d. As shown, Q decreases with increasing ε_r'. For a given ε_r', increasing dielectric loss ε_r'' results in an decrease in Q. As depicted in Figure 4.34b, the changes in Q_d as a function of ε_r'' are similar to those of Q. The Q_{c1} shown in Figure 4.34c is identical for any ε_r'' given in this example and is barely increased due to an increase in ε_r'. This must be due to the fact that the field patterns near cavity walls do not change much as the material load changes. In Figure 4.34d, it is seen that Q_{c2} decreases slightly as ε_r' increases. In comparison with Figure 4.34d, Q_{c2} is much higher than Q_{c1}, which indicates that most of the conducting wall losses are due to the lateral conducting walls. Close examination of Figure 4.34b and 4.34c finds that Q_d and Q_{c1} corresponding to ε_r''=0.039 are of the same order. While for ε_r''=0.39 and 3.9, Q_d is much lower than Q_{c1}. Apparently, TE_{011} is not a good mode to heat low loss material, say ε_r''=0.039, because the EM energy coupled into the dielectric material and lateral conducting walls is almost equal.

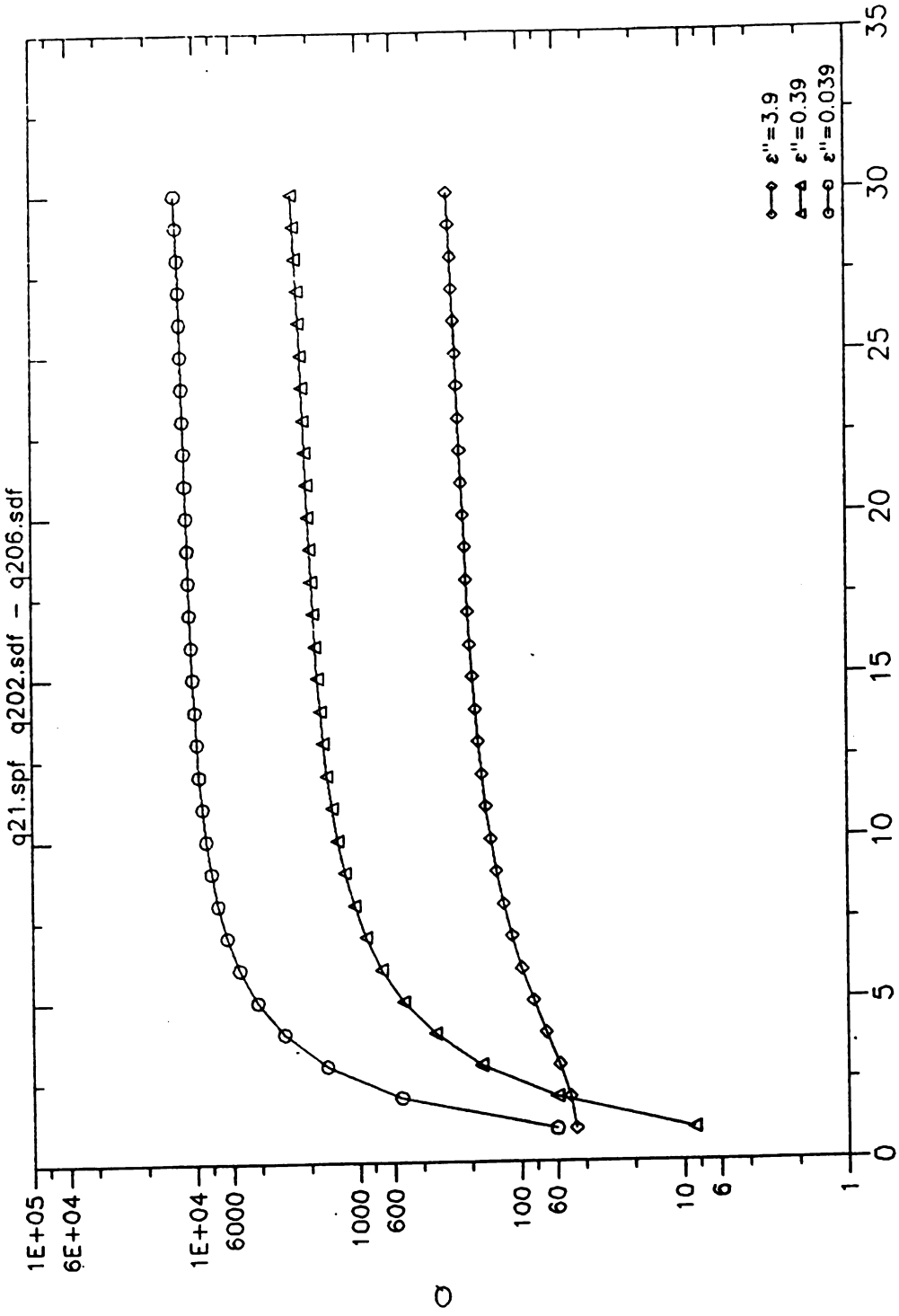

Figure 4.33a Q vs. ε' for HE_{111} mode for various ε'', where a=0.635 cm, b=7.62 cm and f_o=2.45 GHz.

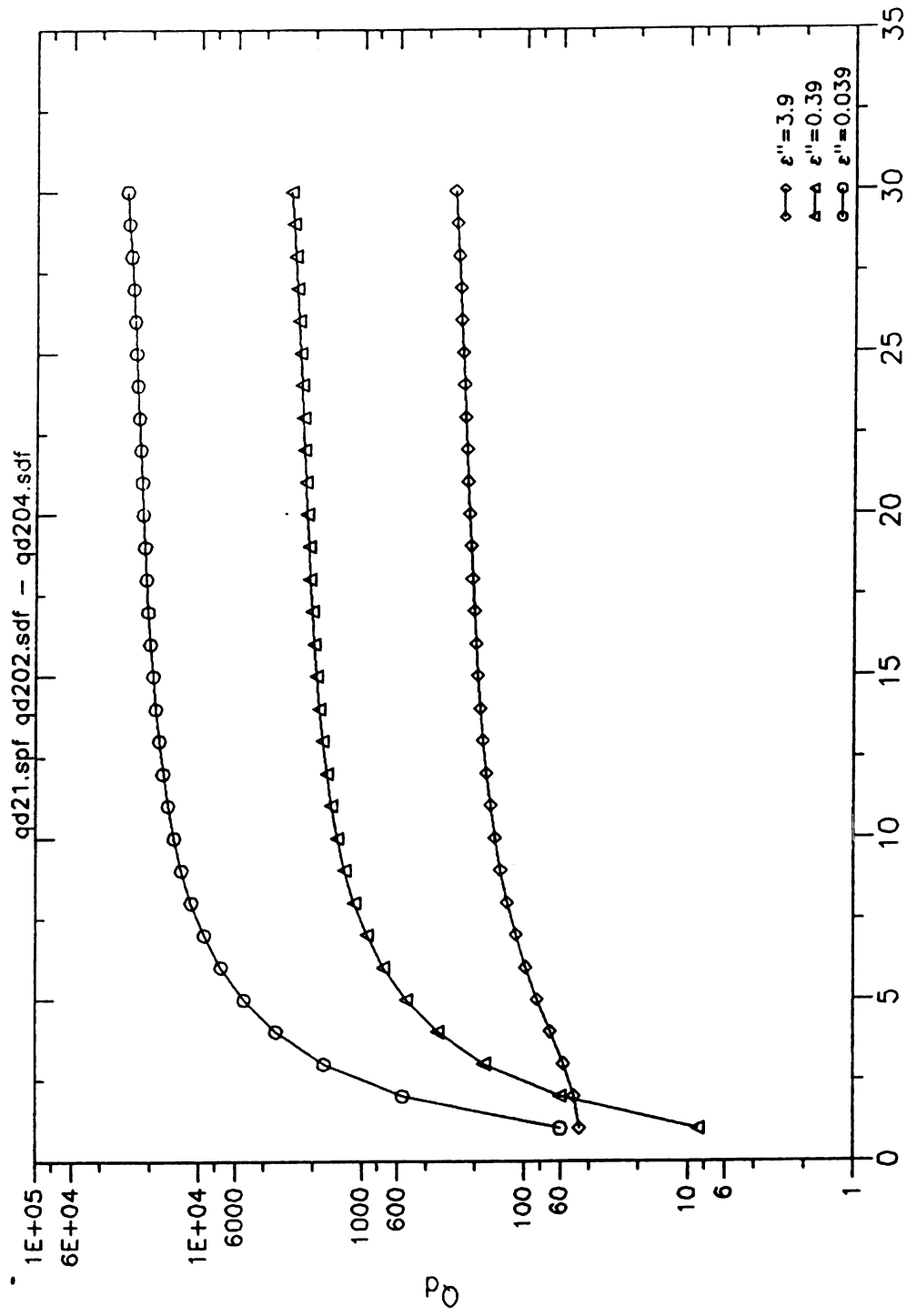

Figure 4.33b Q_d vs. ε' for HE_{111} mode for various ε", where a=0.635 cm, b=7.62 cm and f_o=2.45 GHz.

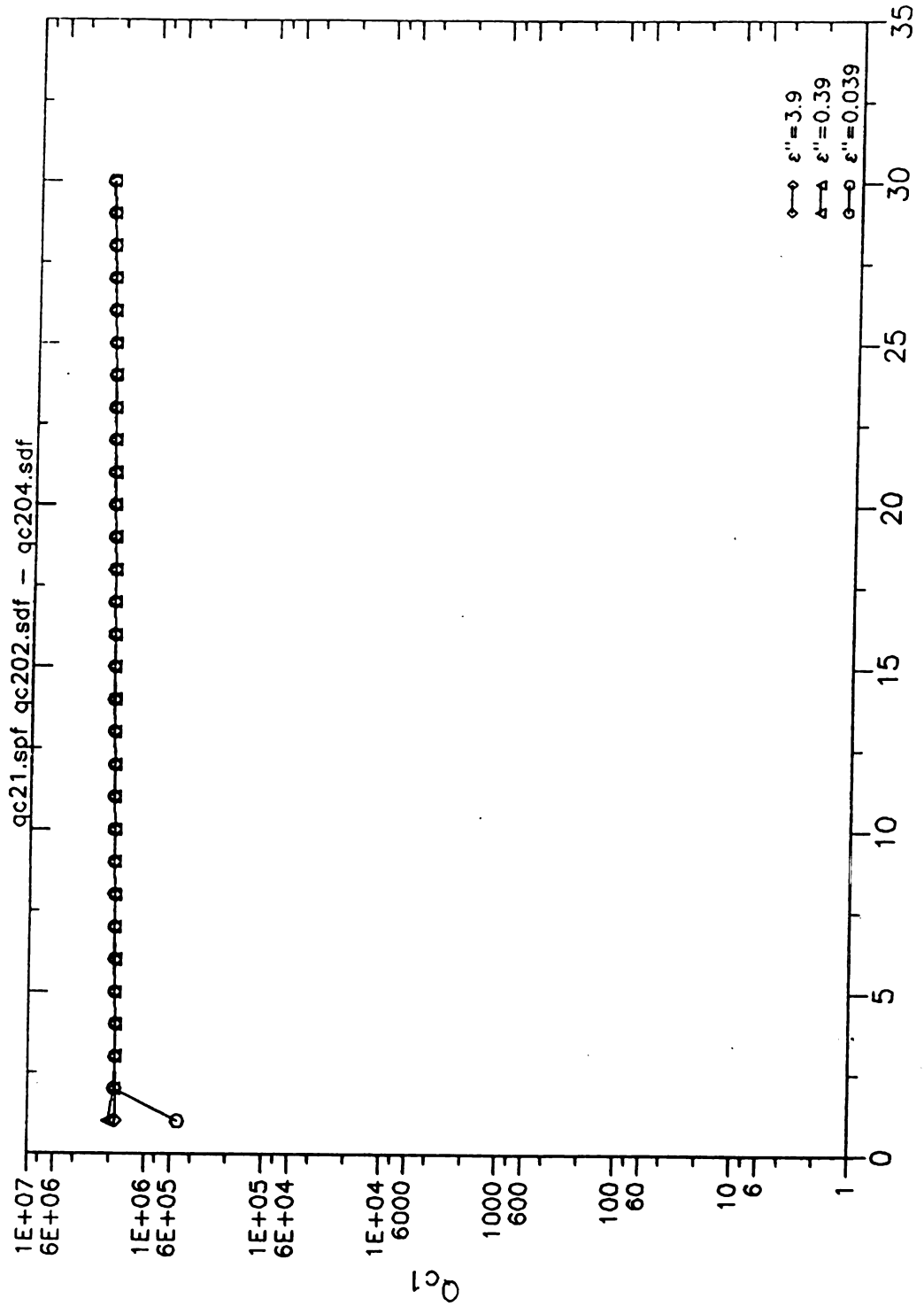

Figure 4.33c Q_{c1} vs. ε' for HE_{111} mode for various ε'', where a=0.635 cm, b=7.62 cm and f_0=2.45 GHz.

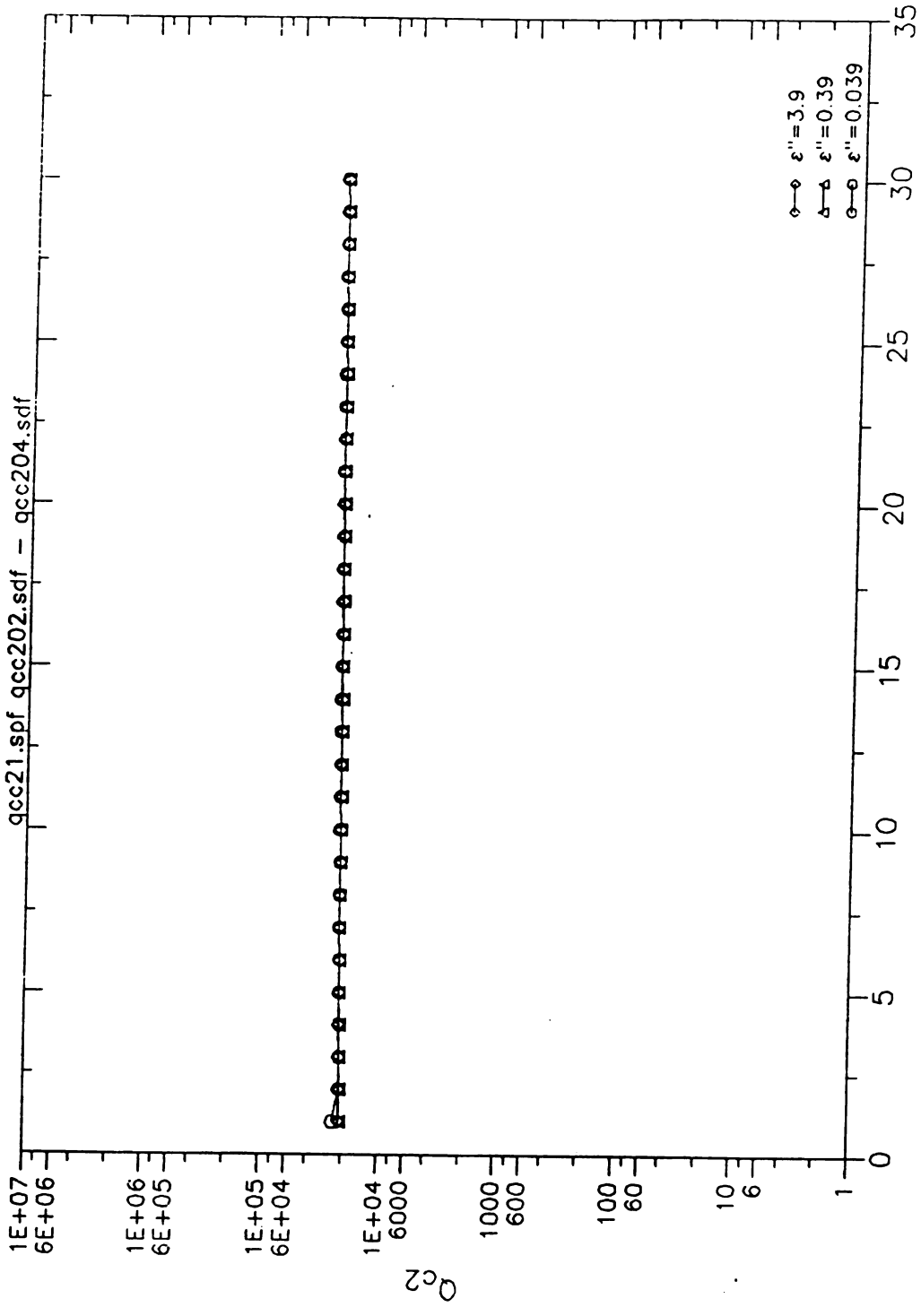

Figure 4.33d Q_{c2} vs ε' for HE_{111} mode for various ε'', where a=0.635 cm, b=7.62 cm and f_0=2.45 GHz

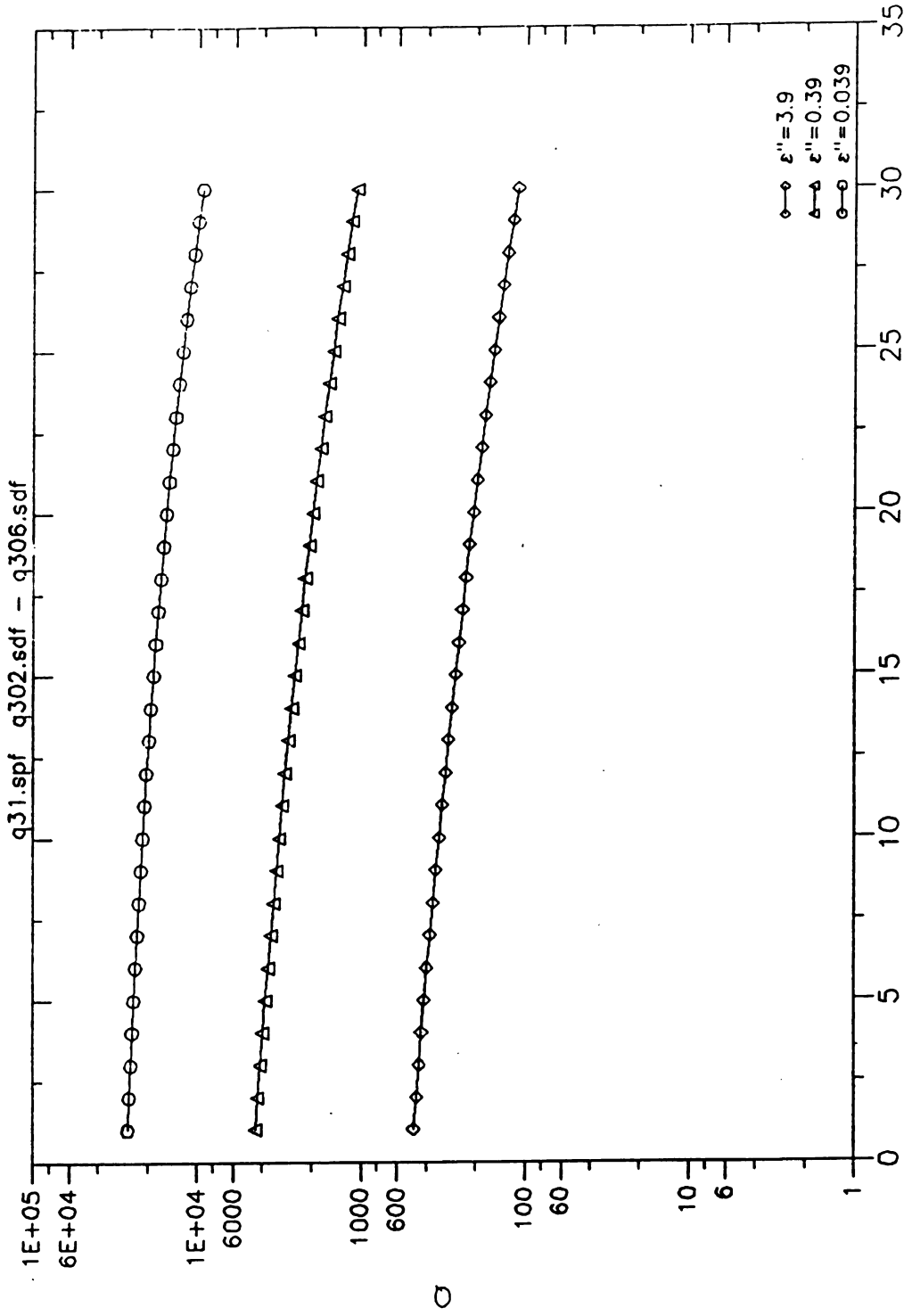

Figure 4.34a Q vs. ε' for TE_{011} mode for various ε'', where a=0.635 cm, b=7.62 cm and f_0=2.45 GHz.

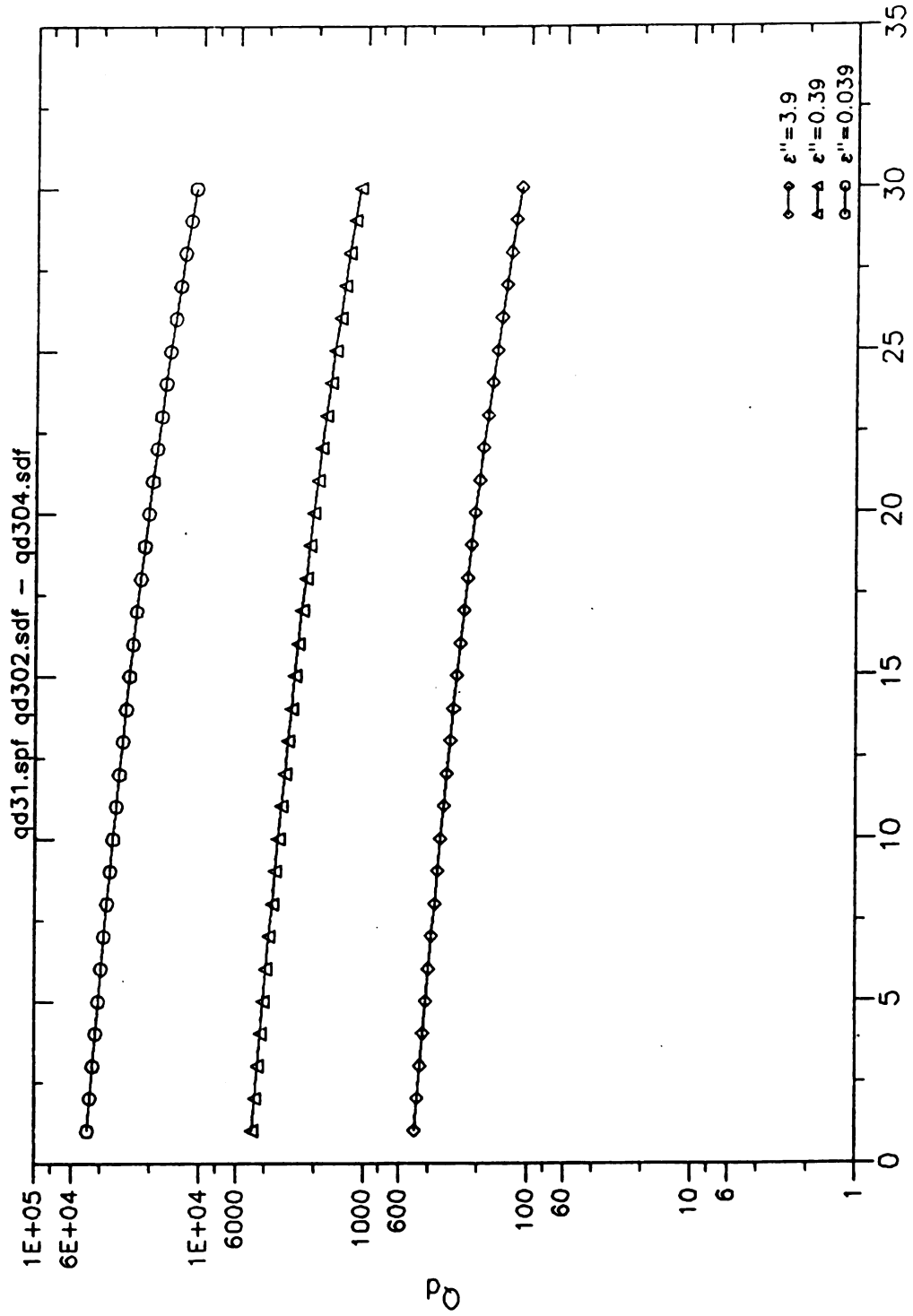

Figure 4.34b Q_d vs. ε' for TE_{011} mode for various ε'', where a=0.635 cm, b=7.62 cm and f_0=2.45 GHz.

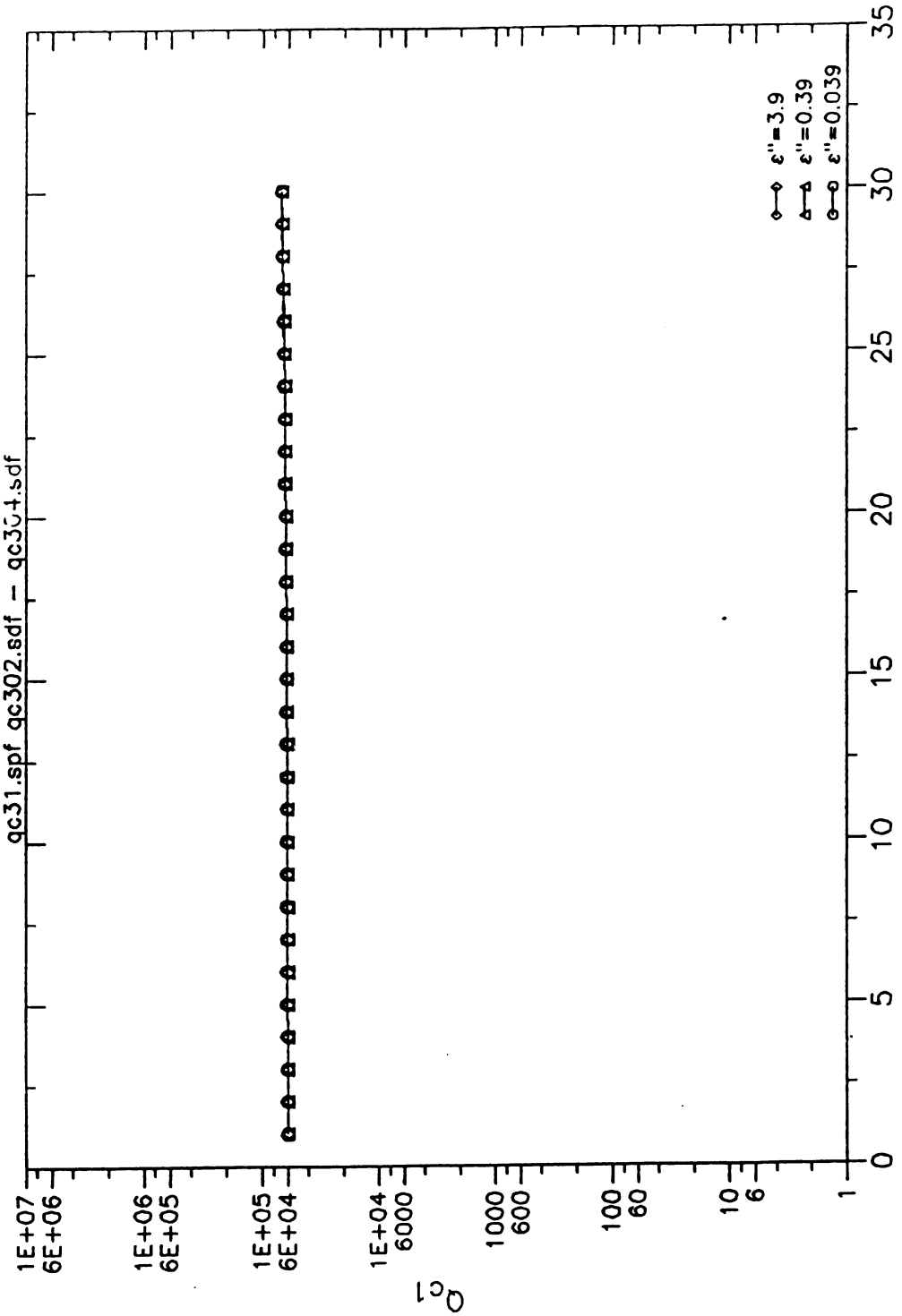

Figure 4.34c Q_{c1} vs. ε' for TE_{011} mode for various ε'', where a=0.635 cm, b=7.62 cm and f_o=2.45 GHz.

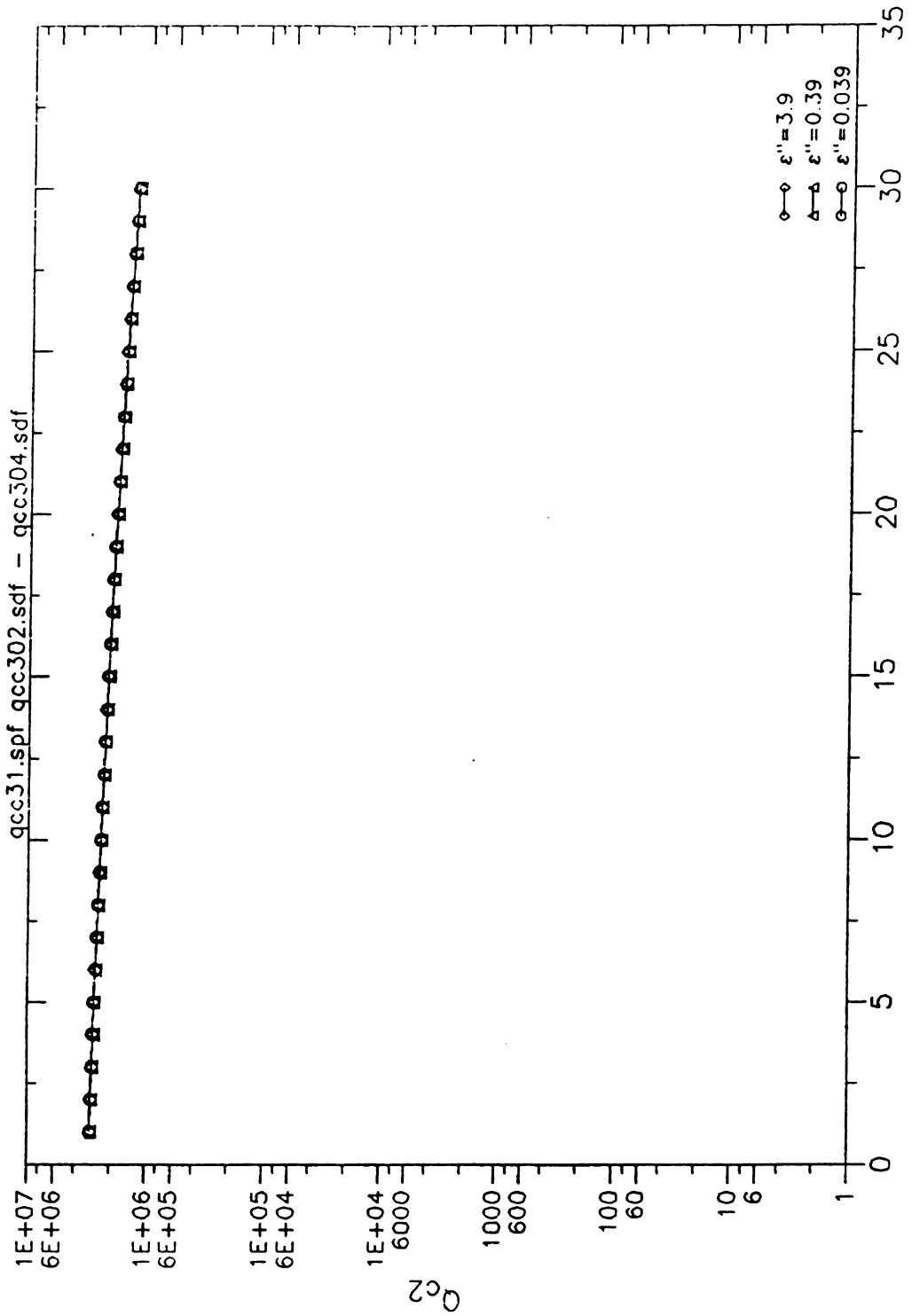

Figure 4.34d Q_{c2} vs ε' for TE_{011} mode for various ε'', where a=0.635 cm, b=7.62 cm and f_0=2.45 GHz

The influence of ε_r'' on Q, Q_d, Q_{c1} and Q_{c2} is investigated for TM_{012}, HE_{111} and TE_{012} for a wide range of ε_r'' in the next eight figures. The radius and ε_r' of the dielectric rod are 0.635 cm and 3.03. As shown in Figures 4.35a and 4.35b, Q and Q_d for HE_{111} decrease with increasing ε_r''. While for TM_{012} and TE_{011}, Q and Q_d decrease with increasing ε_r'' in the low ε_r'' range, but when ε_r'' gets larger, Q and Q_d increase as ε_r'' increases. It is interesting to see that the Q for TM_{012} is the lowest among the three modes when $\varepsilon_r'' < 70$. However, when $\varepsilon_r'' > 70$, the Q for HE_{111} becomes the lowest. It implies that for the particular cavity geometry given in this example, TM_{012} is the best mode to heat materials with $\varepsilon_r'' < 70$ and HE_{111} will achieve better microwave heating when $\varepsilon_r'' > 70$.

The Q_{c1}, as shown in Figure 4.35c, for TE_{011} and HE_{111} modes are almost constant over the range of $0 < \varepsilon_r'' < 1000$. For TM_{012} mode, Q_{c1} is constant only when $\varepsilon_r'' > 100$. In Figure 4.35d, it is seen that Q_{c2} for TM_{012} and HE_{111} modes change only slightly as ε_r'' increases. While the Q_{c2} for TE_{011} mode increases with increasing ε_r''.

The low dielectric loss ranges of $\varepsilon_r'' < 15$ shown in Figures 4.35a through 4.35d are displayed in Figures 4.36a through 4.36d. Close examination of these figures reveals that for very low ε_r'', i.e. $\varepsilon_r'' \to 0$, Q is determined by the conducting wall losses. When ε_r'' becomes larger, Q_d is dominant and hence Q is primarily determined by Q_d.

The changes in the quality factors as a function of rod radius are investigated in Figures 4.37a through 4.37d. The dielectric rod is nylon rod, i.e. $\hat{\varepsilon}_r$=3.03–j0.039, of 0.635 cm radius. As is seen in Figures 4.37a and 4.37b, the Q and Q_d for TM_{012} and TE_{011} modes decrease as rod radius increases. The Q and Q_d for HE_{111} mode increase with increasing rod radius when $a/b < 0.24$. As $a/b > 0.24$, increasing rod radius causes a decrease in Q and Q_d for HE_{111}. The field patterns for HE_{111} displayed in Figure 4.18b and Figures 4.19a through 4.19c explans why the changes in Q for HE_{111} modes are different from those for TM_{012} and TE_{011}. As shown in Figures 4.19c and 4.18b, when a/b increases from 0.0833 to 0.167, more EM energy is distributed in the

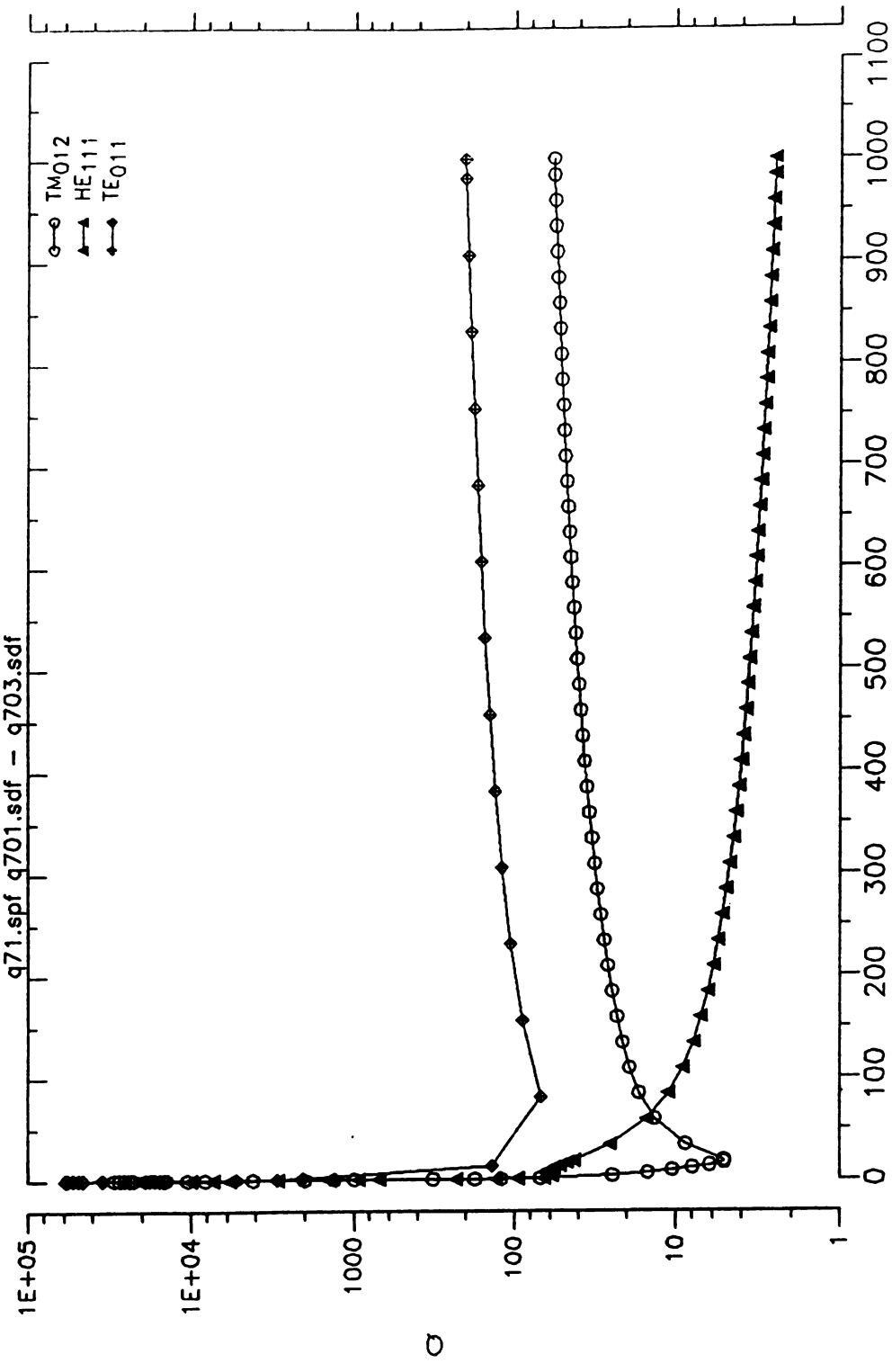

Figure 4.35a Q vs. ε" for various modes, where ε'=3.03, a=0.635 cm, b=7.62 cm and f_0=2.45 GHz.

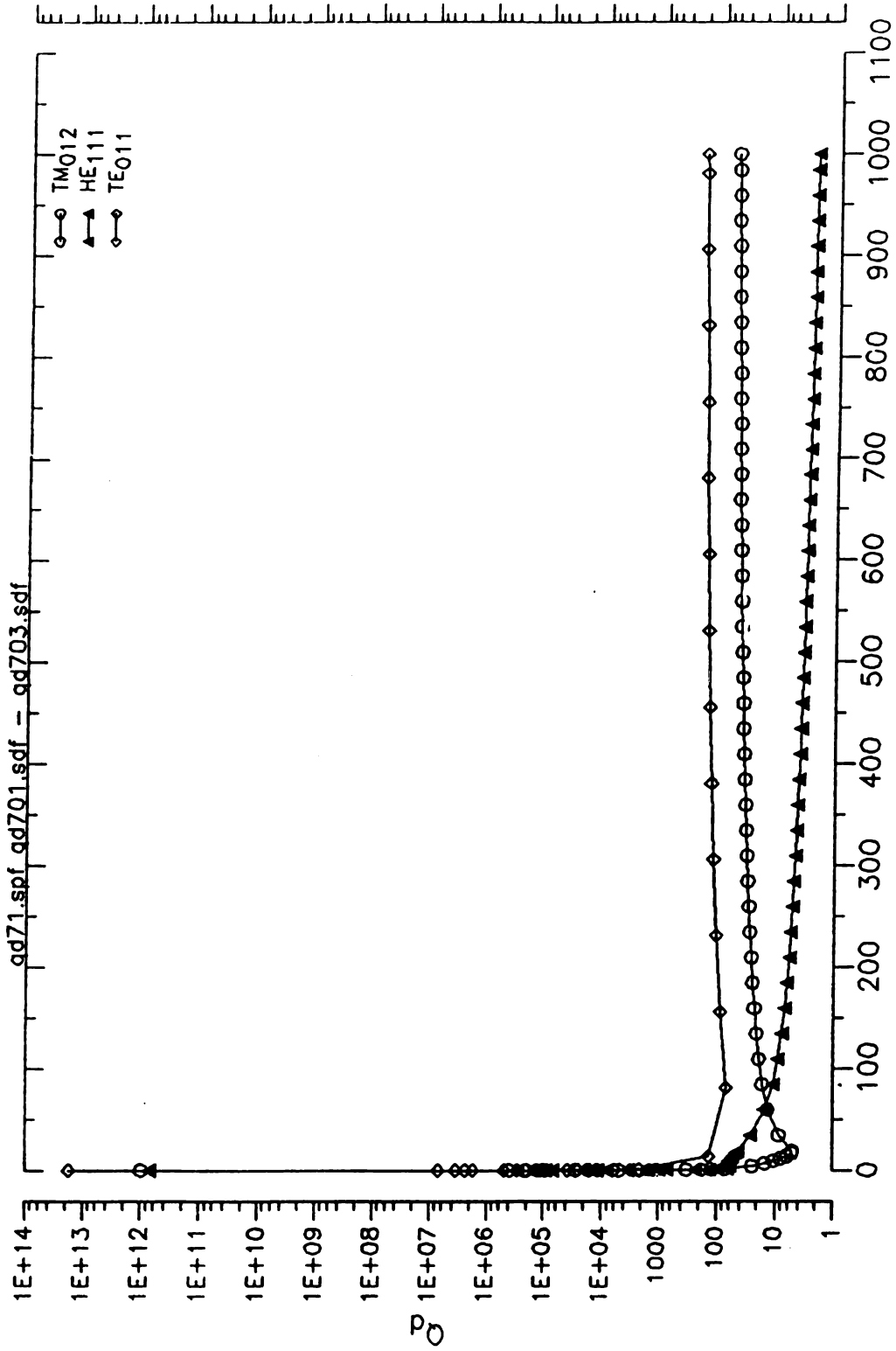

Figure 4.35b Q_d vs. ε'' for various modes, where ε'=3.03, a=0.635 cm, b=7.62 cm and f_o=2.45 GHz.

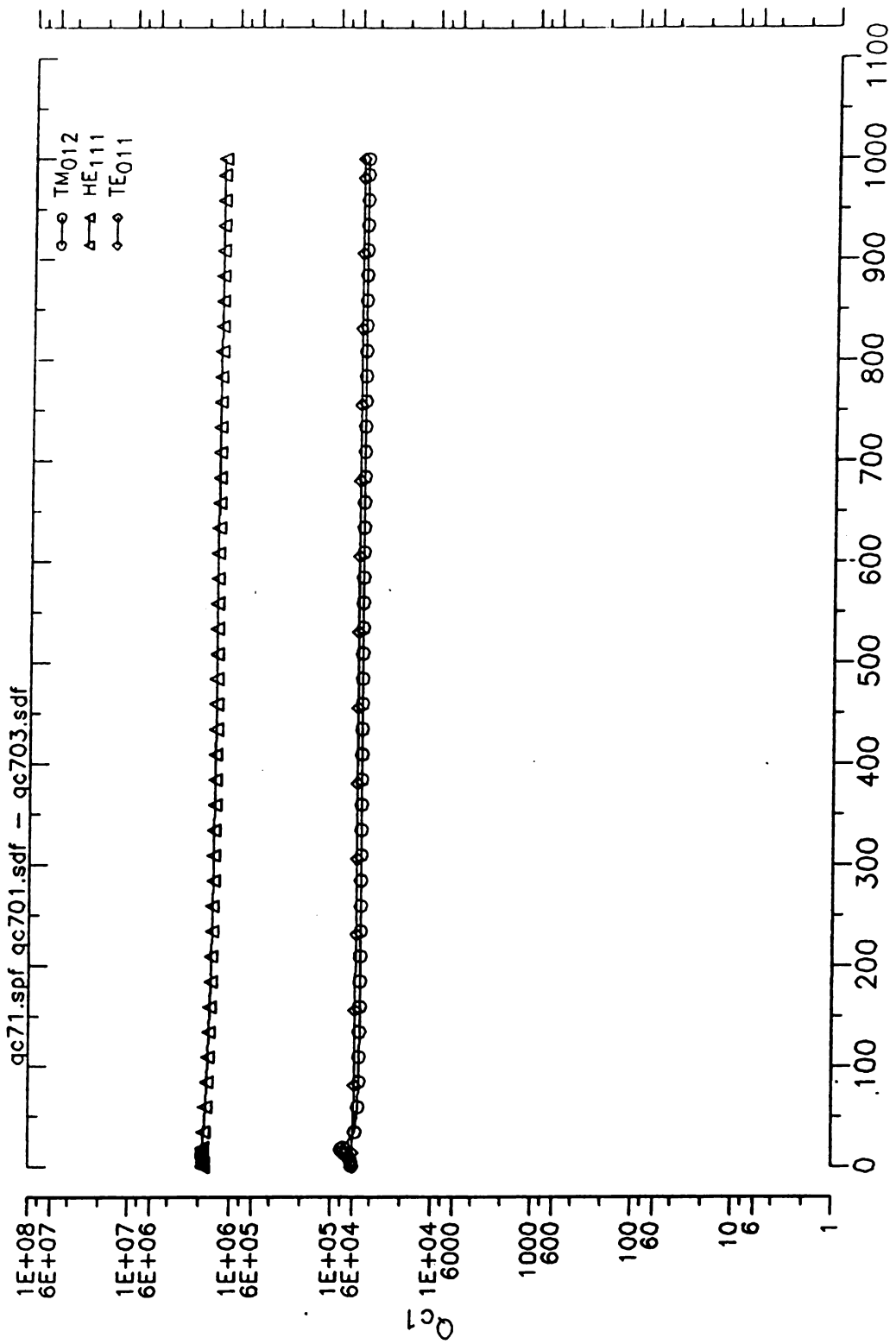

Figure 4.35c Q_{c1} vs. ε'' for various modes, where $\varepsilon'=3.03$, a=0.635 cm, b=7.62 cm and f_o=2.45 GHz.

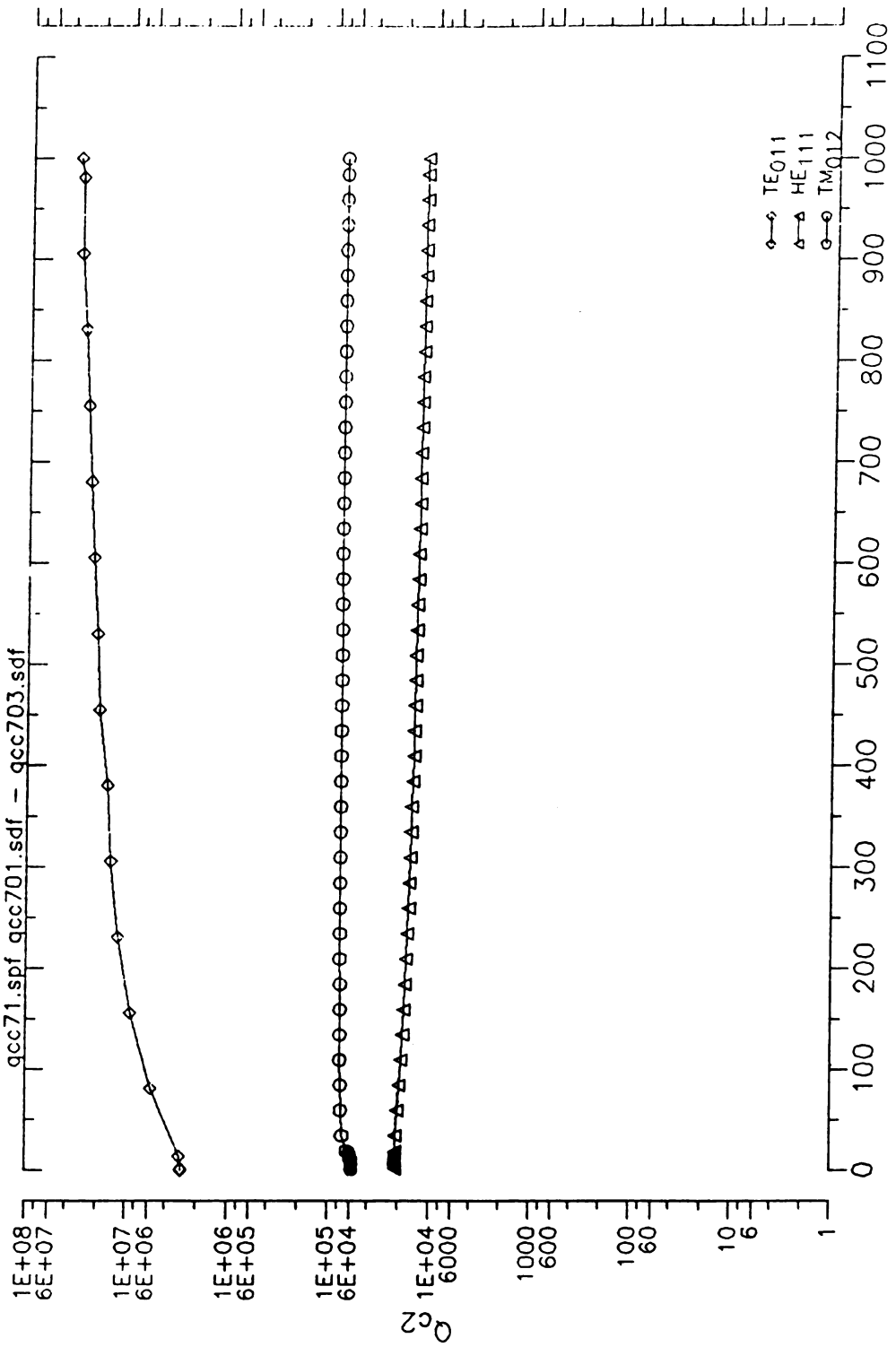

Figure 4.35d Q_{c2} **vs** ε'' **for various modes, where** $\varepsilon'=3.03$, **a=0.635 cm, b=7.62 cm and** $f_0=2.45$ **GHz**

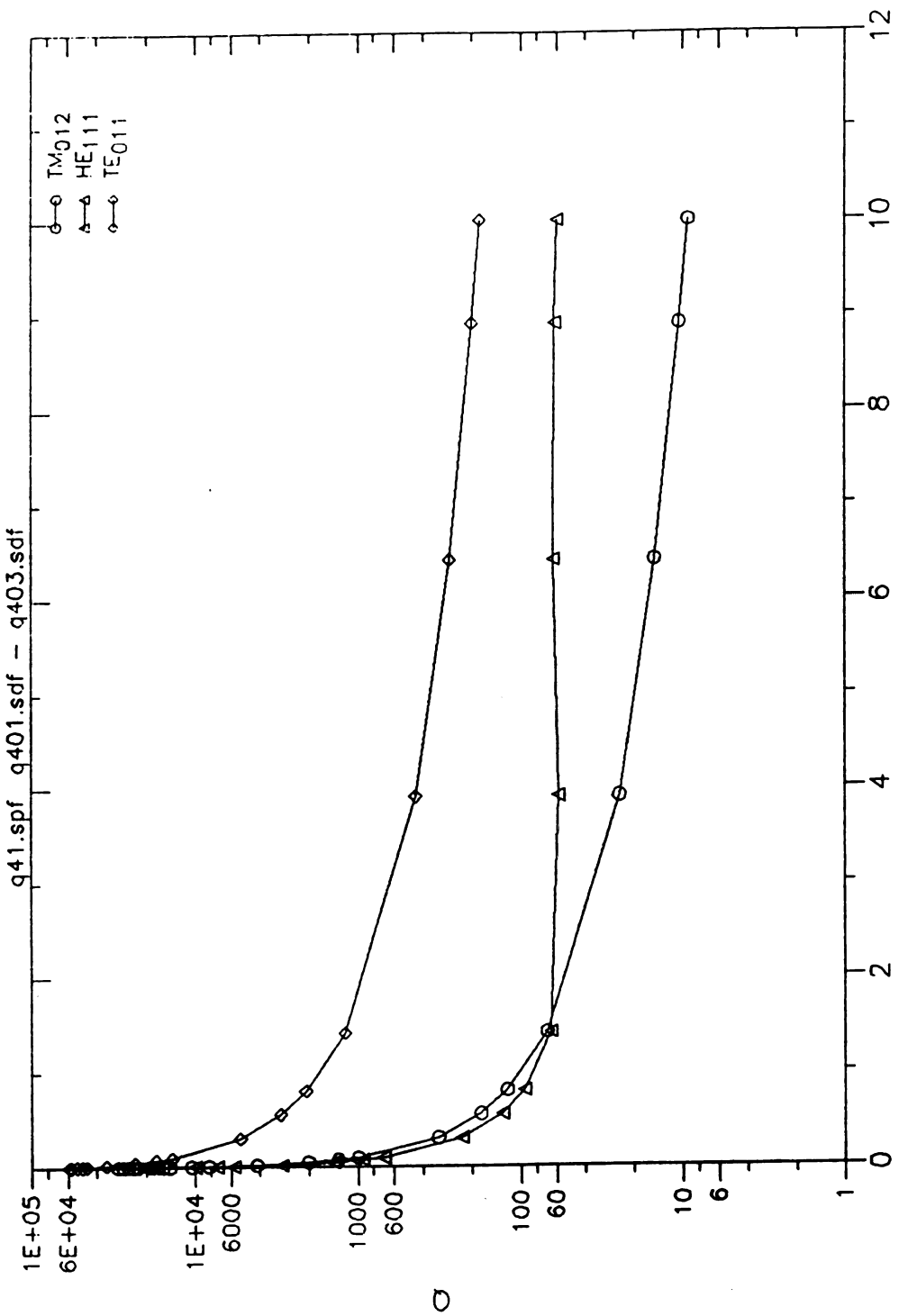

Figure 4.36a Enlargement of the small ε'' portion of Figure 4.35a.

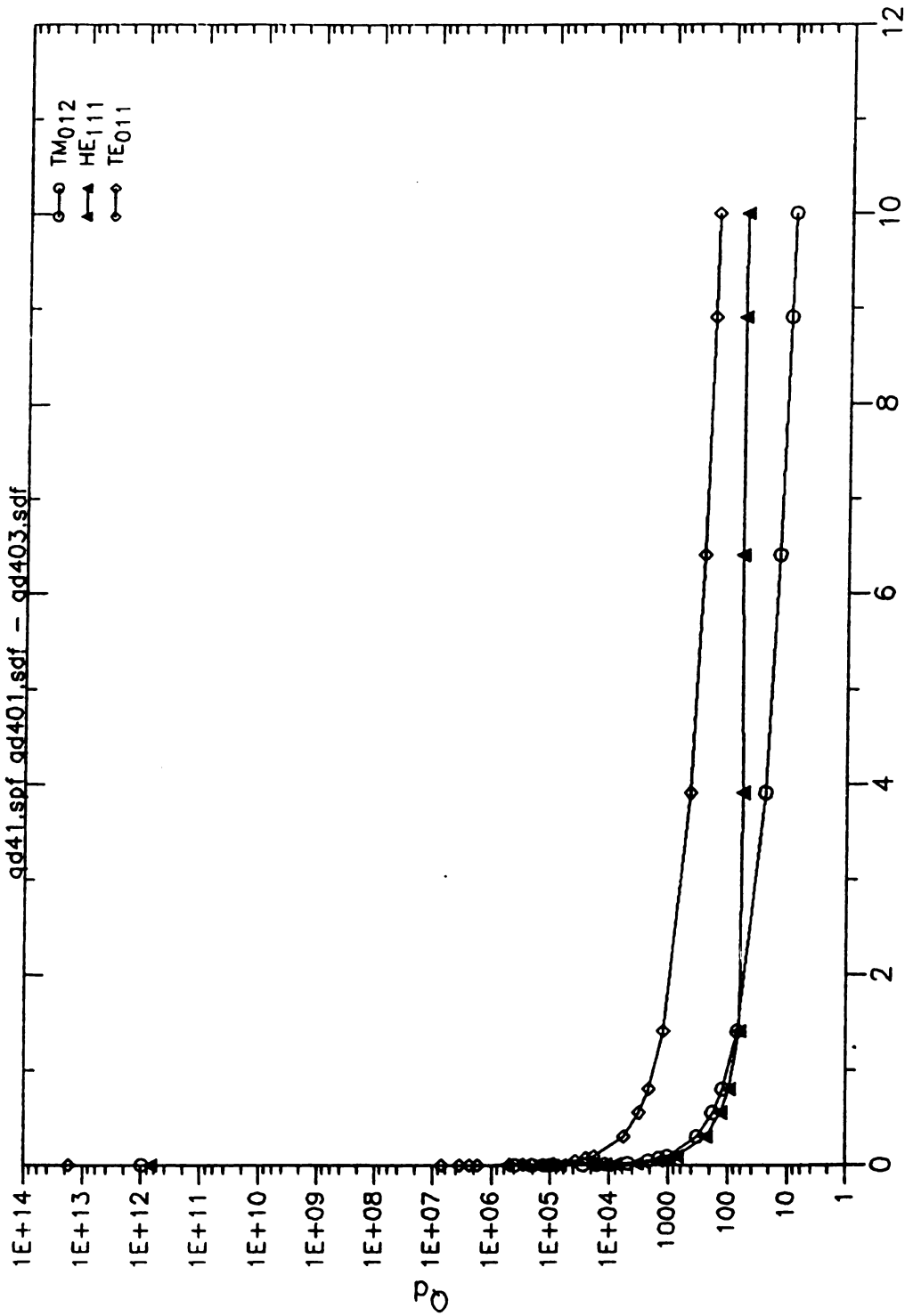

Figure 4.36b Enlargement of the small ε" portion of Figure 4.35c.

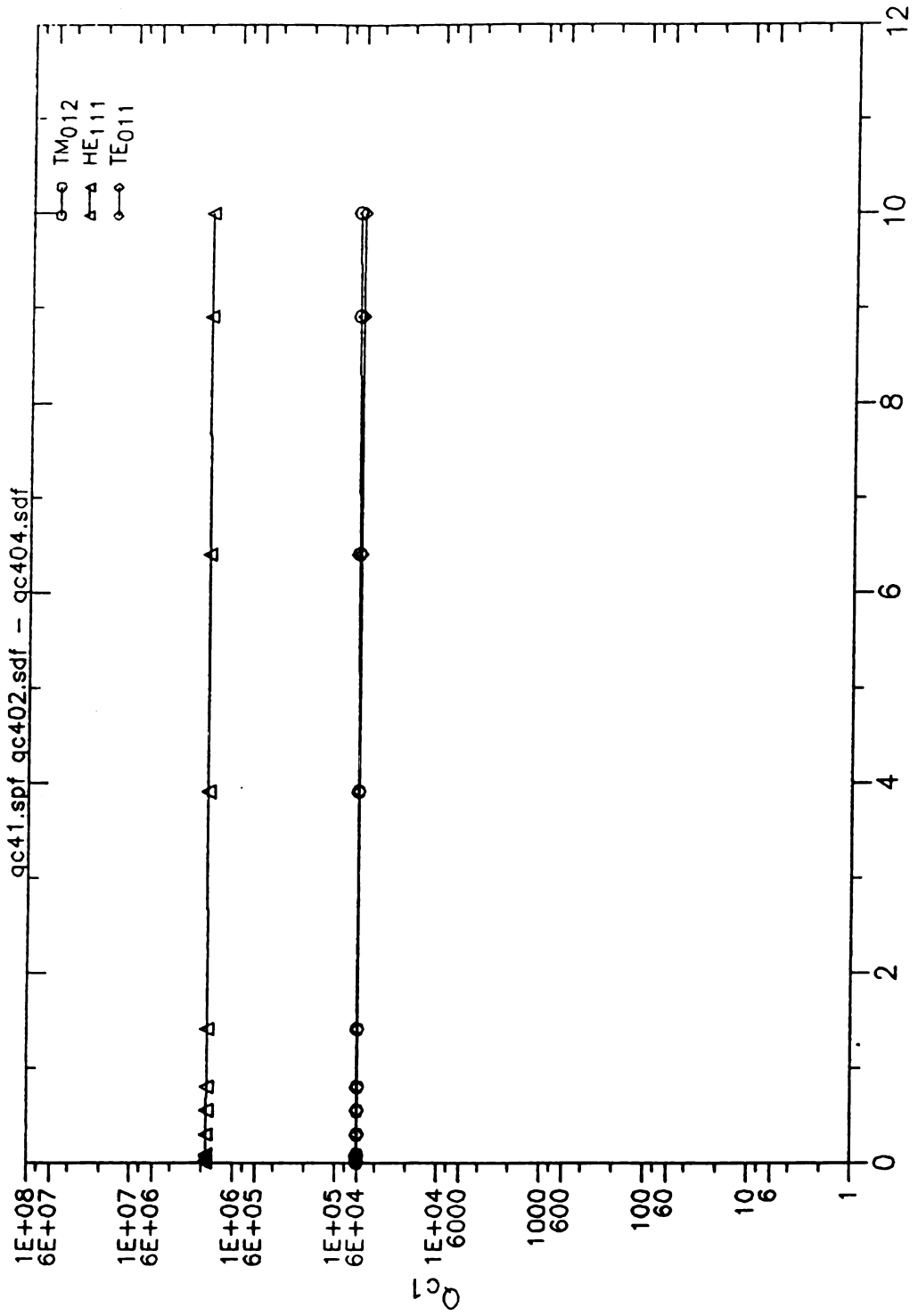

Figure 4.36c Enlargement of the small ε'' portion of Figure 4.35b.

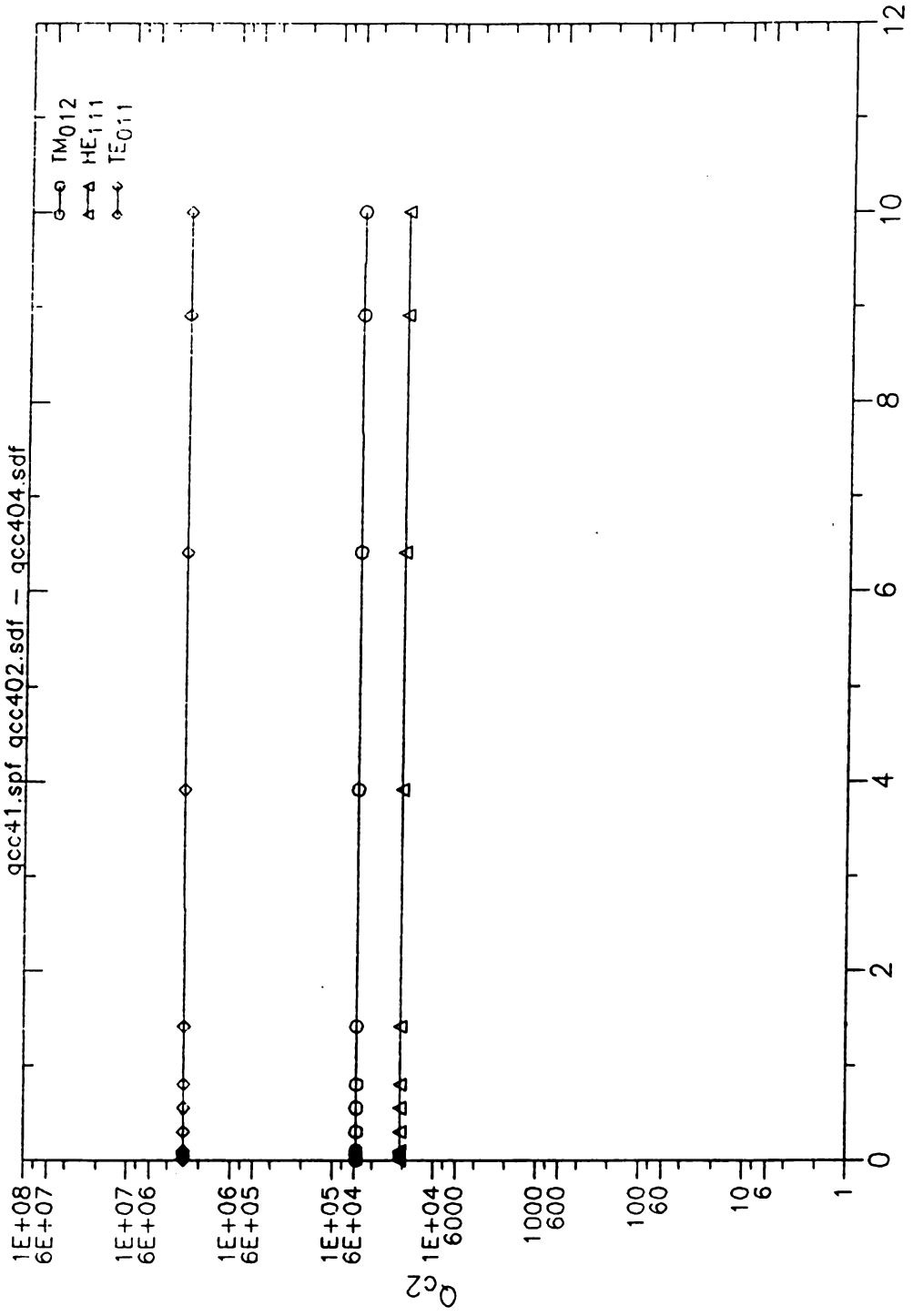

Figure 4.36d Enlargement of the low ε'' portion of Figure 4.35d

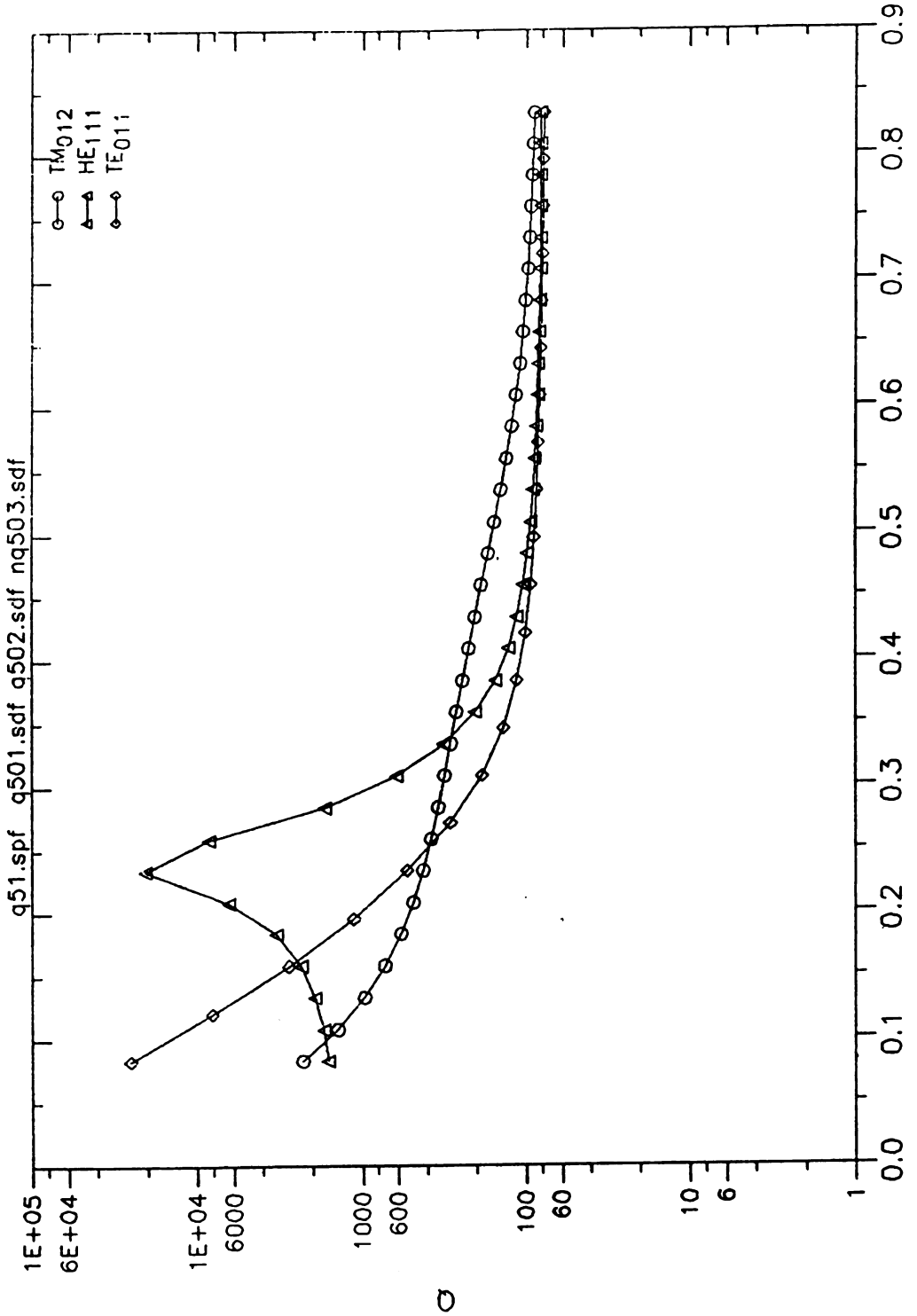

Figure 4.37a Q vs. a/b for various modes, where ε=3.03-j0.039, b=7.62 cm and f_0=2.45 GHz.

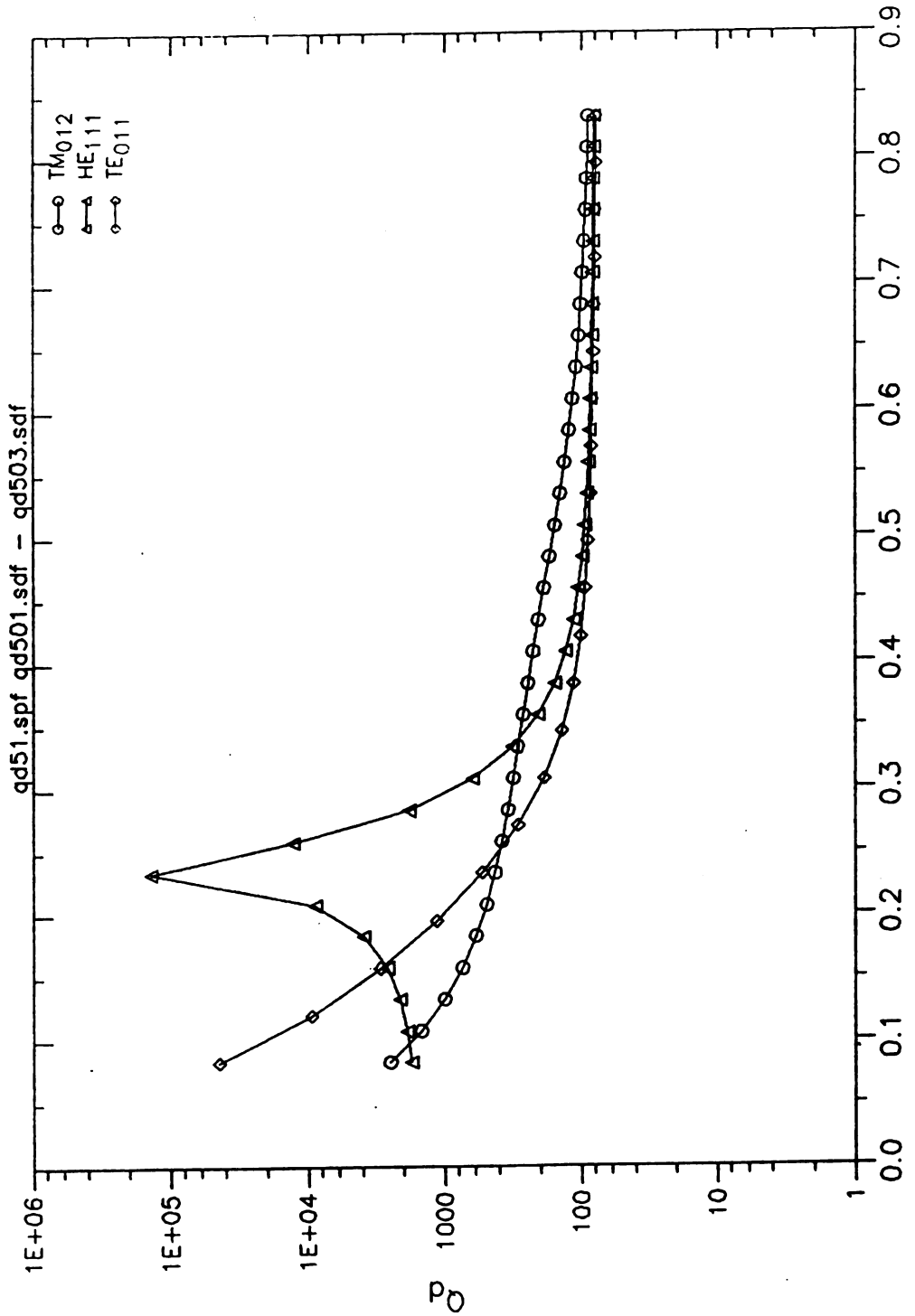

Figure 4.37b Q_d vs. a/b for various modes, where ε=3.03-j0.039, b=7.62 cm and f_o=2.45 GHz.

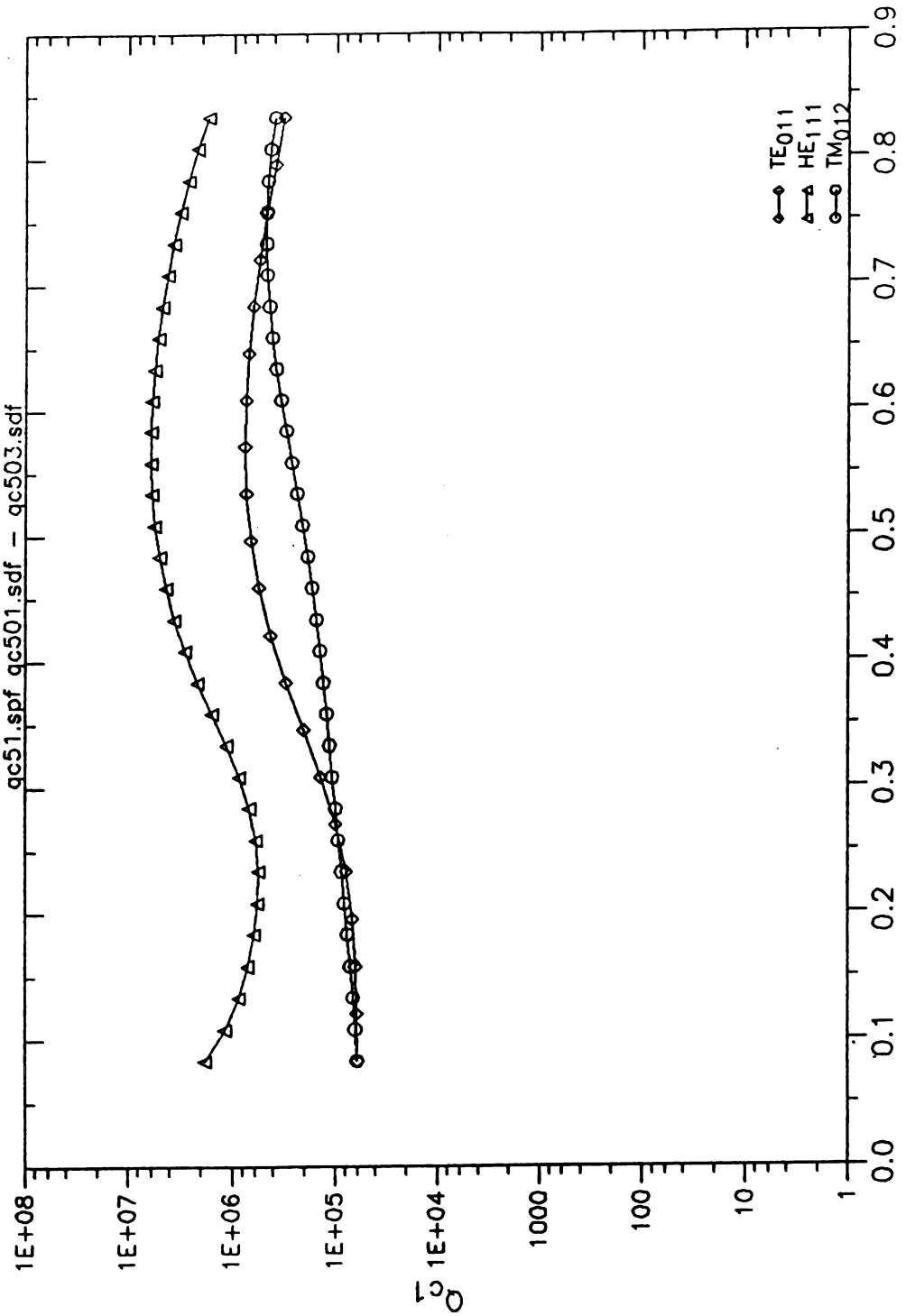

Figure 4.37c Q_{c1} vs. a/b for various modes, where ε=3.03-j0.039, b=7.62 cm and f_o=2.45 GHz.

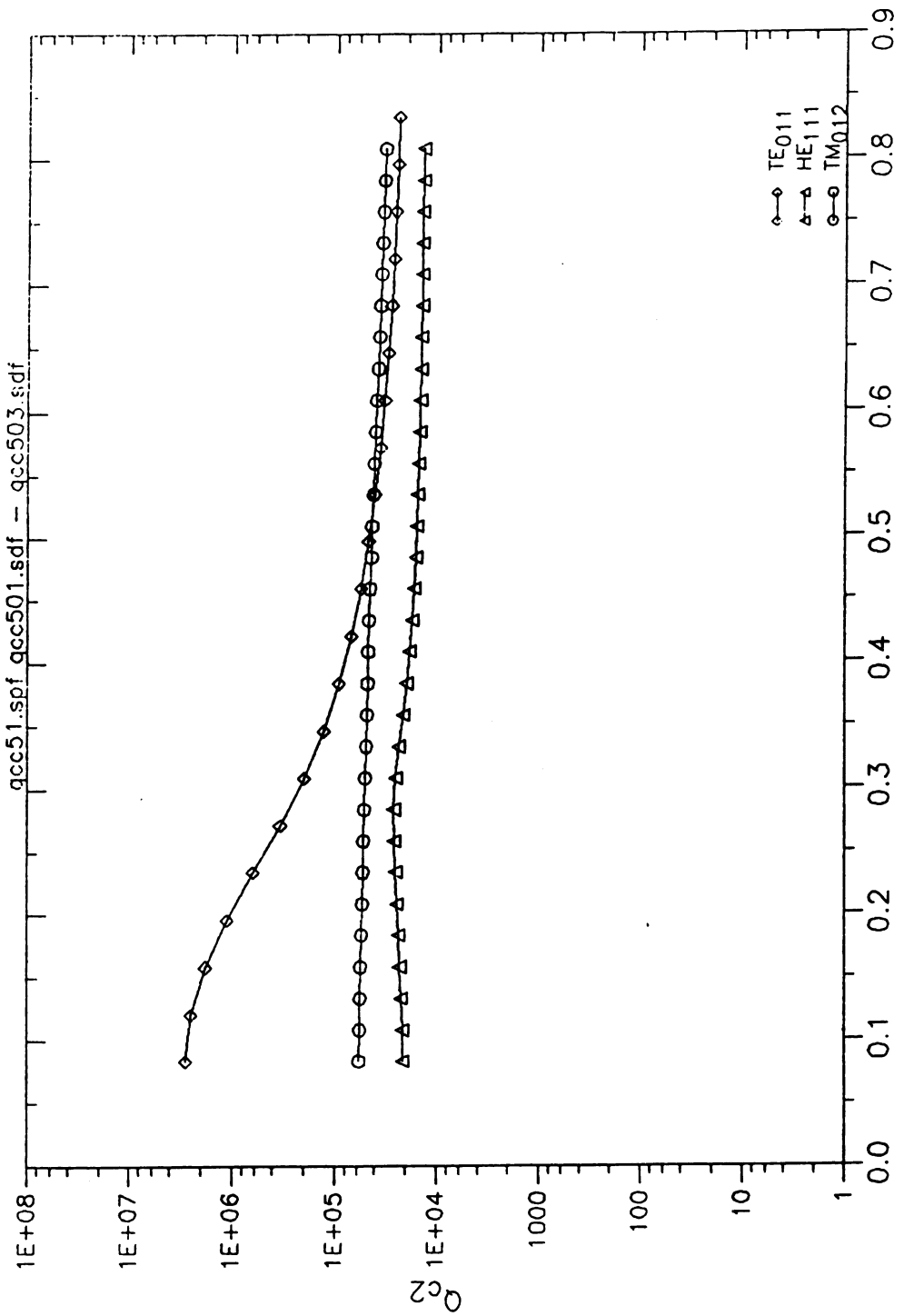

Figure 4.37d Q_{c2} vs. a/b for various modes, where ε=3.03-j0.039, b=7.62 c and f_0=2.45 GHz.

air-filled region as a result of the increase in rod radius, which gives rise to an increase in Q and Q_d. However, when $a/b > 0.24$, the field patterns shown in Figures 4.19a and 4.19b indicate that more and more EM energy is redistributed in the rod as rod radius increases, which yields a decrease in Q and Q_d. Comparing Figures 4.37a through 4.37d, it is found that Q_d is dominant for most of the a/b range. Hence, Q is again basically due to the dielectric losses.

Chapter 5

EXPERIMENTAL SYSTEMS AND TECHNIQUES

5.1 Introduction

The experimental system described in this chapter was used to study the dielectric properties, the absorbed power characteristics and the field distributions of dielectric-loaded cavity applicators using either high power single-frequency or low power swept-frequency techniques. Experiments were conducted to compare the measured field patterns, resonant frequencies, absorbed power and complex dielectric constant with theoretical results given in Chapter 4.

The experimental system consists of: (1) a microwave circuit for generating, transmission and measurement of microwave power, and (2) a cylindrical cavity loaded with different shapes of lossless or lossy materials. An equivalent circuit is presented to explain the coupling mechanism of the microwave energy, the quality factor of the loaded cavity and the experimental techniques from the view point of circuit theory.

Descriptions of the cavity applicator, the experimental system and its equivalent circuit are given in the next two sections. In addition, the diagnostic measurements and associated measurement procedures are described.

5.2 Experimental cavity design considerations and description

5.2.1 Experimental cavity design considerations

The microwave cavity applicator is a section of a right cylindrical waveguide with conducting shorting plates at each end. Due to the presence of the two shorting plates, the field distributions in the cavity are standing wave patterns. The empty cavity modal solutions can be obtained by modifying the homogeneous circular waveguide problem presented in Chapter 3 to satisfy the additional boundary conditions of zero tangential $\vec{E}$ on the two terminating conducting plans. The solutions can be divided

into TM and TE modes. TM modes are the solutions with no longitudinal magnetic field components while the TE modes are the solutions with no longitudinal electric field components.

The resonant frequencies for these two modes are given by, respectively,

$$(\omega_c)_{npq}^{TM} = \frac{1}{b\sqrt{\varepsilon\mu}}\sqrt{x_{np}^2 + (\frac{q\pi b}{L_s})^2} \tag{5.1}$$

$$(\omega_c)_{npq}^{TE} = \frac{1}{b\sqrt{\varepsilon\mu}}\sqrt{x_{np}'^2 + (\frac{q\pi b}{L_s})^2} \tag{5.2}$$

where b and L_s are the radius and length of the cylindrical cavity, respectively, x_{np} and x_{np}' correspond to the pth zeros of the Bessel functions $J_n(z)$ and $J_n'(z)$ respectively. For TM modes, the indices n, p and q may be any integer value and only n and q are allowed to be zero. The indices n, p and q for TE modes may be any integer value but only n is allowed to be zero. If, as is the case in some of the experiments described in this dissertation, the operating frequency is constant at 2.45 GHz, then each resonant mode can be excited by adjusting the cavity length L_s (resonant length) according to equations 5.1 and 5.2 where $\omega_c = 2\pi(2.45\times10^9)$.

There are a number of factors need to be considered in the design of a cavity applicator that is utilized for microwave material processing using single mode excitation. Among these are the cavity dimension for each mode, coupling probe position and dimension, and the effect of material permittivity ε, size, shape and location within the cavity on the excited mode frequency and field patterns. These considerations are described below.

The material shapes considered in this dissertation are either cylindrical rods or slabs. Appropriate cavity modes can be selected for each material shape if the material load can be placed in the proper position within the single mode exciting fields. Materials having different shapes and sizes need to be processed with different

cavity resonant modes. Appropriate mode implies that most of the microwave energy is focused on the material and hence can heat material efficiently and uniformly throughout the power cycle. However, the presence of material load will alter the EM fields and the resonant frequencies from those of the empty cavity in a complex manner depending on the material ε, shape and location in the cavity. Due to the changes of the resonant frequencies as the material is heated, it is necessary to adjust the cavity length and the coupling probe position in the cavity to keep the mode in resonance at 2.45 GHz.

Figure 5.1 displays the transverse electric field patterns for various empty cavity modes. The type and quantity of modes present depends on the cavity dimensions as well as the frequency of operation. Two commercially available brass tubes, 17.8 - cm - i.d. and 15.24 - cm - i.d., were used to build two experimental cavities. These two cavities are named seven inch and six inch cavities respectively according to their radii. In the experiments considered in this dissertation, the excitation frequency is fixed around 2.45 GHz, while the cavity length is adjustable. Therefore, the range of cavity lengths must be determined for a 2.45 GHz excitation operating frequency such that the cavity modes best for the experimental purpose can be selected by length tuning. For instance, a cavity applicator operating at 2.45 GHz can process materials with different electromagnetic modes by adjusting the sliding short position relative to the base plate. The resonant frequency versus cavity length diagrams, i.e. plots of equations 5.1 and 5.2, for these two cavities are displayed in Figures 5.2 and 5.3. Examination of Figure 5.2b indicates that, at 2.45 GHz, seven cavity modes exist for a range of cavity lengths of 0 to 16 cm for the seven inch cavity. Since these modes included those which were suitable for the experimental purpose, it was appropriate to build a seven inch cavity with variable cavity lengths within this range. In a similar manner, as shown in Figure 5.3b, the range of the cavity lengths for the six inch cavity were

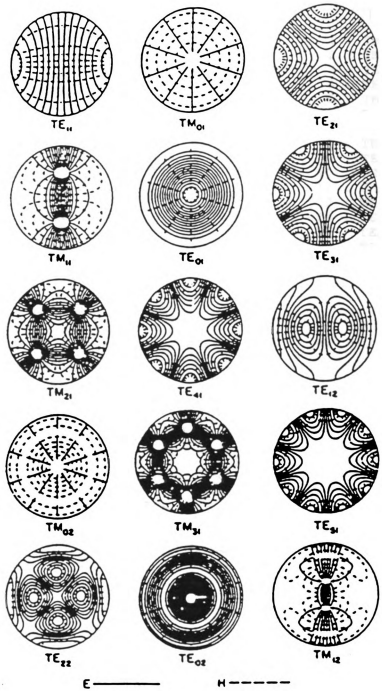

Figure 5.1 Transverse electric and magnetic field patterns for various empty cavity modes

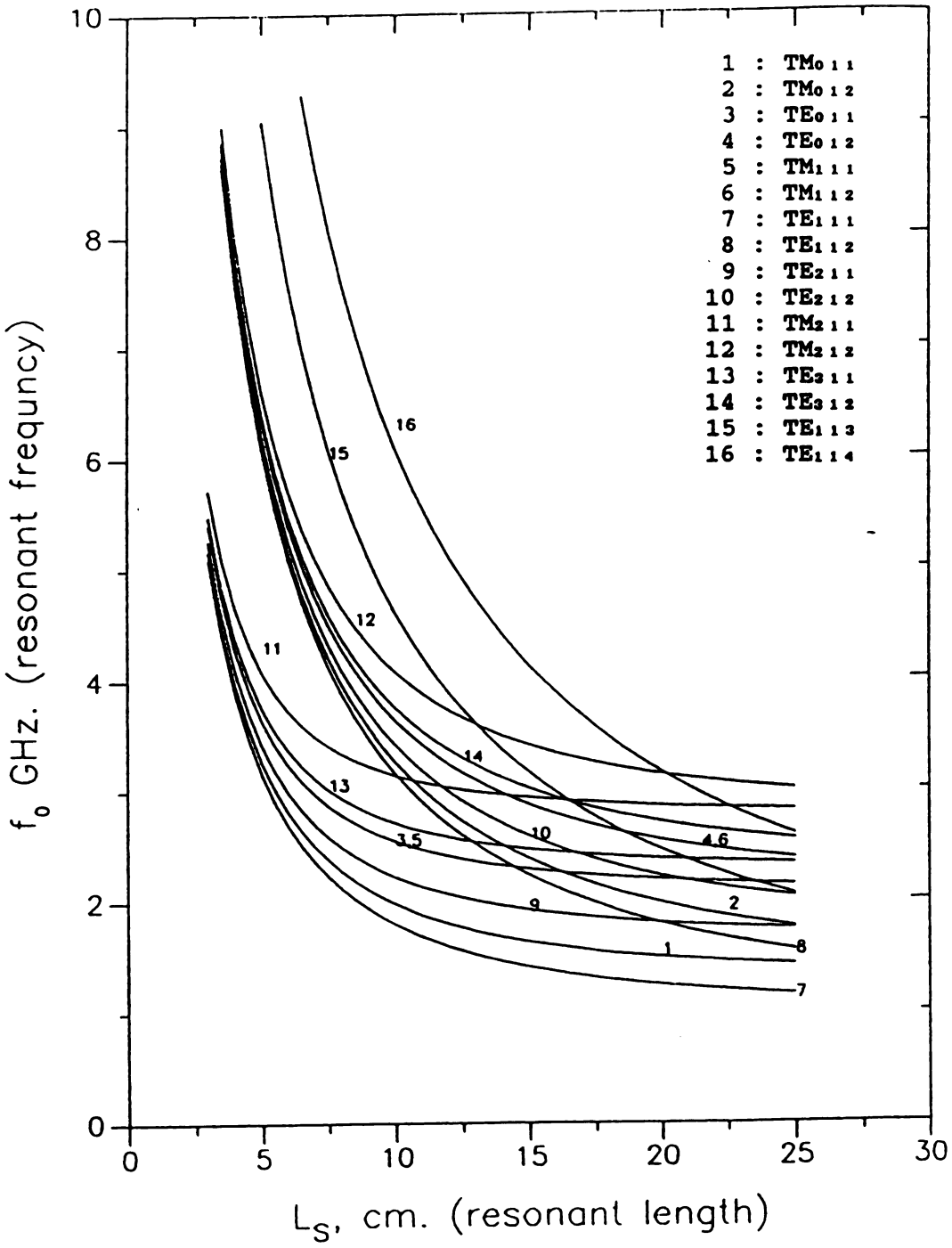

Figure 5.2a Resonant frequency vs. resonant length for seven inch cavity

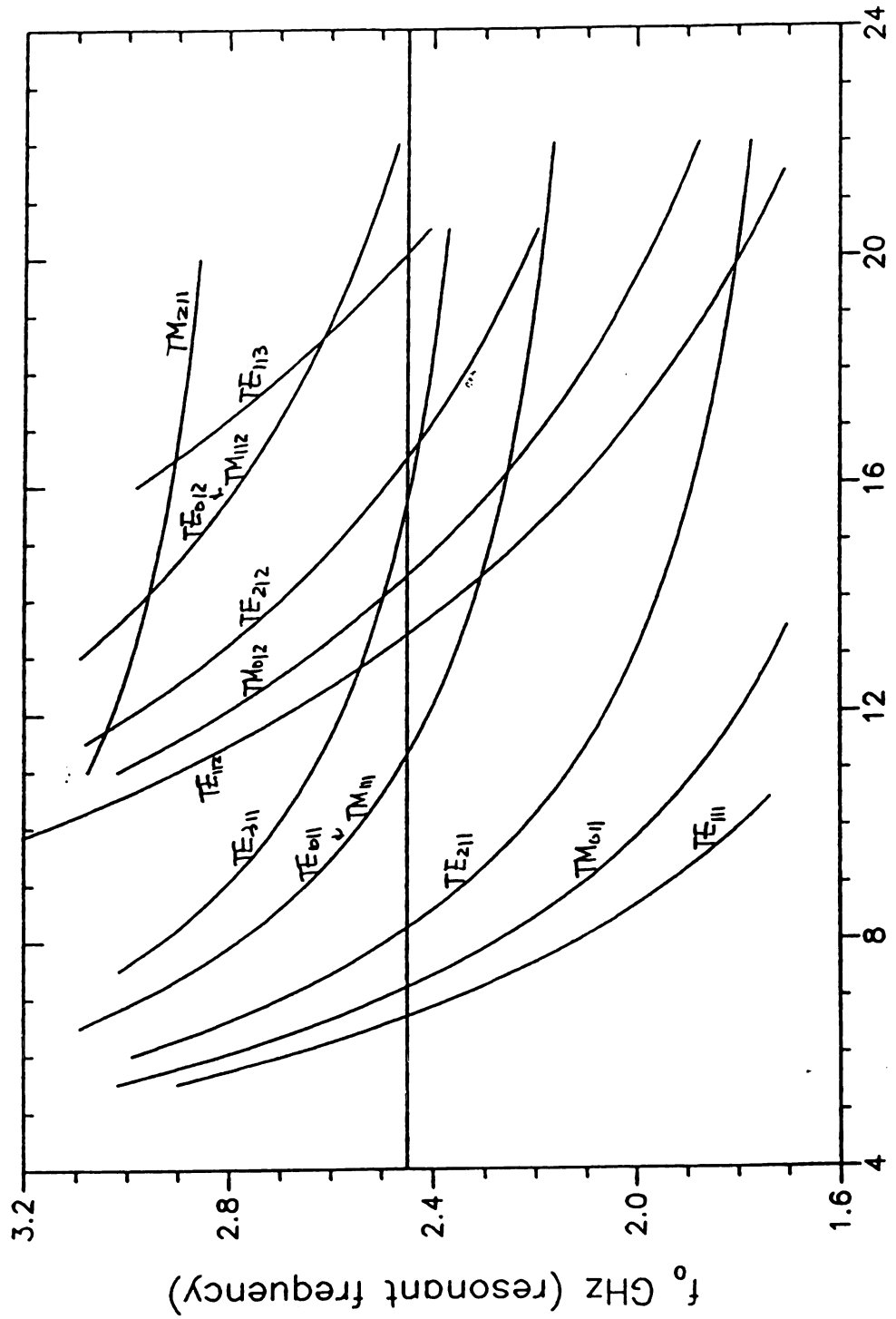

Figure 5.2b resonant frequency vs resonant length

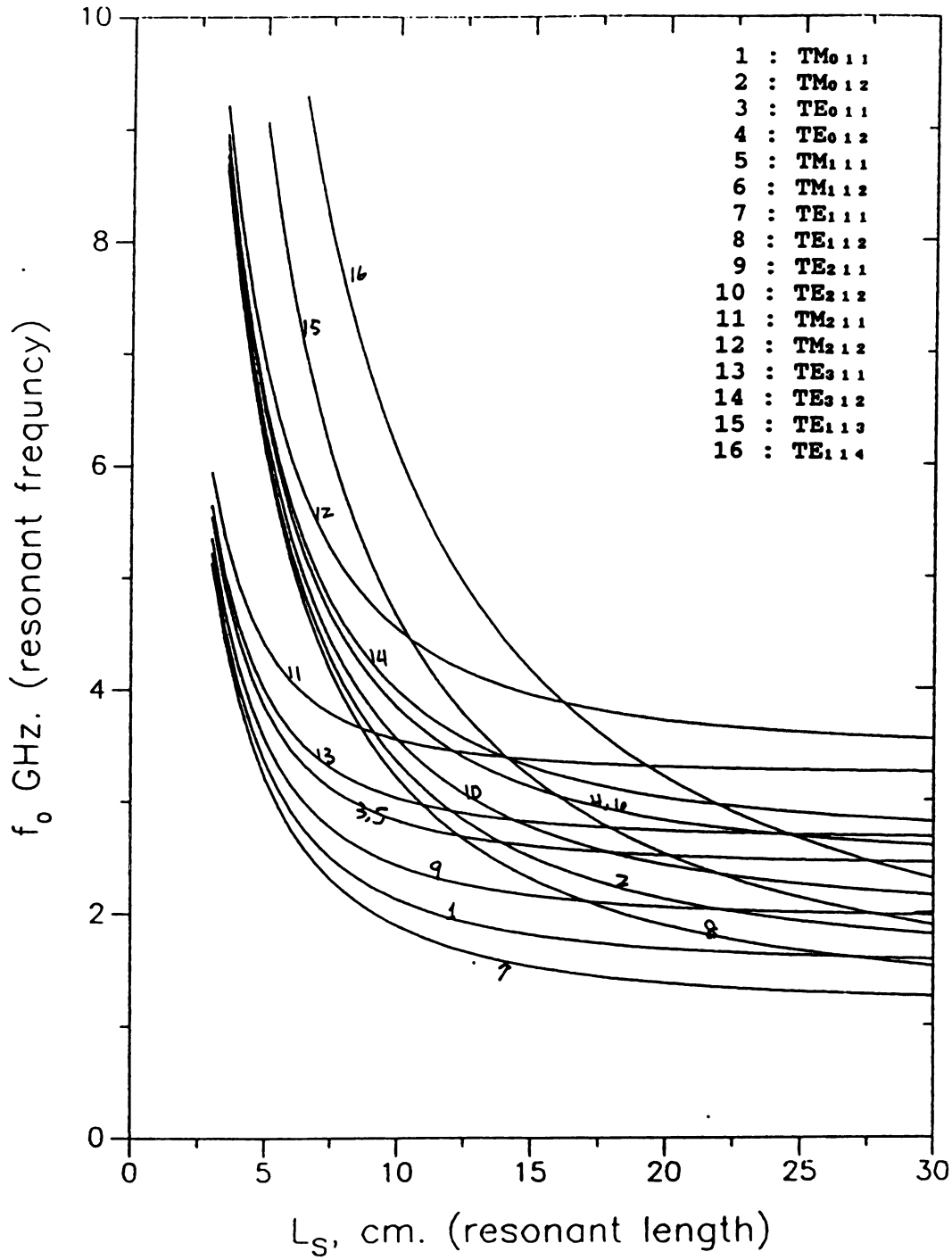

Figure 5.3a Resonant frequency vs. resonant length for six inch cavity

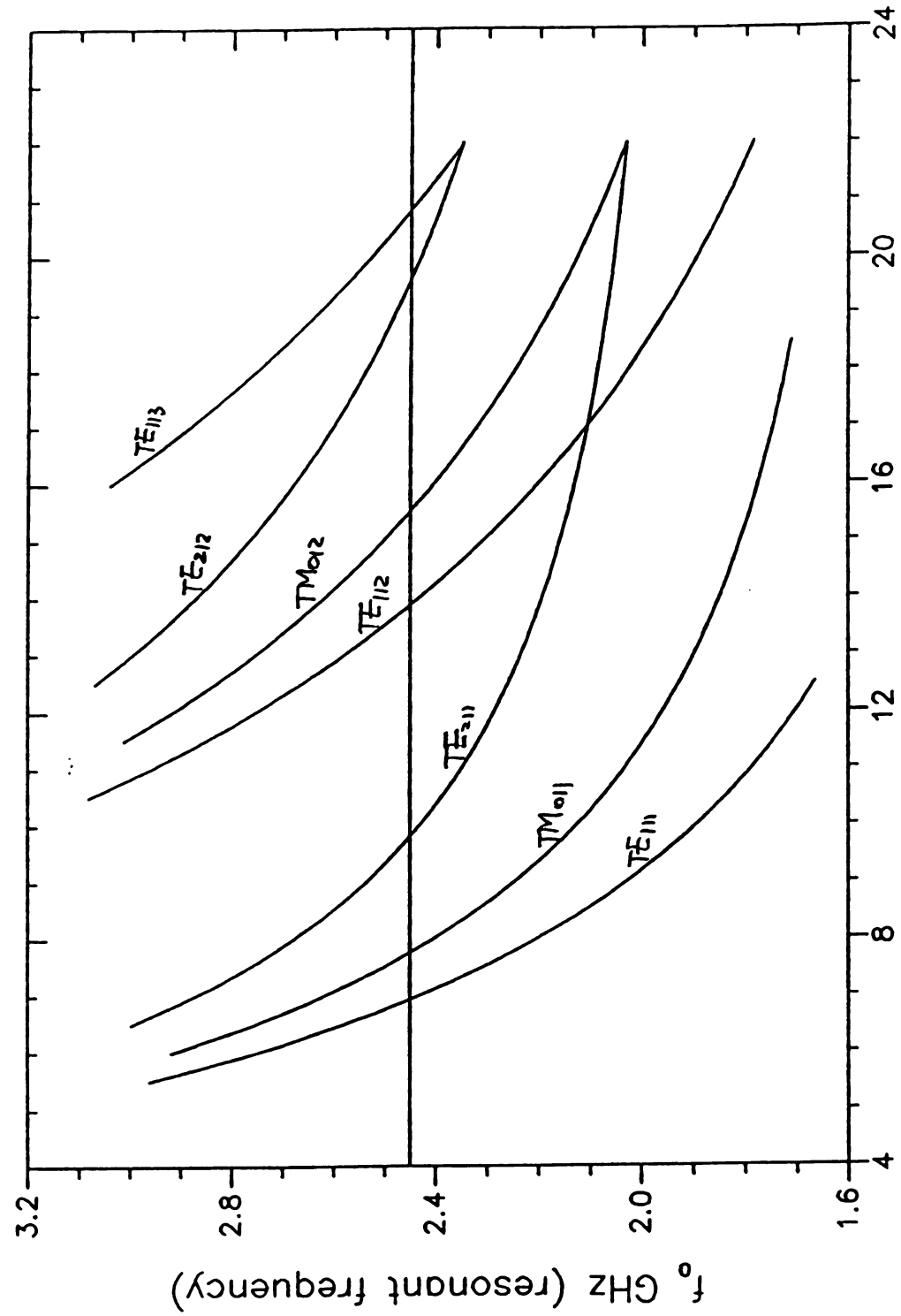

Figure 5.3b resonant frequency vs resonant length

determined to be 0 to 20 cm. In reality, the actual ranges of cavity lengths for these two cavities are shorter than those specified above because the presence of the coupling probes in the cavities limits the movement of the sliding shorts from 6 to 16 cm for seven inch cavity and 5 to 20 cm for six inch cavity.

The resonant frequency vs resonant length curves shown in Figures 5.2 and 5.3 will shift when the material load is placed into the cavity. Curves corresponding to different modes will move differently. Some of them may intersect with each other at the operating frequency as a result of the shifts. As Figure 5.2b shows, at 2.45 GHz the resonant modes adjacent to TM_{012} are not so close as those adjacent to TM_{011}. This may provide a wider tuning range of single mode operation for TM_{012} mode when the cavity is loaded with material.

The reason to locate the coupling probe close to one end of the cavity is to allow a larger range of movement for the sliding short. Intuitively, the size of the probe should be small to minimize the perturbation of the electromagnetic fields in the cavity due to the presence of the probe. However, if the size of the probe is too small, it becomes difficult to convey large amount of power into the cavity. Unexpected arcs may occur at the tip of the coupling probe. The coaxial probe must have a characteristic impedance of 50 Ω so as to match the characteristic impedance of the external feed transmission line. Not until the losses in the coupling probe are carefully studied, can the optimum size of the coupling probe be determined. This is an area for interested researchers to explore.

5.2.2 Experimental cavity description

The two cavity applicators, i.e. a seven inch (17.8-cm-i.d.) cavity with variable cavity length from 0 to 16 cm and a six inch (15.24 - cm - i.d.) cavity with a range of cavity lengths of 0 to 20 cm, are described in detail in this section. A photograph of the seven inch cavity is shown in Figure 5.4. This cavity was made of a cylindrical

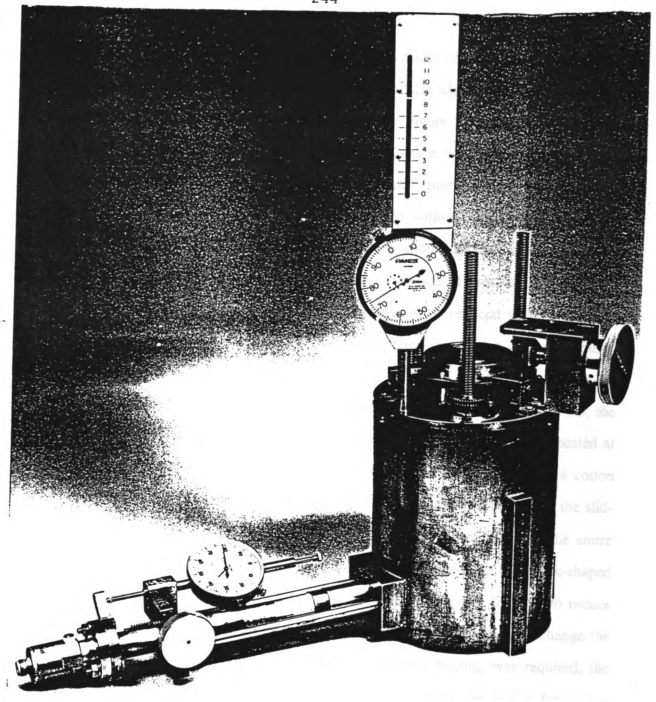

Figure 5.4 Picture of a seven-inch cavity

brass tube (17.8 cm ID, 25.4 cm long and 0.318 cm thick) covered each end with two transverse circular brass short plates. One of the shorts is adjustable to provide a variable cavity length of 6 - 16 cm and as shown in Figure 5.5, the cavity length is denoted by L_s. Adjustment of the cavity length is made by manual rotation of the knob located just above the cavity top, as indicated in Figure 5.4. A micrometer indicator on the sliding shorts is used to measure L_s to within 0.01 mm. There is an access hole 2.25 cm in diameter at the center of the sliding short to allow the placement of loading materials into the cavity interior. Two sets of brass collars are available to fill the access hole allowing the hole diameter to be reduced to 1.27 cm or to be completely closed. The bottom shorting plate is fixed in position during operation and is either soldered to the brass shell as shown in Figure 5.5 or is removable for inserting large radius materials as shown in Figure 5.6. As depicted in Figure 5.5, the cylindrically shaped material load was placed in the cavity through the hole located at the center of the sliding short and suspended in the center of the cavity by a cotton thread. The soldered bottom plate also has a hole of the same size as that in the sliding short so that a long rod can be inserted into the cavity coaxially filling the entire length of the cavity. The removable bottom plate was designed to hold disk-shaped material loads which may be processed with the TE_{111} cavity mode. In order to reduce the disturbance to the *TE* resonant modes, there was no hole in this plate to change the surface currents and the electromagnetic field. If uniform heating was required, the material load dimensions were limited to lengths of less than one half a free space wave length. Silver-plated finger stock is soldered to the movable short plates to provide good electrical contact with the cavity walls. The gears and handles are commercially available and constructed of stainless steal and aluminum respectively.

As can be seen from Figures 5.4 to 5.6, a rectangular brass block with 16, 2.26 mm diameter, diagnostic holes 0.922 cm apart was soldered outside the cavity wall.

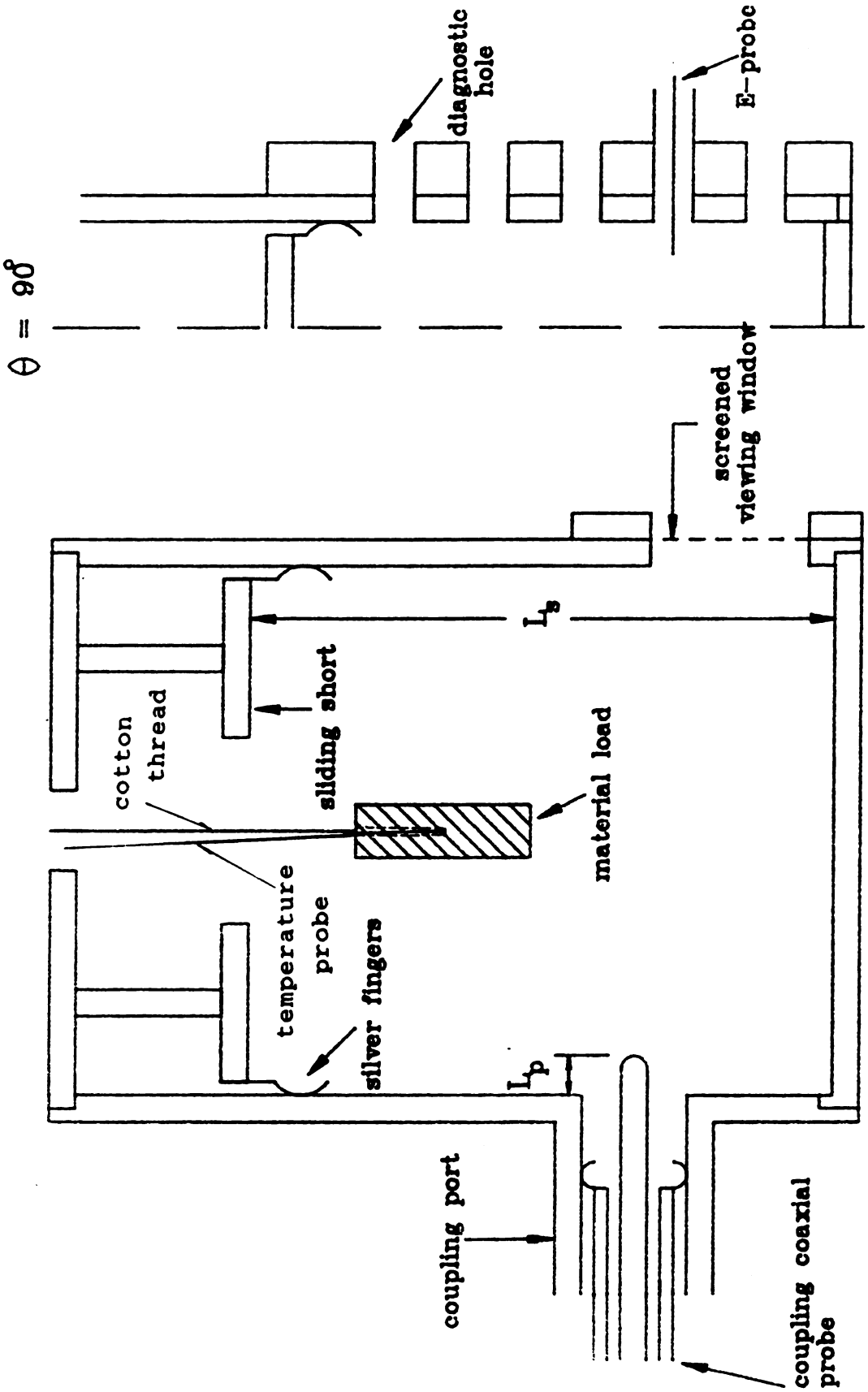

Figure 5.5 side-view of seven inch cavity with fixed bottom plate

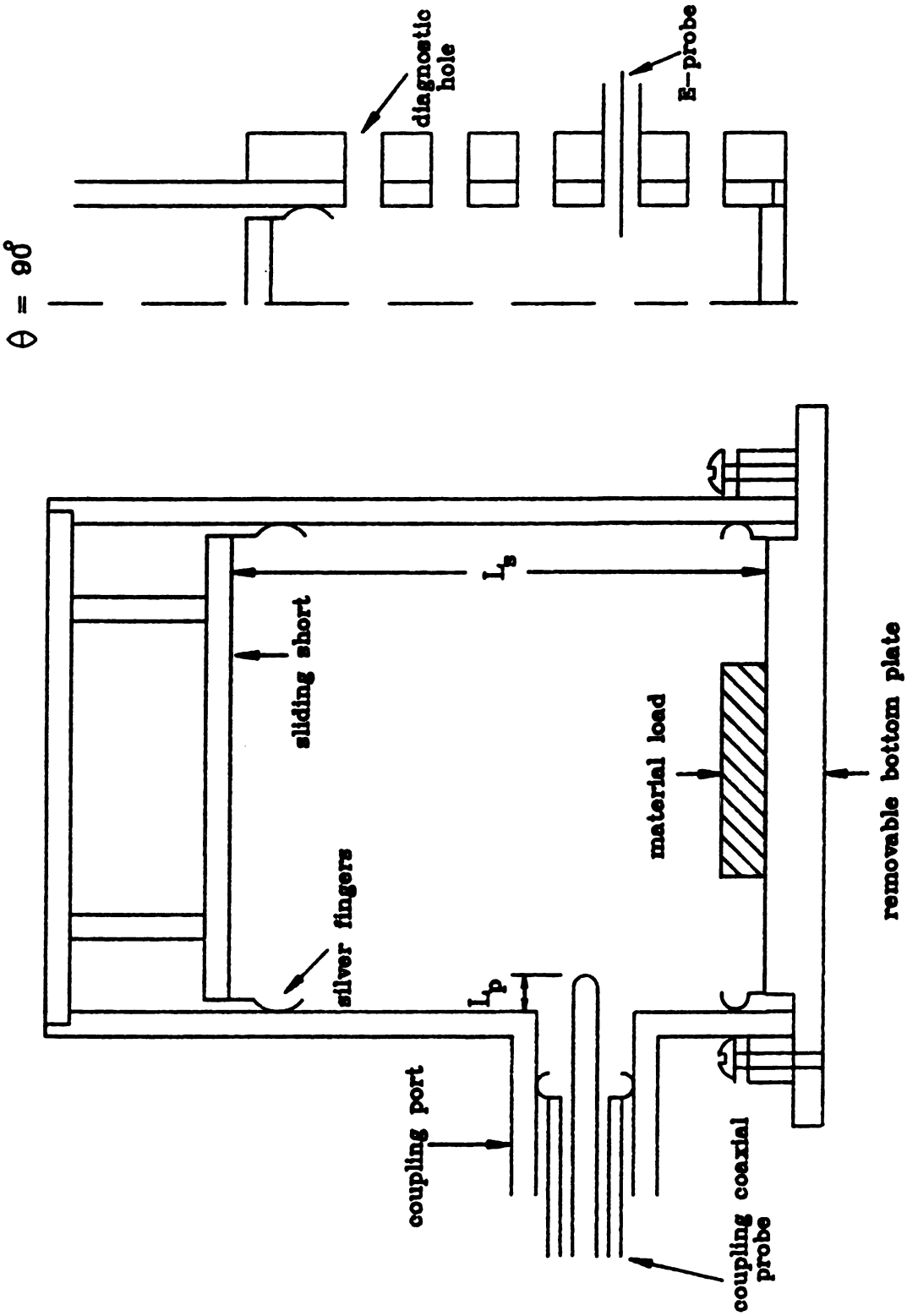

Figure 5.6 side-view of seven inch cavity with removalbe bottom plate

The diagnostic holes were drilled through the cavity wall and the lowest hole was located 0.635 cm above the cavity bottom plate. A 2 - mm microcoax probe, called an E-field probe, could be inserted into the cavity applicator through the diagnostic holes to measure the square of the radial electric field $|E_r|^2$ on the inside surface of the cavity. The penetration of the center conductor of the diagnostic probe is limited to 1.5 mm so that the probe causes minimal perturbation to the resonant mode field patterns and resonant frequency during measurement. Thus, an accurate radial standing wave pattern of a cavity mode can be determined from the diagnostic E-field probe measurements. A copper-screened viewing window on the cavity wall, as shown in Figure 5.5, allowed visual viewing of the material load.

Two coupling ports, which were 4.72 cm above the inside surface of the base plate, were located at 90° from each other. The port openings were 2.77 cm in diameter. Coupling of microwave power into the cylindrical cavity was accomplished with an adjustable coaxial probe inserted through the coupling port. Cavity modes were excited by the EM energy fed from the coupling probe and various coupling conditions could be achieved by the adjustments of the cavity length and the coupling probe position within the cavity. Only one of the two coupling port was used in this dissertation. The 50 - Ω coupling probe has an outer conductor 2.52 cm in diameter and an inner conductor 0.965 cm in diameter. The inner conductor of the coupling probe was extended into the cavity. The depth, denoted by L_p, could be manually varied from 0 to 40 cm. Silver finger stock attached to the center conductor provided excellent electrical contact with the inside of coupling port of the cavity. A reducer (Andrew type 2260B E507C) was adapted to fit the end of the coaxial section providing a means to connect the coupling probe to the external network. Adjustment of the coupling probe depth L_p in the cavity is made by manual rotation of the knobs of the rack and pinion systems shown in Figure 5.4. Similar to the sliding short, a micrometer dial indicator on the coupling probe was used to measure the depth of the probe to

within 0.01 mm.

Figures 5.7 and 5.8 shows the photograph and cutaway view of a six inch (15.24 - cm - i.d.) cavity. A detailed description of this cavity was given in [91]. The basic design is the same as described for the seven inch cavity but the diameter of the brass tube has been reduced and the other dimensions have been scaled appropriately. Only the parts which were made differently from the seven inch cavity will be described in the following. The access hole on top of the cavity was 2.54 cm in diameter. Two sets of brass collars, having holes of 1.27 and 0.635 cm in diameter respectively, and one set of solid brass collar were available to plug the access hole. Several small concentric depressions were located on the inside surface of the fixed shorting plate to allow for the alignment and positioning of cylindrical rod loading materials. The coaxial coupling probe was made smaller to satisfy the electrically thin requirement [91]. The diameters of the inner and outer conductors were 0.20445 and 0.635 cm respectively.

As shown in Figure 5.8, over 500, 2 mm diameter diagnostic probe holes were drilled around the cavity walls and on the bottom shorting plate. The holes were distributed among 16 vertical layers on the walls and five concentric rings on the bottom plate. In addition, a hole was made at the center of the bottom plate. Detailed field patterns along the wall and bottom plate of the cavity were determined by inserting the E-field probe through these diagnostic holes to measure the square of the normal component of the electric field.

5.3 Experimental systems and circuits

5.3.1 Experimental system

The two different microwave systems used in the experiments described in this thesis are depicted in Figure 5.9 and 5.10. As shown they are a low power swept-frequency system and a high power CW single frequency system. The low power

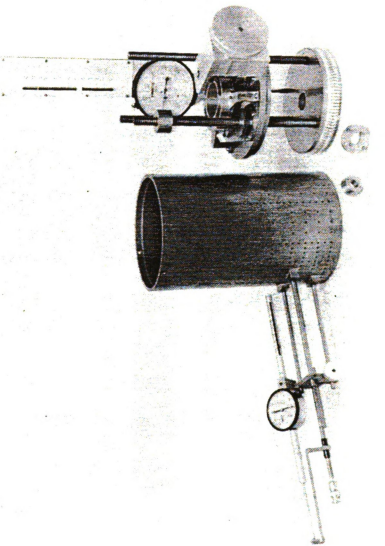

Figure 5.7 Picture of the disassembled six inch cavity applicator

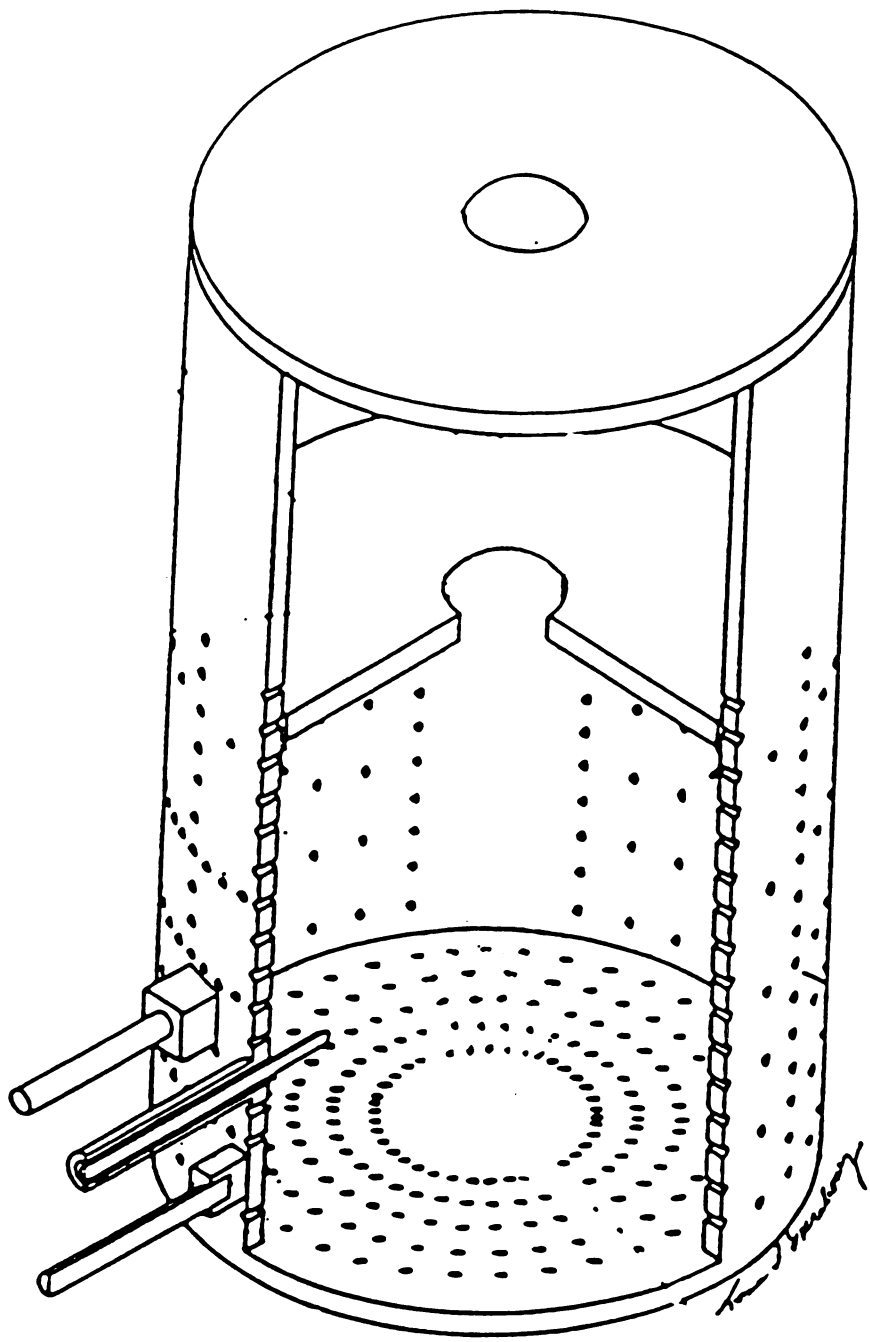

Figure 5.8 Cutaway view of the six inch cavity

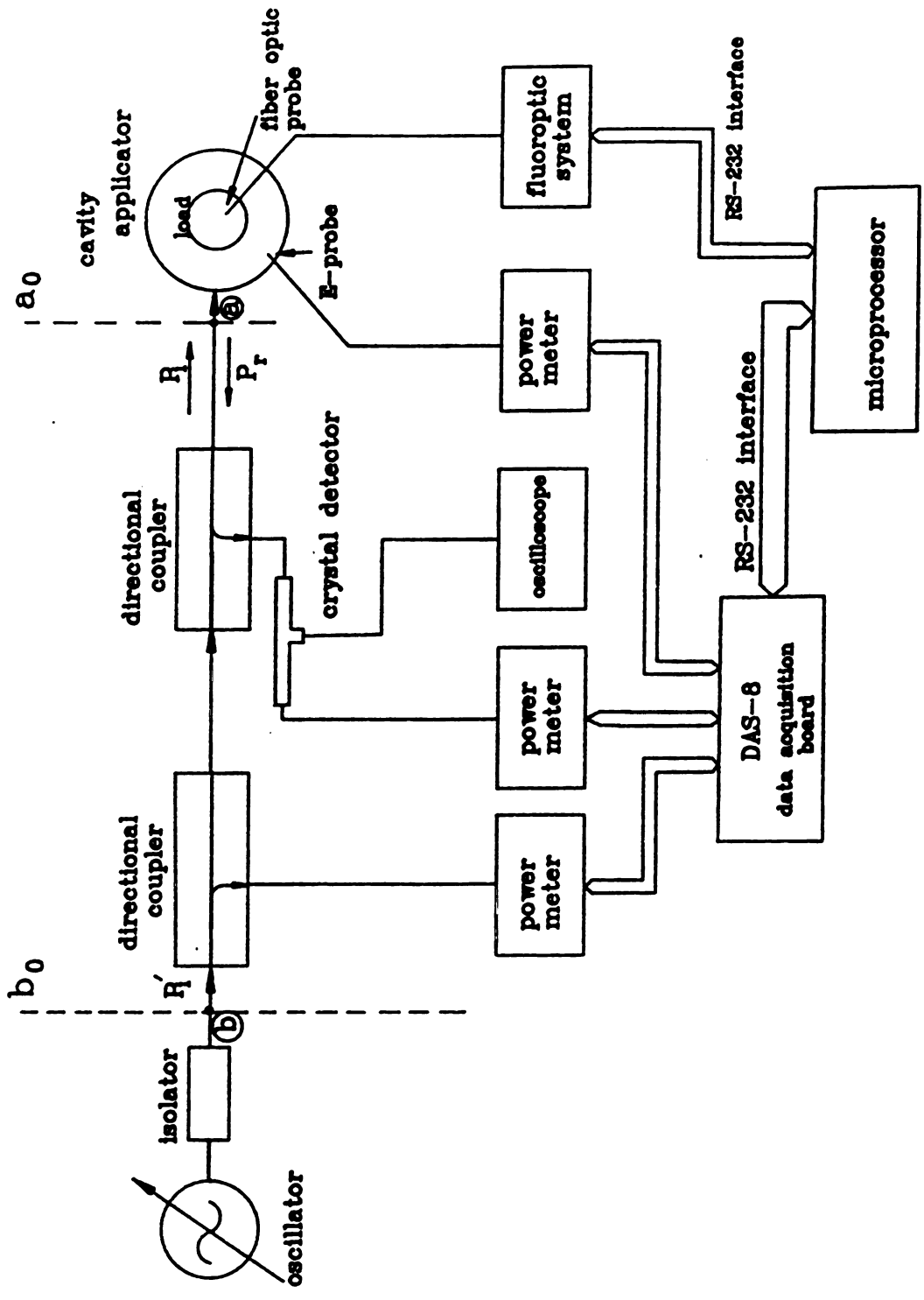

Figure 5.9 low power swept-frequency mode system diagram

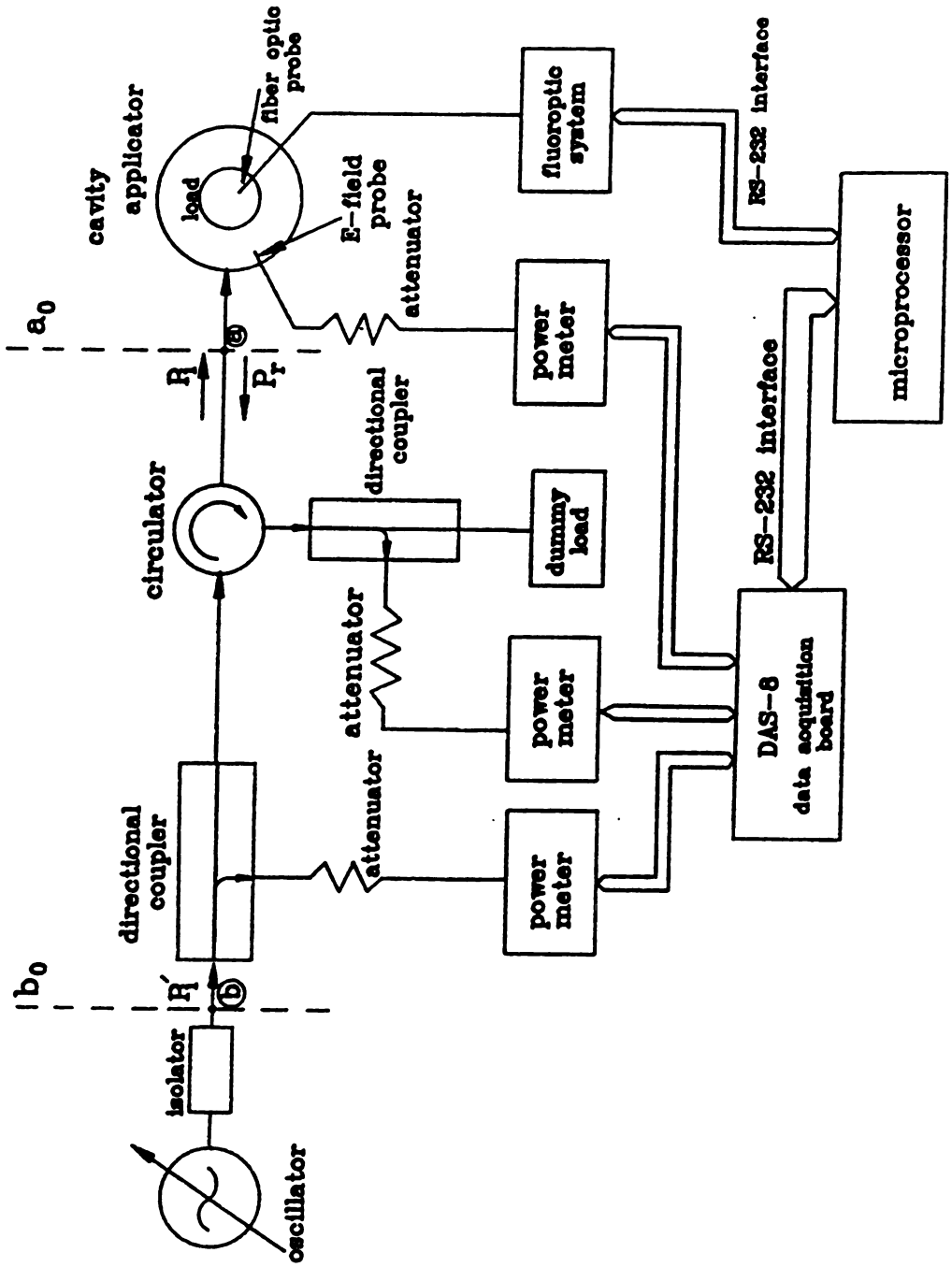

Figure 5.10 high power single frequency mode system diagram

swept-frequency system was used to measure the quality factors and field distributions of both empty and loaded cavities, and to determine the complex dielectric permittivities of dielectric material loads. The high power single frequency mode system was used for microwave heating and on-line diagnosis of lossy materials. Both systems consisted of five functionally independent subsystems: (1) the microwave power sources; (2) the transmission systems; (3) the microwave applicator (cylindrical cavity); (4) the measurement system; and (5) the microcomputer and its interfaces.

The microwave power source was an HP 8350B sweep oscillator connected to a 1.7 - 4.3 GHz HP 86235A RF plug-in with an HP 11869A adaptor. This sweep oscillator is capable of providing 10 - 20 mW of power either at single operating frequency or in the swept mode. For high power application, the sweep oscillator was connected to a Varian TWT amplifier (VA - 1356) which amplified the oscillator signal up to 27 Watts.

The transmission system provided path for the transfer of microwave power. Also, the transmission system provided a connection to the oscilloscope to measure the quality factor and coupling condition, and to the power meters for the purpose of monitoring the incident and the reflected powers and the relative magnitude of the normal component of the electric field on the conducting walls.

As shown in Figures 5.9 and 5.10, the major components in this system comprised two directional couplers (Narda Model 30020). A 30-dB directional coupler was used to sense the incident power and a 20-dB directional coupler was used to measure the reflected power. Whenever the low power swept-frequency technique was employed, the reflected signal was rectified by a crystal detector and displayed on an X-Y oscilloscope. As can be seen from Figure 5.10, in the high power single-frequency system, a circulator (Ferrite Control Co. Model 2620) was used to isolate the reflected power P_r from the incident power P_i. The crystal detector was removed in order not to be damaged by the large amount of reflected power, and the reflected

signal was fed into a matched load. A Marconi coaxial isolator was used to protect the microwave amplifier TWT from the reflected power.

The measurement system was responsible for taking the measurements of input and reflected power levels, relative magnitude of the square of the normal component of the electric field on the cavity walls, the cavity quality factors and the material temperature as well. The measurement system consisted of a two - channel HP 438A digital power meter and the associated HP 8481H sensor heads (0 - 3 W) which were used to measure both incident and reflected powers. An HP 432A microwave power meter and the associated power sensor head together with a microcoax were used to measure the square of the normal electric field on the inner cavity walls through the diagnostic holes. Also included was an HP 130A oscilloscope which was employed to monitor the cavity quality curves to determine the cavity quality factor and the coupling conditions for the low power swept-frequency system. A four - channel fluoroptic thermometer (Luxtron Model 750) was used to continuously monitor either the inner volume or the surface temperature of the material load.

The microcomputer system had three main functions. The first was to provide data bus interfaces with the measurement system for the purpose of data flow between the measurement equipments and the microcomputer. Secondly, the microcomputer activated the function of data acquisition. Thirdly, the microcomputer recorded the incident and reflected power levels, sample temperatures and the the normal electric field components on the cavity walls.

A 8 - channel data acquisition board (DAS - 8) with RS-232 interface was used to obtain the measurements from the power meters and forwarded them to a microcomputer. A serial port with RS-232 interface in the microcomputer was connected to the Luxtron 750 thermometer RS-232 interface, transferring measured temperature readings to the storage buffers of the microcomputer. The data acquisition rate was controlled by the Zennith microcomputer in accordance with the thermometer

temperature update rate. In addition, all measurement readings were recorded and stored in the Zennith microcomputer for plotting, and automatic and intelligent on-line control of the electromagnetic materials processing.

5.3.2 Equivalent circuit of a material-loaded cavity applicator

The quality factor and the coupling mechanism of microwave energy into the cavity applicator can be described using an equivalent circuit. The overall system may be viewed as a one - port network with the single port being the input coupling probe. The reason for this is that in the vicinity of resonance for a single mode, a lumped element equivalent circuit is a good representation of the cavity itself, as illustrated in Figure 5.11 [77, 92]. This figure displays a standard circuit representation for a cavity which is connected to a feed waveguide or transmission line, loaded with material, and excited in the neighborhood of a single mode resonance. When the cavity is empty, the elements G_c, L_c and C_c represent the conductance, inductance and capacitance, respectively, of the excited mode near resonance, and jX the reactive effect of modes far from resonance. The coupling between the input probe and the cavity electromagnetic fields is represented by an ideal transformer of turns ratio m : 1. The reactance effect due to the coupling probe and the susceptance effect due to the aperture through which the probe is fed are embedded in jX. G_L and jB_L are the conductance and susceptance respectively of the material load placed in the cavity.

The elements of the equivalent circuit are related to the fields in the cavity by the following expressions,

(I) Losses in single mode cavity

$$G_c \propto R \iint_S |H_{tan}|^2 \, ds \tag{5.3}$$

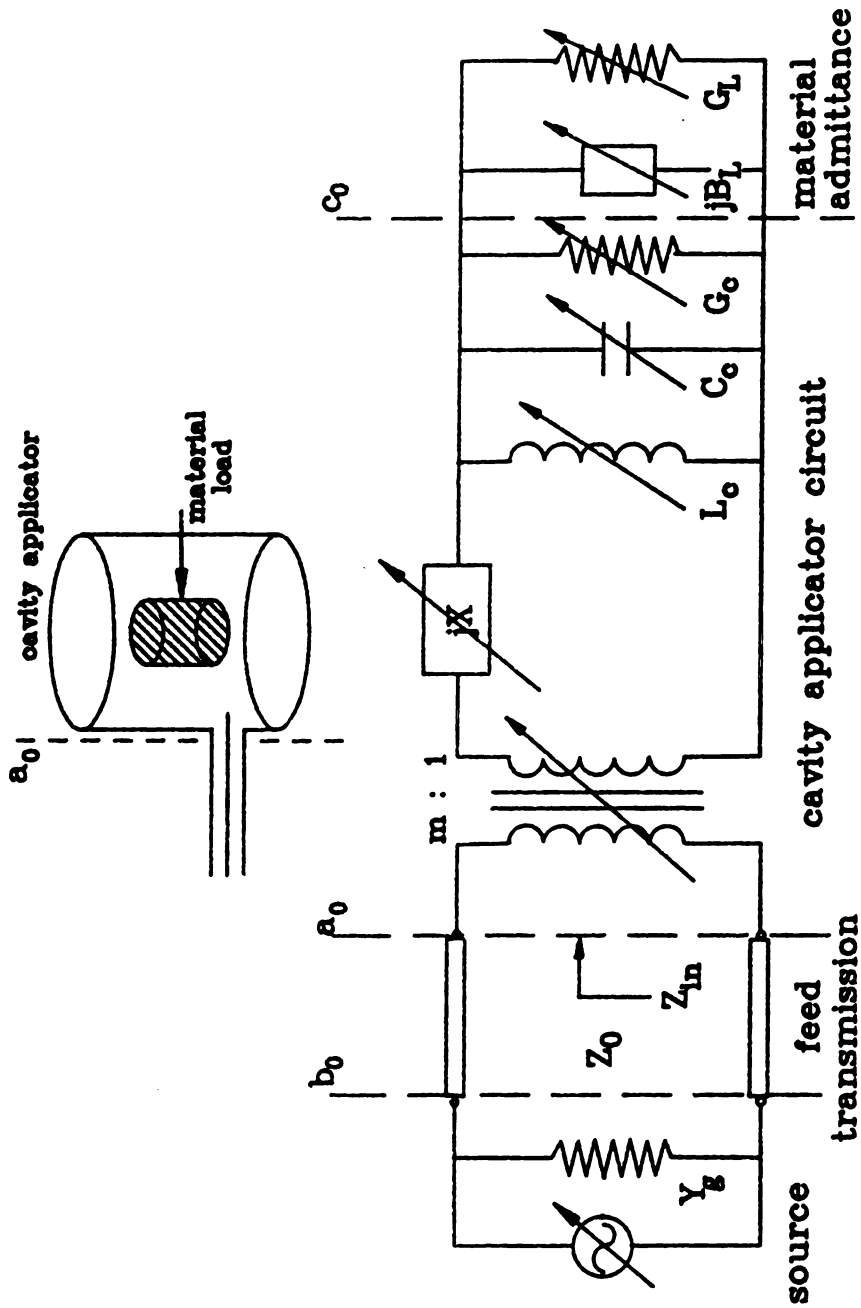

Figure 5.11 equivalent circuit of the material–loaded cavity

$$G_L \propto \frac{\omega}{2} \int\int\int_{V'} \varepsilon'' \mid E \mid^2 dv \tag{5.4}$$

(II) Stored energies in the fields

$$C_c \propto \frac{1}{2} \int\int\int_{V-V'} \varepsilon_0 \mid E \mid^2 dv \tag{5.5}$$

$$L_c \propto \frac{1}{2} \int\int\int_{V-V'} \mu_0 \mid H \mid^2 dv \tag{5.6}$$

$$jB \propto \frac{1}{2} \int\int\int_{V-V'} \varepsilon' \mid E \mid^2 dv + \frac{1}{2} \int\int\int_{V'} \mu_0 \mid H \mid^2 dv \tag{5.7}$$

where

$\hat{\varepsilon} = \varepsilon' - j\,\varepsilon''$

$\omega =$ resonant frequency

$V =$ entire cavity volume

$S =$ cavity surface

$V' =$ material volume

$R =$ intrinsic resistance of the metal (surface resistance)

The input impedance looking into the reference plane a_0 is given by

$$Z_{in} = \frac{P_t + j\,2\,\omega\,(W_m - W_e)}{\frac{1}{2} \mid I_0 \mid^2} = R_{in} + jX_{in} \tag{5.8}$$

where P_t is the total power coupled into the cavity in the steady state. In other words, P_t consists of metal wall losses as well as the power delivered to the material. W_m and W_e are the time average magnetic and electric energies stored in the cavity fields and I_0 is the input current associated on the coupling probe at the reference plane a_0. The terms R_{in} and jX_{in} are the cavity input impedance seen by the feed transmission line from reference plane a_0.

As can be seen from equation 5.8, the input impedance is purely resistive if the time average magnetic and electric energies are equal and purely reactive if there are no losses in the cavity. The reactance is inductive if the time average magnetic energy is greater than the time average electric energy and capacitive for the opposite case.

In order to have maximum power transferred into the cavity, it is required that the reactance and the resistance of the input impedance of the material loaded cavity be equal to zero and the characteristic impedance of the feed transmission line, respectively. This is the critical coupling condition. Under this condition, half of the power generated from the oscillator (microwave power source) is delivered into the cavity. According to circuit theory, the input impedance Z_i looking into a_0 is the total impedance of the secondary circuit transformed to the primary circuit, as depicted in Figure 5.11. That is

$$\begin{aligned} Z_{in} &= Z_{ref} \\ &= m\left\{ \left(\frac{1}{G_c + G_L} \right) + j \left(X + \frac{\omega L_c B_L}{B_L + \omega L_c + \omega^2 L_c C_c B_L} \right) \right\} \end{aligned} \tag{5.9}$$

Close examination of equation 5.9 reveals that the critical coupling condition is achieved by a combination of two adjustments : (1) adjustment of the cavity length to detune the cavity (changing resonant frequency), which results in the changes of L_c, C_c, G_c and jX; (2) adjustment of the depth of the coupling probe in the cavity, which results in the changes of m and jX. Incorporation of these two adjustments will cancel the cavity reactance, i.e., $jX_{in} = 0$, and adjust the cavity resistance to be equal to the impedance of the feed transmission system, i.e., $R_{in} = Z_0$.

Introduction of the material load into the empty cavity will decrease the resonant frequency and change cavity Q. Consequently, the presence of the material load then changes L_c, G_c and C_c and adds additional material conductance G_L and susceptance jB_L to the circuit. G_L and jB_L are functions of material load placement, material volume

and shape, and material properties. During processing, material properties may change, which gives rise to the changes of the resonant frequency and cavity Q. Because of this, L_c, G_c, C_c, G_L, jB_L and jX all change during microwave heating process. So, the continuously variable probe and cavity end plate tunings of the cavity applicator are necessary during processing to cancel the reactance of the input impedance and to adjust the material loaded cavity input resistance to be equal to the characteristic impedance of the feed transmission line.

The definition of the quality factor is

$$Q = \frac{\omega \text{ (total electromagnetic stored energy)}}{\text{total power loss}}$$

From this definition, quality factors associated with different power losses can be defined. The quality factor obtained directly from experiment is called "loaded quality factor" Q_L, which takes into account both the cavity applicator and the external circuit shown in Figure 5.11. The quality factor of the cavity itself (with or without material load) is called "unloaded quality factor Q_u" since it does not account for the loading of the feed transmission line. The third quality factor, "external quality factor Q_{ext}", can be interpreted as the Q corresponding to the power loss due to the external circuit. Note that it is assumed here that the generator (microwave power source) is matched so that the impedance looking from the cavity toward the microwave power source is the characteristic impedance Z_0.

The relation between these quality factors is described by [93]

$$\frac{1}{Q_L} = \frac{1}{Q_u} + \frac{1}{Q_{ext}} \tag{5.10}$$

If Q_{ext} is smaller than Q_u, the power loss due to the external circuit is larger than the power consumed inside the cavity, and hence the cavity is overcoupled. On the other hand, if Q_{ext} is larger than Q_u, the cavity is undercoupled to the external circuit. Only

when Q_{ext} is equal to Q_u, is the power dissipated in the external circuit the same as that dissipated in the cavity. Then the cavity is critically coupled. As can be easily seen from equation 5.10, under critical coupling condition, $Q_u = 2Q_L$. The quality factor is useful in describing the bandwidth of a cavity mode and is an indication of the frequency selectivity of coupling power into the cavity. This is an extremely important factor in designing microwave circuit resonator.

5.4 Experimental procedures and techniques

5.4.1 Definitions

Before introducing the experimental procedures and techniques, some frequently used definitions in this dissertation are described briefly below. A more detailed description can be found in reference [94].

(1) Q-curve (or resonant curve) - a plot of power absorbed by the cavity (with or without material load) as a function of frequency (for a fixed cavity length).

(2) Unloaded quality factor (Q_u) - an indication of the magnitude of the losses in the conducting cavity walls and in the material load. Q_u may also be thought of an indication of the bandwidth of a cavity mode. In this definition, the cavity is not connected to the transmission line.

$$Q_u = \frac{f_r}{\Delta f} \tag{5.11}$$

where f_r is the resonant frequency, Δf is the distance between the half power points on the Q-curve.

(3) Loaded Q (Q_L) - quality factor of the cavity (with or without material load) coupled to the external circuit.

$$Q_L = \frac{f_r}{\Delta f} \tag{5.12}$$

Q_L is normally measured from experimental data and can be related to Q_u, as discussed in section (5.2.2), under critical coupling conditions by the formula

$$Q_u = 2Q_L \tag{5.13}$$

(4) Critically coupled - the impedance looking into the cavity (with or without material load) is matched to the external feed transmission line at resonant frequency. Under this condition, the total input power into the cavity is absorbed and dissipated in the conducting walls and material load, and the reflected power vanishes.

(5) P_i' - incident power measured at the output of the microwave power source, i.e., at the reference point *b* shown in Figures 5.9 and 5.10.

(6) P_i - input power measured at the input of the coupling probe, i.e., at the reference point *a*, shown in Figures 5.9 and 5.10.

(7) P_r - reflected power measured at the reference point *a*, as indicated in Figures 5.9 and 5.10.

(8) P_t - total power absorbed by the cavity includes cavity wall losses as well as dielectric losses.

(9) P_d - power absorbed by the dielectric.

(10) P_c - power absorbed by cavity walls.

(11) P_b - power which is measured by E-field probe is proportional to the square of the radial electric field components near the cavity walls.

Note that the generic meanings of the words "loaded" and "unloaded" in the definitions of Q are not referring to the presence or absence of material load in the cavity. The word "loaded" or "unloaded" describes if the cavity is or is not connected to the external circuit.

5.4.2 Low power swept-frequency measurements

Low power swept-frequency measurements were conducted at power levels of few milliwatts and measured the characteristics of both empty and material-loaded cavities. The experimental measurements included input power P_i, reflected power P_r, resonant frequency f, bandwidth of the resonant mode Δf, coupling probe depth L_p and cavity length L_s. Based on these measurements, the quality factors and the dielectric properties of the material load can be determined. The complex dielectric constant were evaluated by perturbation techniques or theoretical formula. Form these experiments the effect of the material loadings on the cavity operating parameters such as the resonant frequency (resonant length), coupling probe depth, cavity Q and field distributions were investigated.

As stated in Section 5.3, a resonant cavity is excited in discrete cavity modes. When the excitation frequency is fixed, the resonant modes of a cylindrical cavity correspond to distinct resonant lengths. The sweep oscillator was operated in the swept mode at 2.45 GHz center frequency. A cavity mode appropriate for microwave material processing was excited by adjusting L_s and L_p to the correct positions for resonance and critically coupling the cavity. Since the access holes, viewing window, coupling ports and coupling probe caused perturbation to the ideal cavity modes, the experimental eigenlengths of the resonant modes differed from exact theory.

Calibration of the feed transmission line shown in Figure 5.11 is necessary for accurate measurements of the input power level P_i and reflected power level P_r. As indicated in Figure 5.9 to 5.10, points a and b are the reference points used in calibrating the system. Calibration involved supplying a known amount of incident power at b_0 and measuring the power level at a_0. Then the power ratio, m, between P_i and P_i' was established. Using this ratio, the actual available power at the input of the coupling probe can be determined. That is

$$P_i = mP_i'$$

The power readings read from the power meters were corrected by taken into account the attenuations on the directional coupler and attenuators and the loss in the connecting cables. For example, if a 30-dB directional coupler is used for measuring incident power, as was the case for swept-frequency experiment, a 5 milliwatts reading from the incident power meter corresponds to 5 watts at the reference point *b* and the actual input power P_i is m × 5 watts. The total absorbed power by the cavity is given by

$$P_t = P_i - P_r \tag{5.14}$$

Since the coupling probe is not perfectly conducting, microwave power traveling on it is subject to attenuation. The incident power present at the input of the coupling probe is different from that fed into the cavity. Similarly, the reflected power measured at reference point *a* is somewhat smaller than that reflected from the cavity. However, the coupling probe loss is very small compared to the input and reflected powers. The assumption of lossless coupling probe gave no significant drawbacks on the experimental results. The incident power, reflected power and the total absorbed power for the empty cavity are represented by P_{i0}, P_{r0} and P_{t0}.

Cavity Q for any mode is measured by sweeping the cavity over a frequency band and displaying the Q-curve on the oscilloscope. The Q-curve represents the power reflected by the system as a function of frequency for a fixed eigenlength. Figure 5.12 displays such a curve as it would appear on the oscilloscope. The horizontal line is the zero reflected power line. Consequently, the area under the bell-shaped curve is the power absorbed by the cavity in the vicinity of the resonant frequency. Three markers generated by the sweep oscillator are shown on the oscilloscope. Markers one, two and three (m1, m2 and m3) are pointed at the resonant frequency, two half power points, respectively. The distance between markers m2 and m3 is readily read from the sweep oscillator and denoted by Δf. The loaded Q of the empty cavity is obtained using definition (3), i.e., $Q_{L0} = \frac{f_0}{\Delta f}$. If the cavity is critically coupled,

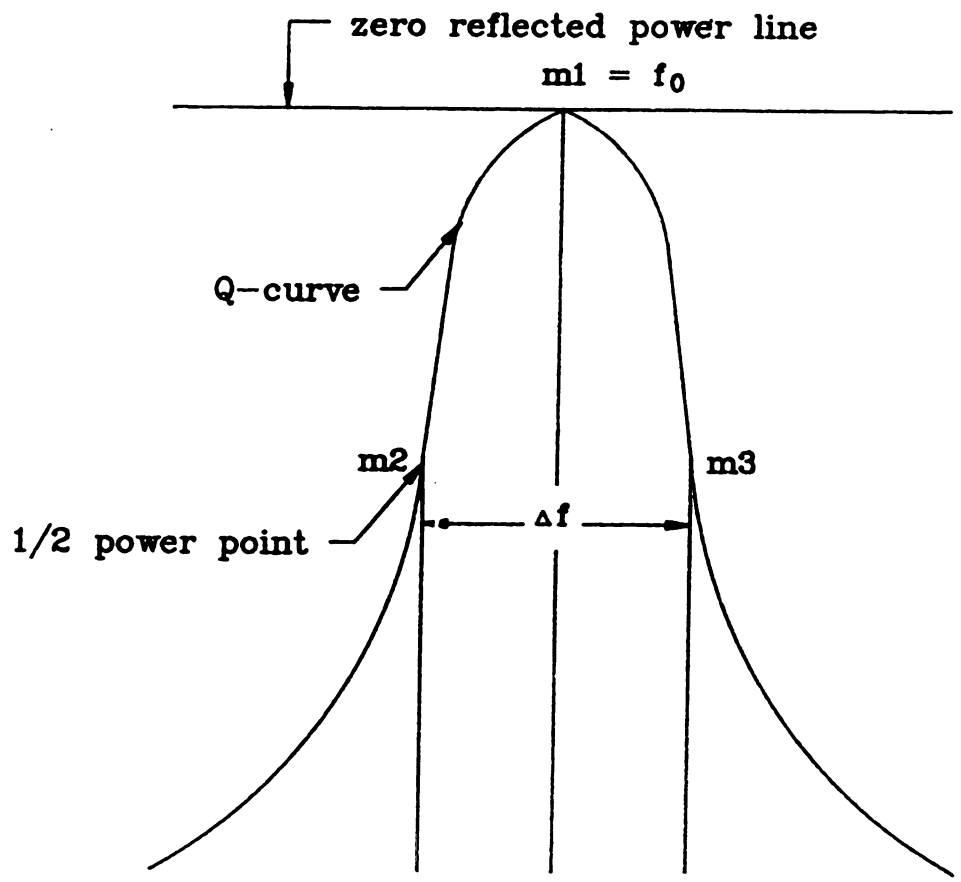

$$Q = \frac{f_0}{\Delta f}$$

Figure 5.12 Q measuremnt using Q-curve

$Q_{x0} = 2Q_{L0}$. The quantities subscripted by 0 refer to empty cavity measurements.

When the material load is placed in the empty cavity, it perturbs the electromagnetic resonant modes excited in the cavity. In general, the resonant frequency decreases and the loaded quality factor changes. The changes in these cavity parameters are complicated functions of material volume, shape, properties and position within the cavity. For small perturbation, the spatial distribution of the fields of the material-loaded cavity is not greatly altered from those of the empty cavity. Only the magnitude of the fields changes. Under this condition, perturbation technique using a quasi-static approximation to the field inside the material can be employed to evaluate the complex dielectric constant of the material [89]. For TM_{011} and TM_{012} modes, the perturbation formulas for cylindrically shaped material are

$$\varepsilon_r' = 1 - \frac{2\tau}{\Delta\tau}\frac{(f_r - f_{r0})}{f_{r0}} \tag{5.15a}$$

$$\varepsilon_r'' = \frac{\tau}{\Delta\tau}\left(\frac{1}{Q_L} - \frac{1}{Q_{L0}}\right) \tag{5.15b}$$

where

$$\Delta\tau = \int_{v'} |E_{x0}|^2 \, dv'$$

$$\tau = \int_{v} |\vec{E}|^2 \, dv$$

f_r = resonant frequency of the material-loaded cavity

f_{r0} = resonant frequency of the empty cavity

v' = material volume

v = entire empty cavity volume

E_{x0} = z component of the empty cavity electric field

$\vec{E_0}$ = empty cavity electric field

For large perturbation, the resonant modes excited in the cavity may become hybrid ones instead of pure TE or TM modes. The theoretical formula given in Chapter 3 is required to determine the dielectric permittivity of the material load.

The resonant frequency and the loaded Q of the loaded cavity can easily be obtained using the oscillator and Q-curve technique. By pointing markers m1, m2 and m3 at the proper positions as shown in Figure 5.13, the new resonant frequency and bandwidth are readily read from the oscillator digital displays.

Since the introduction of the material into the empty cavity detunes the cavity resonance, two adjustments are needed to retune the loaded cavity to critical coupling condition at the resonant frequency. The adjustment of the coupling probe position in the cavity will match the loaded cavity to the external circuit and the adjustment of the cavity length will bring the resonance back at the 2.45 GHz excitation frequency. The cavity length and the coupling probe depth are recorded and compared with empty cavity measurements,

$$\Delta L_s = L_s - L_{s0}$$

$$\Delta L_p = L_p - L_{p0}$$

where the subscript "0" are referring to empty cavity measurements.

5.4.3 High power single-frequency measurements

Though experimental results show that microwave material heating and processing can be achieved using swept-frequency microwave cavity, it is a very inefficient method [95]. Since the microwave source is operated in swept-mode, only small portion of the total incident power in the neighborhood of the cavity resonance is coupled into the cavity applicator. Most of the incident power is reflected and dissipated in the transmission network and the dummy load. In addition, on- line diagnosis of the

material complex dielectric properties during processing is very difficult using this technique. As mentioned in Section 5.4.2, the resonant frequency and quality factor of the material loaded cavity are required for calculating the complex dielectric constant of the load material using perturbation formula. However, material properties may change rapidly during microwave heating. It makes the on-line measurement of the quality factor by Q-curve method almost impossible due to the fast change of Q-curve. As a result, it is evident that the development of a different microwave heating technique is necessary to achieve more efficient heating result and on-line diagnosis of material complex dielectric constant during heating process.

High power single frequency technique has demonstrated high microwave coupling efficiencies of 70% - 95% and on-line process diagnosis [96]. In this method, both heating and diagnosis were accomplished with the same frequency. The operating frequency was constant at 2.45 GHz during the experiments. Since material complex dielectric properties changed during heating, constant adjustment of L_p and L_b were required to maintain the material loaded cavity resonance at 2.45 GHz such that most of the incident power was coupled into the cavity applicator under critical coupling condition. If the exact theory of the loaded cavity were available, one would solve for the complex dielectric constant ε with the knowledge of L_p, f_r and cavity Q. However, because of the unavailability of the theory, perturbation formulas, equations 5.15a and 5.15b, were used to evaluate ε. Therefore, measurements of the resonant frequency and cavity Q during processing are the key data needed to achieve on-line diagnosis.

Due to the single frequency operation, conventional Q-curve technique of quality factor measurement is not applicable. An alternative method for determining Q_u of a material loaded cavity was developed by Rogers [94]. The unloaded quality factor was calculated from the following expression:

$$Q_u = \frac{Q_{u0}\, P_{t0}}{|E_{r0}|^2} \frac{|E_r|^2}{P_t} \tag{5.16}$$

where Q_{u0} is the empty cavity unloaded quality factor, P_t and P_{t0} are the total powers absorbed in the loaded and empty cavities, respectively, E_r and E_{r0} are the radial electric fields at a fixed position within the loaded and empty cavities, respectively. This equation is an approximation based on two assumptions: (1) the presence of load materials in cavity does not alter the field distributions significantly from those of the empty cavity, only the magnitude of the electromagnetic fields change, (2) the relation between the energies stored in the loaded and empty cavities can be expressed as

$$\frac{U_{b0}}{U_b} = \frac{|E_{r0}|^2}{|E_r|^2} \tag{5.17}$$

Rogers showed the evidences of supporting assumption (1). Assumption (2) is carefully examined in the following.

The total energy stored in cavity is defined as

$$U = \int \varepsilon |\vec{E}(\vec{r})|^2 dv \tag{5.18}$$

If assumption (1) is indeed true, the relation can be established

$$\frac{|\vec{E}_0(\vec{r})|^2}{|E_{r0}(r_1)|^2} = \frac{|\vec{E}(\vec{r})|^2}{|E_r(r_1)|^2} = c(\vec{r}) \tag{5.19}$$

where $\vec{E}_0(\vec{r})$ and $\vec{E}(\vec{r})$ are the electric fields in the empty and loaded cavities, respectively, $c(\vec{r})$ is a constant depending on the position within the cavity, r_1 is an arbitrary position within the cavity. According to equations 5.18 and 5.19, the ratio between the total energies store in the empty and loaded cavities is

$$\frac{U_{b0}}{U_b} = \frac{|E_{r0}(r_1)|^2}{|E_r(r_1)|^2} \frac{K_0}{K_1} \tag{5.20}$$

where

$$K_0 = \int_V c(\bar{r})\, dv \tag{5.21}$$

$$K_1 = \int_{V-V'} c(\bar{r})\, dv + \hat{\epsilon}_r \int_{V'} c(\bar{r})\, dv \tag{5.22}$$

Above equations indicate that equation 5.17 is true if $K_0 = K_1$. Close examination of equations 5.21 and 5.22 shows that assumption (2) may not hold for materials of large size, large dielectric constant and lossy materials.

In order to use equation 5.16 to calculate Q_u the ability of measuring the square of the radial electric field at a fixed position within the cavity is necessary. Since the ratio of the E-field probe measurement to the square of the radial electric field at a point within the cavity is a constant, i.e.,

$$\frac{P_b}{|E_r|^2} = \text{constant} \tag{5.23}$$

the following expression can be established under assumption (1),

$$\frac{P_b}{P_{b0}} = \frac{|E_r|^2}{|E_{r0}|^2} \tag{5.24}$$

where P_b is the E-field probe measurement for the material loaded cavity and P_{b0} is the E-field probe measurement for the empty cavity. Equation 5.24 is valid if P_b and P_{b0} are measured at the same point near cavity wall. Accordingly, it is important when measuring Q by this method not to move E-field probe between reading.

According to equation 5.23, the radial electric field patterns near cavity wall were obtained using E-field probe inserted through the diagnostic holes shown in Figure 5.5. Note that when measuring electric field patterns using this technique, the microcoax probe depth within the cavity has to be remained constant throughout the experiments.

Any change of this depth may result in inaccurate electric filed patterns. Detailed description of the determination of an appropriate probe depth is given in [91].

Inspection of equations 5.15 and 5.16 reveals that measurements of the cavity quality factor, P_b, P_r, P_i, L_s and L_p need to be taken in the high power single frequency experiments. Before heating started, the empty cavity quality factor Q_{u0} was made by Q-curve technique, and then the single-frequency low power empty cavity measurements of P_{b0}, P_{r0}, P_{i0}, L_{s0} and L_{p0} were performed. For low power measurements, the input power was typically a few milliwatts. The material temperature was monitored by Fluoroptic Temperature Measurement System. After the initial measurements were recorded, input power was raised to the prescribed level and heating cycle began. During each heating experiment, the input power was maintained constant within the range of 0.5 to 10 W and the cavity was continuously tuned to critically coupled by manually adjusting L_p and L_s to minimum reflected power. Data points of P_b, P_r, P_i, L_s ,L_p and material temperature were taken periodically during heating. As is shown in Figure 5.10, the temperature and power measurements were taken and recorded by a microcomputer at selected data rate which was set by the temperature update rate of the Luxtron 750 Fluoroptic Thermometer. Data points were read every one second or two.

After the heating cycle was complete, the material load was removed from the cavity. Then the empty cavity resonant frequency, f_{r0}, corresponding to each data point position for L_p and L_s measured during processing was determined by swept-frequency method. Cavity Q was calculated using equation 5.16. With the measurements of f_{r0} and cavity Q, the complex dielectric constant of the material for each data point recorded was evaluated using equations 5.15a and 5.15b where f_r is 2.45 GHz.

Chapter 6

EXPERIMENTAL RESULTS

6.1 Introduction

The objectives of the experiments presented in this chapter are (1) to verify the theoretical results given in Chapter 4 and (2) to investigate the microwave heating of solid materials with various dielectric properties using single-mode microwave cavity applicators. The low power experimental measurements of the resonant frequency, resonant length, quality factor and field patterns for various loads were performed and are compared with the theoretical computations of Chapter 4. Load materials included nylon and teflon rods with radii of 0.635 cm and 1.27 cm, and a 0.2 cm inside radius ethylene glycol quartz tube.

Microwave heating experiments were performed to carefully investigate electromagnetic interactions with selected materials and to develop microwave processing and on-line diagnostic techniques. Load materials employed in the heating experiments consisted of lossy materials such as nylon 66 and water-soaked wood cylinders, conducting materials such as three-inch silicon wafers, and anisotropic composite materials such as graphite reinforced epoxy slabs. On-line measured complex dielectric constants of nylon and wet wood were compared with publish data. In addition, the coupling efficiency vs. time was determined in the experiments with wet wood cylinders. The surface temperature of silicon wafers and graphite-epoxy slabs was measured as a function of time during microwave excitation. The influence of the orientation of the graphite fibers on the field patterns and the radial electric field strength near the conducting walls was examined in the low power graphite-epoxy composite experiments.

6.2 Low power measurements (verification of theory)

6.2.1 Introduction

The six-inch cavity described in section 5.2.2 was employed to experimentally verify the theoretical analysis of Chapter 4. As already noted in Chapter 5 this cavity was carefully designed and constructed for precision experimental measurement. Two cavity modes, e.g. TM_{012} and HE_{111} modes, were investigated using various material loading conditions. Experimental measurements included the measurement of resonant frequency, resonant length, quality factor and axial field patterns of the empty and material-loaded cavities excited with the TM_{012} and HE_{111} (or TE_{111}) modes. Cavity loads were finite radius rod materials that uniformly filled the cavity in the axial direction. The TM_{012} and HE_{111} modes were chosen as representative examples of a ϕ independent and a hybrid mode cavity excitation.

The methods used to measure resonant frequency, resonant length, quality factor and cavity field patterns are reviewed in sections 5.4.2 and 5.4.3. All measurements were performed at low power of less than 12 mW in order to avoid microwave material heating and other nonlinear field material interactions. To ensure that the crystal detector was in the linear operation range, quality factors measurements using Q-curve technique were made with input powers of less than 1.9 mW. The radial field patterns at the cavity end plate were measured by inserting a microcoax probe into the diagnostic holes along the angles of 0^o, 90^o, 180^o and 270^o. The configuration of the base plate is displayed in Figure 6.1. As shown, the coupling probe is positioned in the angle of 0^o and the distance of each of the diagnostic holes to the center of the base plate is identified by a ring. The radii of the rings, r_a, r_b, r_c, r_d and r_e are 2.225, 3.294, 4.445, 5.3975 and 6.35 cm, respectively.

The method of determining the optimum microcoax probe depth within the cavity without major perturbation to the cavity resonance was also described in Chapter 5. As shown in Figure 6.2, two microcoax probes of different dimensions were employed for field patterns measurements. Probe "a" was used for TM_{012} mode and probe "b"

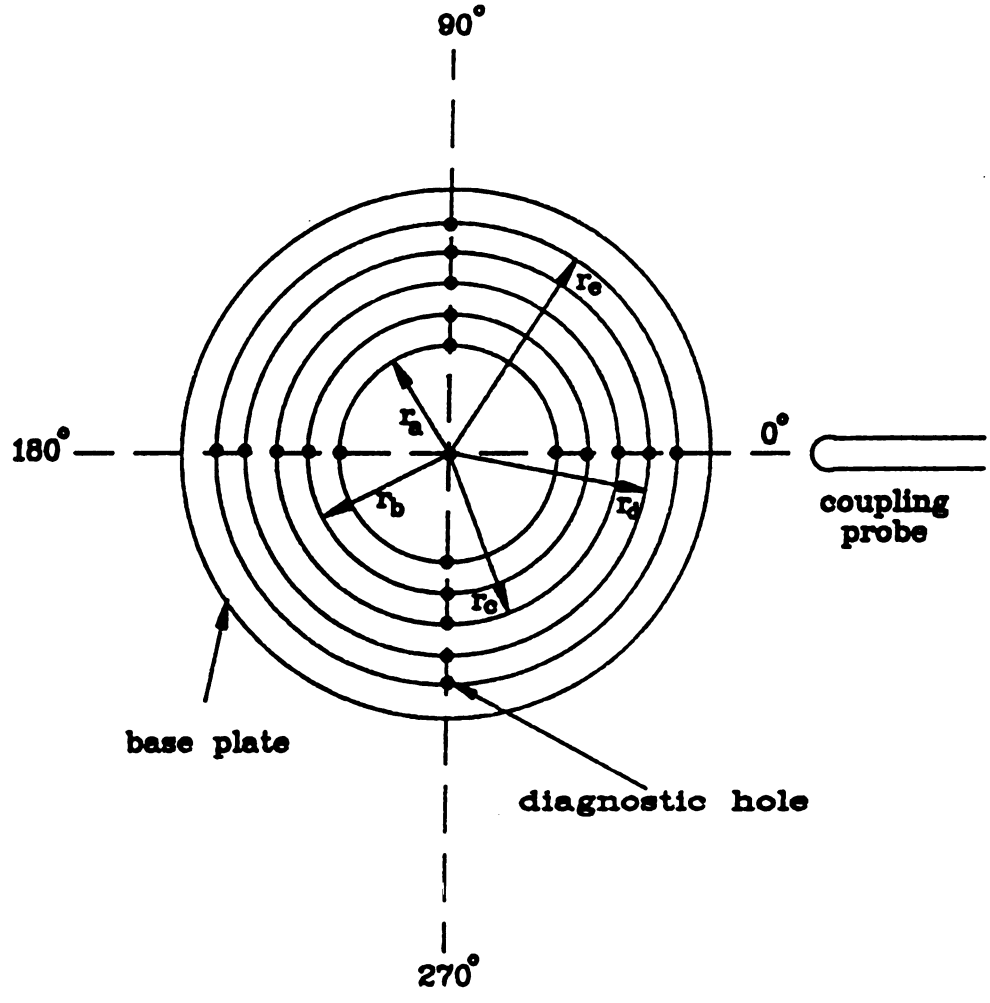

Figure 6.1 Configuration of the base plate

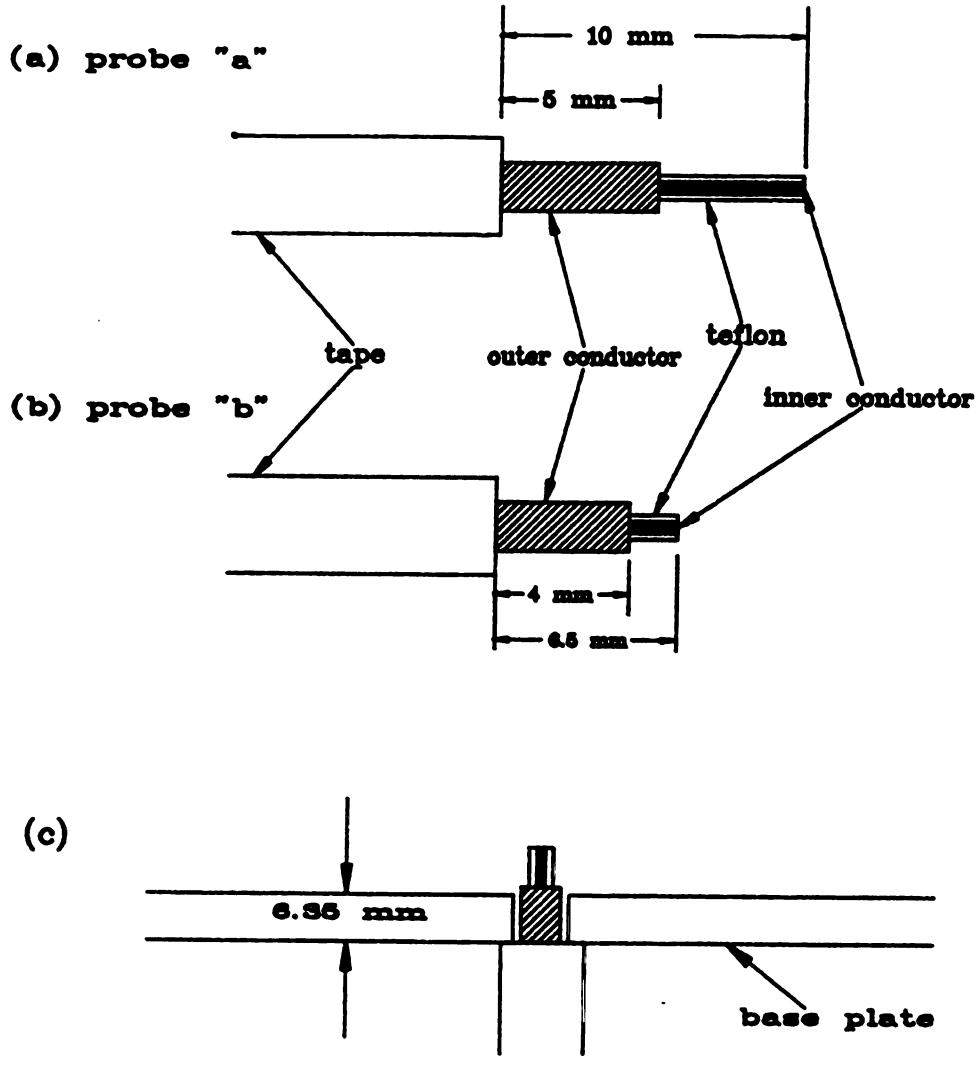

Figure 6.2 Microcoax probes and base plate dimensions

was used for HE_{111} mode. Figure 6.2c depicts the exact probe position in a diagnostic hole on the base plate. Since the thickness of the base plate is 6.35 mm, the actual microcoax probe depths within the cavity were 3.65 and 0.25 mm, respectively, for probes "a" and "b".

6.2.2 TM_{012} mode

The theoretical and measured results for TM_{012} mode are listed in Table 6.1. The resonant frequency, resonant length, coupling probe depth within the cavity, and the quality factor are denoted by f_0, L_s, L_p and Q_0 for the empty cavity, and by f_{01}, L_{s1}, L_{p1} and Q_L for material-loaded cavity. Δf and ΔL_s are defined as $\Delta f = f_0 - f_{01}$, $\Delta L_s = L_s - L_{s1}$. The resonant frequencies and quality factors given in Table 6.1a were measured with the swept frequency technique described in section 5.4.2, where the cavity length was kept at a constant length of 15.5 cm. In order to minimize measurement errors the experimental quality factors were the average of at least three measurements. The resonant lengths listed in Table 6.1b were measured at a constant frequency of 2.45 GHz. Each experimental measurement was taken under critical coupling conditions. In the constant cavity resonant length experiments, cavity was critically coupled by adjusting the operating frequency and the coupling probe depth. In the constant resonant frequency experiments, cavity was matched by adjusting the cavity length and coupling probe depth.

A quartz tube of 0.6 cm radius and 0.1 cm thick was used to contain ethylene glycol for the ethylene glycol experiments. Note that the Δf and ΔL_s in the ethylene glycol experiments were the differences of the resonant frequency and resonant length between the cavity loaded with ethylene glycol and the cavity loaded with empty quartz tube.

As listed in Table 6.1, the theoretical results and experimental measurements of the resonant frequency and resonant length show excellent agreement to within one

TM_{012} mode		f_0 (GHz) empty	f_{01} (GHz) loaded	df (MHz)	Ls (cm) empty	Ls_1 (cm) loaded	dLs (mm)	Lp (mm) empty	Lp_1 (mm) loaded	Q_0 empty	Q_L loaded
Teflon Rod 0.635 cm	theoretical	2.45296	2.439548	13.412	15.5	15.5	--	--	--	28748	14465
	experimental	2.4588	2.4464	12.4	15.5	15.5	--	9.185	9.185	14437	12523
	% error	0.24%	0.28%	7.55%	--	--	--	--	--	49.8%	13.4%
Nylon Rod 0.635 cm	theoretical	2.45296	2.4279	25.06	15.5	15.5	--	--	--	28748	2145
	experimental	2.4588	2.4329	25.9	15.5	15.5	--	8.865	13.32	14437	2880
	% error	0.238%	0.21%	3.35%	--	--	--	--	--	49.8%	34.3%
Nylon Rod 1.27 cm	theoretical	2.45296	2.35606	96.6	15.5	15.5	--	--	--	28748	659
	experimental	2.4606	2.3655	95.1	15.5	15.5	--	9.5	16.565	14437	909
	% error	0.31%	0.38%	1.86%	--	--	--	--	--	49.8%	38%
Ethylene Glycol 0.2 cm	theoretical	2.45296	2.437069	15.891	15.5	15.5	--	--	--	28748	64
	experimental	2.4597	2.4402	14.5 (1)	15.5	15.5	--	8.655	29.56	14437	74
	% error	0.275%	0.128%	8.75%	--	--	--	--	--	49.8%	13.5%

Table 6.1a

TM_{012} mode		f_0 (GHz) empty	f_{01} (GHz) loaded	df (MHz)	Ls (cm) empty	Ls_1 (cm) loaded	dLs (mm)	Lp (mm) empty	Lp_1 (mm) loaded
Teflon Rod 0.635 cm	theoretical	2.45	2.45	--	15.54	15.3953	1.447	--	--
	experimental	2.45	2.45	--	15.588	15.459	1.29	8.37	8.37
	% error	--	--	--	0.31%	0.41%	8.6%	--	--
Nylon Rod 0.635 cm	theoretical	2.45	2.45	--	15.54	15.2815	2.585	--	--
	experimental	2.45	2.45	--	15.589	15.326	2.36	8.62	13.535
	% error	--	--	--	0.32%	0.29%	1.74%	--	--
Nylon Rod 1.27 cm	theoretical	2.45	2.45	--	15.54	14.6326	9.074	--	--
	experimental	2.45	2.45	--	15.6205	14.7205	9.0	9.14	17.895
	% error	--	--	--	0.51%	0.6%	0.82%	--	--
Ethylene Glycol 0.2 cm	theoretical	2.45	2.45	--	15.54	15.3668	1.732	--	--
	experimental	2.45	2.45	--	15.5875	15.377	1.68 (2)	8.605	31.11
	% error	--	--	--	0.34%	0.44%	3.0%	--	--

Table 6.1b

(1) frequency difference between quartz tube loaded cavity and ethylene glycol loaded cavity, f_0 (quartz tube loaded cavity) = 2.4547 GHz
(2) resonant length differece between quartz tube loaded cavity and ethylene glycol loaded cavity, Ls (quartz loaded cavity) = 15.545 cm

Table 6.1 Comparison between theoretical and experimental results for TM_{012} mode, (a) constant resonant length of 15.5 cm, (b) constant resonant frequency of 2.45 GHz.

percent. The experimental Δf's and ΔL_s's also match with theoretical computations to less than ten percent. However the experimental quality factors are quite different from the theoretical results. For the empty cavity, the error percentage in Q_0 is 49.8%. While the error percentages in Q_L for the material loaded cavity vary from 5.6% to 38.0%. In the cases of 0.635 cm and 1.27 cm nylon rods, and ethylene glycol, the experimental quality factors are larger than the theoretical quality factors.

The field patterns of TM_{012} mode shown in Figures 6.3 through 6.6 were measured using single frequency at 2.45 GHz. Figures 6.3a, 6.3b and 6.3c shows the actual magnitude of the measured field strength. Comparison of the experimental and theoretical results is displayed in Figures 6.4b, 6.5b and 6.6b. In these Figures, the experimental field measurements are normalized by a constant such that the theoretical field curve is best fit among the experimental measurements. As shown, experimental and theoretical results have good agreement for all the load materials.

6.2.3 HE_{111} mode

Table 6.2 presents the theoretical computations and the experimental measurements for HE_{111} mode. The experimental results given in Table 6.2a and 6.2b were, respectively, measured at a constant resonant length of 6.94 cm and a constant resonant frequency of 2.45 GHz. As listed in Table 6.2a, the experimental resonant frequencies for all load materials match with theoretical results to within one percent. For 0.635 cm nylon and teflon rods and ethylene glycol, the error percentages in Δf are less than 8%. For the 1.27 cm nylon rod, the error percentage in Δf is 32%. Also seen in Table 6.2a is the very large difference between the theoretical and experimental quality factors. The error percentages in Q_0 are less than 58%. For the material loaded cavity the error percentages in Q_L are between 34.3% and 81.0%. Again the largest error percentage occurs in the experiment with 1.27 cm nylon rod. Note that the coupling probe depth in this experiment was 20.37 mm, which is much longer than the probe depths in other experiments.

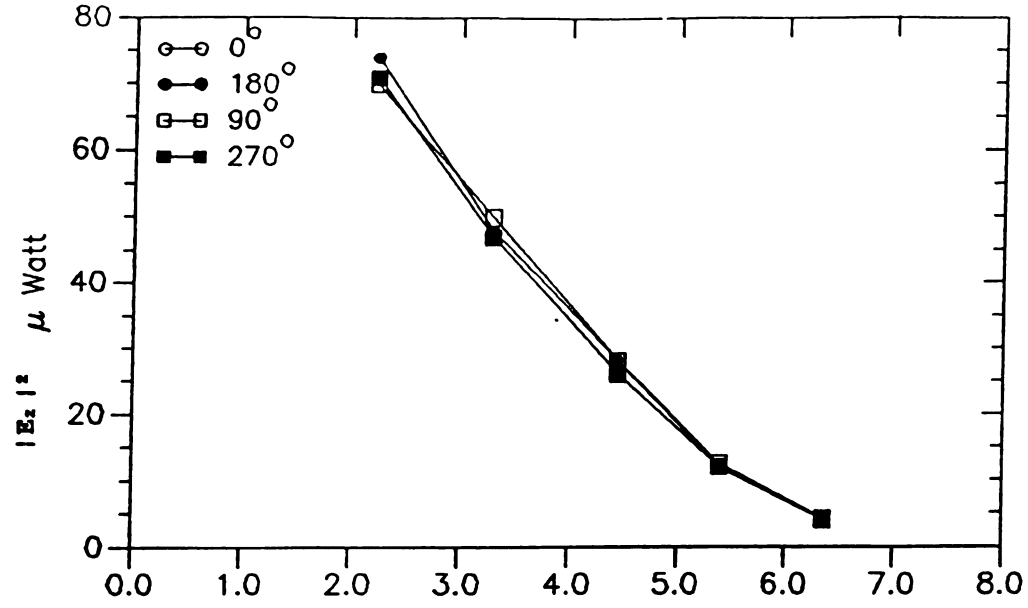

6.3a

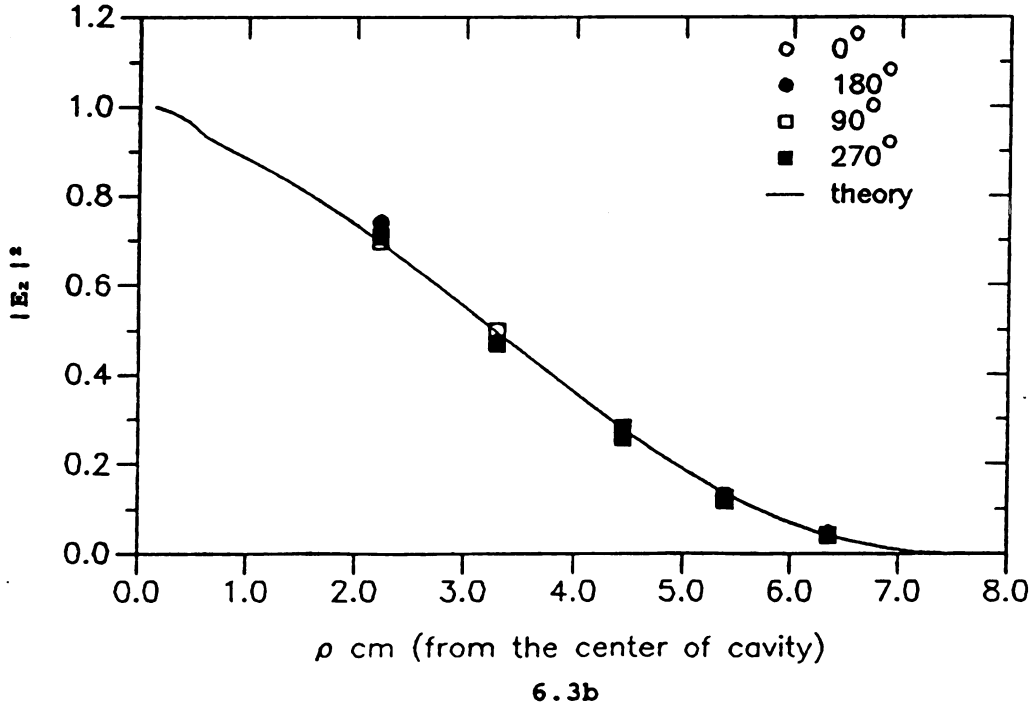

6.3b

Figure 6.3 Field patterns for 0.635 cm teflon rod, TM_{012} mode , (a) actual magnitude, (b) comparison between theoretical and experimental results

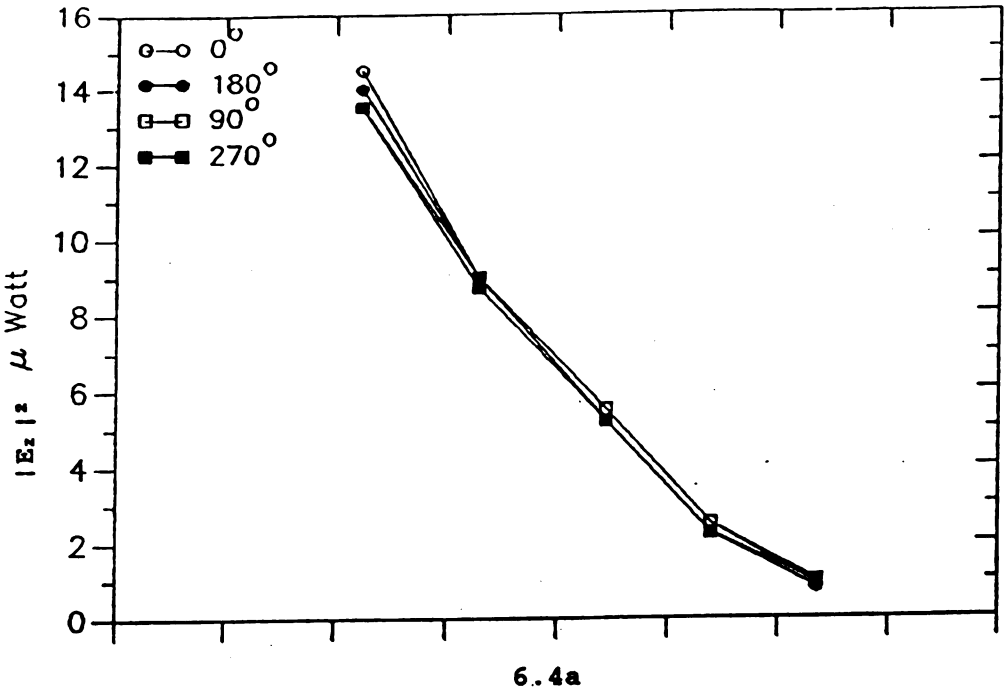

6.4a

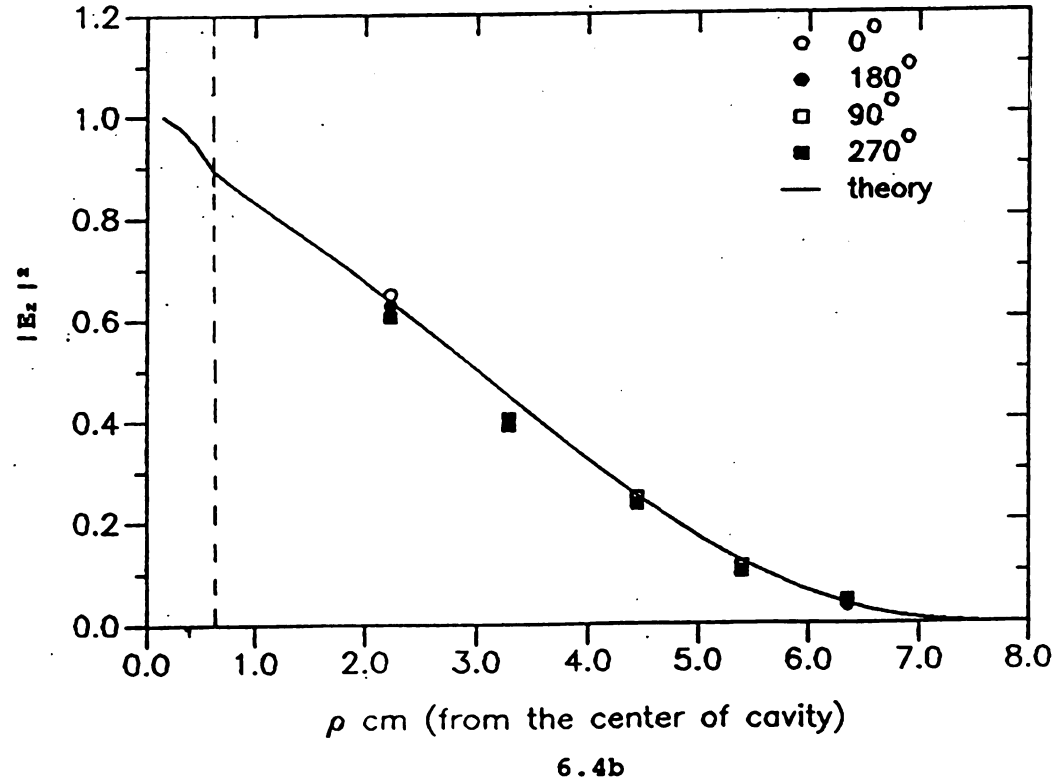

6.4b

Figure 6.4 Field patterns for 0.635 cm nylon rod, TM_{012} mode , (a) actual magnitude, (b) comparison between theoretical and experimental results.

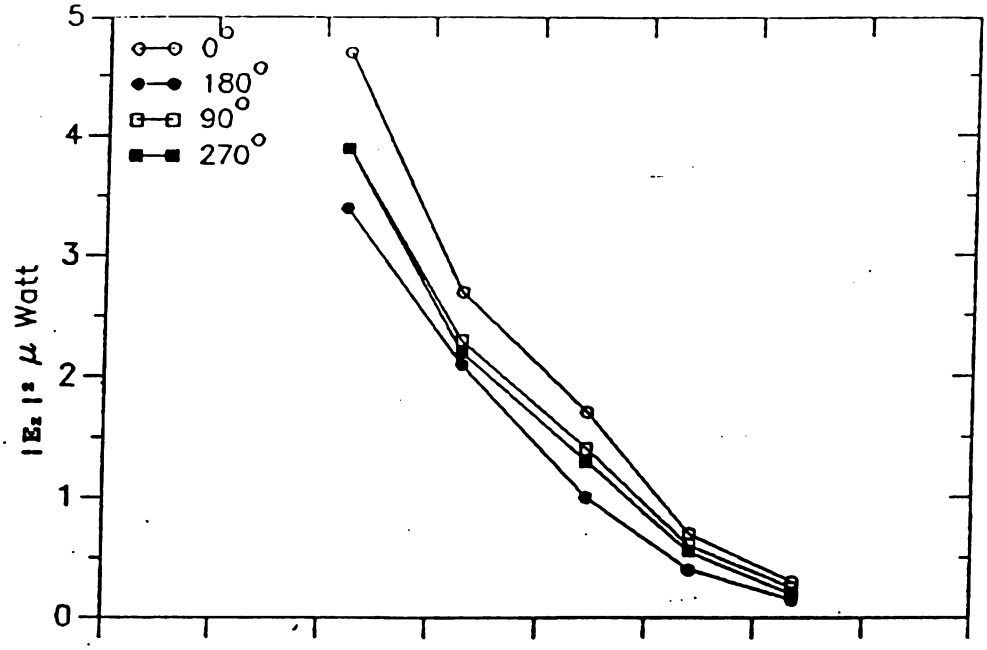

6.5a

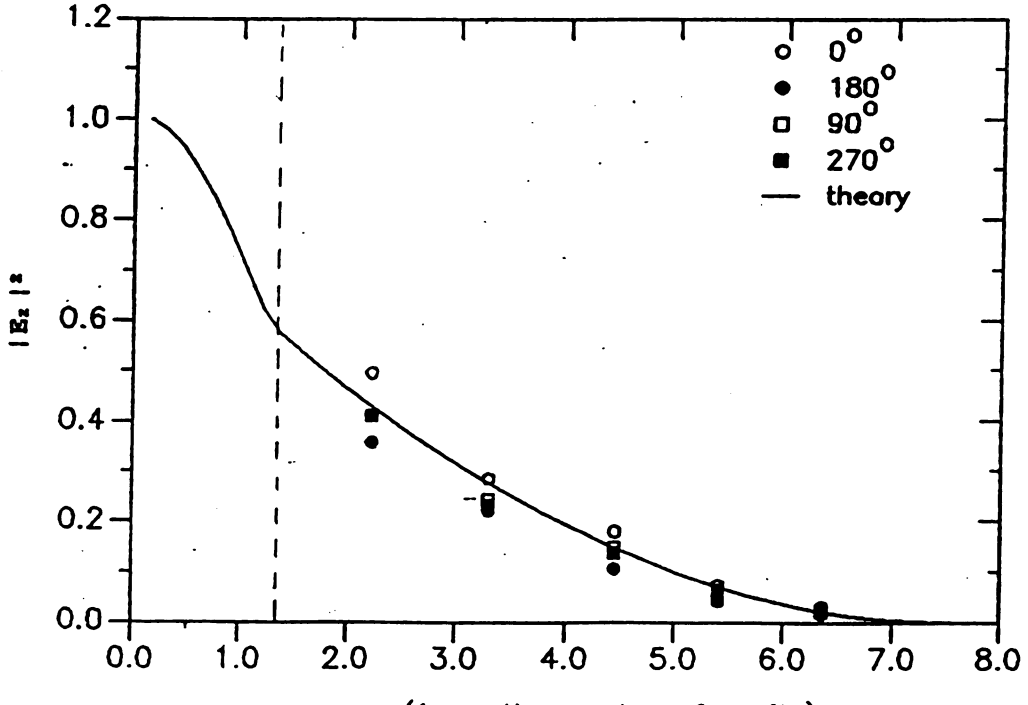

6.5b ρ cm (from the center of cavity)

Figure 6.5 Field patterns for 1.27 cm nylon rod, TM_{012} mode , (a) actual magnitude, (b) comparison between theoretical and experimental results.

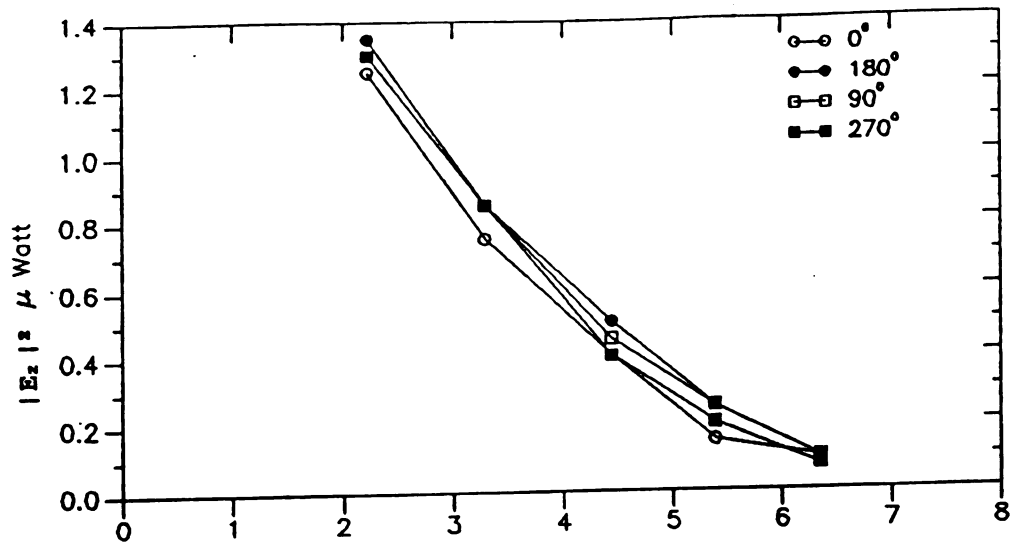

6.6a

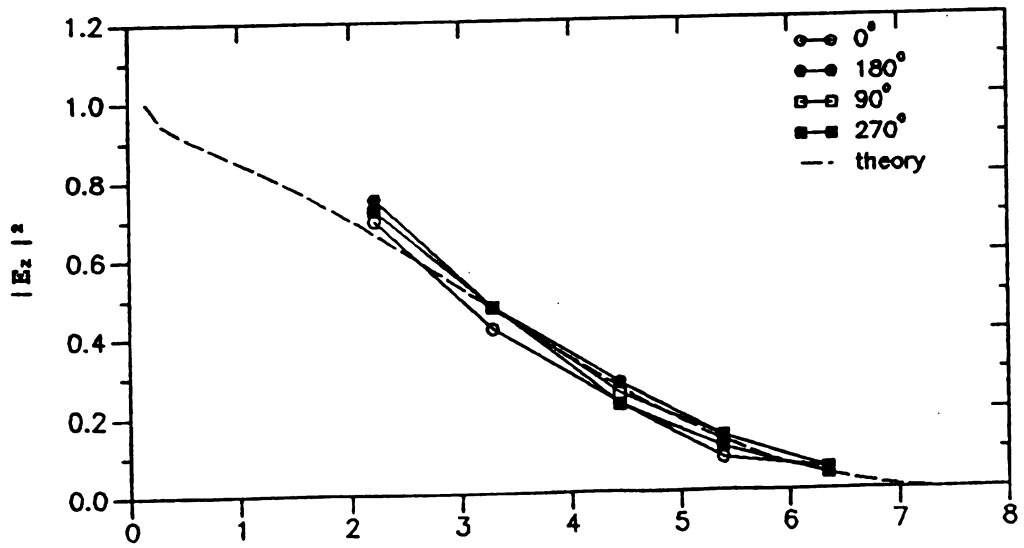

6.6b ρ cm (from the center of cavity)

Figure 6.6 Field patterns for 0.2 cm ethylene glycol, TM_{012} mode, (a) actual magnitude, (b) comparison between theoretical and experimental results.

HE_{111} mode		f_0 (GHz) empty	f_{01} (GHz) loaded	df (MHz)	Ls (cm) empty	Ls_1 (cm) loaded	dLs (mm)	Lp (mm) empty	Lp_1 (mm) loaded	Q_0 empty	Q_L loaded
Teflon Rod 0.635 cm	theoretical	2.45	2.4366	13.4	6.94	6.94	--	--	--	24196	18511
	experimental	2.4474	2.4341	13.3	6.94	6.94	--	7.12	7.12	12811	10359
	% error	0.11%	0.103%	0.75%	--	--	--	--	--	47.0%	44.2%
Nylon Rod 0.635 cm	theoretical	2.45	2.43032	19.687	6.94	6.94	--	--	--	24196	10584
	experimental	2.4474	2.4262	21.2	6.94	6.94	--	7.24	9.08	12811	4902
	% error	0.11%	0.17%	7.73%	--	--	--	--	--	47.0%	34.3%
Nylon Rod 1.27 cm	theoretical	2.45	2.35862	91.38	6.94	6.94	--	--	--	24196	13593
	experimental	2.4422	2.38	62.2	6.94	6.94	--	7.09	20.37	10642	2515
	% error	0.32%	0.9%	32.0%	--	--	--	--	--	56.0%	81.0%
Ethylene Glycol 0.2 cm	theoretical	2.45	2.44659	3.37	6.94	6.94	--	--	--	24196	5505
	experimental	2.4477	2.4422	3.6 (1)	6.94	6.94	--	6.64	9.695	10420	2583
	% error	0.094%	0.179%	6.8%	--	--	--	--	--	57.0%	53.0%

Table 6.2a

HE_{111} mode		f_0 (GHz) empty	f_{01} (GHz) loaded	df (MHz)	Ls (cm) empty	Ls_1 (cm) loaded	dLs (mm)	Lp (mm) empty	Lp_1 (mm) loaded
Teflon Rod 0.635 cm	theoretical	2.45	2.45	--	6.94	6.8913	0.487	--	--
	experimental	2.45	2.45	--	6.93	6.882	0.48	7.075	7.22
	% error	--	--	--	0.14%	0.16%	1.44%	--	--
Nylon Rod 0.635 cm	theoretical	2.45	2.45	--	6.94	6.8685	0.71528	--	--
	experimental	2.45	2.45	--	6.928	6.852	0.76	7.88	9.705
	% error	--	--	--	0.17%	0.24%	6.25%	--	--
Nylon Rod 1.27 cm	theoretical	2.45	2.45	--	6.94	6.60233	3.377	--	--
	experimental	2.45	2.45	--	6.914	6.5205	3.935	7.275	15.545
	% error	--	--	--	0.38%	1.18%	16.5%	--	--
Ethylene Glycol 0.2 cm	theoretical	2.45	2.45	--	6.94	6.92761	0.1239	--	--
	experimental	2.45	2.45	--	6.9375	6.916	0.13 (2)	6.55	10.03
	% error	--	--	--	0.036%	0.17%	4.9%	--	--

Table 6.2b

(1) resonant frequency difference between quartz tube loaded cavity and ethylene glycol loaded cavity, f_0 (quartz tube loaded cavity) = 2.4458 GHz

(2) resonant length difference between quartz tube loaded cavity and ethylene glycol loaded cavity, Ls (quartz tube loaded cavity) = 6.926 cm

Table 6.2 Comparison between theoretial and experimental results for HE_{111} mode, (a) constant resonant length of 6.94 cm, (b) constant resonant frequency of 2.45 GHz

The experimental and theoretical resonant lengths given in Table 6.2b show excellent agreement to less than 1.18%. The experimental ΔL_s's in the experiments with 0.635 cm teflon and nylon rods as well as 0.2 cm ethylene glycol match with theoretical ΔL_s to within 6.25%. In the case of 1.27 cm nylon rod, ΔL_s has an error percentage of 16.% between the experimental and theoretical results.

The field patterns of HE_{111} are displayed in Figures 6.7 through 6.10. As shown, for 0.635 cm teflon and nylon rods and 0.2 cm ethylene glycol rod, the field measurements along 0° and 180° have good agreement with theoretical results. In these cases, the fields along 90° and 270° were zero. This is quite consistent with theory, since theoretically HE_{111} mode exhibits $\cos\phi$ angular variations. As can be seen in Figure 6.9, the experimental field patterns of the cavity loaded with 1.27 cm nylon rod do not agree with theory. In addition, very small fields were sensed along 90° and 270°.

6.2.4 Discussion

The mismatch between the theoretical and experimental quality factors listed in Tables 6.1 and 6.2 is probably because (1) the exclusion of the losses due to the coupling probe in the theoretical formulation, (2) the nonideal structure of the cavity applicator and (3) the measurement errors. The effects of the nonideal structure include the electromagnetic radiation caused by the presence of the access hole and the losses due to the finger stock of the sliding short. The bad contact between the finger stock of the coupling probe and the inside walls of the coupling port would also give rise to inaccurate experimental results. The measurement errors are minimized by taking the average of more than two measurements.

In some cases, the experimental quality factors were larger than the theoretical results. Explanation for this is that the actual field patterns within the cavity are altered from those in theory. If the changes of the field patterns result in either less power losses or more stored energy than it would be in the theoretical model, it is

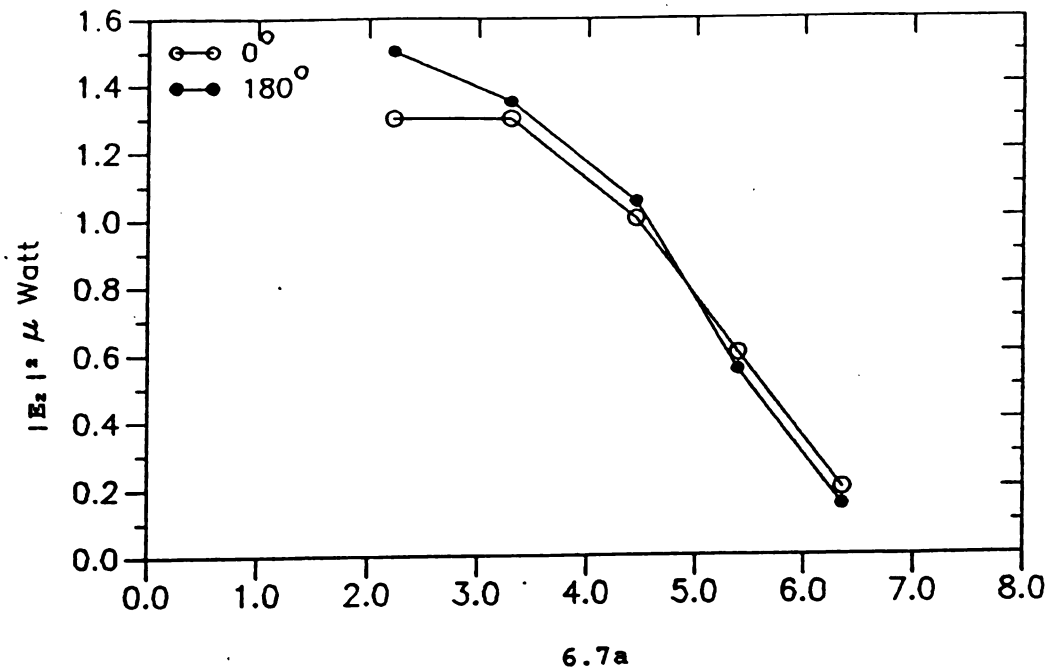

6.7a

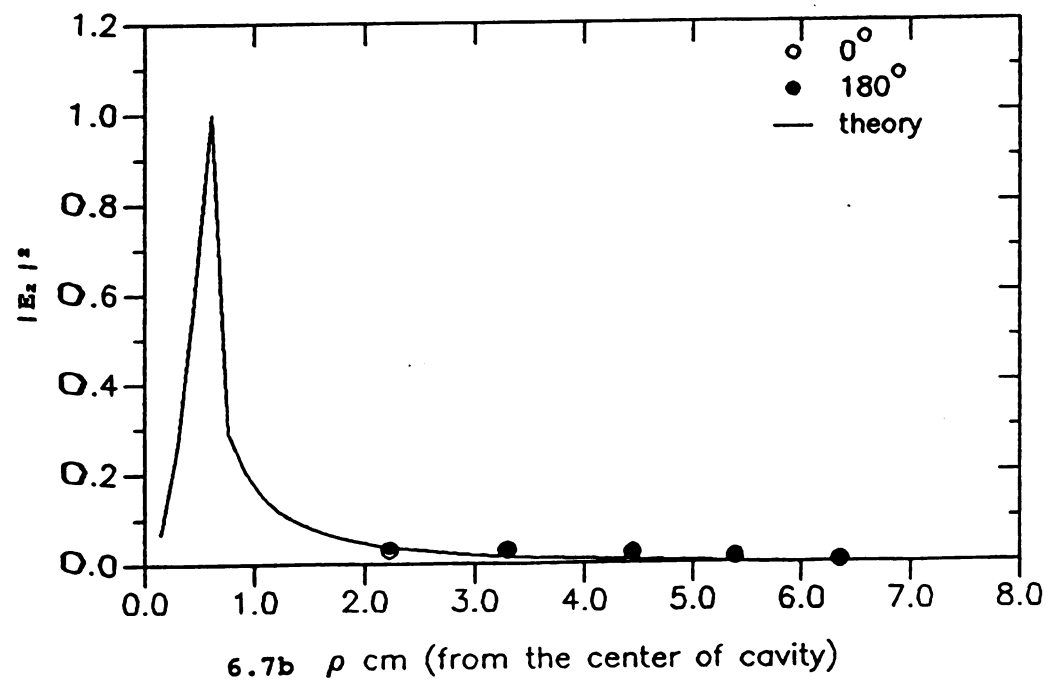

6.7b ρ cm (from the center of cavity)

Figure 6.7 Field patterns for 0.635 cm teflon rod, HE_{111} mode , (a) actual magnitude, (b) comparison between theoretical and experimental results.

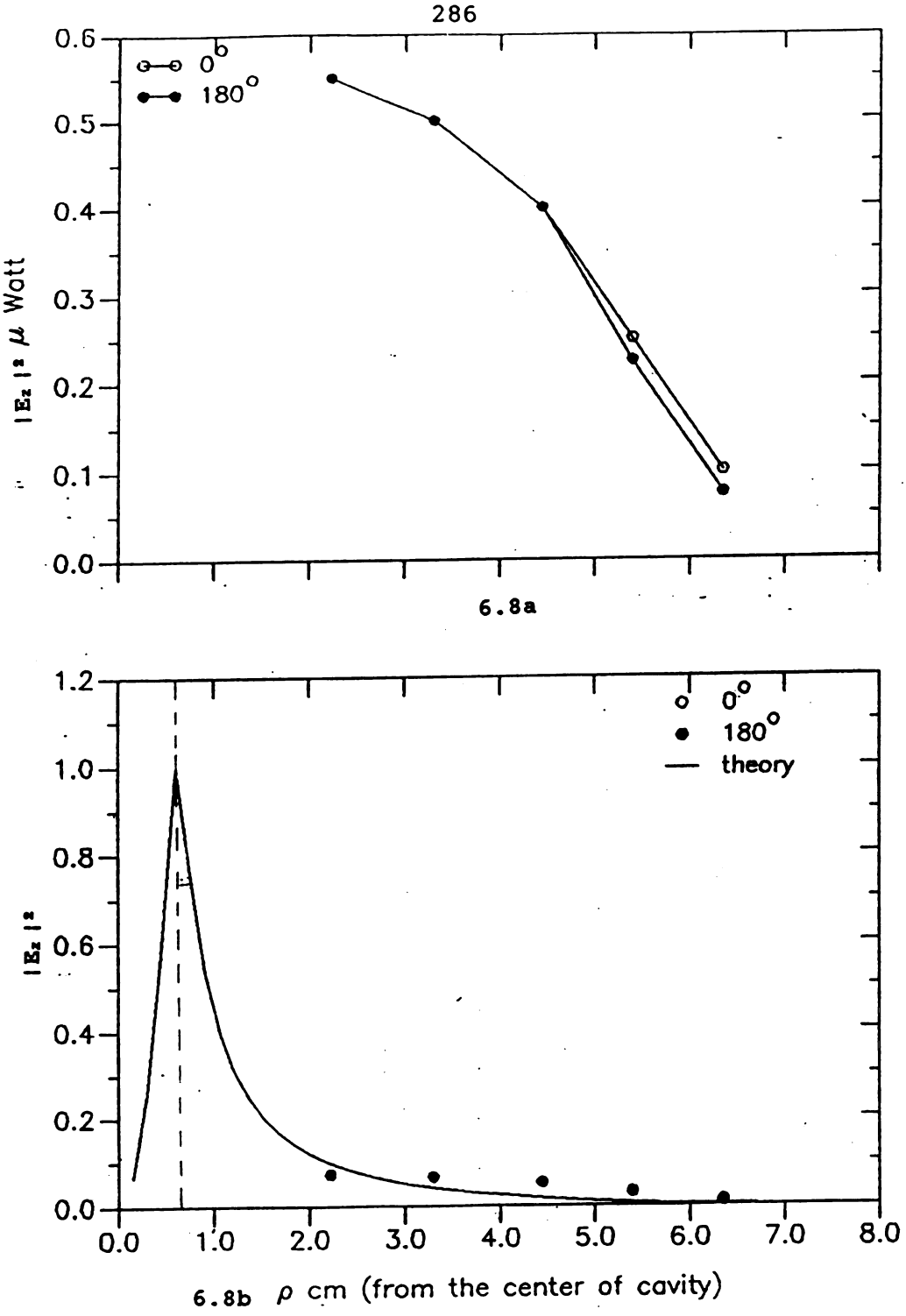

Figure 6.8 Field patterns for 0.635 cm nylon rod, HE_{111} mode , (a) actual magnitude, (b) comparison between theoretical and experimental results.

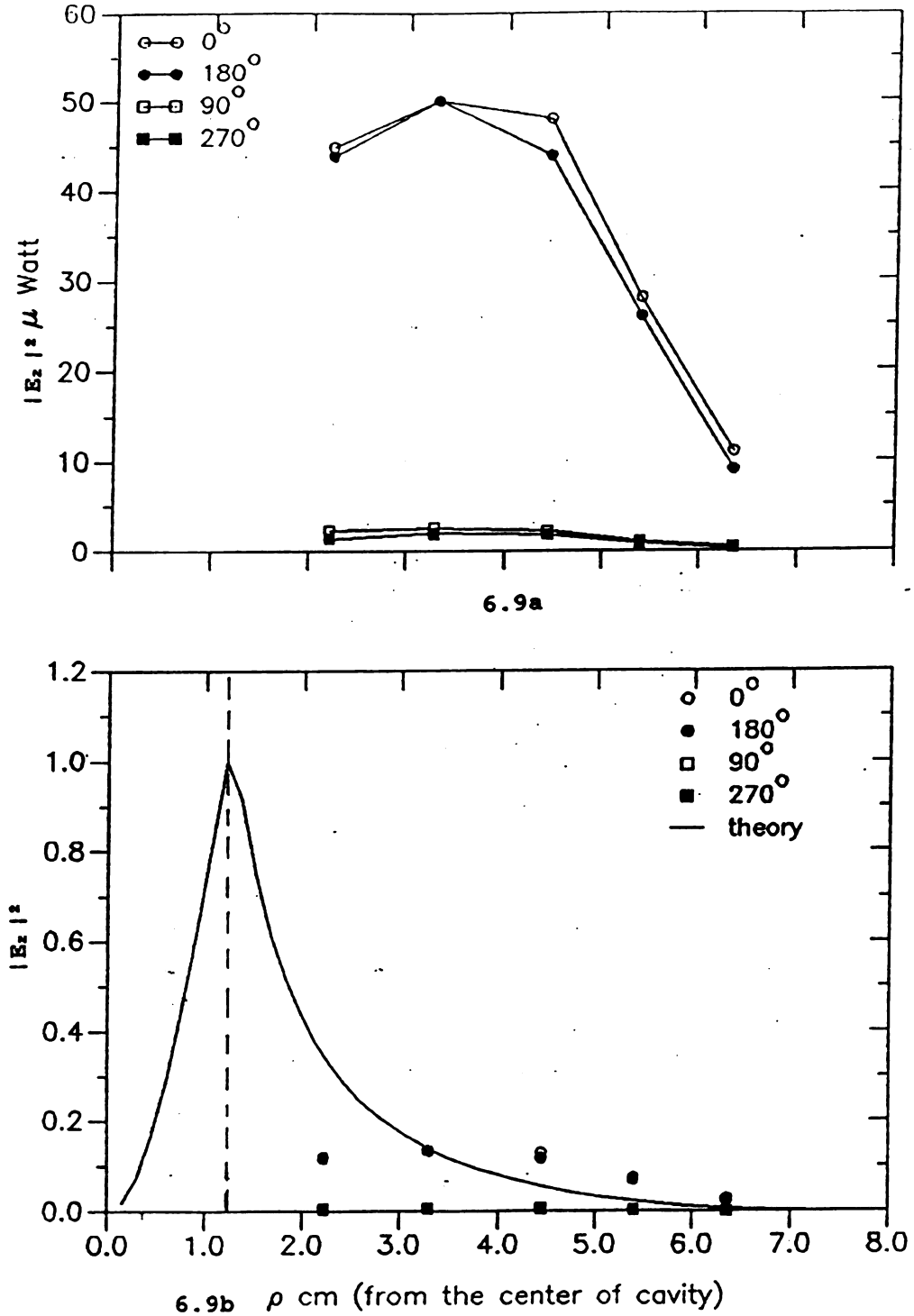

Figure 6.9 Field patterns for 1.27 cm nylon rod, HE_{111} mode, (a) actual magnitude, (b) comparison between theoretical and experimental results.

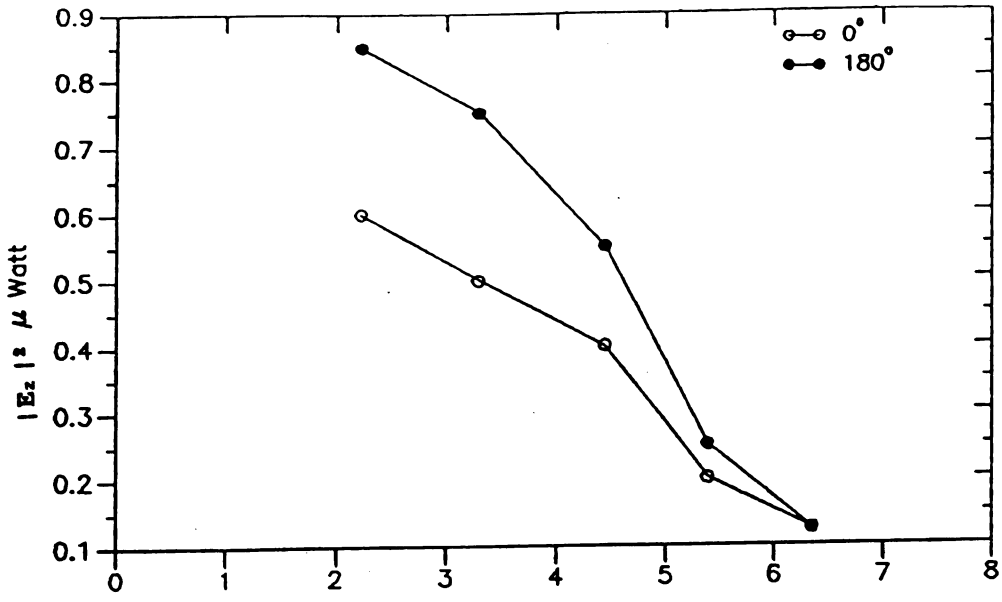

6.10a

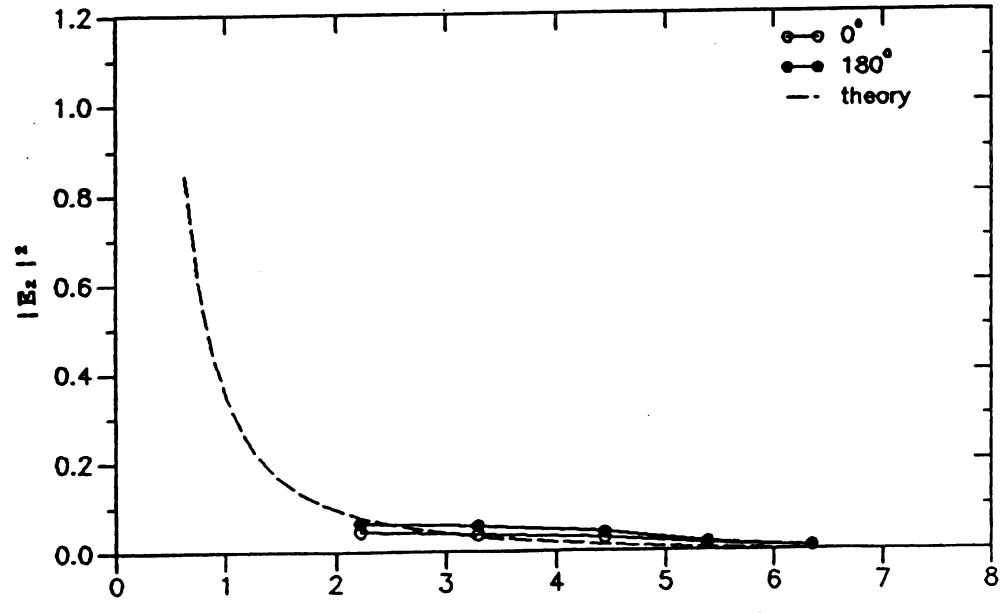

6.10b ρ cm (from the center of cavity)

Figure 6.10 Field patterns for 0.2 cm ethylene glycol, HE_{111} mode , (a) actual magnitude, (b) comparison between theoretical and experimental results.

possible that experimental quality factors are larger than theoretical quality factors. The possible causes of the changes of the experimental field patterns from theory include the perturbation due to the excessive coupling probe depth within the material-loaded cavity, bad contact between the dielectric rod end and the base plate and the bad contact of the fingers around coupling probe with the coupling port.

In the HE_{111} mode experiments with the 1.27 cm nylon rod, the experimental and theoretical results show much differences in Δf's , ΔL_s's quality factors and field patterns. Two explanations may account for the discrepancy. The first is that the coupling probe was extended too deep into the cavity. For instance, as listed in Table 6.2a, L_p in case of 1.27 cm nylon rod was 20.37 mm, which was much longer than the L_p's in the other three cases. The second is the larger access hole on the siding short. In the 1.27 cm nylon rod experiments, the radius of the access hole was 1.27 cm, compared to 0.635 and 0.3 cm in other experiments.

6.3 High power heating measurements

6.3.1 Heating of nylon 66 cylinders

The high power single-frequency measurement technique described in section 5.4.3 was used to heat and diagnose the nylon 66 cylinders of length 3.1 cm and radius 0.65 cm. As is shown in Figure 5.6, the nylon cylinders were placed exactly in the center of a seven-inch cavity excited in TM_{012} mode. In order to measure the internal temperature of the nylon, a fiber-optic temperature probe was inserted axially through a small tight-fitting hole shown in Figure 5.6 into the center of the nylon cylinder. During heating process, each data point of L_s, L_p, P_i, P_r and P_b was taken at one minute intervals. From the measurements, the complex dielectric constant were calculated as described in section 5.4.2 by means of the cavity perturbation formula expressed in equation 5.15.

Variations of the complex dielectric constant as a function of time and temperature are displayed in Figures 6.11 and 6.12, respectively. As shown, the different input powers of 3 and 5 W resulted in different heating cycles. That is, during heating process the complex dielectric constant changes differently for different input powers. As is depicted in Figures 6.11b and 6.12b, nylon changed from a low loss to a very lossy material as heating processed. Also seen is that higher input power gave rise to higher ε_r'' at a given time or at a given temperature. While, as shown in Figure 6.11a and 6.12a, at high temperatures ε_r' dropped and higher input power resulted in smaller ε_r'. The drop of ε_r' at high temperatures during processing was found to be associated with the coupling probe depth within the cavity [97]. The coupling probe was adjusted inward in order to maintain critical coupling as the nylon became lossier during heating. The excessive coupling probe depth within the cavity at high temperatures not only perturbed the nylon loaded cavity but had a nonnegligible influence on the measurements of the empty cavity resonant frequency. Consequently, inaccurate ε_r' was obtained at high temperatures by using the perturbation formula expressed in equation 5.15a.

For comparison, published data [98] is displayed in Figure 6.12a and 6.12b. As shown, below 65° the measured data agrees with published data to within several percent. The decrease of the accuracy at higher temperatures is probably due to the thermal expansion and deformation of the nylon cylinder, changes of the cavity wall temperature, cavity air temperature and humidity, in addition to the effects of the excessive coupling probe depth within the cavity. To fully understand the causes of the inaccuracy of the measured $\hat{\varepsilon}_r$, a careful study of each of the possible factors mentioned above is required. This study is not within the scope of this dissertation.

The heating experiments with the nylon rod demonstrated that the complex dielectric constant can be approximately measured during processing using single mode excitation and cavity perturbation theory. By observing the changes in $\hat{\varepsilon}_r$ or just

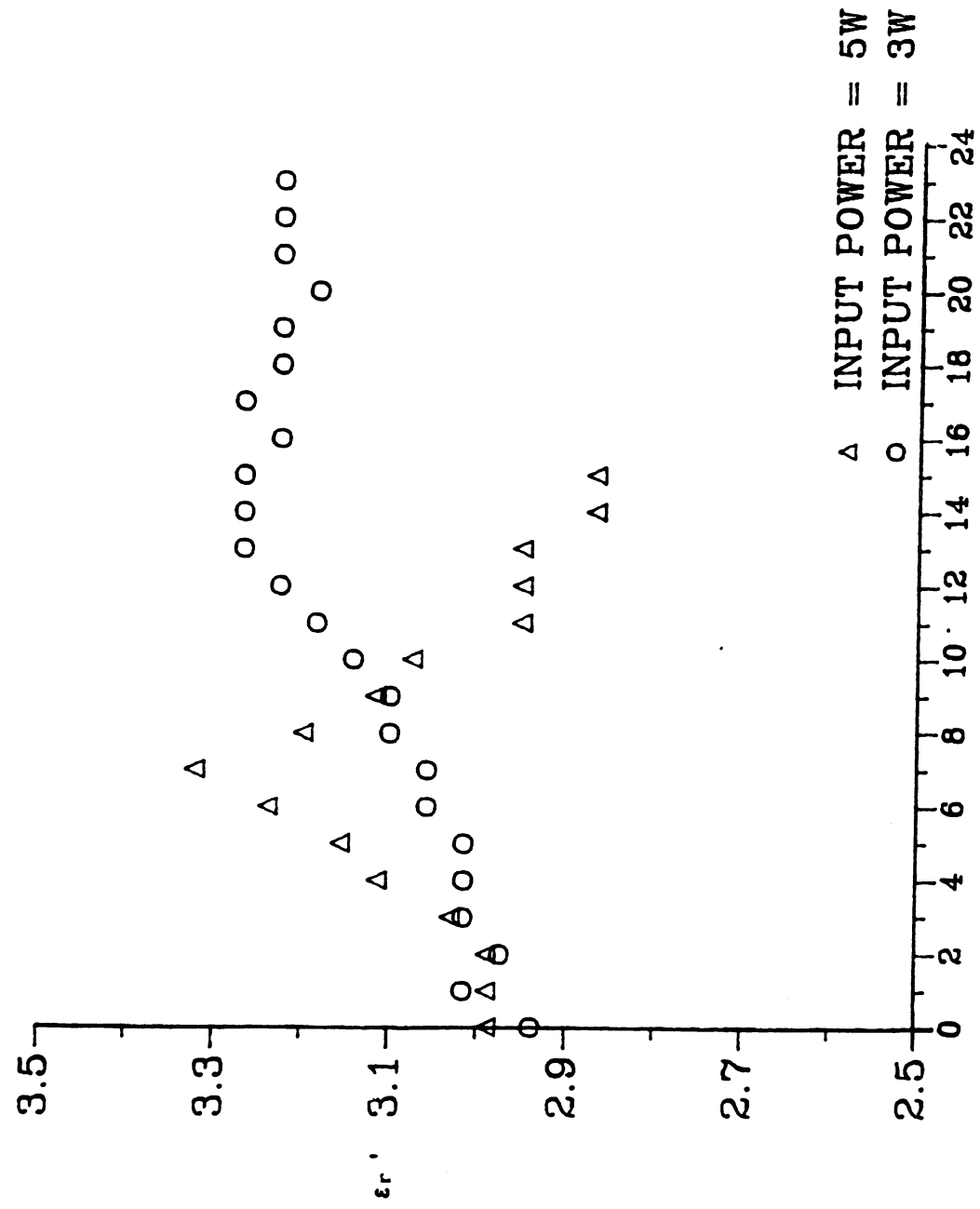

Figure 6.11a ε_r' of nylon 66 versus time

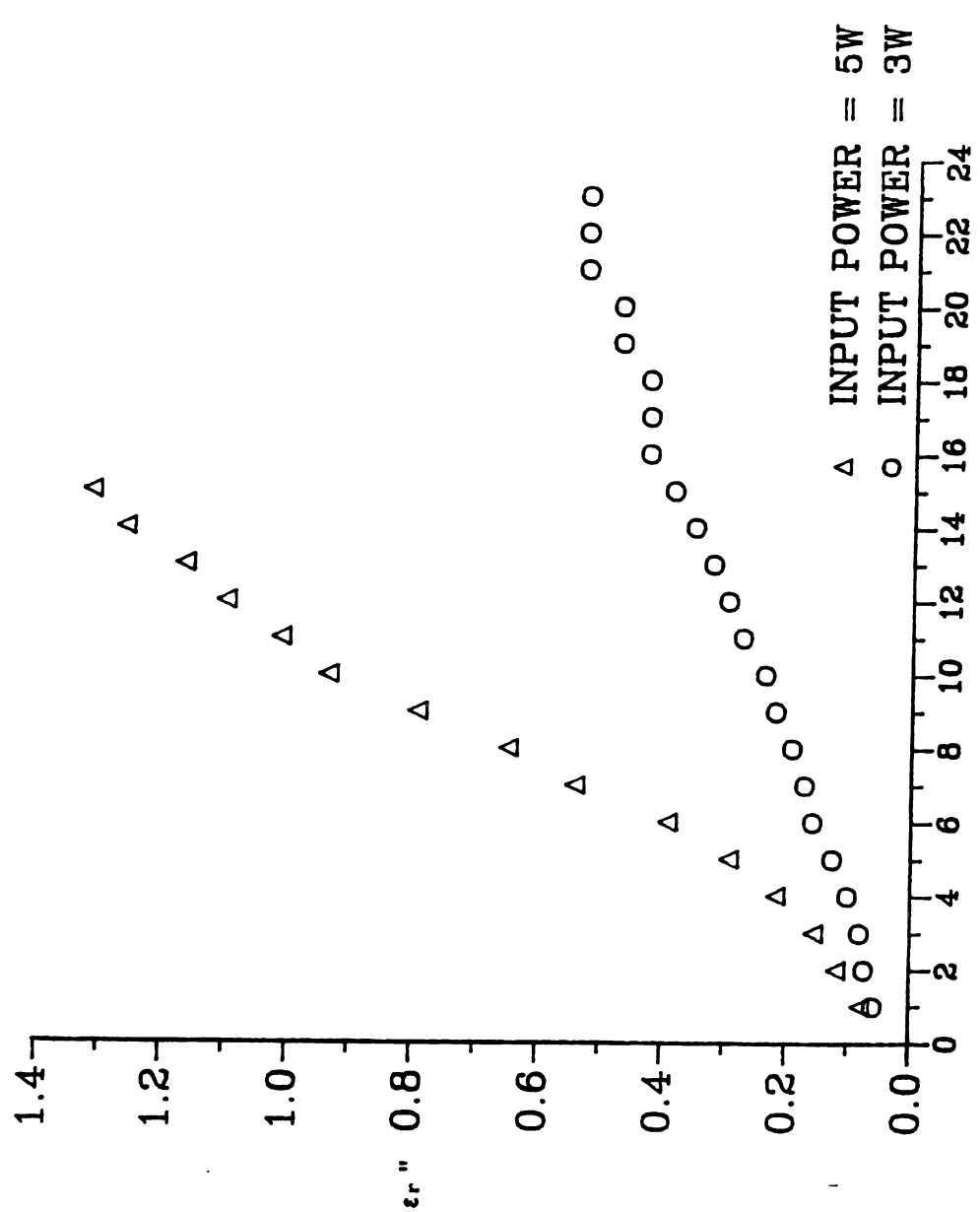

Figure 6.11b ε_r'' of nylon 66 versus time

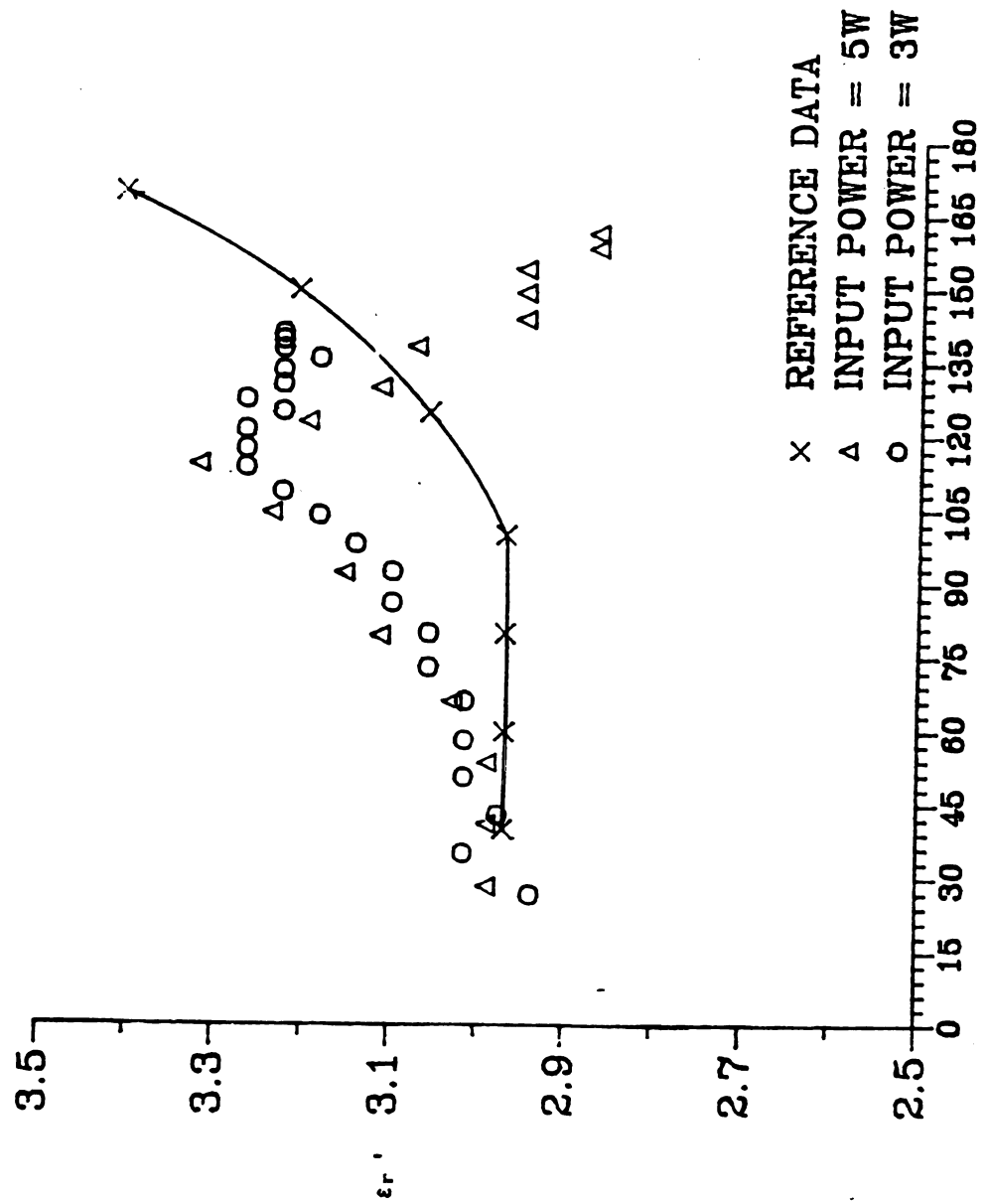

Figure 6.12a ε_r' of nylon 66 versus temperature

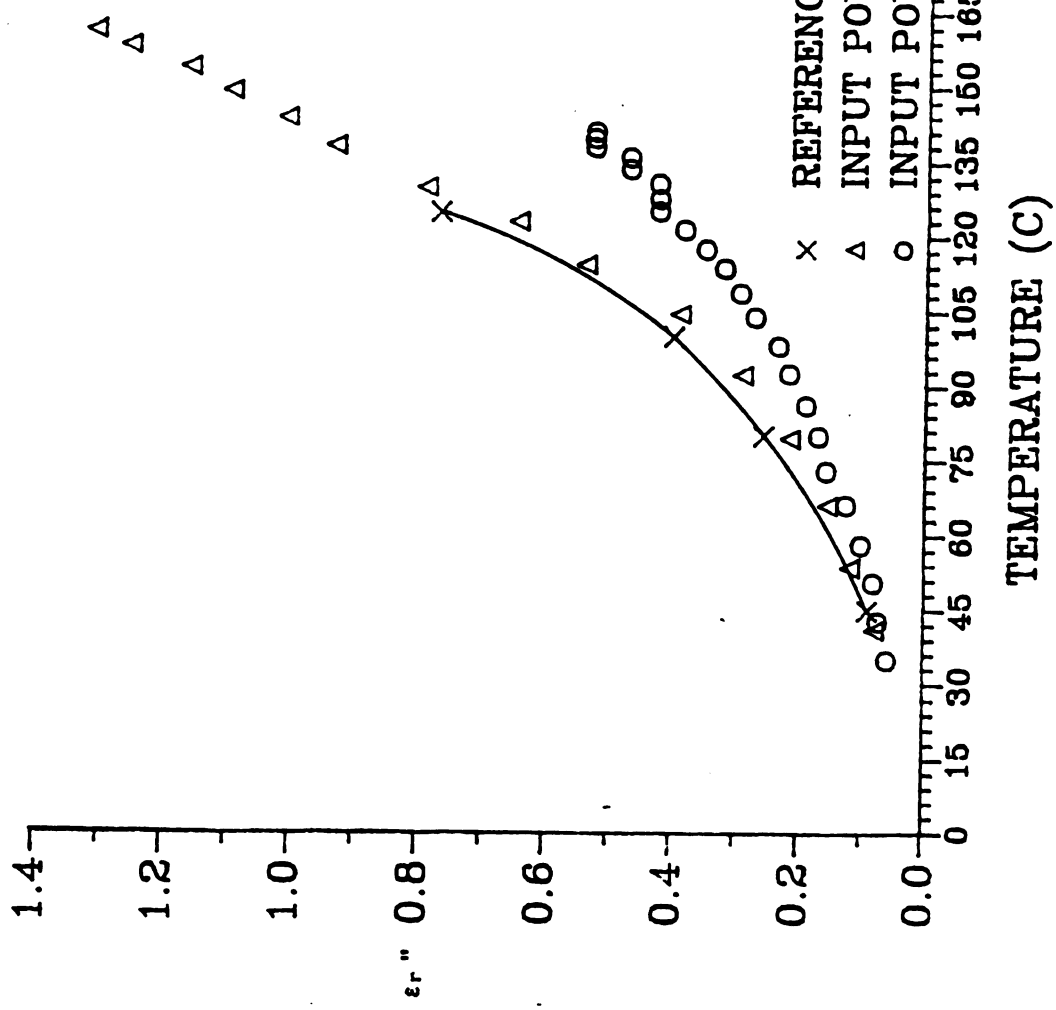

Figure 6.12b ε_r'' of nylon 66 versus temperature

knowing from the experimental measurements of L_s, L_p, P_i, the heating process can be controlled and repeated. This method can be then adopted to build feedback control of the heating process.

6.3.2 Heating of wet wood

Figure 6.13 displays the heating results of water-soaked wood rods of radius 0.455 cm and 3 cm length. By means of the experiment technique described in section 5.4.3, the wet wood heating experiments were conducted with input powers of 5 and 8 W. As is shown, in contrast to the case of nylon rod, ε_r' and ε_r'' of wet wood decreased as heating went on. The decrease of the complex dielectric constant is due to the removal of water from wood while heating. As more water was evaporated, the changes in ε_r leveled out. Hence it is possible to estimate the time when the wet wood is dried by noting the changes in ε_r during processing. As shown, for 5 W input power the wood was dry after 12 minutes. For 8 W input power the wood was dry after 6 minutes and the ε_r is approximately 3.5-j0.3. Again, it is seen different input powers resulted in different heating cycles.

The coupling efficiency of the material loaded cavity is defined as the percent of the input power that is coupled into material. As a result, the coupling efficiency can be expressed as following [97]:

$$\begin{aligned} \text{Eff} &= 100\% \times \frac{P_d}{P_i} \\ &= 100\% \times \left[1 - \frac{Q_u}{Q_{uo}}\right] \end{aligned} \tag{6.1}$$

Where

P_d = power absorbed by the dielectric,

P_i = total power absorbed by the material loaded cavity,

Q_u = unloaded quality factor of the material loaded cavity,

Q_{uo} = unloaded quality factor of the empty cavity.

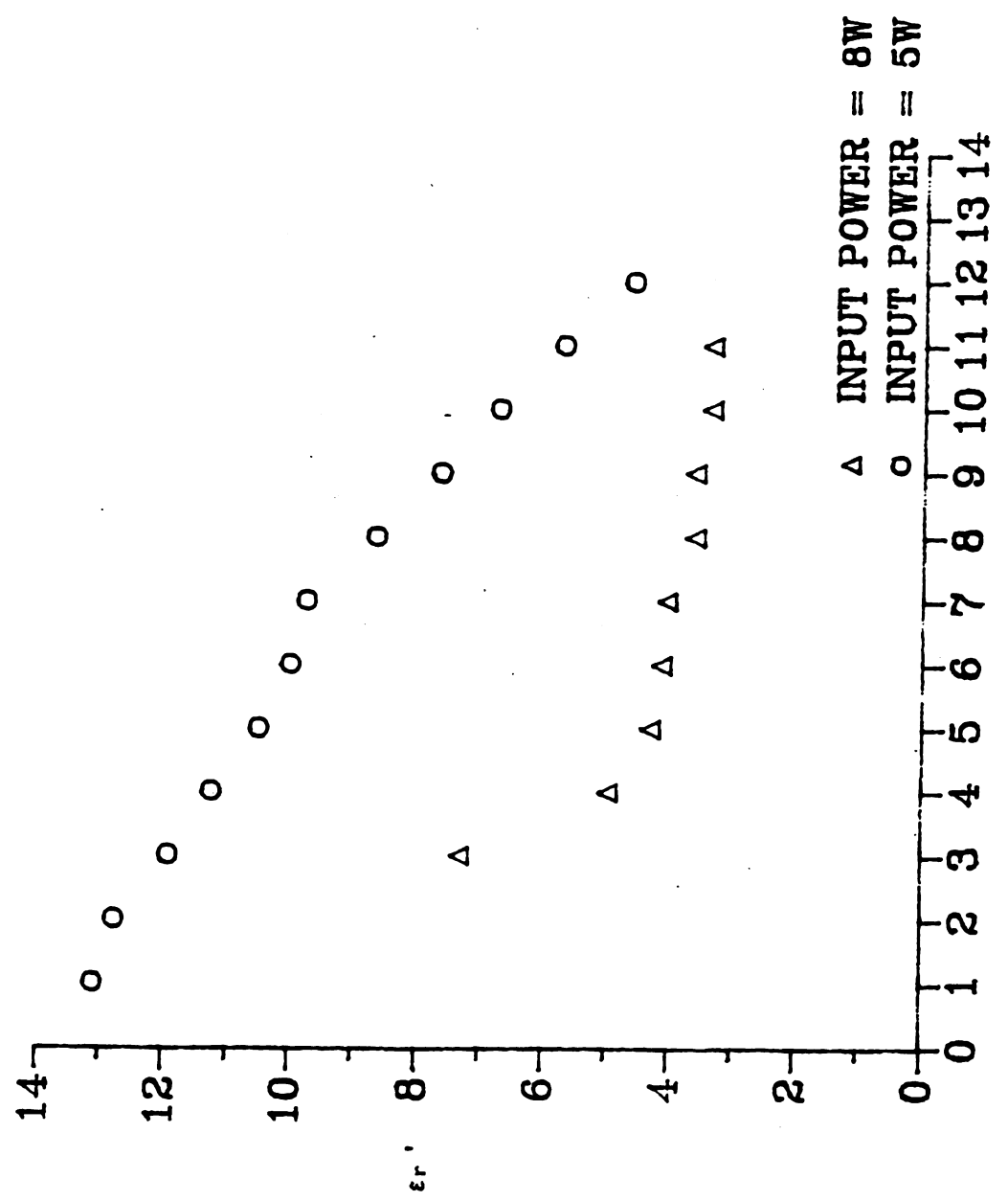

Figure 6.13a ε_r' of wet wood versus time

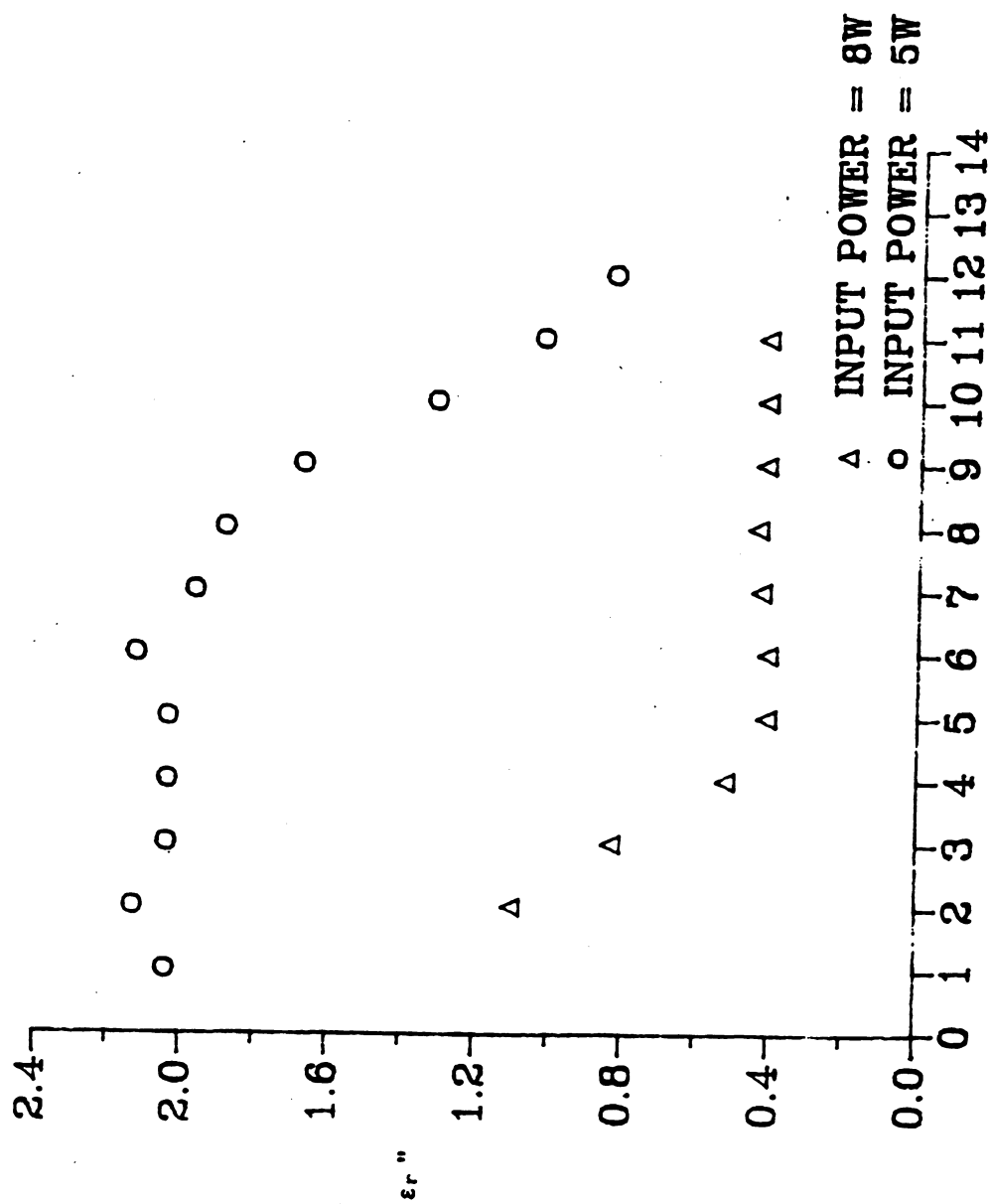

Figure 6.13b ε_r'' of wet wood versus time

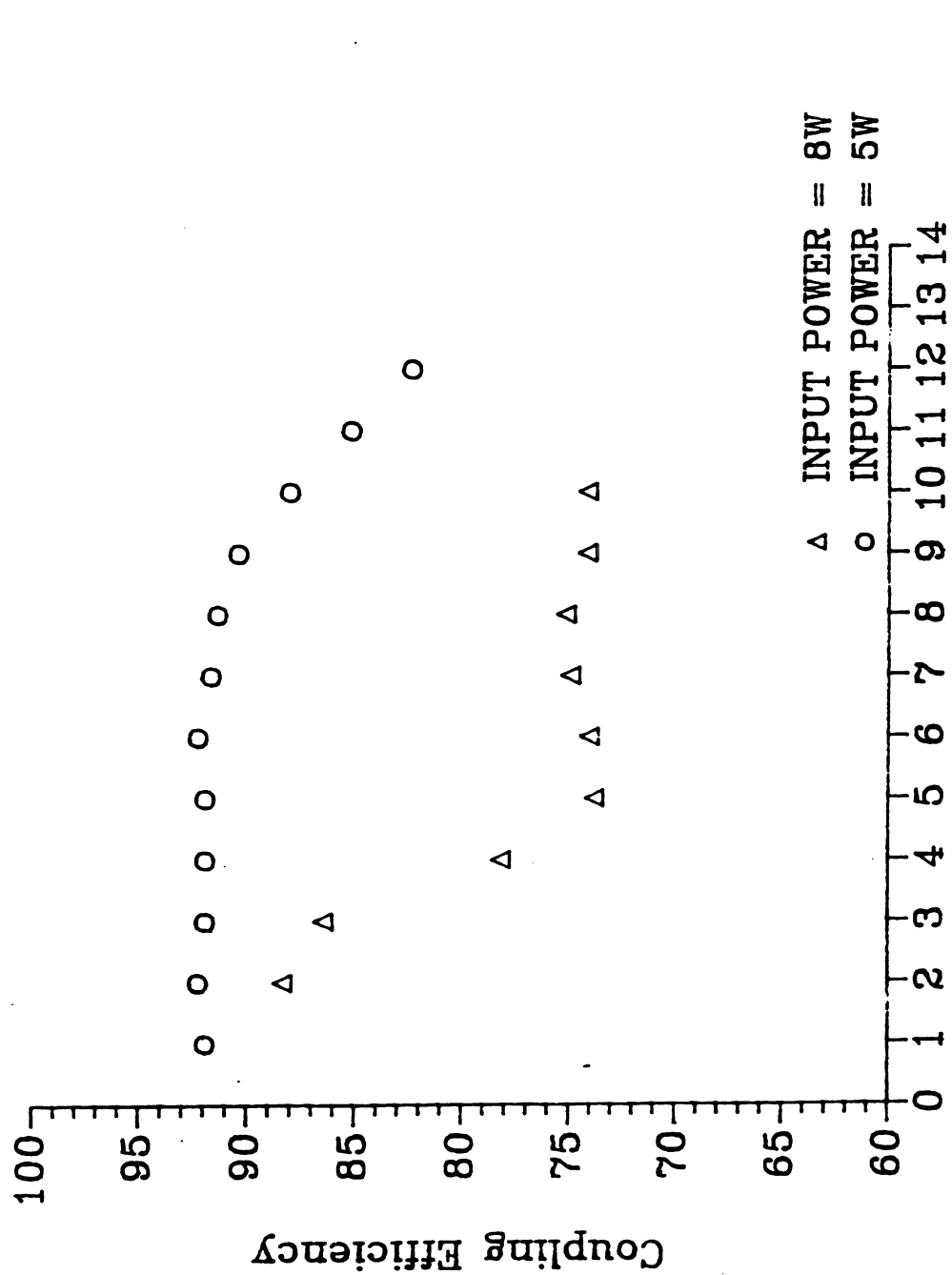

Figure 6.13c Coupling efficiency of wet wood heating versus time

Figure 6.13c shows the coupling efficiency versus time for the wet wood samples. Initially the efficiency was about 90% and then drops to about 70% as heating process continued. It is clear that at constant input power, as drying progressed, the power dissipated in the wood became less, and hence more power was delivered to cavity walls.

6.3.3 Heating of silicon wafer

Three-inch silicon wafers were heated with TE^{m}_{111} mode for a variety of input powers. Note that the superscript 'm' used in the mode designation here and in the later sections is to distinguish the hybrid mode excited in the cavity loaded with slab-shaped materials from the hybrid mode of the cavity loaded with rod-shaped materials and the empty cavity mode, e.g. HE_{111} and TE_{111} in this case. The experimental setup was similar to the one shown in Figure 5.6. The silicon wafer was placed on a teflon ring 1/8 inches above the bottom of the cavity. The center of the wafer was on the cavity axis. The teflon ring caused negligible perturbation to the empty cavity TE_{111} resonance, however, a major perturbation to the cavity was caused by the presence of the wafer. During heating temperatures at two locations were measured by fiber-optic temperature probes. As is shown in Figure 6.14, probe t_1 was on a diameter perpendicular to the axis of the coupling probe and probe t_2 was along the axis of the coupling probe. The temperature probes were placed on the top of the silicon wafer such that the temperatures obtained were the surface temperatures of the wafer. However, these temperature readings probably can represent the "inner" wafer temperature because the wafer is thin and has relatively high thermal conductivity.

Figure 6.14 displays the heating and cooling of the wafer with temperatures at the two locations. Cooling temperatures were obtained by turning off the input power as the heating temperatures reached equilibrium temperatures. As shown, both heating and cooling curves show exponential rise and decay. The rapid heating rate for relatively low power, 5, 7 and 10 W, is significant. Higher input power gives higher

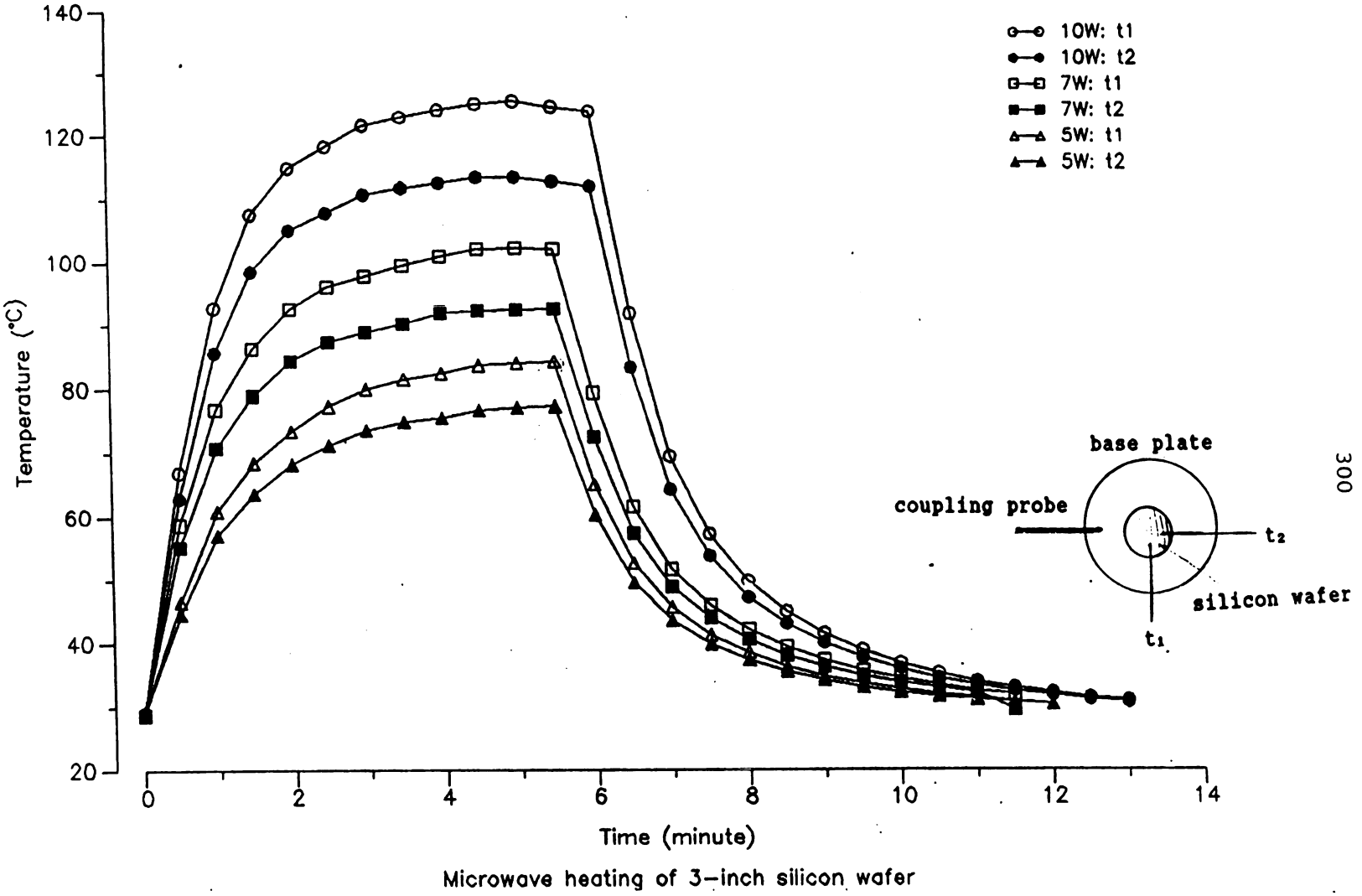

Figure 6.14 Heating of 3-inch silicon wafer, t_1 - perp. to input probe, t_2 - in line with input probe

heating and cooling temperatures. Also seen is that the heating rate is greater on the diameter colinear with the coupling probe. It indicates the heating of the wafer was not uniform. The nonuniformity of the heating is because the field patterns of TE_{111}^{m} mode is not uniform and the possible near zone effects of the coupling probe. Although the heating is nonuniform, it is not as nonuniform as the impressed fields because the good thermal conductivity of the silicon wafer (0.2 cal/cm.sec.degree) helps smooth out this nonuniform heating.

The equilibrium temperatures for 1, 3, 5, 7, 10 and 12 W are shown in Figure 6.15. It appears that the equilibrium temperature of the wafer is linearly proportional to the input power. As expected, higher input power resulted in greater difference between t_1 and t_2.

These experiments demonstrate that single-mode microwave cavity applicator can effectively and rapidly heat semiconducting materials. An equilibrium temperature of 170 C was achieved using moderate 12 W input power in less than 6 minutes. The experiments also demonstrates that the inherent nonuniform heating of the single mode cavity fields can be smoothed out if the processed materials have good thermal conductivity.

6.3.4 Low power and high power heating of graphite reinforced epoxy fiber slabs

These experiments were conducted to study the effects of the graphite reinforced epoxy fiber slab on the field patterns in the cavity applicator as a function of fiber orientation relative to the coupling probe. The microwave heating of the fully cured epoxy-graphite composite materials was also examined. The single-ply graphite reinforced epoxy samples were 8.15x7.5 cm^2 slabs of 2.08 *mm* thick. An alternating-layer slab was made by gluing two identical single-ply slabs together with fiber orientations perpendicular to each other.

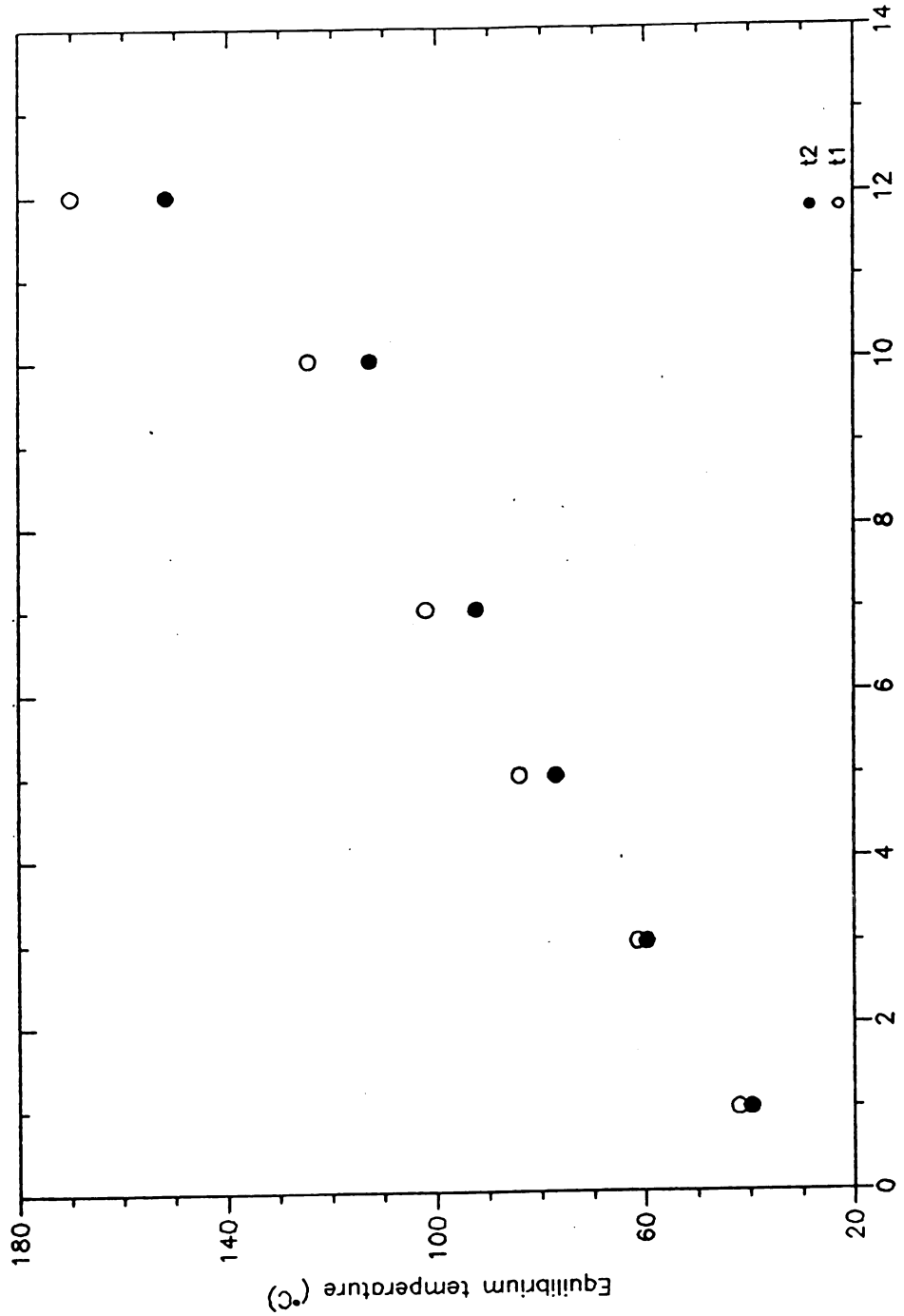

Figure 6.15 Equilibrium temperature versus input power, t_1 - perp. to input probe, t_2 - in line with input probe

A six-inch cavity, as depicted in Figure 6.16, was used in the experiments. As shown, with the diagnostic holes, the radial electric field pattern $|E_\phi|^2$ on the cavity walls can be measured around the cavity circumference and along the cavity axis. TE^m_{111}, TE^m_{211} and TE^m_{112} modes were excited at 2.45 GHz in these experiments. The epoxy-graphite composite was placed either near the top or on the bottom of the cavity for a variety of fiber orientations with respect to the coupling probe. A 1/8 inch teflon ring was used to support the composite sample such that the sample did not contact the conducting surface. Again, the teflon ring itself caused negligible field perturbation to the cavity. Any perturbation to the empty cavity was then considered mainly due to the presence of the composite sample. During heating, temperatures at different locations were measured using a fluoroptic thermometry. The temperature probes were placed underneath the sample such that the temperature readings obtained were the surface temperature of the composite. Field pattern measurements around the circumference of the cavity were made from 0^o to 180^0 to study the field patterns in the cavity and the microwave heating of the composite sample as a function of ϕ. The radial field patterns were measured by inserting a microcoax probe (E-probe) described in section 5.2.2 into the diagnostic holes on the cavity walls. The coupling probe was located at $\phi = 0^o$.

Figure 6.17a shows the comparison of $|E_\phi|^2$ of TE^m_{112} mode around cavity circumference between empty cavity and graphite-epoxy loaded cavity. The sample was placed on the bottom of the cavity and the input power was kept constant at 20 mW. Measurements of the fields were made under critical coupling conditions and at z=2.8 cm height relative to the base plate. As shown, the field patterns for all cases show $\cos\phi$ dependence. Due to the material losses, field intensity in the cavities loaded with composite sample was lower than that of the empty cavity. The field intensity corresponding to the fibers aligned perpendicular to the coupling probe was reduced much more than that corresponding to fibers aligned to the coupling probe.

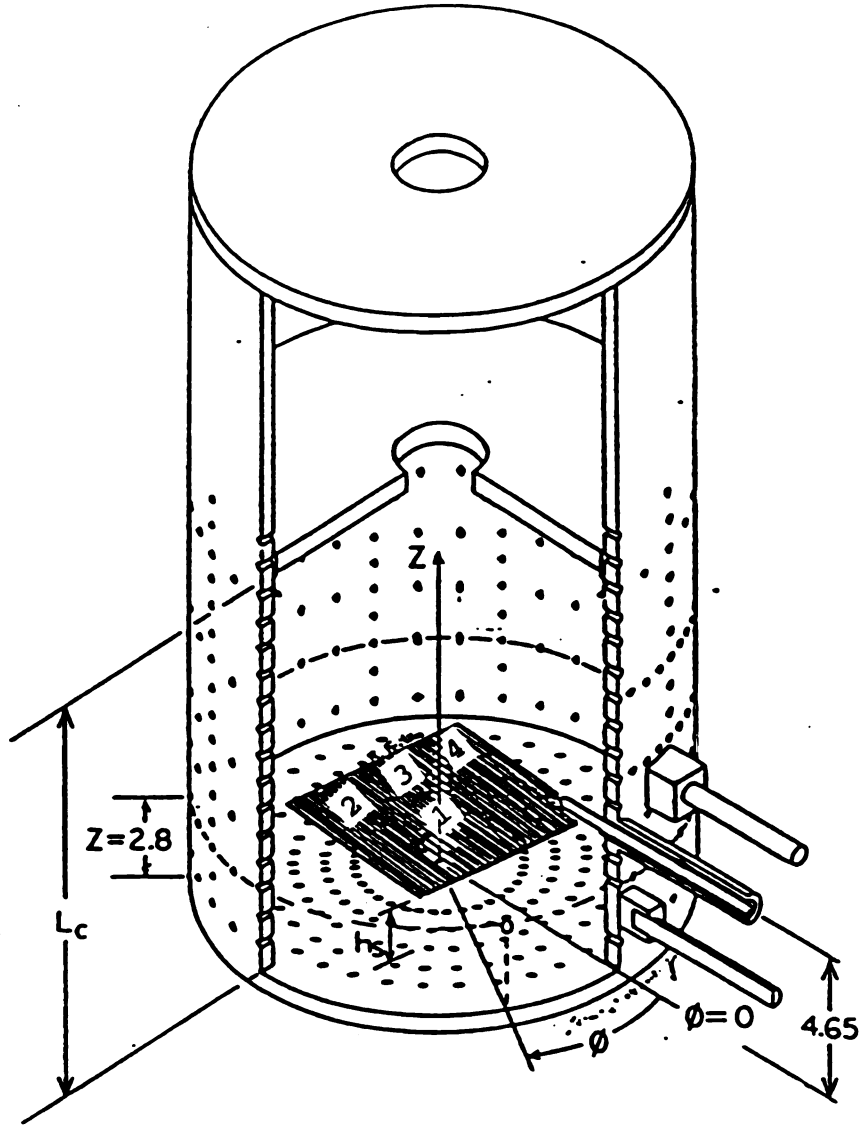

Figure 6.16 Six-inch cavity loaded with graphite-epoxy slab

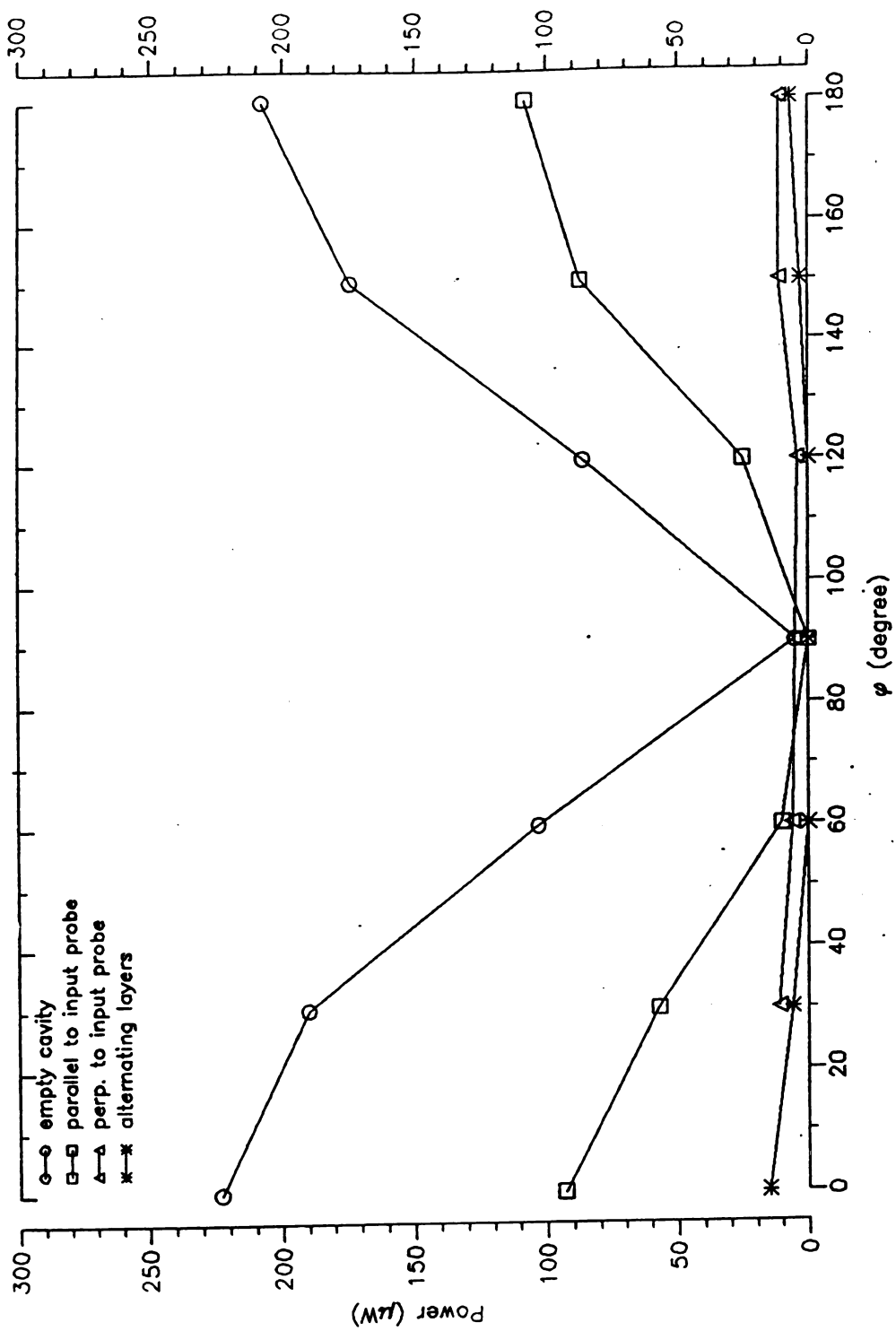

Figure 6.17a Radial electric field versus φ at z = 2.8 cm, TE^{m}_{112} mode, graphite-epoxy slab on bottom of cavity.

It indicates that more microwave power was absorbed by the sample with fibers perpendicular to the coupling probe. Hence, for constant input power, the quality factor of the graphite-epoxy loaded cavity with fibers perpendicular to the coupling probe is the lowest among all cases shown in Figure 6.17a. In other words, better microwave energy coupling into the graphite-epoxy composite can be achieved when the fibers are oriented perpendicular to the coupling probe.

Figure 6.17b depicts the field patterns of the TE_{112}^{m} mode measured at axial position of z=4.65 cm, with the sample positioned on the top of the cavity. As shown, the field patterns still have $\cos\phi$ dependence, and the power readings are larger with fibers aligned to the coupling probe than with fibers perpendicular to the coupling probe. When the composite sample was placed with fiber oriented 45° relative to the coupling probe, the field patterns were shifted about 45° from those with fibers aligned or perpendicular to the coupling probe. However, the patterns still show sinusoidal behavior. Obviously, the change of the fiber orientation rotated the field patterns.

Low power microwave heating experiments were performed using several hundred milliwatts input power. The sample was place on the bottom of the cavity. Figures 6.18a and 6.18b depict the equilibrium temperatures of the graphite-epoxy sample for TE_{112}^{m} and TE_{211}^{m} modes, respectively. As shown in Figure 6.16, equilibrium temperatures were measured at four different locations on the sample surface. It is seen that the same equilibrium temperatures could be achieved using lower incident power when the fibers were perpendicular to the coupling probe. Apparently, much better EM energy coupling into sample can be obtained as the graphite fibers were oriented 90° to the coupling probe. Also found in Figures 6.18a and 6.18b is that the heating is nonuniform. In addition to the near zone effects of the coupling probe and the nonuniform field patterns, the influence of the anisotropic dielectric properties of the graphite composite on the electromagnetic fields may also be one of the causes of the nonuniform heating.

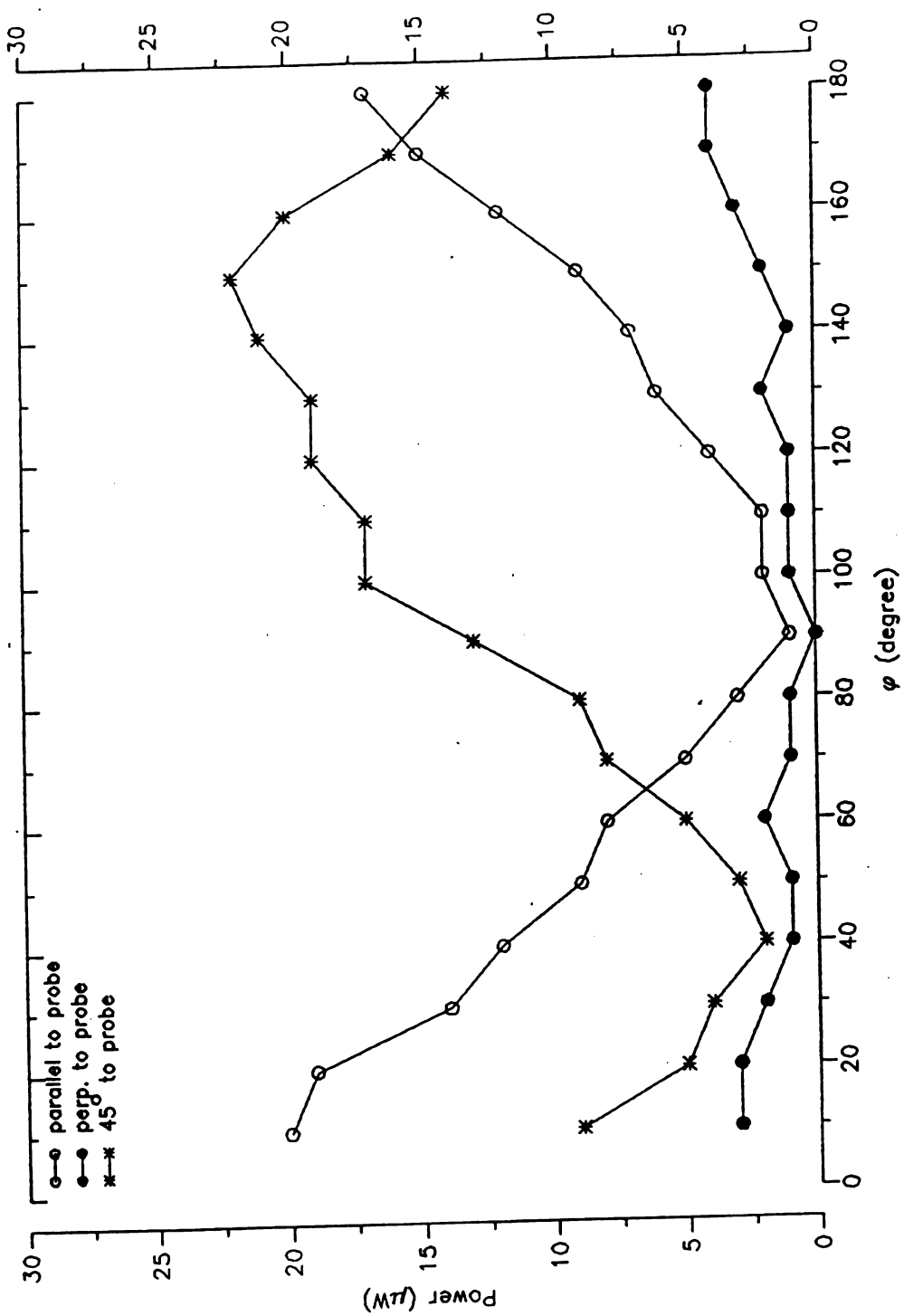

Figure 6.17b Radial electric field versus ϕ at z = 4.65 cm, TE^{m}_{112} mode, graphite-epoxy slab on top of cavity.

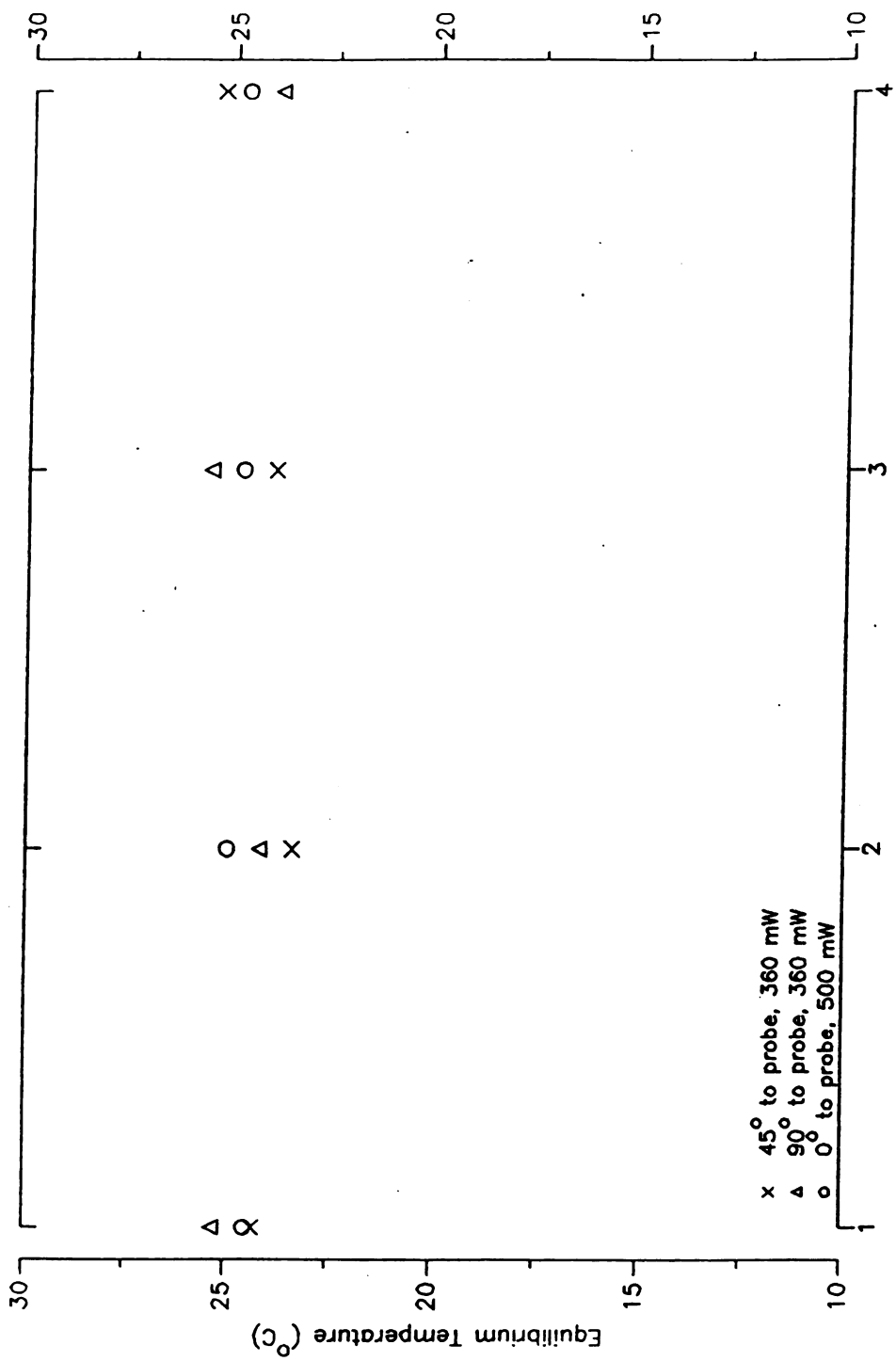

Figure 6.18a Equilibrium temperature versus temperature position, TE^{m}_{112} mode, graphite-epoxy slab on bottom of cavity.

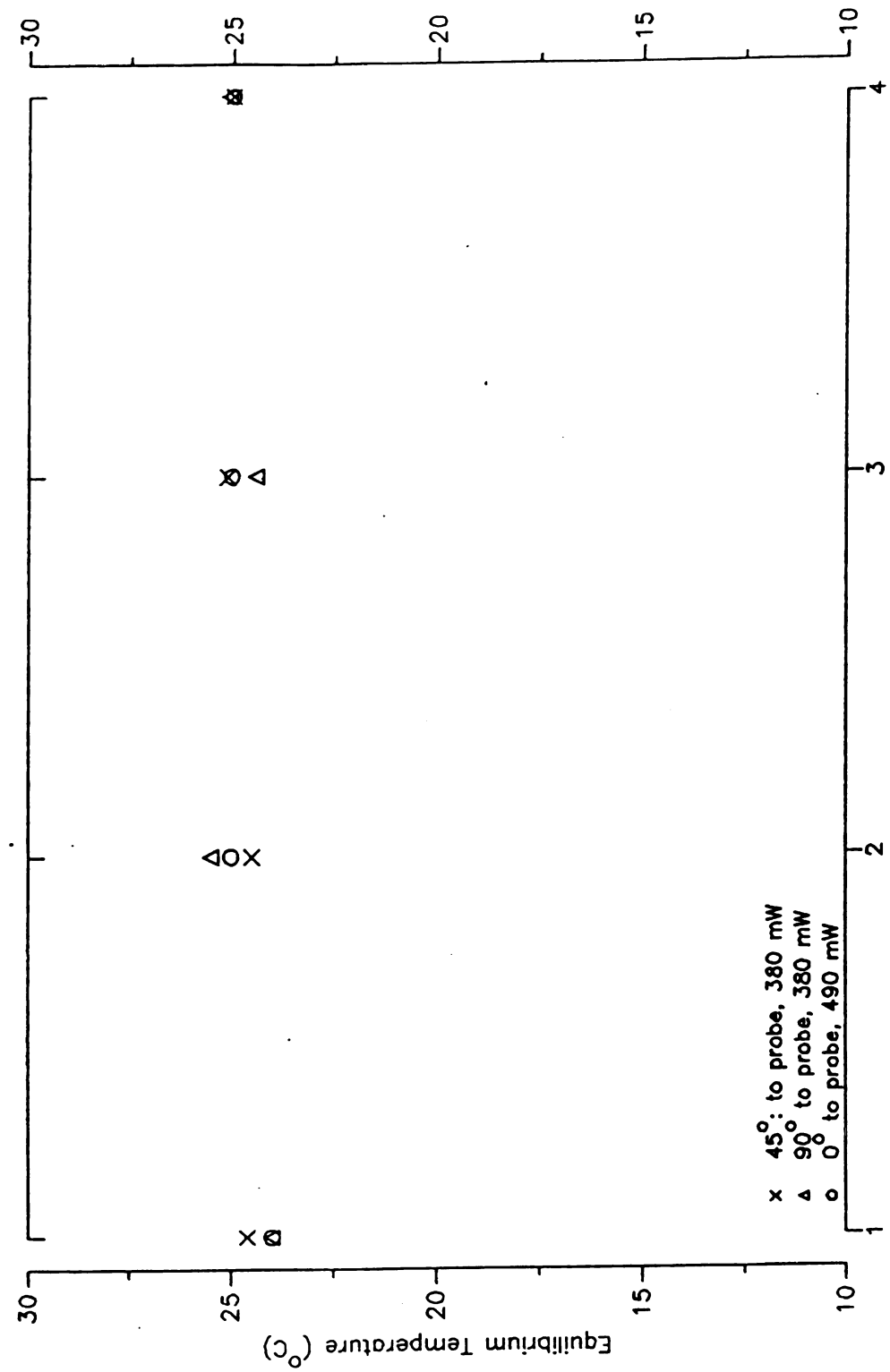

Figure 6.18b Equilibrium temperature versus temperature position, TE^{m}_{211} mode, graphite-epoxy slab on bottom of cavity.

High power heating experments of the graphite-epoxy composite were performed to demonstrate the variation of heating temperature as a function of time for different input powers and fiber orientations. The graphite reinforced fiber epoxy slab was placed on a teflon ring 1/8 inch above the bottom the cavity such that the sample was not in contact with the conducting bottom plate. Heating was conducted using TE^{m}_{111} mode. Similar to the silicon wafer experiments, temperature readings were taken at two different locations on the top of the sample and recorded at 30 seconds interval.

The 5 W experiments is depicted in Figure 6.19a. It is intriguing to see that even at a constant input power, different fiber orientations relative to coupling probe gave rise to different heating cycles. As shown, when fibers were oriented perpendicular to coupling probe, higher heating temperatures were resulted. As disclosed in the low power heating experiments, the heating was not uniform. Interestingly, t_1 was larger than t_2 as fibers were aligned with coupling probe, while the opposite was found as fiber orientation was 90° relative to the coupling probe. Figure 6.19b shows the temperature vs time curves for the 5 and 10 W experiments, where the fibers were perpendicular to coupling probe. As shown, different input powers resulted in different heating cycles. Consequently, for the graphite reinforced epoxy slabs, the heating cycle is not only determined by the input power level but the fiber orientation relative to coupling probe as well.

According to the above experiments, it is found that the sinusoidal pattern of $|E_\rho|^2$ along the circumference of the cavity will not change with the fiber orientation. But the rotation of the sample (the fiber orientation) will cause a shift of the radial electric field pattern in ϕ direction. The quality factor of the cavity loaded with the graphite-epoxy composite is lower with fibers perpendicular to the coupling probe than with fibers aligned with the coupling probe. As a result, better microwave energy coupling into the composite sample, and hence more efficient microwave heating, can be achieved when the fibers of the composite are perpendicular to the coupling probe.

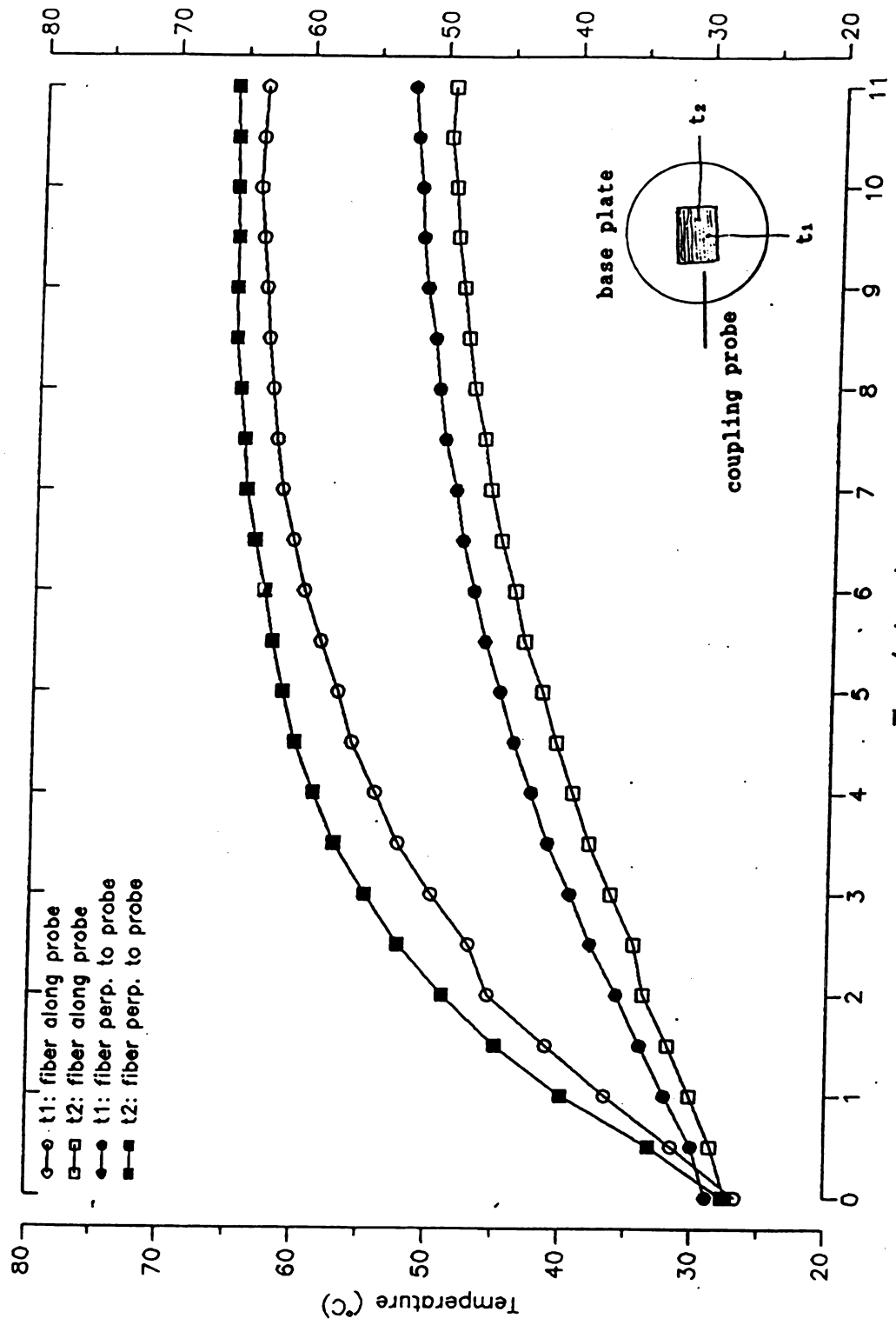

Figure 6.19a Temperature versus time, input power = 5 W.

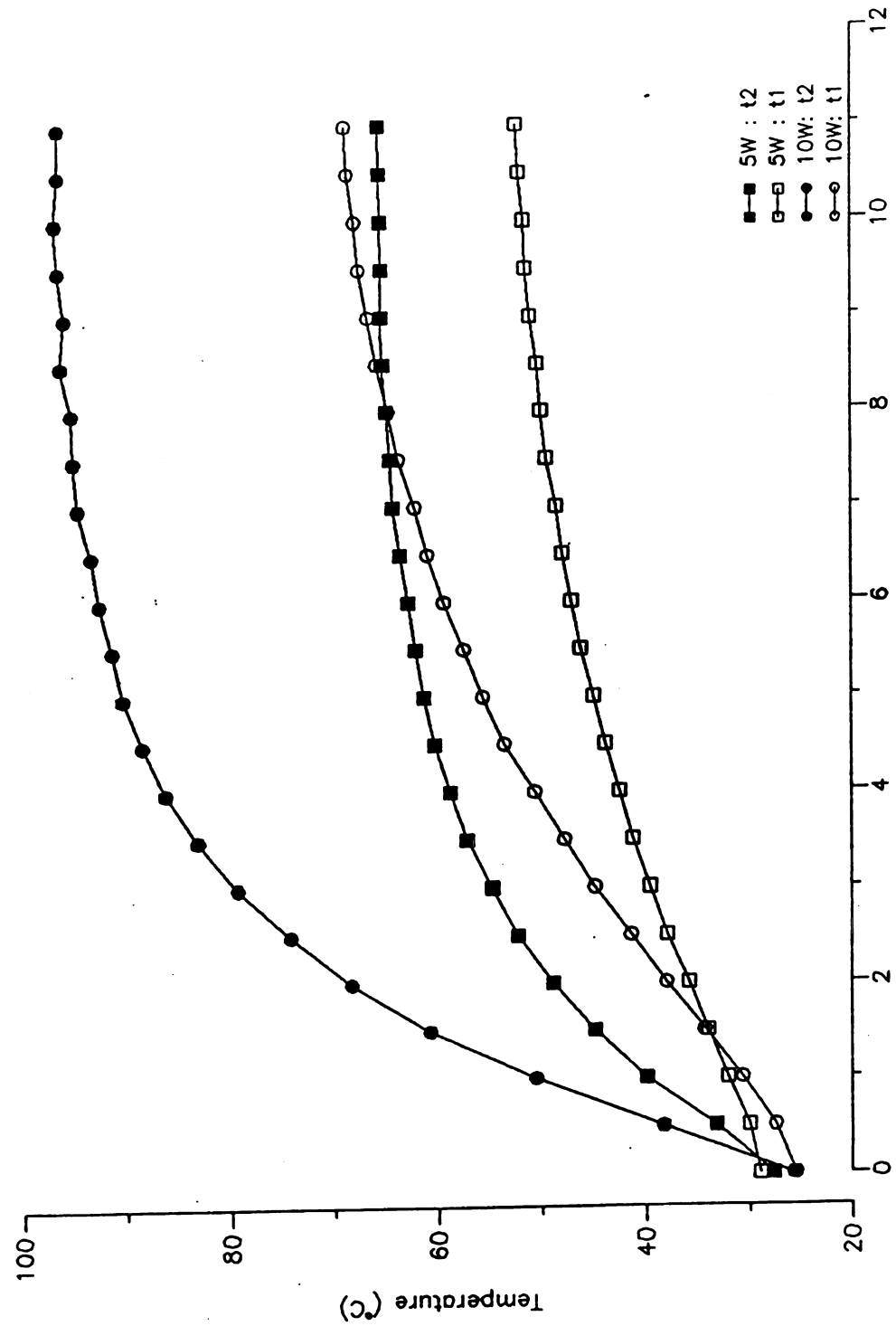

Figure 6.19b Temperature versus time, fiber orientation is perpen. to input probe, t_1 - perpen. to input probe, t_2 - in line with input probe.

6.3.5 Discussion

The heating experiments with nylon and wet wood rods demonstrate high efficiency microwave heating and the on-line measurements of the approximate complex dielectric constant by means of perturbation formula, using single mode microwave cavity. These experiments are controllable and repeatable based on the empirical measurements or by observing the changes in ε_r.

In addition to the regular lossy dielectric materials, the silicon wafers and graphite-epoxy slabs heating experiments demonstrate that the cavity applicator can be used for rapid heating of semiconducting and composite materials. The heating nonuniformity resulted from the nonuniform field patterns can be smoothed out if good thermal conducting materials are processed.

In the graphite-epoxy slab experiments, it has been found that the heating cycle is determined by the input power as well as the orientation of the graphite fibers. As the fibers were oriented perpendicular to the input probe, better microwave energy coupling into the composite samples, and hence better microwave heating, was achieved. The low power experiments with the graphite epoxy composite demonstrate that the shift of the fiber orientation will not change the overall field patterns but causes a shift of the patterns in ϕ direction.

Chapter 7

SUMMARY AND RECOMMENDATIONS

7.1 Summary of results

7.1.1 Theoretical formulation and numerical analysis

The theoretical formulation of a cylindrical cavity loaded with lossy dielectric material was derived. As a central part of the material loaded cavity problem, the classical EM analysis of the homogeneous and coaxially loaded waveguides was reviewed. By means of the mode-matching method, the cavity characteristic equations for cavity-open, cavity-image and cavity-short types, as shown in Figure 1.1, were derived. In addition, a detailed derivation of the stored energy, power absorbed in the lossy dielectric materials and conducting walls and quality factors was presented.

The propagation characteristics, i.e. $\omega - \beta$ and $\omega - \alpha$ diagrams, of a coaxially loaded waveguide were studied numerically as a function of ε_r'' for eight selected waveguide modes. In addition to the $\omega - \beta$ and $\omega - \alpha$ diagrams, the electromagnetic field patterns were investigated for a wide range of ε_r', ε_r'' and rod radius for TM_{01}, TE_{01} and HE_{11} modes. Both slow waves and fast waves were identified in the $\omega - \beta$ diagrams. Whether a waveguide mode is a slow wave or a fast wave is determined by the excitation frequency and the complex dielectric constant and radius of the dielectric rod. It has been shown for slow waves most of the electromagnetic energy is confined in the dielectric rod region. Consequently, efficient microwave heating can be achieved if the electromagnetic mode is excited as a slow wave in the coaxially loaded waveguide region. The selection of the operating frequency and size of the cavity radius and the radius of the dielectric material are major factors of determining the efficiency of microwave coupling and hence microwave heating.

The resonant frequency, resonant length and quality factors of the cavity loaded with lossy dielectric rods were examined numerically as a function of the complex

dielectric constant and the size of the load material for the cavity-short type shown in Figure 3.5. TM_{012}, TE_{011} and HE_{111} modes were considered in these numerical examples. The perturbation formula using quasi-static approximations to the electromagnetic fields within the load material was compared with the exact solutions for TM_{012} mode. The overall quality factor was expressed in terms of the quality factors due to the dielectric losses and conducting wall losses. As expected, for very low loss dielectric material, the overall quality factor is determined by the cavity wall quality factor. As the dielectric rod gets lossier, the quality factor due to the dielectric losses becomes dominant and hence the overall quality factor is determined by the dielectric losses. The study of the quality factors as a function of ε_r'' for a given ε_r' for TM_{012}, TE_{011} and HE_{111} modes has shown that a mode that has lowest Q at small ε_r'' and hence is best for microwave heating for low loss material may not be adequate for heating as material load becomes very lossy. That indicates mode switching may be required to achieve best microwave heating as ε_r'' of the load material changes during processing.

7.1.2 Experimental verification of theory and microwave heating of materials

Two experimental systems, low power and high power systems, were introduced in this research work. An automatic data acquisition scheme using a data acquisition board and a microcomputer was developed for the high power heating system. Experiments conducted with the low power systems were used to verify the theory and to investigate the effects of the anisotropic dielectric materials, e.g. graphite reinforced epoxy slabs, on the electromagnetic field strength and patterns. The high power heating experiments were performed to demonstrate the use of single-mode circular cylindrical resonant cavity applicator as a microwave heating device.

7.1.2.1 Low power experiments

The low power verification measurements of the resonant frequency, resonant length, quality factor and field patterns for TM_{012} and HE_{111} modes were compared with

the theoretical computations of Chapter 4. Load materials included nylon and teflon rods with radii of 0.635 cm and 1.27 cm, and a 0.2 cm inside radius quartz tube containing ethylene glycol.

Except for the 1.27 cm nylon rod in HE_{111} mode, the computed resonant frequency, Δf, resonant length, ΔL, and the axial field patterns near the end plate show very good agreement with the experimental measurements with error percentages of less than 10%. The mismatch between the experimental and theoretical results for the 1.27 cm nylon rod in HE_{111} mode was probably due to the perturbation of the coupling probe and the access hole to the cavity resonance. It is seen that the theoretical quality factors do not agree with the experimental measurements. The explanations for the disagreement are the possible measurement errors and the nondieal structure of the cavity applicator such as the presence of the coupling probe and access hole.

In the low power experiments with the graphite-epoxy composite, it is found that the rotation of the fiber orientation relative to the coupling probe caused a shift of the radial electric field patterns in ϕ direction but the sinusoidal ϕ variation of the field patterns remained unchanged. In addition, at a constant input power, the orientation of the fibers affects the radial electric field strength near the conducting walls, and hence the Q of the material loaded cavity. The electric field intensities measured with fibers aligned perpendicular to the coupling probe were smaller than those measured with fibers alinged and 45^o relative to the coupling probe. The experimental results indicate that better microwave coupling into the lossy composite material was achieved with the fibers oriented 90^o to the coupling probe. That is better microwave heating was obtained with the fibers perpendicular to the impressed electric field.

7.1.2.2 High power heating experiments

The microwave heating experiments demonstrated that single-mode cylindrical cavity applicator can be used for efficient and fast microwave heating of regular

dielectric materials, semiconducting materials and composite materials. Load materials employed in the heating experiments included isotropic materials such as nylon 66 cylinders, water-soaked wood cylinders and three-inch silicon wafers and anisotropic materials such as graphite reinforced epoxy slabs.

The heating experiments with nylon and wet wood cylinders have demonstrated the ability of on-line diagnosis of the complex dielectric properties of materials during processing. The on-line measurement of the complex dielectric constants [96] provides a method of process monitoring to yield processed materials with desired dielectric properties. The heating of wet wood cylinder experiments have shown high coupling efficiencies in excess of 80% using single-mode cylindrical cavity applicator with 8 W input power.

The heating experiments with silicon wafer have shown that the equilibrium temperature is linearly proportional to the input power. 170°C equilibrium temperature was achieved for 12 W input power. The heating and cooling temperature curves show exponential rise and decay, respectively. The temperature measurements at two different locations on the surface of the silicon wafers reveal that microwave heating using single-mode microwave applicator is not uniform. The temperature differences between the two locations were 20°C (11%) for 12 W input power and about 4°C (10%) for 1 W input power.

In the experiments with graphite reinforced epoxy slabs, it is found that the graphite fiber orientation has important influence on the heating temperatures and patterns. The heating temperatures obtained with the graphite fibers 90° relative to the coupling probe were higher than the temperature measured with the graphite fibers aligned with the coupling probe. Hence better microwave heating was achieved if the fibers were oriented perpendicular to the coupling probe. The heating results also show nonuniform patterns. In addition to the input power, it is found that fiber orientation relative to the coupling probe also affects the heating cycle.

7.2 Recommendations

7.2.1 Theory

In previous research [97] it has been demonstrated that the power losses due to the coupling probe were small compared to the losses due to the load material. Hence the overall quality factor would not be influenced much by the exclusion of the quality factor due to the coupling probe in the theoretical model. However the comparison of the theoretical and experimental results for the HE_{111} cavity loaded with 1.27 cm nylon rod in section 6.2 discloses that the major disagreement between the theory and experiments is due to presence of the coupling probe. Because of the near zone effects of the coupling probe, the actual field patterns deviated from the theoretical patterns and thus inaccurate theoretical results of the resonant frequency, resonant length and quality factors were obtained. Hence, It is important to include the coupling probe in the theoretical analysis to account for the near zone effects on the field patterns to improve the accuracy of the theoretical model. The near zone effects may also be reduced by designing a cavity where the near fields of the coupling probe is far from the load material. The quality factor due to the coupling probe should be included in the overall quality factor to increase the accuracy of the theoretical results.

7.2.2 Experiments

Experiments have shown efficient and fast microwave heating of low loss to lossy (conducting) materials. The inherent nonuniform heating using single-mode microwave cavity applicator is the major problem of microwave heating. The nonuniform heating is due to the nonuniformity of the field patterns of microwave cavity resonant modes. Different resonant modes have distinct field distributions and none of them are uniform everywhere in the cavity. Previous works [97] have shown that heating uniformity can be accomplished by placing small load material in the proper position in the single-mode exciting mode fields. For example, a cylinder-shaped load

material placed in the center of a cavity could be heated uniformly in TM_{012} mode, provided the length of the cylinder is less than one quarter guide wavelength. However this method imposes a limitation on the load size. To process materials of larger size uniformly, the cavity size has to been scaled up and the operating frequency is decreased, i.e. for example, a 18" - 915 MHz cavity system. That allows heating of larger size of material load.

One method is proposed in this dissertation to achieve uniform heating without the limitation on the size of the load material.

Mode switching technique

The idea of mode switching is to select some resonant modes that their resultant heating patterns are uniform. During microwave heating, each of the selected modes is excited alternately by switching the excitation frequency of the power source to the associated resonant frequency at a constant switching rate. The cavity length is kept constant in the heating experiments. Idealy the heating will be uniform if the heating modes are properly selected.

Another method of mode switching is to keep the excitation frequency of the power source constant but to change the resonant length from one mode to another alternately while processing. However changing the cavity resonant length mechanically at a fast rate is much more difficult than changing the excitation frequency electronically. Mode switching technique by means of changing excitation frequency is more feasible.

APPENDIX A

FORMULAS FOR EVALUATING THE MATRIX ELEMENTS OF EQUATION 3.102

The formulas for evaluating the the inner products that are defined in equations 3.95a, 3.95b, 3.98c and 3.98d are given in the following equaitons. The matrix elements of equation 3.102 are obtained by substituting these inner products into equations 3.100a through 3.100d. In the following equations the superscript "*" represents complex conjugate.

(I) Nonrotationally symmetric modes ($n \neq 0$)

$$< \hat{E}_i , \hat{e}_j^{TM} > = (\frac{\pi}{2}\nu^*)(\frac{1}{|\omega|^2\hat{\epsilon}\epsilon_1})(\kappa_\rho\kappa_{\rho_1}) \left\{ \left[\tilde{I}^m_{n+1}(\gamma - \alpha\frac{\mu_1}{\mu_0} + \tilde{I}^m_{n-1}(\gamma + \alpha\frac{\mu_1}{\mu_0}) \right] \right.$$

$$+ (\frac{\kappa_{\rho_1}}{\kappa_{\rho_2}}) \left\{ \gamma \left[(A_n(I^m_{n-1} + I^m_{n+1}) - B_n(f^m_{n-1} + f^m_{n+1}) \right] \right.$$

$$\left. \left. + \frac{\mu_2}{\mu_0}\alpha \left[C_n(I^m_{n-1} - I^m_{n+1}) - D_n(f^m_{n-1} - f^m_{n+1}) \right] \right\} \right\} \qquad \text{(A1)}$$

$$< \hat{E}_i , \hat{e}_j^{TE} > = \frac{\pi}{2}(\frac{1}{j\omega\hat{\epsilon}_1})(\kappa_\rho{}'\kappa_{\rho_1}) \left\{ \left[\tilde{I}^e_{n-1}(\gamma + \alpha\frac{\mu_1}{\mu_0}) - \tilde{I}^e_{n+1}(\gamma - \alpha\frac{\mu_1}{\mu_0}) \right] \right.$$

$$+ (\frac{\kappa_{\rho_1}}{\kappa_{\rho_2}}) \left\{ \gamma \left[A_n(I^e_{n-1} - I^e_{n+1}) - B_n(f^e_{n-1} - f^e_{n+1}) \right] \right.$$

$$\left. \left. + \alpha\frac{\mu_2}{\mu_0} \left[C_n(I^e_{n-1} + I^e_{n+1}) - D_n(f^e_{n-1} + f^e_{n+1}) \right] \right\} \right\} \qquad \text{(A2)}$$

$$< \hat{H}_i , \hat{h}_j^{TM} > = \frac{\pi}{2}(\kappa_\rho\kappa_{\rho_1}) \left\{ \left[\tilde{I}^m_{n-1}(1 - \frac{\alpha\gamma}{\omega^2\mu_0\hat{\epsilon}_1}) + \tilde{I}^m_{n+1}(1 + \frac{\alpha\gamma}{\omega^2\mu_0\hat{\epsilon}_1}) \right] \right.$$

$$+ \left(\frac{\kappa_{\rho_1}}{\kappa_{\rho_2}}\right)\left\{\left(\frac{\hat{\varepsilon}_2}{\hat{\varepsilon}_1}\right)\left[A_n(I^m_{n-1} + I^m_{n+1}) - B_n(f^m_{n-1} + f^m_{n+1})\right]\right.$$

$$\left. - \left(\frac{\alpha\gamma}{\omega^2\mu_0\hat{\varepsilon}_1}\right)\left[C_n(I^m_{n-1} - I^m_{n+1}) - D_n(f^m_{n-1} - f^m_{n+1})\right]\right\}\right\} \tag{A3}$$

$$< \hat{H}_i \, , \, \hat{h}^{TE}_j > = \frac{\pi}{2}\left(\frac{1}{j\omega^*\mu}\right)(\nu^*\kappa_\rho{}'\kappa_{\rho_1})\left\{\left[\tilde{I}^e_{n-1}\left(1 - \frac{\alpha\gamma}{\omega^2\mu_0\hat{\varepsilon}_1}\right) - \tilde{I}^e_{n+1}\left(1 + \frac{\alpha\gamma}{\omega^2\mu_0\hat{\varepsilon}_1}\right)\right]\right.$$

$$+ \left(\frac{\kappa_{\rho_1}}{\kappa_{\rho_2}}\right)\left\{\left(\frac{\hat{\varepsilon}_2}{\hat{\varepsilon}_1}\right)\left[A_n(I^e_{n-1} - I^e_{n+1}) - B_n(f^e_{n-1} - f^e_{n+1})\right]\right.$$

$$\left. - \frac{\alpha\gamma}{\omega^2\mu_0\hat{\varepsilon}_1}\left[C_n(I^e_{n-1} + I^e_{n+1}) - D_n(f^e_{n-1} - f^e_{n+1})\right]\right\}\right\} \tag{A4}$$

$$< \hat{e}^{TM}_j \, , \, \hat{e}^{TM}_j > = \frac{\pi}{2}\left(\frac{1}{|\omega|\hat{\varepsilon}}\right)^2 |\nu|^2 \, \kappa_\rho^2 (p^m_{n+1} + p^m_{n-1}) \tag{A5}$$

$$< \hat{e}^{TE}_j \, , \, \hat{e}^{TE}_j > = \frac{\pi}{2} \, \kappa_\rho{}'^2 \, (p^e_{n+1} + p^e_{n-1}) \tag{A6}$$

$$< \hat{h}^{TM}_j \, , \, \hat{h}^{TM}_j > = \frac{\pi}{2} \, \kappa_\rho^2 (p^m_{n+1} + p^m_{n-1}) \tag{A7}$$

$$< \hat{h}^{TE}_j \, , \, \hat{h}^{TE}_j > = \frac{\pi}{2}\left(\frac{1}{|\omega|\mu_0}\right)^2 |\nu|^2 \, \kappa_\rho{}'^2 \, (p^e_{n+1} + p^e_{n-1}) \tag{A8}$$

(II) Rotationally symmetric modes ($n = 0$)

$$< \hat{E}_i \, , \, \hat{e}^{TM}_j > = 2\frac{\pi}{|\omega|^2\hat{\varepsilon}\varepsilon_1}(\gamma\nu^*)(\kappa_\rho\kappa_{\rho_1})\left[\tilde{I}^m_1 + \left(\frac{\kappa_{\rho_1}}{\kappa_{\rho_2}}\right)(A_0 I^m_1 - B_0 f^m_1)\right] \tag{A9}$$

$$< \hat{E}_i \, , \, \hat{e}^{TE}_j > = 2\frac{\pi}{j\omega\hat{\varepsilon}_1\mu_0}(\kappa_{\rho_1}\kappa_\rho{}')\left[\mu_1\tilde{I}^e_1 + \left(\mu_2\frac{\kappa_{\rho_1}}{\kappa_{\rho_2}}\right)(C_0 I^e_1 - D_0 f^e_1)\right] \tag{A10}$$

$$< \hat{H}_i \, , \, \hat{h}^{TM}_j > = 2\pi(\kappa_\rho\kappa_{\rho_1})\left[\tilde{I}^m_1 + \left(\frac{\kappa_{\rho_1}}{\kappa_{\rho_2}}\right)\left(\frac{\hat{\varepsilon}_2}{\hat{\varepsilon}_1}\right)(A_0 I^m_1 - B_0 f^m_1)\right] \tag{A11}$$

$$< \hat{H}_i , \hat{h}_j^{TE} > = (2\pi j)(\frac{1}{\omega^* \mu_0})(\gamma\nu^*)(\kappa_{\rho_1}\kappa_\rho{}') \left[\tilde{I}_1^e + (\frac{\kappa_{\rho_1}}{\kappa_{\rho_2}})(C_0 I_1^e - D_0 J_1^e) \right] \tag{A12}$$

$$< \hat{e}_j^{TM} , \hat{e}_j^{TM} > = 2\pi(\frac{1}{|\omega|\varepsilon})^2 |\nu|^2 \kappa_\rho^2 p_1^m \tag{A13}$$

$$< \hat{e}_j^{TE} , \hat{e}_j^{TE} > = 2\pi \kappa_\rho{}'^2 p_1^e \tag{A14}$$

$$< \hat{h}_j^{TM} , \hat{h}_j^{TM} > = 2\pi \kappa_\rho^2 p_1^m \tag{A15}$$

$$< \hat{h}_j^{TE} , \hat{h}_j^{TE} > = 2\pi (\frac{1}{|\omega|\mu_0})^2 |\nu|^2 \kappa_\rho{}'^2 p_1^e \tag{A16}$$

where

$$A_n = \frac{J_n(\kappa_{\rho_1} a) N_n(\kappa_{\rho_2} b)}{N_n(\kappa_{\rho_2} b) J_n(\kappa_{\rho_2} a) - J_n(\kappa_{\rho_2} b) N_n(\kappa_{\rho_2} a)} \tag{A17}$$

$$B_n = \frac{J_n(\kappa_{\rho_1} a) J_n(\kappa_{\rho_2} b)}{N_n(\kappa_{\rho_2} b) J_n(\kappa_{\rho_2} a) - J_n(\kappa_{\rho_2} b) N_n(\kappa_{\rho_2} a)} \tag{A18}$$

$$C_n = \frac{J_n(\kappa_{\rho_1} a) N_n'(\kappa_{\rho_2} b)}{N_n'(\kappa_{\rho_2} b) J_n(\kappa_{\rho_2} a) - J_n'(\kappa_{\rho_2} b) N_n(\kappa_{\rho_2} a)} \tag{A19}$$

$$D_n = \frac{J_n(\kappa_{\rho_1} a) J_n'(\kappa_{\rho_2} b)}{N_n'(\kappa_{\rho_2} b) J_n(\kappa_{\rho_2} a) - J_n'(\kappa_{\rho_2} b) N_n(\kappa_{\rho_2} a)} \tag{A20}$$

$$\tilde{I}_n^m = \int_0^a J_n(\kappa_{\rho_1}\rho) J_n(\kappa_\rho \rho)\, \rho\, d\rho \tag{A21}$$

$$I_n^m = \int_a^b J_n(\kappa_{\rho_2}\rho) J_n(\kappa_\rho \rho)\, \rho\, d\rho \tag{A22}$$

$$J_n^m = \int_a^b \int N_n(\kappa_{\rho_2}\rho) J_n(\kappa_\rho \rho)\, \rho\, d\rho \tag{A23}$$

$$p_n^m = \int_0^b J_n^2(\kappa_\rho \rho)\, \rho\, d\rho \tag{A24}$$

$$\tilde{I}_n^e = \int_0^a J_n(\kappa_{\rho_1}\rho)J_n(\kappa_\rho'\rho)\,\rho\,d\rho \tag{A25}$$

$$I_n^e = \int_a^b J_n(\kappa_{\rho_2}\rho)J_n(\kappa_\rho'\rho)\,\rho\,d\rho \tag{A26}$$

$$f_n^e = \int_a^b \int N_n(\kappa_{\rho_2}\rho)J_n(\kappa_\rho'\rho)\,\rho\,d\rho \tag{A27}$$

$$p_n^e = \int_0^b J_n^2(\kappa_\rho'\rho)\,\rho\,d\rho \tag{A28}$$

Note that $\kappa_\rho=\frac{x_{np}}{b}$ where x_{np} is the pth zero of $J_n(z)$ and $\kappa_\rho'=\frac{x'_{np}}{b}$ where x'_{np} is the pth zero of $J_n'(z)$.

APPENDIX B

IMPORTANT INTEGRALS USED IN THE ANALYTICAL FORMULATION OF A CYLINDRICAL CAVITY LOADED WITH LOSSY DIELECTRIC MATERIALS

In the analysis of a cylindrical cavity loaded with lossy dielectric materials, it is often necessary to evaluate integrals that involve Bessel functions with complex arguments. This Appendix lists the integrals that are frequently encountered in calculating cavity quality factor. Note that the following equations are valid for lossy materials, i.e. the argument of the Bessel function is complex. If the cavity is loaded with lossless materials, i.e. the argument of the Bessel function is either purely real or purely imaginary, the integrals can be found in [99]. The superscript "*" in the following equations represents complex conjugate.

$$\frac{1}{\kappa_{\rho_1}^*}\int_0^a J_n'(\kappa_{\rho_1}\rho)\frac{nJ_n(\kappa_{\rho_1}^*\rho)}{\rho}\,\rho\,d\rho + \frac{1}{\kappa_{\rho_1}}\int_0^a J_n'(\kappa_{\rho_1}^*\rho)\frac{nJ_n(\kappa_{\rho_1}\rho)}{\rho}\,\rho\,d\rho$$

$$= n\left|\frac{J_n(\kappa_{\rho_1}a)}{\kappa_{\rho_1}}\right|^2 \tag{B1}$$

$$\frac{1}{|\kappa_{\rho_1}|^2}\int_0^a \frac{nJ_n(\kappa_{\rho_1}\rho)}{\rho}\frac{nJ_n(\kappa_{\rho_1}^*\rho)}{\rho}\,\rho\,d\rho + \int_0^a J_n'(\kappa_{\rho_1}\rho)J_n'(\kappa_{\rho_1}^*\rho)\,\rho\,d\rho$$

$$= 4\,Real\left\{\frac{\kappa_{\rho_1}a}{\kappa_{\rho_1}^2-\kappa_{\rho_1}^{*2}}J_n(\kappa_{\rho_1}a)\,J_n'(\kappa_{\rho_1}^*a)\right\} \tag{B2}$$

$$\int_a^b R_n(\kappa_{\rho_2}\rho)R_n(\kappa_{\rho_2}^*\rho)\,\rho\,d\rho$$

$$= 2\,Real\left\{\frac{\kappa_{\rho_2}b}{\kappa_{\rho_2}^2-\kappa_{\rho_2}^{*2}}R_n(\kappa_{\rho_2}^*b)\left[\frac{n}{\kappa_{\rho_2}b}R_n(\kappa_{\rho_2}b)-R_n'(\kappa_{\rho_2}b)\right]\right.$$

$$- \frac{\kappa_{\rho_2} a}{\kappa_{\rho_2}^2 - \kappa_{\rho_2}^{*2}} R_n(\kappa_{\rho_2}^* a) \left[\frac{n}{\kappa_{\rho_2} a} R_n(\kappa_{\rho_2} a) - R_n'(\kappa_{\rho_2} a) \right] \Bigg\} \tag{B3}$$

$$\int_a^b R_n'(\kappa_{\rho_2}\rho) P_n(\kappa_{\rho_2}^*\rho)\, d\rho + \int_a^b \frac{\kappa_{\rho_2}^*}{\kappa_{\rho_2}} R_n(\kappa_{\rho_2}\rho) P_n'(\kappa_{\rho_2}^*\rho)\, d\rho$$

$$= \frac{1}{\kappa_{\rho_2}} \left[R_n(\kappa_{\rho_2} b) P_n(\kappa_{\rho_2}^* b) - R_n(\kappa_{\rho_2} a) P_n(\kappa_{\rho_2}^* a) \right] \tag{B4}$$

$$\int_a^b R_n'(\kappa_{\rho_2}\rho) R_n'(\kappa_{\rho_2}^*\rho)\, \rho\, d\rho + \frac{1}{|\kappa_{\rho_2}|^2} \int_a^b \frac{n R_n(\kappa_{\rho_2}\rho)}{\rho} \frac{n R_n(\kappa_{\rho_2}^*\rho)}{\rho}\, \rho\, d\rho$$

$$= 2\, Real \left\{ \frac{\kappa_{\rho_2} b}{\kappa_{\rho_2}^2 - \kappa_{\rho_2}^{*2}} R_n'(\kappa_{\rho_2}^* b) R_n(\kappa_{\rho_2} b) - \frac{\kappa_{\rho_2} a}{\kappa_{\rho_2}^2 - \kappa_{\rho_2}^{*2}} R_n(\kappa_{\rho_2} a) R_n'(\kappa_{\rho_2}^* a) \right\} \tag{B5}$$

where

$$R_n(\kappa_{\rho_2}\rho) = A_n J_n(\kappa_{\rho_2}\rho) + B_n N_n(\kappa_{\rho_2}\rho)$$

$$P_n(\kappa_{\rho_2}\rho) = C_n J_n(\kappa_{\rho_2}\rho) + D_n N_n(\kappa_{\rho_2}\rho)$$

Note that $J_n(z^*) = J_n^*(z)$ and $N_n(z^*) = N_n^*(z)$.

REFERENCES

1. Irving J. Chabinsky, "Applications of Microwave Energy, Past, Present and Future, 'Brave New Worlds'," Mat. Res. Soc. Symp. Proc., Vol. 124, 1988, pp. 17-29.

2. Hua-Feng Huang, "Temperature Control in a Microwave Resonant Cavity System for Rapid Heating of Nylon Monofilament," Journal of Microwave Power, 11(4), 1976, pp. 305-313.

3. J. K. Sinha and J. Brown, "A New Cavity-Resonator Method for Measuring Permittivity," IEE, Nov. 1960, pp. 522-530.

4. Jes Asmussen, Jr., Raghuveer Mallavarpu and John R. Hamann, "The Design of a Microwave Plasma Cavity,", Proc. IEEE, 62(1), January 1974, pp. 109-117.

5. D. T. Paris, "An Extension of the TE_{01n} Resonator Method of Making Measurements on Solid Dielectrics," IEEE Trans. on Microwave Theory and Tech., March 1964, pp. 251-252.

6. J. Hanfling and L. Botte, "Measurement of Dielectric Materials Using a Cutoff Circular-Waveguide Cavity," IEEE Trans. on Microwave Theory and Tech., March 197?, pp. 233-234.

7. G. Roussy and M. Felden, "A Sensitive Method for Measuring Complex Permittivity with a Microwave Resonator," IEEE Trans. on Microwave Theory and Tech., Vol. MTT-14, No. 4, April 1966, pp. 171-175.

8. Shihe Li, Cevdet Akyel and Renato G. Bosisio, "Precise Calculations and Measurements on the Complex Dielectric Constant of Lossy Materials Using TM_{010} Cavity Perturbation Techniques," IEEE Trans. on Microwave Theory and Tech., Vol. MTT-29, No. 10, October 1981, pp. 1041-1047.

9. C. B. Rosenberg, N. A. Hermiz and R. J. Cook, "Cavity Resonator Measurements of the Complex Permittivity of Low-Loss Liquids," IEE Proc., Vol. 129, Pt. H, No. 2, April 1982, pp. 71-76.

10. U. Farooq, "Sensitive Method of Measuring Dielectric Losses at Microwave Frequencies," IEE Proc., Vol. 134, Pt. H, No. 4, August 1987, pp. 397-399.

11. Ismail I. Eldumiati and George I. Haddad, "Cavity Perturbation Techniques for Measurement of the Microwave Conductivity and Dielectric Constant of a Bulk Semiconductor Material," IEEE Trans. on Microwave Theory and Tech., Vol. MTT-20, No. 2, Feb. 1972, pp. 126-132.

12. E. F. Labuda and R. C. LeCraw, "New Technique for Measurement of Microwave Dielectric Constants," Rev. of Sci. Instrum., Vol. 32, No. 4, April 1961, pp. 391-392.

13. Roger F. Harrington, *Time Harmonic Electromagnetic Fields*, McGraw-Hill Book Company, 1961, pp. 319-324.

14. Shuh-Han Chao, "Measurements of Microwave Conductivity and Dielectric Constant by the Cavity Perturbation Method and Their Errors," IEEE Trans. on Microwave Theory and Tech., Vol. MTT-33, No. 6, June 1985, pp. 519-526.

15. Roger F. Harrington, *Time Harmonic Electromagnetic Fields*, McGraw-Hill Book Company, 1961, pp. 323-324.

16. Werner Rueggeberg, "Determination of Complex Permittivity of Arbitrarily Dimensioned Dielectric Modules at Microwave Frequencies," IEEE Trans. on Microwave Theory and Tech., Vol. MTT-19, No. 6, June 1971, pp. 517-521.

17. Maria A. Rzepecka, "A Cavity Perturbation Method for Routine Permittivity Measurement," Journal of Microwave Power, 8(1), 1973, pp. 3-11.

18. Maria A. Rzepecka and M. A. K. Hamid, "Automatic Digital Method for Measuring the Permittivity of Thin Dielectric Films," IEEE Trans. on Microwave Theory and Tech., Vol. MTT-20, No. 1, Jan. 1972, pp. 30-37.

19. Cevdet Akyel, Renato G. Vosisio and Georges-Emile April, "An Active Frequency Technique for Precise Measurements on Dynamic Microwave Cavity Perturbations," IEEE Trans. on Instrum. and Measure., Vol. IM-27, Dec. 1978, pp. 364-368.

20. Cevdet Akyel and Renato G. Bosisio, "Wide-Range Dynamic Complex Dielectric Constant Measurements Using Micorprocessor Control Techniques," IEEE Trans. on Instrum. and Measure., Vol. IM-28, No. 4, 1979, pp. 272-278.

21. C. Akyel, R. C. Labelle and A.-J Berteaud, "Computer-Aided Permittivity Measurements of Moistened and Pyrolized Materials in Strong RF Fields (Part 1)," IEEE Trans. on Instrum. and Meas., Vol. IM-34, No. 1, March 1985, pp. 25-31.

22. Hans-Juergen C. Blume, "Measurement of Dielectric Properties and Determination of Microwave Emissivity of Polluted Waters," IEEE Trans. on Instrum. and Meas., Vol. IM-29, No. 4, Dec. 1980, pp. 289-291.

23. H. A. Buckmaster, T.H.T. Van Kalleveen, H. Zaghloul and C.H. Hansen, "9-GHz Complex Permittivity Measurements of High-Loss Liauids Using a Variable-Length Reflection Cavity and a Dual-Channel, Double Superheterodyne Signal Processing System," IEEE Trans. on Microwave Theory and Tech., Vol. MTT-35, No. 10, Oct. 1987, pp. 909-916.

24. C. Akyel, R. G. Bosisio, R. Chahine and T. K. Bose, "Measurement of the Complex Permittivity of Food Products during Microwave Power Heating Cycles," Journal of Microwave Power, 18(4), 1983, pp. 355-365.

25. M. Martinelli, P. A. Rolla and E. Tombari, "A Method for Dynamic Dielectric Measurements at Microwave Frequencies: Applications to Polymerization Process Studies," IEEE Trans. on Instrum. and Meas., Vol. IM-34, No. 3, Sept. 1985, pp. 417-421.

26. M. Martinelli, P.A. Rolla, and E. Tombari, "A Method for Dielectric Loss Measurements by a Microwave Cavity in Fixed Resonance Condition," IEEE Trans. on Micorwave Theory and Tech., Vol. MTT-33, No. 9, Sept. 1985, pp. 779-783.

27. T. W. Gault and J. B. Wilson, "Radio Frequency Redrying of Veneer - A Case Study," J. Microwave Power E^2, 1987, p. 179.

28. Ralph W. Bruce, "New Frontiers in the Use of Microwave Energy: Power and Metrology," Mat. Res. Soc. Symp. Proc., Vol. 124, 1988, pp. 3-15.

29. Jean-Marie Thiebaut, C. Akyel and G. Roussy, "Dehydration and Dielectric Permittivity Measurements of a Porous, Inorganic Material (13X Zeolite) Heated with Microwave Power," IEEE Trans. on Instrum. and Meas., Vol. 37, No. 1, March 1988, pp. 114-120.

30. G. Lightsey, C. George, A. Wehr, and G. Bharat, "Evaluation of Microwave and Radio-Frequency Drying in the Acid Hydrolysis of Biomass," J. of Microwave Power and Electromagnic Energy, Vol. 23, No. 1, 1988, pp. 11-15.

31. G. R. Lightsey, C. George and L. D. Russell, "Low Temperature Processing of Plastics Utilizing Microwave Heating Techniques," J. of Micorwave Power, 1986, pp. 86-87.

32. Murray D. Sirkis and Grant W. Conrad, "Heating of Low-Resistivity Semiconductor Ribbons and Wafers with Traveling Microwaves," J. of Microwave Power, 1986, pp. 199-207.

33. M. Sirkis and C. Hou, "A Traveling-Wave Resonator for Heating Low- Resistivity Semiconductor Ribbons and Wafers," 23rd Microwave Power System, 1988, pp. 48-49.

34. Stuart O. Nelson, "RF and Microwave Energy for Potential Agricultural Applications," J. Microwave Power 1985, 1985, pp. 65-69.

35. J. P. Vetsuypens and W. Van Loock, "Microwave Treatment of Grains," J. Microwave Power 1986, 1986, p. 110.

36. C. Gibson, I. Matthews, and A. Samuel, "Microwave Enhanced Diffusion in Polymeric Materials," J. of Microwave Power and Electromagnic Energy, Vol. 23, No. 1, 1988, pp. 17-28.

37. Norman S. Strand, "Fast Microwave Curing of Thermoset Parts," Modern Plastics, Oct. 1980, pp. 64-67.

38. W. Van Loock, "Electromagnetic Energy for Drying Rubber Foam," J. Microwave Power E^2 1987, 1987, p. 178.

39. Wayne R. Tinga, "Fundamentals of Microwave-Material Interactions and Sintering," Mat. Res. Soc. Symp. Proc., Vol. 124, 1988, pp. 33-43.

40. H. Fukushima, T. Yamanaka and M. Matsui, "Microwave Heating of Ceramics and Its Application to Joining," Mat. Res. Soc. Symp. Proc., Vol. 124, 1988, pp. 267-272.

41. David Palaith, Richard Silberglitt, Carl C. M. Wu, Richard Kleiner and E. L. Libelo, "Microwave Joining of Ceramics," Mat. Res. Soc. Symp. Proc., Vol. 124, 1988, pp. 255-266.

42. T. T. Meek, M. H. Brooks, R. D. Blake, J. J. Petrovic, H. Jory and J. V. Milewski, "Microwave Processing, of Ceramics,", J. Microwave Power 1986, 1986, pp. 193-194.

43. S. S. Park, "Thermal Shock Properties of Zirconia-Alumina Composites heated using 2.45 GHz Microwave Radiation," Mat. Res. Soc. Symp. Proc., Vol. 124, 1988, p. 242.

44. R. B. James, "Microwave-Induced Surface Melting of Carbon Composites and Graphite," Mat. Res. Soc. Symp. Proc., Vol. 124, 1988, p. 243.

45. S. Whitehair and J. Asmussen, "Demonstration of a new electrothermal thruster Concept," Appl. Phys. Lett., 44(10), 15 May 1984, pp. 1014- 1016.

46. J. Asmussen, S. Whitehair, M. Hawley and M. Wolak, "Microwave Discharges for Spacecraft Propulsion," 23rd Microwave Power Symp., 1988, pp. 38-39.

47. Stanley J. Whitehair, "Experimental Development of a Microwave Electrothermal Thruster," Ph.D. Dissertation, Michigan State University, 1986.

48. Joseph Root and Jes Asmussen, "Experimental Performance of a Microwave Cavity Plasma Disk Ion Source," Rev. Sci. Instrum., 56(8), August 1985, pp. 1511-1519.

49. I. Hussla, K. Enke, H. Grunwald, G. Lorenz and H. Stoll, "In Situ Silicon-Wafer Temperature Measurements During RF Argon-Ion Plasma Etching via Fluoroptic Thermometry," J. Microwave Power, 1987, pp. 889-896.

50. J. Hopwood, M. Dahimene, D. K. Reinhard and J. Asmussen, "Plasma Etching with a Microwave Cavity Plasma Disk Source," J. Vac. Sci. Technol. B, Vol. 6, No. 1, Jan/Feb 1988, pp. 268-271.

51. J. Hopwood, D. K. Reinhard and J. Asmussen, "Experimental Conditions for Uniform Anisotropic Etching of Silicon with a Microwave Electron Cyclotron Resonance Plasma System," J. Vac. Sci. Technol. B, Vol. 6, No. 6, Nov/Dec 1988, pp. 1896-1899.

52. G. Salbert, J. Hopwood, J. Asmussen and D. Reinhard, "Microwave Plasma Oxidation and Etching for Integrated Circuit Processing," 23rd Microwave Power Symp., 1988, pp. 32-33.

53. T. Roppel, D. K. Reinhard and J. Asmussen, "Low Temperature Oxidation of Silicon Using a Microwave Plasma Disk Source," J. Vac. Sci. Technol. B4, 1986, pp. 295-298.

54. M. Kamo, Y. Sato, S. Matsumoto and N. Setaka, "Diamond Synthesis from Gas Phase in Microwave Plasma," J. of Crystal Growth, 62, 1983, pp. 642-644.

55. M. Sokolowski, A. Sokolowska, B. Gokieli, A. Michalski, A. Rusek and Z. Romanowski, "Reactive Pulse Plasma Crystallization of Diamond and Diamond-Like Carbon," J. of Crystal Growth, 47, 1979, pp. 421-426.

56. Y. Kobayashi, K. Kojima, and S. Yoshida, "Shielded TM_{010} Dielectric Rod Resonator," Electronics and Communications in Japan, Vol. 64-B, No. 2, 1981, pp. 65-71.

57. Kawthar A. Zaki and C. Chen, "Loss Mechanisms in Dielectric-Loaded Resonators," IEEE Trans. on Microwave Theory and Tech., Vol. MTT-33, Dec. 1985, pp. 1448-1452.

58. T. Sphicopoulos, L.-G. Bernier and F. Gardiol, "Theoretical Basis for the Design of the Radially Stratified Dielectric-Loaded Cavities Used in Miniaturised Atomic Frequency Standards," IEE Proc., Vol. 131, No. 2, April 1984, pp. 94-98.

59. D. M. Bolle, "Eigenvalues for a Centrally Loaded Circular Cylindrical Cavity," IRE Trans. on Microwave Theory and Tech., March 1962, pp. 133-138.

60. Y. Kobayashi, N. Fukuoka and S.-I. Yoshida, "Resonant Modes for a Shielded Dielectric Rod Resonator," Electronics and Communications in Japan, Vol. 64-B, No. 11, 1981, pp. 44-51.

61. K. A. Zaki and C. Chen, "New Results in Dielectric-Loaded Resonators," IEEE Trans. on Microwave Theory and Tech., Vol. MTT-34, No. 7, July 1986, pp. 815-824.

62. K. A. Zaki and A. Atia, "Modes in Dielectric-Loaded Waveguides and Resonators," IEEE Trans. on Microwave Theory and Tech., Vol. MTT-31, No. 12, Dec. 1983, pp. 1039-1044.

63. Edward J. Rothwell and Lydell L. Frasch, "Propagation Characteristics of Dielectric-Rod-Loaded Waveguides," IEEE Trans. on Microwave Theory and Tech., Vol. 36, No. 3, March 1988, pp. 594-600.

64. M. S. Leong, P. S. Kooi and T. S. Yeo, "Tunable Double-Ended Dielectric-Loaded Microwave Resonator for Frequency-Stabilisation Applications," IEE Proc., Vol. 128, Pt. H, No. 4, August 1981, pp. 213-217.

65. J. B. Clarricoats and B. C. Taylor, "Evanescent and Propagating Modes of Dielectric-Loaded Circular Waveguide," IEE Proc., Vol. 111, No. 12, Dec. 1964, pp. 1951-1956.

66. A. S. Omar and K. F. Schunemann, "Complex and Backward-Wave Modes in Inhomogeneously and Anisotropically Filled Waveguides," IEEE Trans. on Microwave Theory and Tech., Vol. MTT-35, No. 3, March 1987, pp. 268-275.

67. C. Chen and K. A. Zaki, "Resonant Frequencies of Dielectric Resonators Containing Guided Complex Modes," IEEE Trans. on Microwave Theory and Tech., Vol. 36, No. 10, Oct. 1988, pp. 1455-1457.

68. Rene R. Bonetti and Alie Atia, "Design of Cylindrical Dielectric Resonators in Inhomogeneous Media," IEEE Trans. on Microwave Theory and Tech., Vol. MTT-29, No. 4, April 1981, pp. 323-326.

69. U. S. Hong and R. H. Jansen, "Numerical Analysis of Shielded Dielectric Resonators Including Substrate, Support Disc and Tuning Post," Electron. Lett., Vol. 18, Nov. 1982, pp. 1000-1002.

70. S. Vigneron and P. Guillon, "Mode Matching Method for Determination of the Resonant Frequency of a Dielectric Resonator Placed in a Metallic Box," IEE Proc., Vol. 134, Pt. H, No. 2, April 1987, pp. 151-155.

71. J. Stoer and R. Bulirsch, *Introduction to Numerical Analysis*, pp. 507-515.

72. Andrzej Kedzior and Jerzy Krupka, "Application of the Galerkin Method for Determination of Quasi TE_{i0k} Mode Frequencies of a Rectangular Cavity Containing a Dielectric Sample," IEEE Trans. on Microwave Theory and Tech., Vol. MTT-30, No. 2, Feb. 1982, pp. 196-198.

73. Jerzy Krupka, "Optimization of an Electrodynamic Basis for Determination of the Resonant Frequencies of Microwave Cavities Partially Filled with a Dielectric," IEEE Trans. on

Microwave Theory and Tech., Vol. MTT-31, No. 3, March 1983, pp. 302-305.

74. Jerzy Krupka, "Computations of Frequencies and Intrinsic Q Factors of TE_{0nm} Modes of Dielectric Resonators," IEEE Trans. on Microwave Theory and Tech., Vol. MTT-33, No. 3, March 1985, pp. 274-277.

75. Jerzy Krupka, "Properties of Shielded Cylindrical Quasi-TE_{0nm}-Mode Dielectric Resonators," IEEE Trans. on Microwave Theory and Tech., Vol. 36, No. 4, April 1988, pp. 774-779.

76. Allen W. Glisson, Darko Kajfez and Joseph James, "Evaluation of Modes in Dielectric Resonators Using a Surface Integral Equation Formulation," IEEE Trans. on Microwave Theory and Tech., Vol. MTT-31, No. 12, Dec. 1983, pp. 1023-1029.

77. Roger F. Harrington, *Time-Harmonic Electromagnetic Fields*, McGraw-Hill Book Company, 1961, Chapter 8, pp. 434-436.

78. P. S. Kooi, M. S. Leong, and A. L. Satya Prakash, "Finite-Element Analysis of the Shielded Cylindrical Dielectric Resonator," IEE Proc., Vol. 132, Pt. H, No. 1, Feb. 1985, pp. 7-16.

79. El-Deek M. El-Sayed and Samir S. Farghaly, "Influence of Load Location in Mode Tuning of Microwave Oven," J. of Microwave Power, 18(2), 1983, pp. 197-207.

80. Roger F. Harrington, *Time Harmonic Electromagnetic Fields*, McGraw-Hill Book Company, 1961, Chapter 5, pp. 213-215.

81. M. Tsuji, H. Shigesawa and K. Takiyama, "Analytical and Experimental Investigations on Several Resonant Modes in Open Dielectric Resonators," IEEE Trans. on Microwave Theory and Tech., Vol. MTT-32, 1984, pp. 628-632.

82. William M. Bruno and William B. Bridges, "Flexible Dielectric Waveguides with Powder Cores," IEEE Trans. on Microwave Theory and Tech., Vol. 36, No. 5, May 1988, pp. 882-890.

83. Ri-Chee Chou and Shung-Wu Lee, "Modal Attenuation in Multilayered Coated Waveguides," IEEE Trans. on Microwave Theory and Tech., Vol. 36, No. 7 July 1988, pp. 1167-1176.

84. Maria A. Rzepecka, S. S. Stuchly and M. A. K. Hamid, "Modified Infinite Sample Method for Routine Permittivity Measurements at Microwave Frequencies," IEEE Trans. on Instrum. and Meas., March 1973, pp. 41-46.

85. Robert E. Collin, "Field Theory of Guided Waves," Chapter 5, p. 187.

86. S. D. Conte and Carl de Boor, "Elementary Numerical Analysis, Second Edition."

87. Roger F. Harrington, *Time-Harmonic Electromagnetic Fields*, McGraw-Hill Bood Company, 1961, Chapter 5.

88. Raghuveer Mallavarpu, "An Investigation of the Electromagnetic Behavior of a Microwave Plasma Source over a Wide Range of Pressures and Flow Rates," Ph.D. Dissertation, Michigan State University, 1976.

89. Roger F. Harrington, *Time-Harmonic Electromagnetic Fields*, McGraw-Hill Bood Company, 1961, Chapter 7.

90. A. W. Trivelpiece, *Slow -Wave Proagation in Plasma Waveguide*, San Francisco Press, Inc., 1967.

91. Lydell Lemoine Frasch, "An Experimental and Theoretical Study of a Microwave Cavity Applicator Loaded with Lossy Materials," Ph.D. Dissertation, Michigan State University, 1987.

92. Simon Ramo, John R. Whinnery and Theodore Van Duzer, *Fields and Waves in Communication Electronics.*

93. K. Kurokawa, *An Introduction to the Theory of Microwave Circuits*, Academic Press, 1969.

94. James R. Rogers, "Properties of Steady State, High Pressure, Argon Microwave Discharges," Ph.D. Dissertation, Michigan State University, 1982.

95. J. Jow, M. Hawley, M. Finzel, J. Asmussen, H.H. Lin and B. Manring, "Microwave Processing and Diagnosis of Chemically Reacting Materials in a Single-Mode Cavity Applicator," IEEE Trans. on Microwave Theory and Tech., Vol. MTT-35, No. 12, Dec. 1987, pp. 1435-1443.

96. J. Asmussen, H. H. Lin, B. Manring and R. Fritz, "Single-Mode or Controlled Multimode Microwave Cavity Applicators for Precision Materials Processing," Rev. Sci. Instrum., 58(8), August 1987, pp. 1477-1486.

97. Edward Benjamin Manring, "An Experimental Investigation of the Microwave Heating of Solid Non-Reactive Materials in a Circular Cylindrical Resonant Cavity," Master Thesis, Michigan State University, 1988.

98. A. R. Von Hippel, *Dielectric Materials and Applications*, MIT, Cambridge, MA, 1954, p.361.

99. Darko Kajfez, "Indefinite Integrals Useful in the Analysis of Cylindrical Dielectric Resonators," IEEE Trans. on Microwave Theory and Tech., Vol. MTT-35, No. 9, Sep. 1987, pp. 873-874.

MICHIGAN STATE UNIV. LIBRARIES
31293005857200